Development of temporal phase unwrapping algorithms for depth-resolved measurements using an electronically tuned *Ti:Sa* laser

by

Christos Antoniou Pallikarakis

A Doctoral Thesis

Submitted in partial fulfilment of the requirements

for the award of

Doctor of Philosophy of Loughborough University

January, 2017

Page left intentionally blank

Abstract

This thesis is concerned with (a) the development of full-field, multi-axis and phase contrast wavelength scanning interferometer, using an electronically tuned CW Ti:Sa laser for the study of depth resolved measurements in composite materials such as GFRPs and (b) the development of temporal phase unwrapping algorithms for depth re-solved measurements. Item (a) was part of the ultimate goal of successfully extracting the 3-D, depth-resolved, constituent parameters (Young's modulus *E*, Poisson's ratio *v* etc.) that define the mechanical behaviour of composite materials like GFRPs. Considering the success of OCT as an imaging modality, a wavelength scanning interferometer (WSI) capable of imaging the intensity **AND** the phase of the interference signal was proposed as the preferred technique to provide the volumetric displacement/strain fields (Note that displacement/strain fields are analogous to phase fields and thus a phase-contrast interferometer is of particular interest in this case). These would then be passed to the VFM and yield the sought parameters provided the loading scheme is known. As a result, a number of key opto-mechanical hardware was developed. First, a multiple channel (x6) tomographic interferometer realised in a Mach-Zehnder arrangement was built. Each of the three channels would provide the necessary information to extract the three orthogonal displacement/strain components while the other three are complementary and were included in the design in order to maximize the penetration depth (sample illuminated from both sides). Second, a miniature uniaxial (tensile and/or compression) loading machine was designed and built for the introduction of controlled and low magnitude displacements. Last, a rotation stage for the experimental determination of the sensitivity vectors and the re-registration of the volumetric data from the six channels was also designed and built. Unfortunately, due to the critical failure of the Ti:Sa laser data collection using the last two items was not possible. However, preliminary results at a single wavelength suggested that the above items work as expected. Item (b) involved the development of an optical sensor for the dynamic monitoring of wavenumber changes during a full 100 nm scan. The sensor is comprised of a set of four wedges in a Fizeau interferometer setup that became part of the multi-axis interferometer (7^{th} channel). Its development became relevant due to the large amount of mode-hops present during a full scan of the Ti:Sa source. These are associated to the physics of the laser and have the undesirable effect of randomising the signal and thus preventing successful depth reconstructions. The multi-wedge sensor was designed so that it provides simultaneously high wavenumber change resolution and immunity to the large wavenumber jumps from the Ti:Sa. The analysis algorithms for the extraction of the sought

wavenumber changes were based on 2-D Fourier transform method followed by temporal phase unwrapping. At first, the performance of the sensor was tested against that of a high-end commercial wavemeter for a limited scan of 1nm. A root mean square (rms) difference in measured wavenumber shift between the two of ~4 m^{-1} has been achieved, equivalent to an rms wavelength shift error of ~0.4 pm. Second, by resampling the interference signal and the wavenumber-change axis onto a uniformly sampled *k*-space, depth resolutions that are close to the theoretical limits were achieved for scans of up to 37 nm. Access of the full 100 nm range that is characterised by wavelength steps down to picometers level was achieved by introducing a number of improvements to the original temporal phase unwrapping algorithm reported in ref [1] tailored to depth resolved measurements. These involved the estimation and suppression of intensity background artefacts, improvements on the 2-D Fourier transform phase detection based on a previously developed algorithm in ref [2] and finally the introduction of two modifications to the original TPU. Both approaches are adaptive and involve signal re-referencing at regular intervals throughout the scan. Their purpose is to compensate for systematic and non-systematic errors owing to a small error in the value of *R* (a scaling factor applied to the lower sensitivity wedge phase-change signal used to unwrap the higher sensitivity one), or small changes in *R* with wavelength due to the possibility of a mismatch in the refractive dispersion curves of the wedges and/or a mismatch in the wedge angles. A hybrid approach combining both methods was proposed and used to analyse the data from each of the four wedges. It was found to give the most robust results of all the techniques considered, with a clear Fourier peak at the expected frequency, with significantly reduced spectral artefacts and identical depth resolutions for all four wedges of 2.2 μm measured at FWHM. The ability of the phase unwrapping strategy in resolving the aforementioned issues was demonstrated by successfully measuring the absolute thickness of four fused silica glasses using real experimental data. The results were compared with independent micrometer measurements and showed excellent agreement. Finally, due to the lack of additional experimental data and in an attempt to justify the validity of the proposed temporal phase unwrapping strategy termed as the 'hybrid' approach, a set of simulations that closely matched the parameters characterising the real experimental data set analysed were produced and were subsequently analysed. The results of this final test justify that the various fixes included in the 'hybrid' approach have not evolved to solve the problems of a particular data set but are rather of general nature thereby, highlighting its importance for PC-WSI applications concerning the processing and analysis of large scans.

Acknowledgements

I would like to thank Dr. A. Davila-Alvarez (RA) who, during a sabbatical-leave from the *Centro de Investigaciones en Optica, Loma del bosque 115, Leon Gto 37150 Mexico* (2008-2011) has assisted with the development of the tomographic interferometer. His role has been a key aspect in laying the foundations for the development of the multi-axis tomographic interferometer featured in this work. More specifically, I am thankful for his training in operating and aligning the complex system as well as for his assistance in understanding the software developed before my joining the group.

I would also like to thank Dr. Petros Karapapas of *CYTEC Engineered Materials Ltd*, UK for donating the GFRP samples and the Wolfson School mechanical and electronic workshop for the excellent job in manufacturing the necessary mechanical and electronic hardware required.

Special thanks go to the Wolfson school of Mechanical and Manufacturing Engineering, for the scholarship awarded to perform the enclosed work and the Engineering and Physical Sciences Research Council (EPSRC) for the initial contract (EP/F02861X/1).

Moreover, I would also like to acknowledge Dr. Russel Coggrave CTO and co-founder of *Phasevision Ltd* for his useful advice and inspiration during the four years I spent working part-time in the company.

In addition to the above, I wish to acknowledge my brother, Mr. I. Pallikarakis for his help and unique understanding of computer architecture that were key to building the machine (PC) that was ultimately used for the processing of the data enclosed in this work.

Last but not least, I would like to acknowledge my supervisors Prof. Jonathan Huntley and Dr. Pablo Ruiz for the fruitful conversations, unique academic insight and their continued support and friendship at times it was most needed.

Finally, I would like to thank my family in supporting me to pursue this challenge. None of this would have been possible without their support.

Nomenclature

Abbreviations

ADC	Analog-to-digital converter
ADI	Absolute distance interferometry
ADM	Absolute distance metrology, measurements
AS	Aperture stop
ASE	Amplified spontaneous emission
BBS	Broadband source
BRF	Birefringent filter
BS	Beam splitter
CCD	Charged coupled device
CFRP	Carbon fibre reinforced polymer
CIO	Centre of Investigations in Optics – a laboratory based in Mexico equivalent to the National Physical Laboratory (NPL) in the UK.
CL	Collimating lens
CMOS	Complementary metal-oxide semiconductor
CMM	Coordinate measurement machine
CW	Continuous wavelength
DIC	Digital image correlation (2-D)
DOT	Diffuse optical tomography
DSA	Digital signal amplifier
DSP	Digital signal processor
DSPI	Digital speckle pattern interferometry
DVC	Digital volume correlation (3-D version of DIC)
ESPI	Electronic speckle pattern interferometry
FFT	Fast Fourier transform
FD-LCI	Fourier domain low coherence interferometry
FD-OCT	Fourier domain optical coherence tomography
FL	Focusing lens
FOV	Field of view
FP	Fabry-Perot

fps	Frames per second
FSI	Frequency scanning interferometry
FSR	Free spectral range
FWHM	Full width half maximum
GFRP	Glass fibre reinforced polymer
GPU	Graphics processing unit
HDD	Hard dick drive
HI	Holographic interferometry
IOP	Institute of physics
IR	Infrared
LASCA	Laser speckle contrast analysis
LB	Laser beam
LED	Light emitting diode
LSF	Least-squares fit
MFD	Micro-fluidic device
MI	Moiré interferometry
MM	Magneto motive
MNP	Magnetic nanoparticle
MO	Microscope objective
MRI	Magnetic resonance imaging
MRE	Magnetic resonance elastography
MWI	Multiple wavelength interferometry
NA	Numerical aperture
ND	Neutron diffraction
NDT	Non-destructive testing
NINT	Non-integer value
NIR	Near infrared region
NPL	National Physical Laboratory
OCE	Optical coherence elastography
OCT	Optical coherence tomography
ODT	Optical diffraction tomography
OPD	Optical path difference
OPL	Optical path length
PBS	Pelical beam splitter

PC-OCT	Phase-contrast optical coherence tomography
PM	Parabolic mirror
PMC	Polymer matrix composite
ppm	Parts per million
PSI	Phase shifting interferometry
PSF	Point spread function
PS-OCT	Polarization sensitive optical coherence tomography.
PZT	Acronym for Lead Zirconate Titanate that is an intermetallic inorganic compound whose chemical formula is: Pb $[Zr_xTi_{1-x}]$ O_3 and where: $0 \leq x \leq 1$. It is a ceramic perovskite that shows a marked piezoelectric effect. In other words, it has the ability to change its shape when an electric field is applied to it. Its practical applications include ultrasonic transducers and piezoelectric resonators.
QE	Quantization error
RA	Research associate: *Dr A. A. Davila*
RAM	Random access memory
RM	Reference mirror
RMSE	Root mean square error
ROI	Region of interest
SAW	Surface acoustic wave
SLD	Super-luminescent laser diode
SLM	Spatial light modulator
SOCT	Spectral optical coherence tomography
SS	Swept source
SSI	Supersonic shear imaging
SS-OCT	Swept source optical coherence tomography
STFT	Short-time Fourier transform
SWI	Scanning white light interferometer
TD-LCI	Time domain low coherence interferometry
TD-OCT	Time-domain optical coherence tomography
TFA	Time-frequency analysis
TPU	Temporal phase unwrapping

Ti:Sa	Titanium Sapphire laser
TS	Test sample
TTL	Transistor-transistor logic
UV	Ultraviolet
VFM	Virtual fields method
WG	Wedge
WP	Work package
WS	Wavelength/wavenumber sensor
WS7	High Finesse model Ångstrom of the commercial high-end wavelength meter used to test the performance of the custom made, low cost wavelength sensor (WS) under development in this work.
WSI	Wavelength scanning interferometry
X-Ray μ-CT	X-ray micro-computed tomography

List of symbols

Latin characters

A_o	Amplitude of object wave
A_r	Amplitude of reference wave
`cumsum`	MATLAB function used to calculate the cumulative sum of a series of phase change values
c	Speed of light in vacuum
C	Compliance of test rig.
c_τ	Threshold value used to indicate the point at which a re-referencing event takes place in units of pixels.
D	Optical path difference
d_j	Wedge central thickness, where j indicates the wedge number.
E	Young's modulus
E_1, E_2	Phase unwrapping errors
f	Frequency in Hz
$\hat{f}$	Frequency proportional to the OPD (D) expressed in cycles per scan duration

f_D	Frequency proportional to the OPD (D) expressed in cycles per frame
f_k	Spatial frequency along the k-axis
`fft`	MATLAB function used to perform the Fast Fourier transform
`fftshift`	MATLAB function used to perform the swapping of the four image quadrants
$I(t)$	Intensity of interference signal
$I(k)$	Intensity distribution of a single camera pixel along the wavenumber (k) axis
$\bar{I}$	Mean (averaged) intensity.
I_o	Background intensity
I_b	Estimated free-of-background intensity signal
I_1	Fringe modulation intensity
I_M	Modulation intensity
$\tilde{I}(\hat{f})$	Fourier transform of the intensity $I(t)$
$\tilde{I}^*$	Wavelet transform
$\lvert\tilde{I}\rvert$	Normalised intensity spectrum.
$\lvert\tilde{I}\rvert^2$	Intensity power spectrum
`interp1`	MATLAB function used to perform the linear interpolation of the intensity values onto a uniformly-spaced k-vector
J	Sorting vector used for the sorting of intensity data in ascending order.
k	Wavenumber ($2\pi/\lambda$)
$\check{k}$	Continuous version of the discrete variable k
k_i,k_f	Initial and final wavenumber
k_r	Scalar indicating the magnitude of 2-D Fourier peak radial position.
k_x,k_y	Spatial coordinates in the Fourier-domain that indicate the location of the 2-D Fourier peak along the x and y directions that also correspond to the number of fringes along the x and y image

	coordinates.
L	Distance to be measured
l_c	Coherence length of laser source.
m,n	Spatial indices indicating the number of pixels on CCD sensor (row, column
n	Refractive index of propagation medium
$\bar{n}$	Nominal value of glass wedge refractive index.
$\tilde{n}_{i,j}$	Estimated change in the refractive index of synthetic wedges where (i, j) = (1, 2), (2, 3), (3, 4), (1, 5) during a wavelength scan.
$\tilde{n}_i(t, 0)$	Estimated change in the refractive index of glass wedge (i = 1, 2, 3, 4) during a wavelength scan.
N_f	Number of fringes
N_w	Length of data included in the window function when performing the STFT.
N_p	Number of data points after zero-padding.
N_x, N_y	Number of pixels along the x and y axis of the CCD respectively
N_s	Number of unwrapping steps.
`NaN`	MATLAB entry indicating the presence of unwrapping error in the phase-change data sequence.
N_k	Number of sample independent slices in a depth resolved scan
$\pm P$	+ve and -ve Fourier transform orders that are symmetrical to each other with respect to the d.c.
R	Wedge thickness ratio.
r	Number of resonances
`round`	MATLAB function used for the rounding operator NINT
$S(R_m)$	Cost function used for the optimization of wedge thickness ratio R_m where m indicates the unwrapping step.
SiO_2	Fused silica
Si-OH	Silanol group

$sign(\Delta v)$	Sign of frequency sweep (+1 for increasing and -1 for decreasing frequency)
`spectrogram`	MATLAB function used to perform the short-time Fourier-transform analysis.
t	Non-dimensional time index
t'	Non-dimensional time index corresponding to the camera frame number.
$\mathcal{U}$	Unwrapping operator.
v	Poisson ratio
V_{CH}	Velocity of cross-head in miniature tensile machine.
$\mathcal{W}$	Wrapping operator.
W	Window function
W_n	Window number in STFT.
$\widetilde{W}$	Fourier transform of the window function
x,y	Spatial coordinates of the scattering point measured in a plane perpendicular to the viewing direction (z)

Greek characters

α	Angle along the wedge direction.
γ	Constant associated with the shape of the window function W.
δ	Dirac delta function
δz	Depth resolution
$\delta\lambda$	Wavelength step between two successive frames.
δk	Inter-frame change in wavenumber, wavenumber step
δn	Assumed deviation from the nominal value $\overline{n}$.
$\delta\Lambda$	Optical path difference resolution
$\delta\psi$	Change in phase y between two adjacent wavelengths during a scan.
Δz	Maximum optical path difference between the i^{th} slice within the object and the reference surface (Depth range).

Δn	Refractive index homogeneity
Δk	Total change in wavenumber over a full scan
Δk_r	Total change in the 2-D Fourier peak radial position between the first and last frame recorded during a wavelength scan.
$\Delta\lambda$	Wavelength bandwidth/range
Δv	Frequency range or sweep range
$\Delta\Phi^{i,j}$	Difference in phase between a pair of wedges *i, j* over two successive frames $t' - 1$ and t'that lies in the -2π to +2π range.
$\Delta\Phi_u^{i,j}$	Unwrapped phase change $\Delta\Phi^{i,j}$.
$\Delta\Phi_w^{i,j}$	Wrapped phase change $\Delta\Phi^{i,j}$ onto the principle -π to π range.
$\Delta\Psi$	Total change in phase ψ over a full wavelength scan.
ε	Camera exposure time.
ε_ϕ	Error (rms) in phase.
ε_R	Error in true wedge-thickness ratio *R*.
ε_{rms}	Root mean square error
θ	Angle of refraction with respect to the normal of the front surface of the wedge sensor.
κ	Number of re-referencing events.
λ	Wavelength
λ_c	Centre wavelength of a broadband source
Λ_s	Synthetic wavelength
Λ_o	Optical path difference between the interfering beams.
Λ_M	Maximum unambiguous depth range/optical path difference.
σ_ϕ	Standard deviation of phase noise.
υ	Fringe contrast
ϕ_u	Unwrapped phase
ϕ_w	Wrapped phase

ψ	Phase due to the interference between the front and back surface of the glass wedge.
ω	Non-dimensional frequency representing the rate of change in phase as a function of time.
$*$	Operator used to denote convolution

IMPORTANT NOTES:

Nomenclature: Due to the length of the document and the large number of parameters the reader is advised to consult the individual chapters for definitions of symbols that may appear as duplicates.

Figures: In this work a large number of figures have been included for the purpose of illustration and to aid understanding. The term "reproduced", when used, refers to figures that have been produced by the author from scratch. For the case of diagrams and or schematics, this means that they have been re-drawn, while for the case of plots and graphs this means that the figures have been produced by re-running the appropriate software. In any case, the source is always provided. In places where a reference has not been provided or the term 'reproduced' is not used, means that there have been a significant number of changes introduced to the software required to produce the plots and or graphs. This is particularly true for chapter-5. When a figure has been published elsewhere (journal and or conference paper or other source) this is always referenced. In the aforementioned case the author has checked with the publisher that there are no issues concerning the inclusion of such figures in a PhD thesis.

Table of contents

Page left intentionally blank

Chapter-1: Introduction and research overview

1.1 Introduction

The use of composite materials spans across a large and diverse field of applications. Their performance often becomes a critical factor for the integrity of the structure of which they are part of. Unfortunately, their superior properties are accompanied by complex behaviour. As a result, their functional behaviour is difficult and in some cases impossible to understand and predict. As a result, a number of techniques to assess their mechanical behaviour have been developed. These include destructive and non-destructive approaches. The latter are of particular interest for the obvious reason that they do not involve the destruction of the object under consideration.

Interferometry is one of the aforementioned techniques which provide dense and quick data in a non-destructive manner. Digital speckle pattern interferometry (DSPI) and its predecessor electronic speckle pattern interferometry (ESPI) have become established in the field of displacement measurements of objects with rough surfaces. The reason for their success emanates from the fact that both DSPI and ESPI are full-field techniques and consequently provide dense data coverage over a complete two dimensional surface, as opposed to the limited point wise data offered by strain gauge sensors. The main disadvantage, however, is that their application is limited to surface measurements. As mentioned earlier, composite materials possess an inherently complex structure and are, therefore, characterised as inhomogeneous materials. Moreover, their behaviour is often non-linear. Consequently, surface measurements on such materials can prove insufficient to characterise their behaviour, as they risk missing important sub-surface localised phenomena associated with defects or damage that occurs during the manufacturing process and/or service.

Considering the success of speckle pattern interferometric techniques on surface measurements, in the past decade or so, researchers worldwide have concentrated their efforts in order to extend the application from surface to volumetric measurements. As a result, a wide family of interferometric techniques under the generic name of optical coherence tomography (OCT) have emerged. OCT is a new and exciting imaging modality that was initially developed for applications in

biomedicine. To date, it is still predominantly used in this field as a means of imaging the internal structure of bio-materials such as living tissue and the human cornea. However, advancement in laser technology as well as the continuous development of the technique that have revealed new functionalities has allowed its application to non-biomedical materials. OCT is applicable to weakly scattering materials. In the context of optical measurements, the term weakly scattering refers to materials for which single scatterers are much stronger than their double/multiple counterparts making the assumption of neglecting multiple scattering valid. From the above, it becomes clear that the application of the technique to carbon fibre reinforced polymers (CFRP's) would not be possible due to the high absorption coefficient carbon possesses as an element. This, however, is not the case for glass fibre reinforced polymers (GFRP's). Consequently, since the behaviour of fibrous composites is somewhat similar and is predominantly dependent on geometrical factors, the application of OCT could lead to useful results that characterise fibrous composite structures. An example of the imaging capability of the technique on GFRP composites is shown in figure-1.1 and figure-1.2. The specimens were courtesy of *CYTEC Engineered Materials Ltd*, UK while the OCT system used was a swept source (SS) system from Thorlabs, with a central wavelength λ_c = 1.3 μm, located in the Wolfson School.

1.2 Motivation and relationship to past work

Researchers of the optical engineering group at the Wolfson School of Mechanical and Manufacturing Engineering at Loughborough University have over the past three decades, pioneered the techniques of DSPI and its predecessor ESPI with specific applications to measurements of surface displacement fields. Such information is, however, in general, insufficient to determine uniquely the deformation and stress state **within** the sample. Moreover, such information is insufficient to characterise composite materials due to their inherent inhomogeneous structure and non-linear behaviour.

More recently, the group, and in particular *Dr P. D. Ruiz* and *Prof J. M. Huntley* carried out proof-of-principle experiments that indicate that the techniques can be extended to three dimensions and can, therefore, be used so as to allow the measurement of displacement and strain fields within the volume of scattering materials. [3-8]. Depth resolution is amongst the key parameters that determine the performance of depth-resolved measurements, and can be controlled by varying the ***k***-vector of the wave illuminating the object in two ways:

a. either through changing its direction (a technique so-called tilt scanning interferometry (TSI) [6]),
b. or through scanning its magnitude.

The later method (b) resulted in a pair of techniques called wavelength scanning interferometry, WSI, where the wavelength of a broadband source is tuned sequentially [3, 4] and phase-contrast spectral-domain optical coherence tomography, PC-SOCT where a broadband source is also used but differs from WSI in that all wavelengths are available simultaneously [5, 7].

The aforementioned techniques are now achieving international recognition: for example reference [8] won the **prize for best oral paper** out of 63 presentations at the Speckle '06 International Conference, Nimes, France, in September 2006; and reference [6] attracted comments from the *Proc. Roy. Soc.* reviewers such as "The submission is very interesting and of far-reaching significance. It can certainly be considered as one of the major contributions to the advance of speckle interferometry … over the last three-four years."

1.3 Research goal

The long term goal of this research is to calculate the spatial distribution of the constitutive parameters (Young's Modulus, *E*, Poisson's ratio, ν, etc.) in semi-transparent scattering materials like GFRPs. Measuring the displacement fields within the structure that describe the state of deformation that the material under test has undergone is one of the key issues of this research project. To achieve this, means of introducing the appropriate amount of deformation within the sample need to be developed. Moreover, a system that combines the imaging capabilities of OCT systems with the displacement sensitivity of traditional interferometric techniques also needs developing. Thus, the objectives of this research can be broken down to the following six working packages:

a. Measure all three displacement components.
b. Measure from both sides of the sample.
c. Design and manufacture suitable hardware.
d. Get spatially resolved strain information.
e. Accurately characterise the frequency of the light which provides a ruler and a measure of the system ability to resolve depth information.
f. Hence apply a technique such as the virtual fields method (VFM) to extract spatially resolved modulus distributions [9].

Following the achievements reported in references [3-8], *Dr A. A. Davila*, joined the group during a sabbatical leave from the *Centro de Investigaciones en Optica, Loma del bosque 115, Leon Gto 37150 Mexico* (2008-2011) as a research associate and assisted in the development of the tomographic interferometer. *C.Pallikarakis* (author of this thesis) joined the group as a PhD student in December 2010 and worked closely with *A. Davila* on several aspects related to the development of the multi-axis tomographic system including its assembly, during the one-year period of overlap – figure illustrates the general layout of the multi-axis tomographic interferometer under development, alongside with some of its key hardware components.

1.4 Research methodology

As mentioned earlier, at the time the author joined the *Optical engineering* research group at *Loughborough University* as a PhD student, the development of the multi-axis phase-contrast tomographic interferometer had already been started with *Dr. A. Davila* (RA) and professor *J M Huntley* being the leading investigators. In this section details of how the work evolved are given. At first the original plan is discussed. Second, details on the key parameters that caused the refocusing of the work are given. Finally, the modified objectives of the work are presented alongside with their link to the original objectives.

1.4.1 Original methodology

The technique that would ultimately be used to measure the sought volumetric displacement/strain fields that are necessary to determine the spatial distribution of the elastic constants in composite materials such as GFRPs had already been chosen to be wavelength scanning interferometry (WSI) – the latter being equivalent to the term swept-source optical coherence tomography (SS-OCT) in the field of tomography. It is important to note that OCT is not the only technique capable of providing volumetric data/imaging. X-Ray μ-CT is one attractive alternative solution to OCT; however, it was still at its infancy at the time that this work started and was therefore not chosen. Phase-contrast versions of x-ray μ-CT are now slowly starting to emerge (see for example ref [10]), justifying the importance of phase as a measurand – it can be transformed to almost any parameter of interest i.e. displacement, strain, temperature, pressure etc.

As an alternative to the imaging of phase, image correlation techniques have been under development for two decades or so (almost in parallel to DSPI and its predecessor ESPI) in which the movement of a pattern (speckle pattern or another random pattern that is printed by the user onto the sample of interest) is tracked spatially and leads to the estimation of strain, temperature changes etc. The generic term for the 2-D version of the technique is digital image correlation (DIC) [11] while its extension to 3-D is often called digital volume correlation (DVC) [12]. DVC and its predecessor DIC can be combined with imaging techniques like x-ray μ-CT or OCT to provide the sought depth-resolved displacement fields.

X-ray μ-CT combined with DVC [13-15] has comparable spatial resolution to that of PC-OCT. This is not the case, however, when OCT is combined with DVC with the spatial resolution being less than that of PC-OCT. This is because the size of the sub-volume used for performing the correlation between the deformed and undeformed states is the main parameter that controls the spatial resolution of the system e.g. a sub-volume of $15\times15\times15$ voxels will practically degrade the spatial resolution by a factor of $\times15$. For the above reasons, the method used to extract the depth-resolved information in this work was decided to be PC-OCT or PC-WSI (the two terms are used interchangeably).

Figure-1.4 provides examples of some of the techniques mentioned earlier and their corresponding dimensionality, thereby highlighting the importance of extending computations in 3-D in order to gain improved:

a. Understanding of the physical processes
b. Numerical stability in solving 'inverse problems'.

The above justifies the need for the development of the multi-channel instrument under development in this work (recall figure-1.3) in which a total of six channels are featured – three of which correspond to the three orthogonal displacement components and the other three being complementary to the first set.

Recalling that the ultimate goal of this research is to estimate the 3-D depth-resolved elastic parameters of composite materials such as GFRPs which would in turn allow the study of the effect of defects on their mechanical properties and would thus lead to the development of improved numerical models for stress and strain predictions, a system that is capable of imaging **BOTH** the *intensity* and the *phase* is required – the imaging of the intensity will provide the ability to look within the sample while the imaging of the phase will provide the necessary deformation information between two states (undeformed and deformed state). As the displacement sensitivity ($\lambda/2$) in optical techniques such as WSI is controlled by how short the wavelengths of the light spectrum used are, the laser source chosen was a continuous-wavelength (CW), electronically-tuned Titanium-Sapphire from M-Squared (SolsTiS 300-SRX) that was originally developed for spectroscopic applications. Short wavelengths, however, come at the expense of reduced penetration depths [16]. By illuminating the sample from both sides, this limitation can be supressed and is the reason as to

why a total of six channels were chosen during the design process as opposed to three. With these in mind, work on the development of the tomographic sensor began in 2008.

Figure-1.5 is essentially a block diagram of the work-break-down structure showing the individual work packages (WP) necessary to achieve the long term goal at the time the author joined the group. The fundamental requirement for any WSI application is that the wavenumber k of the light source can be linearly tuned as a function of time. For this reason, an embedded DSP and a WSD were introduced to the purchased Ti:Sa laser by the manufacturer, after request (WP-1). Work packages one to five in figure-1.5 (WP-1 to WP-5 and WP-8 to WP-9) had been initiated by the appointed RA but were continued during the overlap period and beyond (see following sections of this chapter for more details on the actual reasons). The remaining two work packages (WP-6 and WP-7) involving the development of appropriate hardware for the re-registration of the data volumes coming from the six independent interferometers and the introduction of controlled displacements to the GFRP sample were thought to be the main remaining issues at the start of the project. It is for this reason that a significant amount of effort was put towards the development of appropriate hardware during the first two years of this project. A brief description of these is documented in chapter-3. Unfortunately, these were ultimately not used for the reasons listed in the following section (section-1.4.2) but have been included in this document for completeness.

1.4.2 Unanticipated factors

Unfortunately, due to a number of unforeseen factors, the initial methodology outlined in the previous section (see section-1.4.1 and in particular figure-1.5) had to be changed. As a result, the project was focussed away from the initial experimental oriented plan to a numerical and analytical one, based on preliminary experimental data that were captured prior to critical hardware failure. The main reasons that ultimately led to the refocusing of the project are as follows:

a. Highly non-linear laser behaviour that was impossible to foresee at the time (caused long delays that affected the entire plan of work)
b. Critical failure of the electronically tuned CW Ti:Sa laser (affected work packages: WP-1,WP-4 in figure-1.5)

c. Critical issues with the software prepared by the RA (affected work packages: WP-8 and WP-9 in figure-1.5)

As it is evident from figure-1.5, the laser source used in this thesis sits at the core of its novelty and the functionality of the multi-axis tomographic system under development. At the time of purchase (2008) it was the only one of its kind able to produce electronically tuned scans in excess of 100 nm in steps of 1 pm – with the scan range, $\Delta\lambda$, and the wavelength step, $\delta\lambda$, being the two governing parameters which control the depth resolution δz and the depth range, Λ_M, of any tomographic system respectively. Further justification of this can be found in the short history of lasers review in reference [17] and in particular section *25: The solid state laser revolution* and section *26: State of the art lasers in 2010*.

Before proceeding with the details of the laser failure and the associated difficulties with its behaviour, it is worth noting that the particular source used in this work was practically a prototype and the second product the company had commercially produced at the time. Over the last five years the design of the cavity and the wavelength selection mechanism have undergone several improvements (approximately a fifteen version gap between the purchased source and the most up to date one currently in production by M-Squared) leading to a prestigious **IOP innovation award** in 2015.

Apart from the sensitivity of the laser to misalignment (see chapter-4 for more details) one of the many issues encountered right from the beginning was that it was prone to loss in temporal coherence. In simple words, this meant that the recorded images would become completely blurred thereby causing the complete loss of information. After consulting with the company, this was attributed to the synchronisation issues between the BRF (coarse tuning) and the etalon movement (fine tuning stage) during the wavelength selection process. To overcome this issue, the external reference cavity (a component responsible for stabilising the selected wavelength) was removed while a new set of etalons with a much finer FSR replaced the old pair. To perform these changes, the equipment had to be shipped back to the manufacturer and remained there for the duration of approximately eight months starting from December 2010. The latter constitutes part of the reasons for the limited number of experimental data sets captured and analysed in this work.

Following the repairing of the laser and the suppression of the temporal coherence loss issue after the replacement of the etalons, three preliminary data sets were captured. The first was a short scan of 400 frames equivalent to approximately 1 nm with the CCD frame grabber synchronised with the laser at ~ 4.5 fps (Hz), the second and third scans were both ~ 100 nm scans at ~ 5.4 Hz and ~ 6.3 Hz respectively. The actual reasoning behind the choice of such slow scans will become clearer in section-1.4.3 and later in chapter-5.

At a later stage (summer 2013), the PZT responsible for the fine movement of the two etalons failed permanently (more details on how the author reached to that conclusion are given in section-4.4.2). A service engineer from M-Squared was called to inspect the laser (the company refused to allow access to the laser cavity due to trade secret policy) and confirmed the issue. As mentioned earlier, by the time the PZT failure occurred, the design of the product had progressed significantly that it was deemed impossible to repair the current model. Consequently, the group came to an agreement with M-Squared which would ultimately involve the complete replacement of the equipment at a reduced cost of £10,000 instead of the actual cost of £30,000. However, due to the high level of customization required (see next section and also chapter-4 later on) and the accompanying time restrictions, it was decided not to pursue this option for this current project.

1.4.3 Modified methodology

In the view of the eventualities reported in the previous section, the group (the author, the RA and professor J M Huntley) agreed to adjust the objectives of the work and rely to the processing of the limited experimental data prior to the failure of the laser source. This subsection gives details of the basis on which the modified plan was drawn and sets the foundations onto which the novelty of this work lies.

In WSI and SS-OCT the depth encoding frequency shifts separate the signal from within the different slices of the sample under inspection thereby allowing the imaging of its internal structure – this is what is often termed as imaging of the interference signal in the context of depth-resolved measurements. Phase-contrast versions of WSI and SS-OCT take this principle a step further by calculating the displacement-encoding phase maps. The principle onto which the process relies is rather simple and can be summarised in the following three steps:

a. Tune the wavenumber at a constant rate
b. Record the intensity distribution of the interference signal
c. Calculate the Fourier transform of the intensity distribution and extract the phase.

It follows that, if the wavenumber tuning curve is not linear or approximately linear with respect to time, the recovered signal becomes randomized, to an extent analogous to the non-linearity in the wavenumber k, thereby preventing the successful depth-reconstruction of both the intensity and the phase. In order to ensure this, the laser source was customised by the manufacturer as follows:

a. Wavelength-sensitive diode (WSD) incorporated in both coarse and fine tuning feedback loop
b. Etalon scans produce nominally-constant user-defined jump in wavenumber between frames, with TTL pulse to trigger camera
c. Automatic exposure compensation for the laser power-wavelength variations
d. Embedded DSP code modified to automate coarse and fine tuning

The long tuning range offered by the Ti:Sa laser alongside with the aforementioned adjustments should in theory produce depth resolutions of the order of 2.66 μm. However, preliminary results (see chapter-4) demonstrated that the effective depth-resolution is in fact degraded by a factor of approximately $\times 750$. The poor performance was attributed to:

a. Residual etalon mode hops
b. Non-linear behaviour between mode-hops

While the first (a) can potentially be resolved by improving the laser cavity design and the wavelength selection mechanism [18] (significant improvements on these have already been introduced to the most up to date versions of the laser by M-Squared), the second (b) is an intrinsic characteristic to the laser physics. Therefore, in order to overcome this issue, the need of accurate and rapid monitoring of the dynamic changes in wavenumber during a WSI scan becomes apparent.

After realising the importance of accurate wavenumber monitoring for WSI applications with solid-state sources like the Ti:Sa laser source, the objectives of the work where adjusted to developing a system capable of providing:

a. Rapid and accurate Δk monitoring
b. Easy incorporation to the multi-axis WSI system under development

Note that (a) is practically the same as (e) in section-1.3. The block diagram in figure-1.6 illustrates the individual work packages required for the development of the optical sensor for the dynamic wavenumber monitoring and provides the reader with an overview of the contents of this research.

At a first glance the changes between the original and modified methodologies illustrated in figure-1.5 and figure-1.6 respectively may appear significant. However, realising that both the original and the modified methodologies largely rely on phase measurements, the similarity between the two is revealed – both the depth-resolved displacement maps and the rapid and accurate monitoring of Δk require fast, accurate and precise phase measurements. Moreover, as it is evident from the comparison between figure-1.5 and figure-1.6, a number of the initial work packages and in particular WP-5, WP-8 and WP-9 have been directly translated to the modified plan, thereby providing the reader with evidence that the general principle of the main interferometer works.

Conceptually, the principle onto which the instantaneous wavenumber detection was based, was originally reported in ref [19] where a set of simulated fringe patterns with varying fringe densities were analysed using the temporal phase unwrapping algorithm reported in ref [1]. The algorithm was originally developed for shape measurements using the principle of triangulation between a spatial light modulator (SLM) and the camera, and was ultimately employed for large scale, surface metrology applications through the Loughborough University spinoff company *Phasevision Ltd*.

In practice, the development of the wavelength sensor started prior to the author joining the group and before the permanent failure of the laser source, justifying the difficulty in establishing a single strategy. More specifically, the setup for the wavelength sensor, that formulated the seventh channel of the multi-axis instrument, was put together by the RA with a few modifications introduced to it by the author during the one year overlap (see chapter-5 for more details).

As mentioned earlier, during this one year of overlap three data sets were captured. The first was a short scan of 1 nm and involved only the seventh channel of the interferometer (wavelength sensor). The second and third ones were both 100 nm scans but involved two channels of the multi-axis interferometer instead. The first channel involved the intensity distributions from the wedge sensor while the second the intensity distribution from one of the six channels of the main interferometer, corresponding to:

a. A micro-fluidic device (MFD) for testing the imaging capabilities of the integrated system and the analysis algorithms used in this work within scattering materials
b. A stepped, sand-blasted aluminium plate to test the performance of the system and the analysis algorithms when dealing with speckle patterns.

Table-1.1 below provides details on the three data sets captured alongside with some information regarding the key equipment comprising the integrated system. Although these are discussed in the main chapters to follow, they are presented here for the purpose of clarifying the methodology adopted and the novelty of the work. As it is evident from table-1.1, the data acquisition speed for all three data sets is orders of magnitude lower to the scanning speed achievable by the laser source manufacturer. There are several reasons as to why it was decided so. These are:

a. The upper limit on the acquisition speed is not determined by the scanning speed but rather by the number of frames the CCD is capable of capturing per second. Thus, in this case this is 30 Hz.
b. After several trials, it was found that the faster the laser scan speed is the larger the gaps in the wavelength sequence were. This can be readily verified by comparing the size of data set-1 (WS) and data set-2 (WS) in table-1.1 and is linked to the physics of the laser.
c. In order to compare the performance of WS a commercial high-end wavelength meter (WS7) was connected to a low-end laptop whose display was recorded by one of the CCDs. As the monitor refreshing rate was fairly low the scan speed was reduced to avoid blurring of the screen and thus compromising the quality of the independent test.

Table-1.1: Details of the three data sets captured. Green shaded area: Experimental data processed. Blue shaded area: Pending data for processing.

	Data set-1		**Data set-2**		**Data set-3**	
Laser source	Electronically tuned (750-850 nm) CW Ti:Sa pumped by 5W Verdi 532 nm. Ti:Sa max power output of 460 mW at 800 nm and scanning speeds in the order of MHz					
Scan range Δλ	~1 nm (750-751 nm)		~100 nm (750-850 nm)		~100 nm (750-850 nm)	
Wavelength step δλ	2 pm		4 pm		2 pm	
Acquisition speed	4.5 Hz		5.4 Hz		6.3 Hz	
No of channels used	1 out of the 7 available		2 out of the 7 available		2 out of the 7 available	
Data size	WS	WS7 display	WS	MFD	WS	Step plate
	500 Mb	62 Mb	50 Gb	47 Gb	11 Gb	9 Gb
CCD specs	Prosilica GC1380H model with the Sony ICX285 EXview sensor for increased response in the near infra-red (NIR) and 12 bit resolution with speeds of up to 30 frames per second at full resolution (1360 × 1024 pixels)					
PC specs	First generation *i7* quad-core processor, 6GB memory (RAM), an AMD Radeon 6900 HD graphics processing unit (GPU) and a total of seven hard disc drives (HDD) of 1TB capacity each to store the large data sets					
Application	To test the performance of the 4-wedge wavelength sensor (WS) vs a high-end commercial wavelength meter (WS7) for a short scan range.		To test the performance of the WS for the full scan range with slightly higher acquisition speeds and wavelength step as well as to test the imaging capabilities of the system in the wavelength range of 750-850 nm. Micrometer measurements of the central wedge thicknesses were used for verification		To test the performance of the WS for the full scan range with slightly higher acquisition speeds but the same wavelength step as for the short scan as well as to test the performance of the system when dealing with speckle patterns in the wavelength range of 750-850 nm	

During year one of the work data set-1 was processed using a piece of software written in the MATLAB programming language, which was prepared primarily by the RA. The author of this work was also involved in its development while at the same time receiving the necessary training before the RA's departure (end of contract). The joint work (RA and author) resulted in the following publication during the first few months of the research project:

A. Davila, J. M. Huntley, C. Pallikarakis, P. D. Ruiz, and J. M. Coupland, "*Simultaneous wavenumber measurement and coherence detection using temporal phase unwrapping*," Appl. Opt. **51**, 558-567 (2012),

where, the author's contribution started from the experimental determination of the true wedge thickness ratio (see section 3.D in ref [20] and the corresponding section-5.5.1 in this document)

At a later stage of the second year, the wedge data (WS) of data set-2 was processed with the implementation of some modifications to the original software by the author. These involved:

a. Data structure alignment issues associated with the conversion of the images from *.seq* format to a MATLAB readable format. This was partially resolved by the RA but was fully automated by the author to account for the different parameters that accompany the three data sets.
b. The overcoming of memory issues with original code that initially prevented accessing of the data sequence – see destination vector approach in chapter chapter-6.
c. The sorting of the intensity values recorded by the CCD using the extracted unwrapped phase values from the fringe analysis using the conventional 2-D FFT transform – this approach was also implemented in the first publication [20] but had minor effects due to the limited number of frames processed (400 frames) and the relatively slow scanning speed.
d. The resampling of both the intensity and the wavenumber change axis Δk onto a regularly spaced vector.
e. The periodic updating of the frequency at which the phase is evaluated in the Fourier domain – This was suggested as a method to account for the phase shifts owing to the gradual movement of the Fourier peak of interest after several wavelength increments for the case of longer scan ranges in [20].

Following the implementation of the above, the processing of the wedge data of data set-2 commenced and resulted in the second publication during year two of the research:

A. Davila, J. M. Huntley, C. Pallikarakis, P. D. Ruiz, and J. M. Coupland, "*Wavelength scanning interferometry using a Ti:Sapphire laser with wide tuning range*," Optics and Lasers in Engineering **50**, 1089-1096 (2012).

IMPORTANT NOTE: All the data processing and figures enclosed in the above publication were performed solely by the author – The RA had already left at the time.

Although the aforementioned changes to the original software overcame the memory issues encountered previously, the successful data analysis was restricted to 37 nm [21] beyond which severe signal degradation occurs. In the view of this limitation and in an attempt to gain unambiguous access to the full 100 nm scan, the strategy summarised in the work packages WP'-5-WP'-8 of figure-1.6 was employed. This involved the improvement of existing temporal phase unwrapping algorithms with particular attention to the establishment of links between phase unwrapping errors and physical phenomena related to depth-resolved measurements as well as the estimation and partial suppression of systematic and non-systematic errors associated with WSI and the particular laser source.

The development of such algorithms, described in chapters: 5 to 8 of this work resulted in the accessing of the entire scan range and justifies the title: *" Development of temporal phase unwrapping algorithms for depth-resolved measurements using an electronically tuned Ti:Sa laser "* of this research. The practical implementation of the modified strategy resulted in:

a. The complete re-writing of software, in the MATLAB programming language, for the processing of the data sequences of ~ 4,000 lines. Note that the term data processing here refers to work packages WP'-3 and WP'-4 in figure-1.6.
b. The complete re-writing of software using MATLAB for the data analysis and the subsequent figures of ~ 4,000 lines. Note that the term data analysis refers to the implementation of the improved temporal phase unwrapping algorithm (WP'-5 and WP'-8).

The validation of the approach presented was achieved by calculating the thickness of **ALL** four wedges comprising the optical sensor used to provide the sought

wavenumber change axis using at first the proposed algorithm and comparing the results with independent micrometer measurements and the measurements claimed by the wedge manufacturer (CIO Mexico, see appendix-A4). Note that the wavelength meter used for validating the short scan results for the wavelength sensor in [20] was on short loan (2 weeks) from the *National Physical Laboratory* (NPL), Hampton Road, Teddington, Middlesex, TW11 0LW and was not available at the time the aforementioned improvements were achieved. It was, therefore not used.

1.5 Thesis organisation

This short section gives a brief explanation of the contents of the individual chapters featured in this document while at the same time provides the reader with a useful navigation tool (active hyperlinks).

Chapter-1: Introductory chapter that provides an overview of the six year research enclosed in this thesis. As mentioned already, this research was mainly event driven. The chapter gives details of how the work progressed, the critical events that affected the course of this research and the individuals involved in it starting from the conception of the idea up until its completion. Finally, the areas of overlap with previous work are highlighted and the novel aspects for which the author is solely responsible are clarified.

Chapter-2: This is the main literature review chapter in which the critical parameters that determine the performance of the majority of systems within the OCT community are highlighted and discussed. Brief explanations on the working principles of the different types of OCT in the academic community alongside with a detailed description of the mathematical formulae relevant to the technique ultimately used in this work (WSI) are also provided. Finally, a thorough review of the different light sources used in the academic community is provided. This highlights the importance as well as the novelty associated with the use of the Ti:Sa source. It should be noted that shorter and separate literature reviews that are targeted to each of the individual chapters (chapters: 3 to 8)

contained in this document are included in their introductory and/or in some cases the corresponding discussion sections.

Chapter-3: In this chapter a brief summary on the development of the electromechanical hardware associated with the original methodology are provided. As mentioned earlier, these were ultimately not used due to the permanent failure of the laser and the critical issues with the software when dealing with the full length of the scan range offered by the Ti:Sa laser source. However, preliminary experiments at a single wavelength suggest that these work as expected.

Chapter-4: This is the chapter where details of the integrated multi-axis tomographic interferometer under development are given including the optical design of the 6-channel interferometer, the working principle of the Ti:Sa laser source, its customisation and the software used for controlling and synchronising the multiple CCDs with the laser are provided. Finally, the performance of the laser using the data available by the WSD and some preliminary results on the imaging capabilities of the system on glass samples is discussed. The later provide the necessary justification for the development of the four wedge sensor (7^{th} channel of the system) that follows in the next chapter.

Chapter-5: The fifth chapter is a description of the optical design and the principle idea of the analysis algorithms for the four-wedge optical sensor used to characterise frequency of the light coming from the Ti:Sa laser source and which ultimately provides a ruler and a measure of the system ability to resolve depth information. Its performance is assessed using the high-end WS7 wavemeter provided by NPL for a short scan (see data set-1 in table-1.1). The chapter is essentially based on the first publication (see ref [20]). However, all the figures featured in this chapter forward (unless otherwise stated) were produced with the most up to date software. The results are identical to those reported in [20]. This justifies the validity of the proof of principle short scan experiment. More importantly, however, it demonstrates how challenging it is to extend the access from 1 nm to the full 100 nm for this particular source, thereby justifying the work

presented in chapters 6, 7 and 8 later. From a contributions point of view, the material presented from section-5.5 onwards (for that chapter) was the result of joint work between the author and the RA.

Chapter-6: In this chapter the first attempt to extending the access to the full 100 nm scan range is described. Although based on the second publication (see ref [21]) where a similar approach was described, the useful scan range was extended from the 37 nm limit previously reported to the full 100 nm one, owing to the estimation and suppression of intensity background artefacts and the implementation of the 2-D non-integer phase extraction algorithm. In order to validate the achievement, the central thickness of ALL four wedges was compared with independent micrometer readings and the dimensions claimed by the manufacturer with good agreement. However, the main spectral lobes used for estimating the wedge thicknesses showed that the signal suffers from the presence of side lobe structure as the 1-D spectral analysis of the intensity distribution moves away from the higher sensitivity wedge based on which the Δk-axis is calculated.

Chapter-7: In the view of the achievements reported in the previous chapter, in this chapter, an investigation of the systematic and non-systematic errors present in WSI for wide tuning ranges is conducted. These include laser beam induced errors, the presence of angles other than those along the wedge direction, the possibility of the four wedges having different dispersion characteristics and the effect of sample of thickness to name a few (see WP'-6 in figure-1.6). Additionally, links of the aforementioned error sources to phase unwrapping errors (the parameter detectable by the analysis presented) is also attempted. Moreover, a visual tool based on TFA is described for the assessment of the 1-D spectral quality.

Chapter-8: In this penultimate chapter, and in order to reduce the artefacts that were present in the Fourier reconstruction of the depth profile of the four wedges, two modifications to the basic unwrapping algorithm used earlier are introduced. Both approaches are adaptive and involve signal re-referencing at regular intervals throughout the scan. The first is

designed to compensate for the gradual change in spatial frequency of the fringes that arises from the changing wavelength, and requires continual updating of the spatial frequency components at which the phase is evaluated. The second is designed to compensate for the gap that starts to open up between the scaled low-sensitivity phase signal and the high sensitivity phase signal. A hybrid approach combining both methods was found to be the most robust of all the techniques considered, with a clear Fourier peak at the expected frequency and without any spectral artefacts.

Chapter-9: In this final chapter of the work and in the lack of additional experimental two sets of simulated data that closely match the characteristics of the real experimental data analysed earlier are produced and are subsequently analysed .The advantage in doing so lies in that, simulations provide a convenient platform where the performance of the proposed TPU strategy can be assessed in the absence of the inevitable noise and other non-linearities associated with the real experimental data. The results of this final test justify that the various fixes included in the 'hybrid' approach have not evolved to solve the problems of a particular data set but are rather of general nature thereby, highlighting its importance for PC-WSI applications concerning the processing and analysis of large scans.

1.6 Research novelty

The development of the multi-axis tomographic interferometer described in this thesis contains a number of novel aspects, starting from the optical design of the interferometer and stretching all the way to the acquisition and processing of the data. However, as it is often the case with state-of-the-art technology and equipment, this is the result of collaborative work. In this last section of the introductory chapter the overall novelty of the work enclosed is highlighted and is briefly discussed. Moreover, the original contributions of the author are highlighted and distinguished from the work done prior to his arrival, thereby justifying the novelty associated to the development of the analysis algorithms enclosed in this document.

1.6.1 The laser source

As already mentioned earlier in this chapter, the non-linear behaviour of the laser source followed by its permanent failure meant that a significant number of the novel aspects concerning the multi-axis interferometer could not be verified. These include the two mechanical rigs that are briefly described in chapter-3. The first was designed to provide the necessary data sets for estimating the depth-resolved displacement fields in GFRP samples which in turn, would provide the necessary information for the estimation of the 3-D depth-resolved elastic parameters. The second was designed to aid the re-registration of the data volumes from the six channels.

As it will become apparent in the literature review chapter (Chapter-2) and later on in chapters 6 to 8, the use of continuous wavelength solid-state lasers and in particular the electronically tuned CW Ti:Sa laser source used in this work has been limited with the majority of research groups using its pulsed counterpart (see for example references [22-25] that are particularly targeted to NDT of polymer matrix composites). The only report available in the literature in which a CW Ti:Sa laser was used using WSI, can be found in ref [26] where the full 100 nm range was exploited albeit with much larger wavelength steps. The latter is directly linked to the depth-range of the system – the smaller the wavelength-step the larger the depth-range. Moreover, the scanning speed reported in [26] was 250 Hz with a total data size of 128 Mb corresponding to 1024 images/frames collected in 9.5 s.

As the laser source used here is capable of producing scans of 100 nm with wavelength steps down to the pico-meters level, it constitutes one of the novel aspects reported in this work related to the laser. This can be easily verified by comparing the data size of table-1.1 Moreover, the relatively high output power available (~460 mW) and the wavelength spectrum within which the Ti:Sa laser operates allows the use of CCDs that are currently less expensive than those sensitive in the deep IR region of the light spectrum (see for example reference [27]), thereby allowing the construction of the multi-channel OCT system.

1.6.2 The wavelength sensor

The necessity for the development of the wavelength sensor emerged due to the highly non-linear behaviour of the laser source. Commercial wavelength meters are widely available in the market offering unparalleled accuracy and precision in wavelength measurements. However, apart from their relatively high cost and the fact that their acquisition rate is limited to a few hundreds of Hz, the principles of their operation and thus the way their accuracy and precision is achieved is not well documented. As far as the literature is concerned, wavelength detection methods have been available for some time. Simple Fizeau interferometers utilising a single wedge [28, 29] and with a set of wedges [30] have been reported in the literature, whilst an alternative method based on a polarization-sensitive interferometer combined with a homodyne detection system was described in [31].

In brief, the operating principle of the wavelength sensor relies on the use of four wedges with variable sensitivities in Δk. The analysis algorithm starts with the processing of the fringe patterns from the lower sensitivity synthetic wedge and gradually moves to the higher sensitivity one in a three-step process by making use of the temporal phase unwrapping algorithm previously reported in [1]. The latter, although similar to the original strategy in [1], it differs in that the phase signals analysed and used to obtain the final high-sensitivity phase-change signal are scaled by a factor R_m (where m = 1,2,3 corresponding to the unwrapping step) that is linked to the ratio of the central thickness between two successive pairs of synthetic wedges. The concept of synthetic wedges emerged from the limitations and/or difficulties associated to the manufacturing precision of wedges with central thicknesses of 200 μm, 600 μm and 1.6 μm.

In contrast to existing wavelength meters, the proposed one allows the instantaneous detection of incoherent images owing to the mechanical movement of the BRF and the subsequent loss of coherence, thereby making it particularly useful for WSI applications. In addition to the above, the fact that a phase change value is obtained from just one frame means it can be applied to arbitrarily high scan rates, given a camera with sufficiently high framing rate.

1.6.3 The data processing

Although, ultimately, the main interferometer (six-channels) was not used for the reasons previously reported, emphasis to transferring the majority of the novel aspects concerning the data acquisition, processing and analysis to the 7^{th} channel containing the wavelength sensor has been given (recall figure-1.5 and figure-1.6). In order to verify the validity of the analysis algorithms developed in this work and in the lack of any other experimental data, the intensity distributions (fringe patterns) from the wavelength sensor where used instead. In other words, by recalling that phase or in this case phase-change signals can be transformed to practically any parameter of interest, it follows that there is a strong analogy between the process of characterising the frequency of the light source or indeed the accurate extraction of depth-resolved displacement fields. To further clarify this, one only needs to consider that apart from allowing the processing of phase-change and phase signals of wedges with central thicknesses in the micrometer level, the synthetic wedge principle is in effect a practical realisation of phase-change signal multiplexing that allows the characterisation of the instantaneous frequency shifts induced by the laser source. In a similar manner, controlled displacements that follow an exponential sequence could potentially lead to the estimation of depth-resolved displacement fields that are currently limited by the sensitivity of interferometric techniques and phase unwrapping errors.

Joint Work

The performance of the wavelength sensor (WS) was initially tested for a short 1 nm scan and a wavelength step of 2 pm corresponding to 400 frames, versus a commercially available high-end wavelength meter (High Finesse WS7 Angstrom). A root mean square (rms) difference in measured wavenumber shift between the two of ~4 m^{-1} was achieved, equivalent to an rms wavelength shift error of ~0.4 pm.

Strictly speaking, the wedge design was the result of work carried by the RA and the supervisor (professor J M Huntley) and had already been started prior to the author joining the group. However, due to the difficulties encountered with the laser source and the associated delays (8-month period at first and then permanent failure), the experimental validation (see section-5.5.1 or section-3.D in [20]) did not start until the author joined the group. The aforementioned, constitutes the main reason for the inclusion of the author to the first joint publication (see ref [20]).

At a later stage and in an initial attempt to demonstrate the ability of the wavelength sensor to characterise the frequency shifts induced by the laser source as well as to demonstrate the improvement in the depth-resolution of the system and its link to the presence of missing gaps in the signal, a number of additional data processing steps, namely the resampling of the intensity distribution onto a regularly spaced Δk-axis (joint work between the RA and the author) and the demonstration of the effect of signal gaps on the depth resolution of the system (author). These, resulted in the second publication (see reference [21]) where the effective scan range was extended to 37 nm with a the depth resolution close to the theoretical limit. It should be noted that the software used to perform the data analysis was based on that prepared by the RA prior to his leave **but** with several changes to remove bugs that were not easy to identify for the short, 1nm scan.

Original contributions

Although a significant improvement, the fact that only 37 nm out of the total 100 nm available could be used before a curious side lobe structure started to contaminate the main Fourier peak, posed a serious concern with regards to the validity of the proposed method. Moreover, the data presented in [21] refer to the thickest wedge (higher sensitivity in Δk) based on which the wavenumber-change axis was calculated. Recalling that the sensor was designed and incorporated to the multi-axis interferometer in order to provide a 'ruler' onto which the intensity distributions from the six channels (different OPDs to that of the WS interferometer) would ultimately get re-registered, it is possible that errors that are 'coupled' to the calculated Δk-axis will emerge. From a different perspective and although in the text it is suggested the full 100 nm range of the Ti:Sa laser was used, the spectral peak presented in fig-6(b) of reference [26] suggests that only the 55.2 nm (512 frames) of

the total 100 nm (1024 frames) were in fact used. Recent studies [32, 33] have shown that improvement in the axial resolution of OCT systems is still an active field of research. More recently, attempts to overcome the detuning of the laser as well as the fact that accessing the full bandwidth of the laser source is not always as straightforward, an iterative re-weighted l_2 least squares solution to OCT image reconstruction that allows for contiguous spectral sampling over a small bandwidth was proposed (see reference [34]).

The above, constitute the reasons as to why for the remaining of this work (Chapter-6 onwards), all efforts were shifted towards accessing the full scan range offered by the Ti:Sa laser. The proposed approach relies on an in-depth investigation of the link between phase unwrapping errors and systematic and non-systematic errors owing to laser behaviour, material and geometrically induced factors during wide tuning WSI scans. The success of the method was the result of several modifications to the initial analysis algorithm described in chapter-5 and ref [20] and can be summarized in the following few steps:

a. 2-D implementation of the 1-D non-integer Fourier peak detection algorithm originally reported in ref [2] (see chapter-6),
b. Phase estimation using the 2-D non-integer Fourier peak detection algorithm (see chapter-6),
c. Estimation and suppression of intensity background artefacts (see chapter-6),
d. Correction factor to account for the presence of angles along directions other than the wedge-direction (see chapter-7),
e. Instantaneous Fourier peak position extraction using a piecewise LSF method and thee estimation of refractive index dispersion trends, in the absence of other errors, for the four wedges (see chapter-7),
f. Use of a TFA tool based on the STFT for the visual inspection of the signal spectral quality,
g. Adaptive Fourier-peak updating method (see chapter-8),
h. Periodical phase updating method (see chapter-8)
i. Hybrid implementation of (e) and (f) (see chapter-8).

The implementation of items (a), (b) and (c) into the software used for the analysis of the experimental data set, led to the full accessing of the entire scan range. To date

and to the best of the author's knowledge, this is the first time this has been achieved for the particular laser source and for wavelength steps of 2 pm, corresponding to a sequence of ~50,000 frames in place of the 1024 frames previously reported in [26] of which only half was presented. To ensure that the improvement was generic enough and that this was not the result of the inevitable correlation of the wavenumber change axis to the intensity distributions of the thickest wedge used to extract the Δk-axis, a 1-D spectral analysis at the central pixel of each of the four wedges was performed – a process termed as the 'decoupling' of the intensity data for the extracted Δk-axis. Comparison of the extracted central wedge thickness to independent micrometer measurements and the manufacturer data (CIO), suggested that the method works well. However, as the 'decoupling' process progressed, a curious structure appearing on either side of the main spectral lobe started to emerge. Although this was significantly reduced after the implementation of (a), (b) and (c) confirming the initial concerns with regards to the validity of the sensor to provide the necessary 'ruler' for the main six-channel interferometer where the path lengths between reference and the object beams are significantly different.

Considering that the 'ruler' (Δk-axi*s*) is constructed from the four-wedge sensor phase measurements, it becomes clear that the governing error source is the presence of phase unwrapping errors. Despite the fact that the aforementioned mentioned improvements suppressed a significant number of those (see chapter-6 and in particular figure-6.9), it is clear that the extracted high sensitivity phase-change signal still suffers from residual phase unwrapping errors. For this reason a comprehensive error analysis (systematic and non-systematic error sources) is conducted in chapter-7, whereby the identified error sources and their link to phase unwrapping errors are investigated (items (d), (e) and (f) above).

With these in mind, a coordinated and targeted approach to modifying the unwrapping strategy described in chapter-5 so that it accounts for the various systematic and non-systematic errors is provided in the final chapter. By recognising that each wedge constitutes a separate measurement/coordinate system and that each of the four synthetic wedges used in this work are in practice the result of superposition of a pair of wedges at each time, it follows that in the event of a mismatch in geometrical, material and/or in the illumination conditions (recall chapter-7) between the pair of wedges, would violate the assumption of a linear

filtering system [35-37] and would thus lead to significant errors in the unwrapped signal.

To avoid violating the above fundamental assumption, a twofold adaptive approach was introduced to the original phase unwrapping algorithm. The first involved the synchronous updating of the location at which the phase is extracted (see item (g)) while the second involved the periodical updating of the phase-change signal (see item (h)). By combining the two methods (see item (i)) depth resolutions of ~ 2.2 μm (FWHM) for all four wedges were achieved. The obtained central wedge thicknesses for all four wedges are in good agreement as compared with those performed with the micrometer and well within the manufacturing tolerances claimed by the manufacturer – with the exception of one micrometer measurement. Furthermore, the use of the hybrid approach, a combination of several modifications to the initial method described in chapter-5, resulted to an excellent SNR compared to that corresponding to the method used prior to its implementation, thereby justifying the novelty of the work enclosed in this document.

1.7 Figures

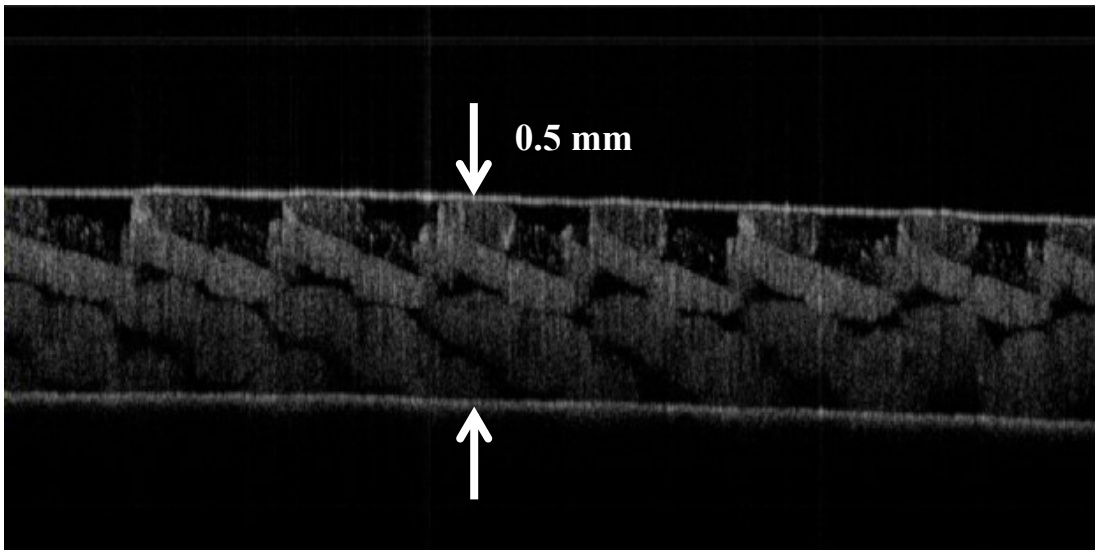

Figure-1.1: Image showing the cross section (line-scan) of 0.5 mm thick GFRP sample using a commercially available SS-OCT system from Thorlabs with a central wavelength λ = 1.3 μm. The sample was courtesy of *CYTEC Engineered Materials Ltd*, UK.

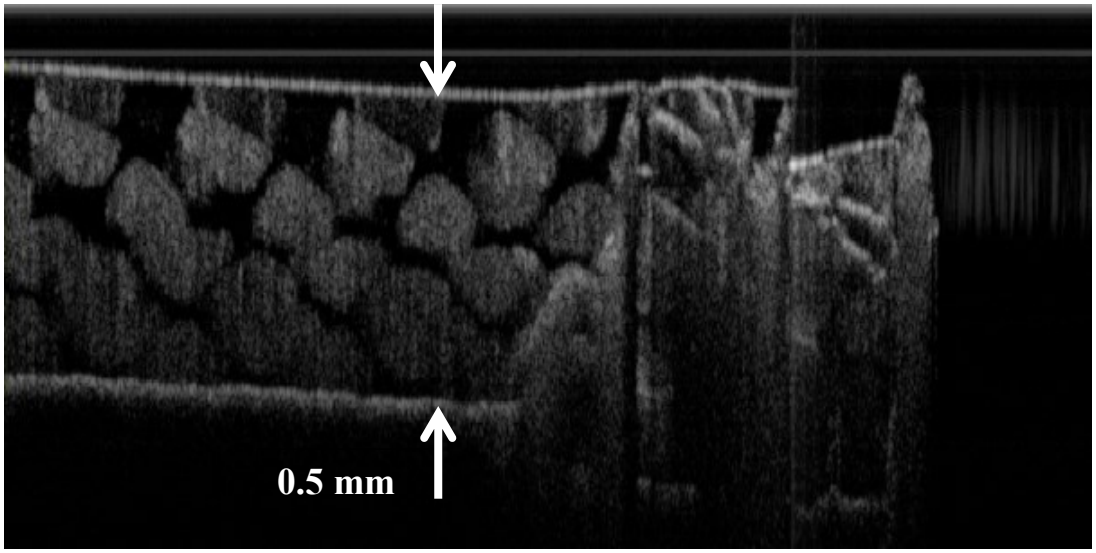

Figure-1.2: Image showing the cross section (line-scan) of 0.5 mm thick damaged GFRP sample using a commercially available SS-OCT system from Thorlabs with a central wavelength λ_c = 1.3 μm. The sample was courtesy of *CYTEC Engineered Materials Ltd*, UK.

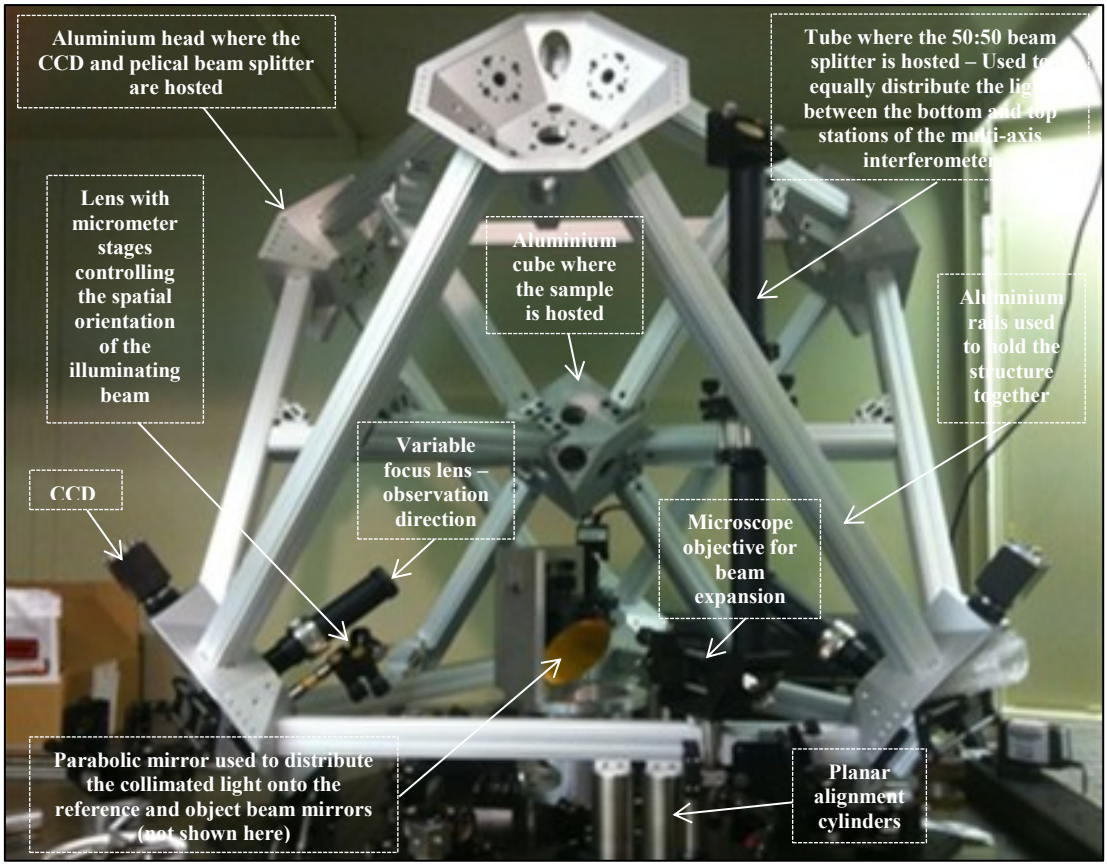

Figure-1.3: Basic layout of the multi-axis tomographic interferometer showing some of the key components and the principle on which the instrument was gradually developed. More information is given in subsequent chapters.

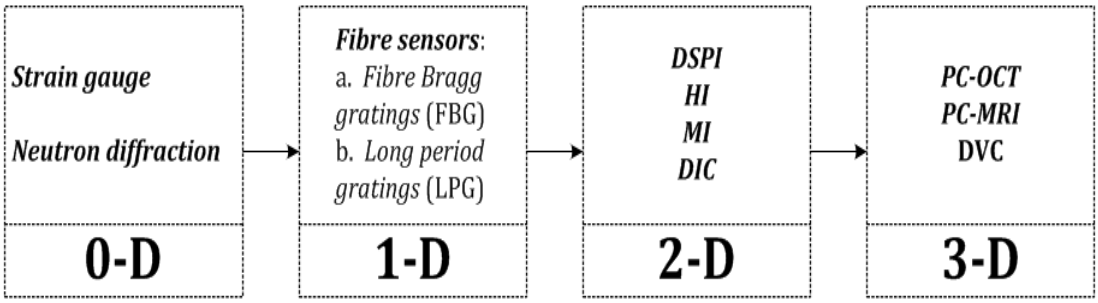

Figure-1.4: Block diagram showing the measurement dimensionality (increasing from left to right) and the related techniques available for practical implementation. HI: Holographic interferometry, MI: Moiré Interferometry, DIC: Digital Image Correlation, PC-OCT: Phase-contrast optical coherence tomography, PC-MRI: Phase-contrast magnetic resonance imaging, DVC: Digital volume correlation.

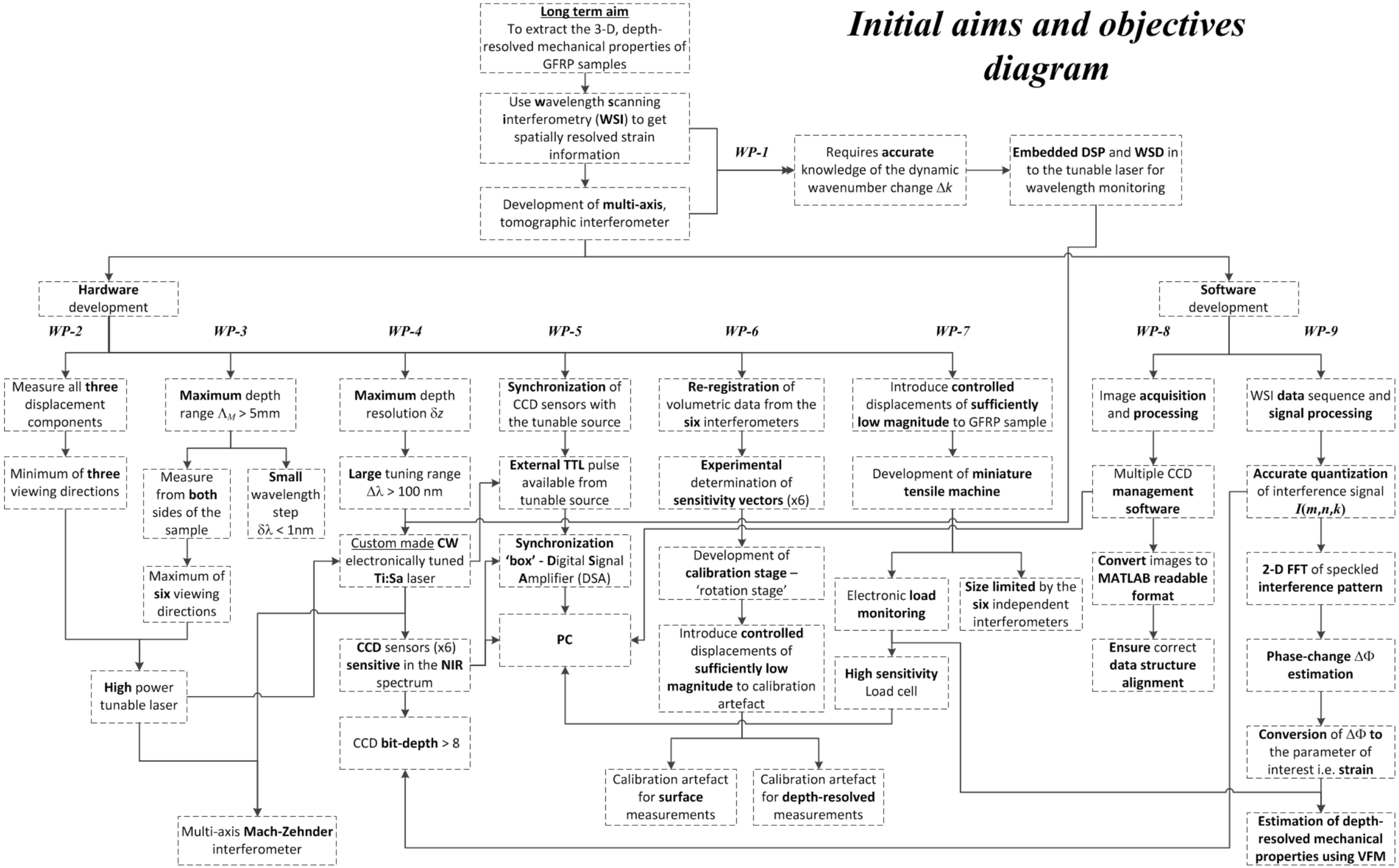

Figure-1.5: Block diagram showing the original work plan drawn and the necessary work packages (WP) for the development of the multi-axis tomographic interferometer using WSI, in order to achieve the long term goal of extracting the 3-D depth-resolved mechanical properties (Youngs modulus E, poisson ratio v etc) of GFRPs.

Modified methodology diagram

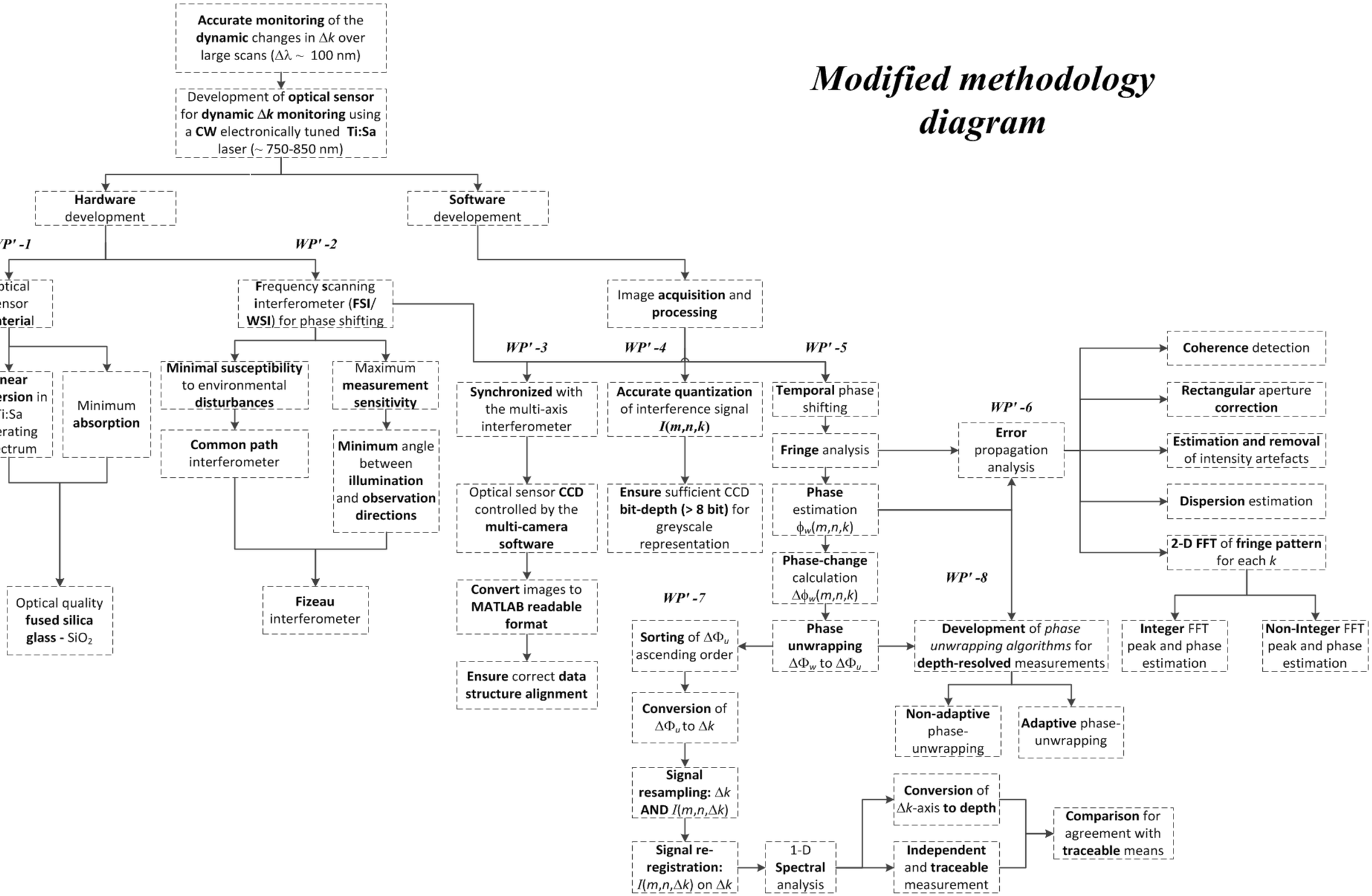

Figure-1.6: Block diagram showing the individual work packages of the modified methodology following the highly non-linear behaviour of the CW and electronically tuned solid-state laser source used in this thesis.

Chapter-2: Literature review

2.1 Composites overview

Composite materials possess superior properties over traditional engineering materials. As a result their application has been predominantly, though not exclusively, in the aerospace and automotive industries. Their superior performance, however, comes at the expense of complex behaviour owing to their complex structure. The understanding of their behaviour is therefore of great importance in order to continue their development and exploit their full potential. There has been a long history of research in the field of composites and the study of their mechanical and functional behaviour. A number of analytical methods have been developed over the years, with the generic approach aiming at predicting the properties of a single lamina from the properties of its constituent materials (micromechanics), followed by reconstruction of the properties of the full laminate (combination of lamina in various sequences) via classical laminate theory (macro mechanics) [38, 39]. A review of the early attempts in micromechanics is provided by [40], while a more recent covering of both micromechanical and macro-mechanical aspects is given by [41]. The latter concludes that the micromechanics of composites is a field that is not yet closed but not as active as in the 1960s.

An even more challenging task is that of predicting and understanding the damage mechanisms of composites. Damage in composites originates from their manufacturing process and/or during in-service operation. Manufacturing processes are responsible for the introduction of defects such as voids, resin rich areas and inclusions. An excellent review on the significance of damage and defects and their detection in composites is provided by [42]. It has been shown that damaged zones containing forms of micro - damage relate to fracture on a macroscopic scale [43]. The zone accompanies the crack propagation and depends on the load history. In a more recent work the importance of such zones was demonstrated in cracking under a variable (fatigue) loading regime [44, 45]. The methods used to date to model the damage have been by and large phenomenological [46, 47].

It is clear that the inherent complexity of composite structures cannot be modelled without the use of simplifying assumptions. Use of the latter, however, causes

significant deviations in predicted response from real data and leads to phenomenological or semi-empirical approaches. From the experimental point of view, a technique with the ability to provide volumetric data on the distribution of the constitutive parameters (E, ν … other elastic constants) of composite structures with sufficient sensitivity and spatial resolution to eliminate the need for simplistic assumptions could prove a powerful tool in the study of damage of composites.

2.2 Interferometric techniques

Phase difference calculations between the scattered waves from a specimen in both an un-deformed and a deformed state allows one to measure displacement fields across the full specimen surface with excellent accuracy (typically sub-μm). The component of displacement that is measured is determined by the geometry of the illumination and observation directions. In interferometry, wrapped phase maps (i.e., maps with phase values lying in the range –π to + π) are often obtained from the fringe patterns using a technique known as phase shifting or phase stepping. The process is often referred to as fringe analysis in the literature and relies on good fringe visibility or indeed good fringe contrast [48]. Fringe contrast is defined as:

$$v = \frac{I_{max} - I_{min}}{I_{max} + I_{min}} \ , \qquad 2.1$$

where the intensities I_{max} and I_{min} are defined by

$$I_{max} = I_o + I_M + 2\sqrt{I_o I_M} \ , \qquad 2.2$$

$$I_{min} = I_o + I_M - 2\sqrt{I_o I_M} \ , \qquad 2.3$$

and where I_o and I_M are respectively the constant ('d.c.') intensity and fringe modulation intensity. This leads to the expression

$$v = \frac{2\sqrt{I_o I_M}}{I_o + I_M} \ , v \in [0,1] \ . \qquad 2.4$$

In traditional electronic speckle pattern interferometry (ESPI), fringes are obtained by correlating two speckle patterns by either subtraction or addition [49]. The subtraction process is often preferred as it reduces optical noise and leads to speckled fringes with high contrast. However, due to the high sensitivity of the process to

environmental instabilities and the possibility to miss fast dynamic events, addition fringes may be used in order to extract the sought phase maps [50] as they eliminate the aforementioned issues. The main drawback of the latter is that fringes are of low contrast resulting in a reduction in signal to noise ratio.

A different approach is reported in [51] which is based on early observations described in [52]. In this work, the fringe pattern is obtained by multiplying instead of adding or subtracting the two speckle patterns. The fringe patterns observed are of low contrast due to the inherently noisy multiplication fringes (any noise content in the speckle patterns is now multiplied). To overcome this issue, a digital filter specific to the application was developed. An in-plane ESPI setup was used which showed that enhancement of multiplication fringes does not require rectification as in the case of subtraction fringes. The main disadvantage highlighted in the paper was that the method does not work if only one single frame is recorded.

2.3 Phase shifting interferometry

All phase-contrast optical techniques rely upon the evaluation of the phase of a fringe pattern (smooth wave-fronts) or speckled pattern, commonly known as interferograms, followed by the subsequent transformation of the latter to the parameter of interest [53, 54]. There are four main steps involved in the analysis of interferograms after the digitization of the intensity distribution as shown in the schematic diagram of figure-2.1. The first step involves the extraction of the phase (ϕ_w) by measuring the intensity as known shifts are introduced between the two interfering waves. In the next step, the phase-change ($\Delta\phi_w$) relative to some reference interferogram is calculated. In the case where the true phase-change value is slightly greater than π, the calculated value will appear to be 2π lower. This is an example of one of the main difficulties in extracting the phase, i.e. the so-called phase ambiguity problem [55]. Phase ambiguity refers to the fact that the phase can only be determined modulo 2π, i.e. the absolute fringe order is unknown. Resolution of this problem, i.e. determining the correct distribution of integer multiples of 2π to be added to the phase-change values in order to remove the 2π discontinuities, has formed the basis of a research field called phase unwrapping in the literature. Finally, in the last step the unwrapped phase map ($\Delta\phi_u$) is converted to the quantity of

interest. If the sought parameter is a displacement field (u) or the extraction of the wavenumber axis (Δk) of a tuneable laser source as in our case, a simple scaling factor is required [54].

2.4 Optical coherence tomography (OCT)

Since the early 1980's, three basic techniques for optical tomography have been adopted: a) optical diffraction tomography (ODT), b) diffuse optical tomography (DOT) and c) optical coherence tomography (OCT). Advances in OCT technology have made it possible to apply the technique to a wide variety of fields ranging from bio-medicine to materials research. An extensive list of OCT applications in bio-medicine is reported in [56-62] which includes tissue engineering, developmental biology, anterior eye imaging and retinal OCT to mention just a few. The extension of OCT to applications other than bio-medicine is fairly new and includes studies of polymer matrix composites (PMC's) [63, 64] and *in situ* testing of wires for breaks [65]. Its high depth and transverse resolutions, the fact that the former is decoupled from the latter, and its high probing depth, are amongst the advantages offered by OCT. Finally, the option of developing various function-dependent image-contrast methods place OCT among the most attractive methods for material studies [66].

The principle, on which OCT operates in order to produce cross sectional images, relies on the synthesis (B-Scans) of point depth scans (A-Scans). The terminology here is adopted from the more familiar technique of ultrasonic imaging. At first, OCT techniques were based on Time-Domain Low Coherence Interferometry (TD-LCI) and later included the implementation of Fourier-Domain Low Coherence Interferometry (FD-LCI). More recently parallel schemes have been introduced to the technique which eliminates the need for lateral scanning. In parallel schemes CCD and CMOS cameras are used as photo detectors. Advances in light sources operating in the Near Infrared Region (NIR) have made possible imaging of media that are strongly scattering in the visible wavelength range [66].

The fundamental difference of OCT techniques when compared with X-Ray Computed Tomography is that OCT techniques work on back-scattered light and therefore the Fourier slice theorem is not applicable. OCT operates on the ODT

principle, i.e. the assumption of singly-scattered photons, in contrast to DOT in which diffusely propagating photons are used [67].

2.4.1 Wavelength scanning interferometry (WSI)

Wavelength Scanning Interferometry (WSI), as well as wavelength sweeping, frequency sweeping or scanning and wavelength shifting which are all equivalent terms that are used interchangeably in the literature, dates back to the early 1980's and was proposed for Absolute Distance Measurements (ADM) by *Bien F et al* [68]. In their work they proposed a method for ADM by changing the wavelength of the source as opposed to the conventional method of phase measurement used to date. The principle of the technique relies upon the fact that in order to determine the optical path difference (OPD) between object and reference waves, the fringe order, the excess fraction and the wavelength are needed. By utilizing a tuneable source the excess fraction between two wavelengths λ_1 and λ_2 was adjusted, while the need to determine the OPD within the synthetic wavelength $\lambda_1\lambda_2/|\lambda_1-\lambda_2|$ was achieved by using a closed-loop frequency locking technique within the shot noise limit of the detector. ADM refers to the use of interferometric techniques for determining the absolute position of an object without the necessity of measuring the continuous displacements as in the case of conventional interferometry [69]. However, it was not until nearly a decade after the concept was proposed by *Bien F et al* that it was practically realized.

ADM is mainly implemented in two schemes namely multiple wavelength interferometry (MWI) and frequency sweeping interferometry (FSI). Both schemes make use of a synthetic wavelength which is much longer than the optical carrier wavelength. The synthetic wavelength increases with decreasing wavelength difference in MWI or sweep range in FSI. The resolution of the final measurement depends on phase measurements on the synthetic wavelength [70].

A typical FSI system is comprised of a Michelson type interferometer that measures the OPD and a sub-system normally based on a Fabry-Perot (FP) interferometer used to measure the frequency sweep range. The synthetic wavelength (Λ) is given by:

$$\Lambda = \frac{\lambda_1\lambda_2}{|\lambda_1-\lambda_2|}\ , \qquad 2.5$$

for MWI and is inversely proportional to the frequency sweep $\Delta\nu$,

$$\Lambda = \frac{c}{\Delta\nu} \ , \qquad 2.6$$

for FSI, where c is the speed of light. The sweep range is obtained by multiplying the free spectral range (FSR) of the FP interferometer by the number of resonances minus one (r):

$$\Delta\nu = r \cdot FSR \ . \qquad 2.7$$

From equations (2.6) and (2.7) it follows that:

$$\Lambda = \frac{c}{r \cdot FSR} \ . \qquad 2.8$$

The measured distance (L) equivalent to the OPD of the interferometer arms is given by:

$$OPD = \frac{N}{2}\frac{\Lambda}{n} = \frac{N}{2}\frac{c}{r \cdot FSR} \ , \qquad 2.9$$

where, N is the number of fringes and n is the refractive index of the propagation medium.

Dandliker R et al reported on a multiple wavelength interferometer (MWI) which increased the measurement range (200 mm) with no phase ambiguity [71], had a resolution of~10 μm and a variable sensitivity. Advances in laser source technology have established the technique in the field of optical metrology. The application of WSI in 2-D and 3-D coordinate measurements in the ATLAS experiment and vibration analysis has been reported by [72, 73] respectively.

It is worth noting that one of the major sources of error is movement or drift of the target during measurement. To compensate for this, most setups employ a second laser source – often called the reference source, of fixed wavelength [69]. However, *B. L. Swinkels et al* recently reported on correction for movement errors without the need for a second non scanning laser source [74]. The technique is applicable only to smooth drifts. The system was based on a Mach-Zehnder arrangement and combined four phase measurements in place of the more usual two previously used. The smooth drifts were achieved by heating the fibres of the system and allowing them to slowly cool down. As a result, slow fringes corresponding to drift only, and fast ones

due to the movement and frequency sweeping, were obtained as illustrated in figure-2.2.

According to [70] there are two factors generating fringes during a measurement using FSI. These are: (a) synthetic wavelength fringes (Λ-fringes) due to frequency sweep and (b) optical wavelength fringes (λ-fringes) owing to changes in distance caused by the drift. The two types are indiscernible and therefore lead to the λ-fringes being misinterpreted as Λ-fringes. As a result, the error due to the drift is amplified by a factor of Λ/λ (equation-7 in [70]). Assuming that drift occurs during a measurement of length L (equivalent to the OPD) and the drift amplitude is denoted ΔL_{drift}, the total number of detected fringes is given by:

$$N = \frac{2n}{\Lambda} L + \frac{2n}{\lambda} \Delta L_{drift} \ . \qquad 2.10$$

Equation-2.10 neglects the effect of drift on Λ-fringes and the influence of wavelength variation on λ-fringes on the basis that these generated effects several orders of magnitude smaller. Rearranging equation-2.10 gives:

$$L = N \frac{\Lambda}{2n} - \frac{\Lambda}{\lambda} \Delta L_{drift} \ . \qquad 2.11$$

Assuming a sweep range (Δν) of 50 GHz corresponding to a synthetic wavelength (Λ) of 6mm and the use of a light source operating in the visible spectrum (i.e. λ ~ 600 nm), yields an amplification factor (Λ/λ) of ~ 10,000. In other words, a 1 nm drift ($\Delta\lambda_{drift}$) would result to an error of 10μm in the measurement. This clearly demonstrates the devastating effect in high precision and accuracy measurements. Minimising the amplification factor is, therefore, of great importance. There are two ways to achieve this, either by increasing the wavelength of the source (λ) to the NIR or by decreasing the synthetic wavelength (Λ), which by direct observation of equation-2.6 corresponds to an increase in the frequency or wavelength scanning range. In the latter case, care must be taken not to increase the sweep duration as this would result in an increase of drift. Another disadvantage of this approach would be the subsequent increase in complexity of the fringe counting process due to the increase in the number of Λ-fringes. Finally, an alternative way is to directly minimise the drift ($\Delta\lambda_{drift}$) via independent relative metrology and actuate a delay line during the sweep [70]. Again this would result in an increase in complexity.

For the above mentioned reasons and under the condition that the assumption of a constant rate of drift holds, equation-2.11 was modified as follows:

$$L = N\frac{\Lambda}{2n} - sign(\Delta v)\cdot V\cdot \Delta t\cdot \frac{\Lambda}{\lambda}\ , \qquad 2.12$$

where $sign(\Delta v)$ is the sign of the frequency sweep (+1 for increasing and -1 for decreasing frequency), V is the drift velocity and Δt is the inter-sample time or sweep duration. This results in the equation

$$L_2 = L_1 + V\cdot \Delta t_3\ , \qquad 2.13$$

where L_1 and L_2 are the OPDs for two consecutive measurements 1 and 2 obtained by direct substitution of the subscripts 1 and 2 in equation-2.12 respectively, and Δt_3 represents the time between the end of the first measurement and the end of the second measurement. Consequently, the drift speed and the corrected absolute distance for the second measurement were obtained using equations 2.7, 2.12 and 2.13.

Following the work of [70] previously summarized, and realizing the importance of the sign of frequency sweeping, the authors of [75] suggested a method utilizing two lasers with opposite scanning directions to cancel drift errors. A precision of approximately 0.2μm for a 0.41m absolute distance measurement was reported. Drift is, however, not the only parameter introducing uncertainty in absolute distance interferometry (ADI) measurements. A comprehensive discussion on the various factors influencing uncertainty is provided in [70] and includes: a) turbulence and vibration, b) scale errors, c) electronics, d) ghost reflections in the detector and optical beam splitters, e) alignment errors, f) dispersive effects and g) laser diode spectral characteristics.

Thickness and refractive index measurements of thin transparent films and 2-D as well as 3-D profilometry are amongst the other fields that WSI has been applied to so far [76-80]. An important observation in the work of [78] is that when performing thickness measurements, a broad bandwidth can actually reduce the accuracy of the measurement, due to the frequency dependence of the refractive index.

The mathematical descriptions that follow aim to demonstrate the depth sensing capability offered by WSI and related techniques, and are adopted from [81]. These

were outlined in [54] and follow the earlier works of *de Groot* and *Surrel* [82-84]. The formulations are initially based on a single scattering surface to relax the mathematical complexity but will be extended to volume scatterers in the next section.

Assuming an opaque surface is illuminated and observed in an interferometric arrangement similar to that illustrated in figure-2.3, where the illumination and observation directions are parallel to the *z*-axis (i.e., the axis that measures the distance along the normal to the surface of zero OPD) then the intensity of the recorded interference signal on the pixels of a photo detector array with indices (*m*, *n*) can be expressed as:

$$\begin{aligned} I(m,n,t) &= \left|A_r(m,n,t) + A_o(m,n,t)e^{i\phi(m,n,t)}\right|^2 \\ &= \underbrace{I_o(m,n,t)}_{DC\ term} + \underbrace{I_M(m,n,t)\,cos[\phi(m,n,t)]}_{Modulation\ term} \end{aligned}, \qquad 2.14$$

where *m*, *n* are spatial indices such that $m = 0, 1, 2,..., N_{m-1}$ and $n = 0, 1, 2,\ldots, N_{n-1}$, *t* is a dimensionless time variable, ϕ is the phase shift between the object and reference waves, and A_r and A_o represent the amplitudes of the reference and object waves, respectively. Their relation to the d.c and modulation terms is described by the following expressions:

$$\begin{aligned} I_o &= A_0^2 + A_r^2 \\ I_M &= 2A_oA_r \end{aligned}, \qquad 2.15$$

The OPD between the reference and object arms of the interferometer is defined as

$$D = 2n_oz(x,y)\ , \qquad 2.16$$

where n_o is the refractive index of the surrounding medium and *x*, *y* are the coordinates of the scattering point measured in a plane perpendicular to *z*. With these in mind, the phase shift (ϕ) between the reference and object wave can be expressed by:

$$\phi = k(t)D(m,n) + \phi_s(m,n)\ , \qquad 2.17$$

where *k* is the wavenumber (2π/λ), λ is the wavelength in vacuum and ϕ_s an unknown potential shift in phase that could possibly arise upon reflection or microscopic

random contributions of scatterers that contaminate the true signal by making amplitude contributions onto the pixel (m, n).

As the name implies, WSI involves scanning of the wavelength (λ) or indeed the wavenumber (k) with time. There are two ways towards achieving this; a) to linearly change λ with time or b) to linearly change k with time. An example of the former is given in [85]. However, the authors had to develop a post processing algorithm to transform the linearly swept wavelength to linearly swept frequency in order to avoid the signal becoming chirped. After Fourier transformation this would result in peak broadening and consequently in a sacrifice in depth resolution of the system (depth resolution will be discussed later in this section). In references [3, 4] the authors scan the wavelength linearly. However, due to the small bandwidth of the source (<0.12 nm) the non-linearity is small enough to be ignored without significantly affecting the results. In the ideal case, therefore, it should be the wavenumber as opposed to the wavelength that should be linearly varied.

$$k(t) = k_c + \delta k \cdot t \ , \qquad 2.18$$

where, k_c is the central wavenumber and δk is the wavenumber increment or wavenumber step as it is often called in the literature with $\delta k \in [-\Delta k/2, \Delta k/2]$ between successive frames and $t \in [-\Delta k/2\delta k, \Delta k/2\delta k]$. Substituting equation 2.18 into 2.17 gives:

$$\phi(m,n,t) = k_c D(m,n) + \phi_s(m,n) + \delta k \cdot D(m,n) \cdot t \ . \qquad 2.19$$

Recall that:

$$\phi(m,n,t) = 2\pi f t \ . \qquad 2.20$$

Differentiating both expressions with respect to time and substituting the differentiated form of equation-2.20 after expressing it in terms of frequency (f) and substituting the result of $d\phi/dt$ obtained from equation-2.19 finally yields:

$$f_D = \delta k D(m,n)/\pi \ . \qquad 2.21$$

The importance of equation-2.21 is that it highlights the fact that a linear variation of the wavenumber with time results in an intensity modulation at a temporal frequency

$f = f_D$ which is proportional to the OPD (D). The units of f are 'cycles per frame'. An alternative way would be to express the frequency in 'cycles per scan duration':

$$\hat{f} = f\,\Delta k/\delta k \ . \qquad 2.22$$

In other words, the depth-encoding frequency shift separates the signal from different slices within the material as illustrated in figure-2.4. In WSI both modulation frequency and phase change between two successive scans are accessible. Their calculation is achieved by means of the 1-D Fourier transform [81], and will be dealt with in the subsequent sections.

In full-field swept source OCT (SS-OCT), which is the name given to WSI in the OCT community, three dimensional imaging of the structure with the best possible lateral resolution throughout also requires scanning of the focus. *Marks DL et al* suggested that by solving the inverse scattering problem, it is possible to reconstruct the full three dimensional volumes while the focus is fixed at one plane. It is known that the lateral resolution of OCT systems is determined by the point spread function (PSF=1.22λ/NA) which in turn is a function of the numerical aperture of the system. Low NA systems can tolerate defocus due to the large depth of field. However, this is not the case for high NA and defocus needs to be taken into account. The authors report on the simulation of an algorithm that recovers the object structure both inside and outside the depth of field and hence allows for focus to be fixed at a particular plane even for high NA systems [86]. Two years later, the same authors reported on a model for SS-OCT with partial coherence that has the advantage of diffraction limited resolution in regions usually regarded as out-of-focus. In their work, they claim that the partial spatial coherence of the source is advantageous, in that it mitigates against multiple scattering effects that are known to be responsible for artefacts in whole-field coherent imaging [87].

2.4.2 Fourier-domain optical coherence tomography (FD-OCT)

Fourier domain OCT (FD-OCT) or spectral OCT (SOCT) as it is often called can be viewed as a parallel version of WSI. In WSI the recorded interference signal is modulated along the time axis. On the other hand, in SOCT the signal is modulated along a spatial axis (spectrometer axis) that samples a range of wavelengths simultaneously as opposed to the sequential sampling that takes place in WSI. As in

WSI, a broadband source (BBS) with a bandwidth $\Delta\lambda$ and a wavelength λ centred at λ_c is also used here to illuminate the reference surface and a sheet of scattering points within the test sample (object). After recombination of the reference and object beams at the beam splitter (BS), the signal is passed through a diffraction grating (G) which spatially separates the different wavelengths. The latter form an interference pattern on a two dimensional photo detector array [5]. A schematic representation of a typical SOCT setup is illustrated in figure-2.5.

Considering that the sample consists of a set of slices, each of which has a thickness equal to the depth resolution of the system δz, then the phase difference between the reference beam and the light backscattered from the j^{th} slice of the sample [5] is:

$$\phi_j(k) = \phi_{j0} + 2kz_j \ . \qquad 2.23$$

Following a similar approach to that in section-2.4.1 the spatial frequency along the k-axis is:

$$f_k = \frac{1}{2\pi}\frac{\partial\phi}{\partial k} = \frac{z_j}{\pi} \ . \qquad 2.24$$

Assuming weak scattering within the material (an assumption normally adopted in OCT) and that the object consists of N_k independent slices, the intensity distribution along the k-axis ($I(k)$) can then be expressed as follows:

$$I(k) = \underbrace{I_0}_{DC} + \underbrace{2\sum_{j=1}^{N_k}\sqrt{I_R I_j}\,cos\left[\phi_j(k)\right]}_{Cross-corelation} + \underbrace{2\sum_{i=1}^{N_k}\sum_{j=i+1}^{N_k}\sqrt{I_i I_j}\,cos\left[\phi_i(k)-\phi_j(k)\right]}_{Autocorrelation} \qquad 2.25$$

Note that equation-2.25 is a generalised form of equation-2.14 and accounts for volume scatterers. Terms I_R and I_j represent the intensities coming from the reference and the j^{th} layer respectively. The cross-correlation term corresponds to the intensity modulation along the k-axis with frequencies $f_{kj} = z_j/\pi$, with the latter being proportional to the optical path difference between the reference and the object surfaces. The third term is associated with the autocorrelation or auto-interference of light from within the object and is closely related to the main assumption in OCT systems of weak scattering. $\phi_i(k)$-$\phi_j(k)$ is the phase difference introduced to the light

scattered from the i^{th} and j^{th} layers within the object and can also be represented in terms of frequencies:

$$\phi_i(k) - \phi_j(k) = 2\pi\left(f_{ki} - f_{kj}\right)k \ . \qquad 2.26$$

That in turn can also be related to the optical path difference between these layers according to:

$$f_{ki} - f_{kj} = \frac{z_i - z_j}{\pi} \ . \qquad 2.27$$

The sought modulation frequency is obtained by the 1-D Fourier transformation of $I(k)$ for a single scattering surface. The mathematical description that follows is the same as that reported in reference [81] but applied in the k-space as opposed to t-space. The Fourier transform of a set of N_k sampled intensity values $I(k)$ can be expressed as follows:

$$\tilde{I}(\hat{f}) = \int_{-\infty}^{+\infty} I(\check{k})\, W(\check{k})\left[\sum_{k'=-\infty}^{\infty} \delta(\check{k} - k')\right] e^{-\frac{2\pi i \hat{f} \check{k}}{N_k}} d\check{k} \ , \qquad 2.28$$

where, δ is the Dirac delta function, $\check{k}$ is a continuous version of the discrete variable k, $W(\check{k})$ is a continuous and even window function which is non-zero only for $|\check{k}| \leq N_k/2$ and $\hat{f}$ is a continuous non-dimensional spatial frequency. Finally, k' is where the sampling takes place. Considering the right hand side of equation-2.28 as the Fourier transform of a sampled (discrete) intensity distribution multiplied by a continuous window function, then by the convolution theorem:

$$\tilde{I}(\hat{f}) = \widetilde{W}(\hat{f}) * \sum_{j=-\infty}^{\infty} \begin{bmatrix} I_o \delta(\hat{f} - jN_k) + \frac{I_M}{2} e^{i\phi_o} \delta(\hat{f} - jN_k - \hat{f}_D) \\ + \frac{I_M}{2} e^{i\phi_o} \delta(\hat{f} - jN_k + \hat{f}_D) \end{bmatrix} . \qquad 2.29$$

In the case of volume scatterers, equation-2.29 takes the form [81]:

$$\tilde{I}(\hat{f}) = \begin{matrix} \left(A_r^2 + \sum_{i=1}^{N_k} A_i^2\right)\widetilde{W}(\hat{f}) + A_r \sum_{i=1}^{N_k} A_i e^{\pm i\phi}\, \widetilde{W}(\hat{f} \pm \hat{f}_{D,i}) \\ + \sum_{i=1}^{N_k} \sum_{j=i+1}^{N_k} A_i A_j e^{\pm i[\phi_i(k) - \phi_j(k)]}\, \widetilde{W}\left[\hat{f} \pm (\hat{f}_{D,i} - \hat{f}_{D,j})\right] \end{matrix} . \qquad 2.30$$

Note that the index (i) takes two different meanings. In the summation symbol, it indicates the i^{th} layer while in the exponential form it is used to express the usual complex quantity ($i = (-1)^{1/2}$). Additionally, all the terms above the Nyquist limit have been dropped for simplicity.

The second term of equation-2.30 (volume scatterers) or equation-2.29 (single scattering surface) provides means of mapping the internal structure of the object under study and needs to be separated from the autocorrelation term to avoid cross-talk [88, 89]. This is usually achieved by moving the reference surface (*R*) away from the object (see figure-2.5 for example). However, this has the undesirable effect of halving the effective depth range of the system [5, 81] (see figure-2.6 and figure-2.7). An alternative way of separating the two terms without the compromise of reducing the depth range of the system was reported by *M, Wojtkowski et al* in reference [90]. The authors demonstrated a way to suppress the autocorrelation term by using phase shifting. Another approach was reported by *Steiner P, Meier C and Koch VM* where a simple background subtraction technique is applied which seems to minimise the artefacts caused by the interference between the autocorrelation and cross-correlation terms [89].

In SOCT, depth range (Δz) is defined as the maximum optical path difference between the i^{th} slice within the object and the reference surface and is limited by the spectrometer resolution. The modulation frequency f_k in equation-2.24 is limited by the Nyquist frequency ($N_k/2\Delta k$). N is the number of pixels required to sample $I(k)$ over a total wavenumber range of $2\pi\Delta\lambda/\lambda^2_c$ [5]. Therefore:

$$\Delta z = \frac{N\lambda_c^2}{4\Delta\lambda} \ . \qquad 2.31$$

The depth resolution, which essentially is the minimum size that can be fully resolved in the Fourier domain by the system, is given by:

$$\delta z = \gamma \frac{\lambda_c^2}{\Delta\lambda} \ , \qquad 2.32$$

where γ is a constant associated with the shape of the window function. For a rectangular window $\gamma = 1$ or $\gamma = 0.603$ depending on whether the resolution is measured as the distance between first zeroes or the FWHM (full width half maximum of the Fourier peak). In the case of a Hanning window, $\gamma = 2$ or $\gamma = 1$ respectively [91]. Strictly speaking, the use of a rectangular window would result in a narrower peak and therefore in a lower depth resolution. However, this comes at the expense of the signal becoming contaminated by side lobes. For this reason, a Hanning window is often used as it reduces the side lobes but increases the width of

the peak. Another type of windowing function was reported in reference [92], with the particular characteristic of all the side lobes on either side of the peak having the same maximum level. Its application, however, also resulted in peak broadening. An alternative way to evaluate the depth resolution is by considering the round trip of the light source giving a theoretical lower limit of $\gamma = 2ln2/\pi$ [66, 90].

From equation-2.31 and equation-2.32 it is clear that the larger the bandwidth of the source, the better the depth resolution of the OCT system. Realizing this, a significant amount of research has been conducted over the past few years in order to develop laser sources with as wide a bandwidth as possible [16, 24, 93, 94]. An excellent summary of the available laser sources for OCT was reported in table-1 in reference [66]. Table-2-1 below is an updated version of the aforementioned table providing a more recent summary of the advances in laser source technology for OCT. The different laser sources have been grouped in terms of the central wavelength (λ_c), bandwidth ($\Delta\lambda$), coherence length (l_C) and deliverable power.

Table-2-1: Examples of sources used in OCT. (Updated table-1 in [66].)

Light source	λ_c (nm)	$\Delta\lambda$ (nm)	l_C (μm)	Power	Ref	Year
SLD	675	10	20	40 mW	[95]	’02
	820	20	15	50 mW		
	820	50	6	6 mW		
	930	70	6	30 mW		
	1300	35	21	10 mW		
	1550	70	15	5 mW		
Kerr lens						
Ti:Sapphire	810	260	1.5	400 mW	[96, 97]	’95,’99
	795	130		1 mW	[98]	’08
Cr:Forsterite	1280	120	6	100 mW	[99]	’96
Cr:LiCAF	715	89		37 mW	[100]	’04

Table-2-1 continued

Light source	λ_c (nm)	$\Delta\lambda$ (nm)	l_C (μm)	Power	Ref	Year
Cr:LiSAF	890	220		few mW	[101]	'91
	1240	40	17	0.1 mW		
LED					[102]	'97
	1300					
ASE fibre sources	1300	40	19	60 mW	[103]	'02
	1550	80	13	40 mW		
Super fluorescence						
Yb-doped fibre	1064	30	17	40 mW	[104]	'98
Er-doped fibre	1550	80-100	16	100 mW	[105]	'98
Tn-doped	1800	80	18	7 mW	[105]	'98
	1300	370	2.5	6 mW	[106]	'01
Photonic crystal fibre	725	370	0.75		[107]	'02
	800	110		30 mW	[108]	'06
	1300	150		48 mW	[108]	'06
Thermal tungsten	880	320	1.1	0.2 μW	[109]	'00
halogen					[110]	'02
Parametric down-conversion						
Krypton Ion/LiO_3	812	200		few pW	[111]	'06

Note: ASE refers to amplified spontaneous emission in laser technology. Source: [112-114].

From the table above, it is evident that solid-state lasers (i.e. Ti:Sa *etc.*) provide a good compromise between available power and bandwidth, thereby placing them at the forefront of laser sources suitable for OCT applications. An interesting approach for increasing the spectral bandwidth of the source was reported by *Tony H. Ko et al.,* where the authors suggested coupling the output from two single SLDs and achieved an overall source spectral width of 155nm [115] (see figure-2.7).

Gong JM et al approached the issue of the source's influence on the resolution from a different angle. They demonstrated that resolution can be improved by means of a

post-processing modeless reshaping of the source spectrum. Their work concludes stating: *'the optimal spectrum has a priori surprising ``crater-like`` shape, providing a 0.74 micron axial resolution in free space, representing a ~50% improvement compared to the resolution using the original spectrum of a white light lamp'* [116].

2.4.3 Phase-contrast optical coherence tomography (PC-OCT)

Phase contrast, as the name implies, refers to the determination of phase. PC-OCT encompasses the family of techniques that is not restricted to imaging the amplitude of the interference signal. Instead it takes advantage of the full potential of the interferometric nature of OCT by allowing, in addition, the calculation of phase maps. The first to have demonstrated PC-OCT in solid mechanics are the authors of [5]. In their work the phase change between two states – a deformed and an un-deformed state, was obtained using the difference of phase equation stated in [54]. The advantage of this approach is that it allowed evaluation of the phase change before and after deformation in a double shot, hence eliminating the need to evaluate each phase separately and subtract them afterwards. The calculation of the out-of-plane displacement was achieved by:

$$w_j = (n_0 - n)d_1 + nd_j \ , \qquad 2.33$$

where, d_1 being the displacement corresponding to the surface of the object (slice 1:S_1) and d_j that of the j^{th} slice (a subsurface slice: S_j) – refer to figures: 2.4, 2.5 for schematic illustrations). Equation-2.33 implies that the refractive index of the material is the same throughout the volume. This, however, is clearly not the case for composite materials. For this reason, the authors suggested that, 'for more complex distributions of known refractive index within the object an integral over [d_1,d_j] and therefore the displacement of shallow slices should be calculated first and used to correct the displacement of deeper ones' [5].

It is worth noting that this assumes *a priori* knowledge of the refractive index of the material and also that it does not change during the loading scheme. The latter being the basis of depth resolved imaging and displacement measurement techniques seen as linear filtering operations [35, 36]. From the above it follows that, since displacement sensitivity is the minimum displacement the system can detect, it depends on the minimum phase change that can be detected by the system [5].

Three years later the same authors reported on a PC-OCT technique to simultaneously measure both in-plane and out-of-plane displacement fields within scattering media [7]. In biomedical applications the technique is predominantly used for flow determination and therefore utilises the Doppler Effect [117, 118].

2.4.4 Optical coherence elastography (OCE)

Disease is known to alter the mechanical properties of tissue on scales spanning from nanoscopic (subcellular) to macroscopic (whole organs). Elastography maps the local mechanical properties of tissue by measuring the deformation in response to mechanical loading. The technique is based on the analysis of images, commonly termed as elastograms in the literature [119], that encode the axial or lateral strains, the elastic moduli and/or the Poisson ratio distributions in tissues. From a historical point of view the method was largely developed as a diagnostic tool using ultrasound in the 1980's and magnetic resonance imaging (MRI) in the 1990's [120]. Optical imaging techniques that date back to the early 1950's were proposed by *Jacques et al.* [121] and Schmitt [122] for elastography applications. A list of insightful and recently published review papers on which the information presented henceforth relies upon can be found in refs [123-125].

OCT-based elastography relies on 2-D cross-correlation algorithms on OCT amplitude images to detect the speckle shifts and consequently estimate motion in OCT image sequences. A good example of the technique was reported by *Kirkpatrick SJ et al* who demonstrated the quantification of displacements, strains and strain rates for both small and large speckle motions [126].

In general, in elastography there are four key parameters that determine the performance of the system. These are:

a. The imaging resolution, also known as depth resolution in the OCT community.
b. The data acquisition speed.
c. Mechanical sensitivity, also known as displacement sensitivity in the field of interferometry.
d. Image penetration, or in other words the depth range of the system.

In optical coherence elastography the depth resolution is in the order of 1-10 μm and is considerably better than that offered by ultrasound elastography and magnetic resonance elastography (MRE).

As far as data acquisition speeds are concerned, OCE offers once again superior data acquisition speeds that span from 10s to 100s of kHz [127], due to the continuous development in laser technology, compared to ultrasound elastography which is limited by the speed of sound and MRE, although multi-kHz 2-D scans have been reported with supersonic shear imaging (SSI) [128].

Displacement sensitivity is another key parameter that is affected by the frequency or the wavelength of the type of wave (light or sound) employed to perform the measurement. A typical value of the measurement sensitivity in DSPI is $\lambda_c/30$ from which it is clear that the smaller the wavelength used the higher the measurement sensitivity. This is an inherent advantage that optical techniques possess over their contenders in the field of non-destructive testing (NDT) like ultrasound and magnetic resonance.

Finally, the image penetration in OCE is significantly lower to that offered by ultrasound elastography and MRE with typical values in the order of a few millimetres. To overcome this limitation, endoscopic or needle versions of OCE have been developed [129].

The first optical coherence elastography technique was reported in 1998 by *Schmitt JM* [122] and was based on a TD-OCT system. It followed seven years after the first demonstration of OCT in 1991 [130]. Ever since the first OCE demonstration, a number of different techniques have emerged which are commonly referred to as OCE in the literature. Classification of the different OCE types can be done in different ways. One approach that is commonly used in the literature is based on the loading scheme used in [123]. For example, in the case of spatial excitation of the sample, OCE techniques are classified as internal or external excitation OCE. If on the other hand a temporal excitation is used, OCE techniques can be classified as either static or dynamic. Figure-2.9 shows a schematic illustration of the loading type classification of OCE techniques. Figure-2.9 (reprinted fig.2 in ref [125]) provides schematic illustrations of (a) external excitation static/quasi-static OCE, (b) external

excitation dynamic OCE and (c) internal excitation dynamic OCE. A demonstration of internal excitation (thermal loading) static/quasi-static OCE can be found in ref [131].

2.4.5 Polarization-sensitive optical coherence tomography (PS-OCT)

Polarization sensitive OCT has been the first and to date the only OCT technique applied as a non-destructive tool for characterization of composite materials [25]. The technique is based on the principle of photo elasticity and typical setups are based on Michaelson interferometers with the necessary additions of optical components for photo elasticity. The technique utilises pulsed broad bandwidth light sources [22] and is based on monitoring the birefringence of the material. Its abilities are not restricted to imaging only the morphology of the structure, but have also been extended to strain-field mapping [22, 132, 133]. It is worth noting that all the works referring to strain or stress field mapping refer to residual stresses that already exist within the structure and are probably induced during the manufacturing process or service of the material in question.

Arne Røyset reported on a novel noise model to monitor the birefringence accurately [134]. Measurement and imaging of backscattered intensity, birefringence, and fast optic axis orientation was reported by [135]. The optic axis orientation was determined from the phase difference recorded in two orthogonal polarization channels.

2.5 Summary of WSI [21]

The absolute measurement of optical path differences by Wavelength Scanning Interferometry has a long history, though several different terms have been used to describe essentially the same technique. For example, optical frequency domain reflectometry was developed to locate defects in optical fibres [136, 137], in the OCT community it is commonly called Wavelength Tuning Interferometry, or 'swept-source' [138, 139]. Variations on the basic theme, called Frequency Scanning Interferometry in [140], have also been developed for large volume metrology applications. Parallel versions of WSI were developed in the mid-90s for profilometry applications [141, 142] in which each pixel of a 2-D array is turned into an independent range sensor. More recently, de Groot described a wavelength

scanning interferometer able to separate the interferograms from two different optical surfaces on a common optical path [143]. A phase shifting formula tuned to the temporal frequency of the surface of interest effectively eliminated the signal from the unwanted surface, allowing an accurate phase map of the first surface to be obtained. The use of phase information to measure 2-D depth-resolved displacement fields takes this idea a stage further. Proof-of-principle experiments on a pair of specularly-reflecting surfaces [3] showed how independent displacement fields associated with rigid body rotation of the two surfaces could be separated. In these cases, a windowed Fourier transform was used to separate the signal from the different surfaces and to extract phase maps. Phase difference maps then encoded the out-of-plane displacement field.

What follows is a summary of the governing equations in WSI and SS-OCT. To avoid complexity, a two-beam interferometer is considered, which is applicable to the case of a single scattered object wave interfering with a reference wave. This produces a single Fourier peak for each camera pixel in the volume reconstructions. Weakly scattering media generally give rise to multiple-beam interference patterns, which result in multiple Fourier peaks. However, the two cases have identical depth resolutions, and unambiguous depth ranges that differ by only a factor of 2 [81].

Consider the light received by a detector at location (x, y) within a 2-D photo detector array. The intensity is given by [91]:

$$I(x,y,k-k_c) = \begin{matrix}\{I_0(x,y) + I_1(x,y)\,cos[(k-k_c)]\Lambda_0(x,y) + \phi_0\} \\ \times W(k-k_c)\end{matrix}\ , \qquad 2.34$$

where k is wavenumber, k_c is the wavenumber at the centre of the scan range, ϕ_0 is a phase offset, Λ_0 is the optical path difference between the interfering beams, I_0 and I_1 are respectively the background (d.c) and fringe modulation intensities, and $W(k\text{-}k_c)$ is a function to represent the case either of windowing the data to reduce spectral leakage, or of a non-uniform laser power during a wavelength scan.

k is changed with time over a total range Δk whilst image sequences are recorded using the 2-D photo detector array. Ideally one aims for a linear variation of k with t, i.e.

$$k(t) = k_c + \delta k \cdot t\ , \qquad 2.35$$

where k_c is the central wavenumber, Δk is the increment in wavenumber between successive frames, and integer variable t ranges from $-\Delta k/\delta k$ to $\Delta k/\delta k$. The Fourier transform of equation-2.34 may be calculated using the Fourier shift and convolution theorems as follows [81] :

$$\tilde{I}(\Lambda) = \left[I_0\delta(\Lambda) + \frac{I_1}{2}\delta(\Lambda - \Lambda_0)e^{i\phi_0} + \frac{I_1}{2}\delta(\Lambda + \Lambda_0)e^{-i\phi_0}\right] * \left[\widetilde{W}(\Lambda)e^{-ik_c\Lambda}\right] \quad 2.36$$

in which the (x, y) dependence has been dropped for clarity, where δ (...) is the Dirac delta function, $\widetilde{W}(\Lambda)$ is the Fourier transform of $W(k)$, and where * represents convolution. A copy of $\widetilde{W}(\Lambda)$ is centred on each of the three delta functions at $\Lambda = 0$ (the d.c term) and $\Lambda = \pm \Lambda_0$ (the cosine term).

2.5.1 Critical parameters in WSI

There are two main parameters that define the performance of WSI system. These are, the depth range (i.e. how deep inside the material the system can image) and the depth resolution or optical path resolution (i.e. what is the smallest size in the internal structure of the material under test that can be resolved by the system).

The maximum unambiguous depth range is given by the Shannon sampling theorem which states that in order to ensure adequate sampling of the $I(x,y,k-k_c)$ signal, the term $k\Lambda_0(x,y)$ in equation-2.34 should not change by more than π between successive k samples. This leads to a maximum allowed value of $\Lambda = \Lambda_M$ where:

$$\Lambda_M = \frac{\pi}{\delta k} , \quad 2.37$$

and where δk is the (constant) wavenumber jump between frames. Any larger Λ values will be aliased onto a lower Λ value thus creating an under-sampling artefact.

The minimum allowed value of Λ, on the other hand, is $\Lambda = 0$, because the cosine function in equation-2.34 is even. Negative Λ values cannot therefore be distinguished from positive ones. We therefore have the allowable path difference range

$$0 \leq \Lambda \leq \Lambda_M \ . \quad 2.38$$

The discrete Fourier transform $\tilde{I}(x.y,\Lambda)$ contains $N_k/2$ positive frequency components, where N_k is the number of k samples, with a separation between sample

points of $2\pi/(N_k\delta k)$. The width of the spectral peak (i.e., distance between zero crossing points) is $4\pi/(N_k\delta k)$ for the case of a uniform spectral profile of width $N_k\delta k$. If the spectrum is not uniform but rather has a non-constant profile $W(k\text{-}k_c)$, then the width of the peak is given by the width of $\widetilde{W}(\Lambda)$. In general we can write the width of the spectral peak as,

$$\delta\Lambda = \gamma \frac{2\pi}{N_k \delta k} \ , \qquad 2.39$$

where the constant γ takes the value 2 for a rectangular window, and 4 for a Hanning window, for example. If, on the other hand, the width is measured on a full width half maximum (FWHM) basis then the corresponding γ values are 1.207 and 2.000, respectively.

The relationship between optical path length resolution, δΛ, and the corresponding depth resolution, δz, depends on the geometry of the illumination and observation directions. For the typical case of backscattered light (illumination and observation directions coincident),

$$\delta z = \delta\Lambda/2n \ . \qquad 2.40$$

2.5.2 Electronically tuned laser sources in WSI

Over the past two decades, wavelength scanning interferometry has become quite popular in the fields of profilometry and absolute distance measurement (ADM) owing to the developments in electronically tuned laser source technology. Table-2.2 below provides a historical review, in chronological order, of the different types of tuned laser sources used in WSI over the last twenty years.

Table-2.2: Historical review in chronological order of the different light sources used in WSI and their corresponding application. λ_c: central wavelength, Δλ: tuning range used in the experimental results of the corresponding reference, Power: max power output of light source, Inter.type: Interferometer setup used.

Source	λ_c	Δλ	Power	Inter.type	Application	Ref
Diode laser	670nm	20nm	10mW	Michelson	Profilometry	[141]
Dye laser	577nn	25nm	300mW	Michelson	Profilometry	[142]

Table-2.2 continued

Source	λ_c	$\Delta\lambda$	Power	Inter.type	Application	Ref
Diode laser	577nm	25nm	2.5mW	Michelson	Topometry	[144]
Dye laser	577nm	4.2nm	300mW	Michelson	Profilometry	[145]
Dye laser	577nm	4.2nm	300mW	Michelson	Profilometry	[146]
Diode laser *SDL TC-40*	776nm	8nm	500mW	Michelson	Height gauging	[147]
Solid state Ti:Sa	791.1nm	102.3nm	300mW	Michelson	NA	[148]
NA	680nm	7.5pm	NA	Fizeau	Flatness test	[143]
Diode laser *SDL TC-40*	775.8nm	6.4nm	500mW	Michelson	Profilometry	[149]
Solid state Ti:Sa	791.15nm	102.3nm	300mW	Michelson	Step gauging	[26]
Diode laser	1556nm	4nm	NA	Fizeau	ADM	[150]
Dye laser	573.8nm	4.28nm	300mW	Michelson	Profilometry	[76]
Diode laser	690.7nm	0.028nm	NA	Fizeau	ADM	[151]
Diode laser	633nm	0.134nm	15mW	Fizeau	Profilometry	[31]
Diode laser	690.7nm	0.25nm	NA	Fizeau	Surface shape and optical thickness	[77]
Diode laser	690nm	0.095nm	NA	Fizeau	Surface shape	[152]
Diode laser	670.15nm	10.1nm	NA	Fabry-Perot	ADM	[73]
Diode laser	690nm	0.095nm	NA	Fizeau	Surface shape and optical thickness	[153]

Table-2.2 continued

Source	λ_c	$\Delta\lambda$	Power	Inter.type	Application	Ref
Shapix™ 2000	840nm	16nm	NA	Michelson	Profilometry	[154]
Diode laser *Agilent 81680A*	1534nm	8nm	15mW	Mach-Zehnder	Effect of detuning in swept sources	[155]
Diode laser	1550nm	4nm	NA	Fizeau	ADM	[156]
Shapix™.	622.5nm	15nm	15mW	Michelson	Height gauging	[157]
Diode laser	637nm	10nm	NA	Fizeau	ADM	[158]
Diode laser	841nm	16nm	NA	Pseudo-Fizeau	ADM	[159]
Custom	1569nm	18nm	5mW	Fizeau	Surface profilometry	[160]

2.6 Summary and conclusions

This chapter has provided a detailed overview of the main developments in the related fields of absolute distance measurement and depth resolved measurement of displacement fields in weakly scattering materials, as well as the light sources used for the optical measurement techniques. It is clear that an optical approach is appropriate to the problem of depth resolved displacement field measurement in composites because of the required spatial resolution. This is of the order of 10 μm or better, to match the length scale of the microstructural features and damage regions. A wide tuning range of 100 nm or more is required to achieve such depth resolutions. Parallel OCT is preferred to scanned pointwise OCT, to ensure the stability when measuring phase difference maps from two different scans. The rest of the thesis describes the development of a system based on an electronically tuneable Ti:Sa source. The fairly limited penetration depth of a few mm will be partially overcome by the use of multiple illumination directions, which will also provide the ability to measure multiple displacement components.

2.7 Figures

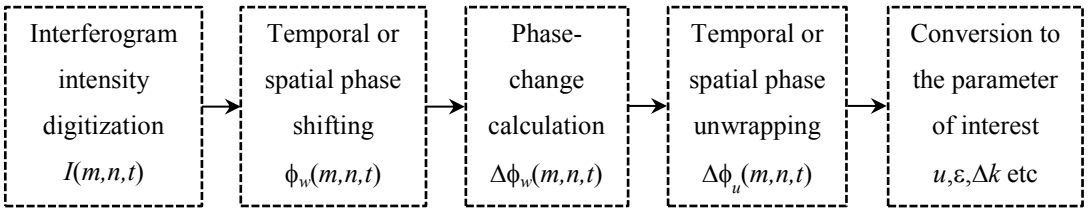

Figure-2.1: Schematic diagram showing the main processes involved in the analysis of interferograms. I (m, n, t) is the intensity distribution in the interferogram with m, n being the spatial indices and t a dimensionless time index. ϕ is the phase of the intensity signal and $\Delta\phi$ the change in phase relative to some reference state. Subscripts w and u indicate whether the phase or phase change is wrapped or unwrapped. Finally, u,ε and Δk are examples of parameters that the unwrapped phase change $\Delta\phi_u$ may be converted to, and correspond to displacement map, strain map or wavenumber axis respectively. Reproduced variation of figure-2.1 in [54].

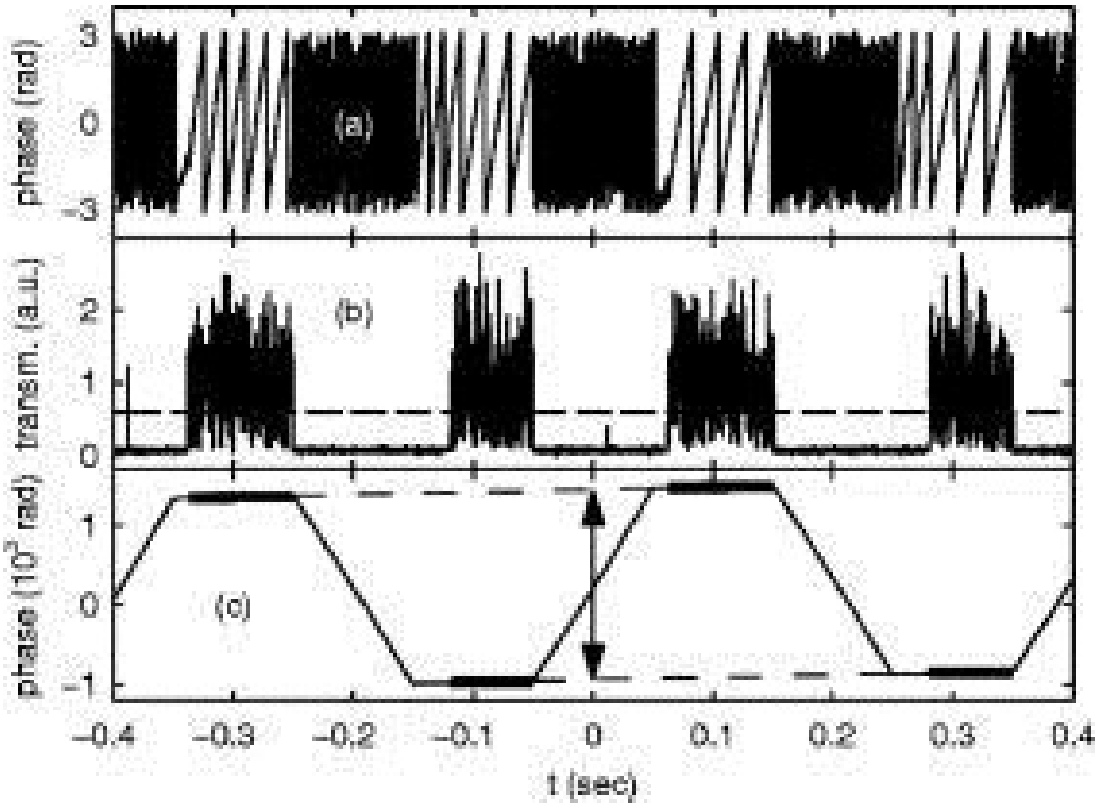

Figure-2.2: (a) interferometric phase, (b) transmission of the Fabry-Perot cavity, (c) unwrapped phase of (a). The dashed line indicates the threshold value. (Figure adopted from [74]).

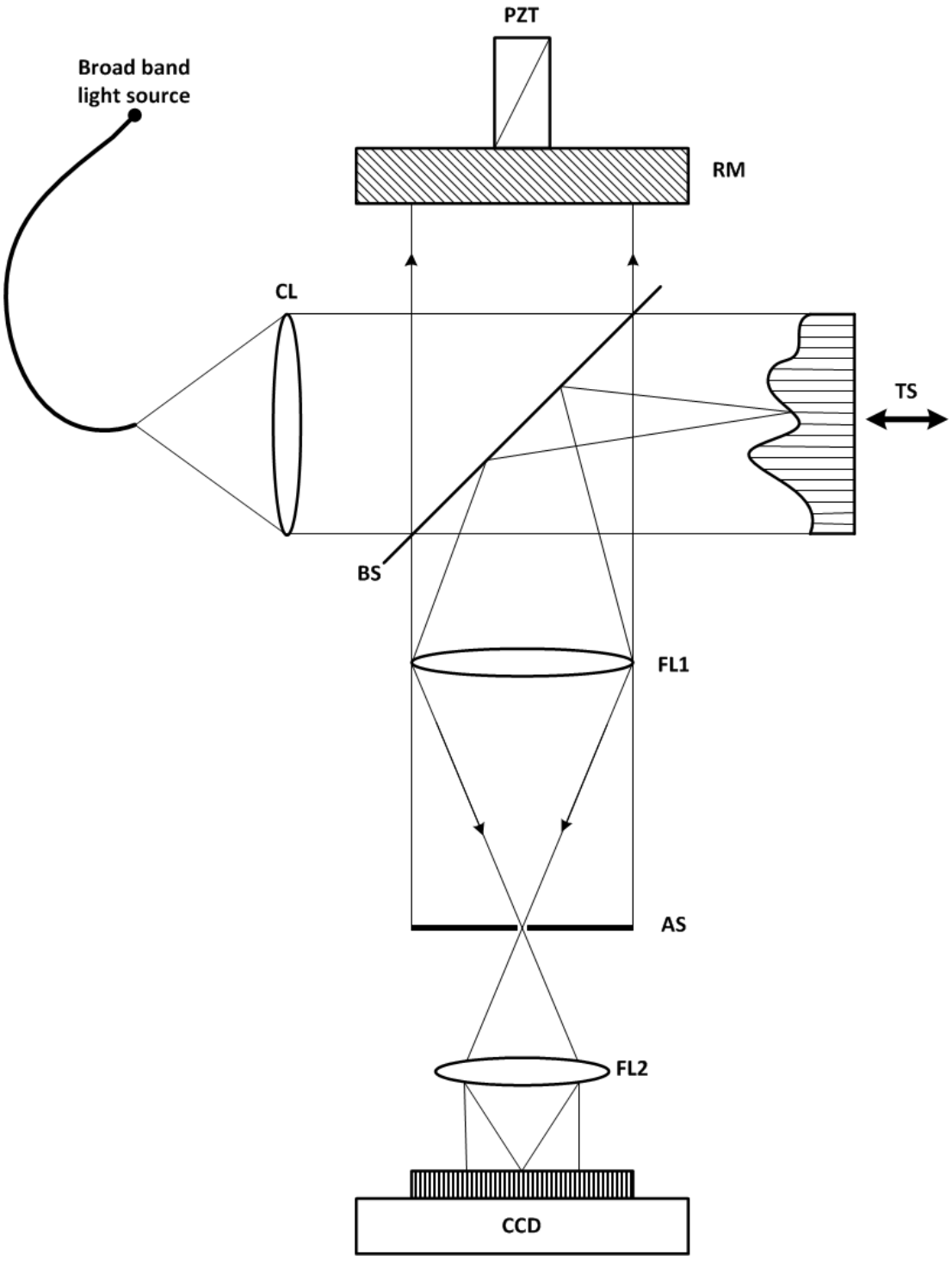

Figure-2.3: Illustration of a typical scanning white light interferometer (SWLI) setup. CL: Collimating lens, PZT: piezo-electric transducer, RM: reference mirror, BS: Beam splitter, TS: Test sample, FL1: Focussing lens 1, AS: Aperture stop, FL2: Focussing lens 2. Source: [81].

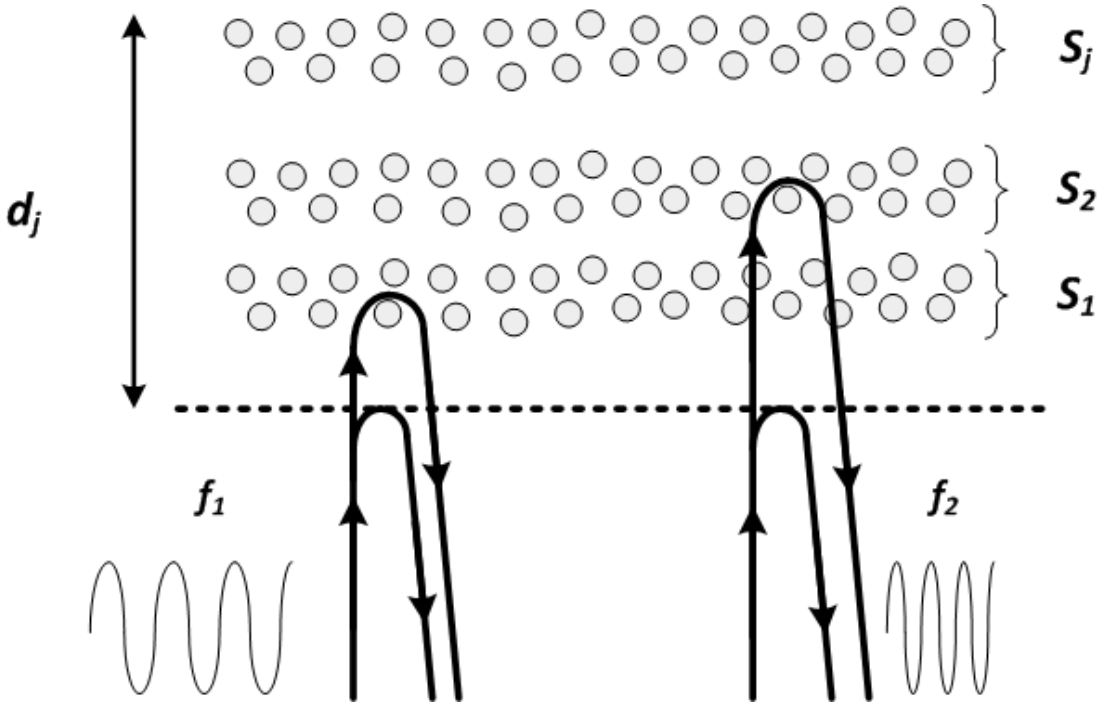

Figure-2.4: Schematic illustration of how the depth encoding frequency shift separates the signal from different slices within the material in WSI. *S*: Slice, *d*: depth, *f*: frequency of light. Source: [161].

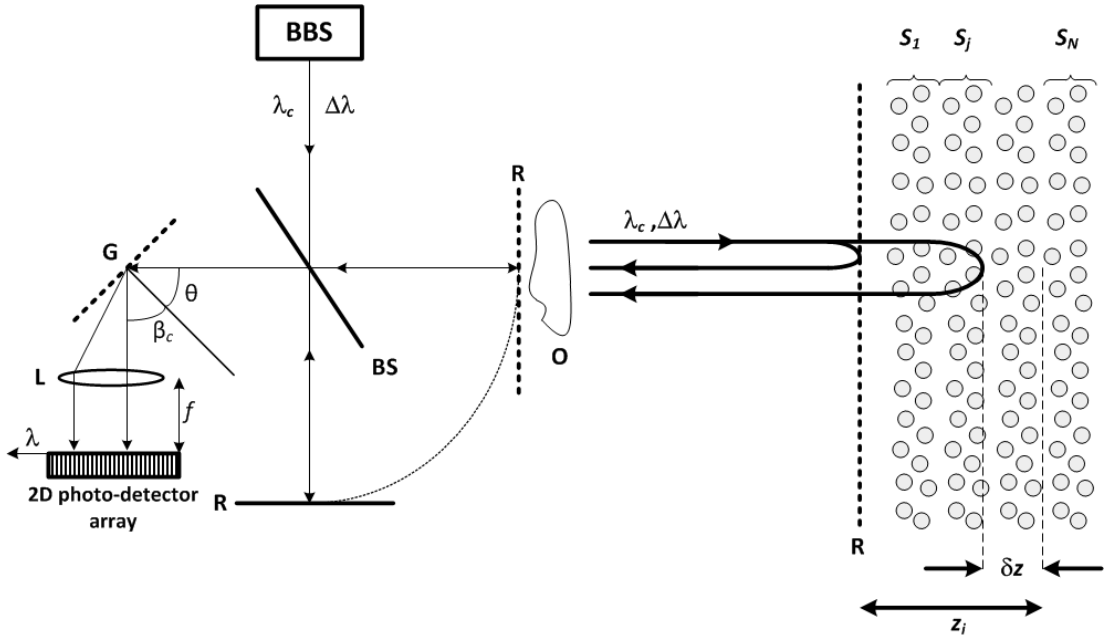

Figure-2.5: Schematic representation of a SOCT system. Broadband source (BBS), beam splitter (BS), object (O), reference mirror (R), diffraction grating (G), lens (L) with focal length *f* and 2-D photo detector array. β_c is the diffraction angle of the central wavelength and θ is the incident angle of the light from the broadband source. Reproduction of fig-1 in reference [5].

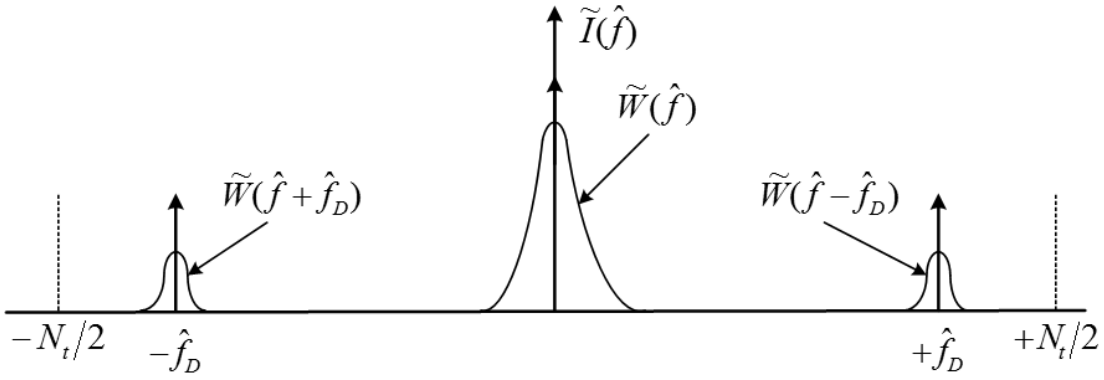

Figure-2.6: Schematic diagram of a 1-D Fourier transformation of $I(k)$ at one pixel in a SOCT system with a sample cosisting of a single scattering surface. (Adopted and adjusted for SOCT, source: figure-2.7 in [81].)

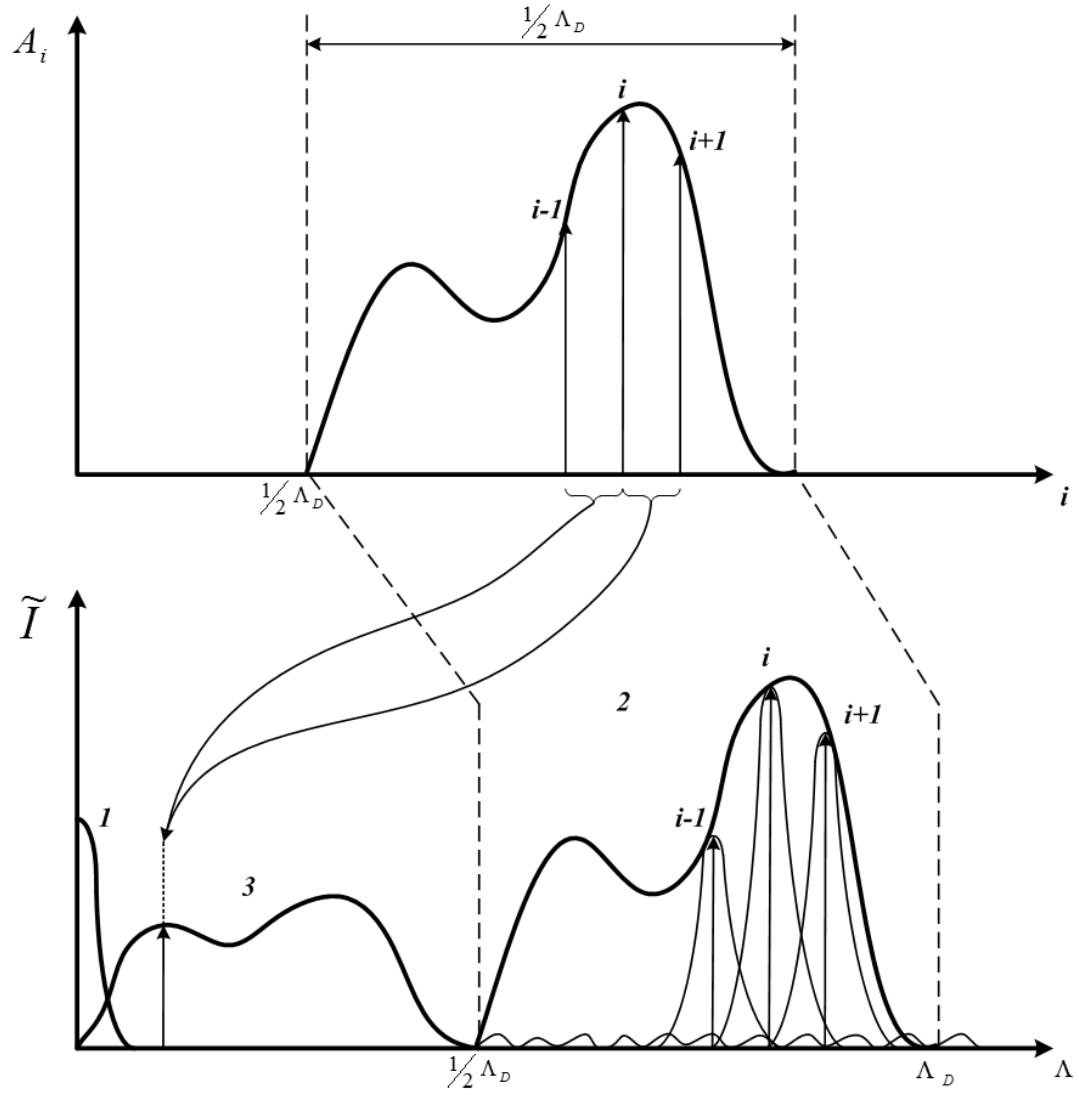

Figure-2.7: Scattered light amplitude distribution N_k scattering layers (top) and reconstruction from the Fourier transform (below) of the intensity at a single camera pixel. Labels 1, 2, 3 correspond to the three terms of equation-2.30. Note that Λ_D is the max allowable OPD. (Adaptation of figure-2.10 in [81].)

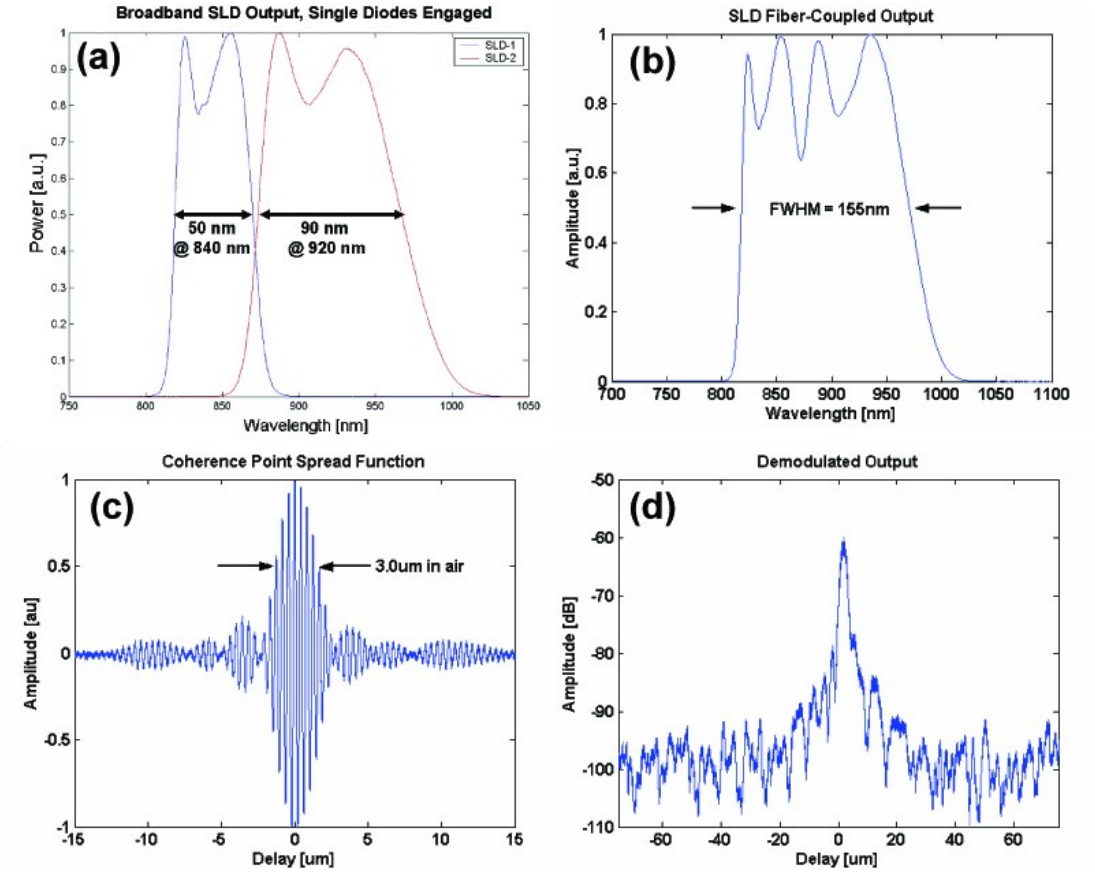

Figure-2.8: (a) Individual output spectra of the two super luminescent diodes. (b) Fibre-coupled multiplexed spectrum of the broadband SLD source. (c) Coherence point spread function of the broadband SLD source. (d) Logarithmic demodulated coherence point spread function. A 3.0 OD filter was used to prevent detector saturation.(Source: fig.2 in [115]).

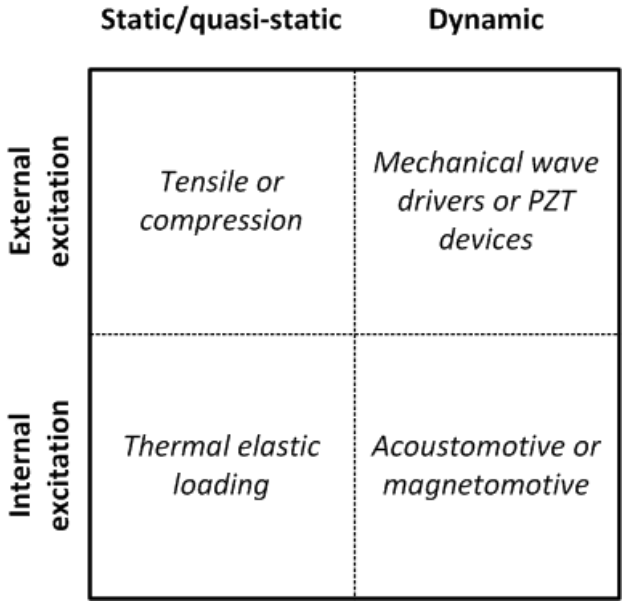

Figure-2.9: Classification of OCE techniques based on loading type scheme. Adaptation of fig.1 in ref [123].

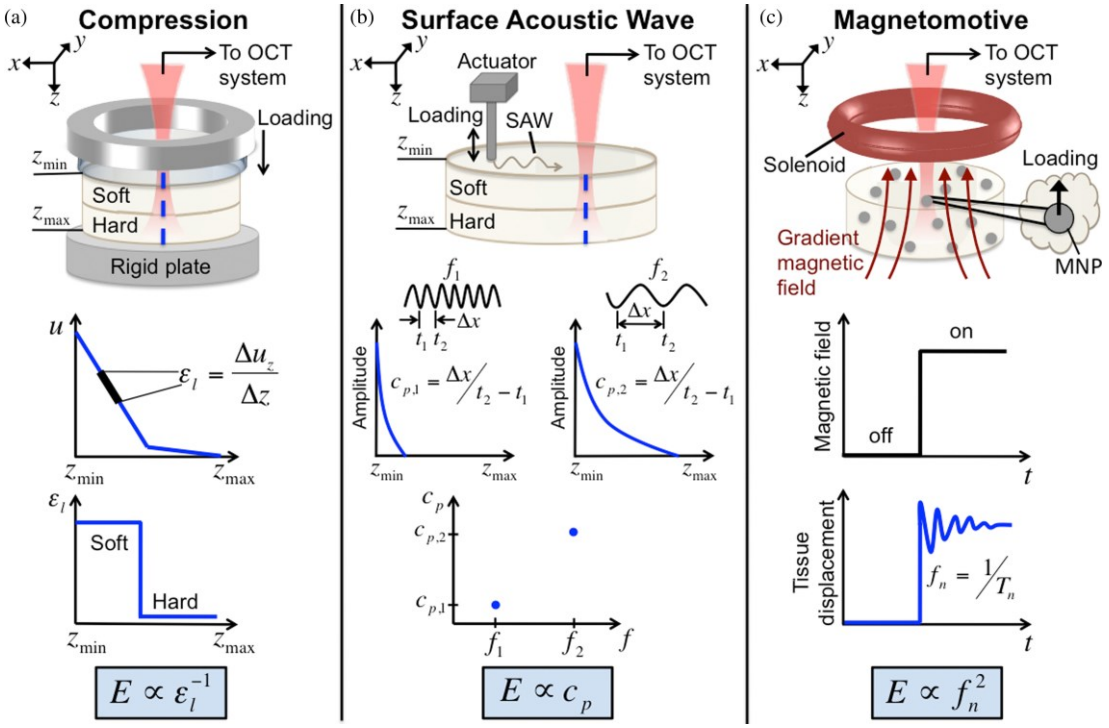

Figure-2.10: Illustrative examples of three different loading schemes commonly used in OCE and elasticity estimation – descriptions from top to bottom: (a) Static/quasi-static loading (compression): concentric loading and on-axis detection in a bi-layer sample; depth-resolved displacement vs depth yield the corresponding local strain ε_l; (b) SAW: periodic loading and off-axis detection; depth-dependent amplitude decay for high and low SAW frequencies f_1 and f_2 respectively; the measured phase velocity c_p is frequency dependent in a layered sample with the higher SAW frequencies depending more on the elasticity of the soft layer whilst the lower SAW frequencies depend on both soft and hard layers; (c) MM: upward movement of magnetic nanoparticles (MNPs) that are embedded in a homogeneous sample in response to a step application of the magnetic field causes a localized load to the surrounding sample; applied magnetic field; corresponding sample response vs time, where f_n is the natural frequency of oscillation and T_n is the period. This is identical to fig.2 in [125] with caption text slightly modified.

Chapter-3: Development of electro-mechanical hardware

3.1 Introduction

The original project aim was to develop a tomographic system able to analyse three-dimensional displacement fields within weakly scattering materials such as glass fibre reinforced polymers (GFRP's). Consequently, it is necessary to develop a device able to introduce the desired displacement boundary conditions to the test sample in an unambiguous manner. A set of intermediate experiments was also devised to align the coordinate systems of the 6 independent interferometers and to test the performance of the system on an ideal weakly-scattering phantom that undergoes pure translation and rotation. Experiments using these devices will ultimately increase the confidence of success when testing the much more complex GFRPs.

During the course of the PhD research, however, failure of the tuneable laser meant that it was necessary to refocus the project to one based on image analysis of existing image sequences. The loading stage and rotation device described in this chapter were ultimately not used, apart from some experiments involving rotation field measurement. They are however documented in this chapter for the benefit of future researchers working on the same or a related project.

3.2 Development of miniature tensile machine

The following section of the report deals with the design of a miniature tensile test machine suitable for installation within the tomographic system shown in figure-1.4. As described in the previous chapter, this is based on the technique called WSI (Wavelength Scanning Interferometry), which it is anticipated will allow the analysis of three-dimensional displacement fields within weakly scattering materials, such as GFRP's (Glass Fibre Reinforced Polymers), by recording a sequence of two-dimensional interference patterns while the wavelength of the light source is tuned at a constant rate [3].

3.2.1 General aspects

The following part of the thesis aims at summarizing and discussing the main design aspects of such a device (i.e. the miniature tensile machine under development),

which occurred during a final year project [162] which the author of this present work closely supervised throughout its course. It should be noted that this design work is a continuation of the work done on the same subject by [163]. Both undergraduate projects were based on a similar project undertaken by [164] as part of their doctoral thesis [165] and relevant publications to it [166, 167]. It is also worth noting the comprehensive work of [168] on the testing procedures of composite materials, on which much of the current work has been based.

Tensile machines are classified into two main types: those which apply a prescribed load to the test piece and those which induce the load by applying a controlled displacement. The former typically deliver the load by means of a servo hydraulic machine while the latter by means of an electro mechanical machine equipped with displacement sensors. Both machines can perform quasi-static tests. Servo hydraulic machines offer both loading regimes whilst allowing for the addition of dynamic loading (fatigue tests). For the current project, however, fixed displacement boundary conditions are more appropriate to reduce the sample motion during the scan time [168].

The mechanical configuration of such experimental rigs has not changed greatly over the years, the main components of which are: the frame, grips, load cell and actuators as illustrated in figure-3.1. It should be noted that the generic machine configuration illustrated in figure-3.1 does not imply that all machines utilize a two column design. Opting for single or dual column design highly depends on the load capacity of the machine, the size of the samples to be tested, the additional equipment for environmental control of the test specimen as well as the required stiffness of the instrument [169]. The latter constitutes one of the most important factors in the design of such instruments and is often expressed in terms of a parameter called compliance (C):

$$C = P/\Delta \,, \qquad 3.1$$

where P is the load applied and Δ is the total displacement of the sample and the individual components of the machine.

There are two fundamental problems to be addressed in mechanical testing, irrespective of the material under test. The first of these is to minimise and ideally

eliminate undesirable interactions between the means of load application and the test material. This is particularly relevant to composites where the load introduced to the material goes through an inherently weak phase (the matrix) and can cause spurious effects. It is therefore important to take care not to overload the outer layers of the fibres as, depending on the construction, these may contribute a disproportionately large amount to its strength and will be inherently susceptible to damage. The second is to produce as nearly a pure state of stress to the sample as possible [168]. Although one could argue such a state to be practically impossible to accomplish, in reality it is achieved by long and thin specimens according to the *Saint Venant's Principle*. The above further highlights the importance of the test piece size as well as the means of transferring the load to the specimen, commonly referred to as the gripping method.

Another important factor which contributes to reliable experimental results is the correct alignment of the test coupon onto the rig. The literature is inundated with evidence of the detrimental effect of small misalignments [170] originating either from the machine or the specimen itself, giving rise to bending and ultimately into large localized stresses.

Finally, a less obvious but nevertheless equally important source of error is the incorrect loading rate of the sample. Composites, particularly the ones with a polymeric matrix, exhibit time-dependent viscoelastic behaviour under load. In the case of constant stress, the strain exhibits time-dependent `creep` while in the case of constant strain or displacement the resulting stress exhibits time-dependent 'relaxation' [171].

3.2.2 Overview and design analysis

One of the main disadvantages of the design developed by [163] was the absence of appropriate bearings to deal with the forces developed in the system. Although the instrument's ultimate goal is not to load the sample to failure, but to introduce (in steps) an overall displacement of the order of a few tens of micrometres, high axial loads nevertheless develop in GFRPs as a result of their high elastic moduli. The selection of the correct type of bearings with sufficient load capacity to deal with the forces developed is therefore an important element of the design. In the light of this change, which is a significant one due to the limited space available to mount the

instrument onto the OCT system, (see figure-3.2 and figure-3.3) it was decided to re-evaluate the entire design.

Several configurations were taken into account while trying to reduce the number of bearings from four in the case of a double-column design to two in the case of a single-column design. Due to the limitations imposed by the design of the main cube (shown in figure-3.3) the single-column design was rejected. More specifically, the location of the holes on the cube where the sample is to be introduced would require the bearings to be offset from the centre of the holes. Such an arrangement was deemed to be unfeasible for a number of reasons:

a. It would introduce a pitching moment onto the moving crossheads, giving rise to unnecessary displacements due to bending.
b. It would over complicate the force analysis, making the correct choice of bearings difficult.
c. It could potentially introduce alignment issues during tests, the importance of which has already been highlighted in the introductory section of this chapter.
d. It would reduce the stiffness of the structure.

The use of guide bars was omitted due to the necessary tight manufacturing tolerances which would raise the cost of the machine. With the above in mind the mechanical configuration was finalised as illustrated in figure-3.4. This shows one half of the machine, with a second identical system applying a force in the opposite direction. The use of two moving crossheads allows the centre of the sample to remain stationary, or to be moved back into the starting position following a load step, which is important to avoid speckle decorrelation associated with large rigid body motion.

As mentioned earlier, due to the limited space provided in the experimental setup, certain components need to be kept to a minimum size while having to fulfil the rest of the design requirements (see product design specification (PDS) in reference [162]) and therefore become critical to the design process of the tensile test machine. These are:

a. The bearing support plates.
b. The lead screws.

c. The gears.

It is important that the size of the bearing support plates is selected such that they do not obstruct the optical paths of the laser beams. Their size is primarily controlled by the size of suitable bearings as well as the diameter of the lead screws. The bearing size will effectively determine the minimum separation of the lead screws which in turn becomes the key stiffness parameter. The length of the lead screws will be determined by the thread pitch and the rotational speeds of the two gears (wheels) shown in figure-3.4 which will combine to produce the required extension of the sample.

3.2.3 Mechanical aspects

In view of the above, the bearing function is primarily to account for the high axial loads developed and secondly to account for the much lower radial loads developed during the machine's operation. It should be mentioned, however, that the two gears contribute to the larger amount of the radial forces present. It is, therefore, important to calculate and include the latter in the bearing calculations. Due to the very low rotational speeds occurring during the operation of the tensile test machine, there are hardly any dynamic phenomena to be taken into account. Spur gears are consequently sufficient for this application. The choice of gears was preferred to that of belts [164-167] due to the long scanning times (about 2 hours) which could result in the polymer belts creeping.

From the above it is evident that in order to calculate the radial force exerted on the bearings by the two rotating gears, the size and power of the motor need to be estimated. This has to be taken into account when deciding the precise size of the thread on the lead screw. Based on the choice of size for the two identical gears, a gear reduction ratio will result. The reduction ratio is a key parameter controlling the loading rate of the test piece. In the current system, the overall reduction arises from the gears and the pitch of the lead screws.

Once the above have been determined, a secure method of mounting the bearing support plate onto the cube needs to be determined. The plate is loaded effectively in three-point bending. With the dimensions of the plate (width, height) known, the thickness can therefore easily be calculated so that the bending of the structure is insignificant.

The previous design was held together by means of three screws. As stiffness is an important factor, the use of locating pins (dowel pin or stud with nut) is a better solution.

3.2.4 Optical aspects

The importance of the loading rate and its effect on viscoelastic creep of polymeric matrix composites has already been highlighted. This parameter, however, strongly affects the nature of the interferograms recorded by the near infrared (NIR) CCD cameras utilized in the tomographic interferometer. It is, therefore, required to choose an appropriate loading rate so that a sufficient number of fringes are obtained at each loading step. As stated above, the system utilizes two independent loading machines attached symmetrically to either side of the cube. This concept was introduced in order to avoid any rigid body motion [167] of the test coupon and to ensure that its centre remains at the centre of the field of view (FOV) at all times. With this loading regime and depending on the displacement introduced at each step, a number of fringes will appear on either side of the static central fringe (see figure-3.5). Although each interferometer has an almost pure out-of-plane sensitivity, the viewing direction of each station is located away from the normal to the sample's surface so there is a component of the sensitivity vector parallel to the in-plane motion of the sample. These fringes will appear to be moving away from the central one and it is the number of those that needs to be reasonably controlled. Each of the moving fringes will correspond to a displacement of order $\lambda/2n$, where λ is the wavelength and n is the refractive index of the material under investigation [36]. Theoretically, a large number of fringes could be obtained without a significant effect on the results. The larger the number of fringes present in the interferogram, however, the more difficult the phase unwrapping process becomes [172-174].

An estimate of the required crosshead speed can be obtained by performing some simple calculations on how fast the fringe patterns will move. The edges of the field of view (FOV) will move at a speed of $\pm (FOV \times V_{CH}) / 2L$ as illustrated in figure-3.5, where V_{CH} is the speed of the crosshead and L is the length of the sample. Note that the factor of two in the denominator arises from the symmetrical nature of the setup. Therefore, the distance moved by one of the edges in time (t):

$$d = (FOV \times V_{CH} \times t)/L, \qquad 3.2$$

If we require N_f fringes across the full field of view, each one corresponding to a displacement of the order of λ/2 (note the refractive index of the material has been omitted to ease the calculations) [48],

$$d = \left(N_f/2\right) \times (\lambda/2), \qquad 3.3$$

The FOV is determined in the current system by the size of the CCD array of the NIR cameras and is approximately 5 mm. Assuming a total number of fringes N_f = 10 over a period of time t = 10 s, an overall length of the sample L = 50 mm and a wavelength λ = 825 nm, the crosshead velocity is readily obtained by equating equations 3.2 and 3.3 resulting in a crosshead speed V_{CH} = 0.124 mm/min.

Another important parameter that needs to be estimated during the design process is the force required to deform the glass re-enforced polymer GFRP specimen. Recalling that each fringe pattern will contain approximately N_f = 10 fringes and that each fringe corresponds to a displacement of order λ/2 we can deduce an estimate for the step displacement required by the tensile machine as follows:

$$d_{step} = \underbrace{N_f \times \lambda/2}_{with\ N=5\ and\ \lambda=825\ nm} \approx 2\ \mu m, \qquad 3.4$$

Since there are two of these machines in the experimental setup, the overall step displacement amounts to 4 μm. Assuming a total number of steps N_s = 14 and rounding the overall step displacement to 5 μm, the overall displacement can be found as follows:

$$d_{total} = N_s \times 2d_{step} = 70\ \mu m, \qquad 3.5$$

Having established the overall displacement required and assuming that this displacement falls well within the linear elastic response region of the composite material, the overall force required can be estimated by direct application of Hooke's Law.

3.2.5 Detailed design of loading stage

The detailed final design of the loading stage is illustrated in figure-3.6, which shows the position of the motor, bearings, load cell and load pin. Two copies of this design were manufactured and assembled in-house. Figure-3.7 shows them after partial assembly and after attachment to the cube. The chamfered corner on the plate of the

left hand machine that attaches to the cube is needed to prevent obstruction of the optical path into the cube. The cube with loading machines attached after reinstallation into the interferometer setup is shown in Figure-3.8. In parallel with the mechanical design, an electronic control unit was designed by the Wolfson School electronic workshop to control the rotation rate of each motor. By driving them in the same direction, the sample is translated within the cube with no loading, whereas driving them in the opposite direction causes loading of the sample with no translation. In addition, the control unit acts as a data logger for the load cell. Figure-3.9 shows the control unit after manufacture.

3.3 Development of calibration artefact

In this section, a second opto-mechanical system is described. The purpose of this system is to establish the ability of the interferometer setup to record and successfully analyse the intensity signals, carrying the sought displacement information, from multiple illumination/observation directions. In this first phase, the design of the experiment was focused on introducing a well-controlled, and easily traceable displacement field onto the sample. Furthermore, prior to testing the more complex GFRP samples which may result in low quality signals induced by multiple scattering, a simpler yet still classified as weakly-scattering material needs to be tested. Consequently, the following part of this section is divided into two main sections, namely the design of the necessary hardware for the introduction of a controlled displacement field, and the samples themselves.

3.3.1 General aspects

As with the loading stage described in the previous section, it is important to make sure that the displacement introduced by the mechanism is sufficiently small to avoid excessive speckle pattern de-correlation. Another important consideration is the instrument's high sensitivity to environmental disturbances like temperature and/or humidity variations, light conditions and external vibrations. Although all of the above were taken into consideration during the design process of the interferometer, it is important to ensure that the design of the displacement device does not introduce unnecessary environmental disturbances throughout the course of its function. Multiple reflections which are a well-known factor contributing towards signal degradation also need to be suppressed wherever possible.

The spatial configuration of the interferometer places strict size limitations on any mechanical device introduced into the setup. The current setup utilizes six illumination and six observation beams (all collimated) that should not be disrupted at any time.

As far as the delivery of the displacement to the sample is concerned, it should be done in a well-defined and controlled manner. In other words, readings should be easy to take, highly repeatable and accurate. Moreover, the displacement introduced should remain constant throughout the duration of each scan and give rise to no more than approximately 4-5 fringes per step to avoid problems with the phase unwrapping. Uncertainty during the introduction of displacement should also be kept to a minimum as the device will be used as a reference to validate the displacement fields obtained from the optical system. Finally, the weight of the device should be kept at reasonable levels to ease the installation procedure.

3.3.2 Conceptual and final design

Although straining of the sample is to be excluded from these first phase experiments, on account of the difficulty in establishing a stable displacement field for a sample under load, these displacements need to be of the most general form possible for an object undergoing pure rigid body motion. Consequently, both translation and rotation displacements are required. In addition, since for this first phase of the experiment only three of the six cameras will be employed and will subsequently be used for measuring the three orthogonal displacement components introduced to the sample (see below), it is desired to ensure that the three displacement components are of the same order of magnitude.

These requirements can be met by introducing a controlled rotation about one of the three diagonals of the cube. There exist already two planar surfaces normal to one of these diagonals, which act as mounting surfaces for the loading machines described in the previous section. The chosen solution therefore consists of a rotation stage mounted onto one of these surfaces with an inner threaded sample holder that also allows translation along the diagonal.

The CAD model for the final design is shown in cross section in figure-3.10, as well as the view from one of the interferometer heads (figure-3.11) to demonstrate that the

rotation stage does not obstruct the beam paths. The manufactured and assembled system is shown in figure-3.12.

3.3.3 Alignment and calibration artefact and phantom

Two cuboid samples of side 3 mm were made, one consisting of steel to act as an alignment and calibration device, the other consisting of a polymer resin with fine titanium powder to act as a weakly scattering volume phantom (see figure-3.13). The original plan was to etch small dots onto the 6 sides of the steel cube with an excimer laser, the positions of which would subsequently be measured to allow the coordinate systems of the 6 viewing directions to be aligned with respect to each other. The plan for the polyester sample was to make depth resolved displacement measurements from each of the three viewing directions and to test for consistency between them using the fact that the imposed sample rotation is common to all three. These plans were put on hold when the laser developed the fault mentioned at the start of this chapter. Nevertheless, initial rotation experiments were carried out on the steel sample, with the laser operating at a single wavelength and using a single measurement station. The two speckle patterns (one recorded before, one after the rotation) and the subtraction ESPI fringe pattern calculated from the two are shown in figures-3.14 to 3.16. The subtraction fringes are of high contrast, and as expected appear parallel to one another and at an angle of approximately 45° to the horizontal axis. This simple experiment thus demonstrates that the various opto-mechanical components, laser and interferometer are working as expected, albeit at just a single wavelength.

3.4 Summary and conclusions

This chapter has provided an overview of two important hardware devices that have been designed and manufactured for the tomographic setup, namely a miniature tensile testing device and a rotation stage. These have been designed to induce controlled displacements of a sufficiently low magnitude and to be small enough to fit into the multi-axis interferometer without obstructing any of the beams. Although these devices were not ultimately used with the tuneable source, preliminary experiments at a single wavelength on the cuboid calibration device have demonstrated that the main elements of the interferometer are working as expected.

3.5 Figures

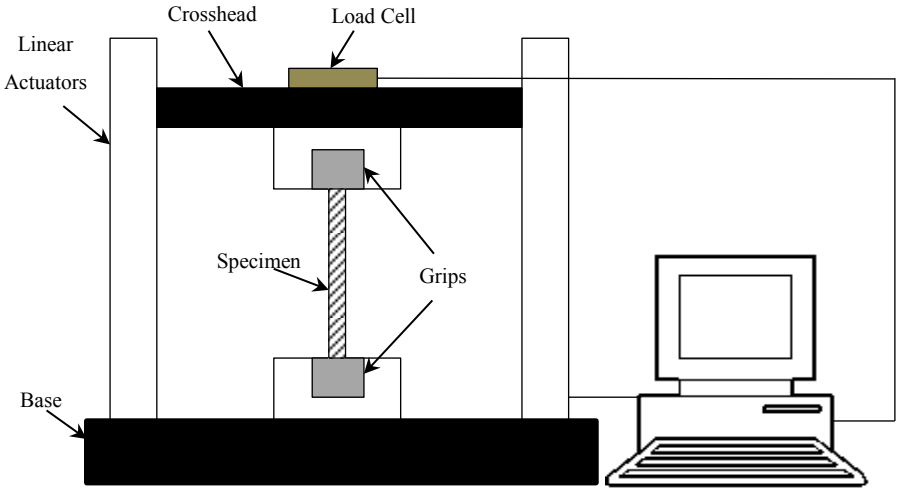

Figure-3.1: Schematic representation of a typical tensile test machine.

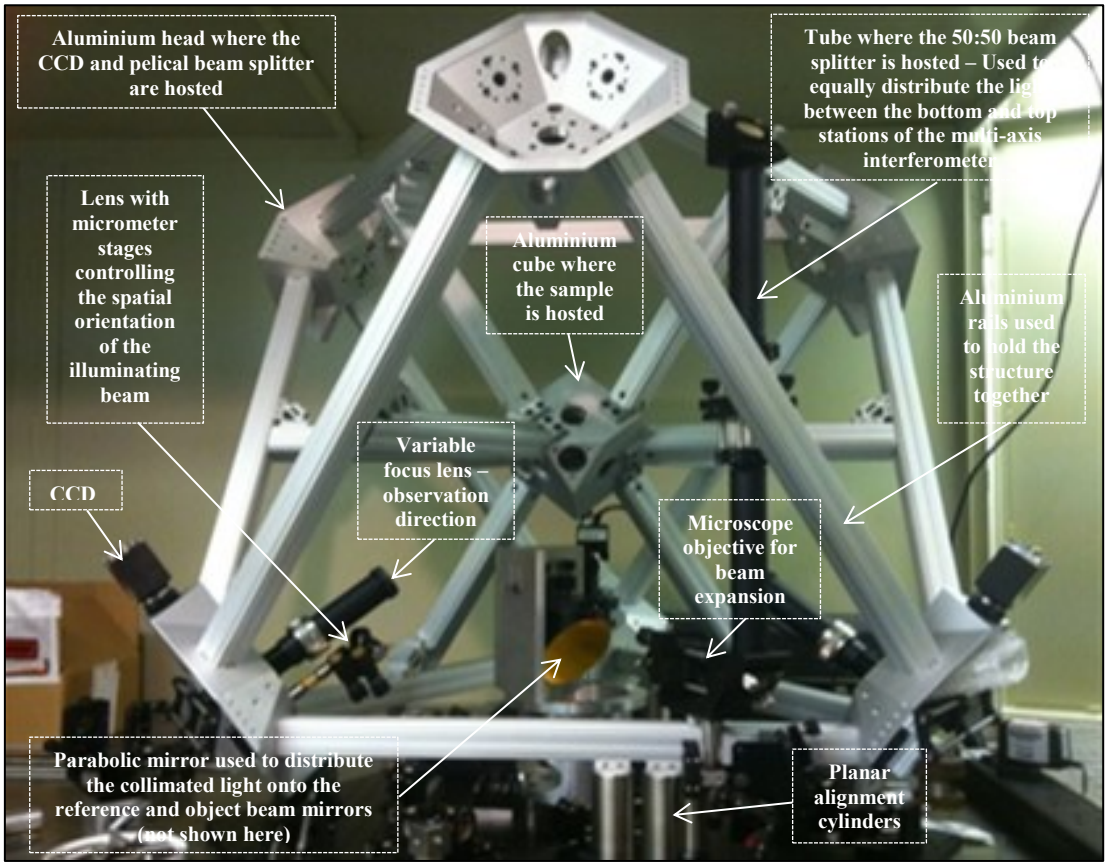

Figure-3.2: Multi-axis tomographic interferometer under development.

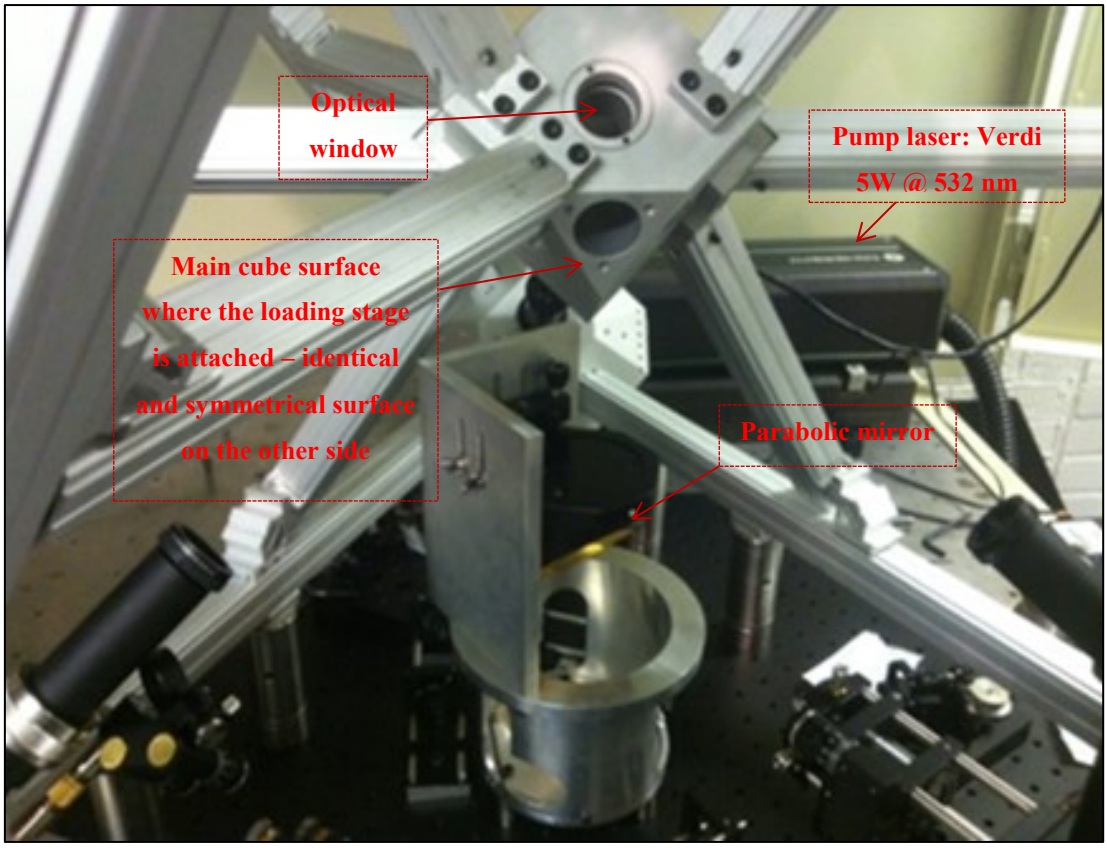

Figure-3.3: Close-up view of the aluminium cube used to host the test samples.

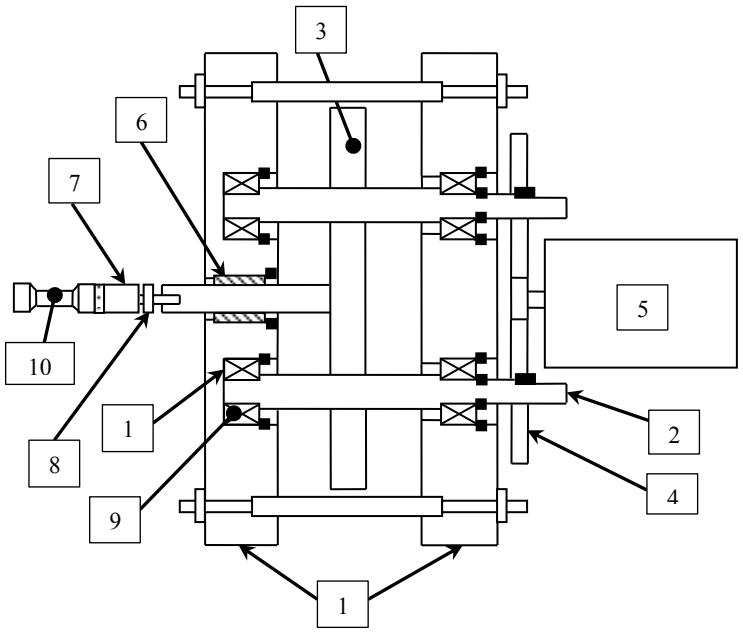

1. Bearing support plates (×2)
2. Lead screws (×2)
3. Moving crosshead; runs along the lead screws and introduces the necessary tensile force
4. Gears (×2); transfer the circular motion provided by the motor to the lead screws
5. Motor (×1)
6. Locating/linear bearings (×1)
7. Sample grip (×1)
8. Load-cell (×1)
9. Bearings (×4)
10. Test sample

Figure-3.4: Schematic diagram showing the key components of the miniature tensile machine under development.

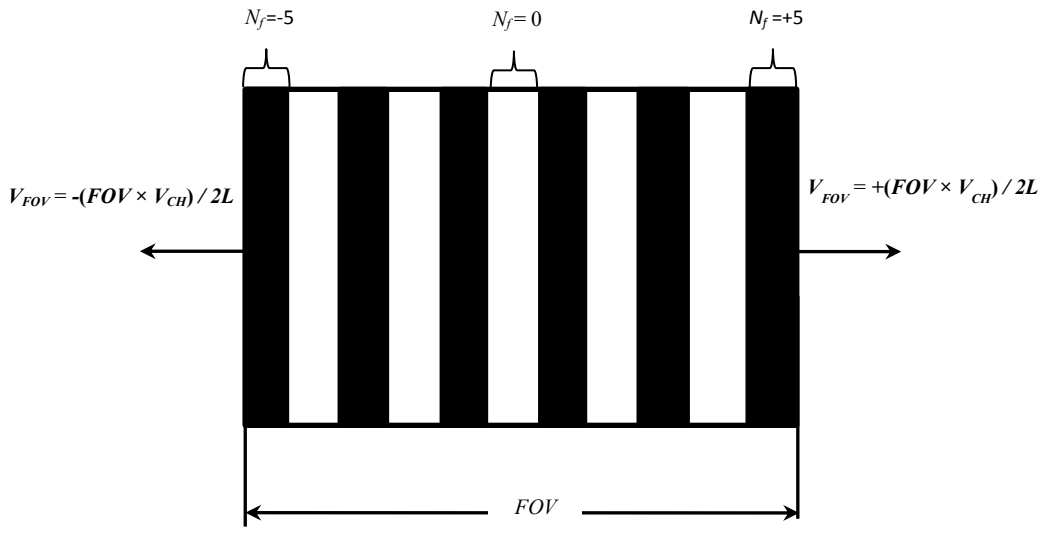

Figure-3.5: Schematic representation of the moving fringes. FOV: Field of view, CH: crosshead and V: speed.

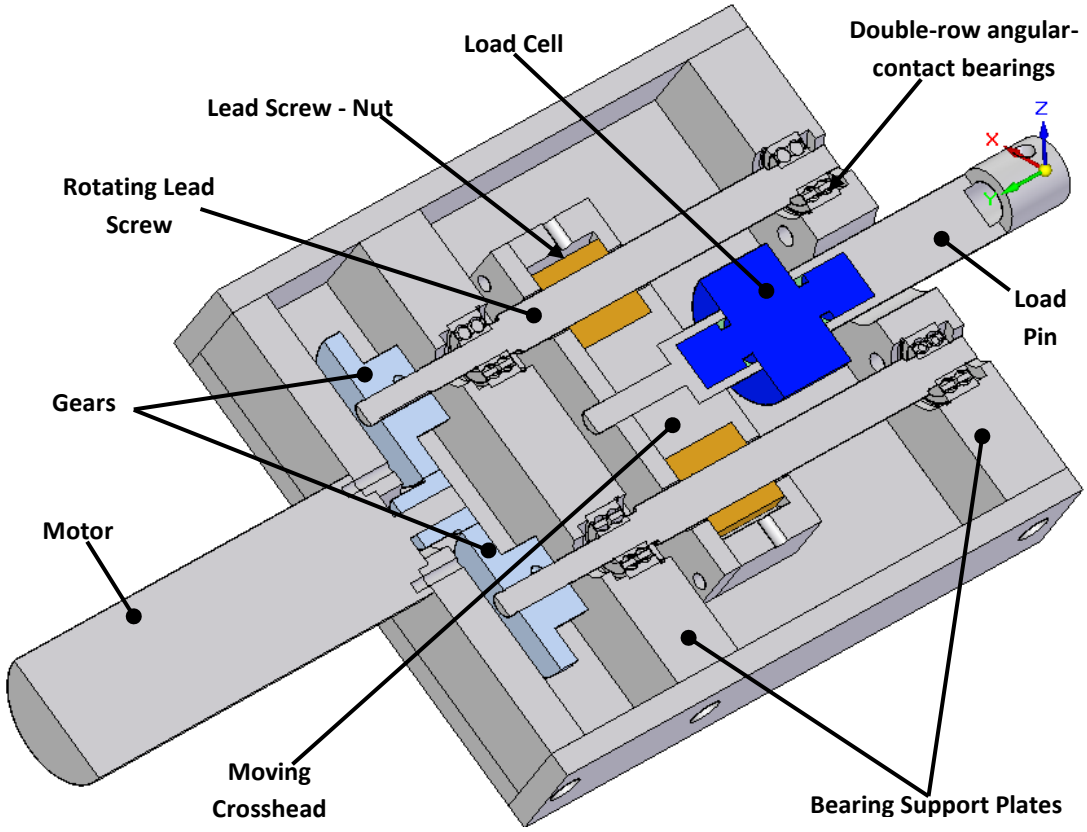

Figure-3.6: Cross-section of the final CAD assembly model for the miniature tensile machine showing the main components.

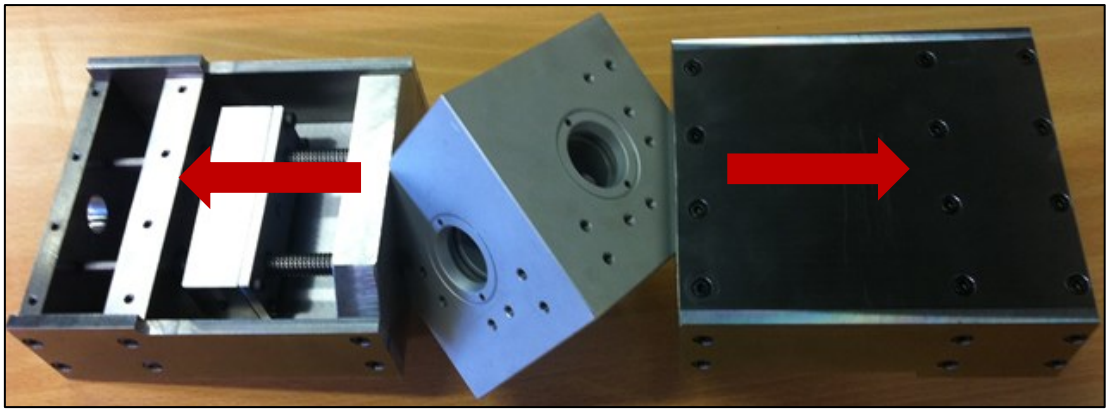

Figure-3.7: Partial assembly showing the arrangement of the two-part miniature tensile machine after manufacture. Arrows indicate the loading direction

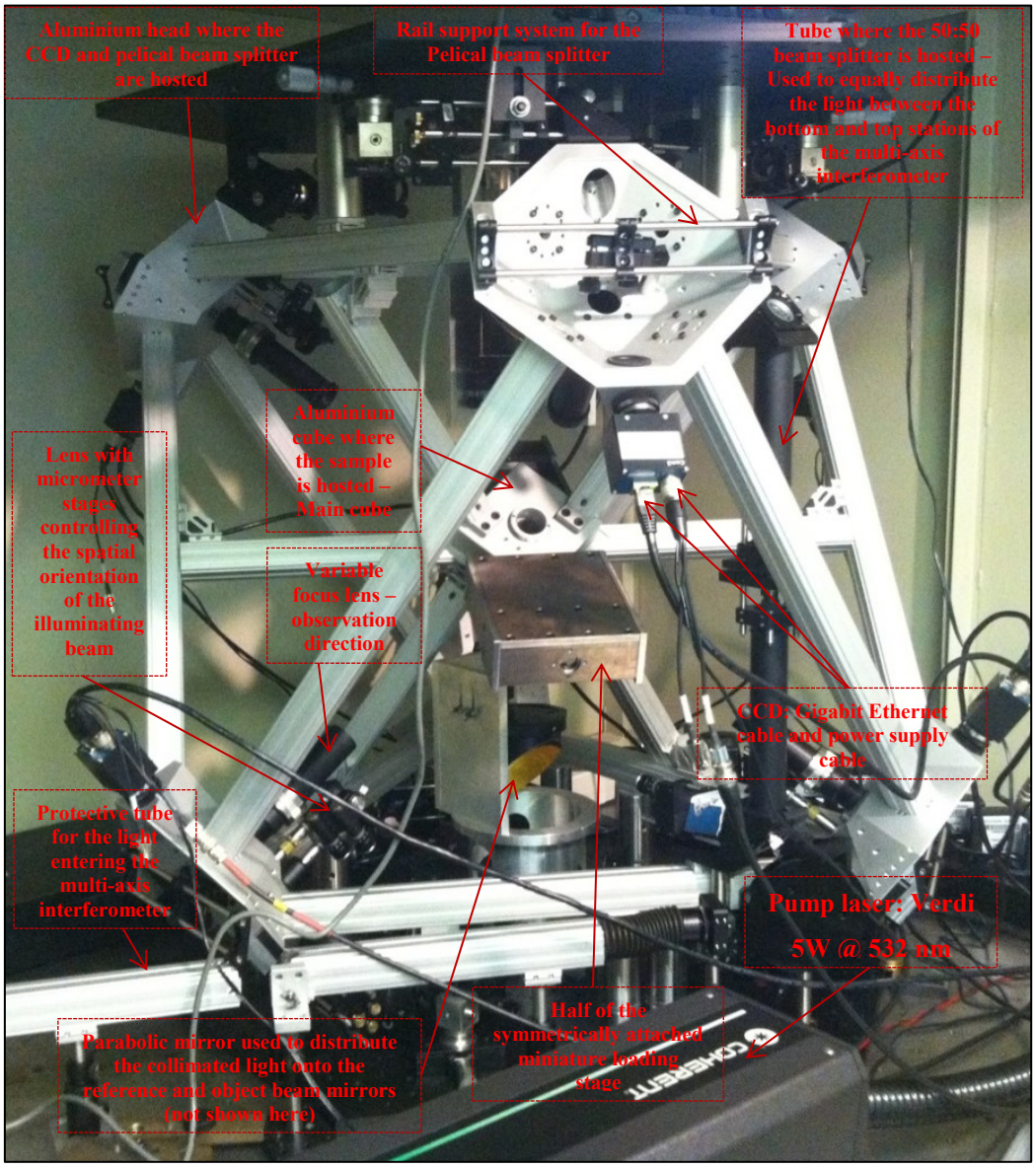

Figure-3.8: Partial assembly of the miniature tensile machine fitted in the multi axis tomographic interferometer under development.

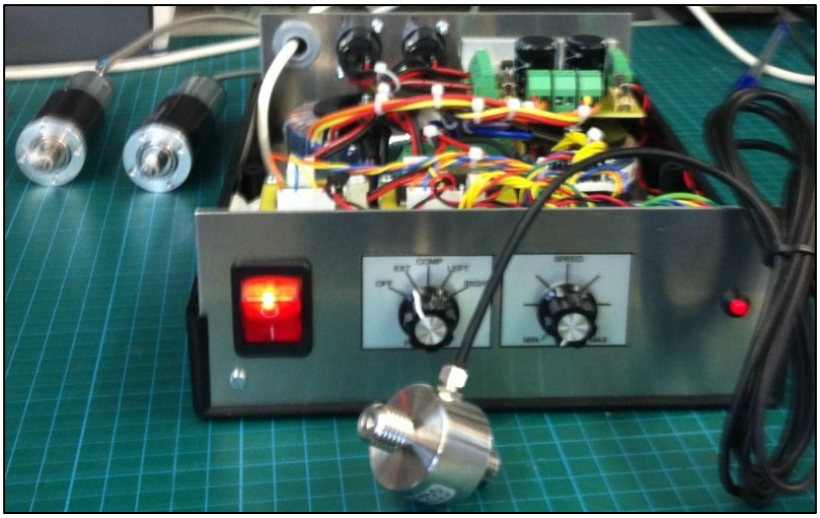

Figure-3.9: Control unit power supply developed by the electronic workshop of Wolfson School at Loughborough University. The unit is used to control: a) the position of the sample inside the host cube b) the load introduced to the sample by controlling the speed of motor rotation and c) is connected to the load-cell (shown at the front) which in turn sends the stored load increments to a text file in the lab PC used to operate the multi-axis interferometer.

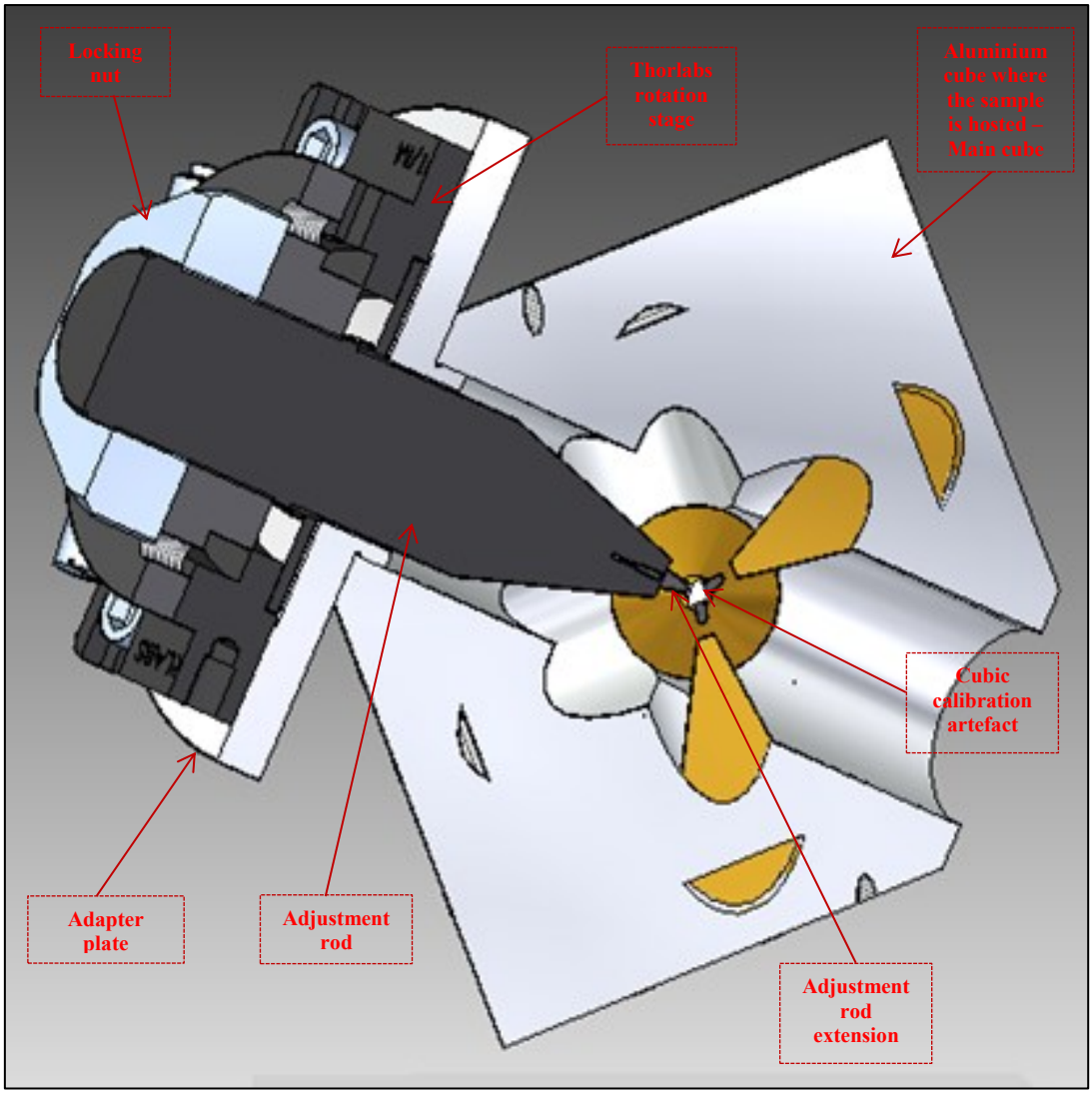

Figure-3.10: Cross section of the CAD model for the rotation stage and calibration cube.

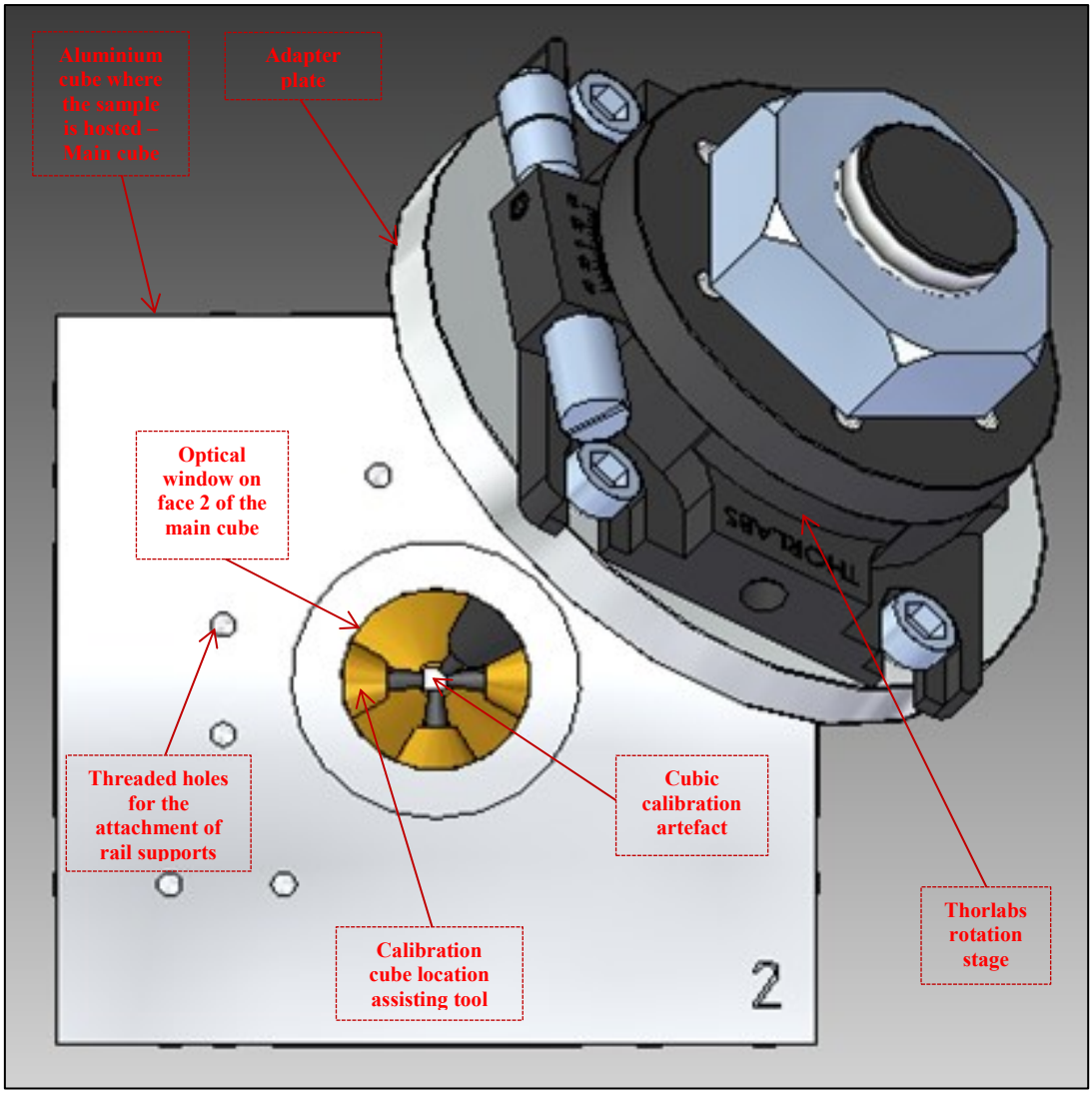

Figure-3.11: Side view of the CAD model showing the calibration artefact assembly from the second view point optical window.

Figure-3.12: Manufactured assembly of the calibration artefact positioning device.

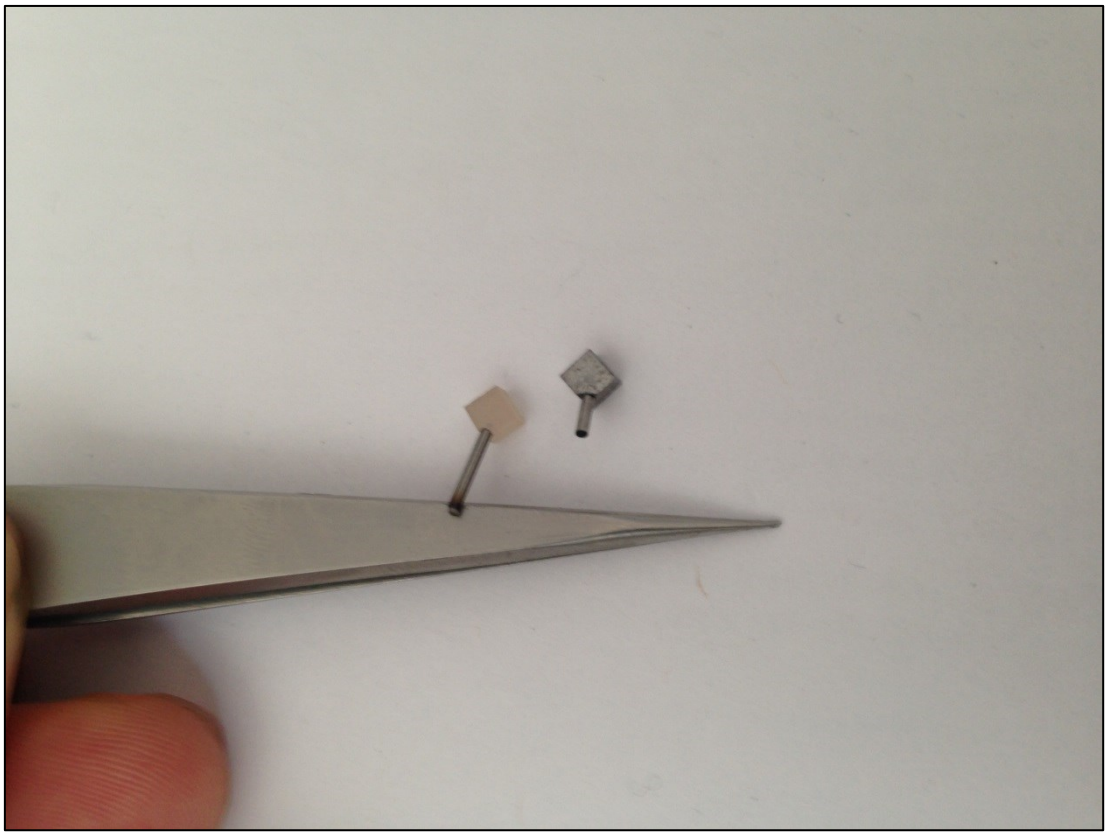

Figure-3.13: Calibration artefacts: (Left) Calibration artefact for depth resolved measurements made out of polymer resin and titanium inclusions, (right) steel cube for alignment of coordinate systems.

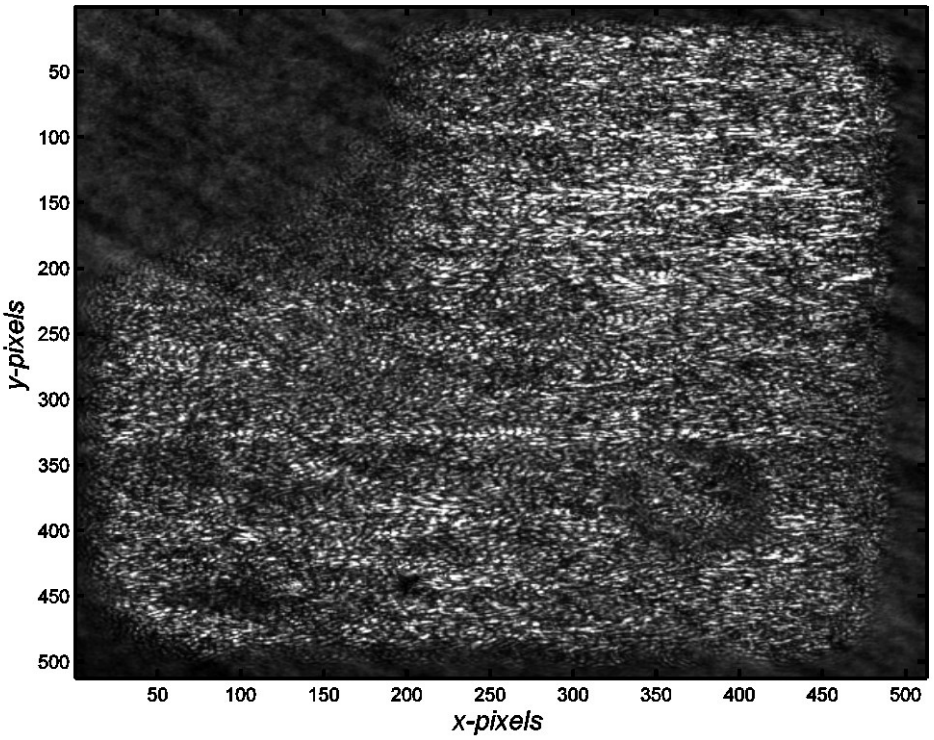

Figure-3.14: Speckle pattern of the steel cube before the induced rotation by the rotation stage.

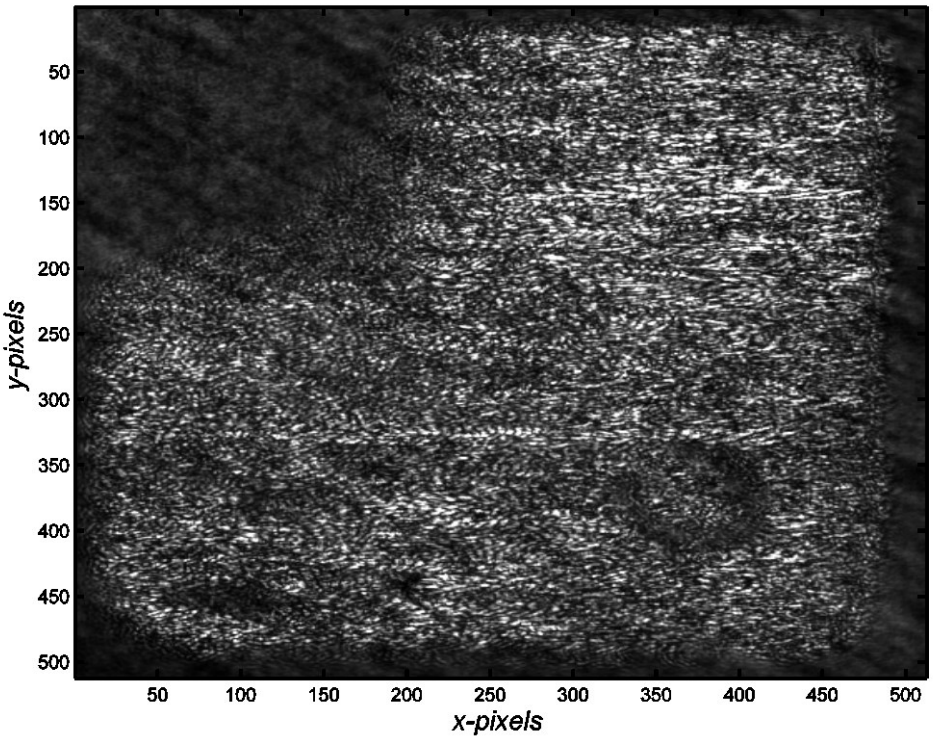

Figure-3.15: Speckle pattern of the steel cube after the induced rotation by the rotation stage.

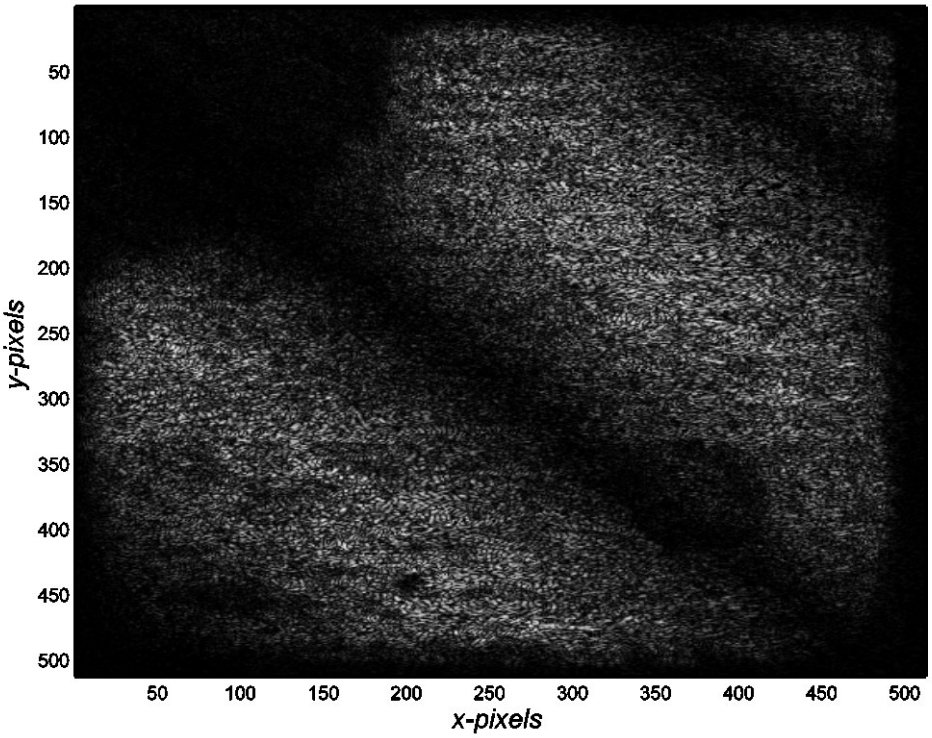

Figure-3.16: Fringes resulting from the subtraction of the speckle pattern after the induced rotation from the corresponding one recorded before the rotation.

Chapter-4: Development of the multi-axis interferometer

4.1 Introduction

In this section of the thesis, a description of the different parts comprising the phase-contrast wavelength scanning interferometer under development is provided. Much of the work described in this chapter was done by *Dr. Abundio Davila-Alvarez* who joined the optical engineering group at Loughborough University as a post doc while on a sabbatical leave from the *Centro de Investigaciones en Optica* (CIO), *Loma del bosque 115, Leon Gto 37 150 México*, for a three year period from 2008 to 2011 and with whom the author worked closely for the last one and a half years of his visit. Moreover, it is worth noting that although some parts of the overall setup description were mentioned in chapter-1 and chapter-3, they are repeated here for three reasons: a) for completeness, b) due to the critical failure of the tuneable source and c) due to major issues with the software development. The aforementioned reasons have caused the refocusing of this thesis on a number of occasions, ultimately forcing the research away from the originally planned experimentally-orientated work, to one relying on the numerical analysis of the limited data sets captured before the critical hardware failure (see chapters 5, 6 and 7).

First a more detailed description of the design process followed for the construction of the multi-axis interferometer than that presented in chapter-1 is given in section-4.2. Second, a brief description of the imaging hardware and the software used to control the seven cameras is provided in section-4.3. Third, section-4.4 is devoted to the key component of the tomographic interferometer under development and is divided into two subsections. Section-4.4.1 provides descriptions of the general principle of operation of the widely tuned Ti:Sa laser source used in this thesis and the necessary customizations to it for WSI applications which were briefly mentioned in ref [21]. In section-4.4.2 the performance of the laser source is assessed by means of preliminary results based on short scans on glass wedges. The results presented are based on work done prior to the author joining the group and were presented in [175]. The aforementioned results provide an insight of the issues associated with the particular laser source (the first of its kind) and are consequently used here to set the ground on which the remainder of the thesis is built.

4.2 Development of optical setup for tomographic displacement sensing

Recalling that the long term goal of this research is to ultimately extract the 3-D depth-resolved mechanical properties of composite materials like GFRP's, the need for multiple illuminations and or observation/s of the sample becomes obvious. The description of the optical setup starts by giving a brief review of the work reported on the 3-D displacement sensing for surface measurements (see section-4.2.1) followed by a review on the current state of the art optical setups used for calculating the depth resolved 3-D displacements to date (see section-4.2.2), thereby revealing some of the novel aspects of the current work.

4.2.1 Optical setups for 3-D-displacement sensing: surface measurements

Although theoretical studies for the determination of 3-D displacements using holographic interferometry date back to the early 70s [176-182], *Takatsuji et al (1995,1997)* were the first to report on an optical setup for the simultaneous measurement of three orthogonal displacement components using ESPI and the Fourier transform method [183, 184]. In this example a total of three object beams and one reference beam, realized in a Mach-Zehnder setup, were used to extract the sought displacements on the surface of the sample (see figure-4.1). The four beam configuration resulted in three two-beam interferometers with the resulting interference patterns carrying the information on the three individual displacement components. A single CCD camera was used for the recording of the three patterns. A setup utilizing two illumination beams and one observation using ESPI was reported by *Sun P (2006)* that was used to extract the 3-D displacement with particular attention to distinguishing between the in-plane and out-of-plane displacement components [185]. *Saucedo-A et al (2010)* used an almost identical setup to that described by *Takatsuji et al* (see figure-4.2) but employed three laser sources (458nm, 532nm and 633nm) to illuminate the sample simultaneously and a high resolution CMOS sensor [186]. *Bhaduri B et al (2011)* reported on an ESPI system that employed two wavelengths (He-Ne laser 632.8 nm and Ar-Ion laser 457 nm) in a modified Michelson setup (see figure-4.3) and a single 3-CCD colour camera to extract the sought 3-D-diplacements [187]. The novel aspect of this setup was that the 3-CCD camera used was able to separate the red (He-Ne laser) and blue

(Ar-Ion laser) beams individually through its red and blue channels, essentially acting as two CCD detectors (see figure-4.3). Finally another modified Mach-Zehnder setup was reported in references [188, 189] using a single laser source but two CCD detectors for the detection of both in-plane and out of plane deformations (see figure-4.4).

4.2.2 Optical setups for 3-D-displacement sensing: depth-resolved measurements

Unlike the many examples of 3-D-displacement measurement on the surface of samples and besides the developments in the OCT community, there is little reported in the field of tomographic sensing of 3-D-displacement measurements. Although phase-contrast schemes of OCT and OCE (see section-2.4.3 and section-2.4.4) are being continuously developed, research is still limited to just a single viewing direction along the depth-axis (see ref [190] for example) owing to the complexity associated with combining multiple data volumes. Another project running in parallel to that described here has recently been reported (see refs [27, 191]. The optical setup used in the aforementioned example features three illumination beams and one observation direction (i.e. a single photo-detector array) in a Mach-Zehnder arrangement (see figure-4.5) and is inherently similar to the optical arrangement described earlier in [183]. The main difference is the use of a mode-hop free broadband tuneable laser source (TSL-510 Type A, Santec Ltd. $\Delta\lambda$ = 100 nm, λ_c = 1310 nm, $\delta\lambda$ = 0.011nm) and the addition of delay lines for frequency multiplexing of the different channels on a single image sequence.

To date, and to the best of the author's knowledge there have been no reports on systems utilizing more than a single CCD in the 1.3 μm region. This is partly due to the high cost of CCDs sensitive to this spectral bandwidth of light but also due to the limited available power output available from tuneable laser sources operating in this region which in turn pose strict limitations on the number of channels light can be divided to in any of the amplitude division interferometers. However, as discussed earlier in section-2.4.2 and section-2.4.4, advances in solid state laser technology have resulted in laser sources with large tuning ranges operating in the region of 700-900 nm and with power output of several hundreds of mW. These have therefore

become an attractive alternative allowing the development of multi-channel setups using multiple low cost CCDs.

4.2.3 Multi-channel Mach-Zehnder interferometer

The brief survey provided above suggests that the Mach-Zehnder interferometer is the most suitable for the measurement of 3-D deformations with a minimum of three illumination directions and one observation direction. Generally, in this type of interferometer two beam splitters and two mirrors are used that allow the reference and object paths to be widely separated and traversed only once in contrast to the Michelson type. The multi-channel tomographic interferometer developed in this thesis is also based on a Mach-Zehnder arrangement. In contrast to the setup illustrated in figure-4.5 the current setup is built on the principle of viewing the sample from a minimum of three and a maximum of six orthogonal directions as illustrated in figure-4.6. Although as far as the number of measurable displacement components is concerned the additional three channels may seem redundant, there are several benefits including them in the setup. As the sensitivity vectors between pairs of opposite channels are practically the same, for the case of symmetrical displacements, the additional channels provide an easy way of checking the validity of the calculated depth-resolved displacements. A less obvious reason is that two of the critical parameters, namely the depth range and the depth resolution of the system are positively affected. Given a specific bandwidth ($\Delta\lambda$) and wavelength step ($\delta\lambda$) the two parameters are practically fixed. However, the introduction of the additional three viewing directions from opposite sides has as a result the doubling of the depth range for the same $\delta\lambda$ and identical depth resolution. In addition, it allows the fraction of the sample that is accessible to the measurement system to be increased for situations where the penetration depth is less than the sample dimensions.

Figure-4.7 provides a schematic illustration of the optical setup to aid understanding of the interferometer working principle. The light emitted by the laser source (~460 mW) is equally split, with one portion directed towards the top station and the other towards the bottom. The two stations are practically mirror images of each other and for this reason the following description refers only to the optical paths for the bottom lower half of the system. The reduced intensity beam is first expanded by microscope objective (MO) and illuminates a 90° parabolic mirror that acts as a

collimator while at the same time changes the direction of the beam. The collimated light is then equally split into three object beams and three reference beams by an equal number of mirrors in a triangular arrangement as illustrated in figure-4.7. It is worth noting that this stage further reduces the intensity of the beam from ~ 260 mW down to a few tens of mW for each of the six beams.

After the successful equal distribution and the subsequent division of light into reference and object beams, the two beams required to produce the interference travel different paths, guided by a series of mirrors, which are traversed only once and are eventually recombined at the pellicle beam splitter. The resulting interference signal is then imaged onto the CCD for that channel. A delay line is introduced in the path traversed by the reference beam that allows adjustment of the optical path difference, and hence the centre frequency of the signal recorded for a given tuning rate of the laser. A variable focus lens is used to image the scattered light from the sample. The angle between the reference and object beams is approximately 5°.

It should be noted that the illustration provided in figure-4.7 is an approximate schematic of the actual system, used here, as a means of describing the general working principle of the interferometer, which would otherwise prove difficult to do so from more accurate representations (see for example figure-4.8). The main drawback of the optical setup described so far is its complexity which makes it difficult to align, particularly as the light is not visible to the eye. This is a common problem with most interferometers that are based on a Mach-Zehnder setup and in most cases a He-Ne laser is used while a sequence of steps involving fine adjustments is repeated until the required quality of the interference pattern is achieved (see appendix-G in ref [48]).

4.3 Hardware and software for image acquisition

In phase-contrast interferometry, the first step prior to analysing the interference pattern involves the recording of the interference signal. As the interferogram is specified by the digitized intensity distribution $I(m,n,t)$ where m, n are the detector spatial indices and t is the time index, it becomes clear that the correct choice of the detector is crucial to the accuracy of the phase measurement.

Errors arising from the digitization of the intensity signal closely resemble those related to the conversion of an analog signal to a digital one using an analog-to-digital converter (ADC). These errors are induced by truncating or rounding the intensity signal to the nearest integer representation and are therefore commonly referred to in the literature as intensity quantization errors (QE) [192, 193].

The first study on the effect of intensity quantization on phase measurement errors was reported by *Brophy, C.P* (*1990*) for phase-shifting interferometry [192]. It was shown, analytically (see eqn.6 in ref [192]), that even though intensity quantization errors are not of a statistical nature, for cases where many bits are used to represent the modulated intensity the quantization error fluctuates rapidly with phase. The effect of quantization errors of CCD cameras and their influence on phase calculation in fringe pattern analysis was revisited by *Skydan, O.A., et al* (*2003*) [193]. In their study cameras with different bit-depths (6, 8 and 10 bits) were tested and the associated phase measurement error quantified. More specifically, it was shown that by increasing the number of grey-scale levels from 64 (6-bit depth CCD: 2^6=64) to 1024 (10-bit CCD) the error in the calculated phase reduced very significantly (see figure-4.9 for example). Moreover, it was highlighted that when the fringe pattern intensity approaches a local minimum or maximum, the quantization error and thus the phase error becomes maximum. The study concludes by comparing the quantization induced phase error between two identical systems where one is using an 8-bit CCD and the other a 12-bit one with the error being 4× smaller for the latter case. It is worth noting that the effective bit-depth of the CCD is nearly always less than the nominal value due to readout noise and shot noise.

Ever since the first report on QE and their influence on the accuracy of phase measurements [192], several research groups have studied this error source [194-197]. More specifically, *Shiyuan, Y.* and *T. Hiroaki* (2004) tested several CCD cameras with 8, 16 and 24 nominal bit depths confirming the significant reduction in phase error as the grey-scale levels of the CCD are increased [194]. Unlike previous studies, of particular importance was the observation that the error reduction below 2^{12} quantization levels is very small (see fig.4 in ref [194]), suggesting that the practical lower limit for a phase measurement system is the use of a 12-bit CCD. More recently, *Song, L. and D.S. Elson* (*2013*) studied the influence of QE on laser speckle contrast analysis (LASCA), a technique used for the measurement of blood

flow and tissue perfusion. It was found that the influence of the mean intensity on the speckle contrast is in many cases due to the quantization of intensity which is digitised with limited bit depth. Provided that the signal level is high enough to use additional grey levels, the use of a 16-bit depth CCD was suggested as a means of removing the contrast bias from the change of mean intensity [197].

On the other hand, increasing the quantization levels of the CCD has the adverse effect of significantly increasing the cost. Another drawback related to high bit depth CCDs, is that they also increase the memory requirements of the system and thus the computational effort for extracting the sought phase maps. For this reason phase retrieval algorithms that aim to reduce errors coming from the digitization of the intensity distribution are being continuously developed [195, 196].

From the above brief review, it is clear that for any phase measurement system using cameras and frame grabbers, the accuracy of the system depends on the accuracy of the acquisition subsystem which in turn is determined by the camera spatial resolution and the bit depth. As the most effective way of reducing intensity quantization errors is by increasing the numbers of bits used to sample the intensity $I(m,n,t)$, the choice of CCD camera was a Prosilica GC1380H model with the Sony ICX285 EXview sensor for increased response in the NIR and 16-bit resolution (with 12-bit true resolution) with speeds of up to 30 frames per second at full resolution (1360 × 1024 pixels). The PC used for storing and processing the images captured by the six CCDs was based on a first generation *i7* quad-core processor, 6GB memory (RAM), an AMD Radeon 6900 HD graphics processing unit (GPU) and a total of seven hard disc drives (HDD) of 1TB capacity each to store the large data sets.

For the recording of the images from the multiple CCDs, specialised software with the brand name *NorPix StreamPix 4* was used. The software offers a state of the art interface and allows the viewing, controlling and image acquisition from multiple cameras simultaneously all in the same user interface (see figure-4.10). Furthermore, *StreamPix* allows the monitoring of CCD input and output lines. As a result, any level change in input or output lines can be configured to trigger user specified events.

In the context of wavelength scanning interferometry an event is characterised by the triggering of the frame grabber each time a different wavelength is emitted by the

tuneable laser source and/or the controlling of the time duration the shutter is open depending on the laser power output. This is a rather important feature that is crucial for the synchronisation of the laser source with the several CCDs used in the system. The current system is also equipped with a digital signal amplifier (DSA) whose purpose is to:

a. amplify the TTL pulse generated by the tuneable source (see section-4.4.1) and format to the range 0 to 5 V,
b. synchronise up to eight cameras,
c. provide power along with the sync signal to each camera and
d. ensure no delay on exposure occurs compared to the master slave setup.

Following the image acquisition and storage all image processing and data analysis presented in this thesis were done in the MATLAB R2013b programming language and relevant toolboxes.

4.4 Development of tuneable laser source

Wavelength scanning interferometry and swept source OCT require the use of highly coherent tuneable light sources. Such sources in the visible or NIR regions are generally not very linear or repeatable, at least over the large scan ranges required for the current work. Two main phenomena are associated with the instability of this type of light source: a) mode hopping and b) laser jitter [198]. Both contribute to limiting the technique from fully exploiting its ability to perform phase measurements. The origins of the mode hops lie in the way wide tuning ranges are achieved [199]. A schematic representation of a typical *Ti:Sa* broadband laser source is shown in figure-4.11.

4.4.1 *Ti:Sa* laser customization

A SolsTis CW Ti:Sapphire laser manufactured by M Squared Ltd [200] has been customized by the manufacturer specifically for this system. The laser operates in a bow tie laser cavity configuration (similar to the configuration shown in figure-4.11), with a gain curve in the near infrared region spanning ~150 nm. The dimensions of the laser cavity result in a cavity mode spacing of 416 MHz or approximately 0.78 pm. The bandwidth of the laser output is reduced significantly using two main components: a birefringent filter (BRF) and an etalon. The BRF reduces the cavity

gain by 7% over a range of ~300 GHz and thus acts as a coarse mode selection device. The etalon has a free spectral range (FSR) of 320 GHz allowing selection of cavity modes over a 0.6 nm tuning range (see figure-4.12 for a schematic illustration of the wavelength selection process described above).

In the laser's normal mode of operation for spectroscopy applications, the motorized BRF is tilted first through the user interface to provide a coarse wavelength adjustment. It is then followed by a fine tuning step using the etalon whose thickness is changed by means of a piezo electric translator (PZT), again through the user interface. Although very precise adjustment is possible (wavelength resolution better than 0.001 nm), it would be impractical to perform a complete WSI scan consisting of upwards of 10,000 individual images, each at a different wavenumber, in this way. The laser was therefore customized by the manufacturer by introducing the following features:

1. The software controlling the embedded digital signal processor (DSP) was modified to perform both the coarse and fine tuning fully automatically.
2. A wavelength-sensitive diode (WSD) was introduced and monitored by the DSP. This became part of a feedback loop to ensure that tilt of the BRF induces a wavelength shift of only a single (as opposed to multiple) etalon FSR.
3. Between movements of the BRF, each etalon scan was implemented as a staircase-like voltage profile to the PZT such that the voltage steps produced a nominally-constant user-defined jump in wavenumber.
4. External TTL trigger pulses were made available, coincident with the etalon scan voltage steps, to initiate the light integration period of the cameras.

5. Automatic changes in timing pulse duration were provided to allow exposure compensation for the change in power output of the laser with wavelength.

The duration of the external synchronization pulses from the laser is controlled by means of a look-up table that is input manually by the user. An initial calibration scan is required to detect the intensity variations (or, more precisely, the combined variation of laser power and camera sensitivity) along the intended wavelength scanning interval. An initial exposure duration, ε_0, is chosen such that almost the full dynamic range of the camera is used at the peak laser power. Mean intensity vs. wavelength $\bar{I}(\lambda)$ data is first obtained by calculating the average grey level over each camera frame where the wavelengths are measured by the WSD and logged by the DSP. In this preliminary step, it is not necessary to have a detailed scan, as the laser gain curve changes smoothly over the ~100 nm *Ti:Sa* tuning range. Only 30 samples are typically sufficient to track the intensity changes.

A polynomial fit $p(\lambda)$ is obtained from the mean intensity values and then normalized to give

$$p_1(\lambda) = p(\lambda)/max(p(\lambda)) \ . \qquad 4.1$$

Assuming a linear camera response, a fully compensated exposure time ε_1 could be calculated as,

$$\varepsilon_1(\lambda) = \varepsilon_0/p_1(\lambda) \ . \qquad 4.2$$

However, this has the drawback that the exposure time diverges as the ends of the usable tuning range are approached. In practice, an alternative compensation scheme calculated as

$$\varepsilon_2(\lambda) = \varepsilon_0\big(2 - p_1(\lambda)\big) , \qquad 4.3$$

provides a partial compensation that corresponds closely to $\varepsilon_1(\lambda)$ for small changes in laser power and yet is limited to a maximum two-fold increase in exposure time as $p_1 \rightarrow 0$. Figure-4.13 shows a typical experimental plot of p_1, $\varepsilon_1(\lambda)/\varepsilon_0$ and $\varepsilon_2(\lambda)/\varepsilon_0$ (maximum laser power = 500 mW, initial pulse duration ε_0 = 600 μs, and polynomial

order = 12). Figure-4.14 illustrates the effect of controlling the width of the camera synchronisation signal so as to adjust its shutter speed in this way over a full 100 nm scan. The shape of the envelope that multiplies the high frequency modulation is seen to be far more uniform for the adjustable shutter speed case (b) than for the constant shutter time (a).

4.4.2 Ti:Sa laser behaviour aspects and limitations

The principle of operation of the wavelength selection for the electronically tuned *Ti:Sa* laser was described in the previous section. Considering that there had been no reports of using this type of source with such a wide tuning range in the relevant WSI and SS-OCT scientific communities (refer back to section-2.5.2 and table-2.2), its behaviour is worth investigating for two reasons: a) due to its uniqueness and b) because the accuracy of the phase measurements to follow (see section-4.5 and chapters 5, 6 and 7) depends strongly on the ability of the customised *Ti:Sa* source to conform with equation-2.35.

To do so a simple experiment that reveals the actual laser behaviour is devised in which the BRF is manually tuned. More specifically, the light emitted by the *Ti:Sa* laser head was directed onto a conventional power meter head that is sensitive only to the laser's spectrum (approximately 0.65 to 1.2 μm). The BRF was then manually tilted by rotating a screw controlling its angle through a full 360-degree rotation in five second intervals while the power (from the power meter) and the wavelength fluctuations (from the user interface of the laser controlling software) were manually recorded. The procedure described above was repeated by tilting the BRF towards the opposite direction for a full rotation for consistency and revealed the same four BRF orders shown in figure-4.15 with the first lasting five seconds and the other three lasting approximately 55 seconds. Unlike the first and second BRF orders where the wavelength fluctuations were limited in the region of 897-905 nm and 888-905 nm respectively, inside the third and fourth orders the wavelength fluctuations spanned much greater regions that were much closer to the laser's normal tuning range of 750-850 nm. It should be noted that at the time, the tuneable source had already started malfunctioning, as is evident from the limited power recorded by the power meter in figure-4.15 and this simple experiment was performed in part as an attempt to understand the reason for the malfunction with the

manufacturer. Unfortunately, the laser eventually failed permanently due to failure of the etalon scanning device. Nevertheless, according to the manufacturer, the second and third BRF orders are the ones within either of which continuous wavelength scanning is achievable with the use of the etalon fine filter.

Another aspect revealed by the experiment described above is the sensitivity of the instrument to misalignment. Although subsequent generations of the CW Ti:Sa laser that are fully automated are now available [201], the current system which was the first ever produced by M-squared lasers that was able to be electronically tuned over the full wavelength range, suffers from the fact that once a full scan is performed manual alignment of the BRF followed by the tuning of the etalon via the user interface is required before the system is ready for the next scan (see appendix-A4 for more details on the laser operating procedure).

As mentioned earlier in section-4.4.1, in theory, the selection of a single mode that corresponds to a single wavelength (determined by the minimum linewidth of the system which in this case is approximately 5 kHz) is performed simultaneously by the BRF and the etalon. In practice, the combined movement of the two complementary to each other wavelength selection mechanisms results in the bypassing of some of the cavity modes inside the BRF order thereby causing the phenomenon commonly termed as mode hopping. This has in turn the undesirable effect of causing the wavelength to jump up and down as the scan progresses and violates the necessary condition for WSI applications which strictly speaking requires the sequential and monotonic tuning of the wavelength or wavenumber of the laser source (equation-2.35).

Figure-4.16 illustrates the presence of mode hops using the recorded wavelength values (λ_{WSD}) from the wavelength sensitive diode (WSD) which are plotted versus the non-dimensional time index t that corresponds to the frame number, for a full 100 nm scan. It is clear from figure-4.16 that certain areas of the tuning range are more affected by the wavelength jitter than others (i.e., around $t \in [9000, 10500]$). One possible reason for this behaviour, according to the manufacturer, is moisture in the air which has certain resonances in this wavelength range, and which is normally dealt with by nitrogen purging of the cavity. However, this solution comes at the expense of increasing the cost and was therefore omitted from the particular system.

Yet another aspect revealed from figure-4.16 is that although a full scan was performed, only 25 of the total 100 nm scanned were recorded by the WSD. This was due to the WSD memory limitations associated with the number of data points in the scan. In this case a wavelength step, $\delta\lambda$, of 2 pm resulted in a data set with 50,000 entries and is consistent with the 100 nm scan. The WSD was put into the system as a guide to aid the understanding of the laser behaviour rather than to act as a real time and accurate wavelength meter.

Finally, the optimum speed of wavelength scanning for such small wavelength steps was experimentally determined from the quality of the captured images to be 6 Hz (see section-5.4 for more details), a value that is much lower than the maximum number of frames that the CCDs of the system can capture every one second (30 fps). This suggests that the speed that the data is acquired in this system is in fact controlled by the speed of the unambiguous scanning of the laser frequency rather than that of the frame grabber.

4.5 Depth-resolved intensity imaging: preliminary results using glass samples

So far a description of the multi-axis tomographic wavelength scanning interferometer under development along with its constituent components has been provided. From the above description it is clear that the behaviour of the laser source is a key aspect to the performance of the system. In this section its ability to perform depth-resolved measurements is assessed using a series of glass wedges (see appendix-A4 for more details) with central thicknesses of 9.6, 12.0, 12.6 and 12.8 mm respectively. The optical setup used for these simple experiments is illustrated in figure-4.17. The resulting interference signal formed from the front and back reflections of the glass samples is imaged onto the CCD while the wavelength of the source is tuned sequentially. By analysing the digitised intensity distribution $I(x,y,t)$, where x,y are the pixel indices of the 2-D CCD array and t is the non-dimensional time index corresponding to the wavelength of the source and therefore the frame number of the data sequence captured, insight into the laser performance is possible.

Figure-4.18(a) shows the intensity signal $I(x,y,t)$ for a short 2 nm scan from which it is clear that certain regions of the signal deviate significantly from the ideal cosine

form (at t ~ 300,600 and 900). One possible reason to explain this signal degradation is the presence of wavenumber jumps caused by the laser mode hops in the scan. In figure-4.18(b) the wavenumber change k_0-k (k =2π/λ) for the short scan is shown as a function of t using the WSD readings, where the presence of wavenumber jumps for t ~ 300 and t ~ 900 is clearly visible. This on the other hand is not the case for t ~ 600, suggesting that either the reading from the WSD for that particular frame is faulty or that there has been some problem with the hardware and/or software used for the data acquisition. As it is difficult, at this stage, to isolate the reason for this occurrence it will be left to deal with in the future. In figure-4.18(c) the intensity distribution, $I(x,y,k_0-k)$, after its re-registration onto the wavenumber change axis, k_0-k, using the WSD readings, is shown from which the effect of small and large wavenumber jumps during the scan on the intensity signal degradation is clear. Moreover, the re-registration step should result in an intensity signal which is varying sinusoidally with k_0-k, the frequency of which is proportional to the OPD through equation-2.19 and equation-2.20 (see section-2.4.1). The intensity signal in figure-4.18(c) is however noticeably less sinusoidal than that of the uncorrected signal in figure-4.18(a), which may be a consequence of the use of the low accuracy WSD readings to perform the correction.

Figure-4.19 illustrates the normalised intensity spectrum $|\tilde{I}|$ for a short (left column of figure) and longer scan duration (right column of figure), with and without re-registration onto the wavenumber axis. The presence of multiple peaks in the intensity Fourier-transform was expected due to the wavenumber jumps that randomise the signal. However, the spectral lobes of the Fourier-transform of $I(x,y,t)$ look cleaner than those of $I(x,y,k_0-k)$. This further confirms that the readings of the WSD used to estimate the wavenumber change are insufficiently accurate to re-register the intensities as a function of wavenumber change and should only be used as a guide.

Figure-4.20 shows the results of performing the same analysis on each pixel along the cross section $x = x_c$ for each of four wedges, where x_c is the pixel index corresponding to the centre of each wedge. Results are shown for a ~2 nm (left column) and a ~25 nm scan (right column). Ideally these should appear as bright lines revealing the shape of the back surface of the four glass wedges. This, however,

is clearly not the case, with the main Fourier peak showing significant splitting and in some cases becoming hardly visible. The most likely reason for this phenomenon is attributed to the presence of wavenumber jumps whose effect in randomising the signal is amplified as the width of the scan is increased. To demonstrate how significant the deviation of the wavenumber change $\delta k(t) = k(0) - k(t)$ from the ideal linear behaviour is, a linear least square fit was performed on the $\delta k(t)$ from the WSD readings (see figure-4.21(a)) to determine the best fit line (figure-4.21(b)) for the first 400 frames only and then extending it for the rest of the sequence, with the difference between the two shown in figure-4.21(c). Note that the reason of performing the LSF to the 400 frames only is to illustrate the detrimental effect that this has if one was to assume that the behaviour of the laser can be safely assumed to follow the same trend for the rest of the sequence. This last point will become clearer from chapter-5 onwards where a short scan lasting 400 frames is analysed followed by the analysis of the full scan range (~50,000 frames) covering the entire 100 nm operating range of the Ti:Sa laser (Chapter-6 onwards).

4.6 Summary

In this chapter a detailed description of the multi-channel wavelength scanning interferometer and its constituent parts has been provided. Unlike in other multi-channel systems previously reported, the current is comprised of by multiple (6×) CCDs owing to the high power output of the *Ti:Sa* laser source. The specifications of the CCDs were carefully chosen so that the well-known issue of quantization errors is reduced by ensuring that sufficient grey levels are available. The broadband source employed in this system was manufactured by M-squared lasers and was initially designed for spectroscopic applications. However, it was highly customised for WSI applications and is therefore a key aspect contributing to the novelty of this research project. Finally, a set of preliminary results using glass samples has been presented that provided insight of the performance and limitations of the system developed so far. An important observation made during the experiments was that the data acquisition speed is determined by the unambiguous wavelength scanning speed rather than the frame grabber speed. One of the main drawbacks revealed was the presence of a significant amount of mode hops throughout the scan durations. These were also confirmed by the readings of the WSD that was put in place as part of a

feedback loop that ensures the selection of a single wavelength. These mode hops have the undesirable effect of causing the wavenumber (k) to deviate significantly from the linear behaviour required for WSI applications. As a result, the phase of the recorded intensity distribution is randomised causing significant artefacts in the computed optical thickness distribution. Although the use of the WSD readings may seem an attractive solution to overcoming this problem, the accuracy is seen to be insufficient to resolve the mode hop issue.

4.7 Conclusions

From the preliminary experiments presented here, it is clear that without precise knowledge of the wavenumber changes during the scan, the imaging of the interference signal of the WSI system developed and consequently the accuracy of phase contrast measurements is significantly compromised. It is for this reason that the remainder of this work is focused on the development of hardware and software that will allow the accurate monitoring of wavenumber changes and will therefore enable successful depth reconstructions and the sought phase measurements.

4.8 Figures

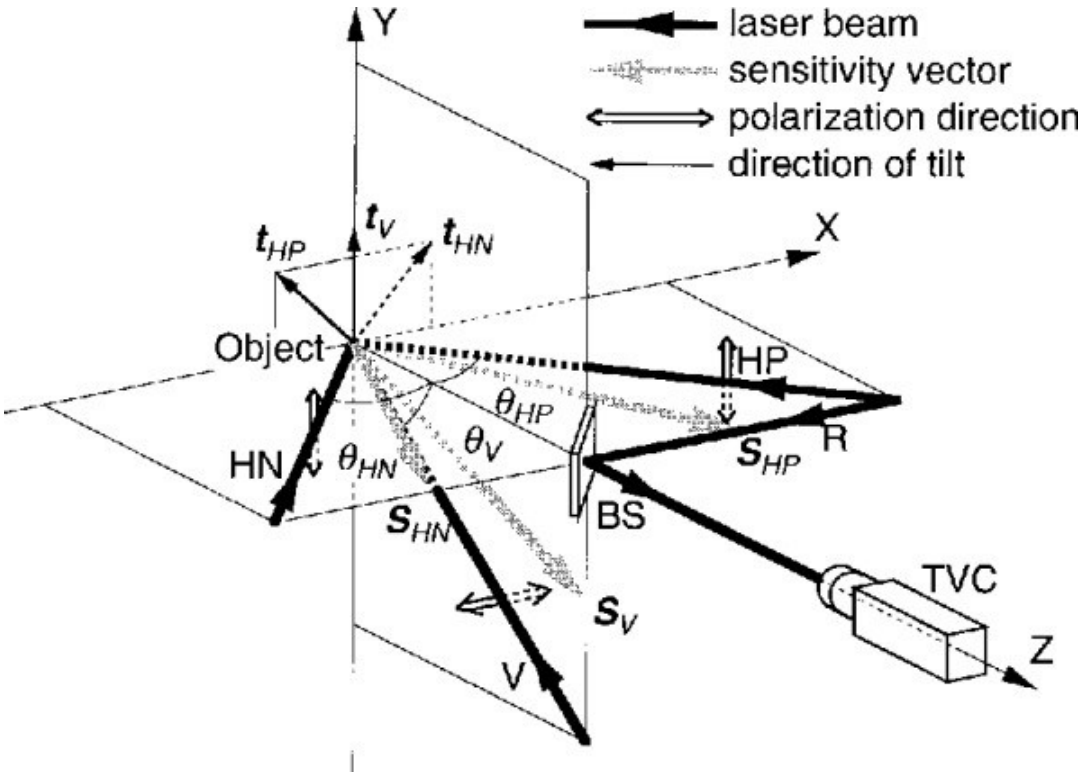

Figure-4.1: Optical configuration of the first setup used for the simultaneous measurement of three orthogonal displacement components using ESPI. Object beams HP, HN, and V illuminate the object at angles θ_{HP}, θ_{HN}, and θ_V, respectively, with respect to the *Z* axis. The scattered light is combined with the reference beam (R) through the beam splitter (BS) and captured with the CCD TV camera (TVC). $\mathbf{s}_{HP}$, $\mathbf{s}_{HN}$, and $\mathbf{s}_V$ are the sensitivity vectors of the interferometer composed of HP and R beams, HN and R beams, and V and R beams, respectively; $\mathbf{t}_{HP}$, $\mathbf{t}_{HN}$, and $\mathbf{t}_V$ are the directions of tilt of the object beams to generate carrier fringes. NOTE: This is a copy of fig.1 in ref [183].

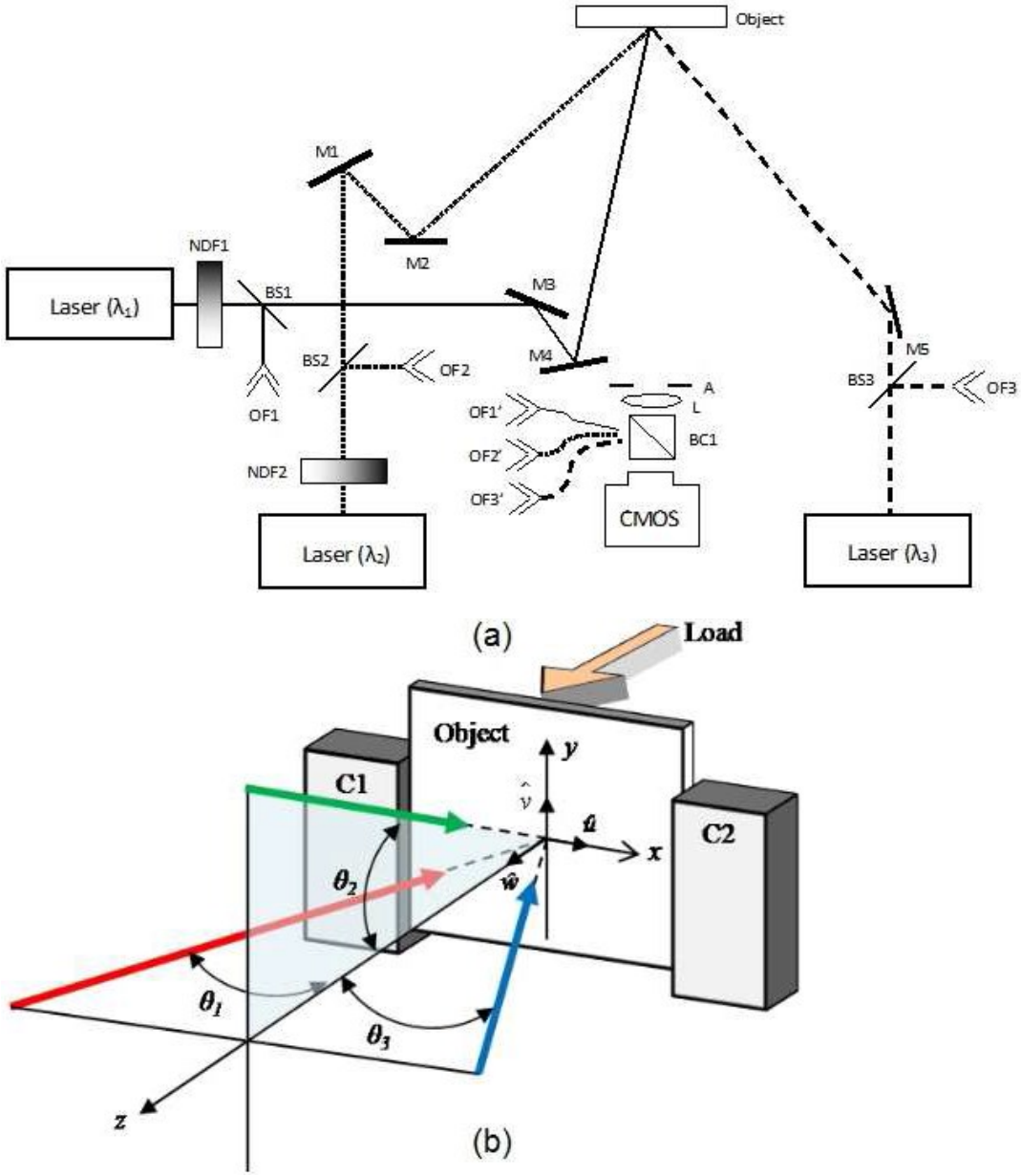

Figure-4.2: (a) Schematic view of the optical set up using three lasers, (b) Mechanical rig used to illuminate and constrain the sample under study. In this geometry $\theta_1 = \theta_2 = \theta_3 = \theta$. NOTE: This is a copy of fig.1 in ref [186].

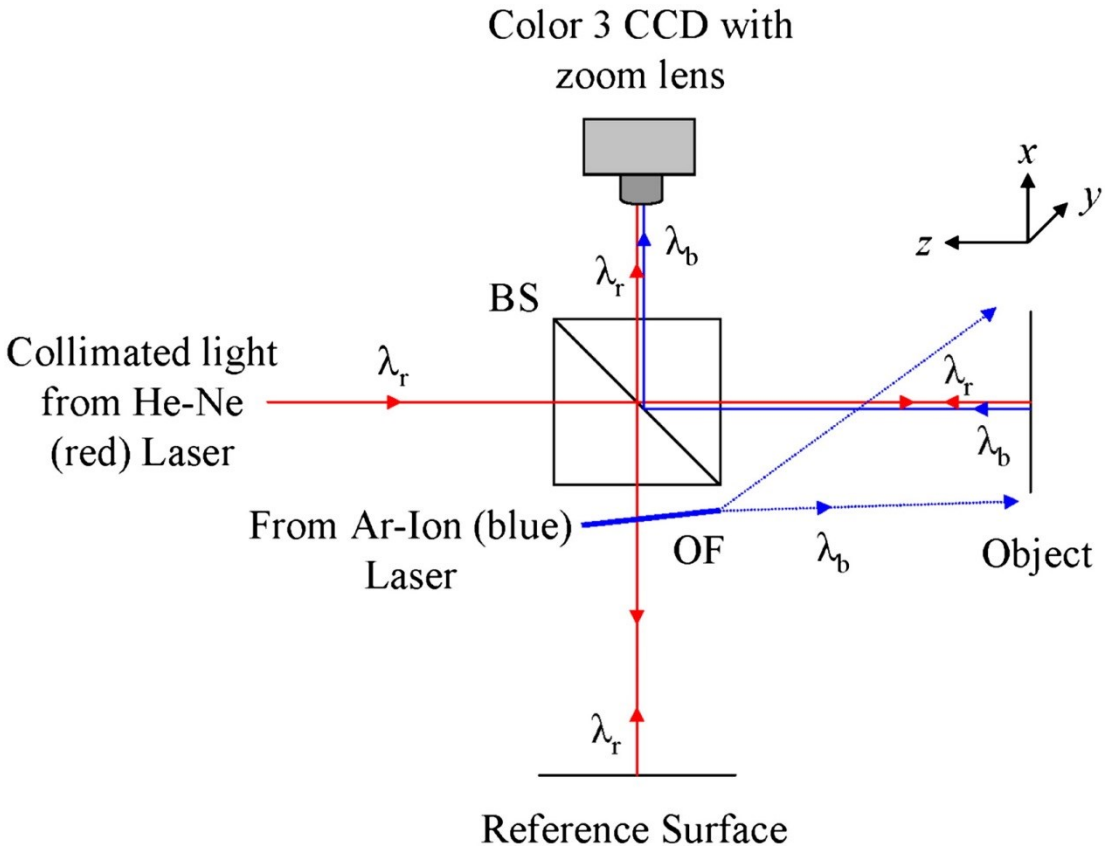

Figure-4.3: Schematic of the optical arrangement for simultaneous 3-D displacement measurement using two wavelength illumination: BS, beam splitter; OF, optical fibre; λ_b, blue wavelength; λ_r, red wavelength; CCD, charge coupled device (copy of fig.1 in ref [187]).

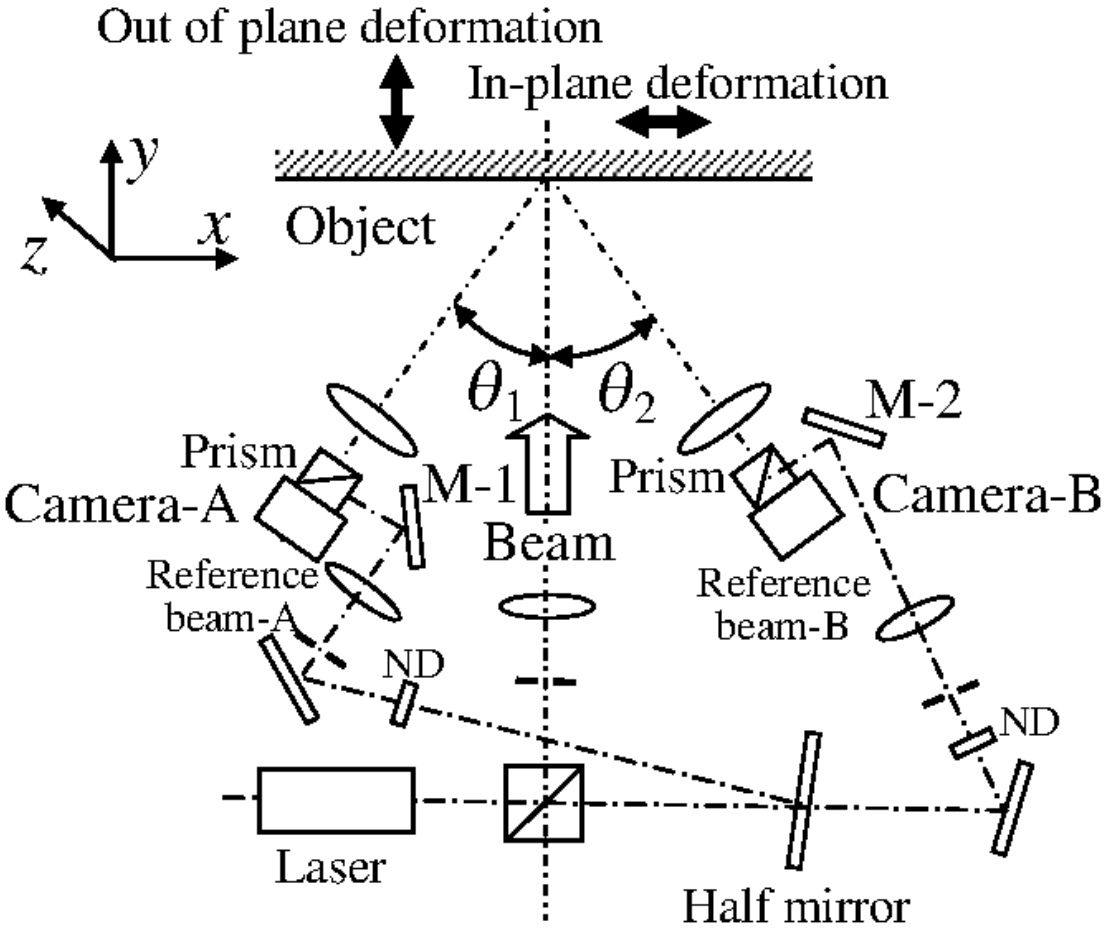

Figure-4.4: Proposed optical system for in-plane and out-of-plane deformation measurements (Copy of fig.3 in ref [188]).

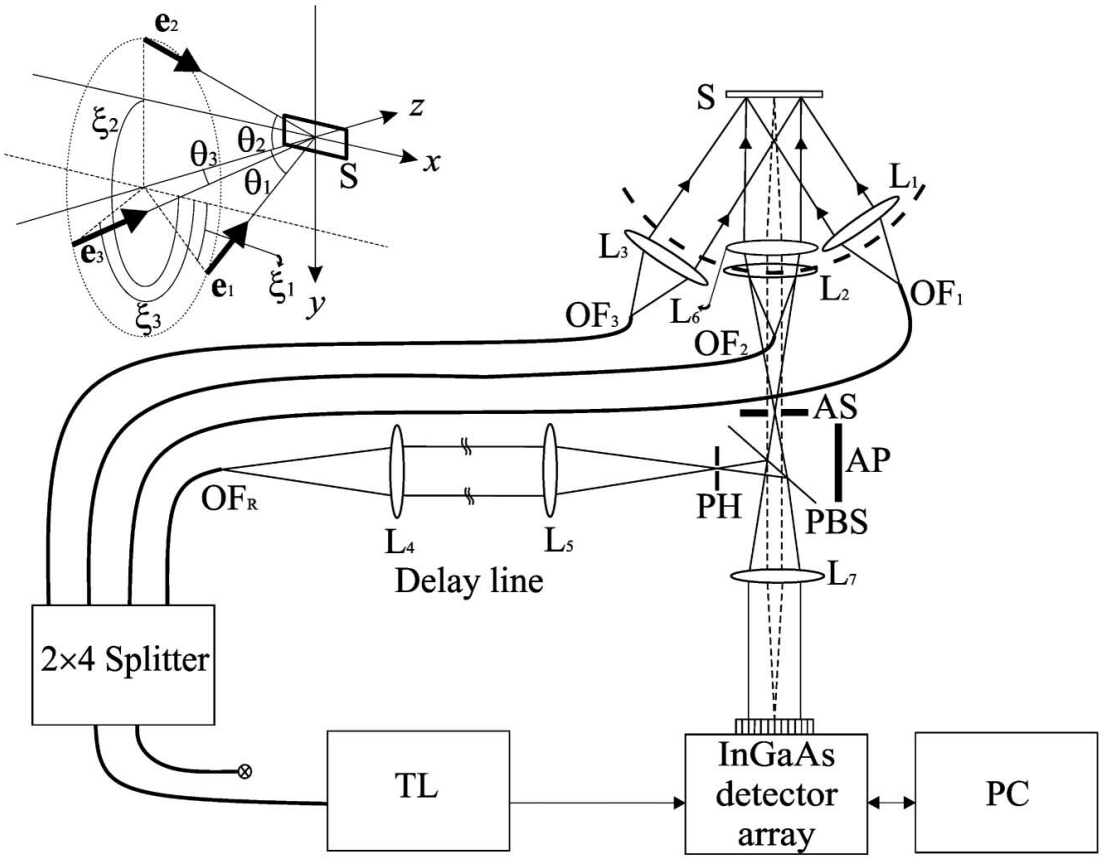

Figure-4.5: WSI setup showing the tuneable laser (TL), 2 × 4 PLC splitter, InGaAs detector, pellicle beam-splitter (PBS), absorber plate (AP), pinhole (PH), aperture stop (AS), sample (S), lenses (L1–L7), optical fibres (OF1,OF2,OF3,OFR), and personal computer (PC). NOTE: This is a copy of fig.1 in ref [27].

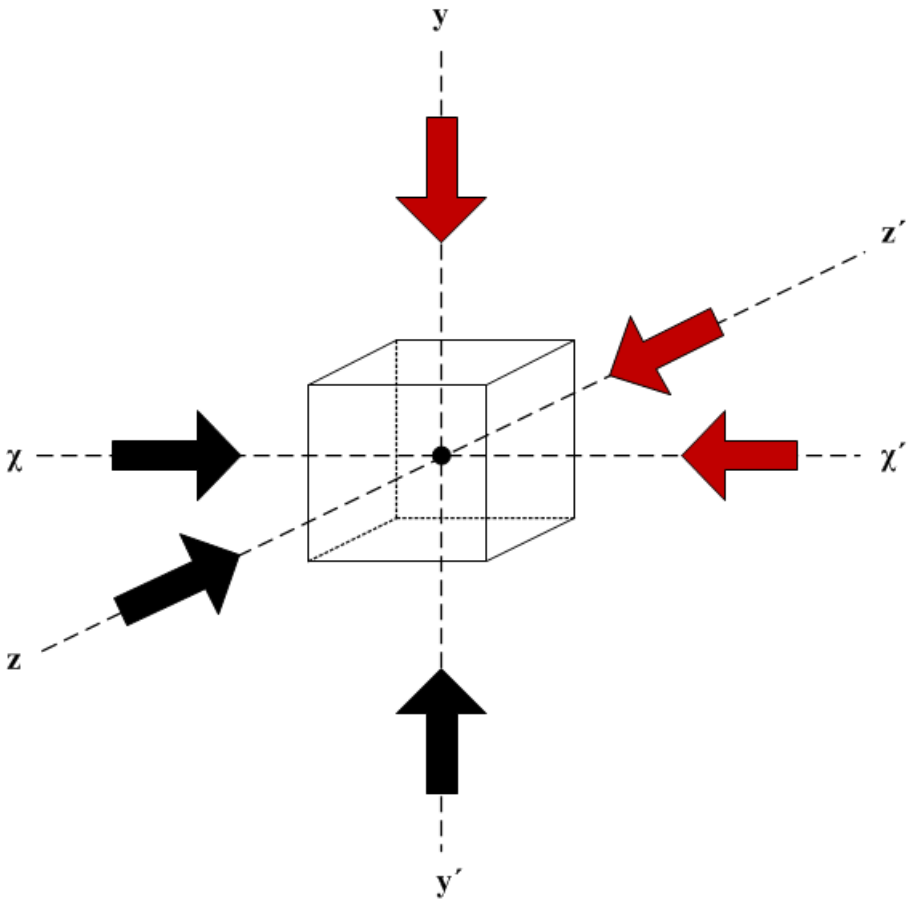

Figure-4.6: Schematic that illustrates the principal geometric layout of a cubic sample viewed from a minimum of three and a maximum of six directions, onto which the multi-axis tomographic interferometer was developed. The black arrows indicate one of the possible sets of the necessary directions to extract the three orthogonal deformation components. The red arrows are complementary as far as the calculation of the displacement components is concerned but can be used as means of ensuring the consistency of the calculated 3-D displacements (complementary red and black arrows have in principle the same sensitivity) as well as for effectively doubling the depth range of the system while the depth resolution remains identical.

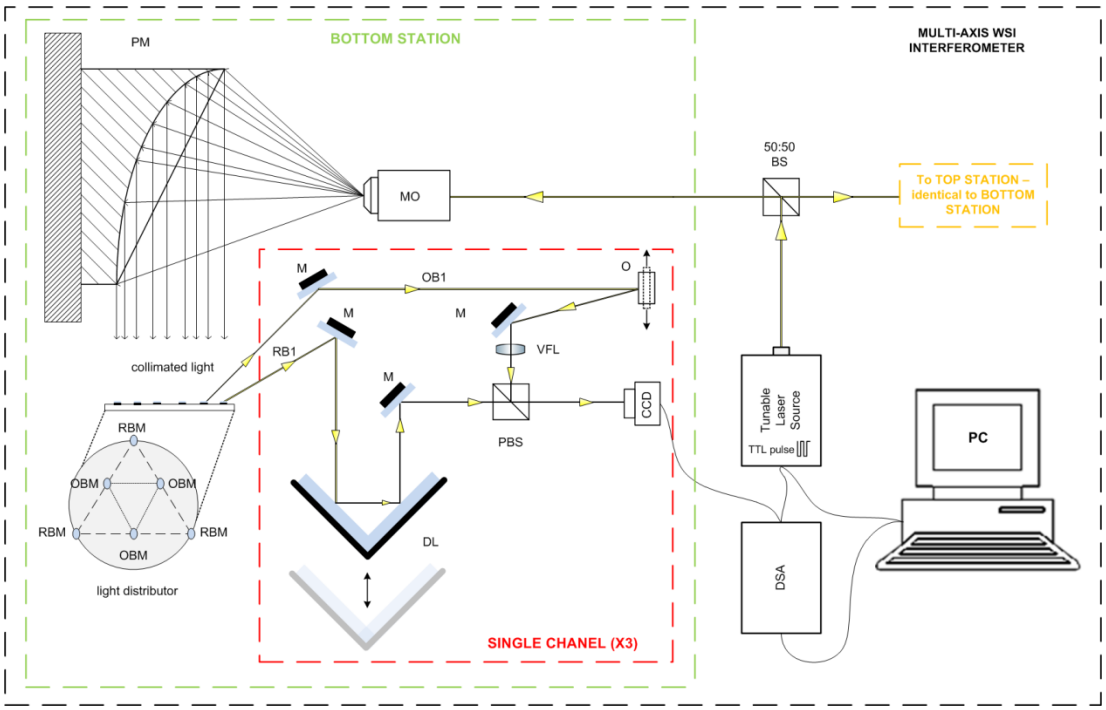

Figure-4.7: Schematic illustration of the multi-channel WSI optical setup. PM: parabolic mirror, MO: microscope objective, M: mirror, RBM: reference beam mirror, OBM: object beam mirror, DL: delay line, PBS: pellicle beam splitter, CCD: charged coupled device, O: object or sample, BS: beam splitter, VFL: variable focus lens, DSA: digital signal amplifier to amplify and format the TTL generated pulse by the laser source to the range 0 to 5 V.

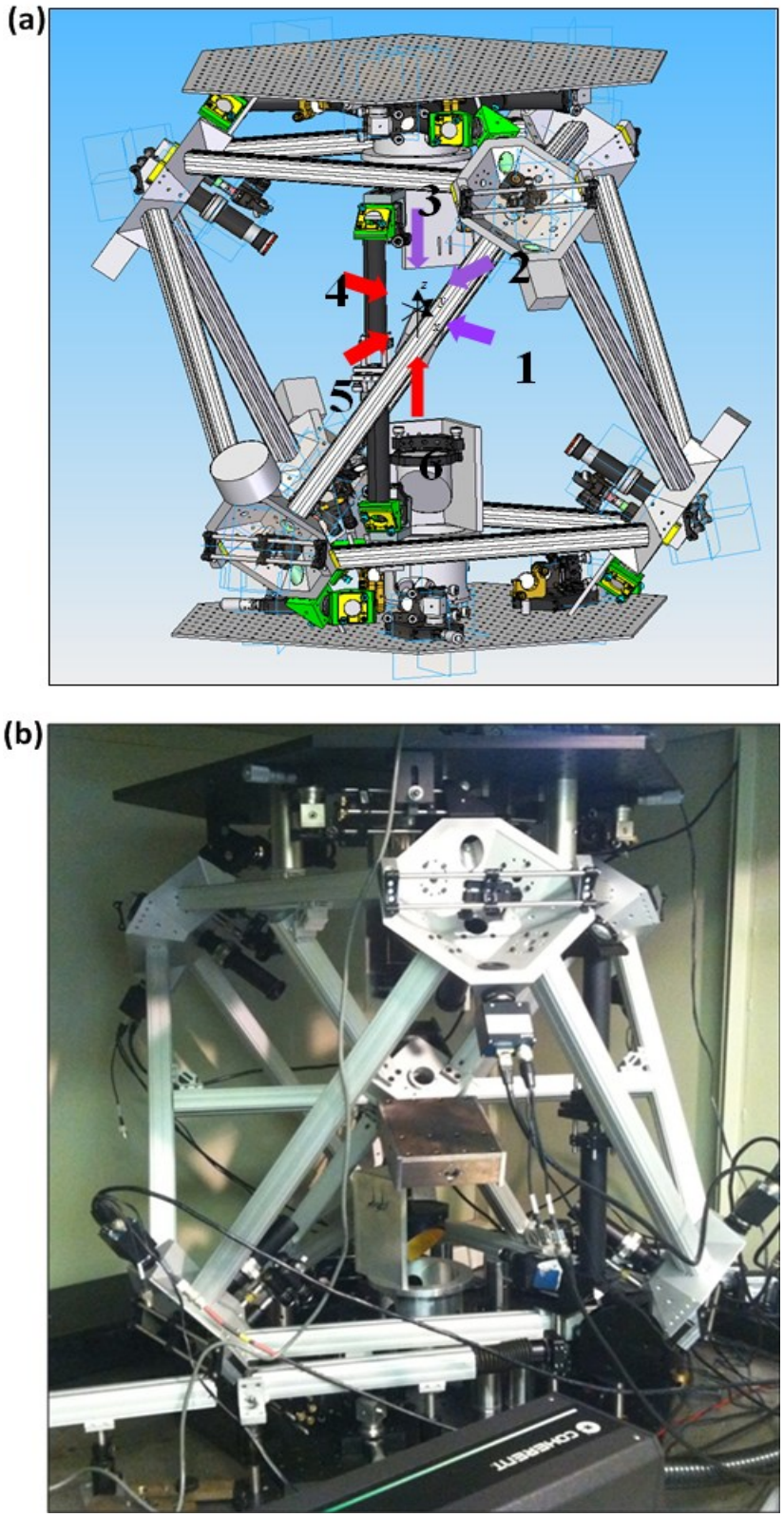

Figure-4.8: (a) CAD model of the multi-axis WSI system under development (reproduced with permission from [175]). The red arrows indicate the sensitivity direction and sense of the bottom station, 3-channel interferometer, while the purple ones correspond to the sensitivity vector direction and sense of the top station 3-channel interferometer (b) Partially complete assembly of the interferometer.

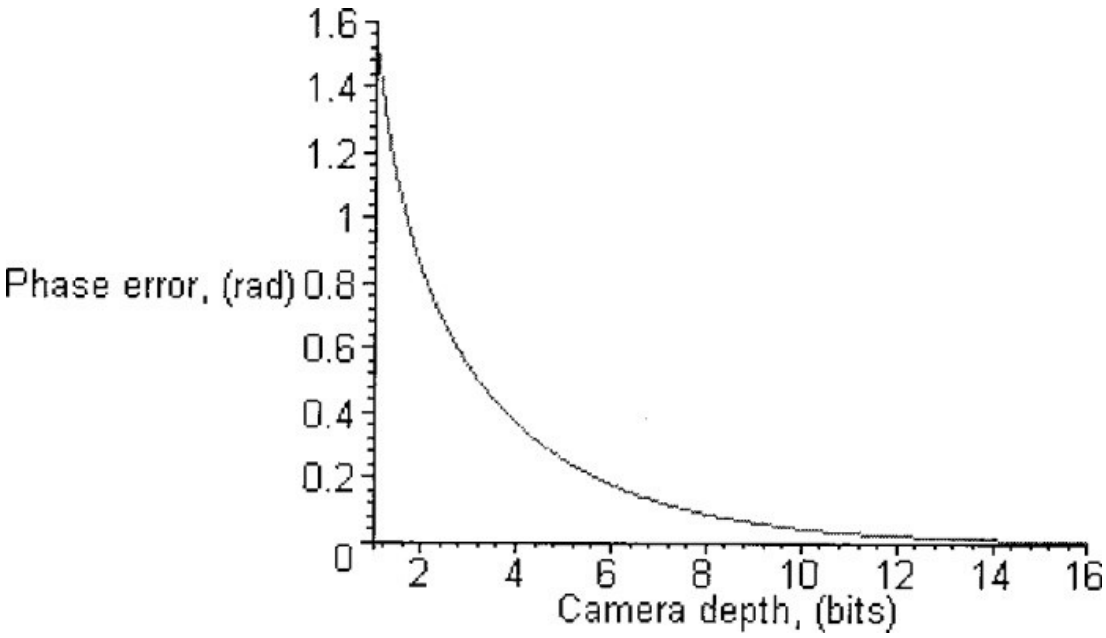

Figure-4.9: Phase measurement error as a function of camera bit-depth illustrating how insufficient grey-scale levels during the digitisation of the modulated intensity affect the measured phase. Copy of fig.3 in ref [193].

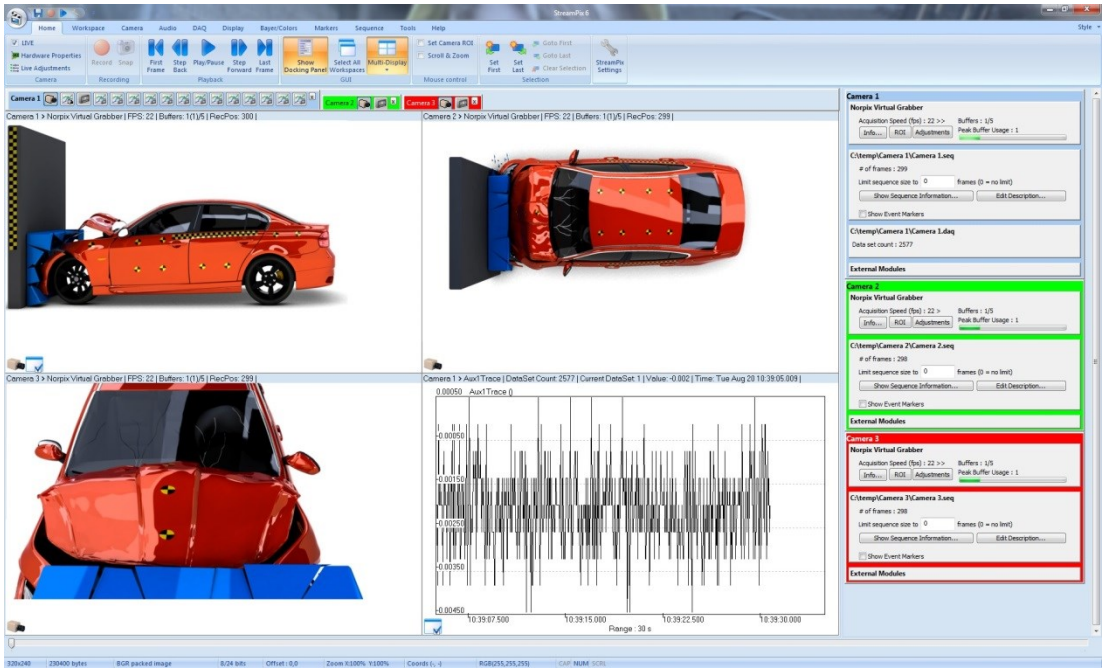

Figure-4.10: Typical *NorPix StreamPix* software user interface that allows easy control of any number of cameras through the same interface. On the left: real time images from the three cameras used in this case. On the right: easy access to the control parameters of each camera such as image size, frame rate, pixel saturation control etc. Adopted from [202] for illustration purposes only.

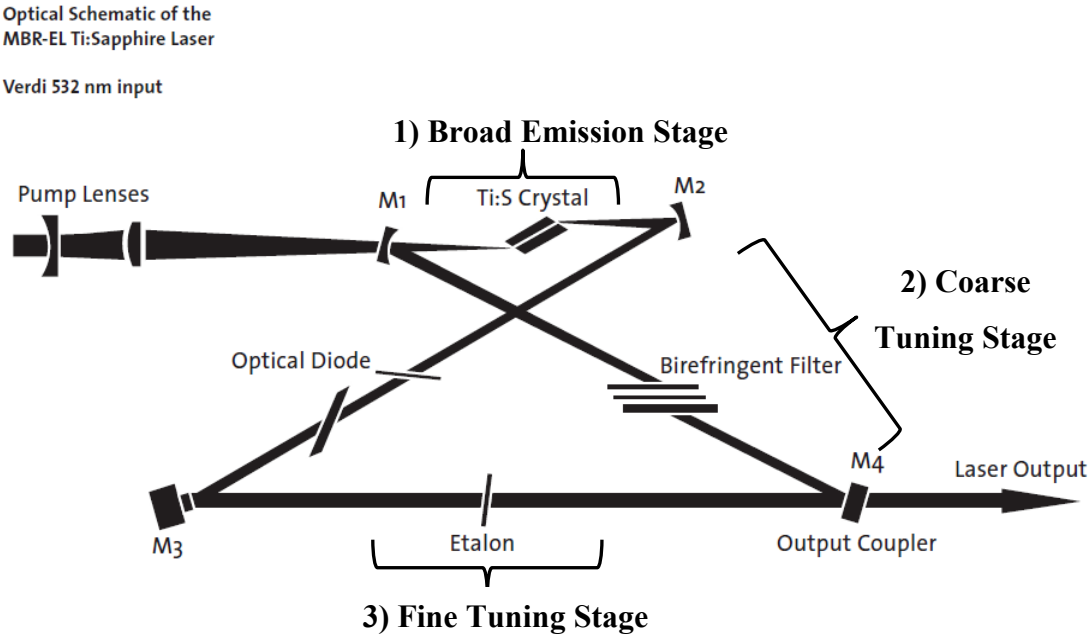

Figure-4.11: Ti:Sa laser operating in a bow tie cavity arrangement. (Adopted from ref [203])

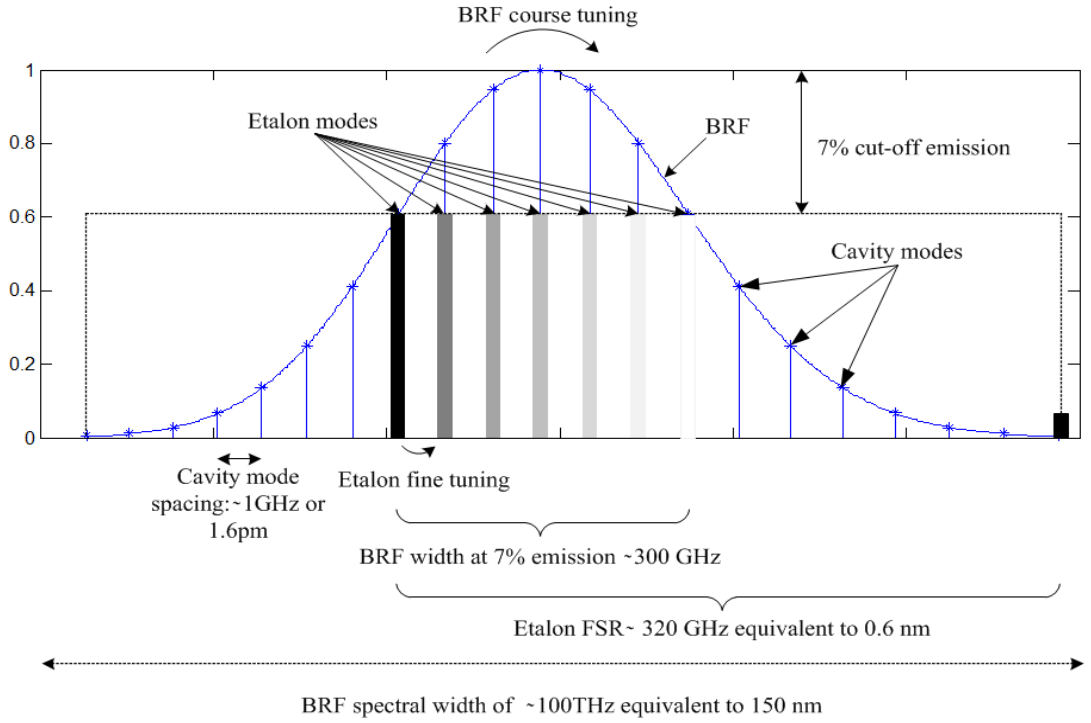

Figure-4.12: Schematic representation of the ideal/theoretical wavelength selection mechanism for the customised *Ti:Sa* laser source for WSI applications. The BRF shown as a Gaussian modulation function (blue line) filters a set of cavity modes while the etalon filters out each cavity mode at 7% cut-off emission (range of black to white bars) in a sequential manner. The BRF is then tilted and a new set of cavity modes is selected followed by the etalon fine tuning until the entire spectrum is covered.

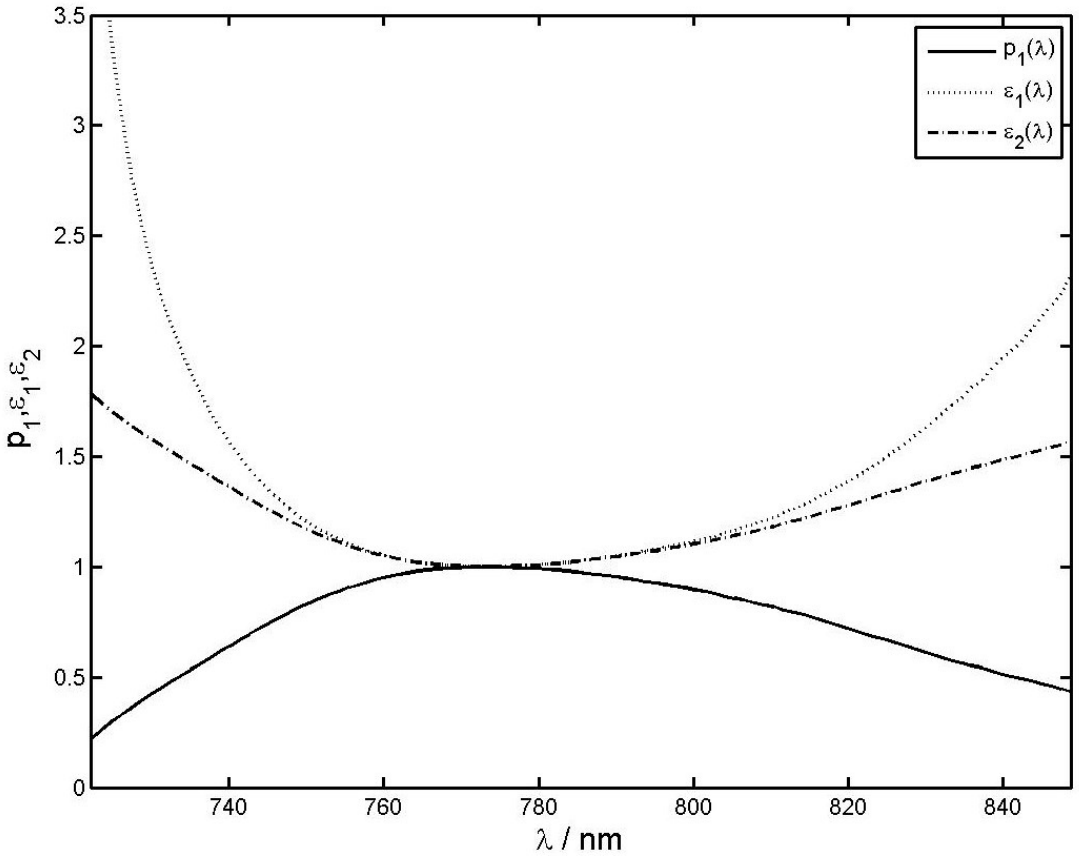

Figure-4.13: Camera exposure duration compensation schemes to account for variation in laser power and camera sensitivity. ε_1: full compensation; ε_2 partial compensation with upper exposure duration limit (Reproduction of fig.1 of ref [21]).

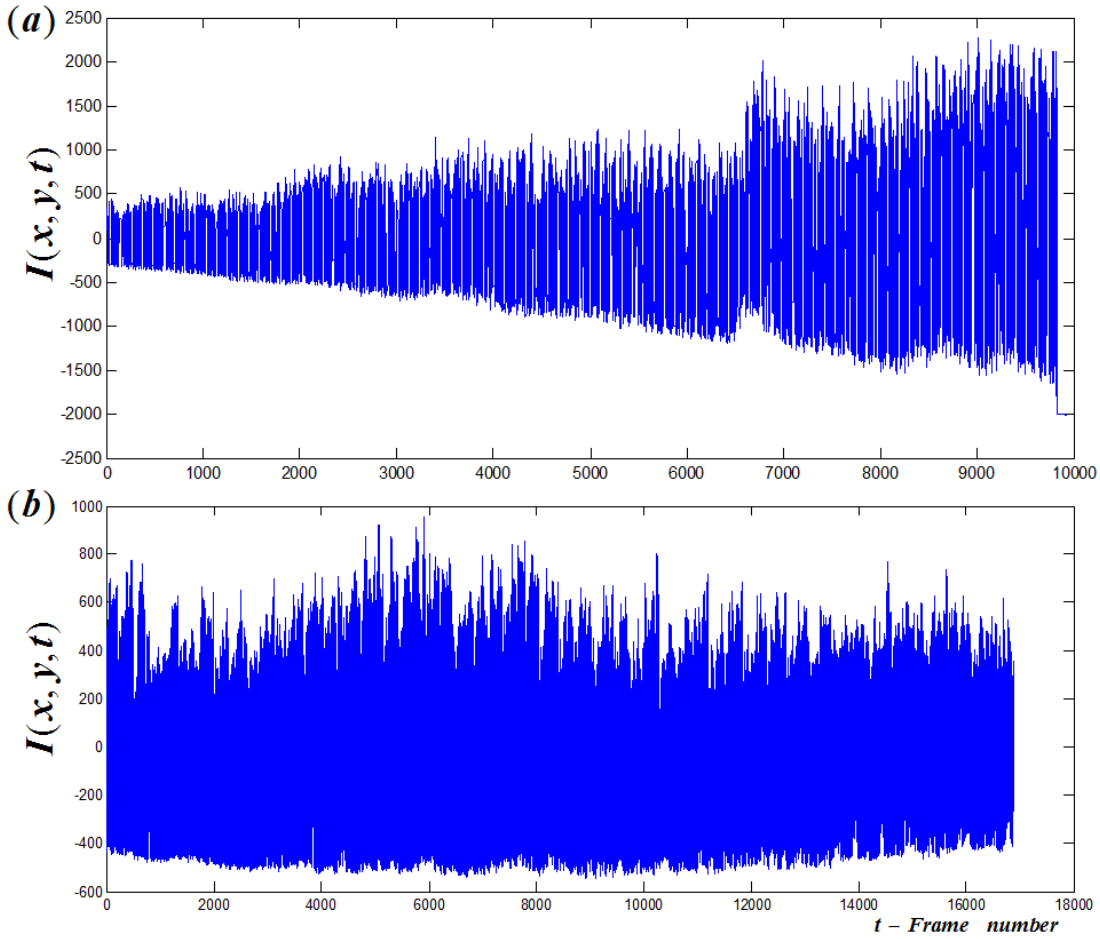

Figure-4.14: Intensity signal $I(x,y,t)$, after subtraction of the d.c level, for a single pixel where x,y are pixel coordinates and t is a non-dimensional time index equivalent to the data sequence frame number for a 100 nm scan range. (a) Fixed rate shutter speed and (b) adjustable shutter speed. Adopted with permission from [175].

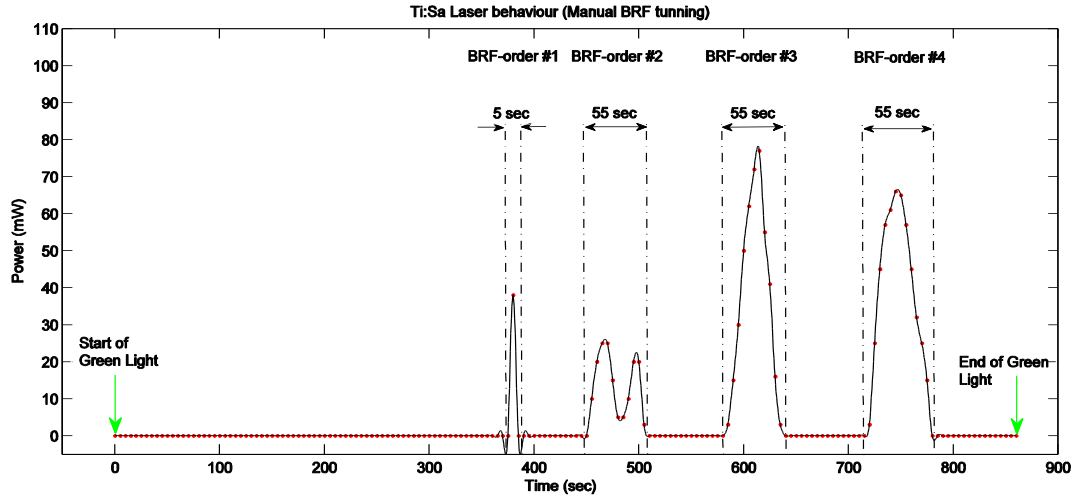

Figure-4.15: Experimental data showing the four BRF orders. Red dots: experimental values of the laser power. Black line: fitted line to the experimental line.

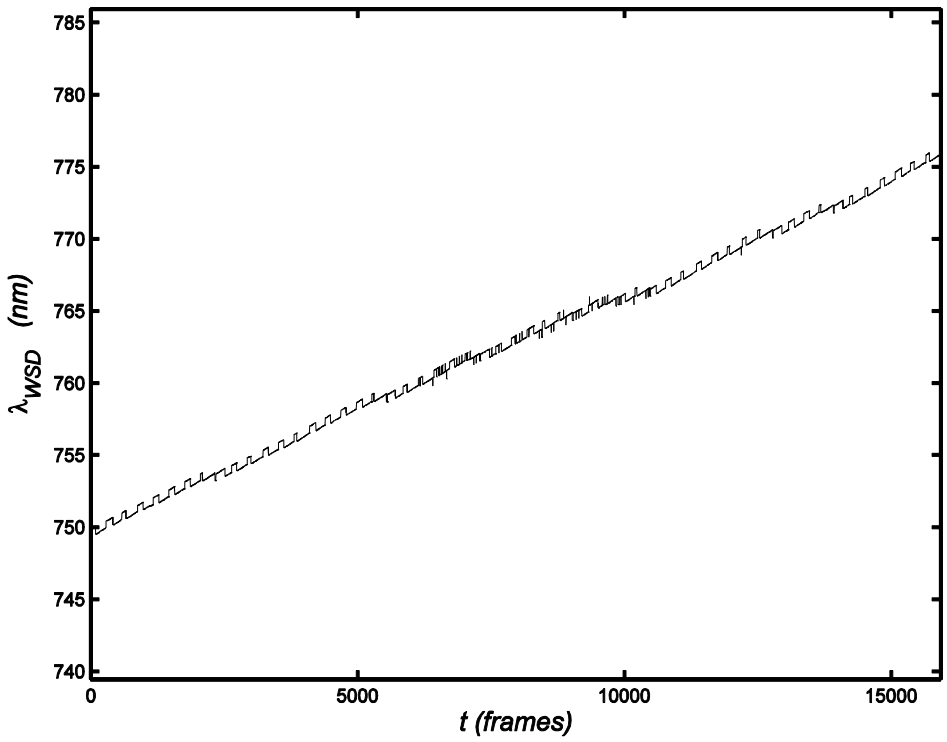

Figure-4.16: Wavelength of the Ti:Sa laser source as a function of the non-dimensional time index t (equivalent to the frame number of the data sequence recorded for a full 100 nm scan (750-850 nm). Note that the WSD can only record a limited number of entries due to memory limitations. This is why the plot stops at approximately 775 nm as opposed to the actual finishing wavelength of 850 nm.

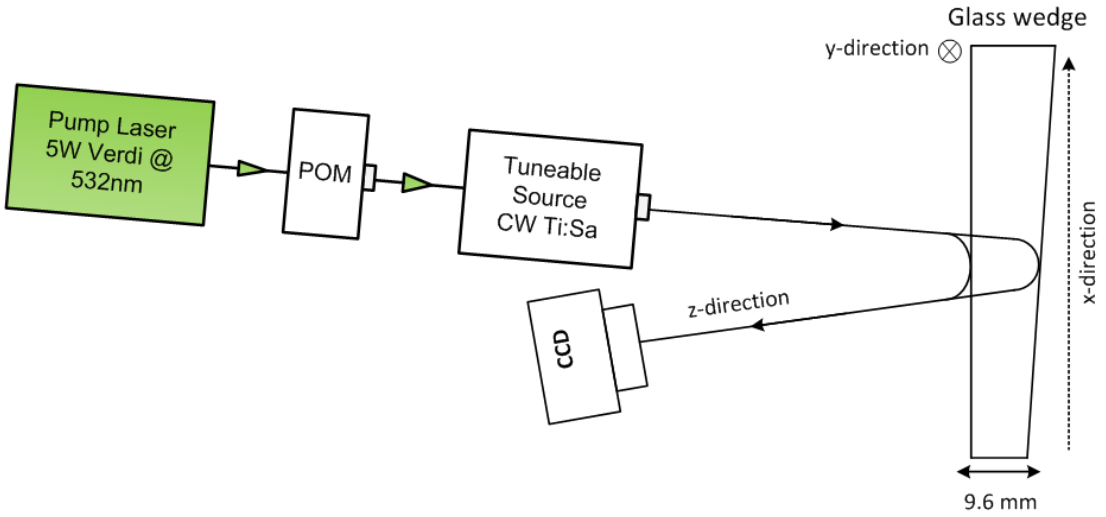

Figure-4.17: Exaggerated experimental optical setup used for assessing the performance of the electronically tuned *Ti:Sa* laser source. Right: glass sample whose front and back reflections form the interference signal $I(x,y,t)$ which is imaged onto the CCD with x, y denoting the pixel coordinates and t the frame number corresponding to the instantaneous wavelength of the laser source. POM: Pump optics module where a set of three mirrors control the spatial orientation of the beam entering the *Ti:Sa* laser head (used for alignment purposes).

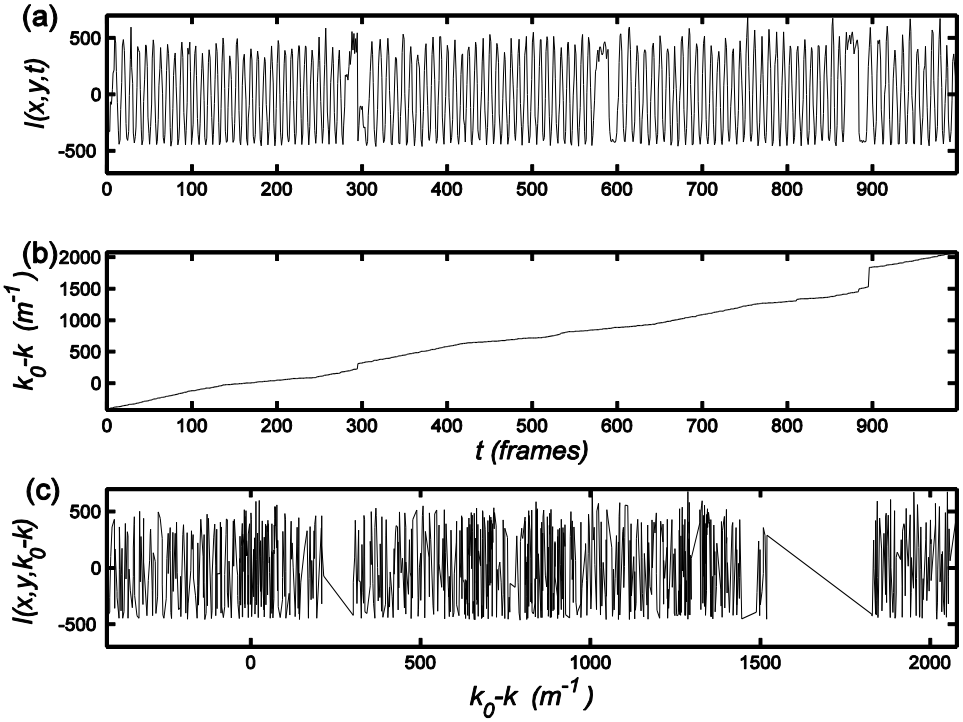

Figure-4.18: (a) Intensity distribution *I(x,y,t)* for a single pixel as function of frame number t for a short scan of ~2nm (1000 frames). (b) Corresponding wavenumber change k_0-k using the WSD readings as function of t. (c) Re-registered intensity signal onto the wavenumber change axis showing the effect that small (t~300) and large wavenumber jumps (t~900) have on the recorded raw intensity data.

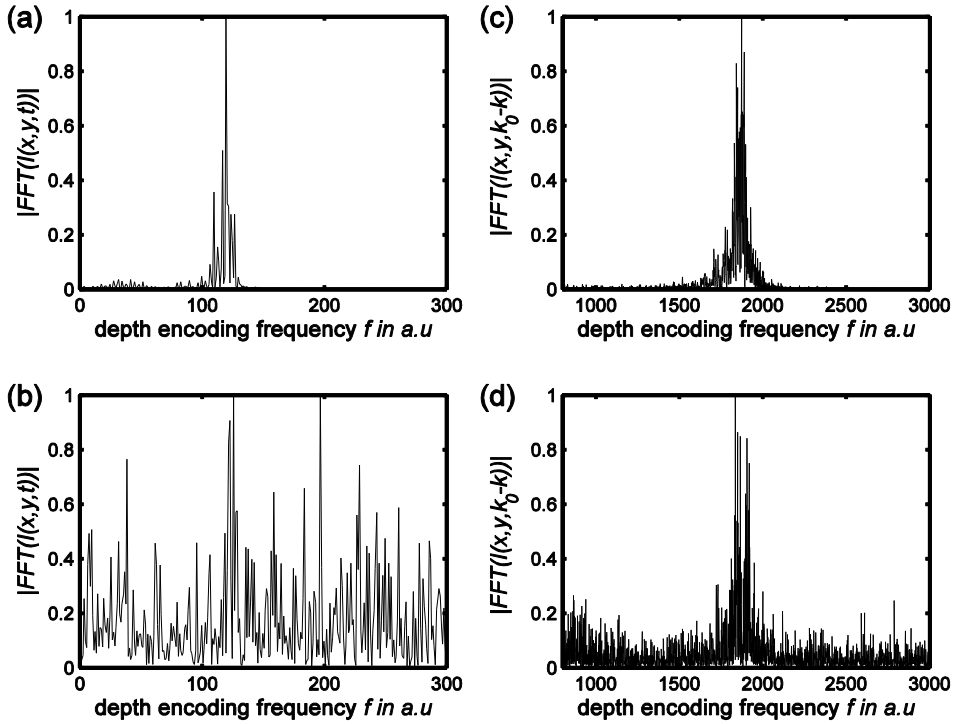

Figure-4.19: Normalised Fourier-transform spectrum of the interference signal $I(x,y,t)$ and $I(x,y,k_0\text{-}k)$ for a short (left column) and a larger scan (right column) for a glass wedge with central thickness of 9.6 mm.

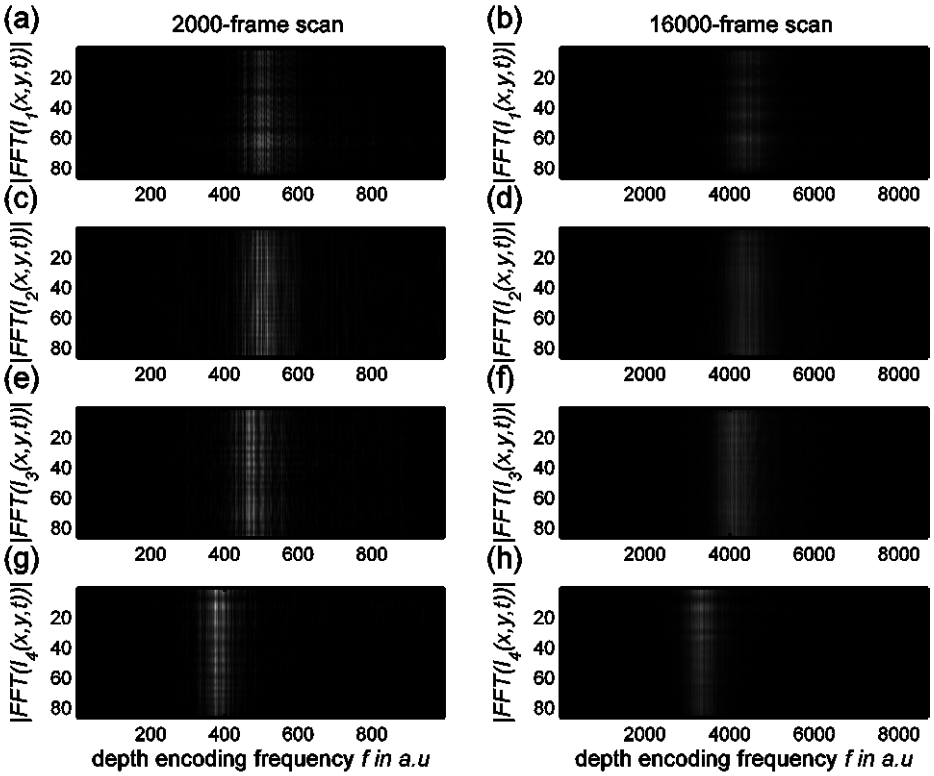

Figure-4.20: Fourier transform spectrum of the intensity distribution $\left|\tilde{I}_i(x,y,t)\right|$ at the central pixel $x = x_c$ and along the y-axis of each of the four glass wedges examined (subscript i = 1,2,34 indicates the wedge number with 1 being the thickest and four the thinnest). Left column: short scan of 2000 frames equivalent to ~ 2 nm. Right column: larger scan of 16000 frames equivalent to ~ 20 nm.

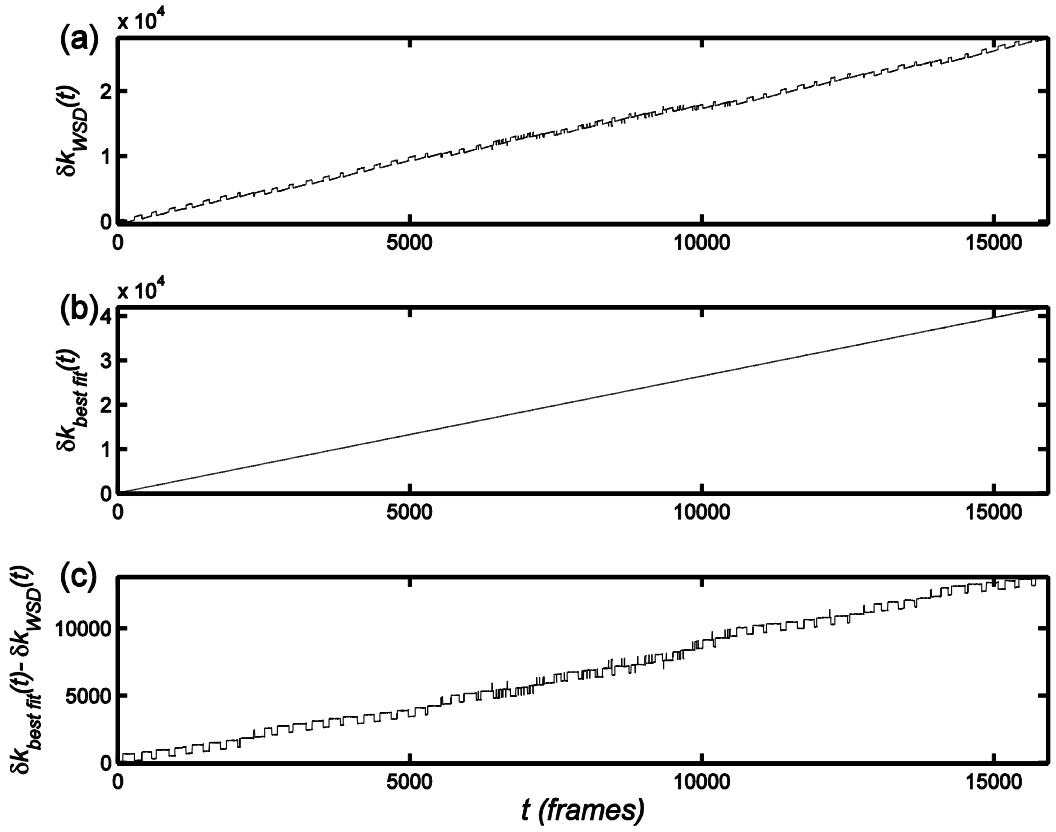

Figure-4.21: (a) Wavenumber change $\delta k(t) = k(0)-k(t)$ calculated using the WSD readings. (b) Best fit line estimated using linear least squares fit to (a) for the first 400 frames only and then extending the result for the rest of the sequence. (c) Difference of the estimated linear best fit from the actual wavenumber change behaviour as recorded by the WSD that demonstrates how significant the deviation from the ideal linear behaviour is.

Chapter-5: Dynamic wavenumber change monitoring

5.1 Introduction

Wavelength scanning interferometry (WSI) and swept-source optical coherence tomography (OCT) provide absolute one-dimensional range maps at each camera pixel. In addition to surface profilometry [26, 158] applications, three-dimensional volumes of both structure and displacement within scattering media can be obtained from the magnitude and phase fields measured by a two-dimensional (2-D) array of such pixels [4, 27, 66]. The image reconstruction algorithms depend, however, on accurate knowledge of the changes in wavenumber, k, over time, denoted here Δk [69]. Tuneable laser technology is constantly evolving. In particular, new semiconductor lasers [204] have achieved ~100 nm scanning capabilities for fibre optics communication wavelengths, and solid state titanium-doped sapphire lasers (*Ti:Sa*) offer similar scanning capability but operate in the near infrared (NIR) with higher output powers. However, for any light source used in WSI applications, precise phase detection is crucial for displacement measurements. A key element for reducing the uncertainty in the phase measurements is to detect the time-varying wavenumber changes at high precision, and simultaneously avoid false readings from temporary incoherence of the light source.

The capabilities of commercial wave-meters are restricted as they usually provide slow responses (typical maximum acquisition rate of order a few tens or hundreds of Hz), determined by the processing time of interferometric data, and do not provide instantaneous light coherence detection [205]. Wavelength detection methods with high sensitivity have been available for some time. The most precise ones are based on measurement of the fringe patterns from a Michelson interferometer. For increased precision, the fringes are compared with a wavelength stabilized reference (see, for example, the Bristol Instruments model 621A). In this particular example, wavelengths are measured to an accuracy of ±0.2 parts per million by counting fringes while an internal mirror is displaced. However, the need for temporal scanning makes this approach unsuitable for instantaneous wavelength measurements.

The approach to be adopted in this project therefore involved tracking wavenumber changes by the use of a 7th camera that images the interference patterns produced by a set of wedges. As the thickest wedge is 2-3 times thicker than the anticipated maximum sample depth, and because the wedge is a smooth wavefront interferometer rather than one involving speckled wavefronts as is the case for the depth-resolved measurements on composites, the phase changes measured from the wedges will be more precise than those from the sample and can therefore be used to infer to sufficient accuracy the changes in wavenumber over time. Furthermore, the phase measurements will be precisely synchronised with those from the other six cameras as identical exposure timing pulses are applied to all the cameras in the system.

5.2 Wavenumber monitoring in WSI

The interference pattern from a wedge changes according to the phase shifts introduced by the tuning of the wavelength of the broadband source thereby allowing this phenomenon to be used as means to monitor the wavenumber changes. A single wedge, however, is insufficient to provide such measurements with sufficient sensitivity for the large wavenumber range of a 100 nm scan. The following analysis starts with the fundamental equations for a single wedge.

5.2.1 Theoretical aspects: general wedge equations

Consider a thin, transparent wedge, of angle α and refractive index n that is imaged onto a photo detector array. Let d_j denote the thickness of the wedge at the centre of a region of interest from which phase values are computed. The phase difference ψ between light reflected from front and back surfaces, refracted at angle θ to the normal of the front surface, may be written [206, 207]:

$$\psi_j(x) = k(2nd\cos\theta + \lambda/2), \qquad 5.1$$

where, $d = d_j + x\tan\alpha$, is the local wedge thickness, k is the wavenumber (=$2\pi/\lambda$, where λ is the wavelength), and x is a spatial coordinate. Strictly speaking, equation-5.1 is correct only for a thin plane-parallel plate, i.e. for the case $\alpha = 0$. It is, however, possible to show it is also applicable with minor changes to the more

general case of nonzero wedge angle α. To do so, consider the general case of a wedge as illustrated in figure-5.1.

The interferometric phase, Ψ_B, resulting from the interference between the reflection of light from the back and front surfaces of the wedge in question at any given wavenumber (k), is given by:

$$\Psi(k) = k \cdot OPL_{BS} - k \cdot OPL_{FS}, \qquad 5.2$$

where the parameters OPL_{FS} and OPL_{BS} denote the optical path lengths for the front and back surfaces of the wedge. For a camera focused on the front surface of the wedge (plane across line OCB), the light received from a given point B is a coherent superposition of contributions from paths OAB and DB (neglecting multiple reflections). In order to relate the interference phase $\Psi = \Psi_B$ to the wedge thickness at point B ($d = d_B$) in figure-5.1, the following set of path lengths need to be considered:

$$\left.\begin{aligned} OA &= AC/\cos\theta = d_C/\cos\theta \\ AB &= AC/\cos(\theta + 2\alpha) = d_C/\cos(\theta + 2\alpha) \\ OC &= d_C \tan\theta \\ CB &= d_C \tan(\theta + 2\alpha) \\ DB &= OB \sin\theta' = (OC + CB)\sin\theta' \\ &= d_C(\tan\theta + \tan(\theta + 2\alpha))\sin\theta' \end{aligned}\right\}. \qquad 5.3$$

Thus, using the group of equations-5.3, the general interferometric phase in equation-5.2 may be written as:

$$\left.\begin{aligned} \Psi_B &= n \cdot k \cdot (OA + AB) - k \cdot (DB) \\ &= n \cdot k \cdot d_C \left(\frac{1}{\cos\theta} + \frac{1}{\cos(\theta+2\alpha)}\right) \\ &- k \cdot d_C \cdot \sin\theta' \,(\tan\theta + \tan(\theta + 2\alpha)) \end{aligned}\right\}, \qquad 5.4$$

where n is the refractive index in the medium, and the refractive index of the surrounding air is assumed to be 1. From Snell's law, $\sin\theta' = n\sin\theta$. Therefore:

$$\Psi_B = n \cdot k \cdot d_C \left\{\frac{1}{\cos\theta} + \frac{1}{\cos(\theta+2\alpha)} - \sin\theta\,[\tan\theta + \tan(\theta + 2\alpha)]\right\}. \qquad 5.5$$

As the interferometric phase of interest is that at point B, it makes sense to express the above equation in terms of d_B. Once again, from the ray tracing diagram illustrated in figure-5.1:

$$\left.\begin{aligned} d_B &= d_C + CB\tan\alpha \\ &= d_C[1 + tan(\theta + 2\alpha)\tan\alpha] \end{aligned}\right\}. \qquad 5.6$$

Consequently,

$$\Psi_B = \frac{n\cdot k\cdot d_B\left\{\frac{1}{\cos\theta}+\frac{1}{cos(\theta+2\alpha)}-sin\,\theta[tan\,\theta+tan(\theta+2\alpha)]\right\}}{[1+tan(\theta+2\alpha)\,tan\,\alpha]} \qquad 5.7$$

Using trigonometric identities, the bracketed term in the numerator of equation-5.7 can be simplified as follows:

$$\left.\begin{aligned} \frac{1}{\cos\theta} - sin\,\theta\,tan\,\theta &= \frac{1-sin^2\theta}{\cos\theta} = cos\,\theta \\ \frac{1}{cos(\theta+2\alpha)} - sin\,\theta\,tan(\theta+2\alpha) &= \frac{1-sin\,\theta\,sin(\theta+2\alpha)}{cos(\theta+2\alpha)} \end{aligned}\right\}.$$

Thus, it follows that:

$$\left.\begin{aligned} \Psi_B &= n\cdot k\cdot d_B\frac{[cos\,\theta\,cos(\theta+2\alpha)+1-sin\,\theta\,sin(\theta+2\alpha)]}{cos(\theta+2\alpha)[1+tan(\theta+2\alpha)\,tan\,\alpha]} \\ &= n\cdot k\cdot d_B\frac{[cos\,\theta\,cos(\theta+2\alpha)+1-sin\,\theta\,sin(\theta+2\alpha)]}{cos(\theta+2\alpha)+sin(\theta+2\alpha)\,tan\,\alpha} \end{aligned}\right\}. \qquad 5.8$$

Further simplification of the above expression is possible by making use of the identity $\cos(A+B) = \cos A\cos B - \sin A\sin B$, in both the numerator and denominator (after substituting for $\tan\alpha = \sin\alpha/\cos\alpha$). The reduced expression for the interferometric phase at point B is, therefore, given by:

$$\Psi_B = n_m k d_B \underbrace{\left[\frac{cos\,2(\theta+a)+1}{cos(\theta+\alpha)}\right]cos\,\alpha}_{f(\theta,\alpha)}. \qquad 5.9$$

A quick check on this equation can be performed by considering the limiting case $\alpha = 0$; Equation-5.9 then reduces to that for a plane-parallel plate (equation-5.1), as expected.

Whilst classical two beam interference is a valid assumption for a thin plane-parallel plate with low reflectivity front and back surfaces, non-sinusoidal intensity distributions resulting from multiple beam interference become more significant with increasing reflectivity of front and/or back surfaces. The resulting multiple reflections can, however, be handled by the 2-D Fourier transform provided the aliased higher harmonics do not interfere with the fundamental fringe frequency during the phase estimation process described in Subsection-5.4.

With this in mind, the successive phase changes in ψ, denoted henceforth δψ, owing to the sequential changes in wavenumber (δk) between successive frames may be expressed by:

$$\delta\psi_j(t, t-1) = nd_j\delta k(t, t-1)f(\theta, \alpha)\,, \qquad 5.10$$

where t denotes the frame index (t = 0, 1, 2…, N_t-*1*) but can also be considered as a dimensionless time index. Integration of equation-5.10 over the entire time sequence yields:

$$\Delta\Psi_j(t, 0) = nd_j\Delta k(t, 0)f(\theta, \alpha)\ , \qquad 5.11$$

In WSI, the target δk value between two adjacent frames is the one that induces a phase change of~ π/2 between the waves reflected respectively from the front and back of a sample of thickness T. This places the resulting temporal frequency midway between the zero frequency and Nyquist frequency points in the Fourier depth reconstruction. Unfortunately, laser mode hops can cause δψ values to fall well outside the desired range – π to π and since only the wrapped phase is measured, Δk is estimated incorrectly. Providing that an upper bound Δk_m can be defined for Δk based on the physics of the tuneable laser, a reduced value for d_j can be chosen such that:

$$d_j < \frac{\pi}{nd\Delta k_m f(\theta,\alpha)}\ , \qquad 5.12$$

which ensures that the right-hand side of equation-5.10 always lies in the range -π to π. However, this has the undesirable consequence of also scaling down the magnitude of the phase changes produced during the rest of the scan, and hence degrading the accuracy of the wave number estimation by the same factor.

As mentioned earlier, two of the key aspects in any depth-resolved imaging technique, like WSI, are the depth resolution and depth range, denoted δz and Δz respectively. The two crucial parameters, which constitute a performance measure, are in turn linked to the wavenumber range Δk and the wavenumber step δk. It is, therefore, desirable to have as wide a wavenumber range as possible with the smallest possible wavenumber step.

5.2.2 Phase unwrapping using a set of wedges

The analysis so far (refer to chapter-3), suggests the use of a single wedge is insufficient to reconstruct a wide enough Δk with sufficient sensitivity in δk to allow for successful depth-resolved imaging of both intensity and phase. To overcome this problem, a solution is proposed here to use a set of wedges of varying thicknesses allowing for high Δk resolution without compromising the width of the operating range. This is done by recognising that, by sequential subtraction of phase change values between pairs of wedges in turn, a variety of phase sensitivities for a given wavenumber change can be achieved. The use of phase differences between wedges is proposed, rather than just the phase values from the individual wedges. This is because it would be impractical to make a wedge thin enough to satisfy inequality 5.12, whereas it is easier to make two wedges whose thickness difference satisfies the same inequality. The remainder of this chapter is dedicated to mathematically expressing and validating the proposed solution.

Let the difference in the phase change between frames $t' - 1$ and t' and between the wedges *i* and *j* be denoted by:

$$\Delta\Phi^{i,j}(t', t'-1) = \delta\psi_i(t', t'-1) - \delta\psi_j(t', t'-1) \ , \qquad 5.13$$

where $\delta\psi_i$ and $\delta\psi_j$ correspond to the phase changes due to the physical wedge thicknesses d_i and d_j, as well as the incremental wavenumber change δk between two successive frames. Assuming that $\delta\psi_i$ and $\delta\psi_j$ are each wrapped onto the range $-\pi$ to π, then $\Delta\Phi^{i,j}$ lies in the range: -2π to 2π. It is, therefore, convenient to wrap this onto the principal range of $-\pi$ to π by the wrapping operator:

$$\Delta\Phi_w^{i,j}(t', t'-1) = \mathcal{W}\{\Delta\Phi^{i,j}(t', t'-1)\} \ , \qquad 5.14$$

where $\mathcal{W}$ is defined mathematically later in this section. The wrapped phase change, $\Delta\Phi_w^{i,j}$ calculated in this way, can be thought of as the change produced by a wedge with a synthetic thickness:

$$d_s^{i,j} = d_i - d_j \ . \qquad 5.15$$

Provided d_s satisfies the same inequality given by 5.12, i.e.

$$d_s^{i,j} < \frac{\pi}{nd\Delta k_m f(\theta,\alpha)} \ , \qquad 5.16$$

the incremental wrapped phase change between a given pair of successive frames equals the true (unwrapped) phase change between those frames. Therefore, the running sum of incremental wrapped phase changes,

$$\Delta\Phi^{i,j}(t,0) = \sum_{t'=1}^{t} \Delta\Phi^{i,j}(t', t'-1) \ , \qquad 5.17$$

represents the true unwrapped phase change between frame 0 and the current frame *t*, i.e.

$$\Delta\Phi_u^{i,j}(t,0) = \Delta\Phi^{i,j}(t,0) \, . \qquad 5.18$$

We denote the indices defining the pair of wedges that satisfy the inequality in 5.16 as $i = i_1$, $j = j_1$. The resulting temporally unwrapped phase change $\Delta\Phi_u^{i_1,j_1}(t,0)$ provides the reference signal for the subsequent unwrapping across wedge thickness. Suppose a second pair of wedges, denoted $i = i_2$, $j = j_2$, are not sufficiently close in thickness to satisfy 5.16. $\Delta\Phi^{i_2,j_2}(t,0)$, can still be calculated according to equation-5.17, yet it cannot be guaranteed to equal the correctly unwrapped phase change $\Delta\Phi_u^{i_2,j_2}(t,0)$, because some of the $\Delta\Phi_w^{i_2,j_2}(t', t'-1)$ values in equation-5.17 may miss one or more 2π phase jumps. We can, however, use the reference signal $\Delta\Phi_u^{i_1,j_1}(t,0)$ to unwrap $\Delta\Phi^{i_2,j_2}(t,0)$ in the following way. According to equations 5.1 (or indeed the more precise in our case equation-5.9) and 5.10, the expected phase change $\Delta\Phi^{i_2,j_2}(t,0)$ is a factor R_1 greater than $\Delta\Phi_u^{i_1,j_1}(t,0)$, where:

$$R_1 = \frac{d_s^{i_2,j_2}}{d_s^{i_1,j_1}} \ , \qquad 5.19$$

Therefore, a scaled phase change signal $R_1\Delta\Phi_u^{i_1,j_1}(t,0)$ can be used to unwrap $\Delta\Phi^{i_2,j_2}(t,0)$, according to the following expression:

$$\Delta\Phi_u^{i_2,j_2}(t,0) = \mathcal{U}\{\Delta\Phi^{i_2,j_2}(t,0), R_1\Delta\Phi^{i_1,j_1}(t,0)\} \ , \qquad 5.20$$

where $\mathcal{U}\{\Phi_A, \Phi_B\}$ represents the unwrapping operator that subtracts an integral multiple of 2π from a given phase value Φ_A such that Φ_A-Φ_B lies within the range $-\pi$ to π, that is:

$$\mathcal{U}\{\Phi_A, \Phi_B\} = \Phi_A - 2\pi NINT\left(\frac{\Phi_A - \Phi_B}{2\pi}\right) , \qquad 5.21$$

and where NINT denotes rounding to the nearest integer. At this stage it is convenient to note that the wrapping operator used in equation-5.14 is defined in terms of the unwrapping operator such that

$$\mathcal{W}\{\Phi_A\} = \mathcal{U}\{\Phi_A, 0\} . \qquad 5.22$$

Once the $\Delta\Phi_u^{i_2,j_2}(t,0)$ sequence of unwrapped phase values has been obtained by equation 5.20, this can be used to unwrap a third sequence of phase values, measured from a third pair of wedges that are specified by the indices $i = i_3$, $j = j_3$ and that have a greater synthetic thickness $d_s^{i_3,j_3}$ than those of the second sequence. These can then be used to unwrap a fourth sequence, and so on, until finally the phase data from the thickest wedge alone has been unwrapped, which gives the maximum possible sensitivity from the chosen set of wedges. At the m^{th} step in the sequence, equations 5.19 and 5.20 become:

$$R_m = d_s^{i_{m+1},j_{m+1}} / d_s^{i_m,j_m} , \qquad 5.23$$

$$\Delta\Phi_u^{i_{m+1},j_{m+1}}(t,0) = \mathcal{U}\{\Delta\Phi^{i_{m+1},j_{m+1}}(t,0), R_m \Delta\Phi^{i_m,j_m}(t,0)\} . \qquad 5.24$$

The equations above were originally derived in [1] for the case of shape measurement by projected fringes, in which an exponentially growing sequence of fringe frequencies was used to achieve exponentially growing depth-measurement sensitivity. The current case is analogous in that an exponentially growing sequence of synthetic wedge thicknesses is used to achieve exponentially growing Δk-measurement sensitivity. This can be produced by choosing the d_j according to the following rules:

$$\left.\begin{array}{l} d_1 = d_0 R^{s-1} \\ d_j = d_1 - d_0 R^{j-2}, where\ j = 2,3,..,s \end{array}\right\} , \qquad 5.25$$

where d_0 and R, are constants and s is the total number of wedges required. A lower bound on the synthetic thickness difference $d_s^{min} = d_s^{i_1,j_1}$ may be defined using inequality 5.16. Taking into account that for the particular laser source used in this thesis (see chapter-3 for more details) wavenumber jumps (Δk_m) as high as 6000 m^{-1}

may occur, which result in a $d_s^{i_1,j_1}$ value of 175 μm or less for n = 1.5. Since the designed WSI system described in this thesis aims at inspecting specimens approximately 5 mm thick, a convenient upper limit for the synthetic thickness difference d_s^{max} is twice the maximum specimen thickness. Thus, for N_s unwrapping steps used to span the d_s range of d_s^{min} to d_s^{max}, the optimal choice of thickness ratio for each step would be $R_1 = R_2 = \cdots = R_{N_s} = R$, where:

$$R = \left(\frac{d_s^{max}}{d_s^{min}}\right)^{1/N_s} . \qquad 5.26$$

Keeping equal thickness ratios throughout the entire sequence of unwrapping steps is desirable because noise as well as the phase signal gets amplified by R.

Noise-amplification-induced phase unwrapping errors pose a threat in the case where the amplified phase noise falls outside the range -π to π. To avoid this, and by denoting the standard deviation of phase noise present in the signal by σ_ϕ, the following requirement needs to be satisfied:

$$\left|R\sigma_\phi\right| \ll \pi . \qquad 5.27$$

This suggests that an appropriate upper limit on R is approximately 10, for a typical value $\sigma_\phi \approx 2\pi/50$. Substituting the values $d_s^{min} = 175\,\mu m$ and $d_s^{max} = 10\,mm$ into equation-5.26 gives the values R = 57, 7.6, 3.9, 2.7 for N_s = 1, 2, 3, and 4, respectively. Upon completion of the multi-step phase unwrapping process, the sought wavenumber change axis Δk (t, 0) may be computed as follows:

$$\Delta k(t,0) = \frac{\Delta\Phi_u^{i_{N_s+1},j_{N_s+1}}(t,0)}{n d_s^{max} f(\theta,\alpha)} , \qquad 5.28$$

It is worth noting that if a phase unwrapping error does occur when applying equation-5.20 it affects only the δk value at a single frame and does not propagate throughout the rest of the phase sequence. Another important remark is that in equation-5.28, n is assumed to be independent of the wavelength. Strictly speaking, this is not true in most cases and a more accurate treatment of the dispersion is presented in Chapter-7.

As far as the dimensional characterization of the wedge is concerned, its lateral dimensions are determined by the size of the wave-front as well as the magnification of the imaging lens used. Finally, the remaining parameter - the wedge angle α - can be expressed in terms of the number of fringes N_f across the field of view of a wedge with width W by:

$$\alpha = N_f \lambda / 2nW \ , \qquad 5.29$$

provided that a small illumination angle is used. N_f is chosen in turn to be a convenient number for the subsequent fringe analysis, a value 10 or 20 being reasonable.

5.3 Experimental setup description

In this section a brief description of the optical setup used for the dynamic wavenumber change monitoring is provided. The setup was originally developed by A. Davila and J. M. Huntley with a few modifications added at the time the author joined the research group. The description starts with the design and manufacture of the four wedges comprising the optical sensor used in this thesis, followed by the description of the interferometer setup.

5.3.1 Wedge design and manufacture

A four-wedge sensor, with each wedge having a polished area of 30 × 7.5 mm^2, and with target thickness values equal to 12.8, 12.6, 12.0, and 9.6 mm ± 0.05 mm (denoted wedges 1-4, respectively), had previously been manufactured from fused silica to a flatness of $\lambda/10$ by a commercial optical component supplier. This set of wedge thicknesses is defined by the two equations in 5.25 with the parameters d_0 = 200 μm, s = 4, and R = 4. The specified wedge angle α was 2 min ± 0.2 min. The four wedges were stacked adjacent to one another, in order 1–4 along their largest unpolished surfaces, to form a 30 × 30 mm^2 wave-front sensor. One polished face of each wedge was aligned by gravity to a flat surface while the adjacent sides were cemented together as shown in figure-5.2 (left).

The composite optical element formed by the bonded wedges was placed in a gimbal mount for alignment purposes with the other components of the setup as shown in figure-5.2 (right).

5.3.2 Optical setup (Fizeau interferometer)

Phase shifting interferometry (PSI) is a well-established technique in the field of optical metrology. Interferometers of this type utilize a monochromatic laser source and a set of piezo-electric transducers (PZT) that are used for introducing the required phase shifts (typically in steps of ¼ waves) realised in a Fizeau setup. Most phase shifting formulae require one or at most two cycles of the cosine wave and allow phase to be calculated to an accuracy of typically 1/30th to 1/100th of a fringe, with a typical fringe separation distance of λ/2. Consequently, for a light source with λ = 800 nm the fringe separation is 0.4 μm resulting in an accuracy of approximately 10 nm.

An alternative way of performing temporal PSI is achieved by introducing small shifts in the frequency of the light source. This requires the use of a narrowband source whose wavelength is scanned sequentially and eliminates the need for any mechanical movement in the setup. Although a tuneable light source is used in the current setup, this was not the method used here because of the lack of *a priori* knowledge of the laser scan behaviour. Instead spatial phase shifting was used which allowed phase values to be obtained from a single interferogram consisting of approximately parallel uniformly-spaced fringes.

As with a traditional PSI setup (see figure-5.3 for a representative example), the optical setup incorporating the four-wedge optical sensor was also built in a Fizeau arrangement as illustrated in figure-5.4. The tuneable *Ti:Sa* laser manufactured by M-Squared Lasers, as used in the main interferometer, was used to illuminate the composite optical element. The laser beam LB was expanded and collimated by an achromatic doublet to illuminate the four wedges. The angle of illumination was approximately 2 deg. The back-reflected light was collected by Lens L2, which with lens L3 forms an afocal system for the observation of fringes over the CCD (see figure-5.4 for a schematic representation of the setup adopted from [20]).

The CCD camera was a Prosilica GC1380H model with the Sony ICX285 EXview sensor for increased response in the near infra-red (NIR) and 12-bit resolution with speeds of up to 30 frames per second at full resolution (1360 × 1024 pixels). A sample image of the four wedge interferograms is shown in figure-5.5(a). The fringe orientation and spacing vary from one wedge to another due to the difficulties in

manufacturing a set of wedges with completely consistent wedge angle and orientation. However, the variation between the wedges is automatically handled by the 2-D Fourier transform phase extraction procedure described in the next section. One complicating feature of the analysis is that laser mode hops, arising due to the mechanical movement of the BRF during wavelength tuning, resulted in a temporary loss of laser light coherence causing some of the images in the recorded sequence to become blurred (see figure-5.5(b) for a representative example of such an event). The issue is also addressed in the next section.

5.4 Fourier transform phase estimation and coherence detection

The image acquisition software used (*Norpix-4*) allowed the recording and storing of large image sequences at video frequencies. The aforementioned sequence consists of a stack of fringe patterns, similar to those shown in figure-5.5(a), essentially forming a 3-D fringe pattern with each recorded image synchronized to a particular wavelength of the tuneable laser (see figure-5.6).

However, the presence of blurred images in the sequence poses a threat to the accuracy of the phase extraction process. In order to assess the reliability of the phase estimation process, a coherence detection procedure, based on analysing the fringe contrast from the set of wedges using the ratio of the zero and first positive order amplitudes in the 2-D Fourier transform, had been put in place by A. Davila. Figure-5.7 shows how the amplitude of the first order peak is reduced when incoherent emission of the *Ti:Sa* laser occurs. By defining a threshold value for the contrast, images recorded with incoherent light are detected: they are tagged as unreliable, and subsequently they are discarded from the measurements.

In order to extract the required phases, each of the compound fringe patterns was broken down to smaller regions of interest (ROI) corresponding to the area of each wedge, followed by a 2-D Fourier transform (see figure-5.8). As the slope of the wedge produces approximately parallel uniformly spaced fringes, its 2-D Fourier transform gives three main orders labelled as d.c, +P, and –P. The associated phase is obtained from the arc tangent of the imaginary over the real parts of the resulting complex value found at the detected maximum of the positive frequency order (labelled +P).

Errors during the manufacturing stage of the wedges (e.g. surface flatness) and/or imperfect beam collimation resulting in a spherical wave-front as opposed to the required plane wave-front, can however cause the fringes to deviate from the ideal case of fringes of equal spacing, particularly around the edges. To suppress these edge effects, and spectral cross-talk in the frequency domain, a 2-D Hanning window is applied to the interference pattern from each ROI of all the recorded frames prior to the 2-D Fourier transformation of the signal. The benefit of this approach to phase extraction, in addition to its 'single shot' nature, is that the signal from a large number of pixels ($>10^5$) is concentrated onto a small region of the Fourier domain, thus providing a very high signal to noise ratio for the phase value at the centre of each ROI.

In its basic form, the resulting location of the estimated phase for each of the fringe patterns corresponds to that at the image pixel at the origin of the ROI. This position can, however, be shifted to the centre of the ROI by swapping the four image quadrants prior to performing the 2-D Fourier transform. This is easily done, for example, by using the `fftshift` function in the MATLAB programming language (see figure-5.9 for a schematic illustration that explains the principle of image-quadrant swapping and the corresponding shift in the location the phase is calculated). This procedure allows the phase to be computed at the centre of the ROI where the signal to noise ratio is highest and where the fringes are closest to being parallel and equally spaced.

5.5 Experimental validation: results from a short wavenumber scan

So far, for the unwrapping procedure described in section-5.2.2 it has been implicitly assumed that the wedge thickness values d_i are known. This may be possible if the most cutting edge manufacturing processes are employed at the expense of high manufacturing cost. The four wedges comprising the optical sensor here are, however, far from perfect as the interferograms (e.g., figure-5.5(a)) reveal. In practice, no manufacturing process is perfect and small deviations equivalent to just a small fraction of the normal manufacturing tolerances are inevitable in almost any process. Considering the sensitivity of the technique used here, these deviations are likely to cause significant unwrapping errors. Absolute distance metrology (ADM) is one approach that could be used to verify the wedge profiles. It is, however,

inconvenient as it usually requires expensive instrumentation. In the following section, a simple low-cost procedure for computing the required wedge thickness ratios R_m is described. The procedure is validated using direct measurement of wavelength during a scan with a commercially available high-end wavelength-meter (High Finesse model Ångstrom WS7; acquisition rate: up to 400 Hz; absolute accuracy at 800 nm = 0.13 pm [205]).

5.5.1 Determination of true wedge-thickness ratios

Assuming the value of R_m for the m^{th} step is chosen correctly, the terms $R_m \Delta\Phi_u^{i_m,j_m}(t,0)$ and $\Delta\Phi_u^{i_{m+1},j_{m+1}}(t,0)$ in equation-5.24 will agree with each other. Deviations between the two will be due to experimental phase noise, which in the case of $\Delta\Phi_u^{i_m,j_m}(t,0)$ is amplified by R_m. Provided R_m is not too large, these noise-induced phase deviations will be typically a small fraction of 2π. On the other hand, in the event of a small error present in the assumed value of R_m, the two terms will start to deviate from one another as the scan progresses. Naturally, the unwrapping function (equation-5.24) will limit the magnitude of these excursions to ±π, while the rms deviation between them will, for a sufficiently long scan, be that of a random variable with uniform probability density function over the range -π to π, which is $\pi/\sqrt{3}$. Consequently, the proximity of a postulated value for R_m to its true value can be tested by calculating the value of S given by:

$$S = \sqrt{\frac{\sum_{t=1}^{N_t}\left[\Delta\Phi_u^{i_{m+1},j_{m+1}}(t,0) - R_m \Delta\Phi_u^{i_m,j_m}(t,0)\right]^2}{N}}\ , \qquad 5.30$$

Indeed, equation-5.30 can be regarded as a 1-degree of freedom cost function that should be minimised during an optimisation of the unknown variable R_m. From equation-5.24 it is evident that $\Delta\Phi_u^{i_{m+1},j_{m+1}}(t,0)$ depends nonlinearly on $\Delta\Phi_u^{i_m,j_m}(t,0)$, so that in general an iterative solution is required for determining the optimum R_m. For step 1, involving wedge pairs 1,2 and 2,3, (see figure-5.10) a linear least squares fit was performed to the initial portion of $\Delta\Phi_u^{i_{m+1},j_{m+1}}(t,0)$ and $\Delta\Phi_u^{i_m,j_m}(t,0)$ versus t curves, with the initial estimate for R_m taken to be the ratio of their respective gradients. For the remaining steps, a slightly different approach was followed. As the corresponding phase changes underwent much more frequent 2π phase jumps, the initial estimates for R_m were computed based on a simple ratio of

the thickness differences as derived from micrometre measurements from the edges of the wedges. Recognising that there is only one free parameter in equation-5.30, subsequent refinement of the initial estimates was quickly and simply achieved by manual iteration.

In the remaining part of this section an illustration of the general approach described earlier in section-5.2.2 is provided, using experimental data lasting 400 frames (approx. 1 nm scan range) and a total of four wedges. The wavelength step (δλ) and the frame rate acquisition during the scan were set to 2 pm and 6 Hz respectively. Schematic illustrations of the relevant phase changes and other key parameters related to the experiment are provided in figure-5.10 and figure-5.11 to aid understanding.

The temporally unwrapped time-varying phase difference values for wedge pairs 1 and 2 ($\Delta\Phi_u^{1,2}(t,0)$), as well as for 2 and 3 ($\Delta\Phi^{2,3}(t,0)$) are shown in figure-5.12. In terms of the notation used in section-5.2.2, the relevant wedge indices are $(i_0, j_0) = (1, 2)$ and $(i_1, j_1) = (2, 3)$. It is worth noting at this stage that temporally unwrapped in this context refers to the cascade of three simple operations; differentiating, wrapping and integrating [208] but does not necessarily imply that the treated, in this manner, signal is free of 2π-ambiguities. For example, the synthetic wedge thickness $d_s^{1,2}$ is small enough to satisfy the inequality given by 5.16 and thus able to cope with large wavenumber jumps of ~6000 m^{-1} that occur after frames t = 74, 150, 163, 238, and 245. An independent check described in section-5.2.2 was carried out to ensure that the inequality (5.16) for this particular wedge pair (1 and 2) was held. Consequently, by simply taking the cumulative sum of consecutive re-wrapped (onto the principal range -π to π), phase differences is sufficient to retrieve the true, unwrapped $\Delta\Phi_u^{1,2}(t,0)$ as specified by equation-5.18.

Unlike $d_s^{1,2}$, the thickness difference $d_s^{2,3}$ does not satisfy 5.16. This, in turn explains the presence of 2π phase errors in the temporally-unwrapped signal $\Delta\Phi^{2,3}(t,0)$ as shown in figure-5.12. The errors become even more evident once the scaled up version of the phase signal from wedges 1 and 2, i.e. $R_1\Delta\Phi_u^{1,2}(t,0)$ is plotted on the same axis (with the value R_1 = 10.314 determined by the procedure outlined earlier). Figure-5.13: illustrates the result of unwrapping $\Delta\Phi^{i_1,j_1}(t,0)$ using as a reference

signal the $R_1\Delta\Phi_u^{i_0,j_0}(t,0)$ according to equation-5.24. The two signals appear to be in close agreement with a root mean square difference of 0.4602 rad and with $\Delta\Phi_u^{2,3}(t,0)$ clearly possessing a much better signal to noise ratio than that of $R_1\Delta\Phi_u^{1,2}(t,0)$. This is of course attributed to the fact that the amplification factor R_1 affects not only the signal itself but also its associated phase errors.

In figure-5.14 and figure-5.15 the results of repeating the same process for steps 2 and 3 are shown. Step 2 refers to the use of previously unwrapped $\Delta\Phi_u^{2,3}(t,0)$ from step 1 as the reference signal in order to unwrap $\Delta\Phi_w^{3,4}(t,0)$ from wedges 3 and 4. Similarly, in step 3 the resulting $\Delta\Phi_u^{3,4}(t,0)$ is then used to unwrap $\Delta\Phi_w^{1,5}(t,0)$. Note that the superscript '5' refers to a fictitious fifth wedge that has zero thickness and hence $\Delta\Psi_5(t,t-1)=0$, for all t (see equation-5.11). This fictitious wedge allows one to apply the same general equations: 5.13, 5.14, 5.16, 5.17 and 5.24, derived earlier, while obtaining maximum sensitivity through the use of the maximum available wedge thickness of 12.8 mm. The ratios used were R_2 = 3.1242 and R_3 = 5.42975 for these two steps.

Finally, as a last check to validate the multi-step phase unwrapping approach, the effect of choosing an incorrect R_m is investigated. Choosing step 2 for this investigation, deviations of 1.12 and 0.87 below and above the true value of R_2 = 3.1242 were introduced. These were seen to have caused deviations approaching ±π between $R_2\Delta\Phi_u^{2,3}(t,0)$ and $\Delta\Phi_w^{3,4}(t,0)$ as illustrated in figure-5.16 with R_2 = 3.1242 shown at the top. The rms deviation between $R_2\Delta\Phi_u^{2,3}(t,0)$ and $\Delta\Phi_w^{3,4}(t,0)$, denoted ε_ϕ, for the three values of R_2 were 0.046, 1.7133, and 1.8871 rad. A plot of ε_ϕ versus R_m (see figure-5.17) illustrates how finding the minimum of the cost function given in equation-5.30 can be used to optimize the choice of R_m.

5.5.2 Measurements from a single wedge

In previous sections, phase measurements from one region of interest on two consecutive but separate wedges were described. A similar procedure may, in fact, be adopted for two ROIs lying on the same wedge. In the following section, the benefits of doing so are discussed and validated. It should be noted that the previous notation can still be applied here by simply interpreting the indices $i = i_0$ and $j = j_0$, as labels to

the two distinct ROIs lying on the same wedge as opposed to two distinct wedges used earlier.

The first benefit of the single wedge analysis is that it allows one to test that the required condition described by inequality-5.16 is held for $d_s^{i_1,j_1}$, by simply applying equation-5.24 to the phase signal from the two ROIs with each region having a slightly different thickness due to the wedge angle. Consequently, as the two ROIs are brought closer, the synthetic thickness $d_s^{i_0,j_0}$ can be made arbitrarily small. In order to verify that $d_s^{i_1,j_1}$, did indeed satisfy the inequality in 5.16 two ROIs situated at the two extreme ends of wedge 1 were used. The aforementioned justification step can be regarded as step 0 in the general scheme outlined earlier, with the resulting thickness ratio R_0 taking the value of 8.6787.

The second benefit from the use of two windows on the same wedge is that it allows the absolute measurement of wavelength, thereby providing a useful guide for the alignment between different scans and in dispersion correction (see Chapter-7 for more details on this aspect). Finally, the use of absolute wavelength measurements as opposed to the changes in wavenumber that have been considered so far, make it easier to compare the performance of the composite sensor to that of commercially available wave-meters.

According to equation-5.23, the R_0, R_1, R_2,…,R_{Ns}, values, which are determined by the procedure described earlier, are related to $d_s^{i_{N_s+1},j_{N_s+1}}$ and $d_s^{i_0,j_0}$ as follows:

$$d_s^{i_0,j_0} = \frac{d_s^{i_{N_s+1},j_{N_s+1}}}{R_0 \times R_1 \times R_2 \times \ldots \times R_{N_s}} \ , \qquad 5.31$$

where $d_s^{i_{N_s+1},j_{N_s+1}}$ corresponds to wedge thicknesses of the order of mm or tens of mm and can be measured to sufficient accuracy with a mechanical probe such as a micrometre. The thickness difference between the centres of the two ROIs can, therefore, be determined using equation-5.31. The fact that there is a continuous path between the two ROIs means that for any given frame *t*, the phase difference between their centres,

$$\Delta\Psi = \Psi\left(x_{i_0}, y_{i_0}, t\right) - \Psi\left(x_{j_0}, y_{j_0}, t\right) \ , \qquad 5.32$$

can be computed with no 2π ambiguity by counting fringes along any chosen path between them. This is conveniently achieved by the 2-D version of the Takeda Fourier transform method [209], followed by spatial unwrapping of the resultant wrapped phase maps. The wavelength used to record the current frame is then given, using equation-5.9, as:

$$\lambda = \frac{2\pi n d_s^{i_0,j_0} f(\theta,\alpha)}{\delta\psi} \ . \qquad 5.33$$

Figure-5.18 shows the fringe pattern from wedge 1 in frame 1, with the white boxes indicating the positions of the two ROIs, while the corresponding wrapped phase-map is shown in figure-5.19. The phase difference between the centres of the two ROIs can be easily estimated by counting the number of fringes spanning across the region marked by the two crosses to be $\sim 31 \times 2\pi$. However, a more precise value of $\delta\Psi$ = 195.941 rad is obtained by computing the difference between the unwrapped phase values at the two crosses. By substituting R_0 = 8.6787 and the other R_m values as stated earlier in section-5.5.1, a $d_s^{i_0,j_0}$ value of 8.4 μm is obtained. Substituting this and the $\delta\Psi$ value obtained earlier into equation-5.33 and assuming a constant value for the refractive index of n = 1.45395 yields a wavelength value of 782.5 nm. A value of 764.8 nm was reported by the wave-meter. Strictly speaking the fact that n is dependent on λ implies that equation-5.33 should be solved iteratively. However, the weak dependence of n on λ for the limited scan used here indicates that there is no need to do so. (Only 400 frames were recorded, equivalent to a 1nm scan in the region of 764.81nm – 765.81nm) – see figure-5.20. The accuracy is not particularly high due to the use of only the pair of wedges with the lowest thickness difference; however, agreement to within 2.5% is considered acceptable. Subsequent changes in wavenumber are determined to a much higher accuracy, as we have already seen, through the use of the thicker wedges.

In order to validate the method proposed in this thesis for the dynamic monitoring of wavenumber changes, the final result of the analysis was compared to the wavelength measured simultaneously with a commercial wave-meter. This was a loan instrument and no simple way existed to log the wavelengths in synchronisation with the camera frames. To solve this problem, a second identical camera triggered by the same exposure pulses as the one that recorded the wedge images was used to

capture images of the PC screen that displayed the wave-meter readings. An example is shown in figure-5.21. Each of the recorded images was then analysed using a widely available optical character recognition (OCR) program. Moreover, to eliminate errors due to electronic delays, the scanning speed was reduced to 4.5 Hz.

A comparison between the results of the analysis described here, and the wavenumber versus frame number as measured by the commercial wave-meter, is shown in figure-5.22 where the offset from the initial wavelength value has been removed. The agreement is seen to be close, with a rms deviation between the two signals of 3.86 m^{-1}, i.e., 0.44 × 10^{-3} of the wavenumber range covered here. The most likely source of this discrepancy is the error in wedge thickness measurement by the micrometre, which results in an error in the scaling factor $ndf(\theta,\alpha)$ relating phase change to wavenumber change [using equation-5.11] of order 5 μm in 12 mm ≈ 4 × 10^{-4}. By comparison, the error arising from the approximation $f(\theta,\alpha)\sim 2\cos\theta$ [i.e., by assuming the parallel plate formula of equation-5.1] is approximately 20× smaller. The variability in refractive index of fused silica is smaller still with a typical relative value of ∼1 × 10^{-5} [210].

5.6 Discussion

Wavelength detection methods have been available for some time. Simple Fizeau interferometers utilising a single wedge [28, 29] and with a set of wedges [30] have been reported in the literature, whilst an alternative method based on a polarization-sensitive interferometer combined with a homodyne detection system was described in [31]. In this present chapter an alternative method for dynamic monitoring of the time-varying wavenumber is provided, based on whole-field analysis of wave-fronts using interference patterns generated by an array of wedges. Unlike others (see for example the aforementioned [28-30]), the method also allows the instantaneous detection of incoherent images owing to the mechanical movement of the BRF and the subsequent loss of coherence, thereby making it particularly useful for WSI applications. The fact that a phase change value is obtained from just one frame means it can be applied to arbitrarily high scan rates, given a camera with sufficiently high framing rate.

To limit the phase errors that would normally arise from the use of wedges and the fact that the arms of the interferometer are not balanced [142] a modification to the phase equation for a plane parallel plate was proposed. The wrapped phase values were computed from 2-D transformation of the interference patterns from each wedge, while the instantaneous coherence detection was based on a fringe contrast analysis. As speed and accuracy are of primary importance in WSI applications, the use of the reverse exponential temporal unwrapping algorithm [1, 211] is more appropriate to the complex Fourier transform ranging algorithm [149]. Therefore, by choosing the wedge thicknesses to follow a reverse exponential sequence the algorithm described in [1] can be implemented to provide Δk measurement to high accuracy and precision without the errors that would arise from a single wedge in the presence of large wavenumber jumps. As a result, dynamic acquisition of wavenumber changes that is limited only by the speed of the wavelength scanning mechanism and/or the camera used to detect the interference patterns was achieved.

To compensate for errors induced by the manufacturing tolerances which in turn may cause the wedge thicknesses to deviate significantly from the ideal reverse exponential sequence, a simple method to characterise the wedge thicknesses based on micrometre readings was implemented. Moreover, the method allowed the dynamic monitoring of absolute wavelength. Agreement to within 2.5% between the wavelength values obtained from the composite sensor and those from the high end wavelength meter was observed. However, when *changes* in wavenumber were computed, instead of the absolute values, much better agreement to within approximately 0.4 pm was achieved between the two independent measurements over the scan range used. Two reasons were suggested to explain the mismatch in accuracy between the two: a) a potential error in the micrometre measurements and b) the effect of refractive index dispersion. It is worth noting that whilst the dependency of the refractive index to the wavelength of the source may be negligible for a short scan of only 1 nm, this will certainly not be the case for larger scans and a more accurate treatment of the effect of dispersion will be required. A higher level of accuracy in absolute wavenumber monitoring is possible through the use of more wedges.

The significance of the approach described in this chapter lies in that it provides easy synchronisation between the camera used for the wavenumber monitoring and the

identical ones used to image the 3-D displacement of the sample. More specifically it will allow the registration of the interference signal between the deformed and undeformed states of the sample with several cameras to several WSI directions.

5.7 Conclusion

Wavelength scanning interferometry and swept-source optical coherence tomography require accurate measurement of time-varying laser wavenumber changes. In this chapter a method based on recording interferograms of multiple wedges to provide simultaneously high wavenumber resolution and immunity to the ambiguities caused by large wavenumber jumps is described. All the data required to compute a wavenumber shift are provided in a single image, thereby allowing dynamic wavenumber monitoring. In addition, loss of coherence of the laser light is detected automatically. The chapter gives details of the analysis algorithms that are based on phase detection by a two-dimensional Fourier transform method followed by temporal phase unwrapping. A simple but robust method to determine the wedge thicknesses, which allows the use of low-cost optical components, is also described. The method is illustrated with experimental data from a *Ti:Sa* tuneable laser, including independent wavenumber measurements with a commercial wave-meter. A root mean square (rms) difference in measured wavenumber shift between the two of $\sim$4 m^{-1} has been achieved, equivalent to an rms wavelength shift error of $\sim$0.4 pm.

5.8 Figures

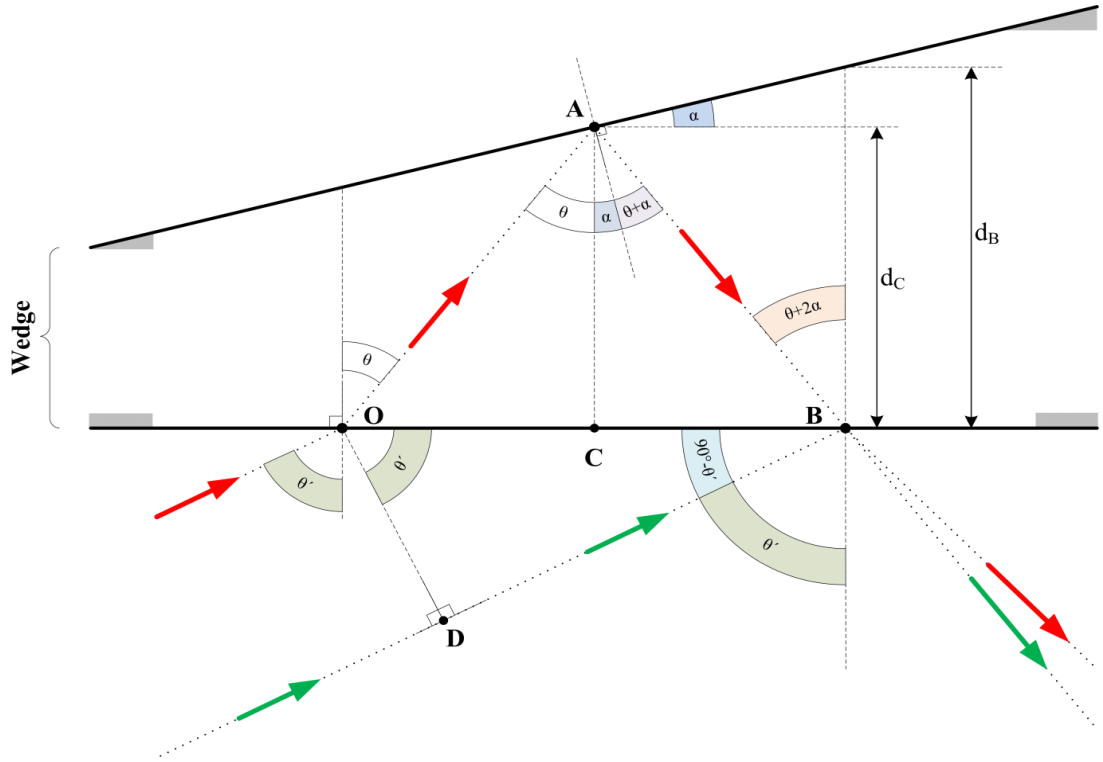

Figure-5.1: Wedge ray-tracing diagram. Green and red arrows indicate front and back reflections. B is the location where interference between the two wavefronts takes place (and also the corresponding point in the image plane of the camera) while d_B is the corresponding wedge thickness at that point. α and θ are the wedge angle and the angle of refraction, respectively, while d_C is the central wedge thickness.

j	*1*	*2*	*3*	*4*
d_j *[mm]*	12.8	12.6	12	9.6
t_j *[mm]*	0.2	0.8	3.2	–

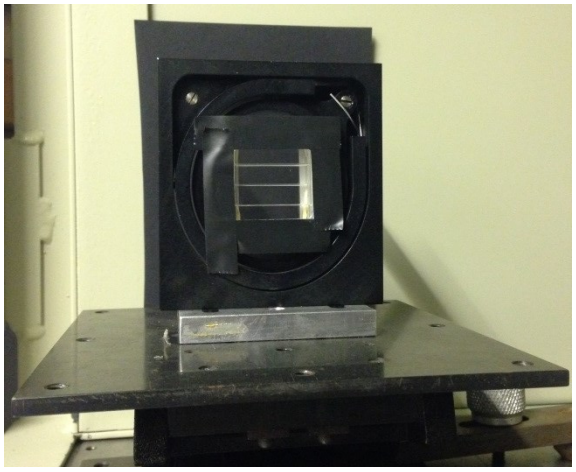

Figure-5.2: (Left) Wedge assembly with associated central thicknesses (d_j) and synthetic thicknesses (t_j). (Right) Wavefront sensor assembly on gimbal mount.

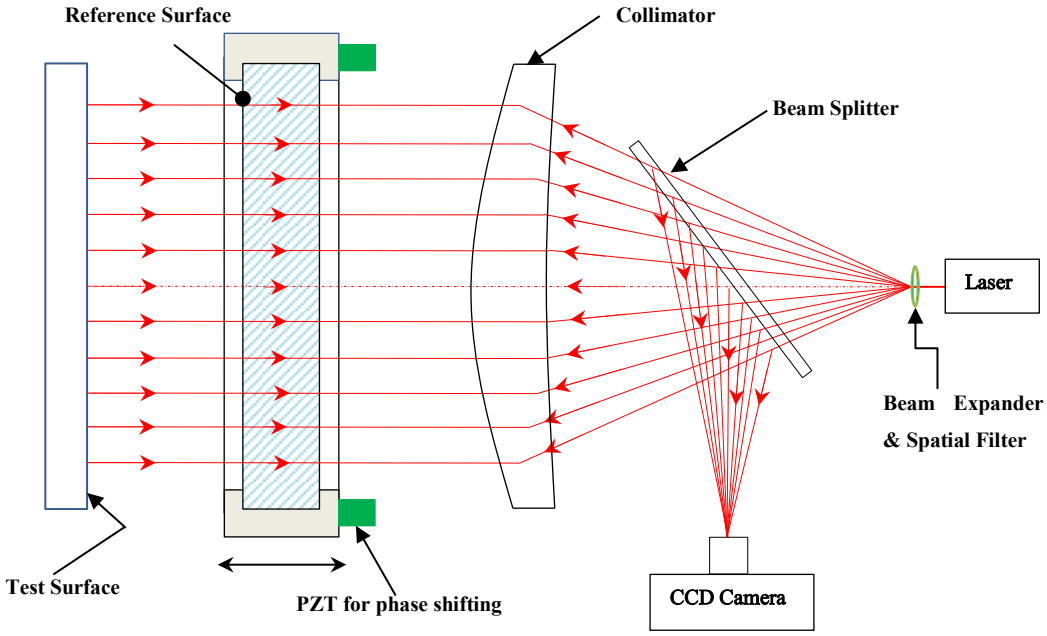

Figure-5.3: Typical Fizeau interferometer setup for PSI applications.

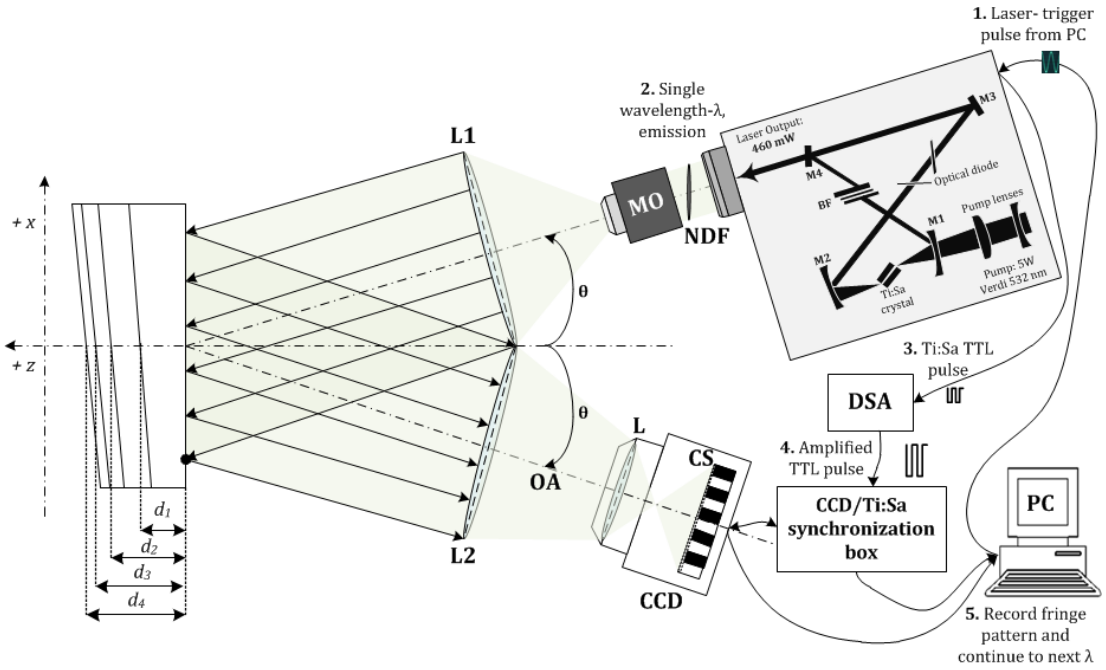

Figure-5.4: Overview of the Fizeau interferometer with the wedge sensor on the left (set of four wedges with thickness increasing along +*x*). NDF: neutral density filter, MO: Microscope objective L1: collimating lens, L2: Focussing lens, L: Camera lens, CS: camera cover slip, CCD: Charged coupled device, OA: Optical axis, DSA: Digital signal amplifier, θ: angle formed between the viewing direction (CCD optical axis shown as dotted line) and the *z*-direction (approx. 2°) also termed as the refracted angle of the illuminating beam.

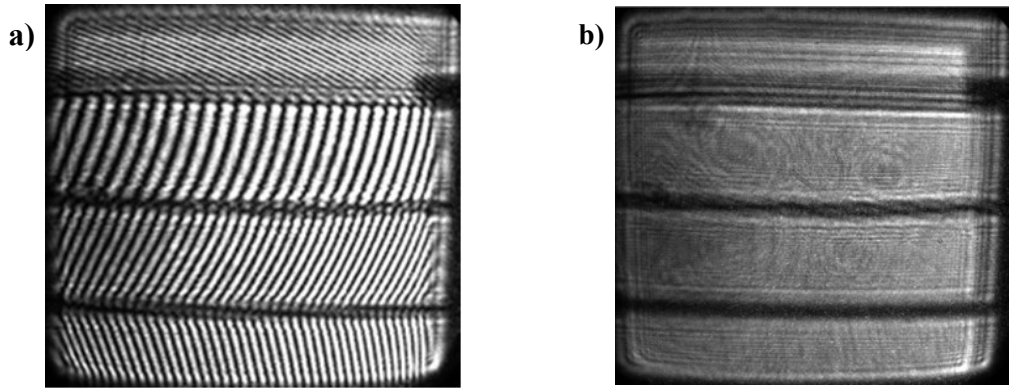

Figure-5.5: a) Wedge fringe patterns at a wavelength of 750 nm, where the thickest wedge is at the top and the thinnest at the bottom. b) Blurring of the wedge fringe patterns when coherence is lost due to mechanical movement of the BRF. Figure reproduced from [20].

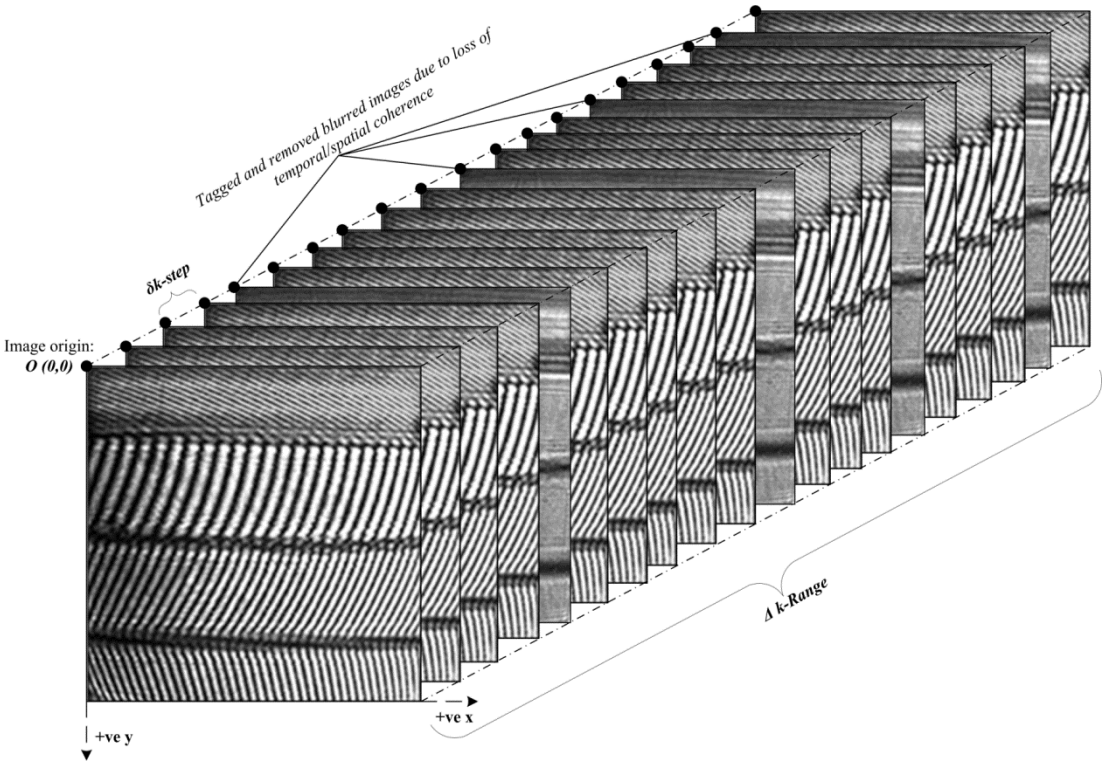

Figure-5.6: Concatenated 2-D image sequence to form a 3-D fringe pattern.

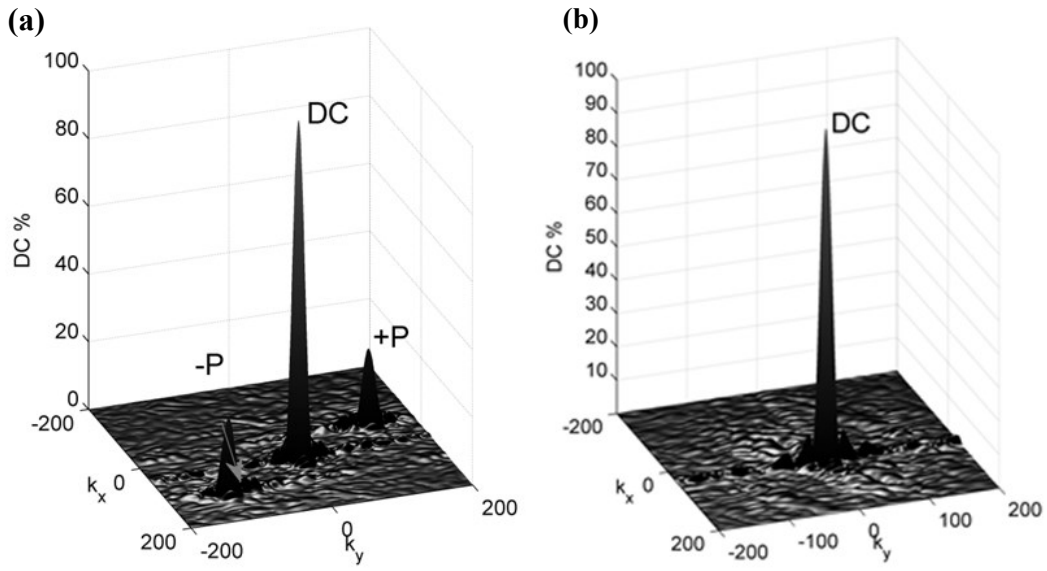

Figure-5.7: (a), (b) 2-D Fourier transforms of the fringe patterns from the top wedge shown in figure-5.5 (a) and figure-5.5 (b) respectively. Figure reproduced from[20].

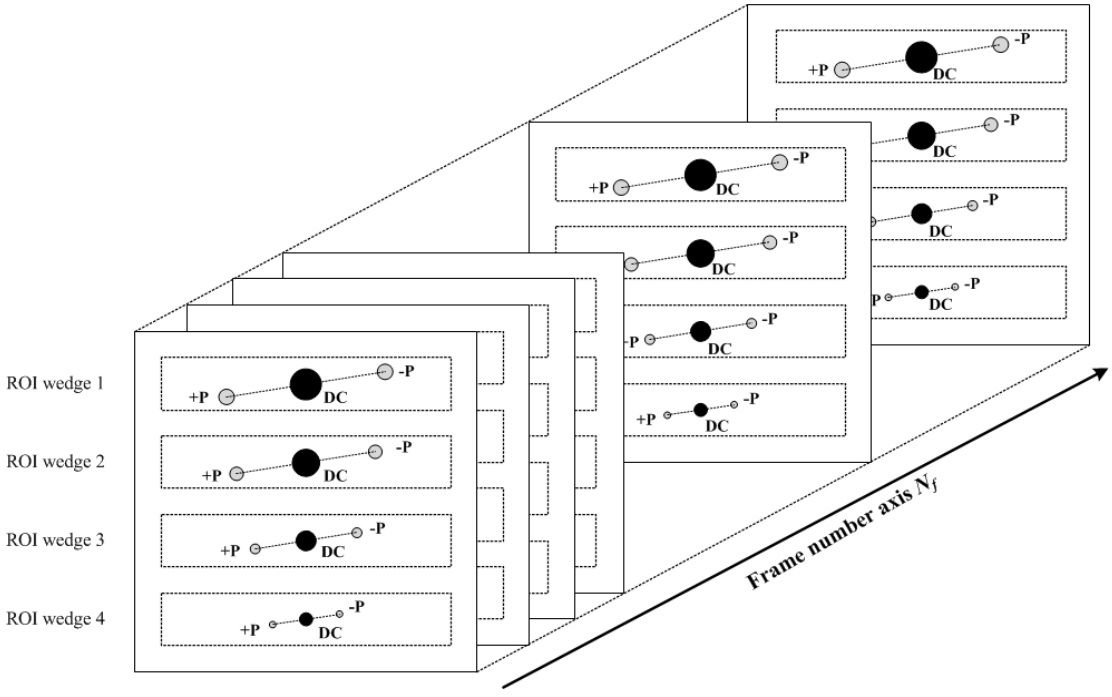

Figure-5.8: Schematic representation of a typical image sequence, after the removal of blurred images, showing the chosen ROIs for each wedge (dotted parallelograms) as well as the complex amplitude of the 2-D Fourier transforms. The big central black spots show the d.c components while the others represent the +ve and the -ve components of the Fourier transform. The distance of the symmetrical to the d.c component +ve and –ve orders is variable to reflect on the variability of the individual wedge angles.

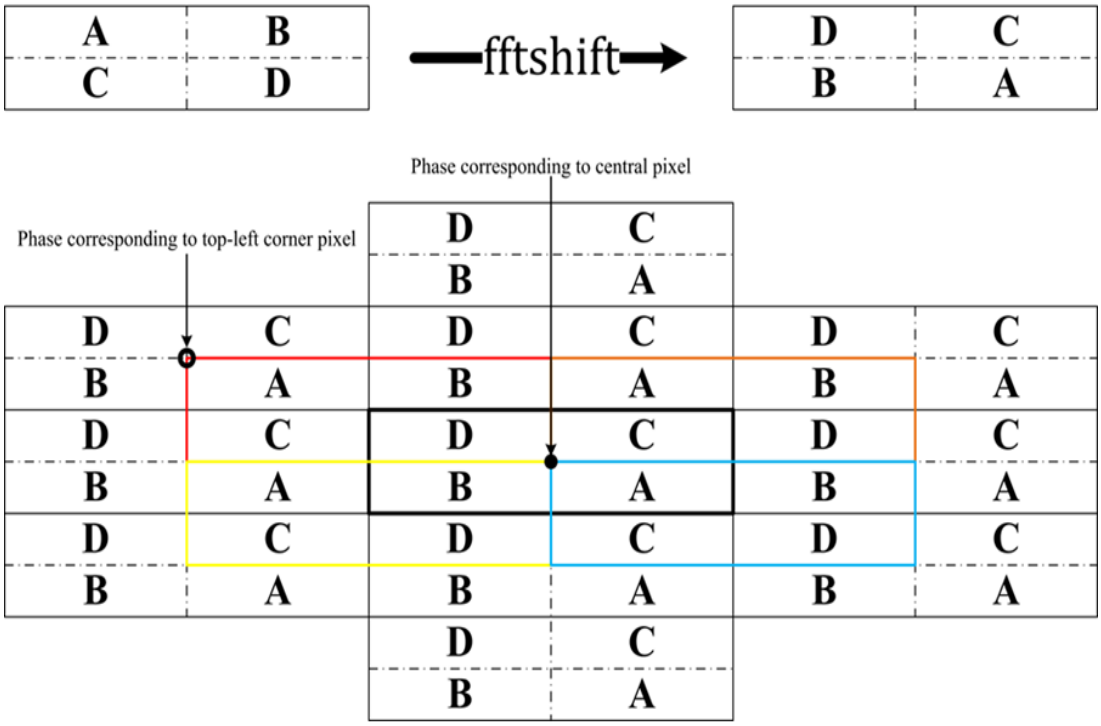

Figure-5.9: Visual means to demonstrate how the location of the extracted phase can be shifted from the image origin to the centre using the `fftshift` function in MATLAB. Letters A, B, C and D denote the four quadrants. As the 2-D Fourier transform is an operation that essentially spans through $\pm\infty$ in both x and y directions the shuffled quadrants show the shifting of the phase computation to the centre of the image.

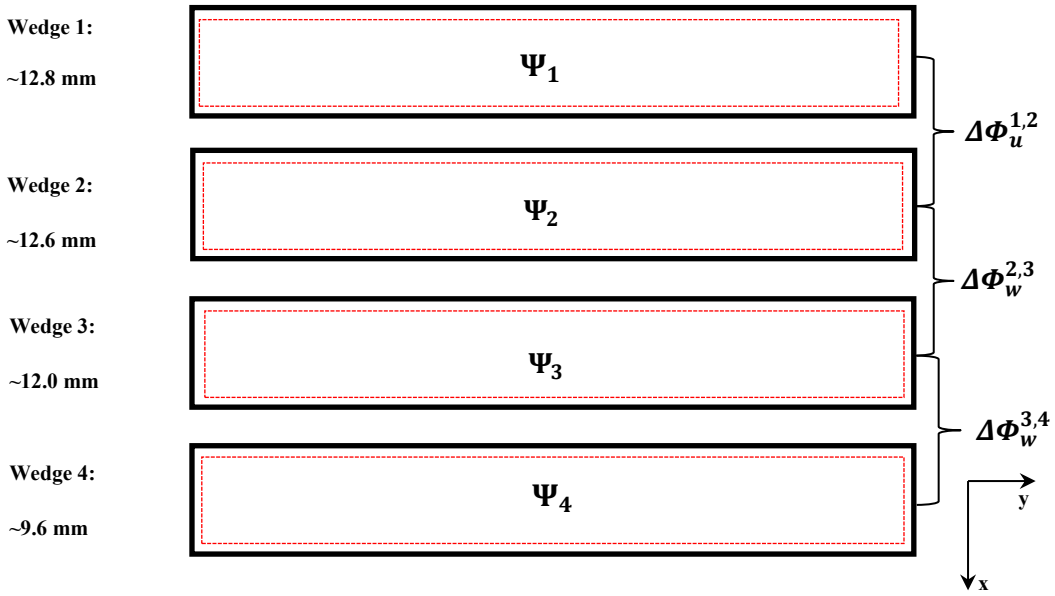

Figure-5.10: Schematic showing the four-wedge optical sensor for the experiment and the four phase changes used in this thesis. Note that the last phase change is between wedge-1 and a fictitious wedge-5 with zero thickness (in other words: $\Delta\Phi_w^{1,5} = \Psi_1$).

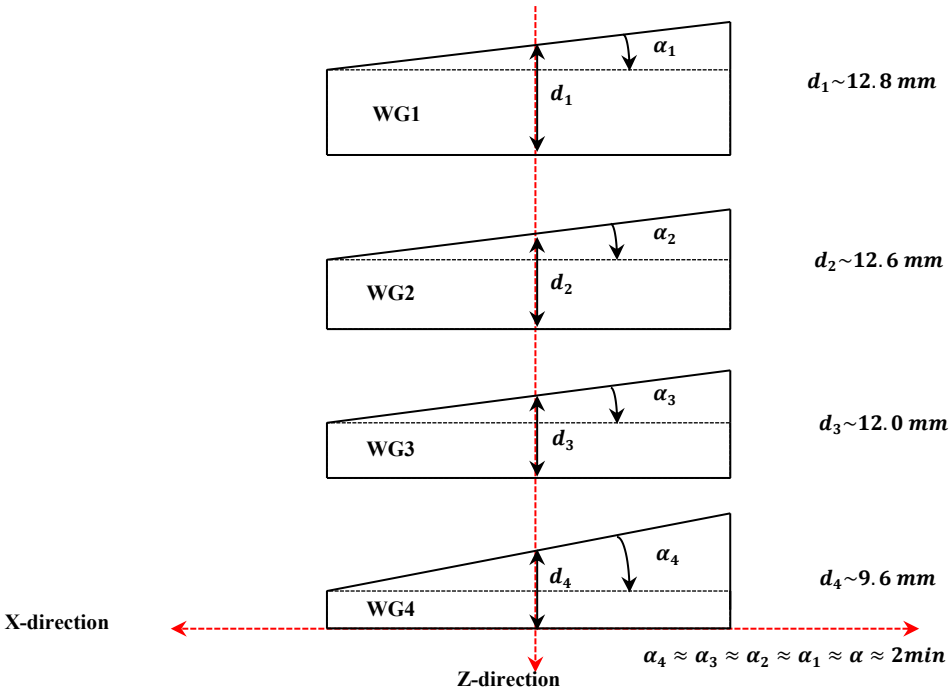

Figure-5.11: Schematic showing the four wedges in an expanded view with their associated central thickness dimensions. Note that the Z-direction and the optical axis of the camera are at a slight angle.

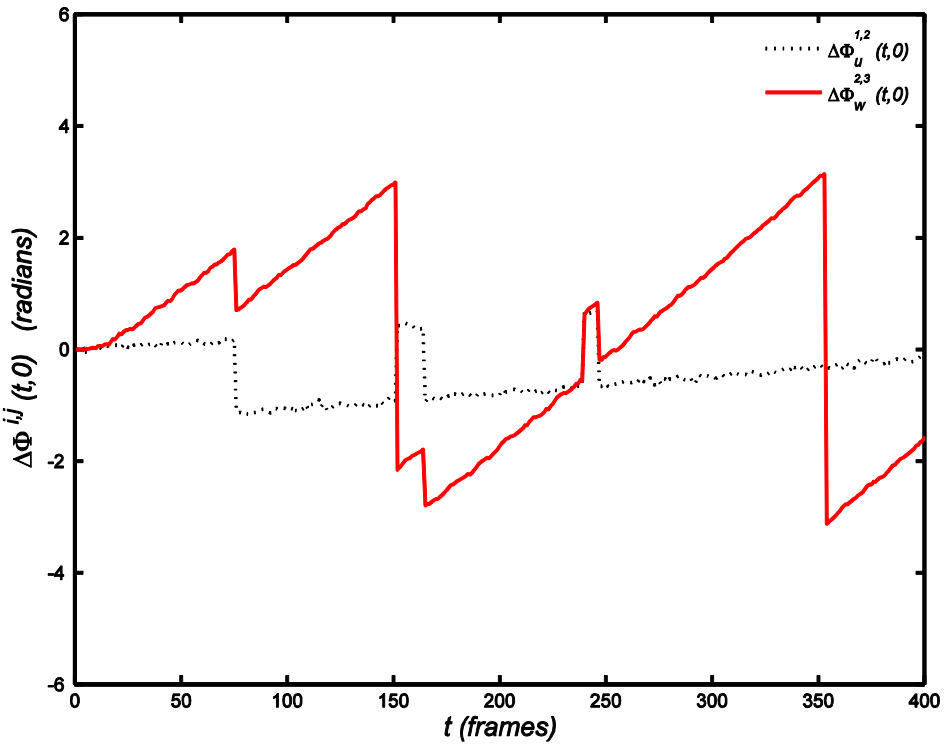

Figure-5.12: Measured phase change over a wavelength scan of 400 frames for step 1 (wedge pairs 1, 2 and 2, 3). Temporally unwrapped phase signals $\Delta\Phi_u^{1,2}(t,0)$ (dotted black line) and $\Delta\Phi^{2,3}(t,0)$ (continuous red line).

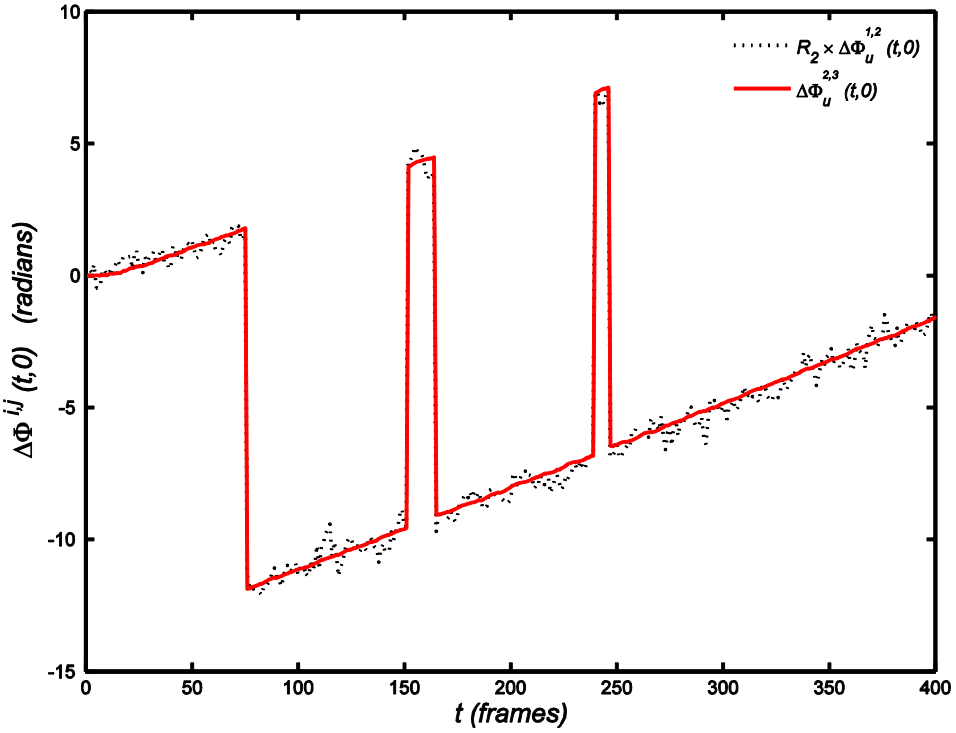

Figure-5.13: Measured phase change over a wavelength scan of 400 frames for step 1 (wedge pairs 1, 2 and 2, 3). Scaled thin wedge phase signal $R_1\Delta\Phi_u^{1,2}$ (black dotted line) and the resultant unwrapped thick wedge signal $\Delta\Phi_u^{2,3}$ (continuous red line) after unwrapping according to equation-5.24.

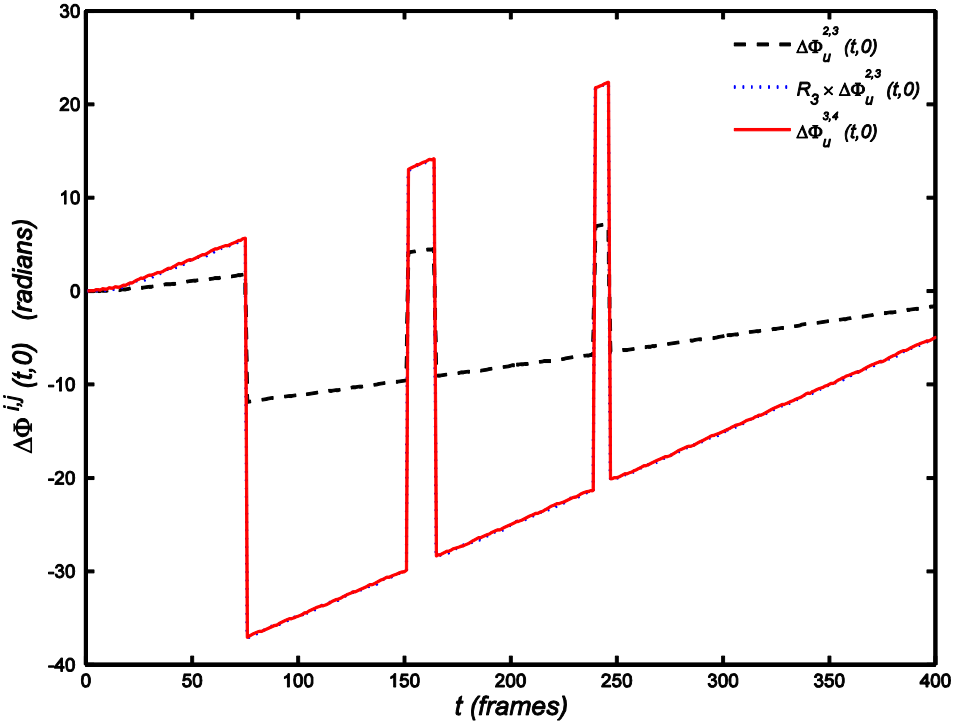

Figure-5.14: Unwrapped phase change values over a wavelength scan of 400 frames. Step 2 (in which wedges 2 and 3 are used to unwrap the difference between wedges 3 and 4).

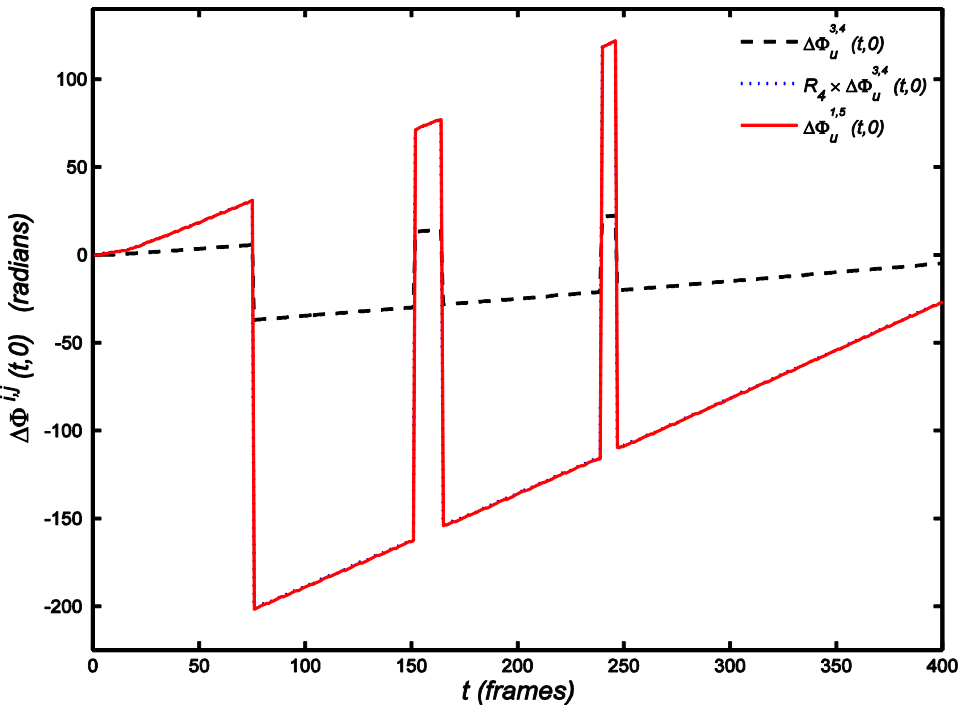

Figure-5.15: Unwrapped phase change values over a wavelength scan of 400 frames. Step 3 (in which wedges 3 and 4 are used to unwrap the phase of wedge 1).

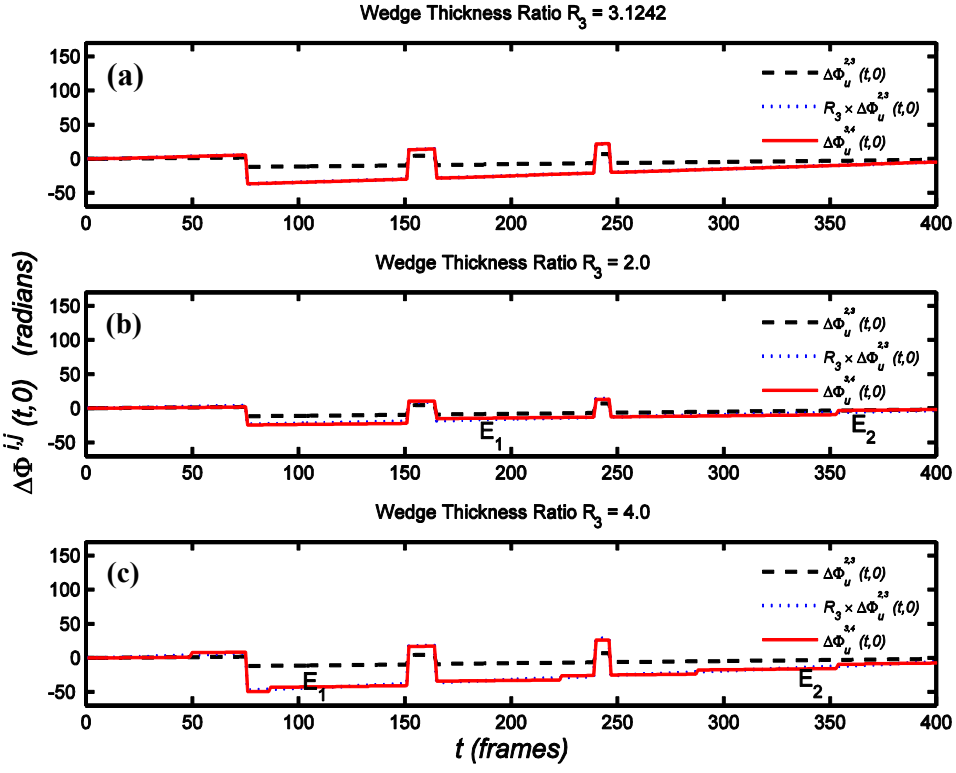

Figure-5.16: (a) Previous figure-5.14 for comparison of phase unwrapping errors, where the optimal thickness ratio R = 3.1242 has been used to unwrap the high-sensitivity phase data. Incorrect R_2 ratios (R_2 = 2, (b) and R_2 = 4, (c)) result in unwrapping errors E_1 and E_2 together with linear portions of incorrect slope in between.

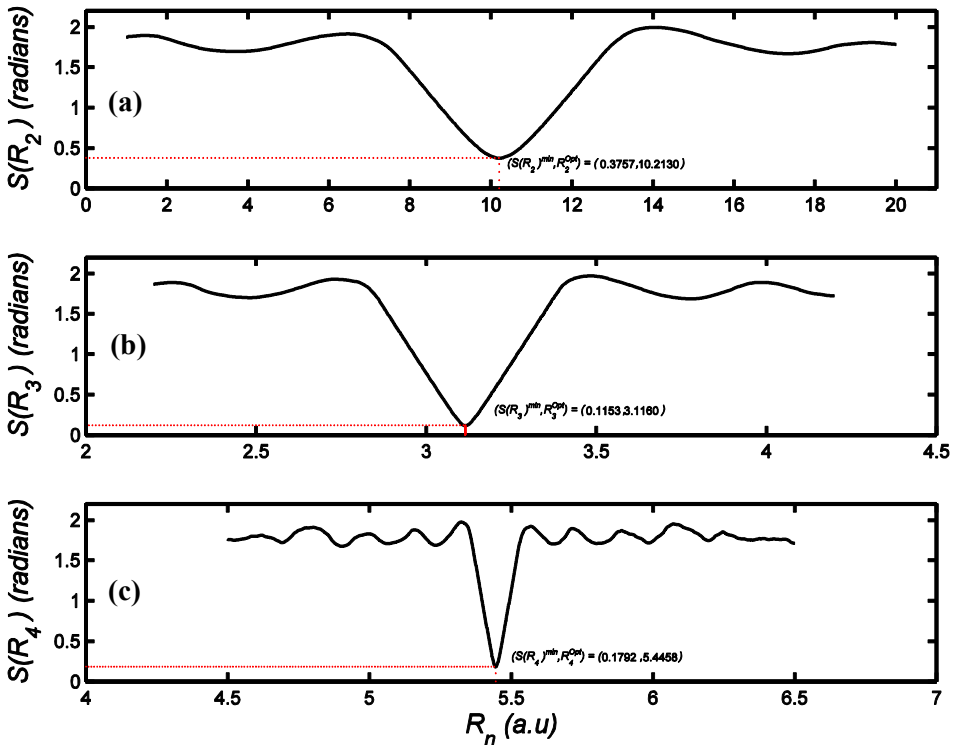

Figure-5.17: Cost function $S(R_m)$ (equation-5.30) for: (a) step $m = 1$, (b) step $m = 2$ and (c) step $m = 3$. Note: $m = n$.

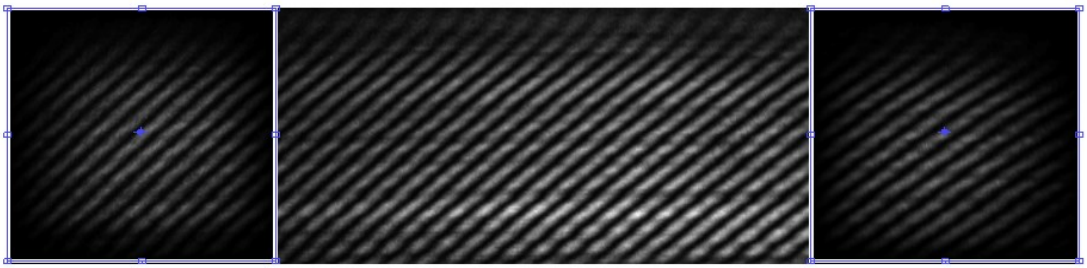

Figure-5.18: Fringe pattern at 764.81 nm: intensity distributions from wedge 1 after application of Hanning window. Rectangular boxes show the regions from which phase values were extracted, with their centres indicated as crosses. Reproduced from [20].

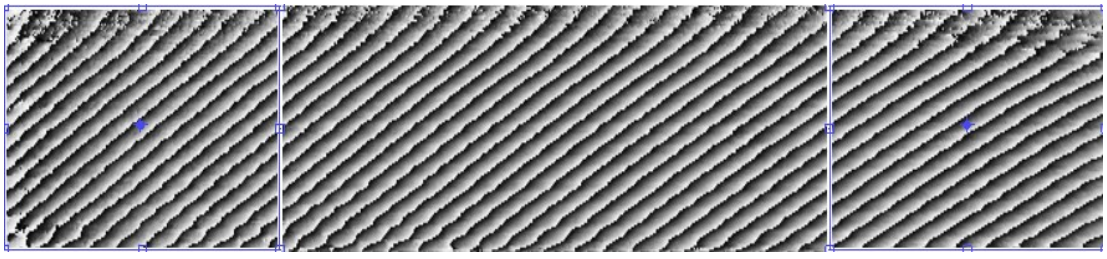

Figure-5.19: Corresponding wrapped phase-map from wedge 1 (764.81 nm). Reproduced from [20].

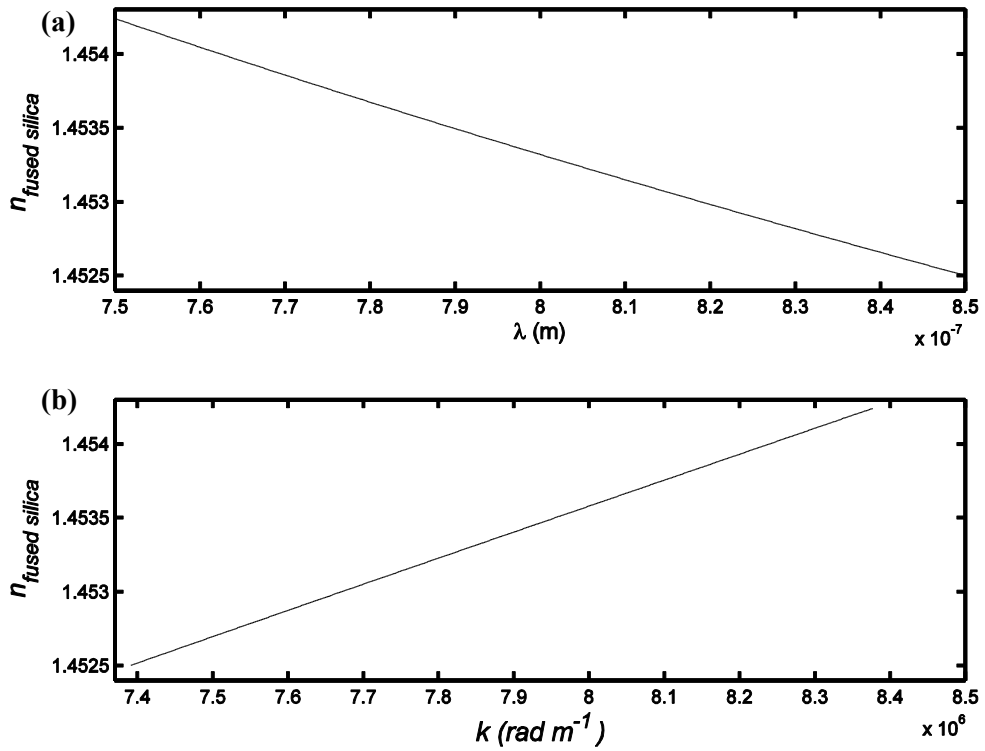

Figure-5.20: Fused silica refractive index dispersion curve for (a) the wavelength range from 750 to 850 nm and (b) the corresponding wavenumbers for the same wavelength range. The plots were produced using equation-1 in [210].

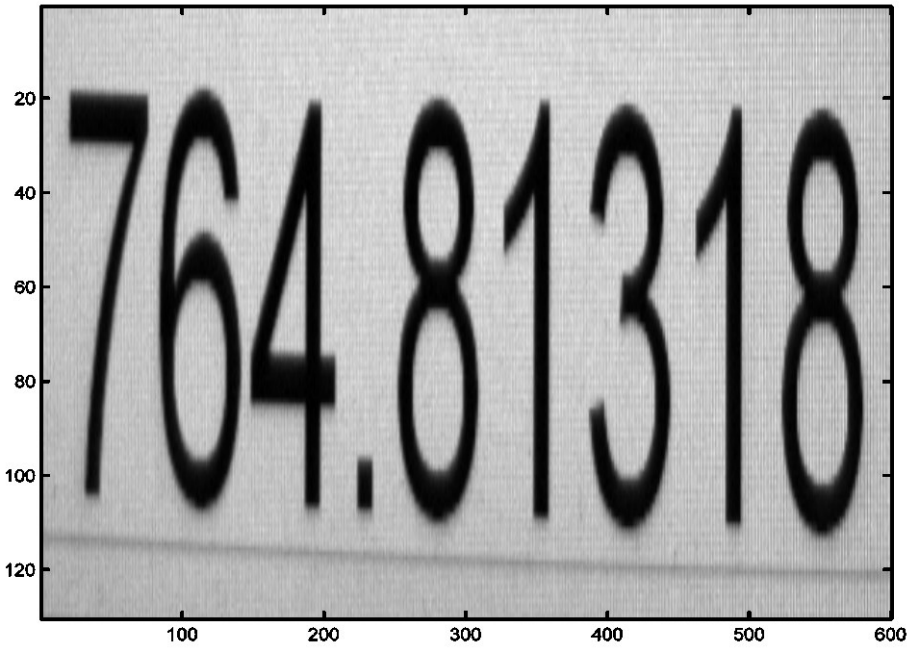

Figure-5.21: Image of the PC-screen displaying the wavelength-meter reading. Upon completion of the short scan the sequence of images was read using a readily available OCR algorithm and was converted to a MATLAB 1-D-array for the subsequent performance comparison between the commercial instrument and the optical sensor described in this thesis.

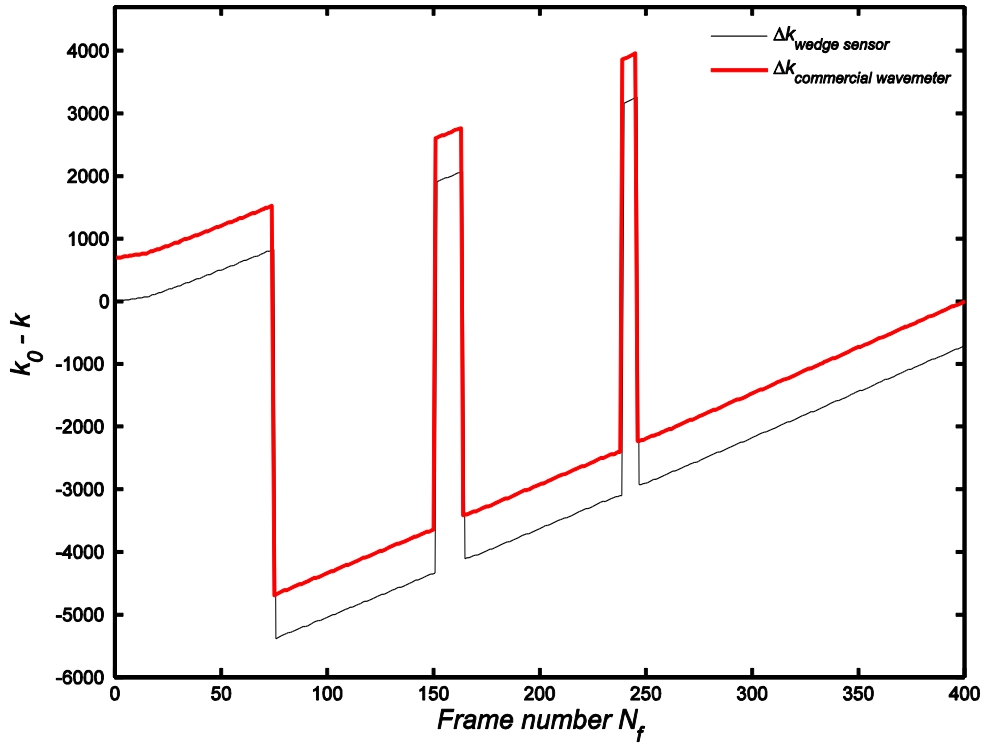

Figure-5.22: Calculated wavenumber changes from the four-wedge optical sensor using the procedure described in this chapter (solid black line) and the corresponding changes measured simultaneously by the commercial wave-meter (solid red line with an offset of 700 m^{-1} to aid visualisation). The rms deviation between the two curves was 3.86 m^{-1}.

Chapter-6: Data analysis in phase-contrast WSI

6.1 Introduction

Wavelength scanning interferometry (WSI) can be regarded as a volume imaging technique in which 2-D image sequences are recorded while the wavenumber of the light source is changed over time. The intensity of the light from a given scattering point is modulated by a temporal carrier whose frequency is proportional to the optical path difference between the object and reference waves. Provided that contributions from neighbouring scattering points can be neglected (assumption for weakly-scattering materials), one-dimensional Fourier transformation of the signal at each camera pixel separates the contributions from different regions in the measurement volume according to their distance from the zero optical path difference (OPD) surface. The approach has been used both for 3-D profilometry of opaque surfaces [26, 141] and for depth-resolved displacement field mapping in weakly-scattering materials [3, 81]

Like in any other tomographic technique, the two key parameters in WSI are the optical path difference resolution, $\delta\Lambda$, and the unambiguous depth range Δz. The former varies inversely with the total wavenumber scan range Δk, whist the latter is proportional to $N_f\delta\Lambda/n$, where N_f is the total number of recorded frames spanning Δk and n is the refractive index. It follows that, in order to achieve sufficiently good depth resolution without compromising the depth range, a laser source featuring both a wide tuning range and fine frequency resolution is required. Thus, the high-power (up to 600 mW) offered by the continuous-wavelength titanium sapphire (*CW Ti:Sa*) laser previously described in Chapter-3, along with its wide tuning range of ~100 nm and its fine wavelength resolution (down to 0.001 nm), make it suitable for WSI.

In spite of its capability to operate over such an extended range compared to those offered by the laser diodes used in earlier studies [3, 81], the main challenge with a *Ti:Sa* laser is the nonlinear variation of wavenumber with displacement or rotation of the BRF or etalon. This behaviour is due to the physics of the wavelength selection devices in the laser cavity which in turn lead to the large wavenumber jumps – see Chapter-4 for more details with regards to the behaviour and customization of the laser source. Although the algorithms in the embedded digital signal processor (DSP)

in the *Ti:Sa* laser source have been modified by the manufacturer to reduce the nonlinearities of the scan, it has proved difficult to fully suppress the issue.

In order to further supress this problem and thus improve the quality of the volume reconstructions, two fringe analysis techniques are implemented. The first involves the phase estimation described in Chapter-5 while the second is concerned with the analysis of the 1-D temporal signals obtained from each camera pixel for the duration of a full 100 nm scan.

This section of the thesis is concerned with the majority of data analysis involved in phase-contrast wavelength scanning interferometry. The term data analysis here refers to: a) the reconstruction of the Δk-axis from the phase measurements obtained with the four-wedge sensor described earlier and b) the subsequent resampling and registration of the raw intensity data onto that axis. The ultimate purpose of such an approach is to demonstrate the importance of a precise and accurate Δk-axis for phase-contrast tomographic instruments that do not necessarily feature *'balanced'* reference and object arms.

First, an in-depth description of the Fourier-transform phase calculation that was briefly described in section-5.4, is provided in section-6.2. A number of issues associated with the algorithm are addressed and an improved approach is proposed.

6.2 Fourier-transform phase extraction

The precise and accurate measurement of phase is of paramount importance in any phase contrast scheme. The following section provides an in-depth description of how the interferometric phase from the four-wedge optical sensor described earlier in chapter-5 (section-5.4) is extracted, followed by an analysis of some of the factors that may compromise the precision of this process.

For a wave-front from a perfectly formed wedge i.e. one with perfectly flat front and back surfaces and a constant wedge angle α, the spatial distribution of phase can be described as follows:

$$\Psi(x,y) = \Psi_0(x,y) + 2\pi\left(xk_x/N_x + yk_y/N_y\right), \qquad 6.1$$

where x,y are the spatial coordinates, k_x,k_y are the spatial frequencies and N_x,N_y are the total number of samples in x and y. Consequently, the corresponding intensity distribution (fringe pattern), $I(x,y)$, is given by:

$$I(x,y) = d.c. + cos[\Psi(x,y)] \ , \qquad 6.2$$

The paper published by Takeda *et al* [209] in the early 80's was the first to point out the significance of the Fourier transform as a tool to analyse fringe patterns with spatial carriers. In accordance to their work, the wrapped phase can, therefore, be retrieved as follows:

$$\Psi(x_0,y_0) = \ tan^{-1}\left\{\frac{\Im[\tilde{I}(k_x,k_y)]}{\Re[\tilde{I}(k_x,k_y)]}\right\} \ , \qquad 6.3$$

where, $\tilde{I}$, is the Fourier transform of I, $\Im$ is its imaginary part and $\Re$ its real part. Note that the wrapped phase computed in this manner, corresponds to that at the image origin $(x_0, y_0) = (0, 0)$. Taking into account the infinite and symmetric nature of the Fourier transform, the location of the extracted phase can be shifted to the centre of the image, $(x_c, y_c) = (N_x/2, N_y/2)$, by swapping the image quadrants prior to Fourier transformation (see figure-5.9).

In practice, the *d.c* offset is never zero because measured intensity is always positive or zero, and the Fourier transform of a fringe pattern described by equation-6.2 therefore consists of three orders, namely the d.c. peak and two side lobes. The three peaks are located at spatial frequencies $(f_x,f_y)=(0,0)$, for the d.c peak, and $(f_x,f_y)= \pm (k_x, k_y)$, for the two symmetric side lobes as shown in figure-6.1(a). In this case, the required phase (plus the carrier, if one is present) is normally computed by isolating the positive frequency lobe followed by numerical extraction of its spatial location and the subsequent application of equation-6.3. Frequency isolation is usually achieved by multiplying the transform by an appropriate shifted 'top hat' window. The removal of the spatial carrier, on the other hand, is done by a process known as demodulation involving the shifting of the isolated peak back to the Fourier image-plane origin (0,0) [54, 209]. In the current case, there is no spatial carrier, however, the non-zero wedge angle ensures that the positive and negative frequency lobes are well-separated. In addition, the fact that the wedge angle is primarily along the x-axis means that we can assume the side lobes to lie close to the f_x axis.

6.2.1 Integer phase calculation

Figure-6.1(b-d) shows a practical way of selecting the positive frequency lobe in such a case. It was originally proposed and implemented by A. Davila, but has since been improved by the current author as will be described in subsequent sections. The approach involves three steps where, at first, half of the Fourier spectrum is set to zero. Second, as the d.c always appears at the origin, the neighbouring region to the origin is also set to zero. Finally, by swapping the quadrants of the Fourier plane (shown as A, B, C, D in figure-6.1), the peak of interest is placed towards the centre of the Fourier plane. The swapping of the four quadrants is equivalent to moving the origin of the Fourier plane from the bottom left corner to the centre. The three-step process described above is similar to filtering out the negative frequency lobe while at the same time it provides a simple way of removing the d.c offset. Note that the rectangular window, shown in red in figure-6.1(c) and figure-6.1(d), is an alternative to the shifted 'top hat' window mentioned earlier.

6.2.2 Non-integer phase calculation

The procedure described in the previous section, which was initially put together by A. Davila, may be considered as similar to the Takeda Fourier transform method. However, it does not involve transforming back to the spatial domain and calculating the phase at each pixel. Instead, the phase is calculated at just one pixel (central pixel in the ROI) in the spatial domain from the phase at the point P in the spatial frequency domain. This method termed 'integer phase calculation' was used for the computation of the total change in wavenumber for the proof of principle short scan in chapter-5 (section-5.4) and in [20]. It did, however, have a number of defects such as (a) measuring the peak position only to the nearest integer and (b) masking out the d.c peak, rather than removing the d.c term at source, thereby introducing the potential for phase errors due to the d.c. peak's side lobe structure in the case of low spatial frequency fringe patterns.

One significant improvement made on the original Davila method was therefore to identify the peak location to sub-pixel accuracy, and then measure the phase at this true peak, rather than at the nearest integral spatial frequency values. An algorithm to estimate the location of a peak in the spatial frequency domain to sub-pixel accuracy was proposed by *Huntley J.M* [2]. The proposed solution, which was based on a

discrete Fourier transform of the recorded speckle fringe patterns coupled with an optimization algorithm based on a *Newton-Raphson method*, resulted in a significant improvement in the accuracy and precision of the sought displacement vector. Although at this stage we are not concerned with displacements, the significance of such an approach may be realized by recalling that the fine wavelength step resolution used in a phase-contrast wavelength scanning interferometry scheme will almost always produce interferograms with a non-integer number of fringes across the field of view. Therefore, the use of an algorithm which is immune from such rounding errors is most likely going to improve the quality of the phase estimation process and is thus worth investigating. Another possible factor contributing to limiting the accuracy and precision of the phase extraction process is that related to the imaging geometry. Its effect was demonstrated by the same author, a few years later, by pointing out that, when compared to that for a square image, the Fourier-peak of interest for a non-square image is broadened along the frequency axis corresponding to the short image side [212].

To demonstrate the effect of non-square imaging geometry and non-integer spatial frequencies on phase errors, simulated data sets with varying imaging dimensions and spatial frequencies in the absence of a *d.c.* offset are compared using the algorithm described in the previous section and that described in [2]. In addition to the above, the validity of the proposed method for extracting the phase corresponding to the centre of the region of interest by swapping the image quadrants prior to phase extraction is also tested. More specifically, the chosen parameters for the numerical case study conducted are as follows:

a. Square imaging geometry (512 × 512 pixels) with integer spatial frequencies ($k_x = 15$, $k_y = 12$) - see figure-6.2.
b. Square imaging geometry (512 × 512 pixels) with non-integer spatial frequencies ($k_x = 14.45$, $k_y = 12.43$) - see figure-6.3.
c. Non-square imaging geometry (714 × 86 pixels) with integer spatial frequencies ($k_x = 15$, $k_y = 12$) - see figure-6.4.
d. Non-square imaging geometry (714 × 86 pixels) with non-integer spatial frequencies ($k_x = 14.45$, $k_y = 12.43$) - see figure-6.5.

By visually comparing figure-6.2 and figure-6.3 (correponding to cases of a and b above), it is obvious that in the presence of non-integer spatial frequncies the shape of the Fourier peak appears to be broadened (see for example figure-6.2 (a) and figure-6.3). Moreover, the effect of swapping the image quadrants prior to transformation is now more apparent as shown in figures 6.2(d) , 6.3(d). A less obvious, yet quite intetresting point is that related to the precision and accuracy of the phase estimation in the presense of non-integer k_x, k_y. Using equation-6.1 the 'true' phase at the image origin and centre can be computed and can, therefore, serve as a valid reference to test the precision of the phase extraction. In order to aid the comparison of the numerical results from the two algortitms used to extract the phase, the relevant data are presented in tabular form (see tables 6.1-6.2 below)

Table-6.1: Tabular form of the results from a simulated fringe pattern for a square image (512 × 512) with integer k_x, k_y of 15 and 12 respectively, showing the estimated phase values by the Fourier transform method ('integer phase calculation'), the sub-pixel Fourier transform phase value ('non-integer phase calculation') and their corresponding deviation from the true phase

True phase Ψ_{true}		**Integer-based phase calculus $\Psi = \Psi_{int}$**		**Non-integer based phase calculus $\Psi = \Psi_{non\text{-}int}$**	
Origin	*Centre*	*Origin*	*Centre*	*Origin*	*Centre*
0.3313 rad	-2.81029 rad	0.3313 rad	0.3313 rad	0.3313 rad	-2.8102 rad
Deviation from true value:		$\lvert\Psi_{true} - \Psi\rvert$	$\lvert\Psi_{true} - \Psi\rvert$	$\lvert\Psi_{true} - \Psi\rvert$	$\lvert\Psi_{true} - \Psi\rvert$
		0 rad	3.1416 rad	1.7542e-14 rad	5.3291e-15 rad

Table-6.2: Same as table-6.1, but for a square image (512 × 512) and non-integer k_x, k_y of 14,45 and 12.43 respectively.

True phase Ψ_{true}		**Integer-based phase calculus $\Psi = \Psi_{int}$**		**Non-integer based phase calculus $\Psi = \Psi_{non\text{-}int}$**	
Origin	*Centre*	*Origin*	*Centre*	*Origin*	*Centre*
0.3421 rad	-0.0348 rad	3.1014 rad	3.1014 rad	0.3424 rad	1.3052 rad
Deviation from true value:		$\lvert\Psi_{true} - \Psi\rvert$	$\lvert\Psi_{true} - \Psi\rvert$	$\lvert\Psi_{true} - \Psi\rvert$	$\lvert\Psi_{true} - \Psi\rvert$
		2.7593 rad	3.1363 rad	2.5839e-04 rad	1.3400 rad

As seen from the tabular data above the integer-based algorithm significantly underestimates the phase at the centre by nearly 9.5× for case-a, while it overstimates both the phase at the origin and that at the centre by approximately 8× and 9× respectively for case-b. The performance of the non-integer algorithm on the other hand, shows more promising results albeit it overestimates the true phase at the

image centre suggesting that for non-integer values of spatial frequncies the swapping of the image quadrants prior to phase extraction does not yield the true phase at the centre. The analysis for a non-square imaging geometry gives very similar results as seen from table-6.3 and table-6.4 shown below.

Table-6.3: Same as table-6.1, but for a non-square image (714 × 86) and integer k_x, k_y of 15 and 12.

True phase Ψ_{true}		**Integer-based phase calculus $\Psi = \Psi_{int}$**		**Non-integer based phase calculus $\Psi = \Psi_{non\text{-}int}$**	
Origin	*Centre*	*Origin*	*Centre*	*Origin*	*Centre*
1.0087 rad	-2.13287 rad	1.0087 rad	1.0087 rad	1.0087 rad	-2.13287 rad
Deviation from true value:		$\lvert\Psi_{true} - \Psi\rvert$	$\lvert\Psi_{true} - \Psi\rvert$	$\lvert\Psi_{true} - \Psi\rvert$	$\lvert\Psi_{true} - \Psi\rvert$
		6.6613e-16 rad	3.1416 rad	1.5099e-14 rad	9.77e-15 rad

Table-6.4: Same as table-6.1, but for a non-square image (714 × 86) and non-integer k_x, k_y of 14.45 and 12.43, respectively

True phase Ψ_{true}		**Integer-based phase calculus $\Psi = \Psi_{int}$**		**Non-integer based phase calculus $\Psi = \Psi_{non\text{-}int}$**	
Origin	*Centre*	*Origin*	*Centre*	*Origin*	*Centre*
1.0441 rad	0.6671 rad	-2.4923 rad	-2.4923 rad	1.0444 rad	1.9889 rad
Deviation from true value:		$\lvert\Psi_{true} - \Psi\rvert$	$\lvert\Psi_{true} - \Psi\rvert$	$\lvert\Psi_{true} - \Psi\rvert$	$\lvert\Psi_{true} - \Psi\rvert$
		3.5364 rad	3.1594 rad	2.9372e-04 rad	1.3219 rad

The case study above highlights the benefit of sub-pixel accuracy in detecting the location of the Fourier peak of interest. Although an error is present in the estimated phase for non-integer spatial frequencies of the fringes, it is significantly lower than the case for integer pixel phase estimation.

Finally, the answer to the natural question as to why the phase should preferably be evaluated at the centre of the region of interest as opposed to the image origin is related to the manufacturing quality of the sensor itself. The likelihood of deviations from flatness towards the edges of the four wedges is higher than that at the centre. While a perfectly flat wavefront would give equally spaced parallel fringes, a curved wavefront would result in fringes with a level of curvature related to the deviation from flatness. In addition to that, the presence of edge effects owing to unwanted reflections around the edges of the optical sensor may further contaminate the signal.

To ensure their effect is kept to a minimum, a 2-D Hanning window was applied to the recorded fringe patterns which gives maximum weight towards the centre of the image and minimum at the edges.

6.2.3 Estimation and suppression of background intensity-artefacts

So far, the analysis presented in the previous section did not account for the effect of the *d.c.* term on the phase estimation process. As pointed out by *Huntley J.M.* the zero-order peak has the undesirable effect of shifting the location of nearby peaks in the frequency domain [2]. The background intensity in speckled interferograms is a well-established factor known to affect the accuracy of phase related measurements. The study by Kaufmann *et al* was amongst the first to point out the significance of the diffraction halo on phase errors by means of numerical analysis of 1-D photodiode data [213]. In their study, two approaches for removing the diffraction halo were examined. The first involved the direct subtraction of the estimated diffraction halo, while the second was based on the ratio of the recorded fringe pattern over the estimated halo. The term "*background"* is rather generic and is often mixed with the more familiar *d.c.* term used in signal processing where in most cases it is associated with the mean value of the signal. To clarify this, consider the ideal case of a digitized fringe pattern as stated in [2]:

$$I(x,y) = I_0(x,y)\{1 + cos[2\pi(xk_x/N_x + yk_y/N_y) + c]\}, \qquad 6.4$$

where $I_0(x, y)$ is the intensity background and c is a constant. For the setup described in section-5.3, there are two additional factors contributing to the measured intensity distribution that are not included in equation-6.4:

a. Intensity variations owing to the combined variations of the laser power and camera sensitivity during the scan which strictly speaking therefore introduce an additional time dependence which is not present in equation-6.4
b. Multiple reflections inside the wedges resulting in harmonics of the fundamental frequency.

The former is mostly dealt with using the variable exposure compensation method as described in chapter-4 section-4.4.1. The latter is not a major effect as the higher harmonics appear at different locations in the 2-D Fourier transform and therefore should not interfere with the phase detection at the principal peak.

Recalling that the direct subtraction of $I_0(x, y)$ from the recorded signal prior to Fourier transformation is preferable to calculating the Fourier transform of $I(x, y)$ / $I_0(x, y)$ the former will be adopted in the following analysis [2]. Both authors in [2, 213] estimated the background intensity by recording its effect prior to the measurements. More specifically, the former used a total number of 16 frames before the recording of the speckled fringe patterns which were subsequently used for estimating the diffraction halo by averaging the contributions of each pixel. Although this could formulate a perfectly valid approach in determining the effect of multiple reflections in the 4-wedge sensor, it would on the other hand suffer from inaccuracies on account of the fact that laser scans are not necessarily identical to one another. Instead, an approach which is similar to that described in [2] is adopted but differs in that the entire scan sequence, consisting of ~ 50,000 frames, is used for estimating the diffraction halo thereby reducing uncertainties related to scanning consistency. By averaging such a large number of frames, the interference fringe amplitude can reasonably be assumed to be reduced to negligible levels. However, changes in halo shape as the scan progresses are not taken into account by the proposed procedure.

The proposed algorithm for estimating the background term after removing the non-linear effects due to the laser power variations and the sensitivity in the photodetector is as follows. The recorded intensity distribution of the fringe patterns along the k-axis can then be written as:

$$I(x, y, k_t) = I_0(x, y)\{1 + cos[2\pi(xk_x(k_t)/N_x + yk_y(k_t)/N_y) + c(k_t)]\}, \quad 6.5$$

where x,y are the spatial coordinates of the individual regions of interest for each of the four wedges (see figure-6.6), k_t is the instantaneous wavenumber of the source in frame t and N is the total number of recorded frames for a full 100 nm scan (in this case 48,971). An estimate of the background intensity $I_0(x,y)$ can then be calculated from the following expression:

$$\bar{I}_0(x, y) = \sum_{t=0}^{N-1} I(x, y, k_t), \quad 6.6$$

The sums:

$$s_1(k_t) = \sum_{x=1}^{Nx} \sum_{y=1}^{Ny} I(x, y, k_t) \ , \quad 6.7$$

$$s_2 = \sum_{x=1}^{Nx} \sum_{y=1}^{Ny} \bar{I}_0(x, y) \ , \quad 6.8$$

can then be regarded as estimates of the zero frequency Fourier components of $I(x,y,k_t)$ and $\bar{I}_0(x,y)$ respectively. Consequently, the free-of-background-intensity signal, I_b, can then be approximated as follows:

$$I_b(x,y,k_t) = I(x,y,k_t) - (s_1/s_2)\bar{I}_0(x,y) \ , \qquad 6.9$$

A visual representation of the estimated diffraction halo by implementing the algorithm described above is shown in figure-6.7. To demonstrate the combined effect of the improvements implemented so far related to the phase extraction process, a comparison of the resulting phase-change from the last unwrapping step in chapter-5 using the integer based phase calculation approach and that which combines the removal of the background intensity and the sub-pixel peak detection algorithm is provided in figure-6.8. The difference between the two approaches is at first sight not very obvious. However, by zooming in to the four regions of the full sequence that were previously most affected by phase unwrapping errors, the superiority of the proposed approach becomes evident, as demonstrated in figure-6.9. As indicated in figure-6.9(d), although the majority of the phase unwrapping errors have been suppressed, some residual phase unwrapping errors are still present. These errors will be ignored for now as their origin and effect are different from those considered in the current chapter and will be dealt with later in chapter-7.

6.3 Registration of raw intensity data onto Δk-axis

The camera and the 4-wedge optical element, in effect constitute a wave-meter that is precisely synchronised to the other cameras in the system. The intensity data from a given pixel in any camera can then be located at the correct position along the Δk axis. The raw intensity data can then be temporally interpolated onto a regularly spaced wavenumber change vector. The numerical analysis presented in this chapter describes this process for the case of a full scan of 100 nm (λ_{start} = 750 nm to λ_{end} = 850 nm with a nominal wavelength step $\delta\lambda$ = 4 pm).

6.3.1 Non-uniform *k*-space sampling

The data processing for WSI involves one-dimensional spectral analysis of the recorded time-varying signal at each pixel, $I_t(x, y, t)$. In what follows, we focus on

the j^{th} pixel with image plane coordinates $x = x_j$, $y = y_j$. The assumption in previous WSI implementations [3, 81], which used narrow tuning ranges, was that:

$$I(x_j, y_j, k) = I_t(x_j, y_j, t) \ , \qquad 6.10$$

with k and t related through the following expression:

$$k(t) = k_c + \delta k \cdot t \ . \qquad 6.11$$

Thus a discrete Fourier transform of the sampled 3-D intensity volume $I_t(x_j, y_j, t)$ along the t axis provides a scaled version of $\tilde{I}(\Lambda)$ for the jth pixel, where Λ is the optical path difference between the reference and object beams. As discussed in Section 6.2, this should consist of three delta functions, one at $\Lambda = 0$ (the d.c term) and the other two at $\Lambda = \pm \Lambda_0$ (the cosine term), convolved with the Fourier transform of the window function, $\widetilde{W}(\Lambda)$.

To investigate the validity of equation-6.10 and equation-6.11, to the much longer sequences offered by the *Ti:Sa* laser, and to illustrate some of the issues involved in the data analysis, the 3-D data sets $I_t(x,y,t)$ from the camera recording the wedges are used. As a first step, the ability of the laser to emit distinct wavelengths during a full scan was assessed by comparing the wavenumber change between successive frames to an appropriately chosen threshold value $\delta\kappa$ such that:

$$\delta\kappa = c \cdot \delta k_{step} \ , \qquad 6.12$$

where c is a constant and δk_{step} is the user defined wavenumber step between successive frames such that:

$$\left.\begin{array}{c} 0 < c \leq 1 \\ 19.635\ m^{-1} < \left|\delta k_{step}\right| < 9817\ m^{-1} \end{array}\right\} . \qquad 6.13$$

Note that the latter is a parameter required by the software controlling the laser wavelength selection which for a perfect scan would be identical to δk in equation-6.11. Apart from providing a first indication as to how linear the scan is, this intermediate data processing step also acts as a memory efficient way to deal with the large data sets. Equation-6.12 is essentially a criterion used to decide: a) which frames are static (i.e. no significant change in k was produced by the tuneable laser source) and b) which slice of the 3-D intensity volume should each frame be placed

at. The second point is important because the laser wavenumber can sometimes decrease as well as increase with time. Shuffling of the frames is needed to ensure that the wavenumber increases monotonically with frame index before subsequent interpolation steps. This is conveniently handled by creating a 'sorting vector' J where the t^{th} element of J specifies position in the 3-D intensity volume of the t^{th} frame. By doing so the need for a subsequent sorting step is dropped, thereby saving an additional 3-D array and thus using only part of the initial memory requirements.

Figure-6.10 and figure-6.11 show the three-step process that produces the memory efficient sorting vector J used for the subsequent data analysis. By choosing a value of $c = 0.9$ and $\delta k_{step} = 32$ m^{-1} to match the wavelength step of 4 pm used for this data set, a reduction in the size of the original data set (initial size: 48,971 frames) of more than 50% (final size: 15,822 frames) was achieved.

Figure-6.12 shows the power spectrum $\left|\tilde{I}_t(x_j, y_j, \Lambda)\right|^2$ for one pixel near the centre of the thickest wedge, over the full range of positive optical path lengths (d.c to Nyquist limit). In this case the δk value needed to convert the non-dimensional optical frequency to optical path length (see equation-6 in [21]), was estimated as the total wavenumber change measured by the wavelength sensitive diode (9.81×10^5 m^{-1}, corresponding to a wavelength range of ~100 nm), divided by the total number of frames (15,822). In addition, the horizontal axis has been scaled by $(1/2n)$ to convert from optical path difference to physical thickness of the wedge. Initially, a constant change in wavenumber between frames was assumed here which allowed the power spectrum to be calculated by the use of a fast Fourier transform algorithm (`fft` in MATLAB).

One important aspect revealed is that the expected single peak is split into multiple peaks covering a broad range of frequencies as shown in figure-6.12. A Gaussian fit to the spectrum in the region of the peak, shown in red, has a mean value of ~ 10.2 mm and a full width half maximum (FWHM) value of 1.0410 mm. The mean value significantly underestimates the true wedge thickness (12.755 mm) while the FWHM value is 750× the expected resolution figure of 2.66 μm (FWHM value obtained from equation-6 and equation-7 in [21] with $\gamma = 1.207$). Clearly, the most likely reason for such large disagreement between the theoretical and experimental values for the optical path difference resolution, $\delta\Lambda$ and the depth resolution δz is that the linear

scan in k-space assumption (see equation-6.11) is not satisfied for such large tuning ranges.

From figure-6.13(a), it is clear that while the full tuning curve of (k-k_c) versus t appears to be approximately linear, when a short section is enlarged, etalon induced mode-hops become clearly visible. In addition to that, a degree of nonlinear behaviour between the mode-hops is seen as shown in figure-6.13(b). In figure-6.14(a), the intensity signal corresponding to the same t-range as that used in figure-6.13(b), shows how the mode hops essentially randomize the phase of the interference signal. As a result, the expected narrow Fourier peak is significantly broadened and split, thus eliminating the main benefit of the long tuning range. Furthermore, between the mode hops, the gradient of the (k-k_c) versus t tuning curve is significantly less than the average gradient, thus leading to a downshift in temporal frequency and hence underestimation of the optical path difference.

6.3.2 Fourier-transform of non-uniformly distributed intensity data

One solution to the problem outlined in the previous section is to use the measured k values, instead of the assumed vector of linearly spaced k values, when performing the 1-D Fourier transform along the t axis of $I_t(x_j,y_j,t)$. Algorithms have been developed for Fourier transformation of non-uniformly sampled data (see for example [214]). However, to the best of our knowledge, no fast algorithms exist. With typical N_f values of at least 10^4, the computation time of the fast Fourier transform (FFT) algorithm is reduced by a factor of at least $\sim N_f / \log_2(N_f) \approx 750$ compared to a non-fast discrete Fourier transform. In view of the large data volumes, interpolation onto a linearly-spaced vector of k values followed by a FFT is a better option.

The re-sampling of the signal is performed by first sorting the measured (k-k_c) vector into monotonically increasing order, and then using the re-ordering vector J described earlier to sort in the same way the corresponding intensity values $I_t(x_j,y_j,t)$ as was shown earlier in figure-6.11. A linear interpolation of the intensity values to a uniformly-spaced k vector is then achieved using the MATLAB `interp1` function. Figure-6.14(b) shows the pixel intensity data $I(x_j,y_j,k\text{-}k_c)$ following interpolation of the $I_t(x_j,y_j,t)$ data from figure-6.14(a). The four wavenumber jumps displace the

interference signal to the correct positions in k space, ensuring phase continuity between signals on either side of the mode hops.

6.3.3 Effect of *k*-scan gaps

In the example shown in figure-6.13(b) four mode hops that result in an upwards jump in wavenumber are clearly visible. From figure-6.14(a) and figure-6.14(b), it is evident that the interpolation procedure described in the previous section is unable to provide valid data in the regions where the aforementioned mode hops occur. This is in fact one of the main disadvantages of any interpolation procedure for regions where the data density is poor and has, thus, formed the basis of research in treating non-uniformly sampled data as mentioned earlier.

One way of handling the random, laser-induced gaps in the k range would be to interpolate the vector of frame indices (t) using the vector of linearly spaced k values on which the experimental (k-k_c) values were interpolated as described above. This allows the gradient, dk/dt, to be estimated on the interpolating k vector such that:

$$W_1 = \begin{cases} 1, \forall k: dk/dt \leq c_2 \\ 0, \forall k: dk/dt > c_2 \end{cases}, \qquad 6.14$$

where c_2 is a threshold value for the wave number gradient which in this case was chosen to be 2.9× the mean value, i.e. $2.9\times\Delta k/\Delta t$. Δk and Δt refer to the total changes in k and t respectively, over a full scan duration. This is equivalent to multiplying the interpolated data by a window function, $W_1(k\text{-}k_c)$, that takes the value 1 for all k values for which dk/dt lies below the specified threshold, but zero elsewhere. Figure-6.15(a) shows the experimental window function, $W_1(k\text{-}k_c)$, for the example shown in figure-6.14 (b), with the windowed interpolated intensity data $W_1(k\text{-}k_c)\ I(x_j,y_j,k\text{-}k_c)$ over the same range shown in figure-6.15.

Given that the point spread function (PSF) of the WSI system in the axial direction is equivalent to the Fourier transform of the window function, $|\widetilde{W_1}(\Lambda)|$, the representation of the missing data in terms of the window function allows one to examine the effect of such gaps on the depth resolution of the system. Figure-6.16 illustrates this issue for a mid-scan range, showing (**a**) the isolated window function and (**b**) the windowed sample intensity data after interpolation. The normalised Fourier transform of the window function, $|\widetilde{W_1}(\Lambda)|$, is shown in figure-6.17(a),

compared to the Fourier transform of '*k*-gap free' top hat window function of equal length. The interesting observation is that the axial resolution (i.e. depth resolution of the system) is almost completely unaffected by the presence of the multiple zeros in the window function representing the laser-induced gaps in *k*-space. The price to be paid is, however, more apparent when a wider range of $\left|\widetilde{W_1}(\Lambda)\right|$ is considered. The long range side lobes become more significant whilst at the same time they are seen to decay at a slower rate than those for a top-hat window function of equal width as shown in figure-6.17 (b). One possible reason for the long range artefacts could be that they are caused by the sharp edges within the window function; convolution of the window with a smoothing function could potentially reduce the effect, but was not attempted here.

In order to further investigate the effect of *k*-gaps, a comparison between the experimental and theoretically predicted depth resolutions for different sections of the signal is provided. Figure-6.18 (a), shows an example of a small portion of the full scan, that is sufficiently short ($\Delta k = 4.6 \times 10^3$ m^{-1}) for it to lie between etalon mode hops, with its corresponding spectrum shown in figure-6.18 (b). The theoretical depth resolution in the glass, obtained from equation-7 in [21], is 946.4 μm between the first minima on either side of the central lobe and is shown by the distance between the vertical dashed lines in red. These almost coincide with the first minima of the experimental transform. The corresponding signal for a mid-range scan, which now encompasses multiple mode hops, is shown in figure-6.18 (c). As anticipated by the results in figure-6.17, the depth resolution (55 μm) in figure-6.18 (d) is practically unaffected by the presence of the mode hops and is still close to the theoretical value (47.5 μm), which is again indicated by the distance between the vertical dashed lines. Finally, figure-6.18 (e) and figure-6.18 (f), show the signal and its transform respectively, for a full scan range, ($\Delta k = 1.00784 \times 10^6$ m^{-1}, $\Delta\lambda = 80.1$ nm). Once again the experimental depth resolution (10.8 μm) is close to the theoretical value (4.3 μm), although the deviation of the zero crossing points from their corresponding theoretical ones is now somewhat more significant. The results for the three scan ranges illustrated in figure-6.18 are grouped in tabular form in table-6.5 below.

Table-6.5: Tabular form of the results illustrated in figure-6.18 showing a comparison between the theroretical and experimentally measured depth resolutions for the three scan ranges and the corresponding zero-crossing point drifts (i.e., deviations from the theoretical value) for each case.

Scan-range			**Depth resolution (δz)**		**Zero crossing point drift**	
Δk (m^{-1})	*Δλ (nm)*	*Scan %*	*Experimental*	*Theoretical*	*Left*	*right*
4.568×10^{-3}	0.4085	0.45	976.0 μm	946.4 μm	14.8 μm	14.8 μm
9.096×10^{4}	8.0521	9.00	55.0 μm	47.5 μm	4.5 μm	3.0 μm
1.00784×10^{6}	80.5031	100	10.8 μm	4.3 μm	4.5 μm	2.0 μm

It is clear from this table that, as one might expect, the short-scan-range Fourier transform has a peak width closest to the theoretical value (in fractional terms) and that as more gaps are introduced for the medium and full-range scans, the width of the Fourier peak (as a fraction of the theoretical value) is somewhat increased.

6.4 Independent wedge measurements

One of the main research aims in this chapter has been the development of signal processing procedures that allow the successful and unambiguous decoupling of the Δ*k*-axis from the intensity signal. For this reason, the procedure described above involving the resampling and re-registration of the raw intensity data onto a regularly spaced wavenumber change was implemented. The results of the aforementioned procedure seems to be quite promising in that, now, unlike in previous work (see reference [21]) where the useful scan range was limited to 37 nm out of the approximately 100 nm available, the full scan range can be used. Moreover, the experimental depth resolution of the system acquired by evaluating the point spread function in the axial direction is quite close to its theoretical counterpart for the same wavenumber change.

One issue with the analysis presented so far is that the spectral analysis has been applied to the data from the highest sensitivity wedge, which was also the wedge that provided the unwrapped signal to estimate wavenumber change. It makes sense to perform the same spectral analysis on the other three wedges, which were only indirectly involved in the calculation of wavenumber change, to ensure that the

results from the thickest wedge were not influenced by a correlation between the two. Figures 6.19(b), 6.20(b), 6.21(b), 6.22(b) show the spectrum of wedge intensity in OPD-descending order, starting from the highest sensitivity (thickest) wedge. The width of the experimental peak is close to that of the theoretical peak for each wedge. This clearly demonstrates that the results from the thickest wedge described earlier were not appreciably influenced by the fact that the wavenumber values are derived directly from the same wedge. For the case of the thinnest wedge, however, some significant side lobe structure is seen as shown in figure-6.22 (b), a fact that is discussed in the next sub-section.

6.4.1 Effect of phase unwrapping errors

One interesting observation that emerged during the calculations in the previous paragraph is that related to the build-up of artefacts around the main spectral lobe as the optical path difference starts to deviate from that used for the total Δk computation (see figure-6.21 (b) and figure-6.22 (b) for example). To investigate the cause of such discrepancies it would be interesting to compare the results of the data processing described in section-6.3 using the two different phase extraction algorithms discussed in section-6.2 earlier.

Figures 6.19-6.22 provide a visual comparison between the two phase extraction approaches using a) the integer-based method and b) the improved algorithm involving the removal of the diffraction halo and the use of the more accurate and precise phase extraction algorithm based on a sub-pixel (non-integer) peak detection technique. The benefits of using the proposed approach are not so evident with the thickest wedge, with the integer based phase calculation based method resulting in a clear, free from side lobes spectrum as shown in figure-6.19 (a). As the OPD differs from that for the thickest wedge, the side lobe structures around the main frequency peak become more significant as shown in figure-6.21(a) and figure-6.22(a). Although these artefacts are present in both cases, it is clear that the improved algorithm suppresses these quite significantly (refer to the comparison between figure-6.21 (a) with figure-6.21 (b) and figure-6.22 (a) with figure-6.22 (b)).

A second, quite important observation is that the location of the spectral peak corresponding to the wedge central thickness is shifted for all four cases examined here. It is, therefore, interesting to compare the measured wedge thicknesses using

the three different methods, amongst each other and finally to the manufacturer's data. Note that *Method-A* is used here to denote the integer-based phase extraction algorithm described in section-6.2.1. *Method-B* refers to the subpixel phase accuracy approach in section-6.2.2 after the diffraction halo removal. *Method-C* on the other hand refers to the independent thickness measurements using a conventional micrometre. These were taken by measuring the thickness of each wedge at the edges and then using linear interpolation to extract the central thickness to avoid damaging the sensitive equipment.

Table-6.6: Tabular form of the resulting central wedge thickness using the three different methods in comparison to the manufacturer's data. *Method-A* and *Method-B* denote the two algorithms described in section-6.2 while *Method-C* refers to the independent measurements using a conventional micrometer. For the manufacturer's data the three digit figures denote the target value while the superscript entries set the minimum and maximum values as given by the allowed tolerance.

	Central wedge thickness $d_c^{W_n}$ mm			
W_n	*Method-A*	*Method-B*	*Method-C*	*Manuf. Data*
1	12.7471	12.7516	12.7550	$12.8^{12.8500}_{12.7500}$
2	12.6740	12.6780	12.6600	$12.6^{12.6500}_{12.5500}$
3	11.9216	11.9265	**12.4350**	$12.0^{12.0500}_{11.9500}$
4	9.5747	9.5813	9.5900	$9.6^{9.6500}_{9.5500}$

Table-6.6 above provides a summary of these measurements. It is evident that the results obtained using *Method-B*, are in general close to the micrometre measurements, the manufacturer's data and in most cases fall well within the claimed tolerance limits (±0.05 mm). The major disagreement between *Method-C* and the rest, highlighted in red, for wedge-3 is most likely due to human error while reading the micrometer. Note that the sub-pixel peak detection algorithm modified to process 1-D-signals was used to extract the optimised spectral peak location which was then converted to length units for both *Method-A* and *Method-B*.

In view of these results and recalling that the main advantage of *Method-B* over its predecessor, *Method-A*, was that a significant number of the phase unwrapping errors in the final phase signal (recall figure-6.9) was removed, it is suggested that the effect of phase unwrapping errors is of high importance. The unwrapping errors on

the final wedge data simply result in a shift along the wavenumber axis by a whole number of intensity cycles which is impossible to detect when the intensity data from the same wedge were used to evaluate the depth resolution of the system at first and later to extract the central wedge thickness. However, by using intensity data from the other three wedges the true impact of the unwrapping errors is revealed and twofold: a) taking the form of secondary lobes around the main spectral peak and b) distorting the Δk-axis and in turn causing errors in measuring the true thickness of the wedges. It is, therefore, worth investigating how to remove as far as possible these errors. This will be the subject of research in the following chapter.

6.5 Discussion

Various phase related errors have been reported in the literature on several occasions termed as phase instabilities in [215], multiple interference in [216, 217] and phase jitter in [198], which are known to contribute towards signal degradation. Scanning and other non linearities have also been reported in the literature [66, 77, 153, 218]. Hibino *et al.* used a 19-sample algorithm to suppress the effects of multiple interference, which was in turn used to measure a 20 mm thick BK7-glass plate. In this chapter, some errors of this type that limit successful depth reconstructions in a PC-WSI scheme were identified and appropriate methods to overcome them were devised.

At first, a simple yet effective way to shift the location of the extracted phase of the recorded fringe patterns from the image origin to the centre of the image by swapping the image quadrants prior to Fourier transformation. Initially, numerical simulations were used to demonstrate the validity of the method. At a later stage, however, the method was further validated using real data by successfully measuring to an acceptable degree of accuracy the individual wedge thicknesses.

A summary of the main observations made in this chapter is as follows:

1. Swapping of the image quadrants prior to Fourier transformation can be used to extract the phase at the image centre. This was proven using numerical simulations and later by successfully measuring the central thickness of the wedges.

2. The geometry and size of the region of interest plays an important role in the accuracy and precision of the extracted phase.
3. By implementing the sub-pixel peak detection algorithm developed by J.M.Huntley in [2], the phase is extracted from the point in the frequency domain with maximum signal to noise ratio and therefore results in a more accurate phase estimation procedure than that previously used.
4. A brief analysis of the different factors contributing to the generic term "*background intensity"* has been given, together with a simple way to estimate and remove it from the overall signal. Its overall effect on phase errors is assessed and its link to fringe contrast is demonstrated.
5. It was shown that laser mode hops and other nonlinearities in the scans prevent successful depth reconstructions using the standard 1-D-Fourier transform approach. A method involving the re-sampling and re-registration of raw intensity data onto a regularly spaced wavenumber change vector was proposed. The reconstructed Δk axis resulted from the highly sensitive optical sensor developed earlier. As a result, full access to the entire scan duration which was previously limited down to approximately 40 nm out of the total 100 nm available, was achieved [21].
6. Missing gaps in the data due to upward etalon mode hops have negligible effect on the experimentally measured depth resolution, which is close to its corresponding theoretical one.
7. Significant side lobe structure appears on either side of the main spectral peak, and is worse for the shorter OPD wedges than for the longest OPD wedge. The missing gaps in the data result in identical time-domain window functions for all four wedges, and thus identical side lobe structure in the frequency domain, and therefore cannot be the main cause of such artefacts. Phase unwrapping errors are a more likely cause since they result in a distortion of the Δk axis which affects the different wedges to different extents.
8. It was demonstrated that by supressing some of the unwrapping errors in the signal the measured thickness gets closer to the specified value and to the independent micrometre measurements. Residual phase unwrapping errors

are thus classified as a very significant source of errors in the overall measurement process.

6.6 Conclusions

A tuneable CW *Ti:Sa* laser with large scanning ranges (>100 nm) and wavelength steps down to a few pico-meters has been developed for wavelength scanning interferometry applications. Modifications to the embedded DSP algorithms controlling the mode selection devices in the laser have allowed high speed linear scans of several tens of thousands of frames at rates of up to 30 frames s^{-1}, with variable exposure time to compensate for wavelength variation of laser power output and camera sensitivity. However, mode hops and other nonlinearities in the scans prevent successful depth reconstructions by the standard approach of 1-D Fourier transformation of the image sequences on a pixel wise basis. A solution to this problem has been developed, which involves measuring wavenumber changes from the phase changes in the interferograms from four wedges. The measured wavenumber changes are then used to resample the intensity signals on a regularly spaced wavenumber vector. With these improvements, depth-resolutions approaching the theoretical values are achievable for the full scan. Missing gaps in the data due to upward etalon mode hops have negligible effect on the depth resolution, but result in some long range signal leakage. Although the missing data gaps are a contributory source of the side lobe structure, the main cause is believed to be residual phase unwrapping errors. These will cause highly undesirable reconstruction artefacts in the eventual application of the system, and additional approaches to reducing unwrapping errors further are therefore considered in the next chapter.

6.7 Figures

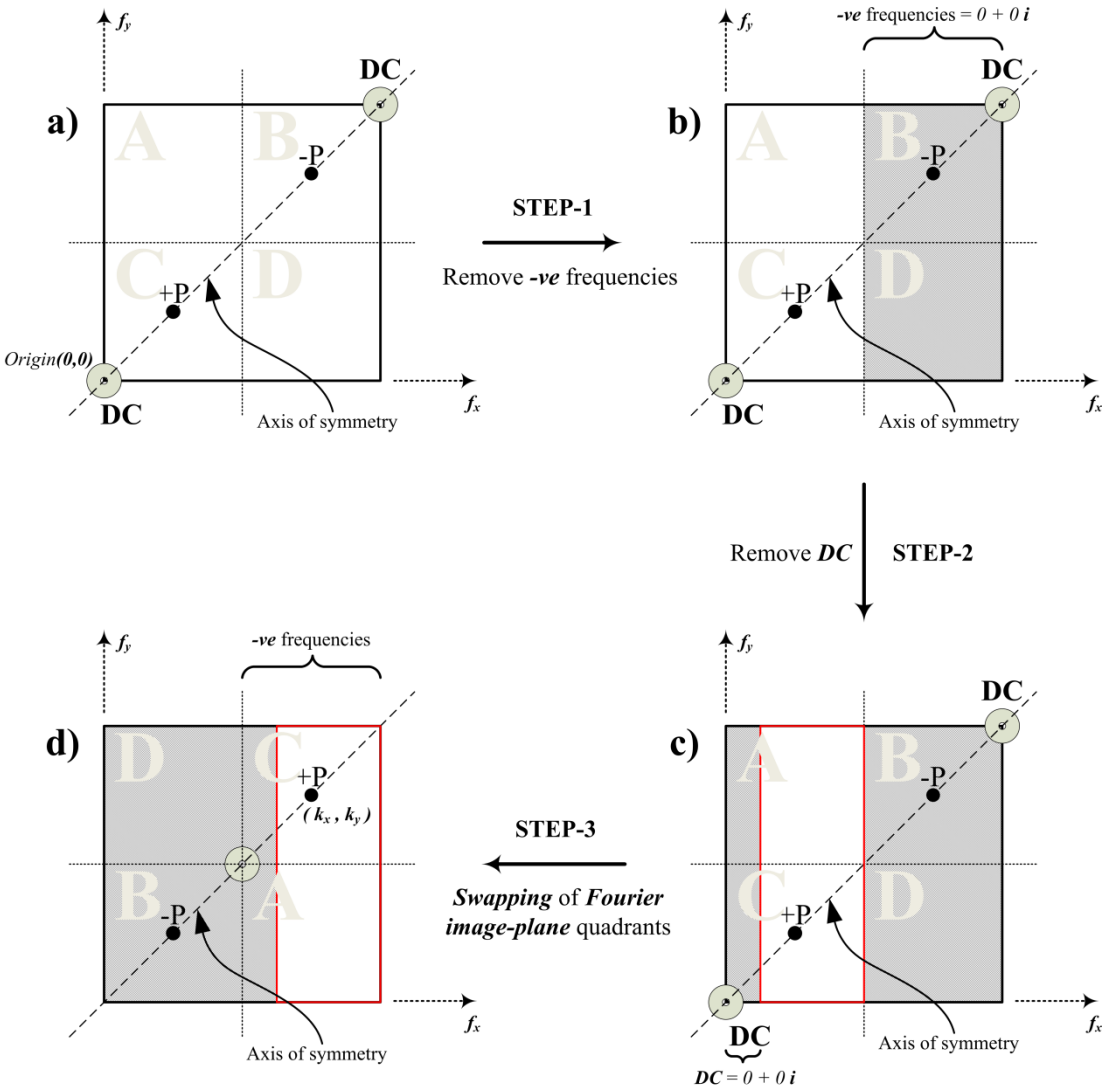

Figure-6.1: Diagram showing the three steps involved in the integer-based Fourier transform phase extraction process for an image $\mathcal{M}_{m\times n}$ with $m = n$ and $m, n \in 2\mathbb{Z}$, where a) shows the three peaks (d.c and ±P), b) shows the first step where the negative frequencies are set to zero, c) shows the second step where the d.c offset is removed by setting its neighbouring region also to zero and d) shows the final step where the positive peak is shifted in the negative frequency region and its spatial coordinates are extracted.

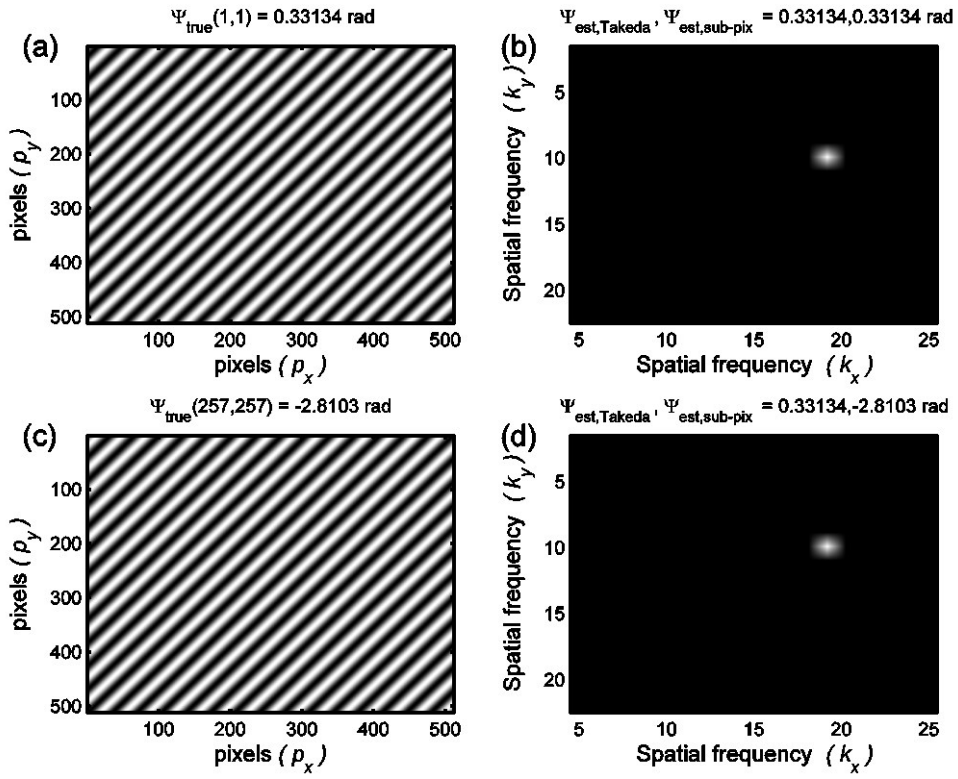

Figure-6.2: Simulated fringe pattern using equation-6.1 to demonstrate the effect of swapping the image quadrants prior to 2-D-Fourier transformation on the location of the phase computed using the 'Fourier transform method'. a) Simulated fringe pattern with k_x =15, k_y = 12, N_x = N_y = 512, d.c = 0 and the corresponding phase value at the image origin Ψ(1,1) in radians using equation-6.1.b) Plan view of the 2-D-Fourier transform of the fringe pattern in a), showing the location of the 2-D-Fourier peak in the spatial frequency domain and the phase computed using equation-6.3. c) Fringe pattern in a) after swapping the image quadrants and the phase at the image centre Ψ(257,257) using equation-6.1. d) Same as b) but for the fringe pattern in c).

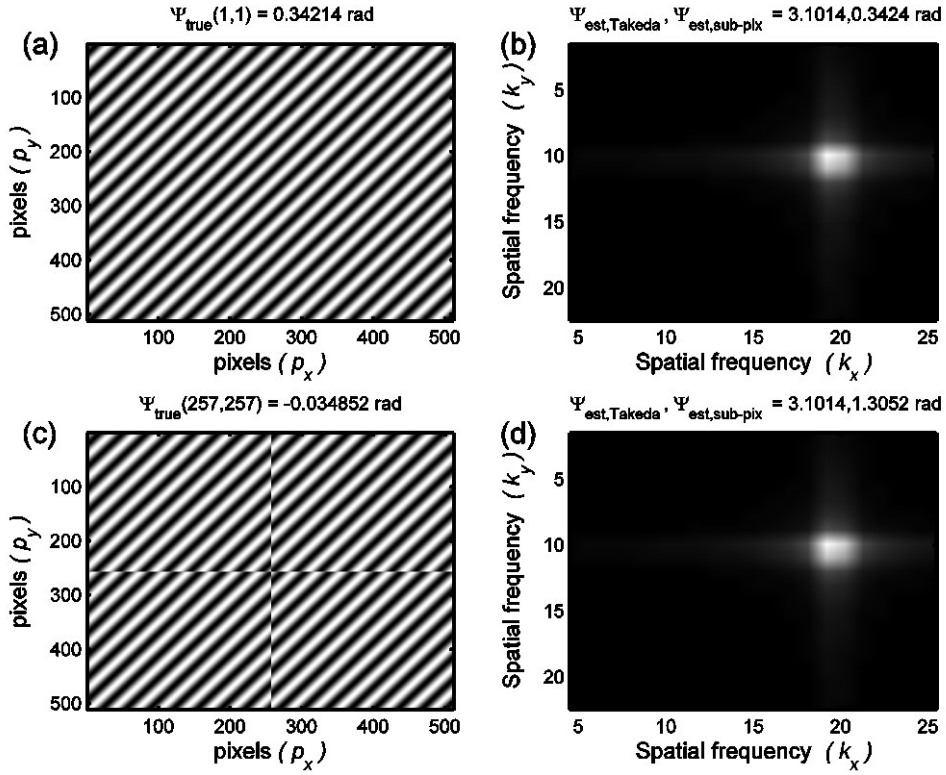

Figure-6.3: Demonstration of the effect of non-integer k_x, k_y values by means of numerical simulation. Same as figure-6.1 but with $k_x = 14.45$ and $k_y = 12.43$.

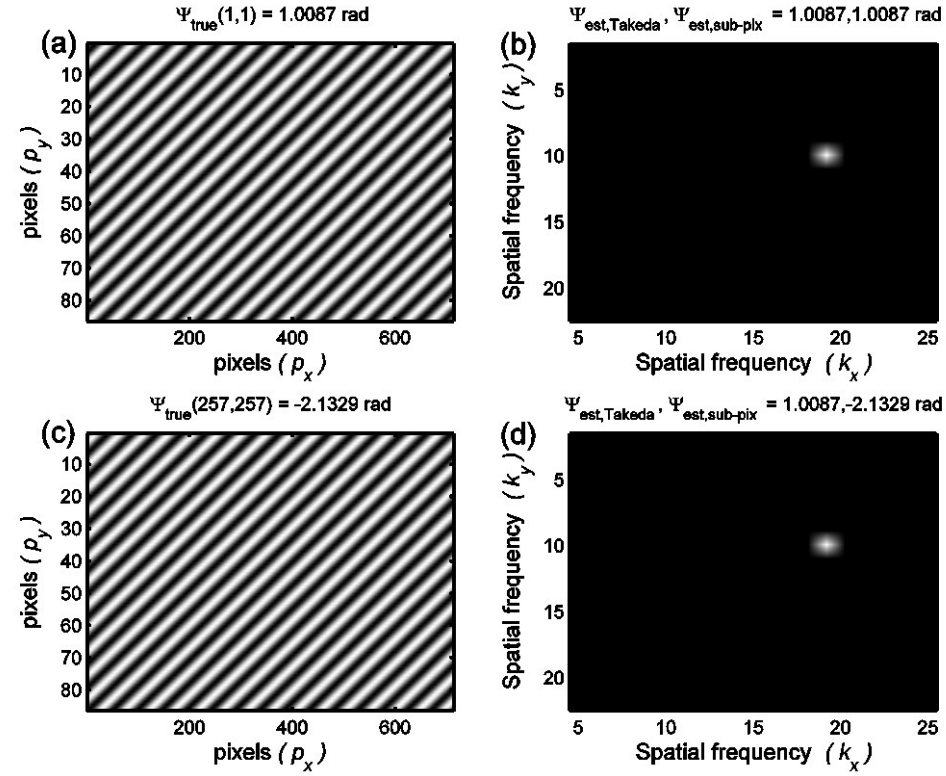

Figure-6.4: Demonstration of the effect of non-integer k_x, k_y values by means of numerical simulation. Same as figure-6.1 but with $N_x = 714$, $N_y = 86$.

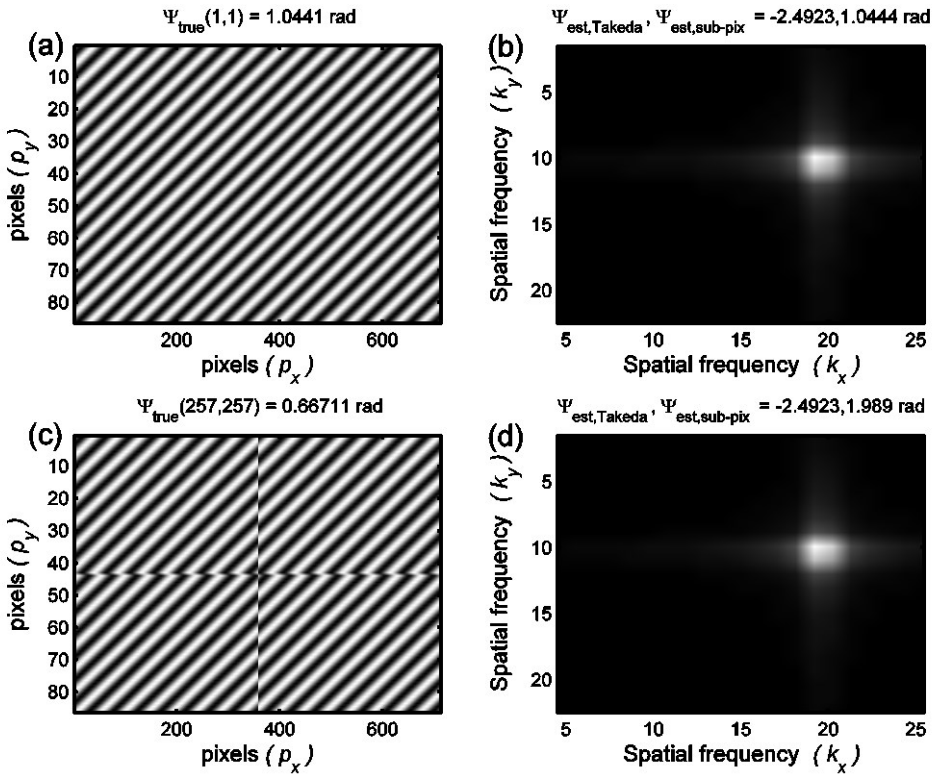

Figure-6.5: Demonstration of the effect of non-integer k_x, k_y values by means of numerical simulation. Same as figure-6.4 but with k_x = 14.45 and k_y = 12.25.

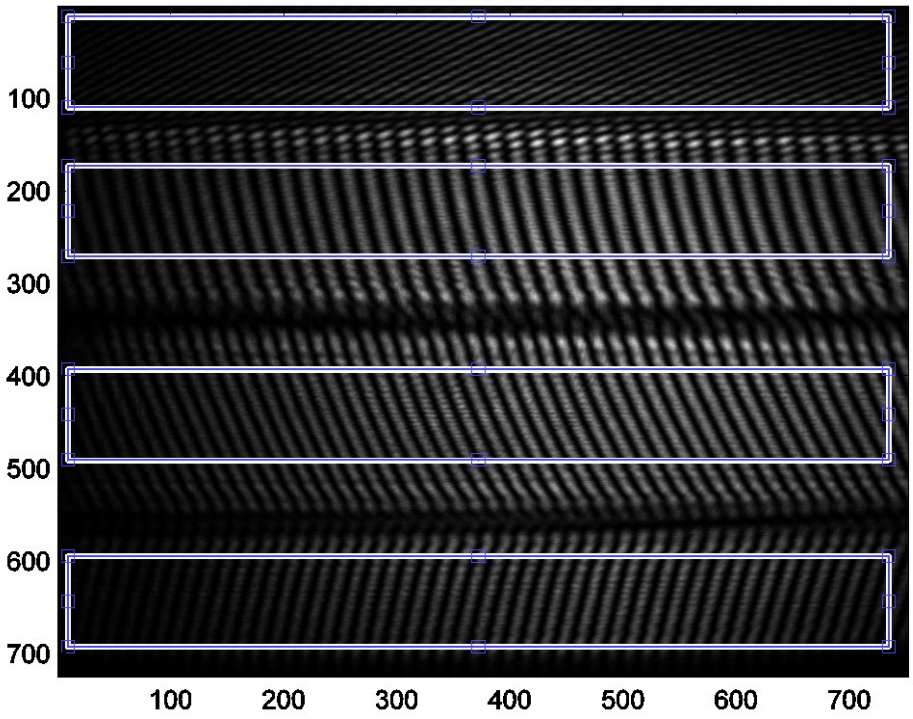

Figure-6.6: First image of the recorded 48,971 image sequence for a full 100 nm scan, showing the identical regions of interest (ROI) for each wedge - ROI size of 714 × 86 pixels.

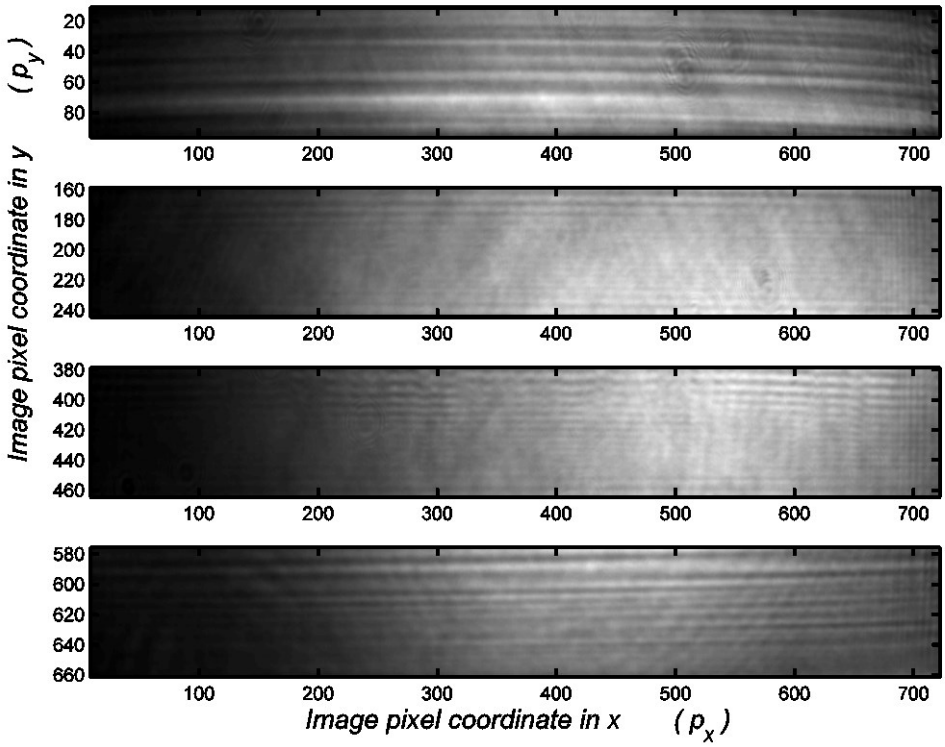

Figure-6.7: Visual representation of the estimated 'halo' for each of the four wedges as described in section-6.2.3, with the thickest wedge at the top.

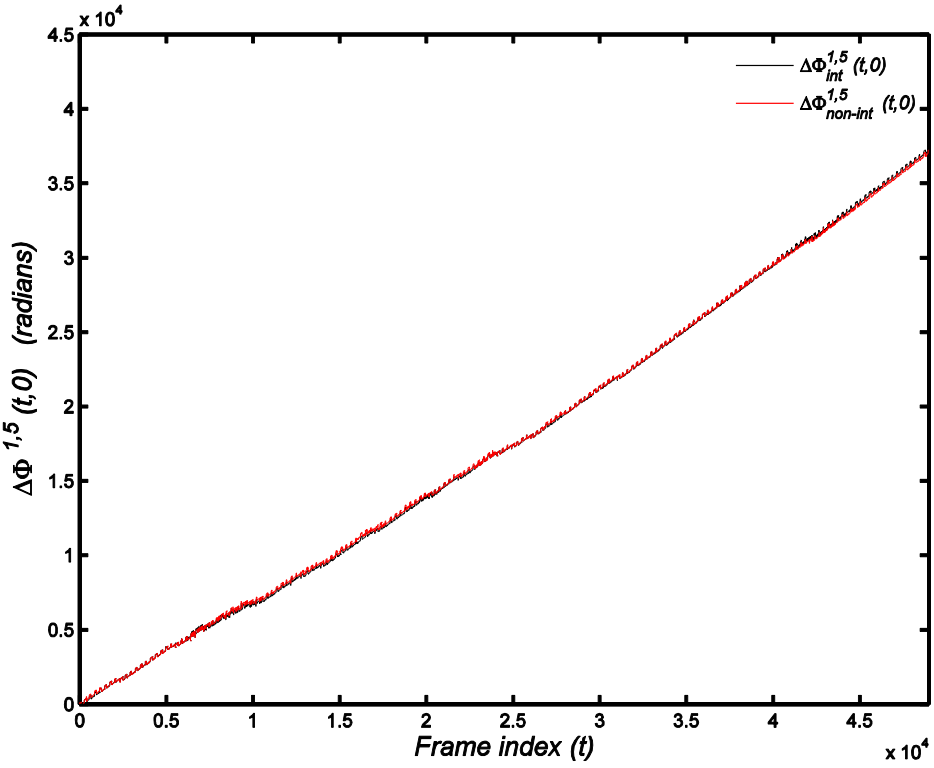

Figure-6.8: Comparison between the phases extracted from the thickest wedge using the integer based phase calculation method and the non-integer based phase calculation method with the diffraction halo removed.

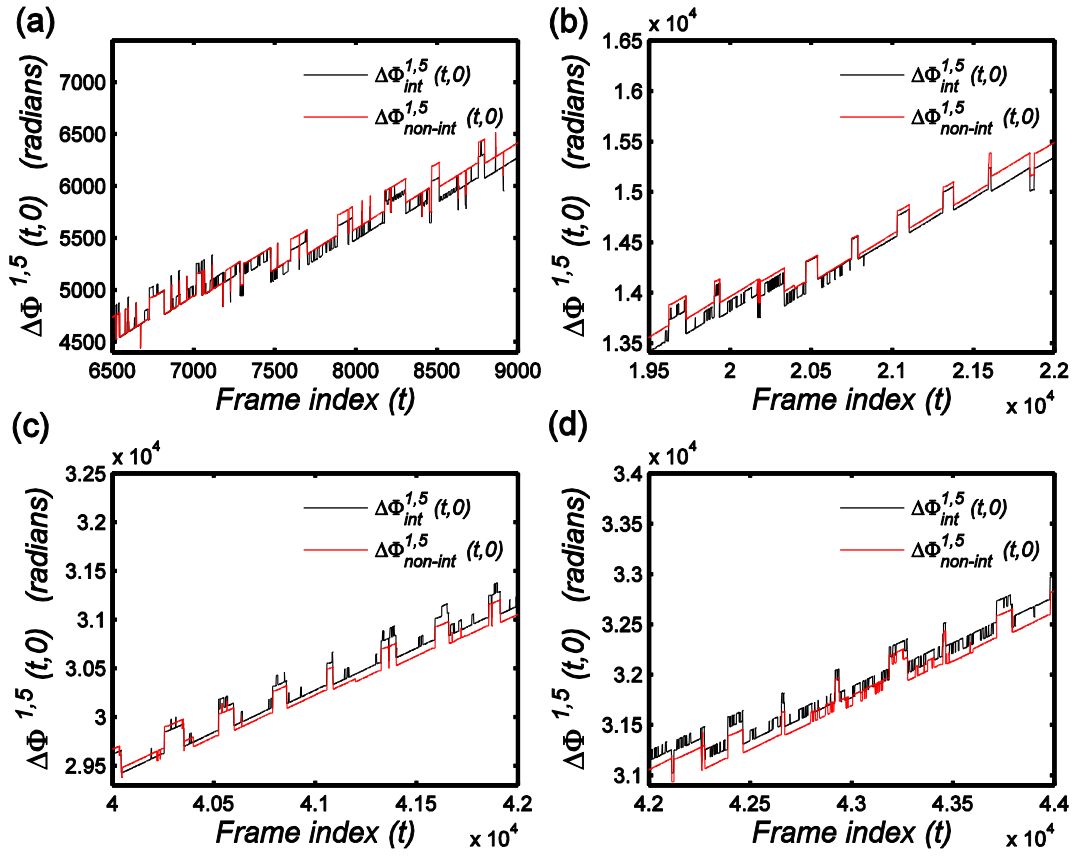

Figure-6.9: Comparison of the extracted phase using the two algorithms described in sections 6.2.1-6.2.3. (a) - (d): sections of the full sequence with the highest density of phase unwrapping errors (black line) and the evident improvement (red line).

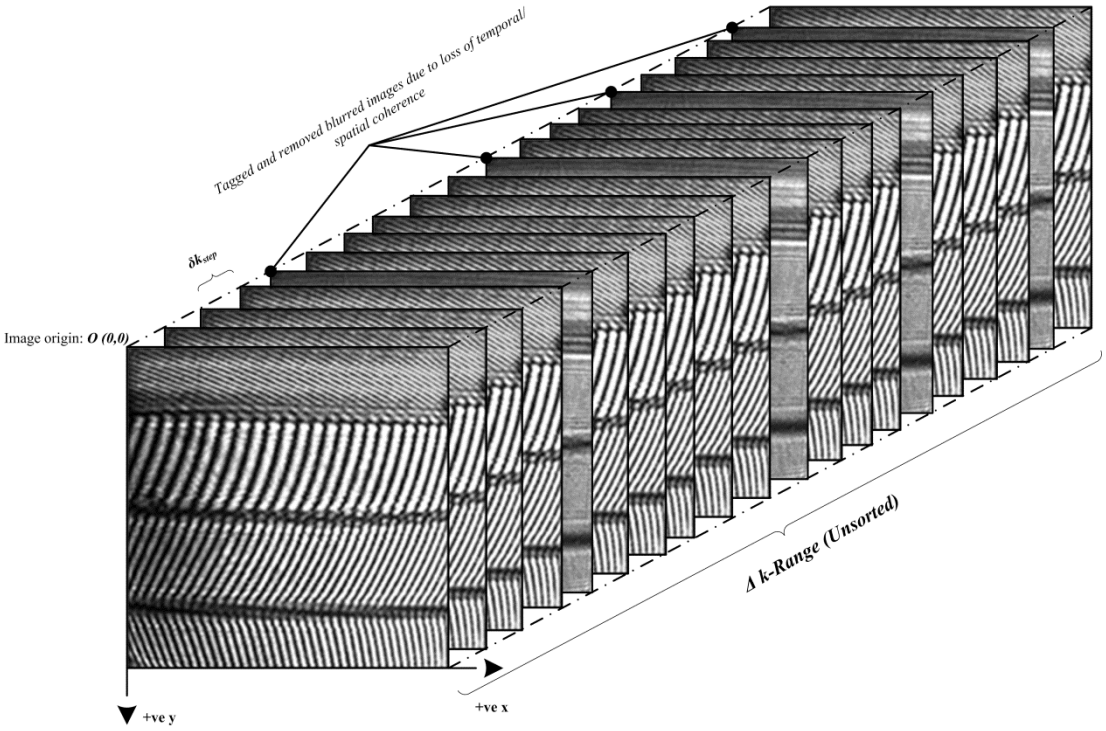

Figure-6.10: Initial data sequence prior to sorting. Reproduction of figure-5.6

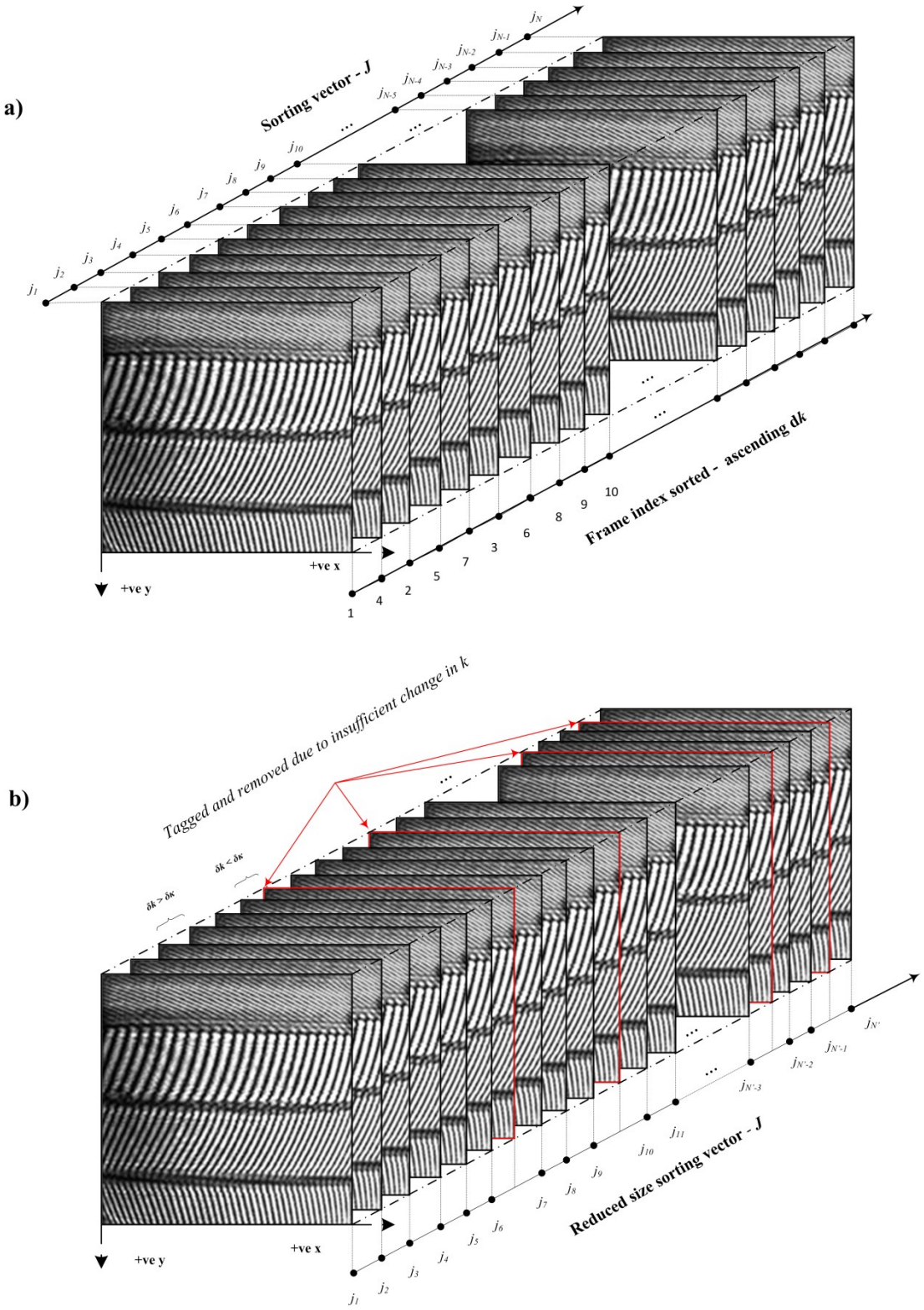

Figure-6.11: (a) sorted 2-D image sequence in ascending δk where the index of each frame is stored in the sorting vector *J*. (b) Reduced size vector J after removing duplicate frame entries according to equation-6.12

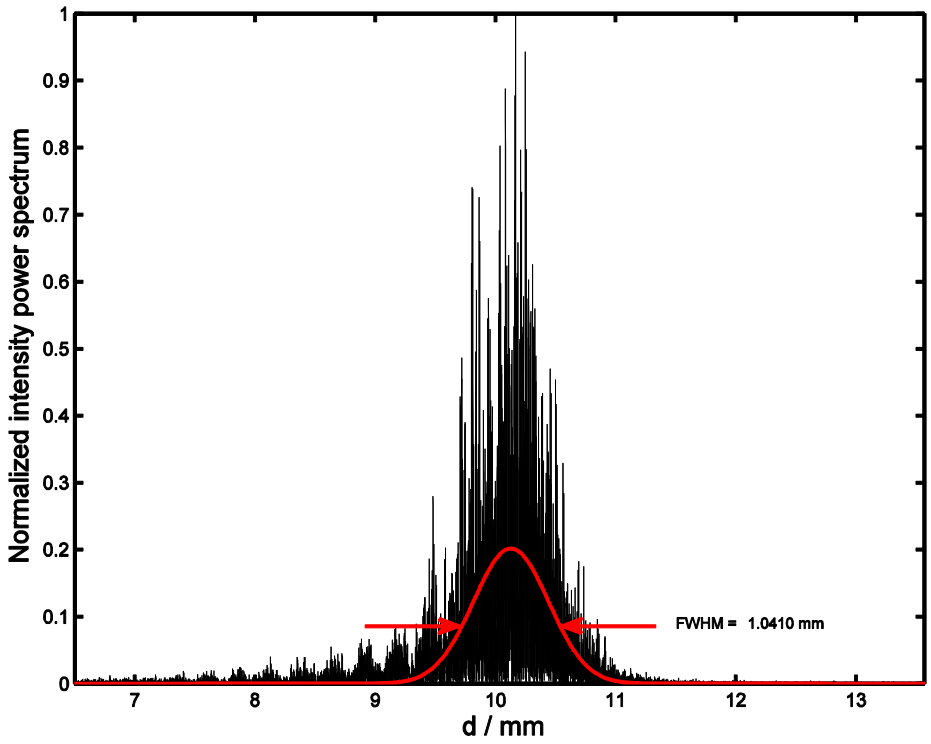

Figure-6.12: Power spectrum $\left|\tilde{I}_t(x_j, y_j, \Lambda)\right|^2$ for one pixel near the centre of the thickest wedge (black); best fit Gaussian distribution (red).

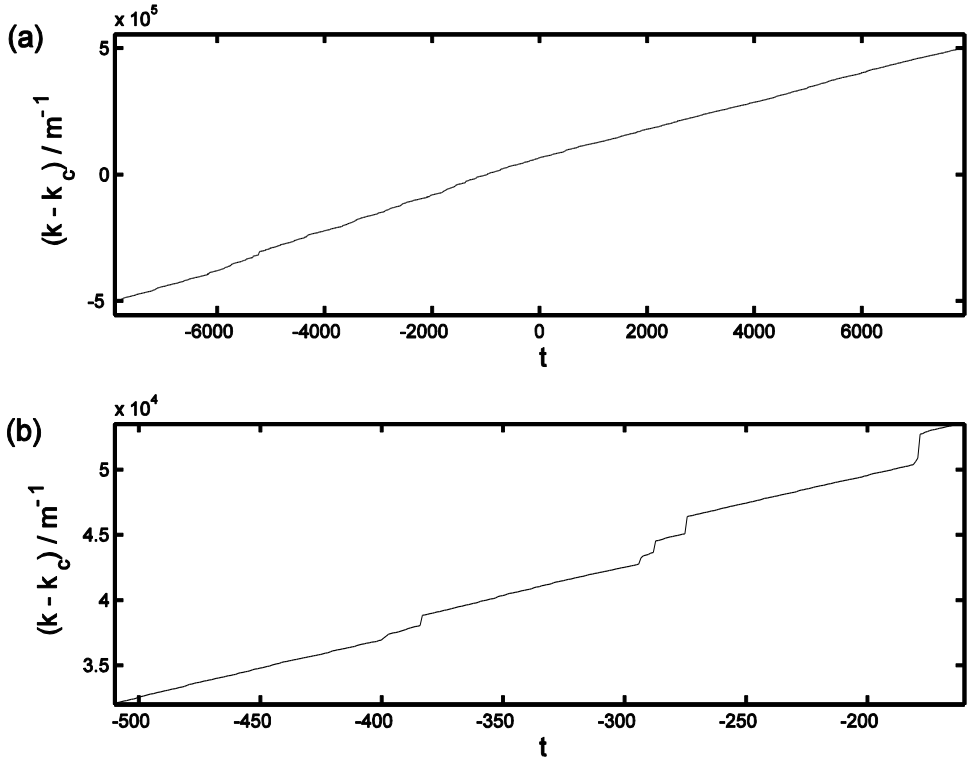

Figure-6.13: Wavenumber change (k-k_c) as a function of non-dimensional time, t. (a) Full range; (b) sub-range from (a) showing mode hops.

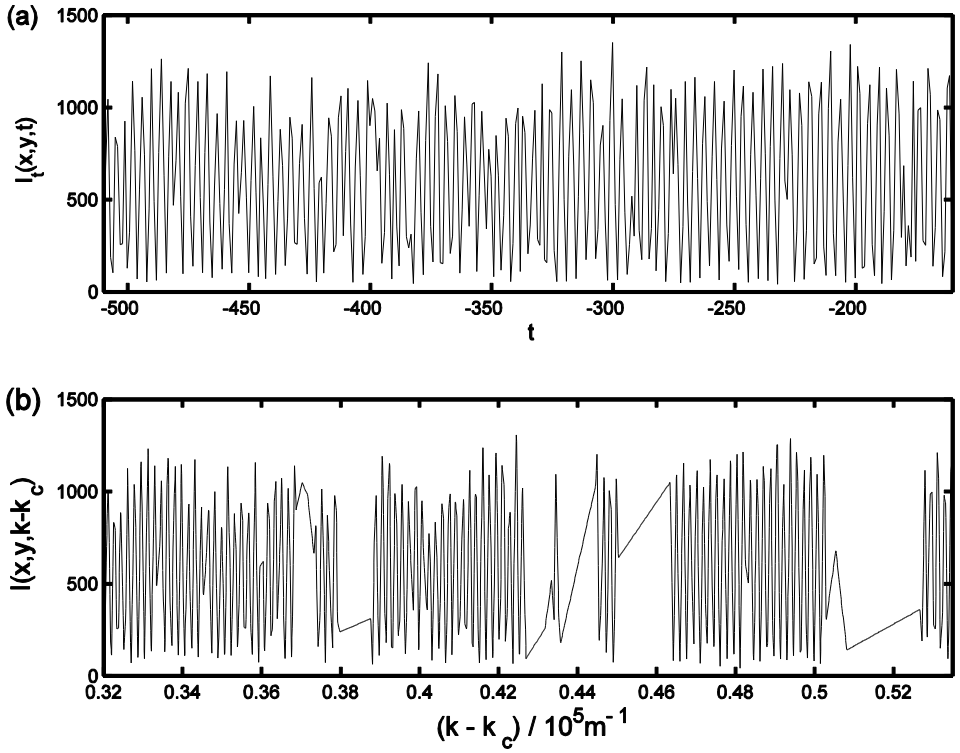

Figure-6.14: (a) Raw intensity signal, $I_t(x_j,y_j,t)$, prior to resampling, corresponding to the same t-range to that shown in figure-6.13(b); (b) Resampled and re-registered intensity signal, $I(x_j,y_j,k-k_c)$, onto the linearized wavenumber change axis, $k-k_c$, using linear interpolation for the same t-range as (a).

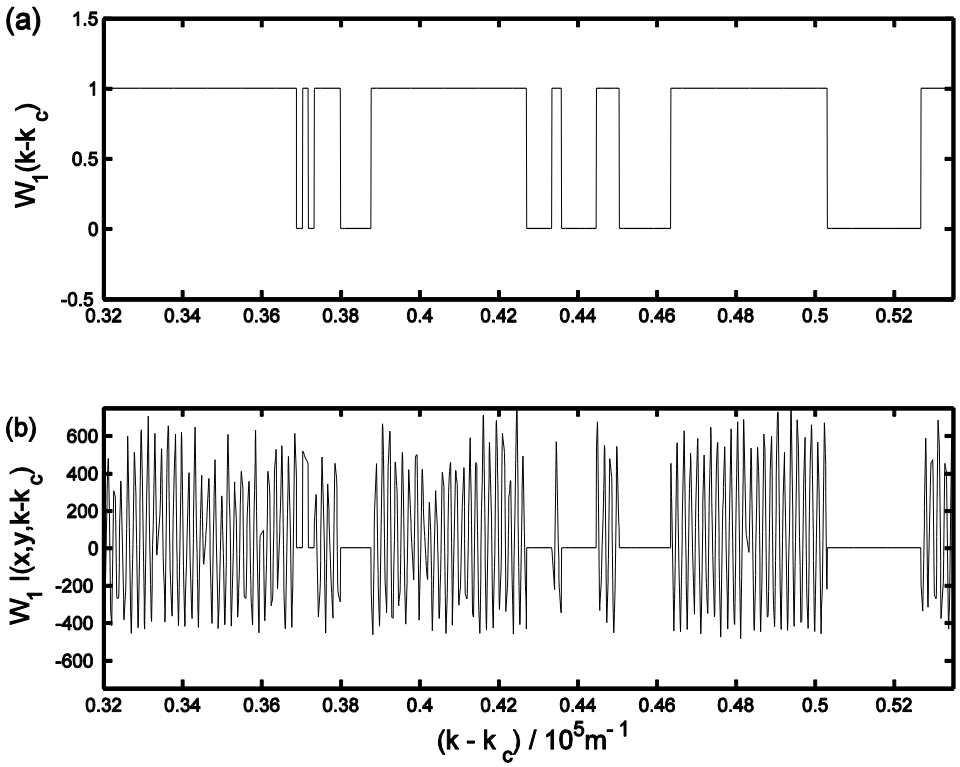

Figure-6.15: (a) Window function $W_1(k-k_c)$ over the same range as for figure-6.14; (b) Windowed interpolated intensity data, $W_1(k-k_c)\ I(x_j,y_j,k-k_c)$, over the same range.

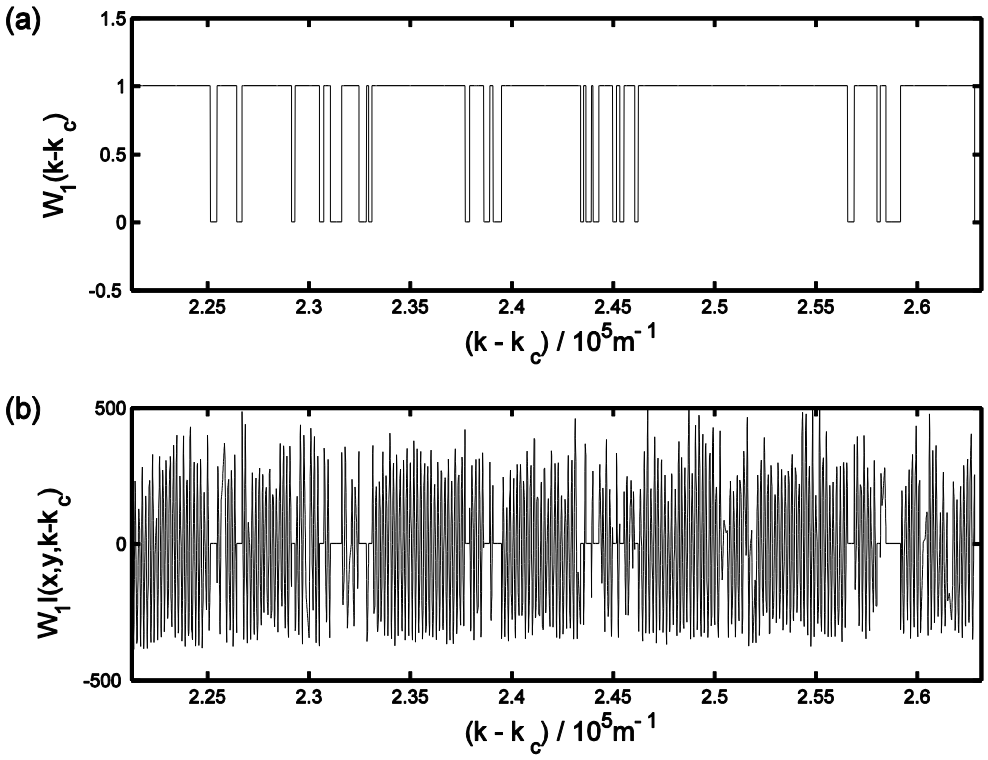

Figure-6.16: (a) $W_1(k\text{-}k_c)$ and (b) windowed Intensity data.

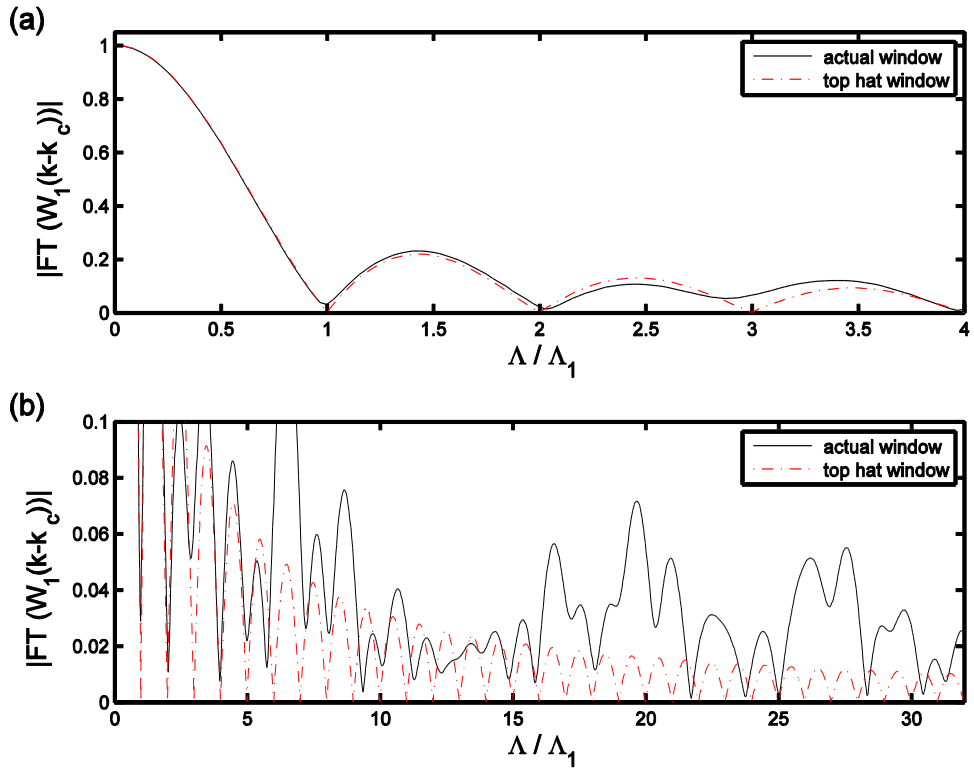

Figure-6.17: (a) $\left|\widetilde{W_1}(\Lambda)\right|$ for the window function in figure-6.16(a) compared to the Fourier transform of a 'gap-free' top-hat window function of equal width; (b) same as (a) but over a wider Λ range. Λ_1 is the position of the first zero in $\left|\widetilde{W_1}(\Lambda)\right|$ for the top-hat function.

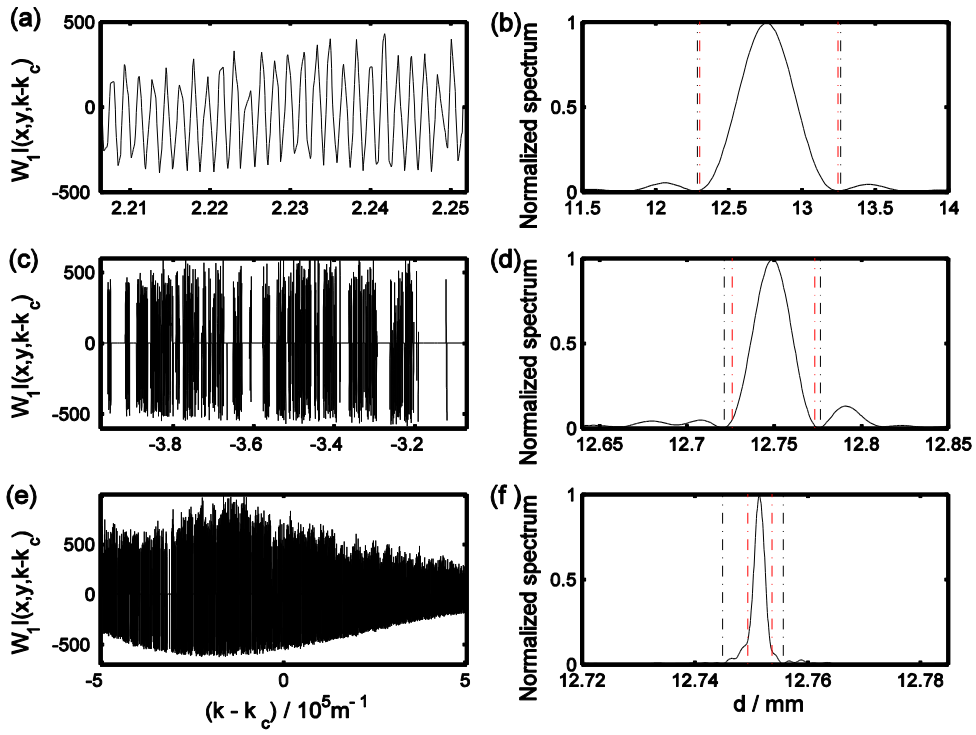

Figure-6.18: Signals for short (a), medium (c) and full-range (e) scans, and their corresponding Fourier transforms (b, d, and f). Theoretical and experimental depth resolutions (full width down to zero crossing points) are shown by the dashed lines in red and black respectively.

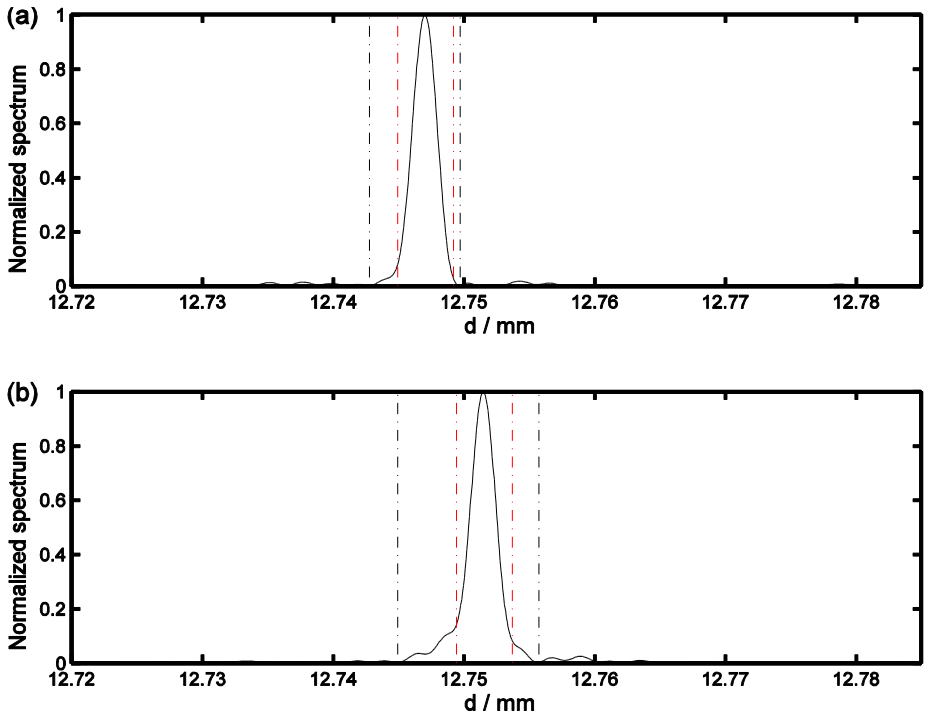

Figure-6.19: Decoupling of intensity data from the Δ*k*-axis for **wedge-1**: a) Using the integer-based method and b) using the improved method described in section-6.2. The red and black dashed lines show the theoretical and experimental depth resolutions respectively**.**

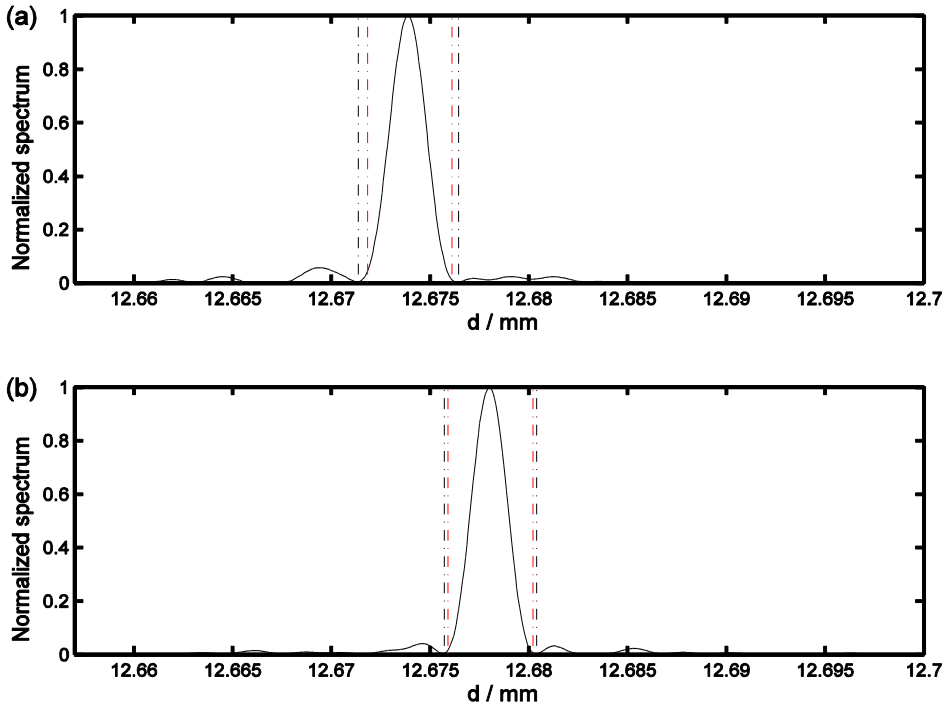

Figure-6.20: Decoupling of intensity data from the Δ*k*-axis for **wedge-2**: a) Using the integer based method and b) using the improved method described in section-6.2. The red and black dashed lines: theoretical and experimental depth resolutions

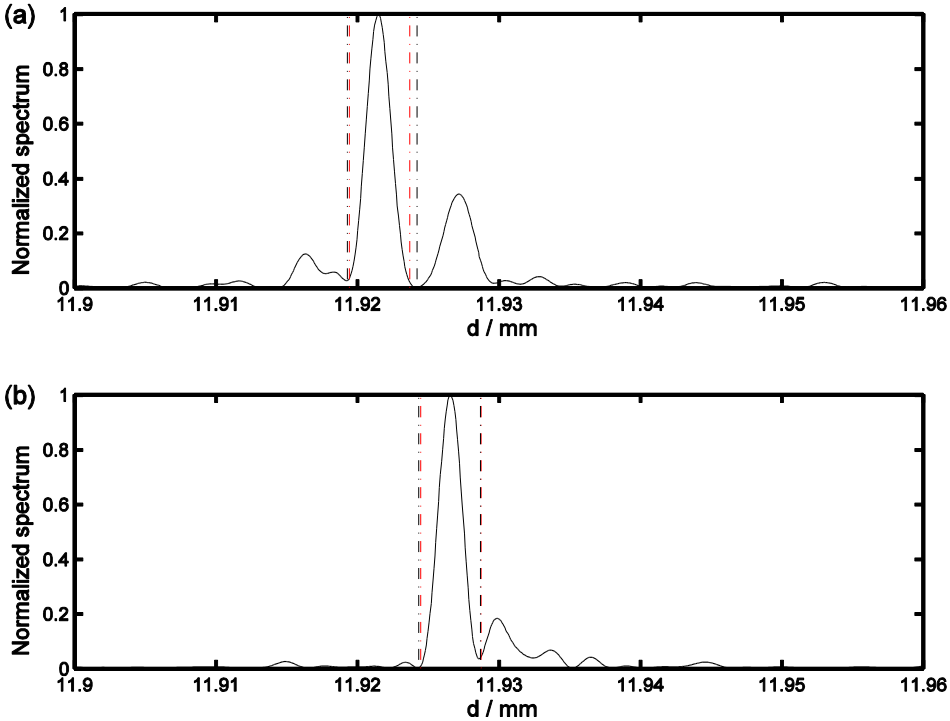

Figure-6.21: Decoupling of intensity data from the Δ*k*-axis for **wedge-3**: a) Using the integer based phase calculation method and b) using the improved method described in section-6.2. The red and black dashed lines show the theoretical and experimental depth resolutions respectively. Significant side lobe is starting to build up a) with some of it suppressed in b).

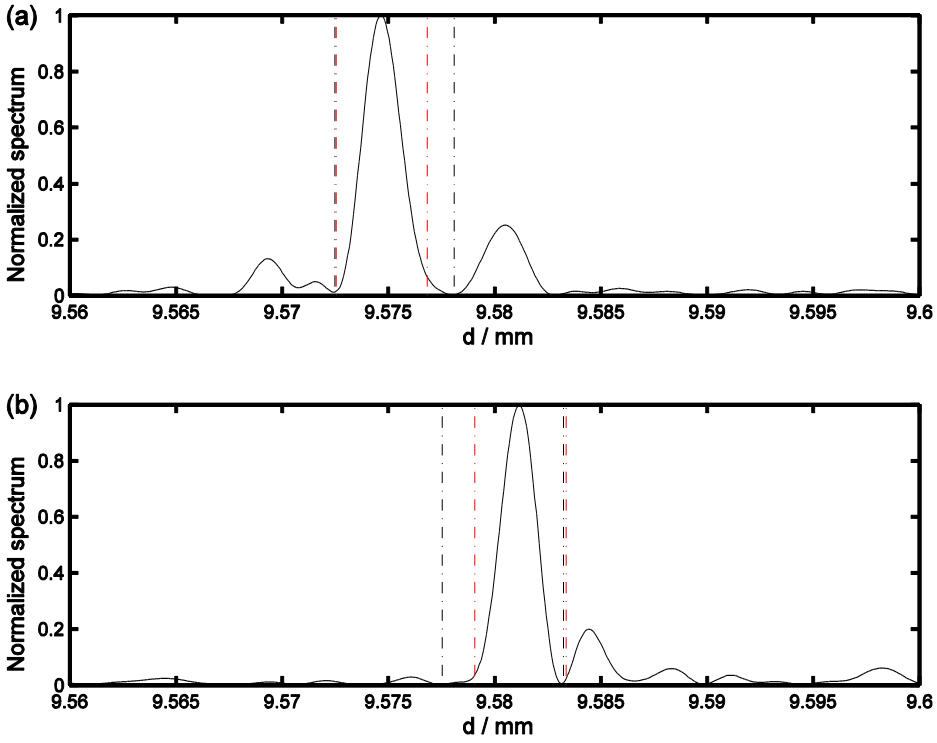

Figure-6.22: Decoupling of intensity data from the Δ*k*-axis for **wedge-4**: a) Using the integer based phase calculation method and b) using the improved method described in section-6.2. The red and black dashed lines show the theoretical and experimental depth resolutions respectively. Significant side lobe is starting to build up a) with some of it suppressed in b).

Chapter-7: Identification of error sources in wide tuning range WSI

7.1 Introduction

In Chapter-6, a significant improvement in data processing, owing to the removal of the diffraction halo (digitization of the intensity distribution along the wavenumber axis, k) and the improved phase extraction algorithm (phase-change $\Delta\phi_w$ calculation), allowed a full 100 nm scan too be analysed in contrast to the more limited 37 nm scan range previously reported in [21] with the same setup. The main reason for such a significant improvement was attributed to the reduction of the phase unwrapping errors in the phase signal used to extract the sought wavenumber axis, Δk. In spite of the aforementioned improvement, however, a curious phenomenon was observed, namely a build-up of side lobe structure around the main spectral peak that is worse for the shorter OPD wedges than for the longest OPD wedge.

The investigation of the root cause of such errors and the development of appropriate tools for their subsequent suppression will be the main focus of this chapter. More specifically, in section 7.2 of this chapter a method based on time-frequency analysis (TFA) to assess the performance of the algorithm developed so far is described. TFA methods date back to the mid 70's [219] and have found a wide variety of applications in power quality analysis [220-223], fault detection [224], biometric authentication [225] and interferometry [226-229].

One of the limiting factors to successful depth reconstruction in optical coherence tomography (OCT) is dispersion [230-232]. That is, the dependency of the refractive index n to the wavelength of light λ or the wavenumber k ($2\pi/\lambda$). The standard technique to avoid this problem has for a long time been to introduce a dispersive element in the sample arm of the interferometer that matches the dispersion in the object arm. The development of broadband sources with wide tuning ranges, such as the *Ti:Sa* laser used in this thesis, has significantly improved the depth resolution of OCT systems to the few μm level. However, as dispersion is in general a depth dependent phenomenon a corresponding depth dependent compensation is complex and cumbersome to achieve in this manner – see for example references [233, 234].

As a result, a large number of digital methods have been developed instead to provide automatic dispersion compensation – see references [235-238] for representative examples.

Apart from the obvious degradation in depth resolution, dispersion is also responsible for additional phase terms [230]. Considering that the accuracy and precision of the reconstructed wavenumber change axis relies on the measurement of the laser induced phase shifts an in-depth investigation of dispersion induced phase shifts is given in section-7.3 alongside other factors like laser beam induced errors and material induced errors. The chapter concludes by identifying the main error sources during a full 100 nm scan, thereby paving the way towards the development of appropriate methods for their subsequent suppression.

7.2 Temporal and spatial signal analysis

Over the last two decades, the Fourier-Transform (FT) representation of intensity data has been established as the most prominent approach in the field of interferometry [82-84]. In parallel with the FT representation, an alternative technique, often termed as wavelet analysis within the field of digital signal processing, was used to detect local variations in the signal frequency [54]. *Berger E, et al* used the wavelet transform (WT) to filter noisy speckled interferograms and to identify features of interest [226, 227]. *Kaufman G H* and *Galizzi E G* also used the wavelet method to reduce speckle noise and study transient phenomena in TV holography [239]. Recalling that the parameter of interest in interferometric signals is the evaluation of phase, *Cherbuliez M et al* proposed the wavelet transform as the method to extract the sought phase from a time-varying signal with a temporal carrier [228]. The method has predominantly been used to study speckled data; however, it can be used as a method to assess the performance of the algorithm used on the wedge data. To help determine which approach best fits as a suitable criterion for evaluating the performance of the algorithm developed so far, a brief description on the wavelet analysis approach and the simpler short-time Fourier-transform method is given in section-7.2.1 and section-7.2.2 respectively.

7.2.1 Wavelet analysis approach

First, a brief description of the conventional *Fourier* transform method is given and its links to the wavelet transform are highlighted. Following the approach described by *de Groot* [82] and *Surrel* [83, 84], the Fourier transform of a set of *M* sampled intensity data *I*(*t*) where *t* = 0,1,2,…,*M*-1 is given by:

$$\tilde{I}(k_t) = \sum_{t=0}^{M-1} I(t)W(t)e^{-2\pi i k_t t/N} \ , \qquad 7.1$$

where *W(t)* is a continuous window function, k_t is a continuous non-dimensional temporal frequency and *N* is the number of samples per cycle of the carrier. According to *Cherbuliez M et al* [228] on the other hand, the equivalent one-dimensional wavelet transform may be written as follows:

$$\tilde{I}^*(k_t, t) = \sum_{t'=(-M+1)/2}^{(M-1)/2} I(t+t')W(k_t, t')\, e^{-2\pi i k_t t'/N} \ . \qquad 7.2$$

Comparing the two equations above one can notice two differences between the wavelet transform $\tilde{I}^*(k_t, t)$ and the Fourier transform $\tilde{I}(k_t, t)$. That is, a) an unimportant shift in the limits on the summation and b) that the shape of the window function is now dependent on k_t.

Consider a symmetrical Gaussian window function as the one used in [54], such that:

$$W(k_t, t) = \frac{k_t}{N} e^{-k_t^2 t^2/2N^2} \ . \qquad 7.3$$

When the window function $W(k_t,t)$ is multiplied by the complex exponential in equation-7.1 it is an example of a Morlet wavelet. The intuitive advantage of wavelets over constant time-duration windows is that they are adaptive. Therefore, it follows that the wavelet window used for searching fast changing signals will automatically be short compared to one used for slower signals, thereby ensuring that the same number of oscillations occur within the window at each one time.

As we have seen earlier in Chapter-6, prior to Fourier transformation of the intensity signal, the extracted wavenumber change from the four wedge sensor is interpolated onto a uniformly spaced *k*-space followed by resampling and re-registration of the intensity signal onto the final Δk-axis. One of the reported issues of using the wavelet transform for TFA in non-uniformly sampled data is that the resampling operation induces unwanted low-pass filtering and artefacts in the spectrum of non-uniform

data [240-242], thereby negating the use of adaptive window sizing offered by the method. Arguably, this issue was demonstrated by examining the effect of *k*-scan gaps earlier (see Chapter-6 section-6.3.3 and the figures therein) and was shown to be negligible.

7.2.2 Short-time Fourier-transform approach

To avoid the unnecessary complexity associated to the variable window function size required by the wavelet transform approach, a simpler tool termed the short-time Fourier-transform (STFT) method will be used here instead. Its mathematical description is almost identical to equation-7.2 with the exception that the dependency of the window function to the frequency k_t is now dropped. The STFT method has been used for the determination of phase and phase derivatives in fringe pattern analysis in 1-D [243], and later in 2-D [244, 245]. The method has been suggested for refractive index measurement in [243], phase shifter calibration in [244] and local frequency measurement in [245]. However, none of the aforementioned publications provide real life practical applications. The main focus of this section will be limited to the use of STFT in studying the behaviour of the local frequency k_t across different segments of the total scan duration.

Finally, it has been reported that errors associated with the STFT stem from end effects or transient signals present in the measured time-domain output blocks that are uncorrelated with the respective input block [246]. Moreover, in recent studies [247, 248], it was shown that the magnitude of the transient effects can be reduced with the use of a window function like the well-known Hanning-window, while the variance of the frequency estimates can be reduced by introducing a percentage of overlap between each block, owing to the increase in the number of averaging blocks. The choice of window function used for the TFA was a Hamming-window $W(t)$:

$$W(t) = \alpha - \beta \cos\left(\frac{2\pi t}{N_w - 1}\right), \qquad 7.4$$

where $\alpha = 0.54$, $\beta = 1-\alpha = 0.46$ and N_w is the fixed length of the window function. Table-7.1 below provides a summary of the parameters used henceforth anywhere in the text where the STFT is be used.

Table-7.1: Summary of the short-time Fourier-transform parameters used for producing the spectrograms of figure-7.1 and figure-7.2. The same parameters hold for all spectrograms unless otherwise stated

Short-time Fourier-transform (STFT) parameters	
Total number of data points in scan sequence N_t	125155
Window function type $W(t)$	Hamming
Number of data points in each window N_w	8192
Percentage overlap	98%
Zero-padding factor in number of data points N_p	16384

Figure-7.1(a) and figure-7.1(b) show the absolute value of the resulting spectrograms following the implementation of STFT for the intensity data of wedges one and two respectively where the line $k_t = 1$ stretching across the width of the figure is where the Fourier peak should appear. The thick white lines, on the other hand, indicate the actual location of the Fourier peak. Finally, W_n is the window number and is effectively a dimensionless time index similar to t used earlier. Apart from some small fluctuation in the width of the Fourier peak indicated by the widening and thickening of the white lines as well as some level of reduction in the amplitude of the Fourier transform (decaying colour of the white lines from $W_n = 700$ onwards), in both figures the location of the peak is consistent and coincides with line $k_t = 1$ as expected. However, this is not the case for the spectrograms of the intensity data for wedges three and four. As shown in figure-7.2(a) and figure-7.2(b), around the region where $W_n \in (400,550)$ the location of the Fourier peak is not unique and in some cases it even completely vanishes. Furthermore, unlike figures 7.1(a) and (b) its location is no longer coincident with the $k_t = 1$ line showing a relative amount of oscillation around $k_t = 1$, particularly towards the end region where $W_n \in (700,912)$ for wedge three but also at the very beginning for wedge four. The spectrogram results shown in the aforementioned figures are quite consistent with figures 6.19(b), 6.20(b), 6.21(b) and 6.22(b) in that they all illustrate the fact that for the thinner wedges the data quality is reduced. However, they also provide the additional information of whereabouts within the scan the problems are arising.

7.2.3 Wedge thickness-ratio variation

As it was mentioned earlier (Chapter-6) the main reason for the observed signal degradation is likely to be the presence of residual phase unwrapping errors. To further investigate the validity of this assumption a simple test is devised involving two key quantities. That is phase unwrapping errors and the wedge thickness ratio R_m (where m is the index indicating the unwrapping step and in this case is equal to 1). Prior to the 1-D optimization using equation-5.30, the ratio R_1 for the first unwrapping step involving pair of wedges (1,2) and (2,3) was estimated to be equal to the ratio of their respective central thicknesses as indicated by equation-5.23 and the results for Method-B in Table-6.6, i.e. R_1 = (12.7516-12.6780)/(12.6780-11.9265) = 10.21. This is quite close to the optimum value of 10.314 used.

R is in effect a spatial parameter which should naturally, in the absence of any changes in the physical thickness of the wedges, remain constant throughout the duration of the scan. To test this assumption, the scan sequence was divided into segments of equal length (590 frames long each), for each of which the unwrapping process described in chapter-5 and the 1-D-optimisation for R, was performed individually. Figure-7.3(a) shows in green the unwrapped phase change $\Delta\Phi_u^{1,2}(t,0)$ scaled by the optimum ratio $R_{opt}^1 = 11.219$ for the first scan section where $t \in$ [1,590], in red the unwrapped phase change $\Delta\Phi_u^{2,3}(t,0)$ using $R_{opt}^1 \times \Delta\Phi_u^{1,2}(t,0)$ and in blue the unwrapped phase change $\Delta\Phi_u^{1,2}(t,0)$ scaled up by $R_{opt}^{15} = 9.501$. Note that, the superscripts 1 and 15 in R_{opt} are used to indicate the optimum R-ratios for the initial and 15th segment (for which $t \in$ [1,590] and $t \in$ [8261, 8850] respectively), out of the total 82 segments that the data sequence was divided into. Figure-7.3(b) on the other hand shows similar plots to those in figure-7.3(a) with the only difference being that the unwrapped phase change shown in red for the segment where $t \in$ [8261, 8850] was obtained using the optimum ratio for the first segment with $t \in$ [1,590]. Finally, figure-7.4(b) shows the resulting unwrapped phase change $\Delta\Phi_u^{2,3}(t,0)$ in red using $\Delta\Phi_u^{1,2}(t,0)$ scaled by optimum ratio $R_{opt}^{15} = 9.501$ for that section. Note that figure-7.4(a) is identical to figure-7.3(a) and is reproduced to aid the following comparison. Close inspection of the plots shown in the aforementioned figures yields a number of notable remarks. More specifically:

a) In figure-7.3(a), after the second wavenumber jump at t = 300, a gap between all three plots is starting to build up. As expected given the difference in between R_{opt}^{1} and R_{opt}^{15}, the deviation for the blue line is largest, whereas the red and green lines follow another one another more closely. However, whereas the red curve lies under the green curve for t between 300 and 400, it lies above it for t > 430, suggesting that an unwrapping error has occurred between t = 400 and 430.The optimization process would have therefore apparently returned a value for R_1 that, whilst it minimizes the cost function, is nevertheless too high in this case.

b) In the same figure, at t = 400 a smaller jump occurs that causes the red and green lines to significantly deviate from the blue. At this stage, it is unclear whether this small upward hop is in fact due to a laser induced mode hop or it is caused by an unknown error source. The fact that it occurs in all three lines is reassuring suggesting that this is a laser-induced behaviour. A more in-depth investigation on this matter will be given in a subsequent section.

c) In principle, given that the correct ratio for the unwrapping step is chosen, the unwrapped phase change shown in red should follow the blue line closely. However, the gradient of the unwrapped phase change shown in red tends to vary, appearing below the green line and then on top of it at the end of the segment (see figure-7.3(a))

d) In figure-7.3(b), apart from the expected mismatch in the gradients between the red and blue lines owing to the deliberate choice of an incorrect R_{opt} for that segment of the scan, unwrapping errors are starting to become visible (see region just before t = 8700), thereby illustrating that unwrapping errors can be caused by incorrect R-ratios.

e) In figure-7.4(b) on the other hand, even though the correct R-ratio was used for the corresponding segment of the scan, the unwrapped phase change $\Delta\Phi_u^{2,3}(t,0)$ still suffers from a significant amount of unwrapping errors starting at t = 8455 and t = 8800. Moreover, the small downward step occurring at t = 8400 in both green and blue lines is not resolved by the unwrapped phase which was in fact the case in figure-7.3(b) as well.

Finally, figure-7.5 shows in black the optimum ratio R as a function of position W_n with the latter referring to the scan segment and n being the index of the 82 in total

sections (n = 1, 2 ... 82). The line situated at R = 10.550 shown in red indicates the average value of the optimum R over the total 82 sections and is fairly close to the optimized R of 10.314 value previously reported in chapter-5 and in [20] for the limited 400-frame scan. The reasons as to why the fluctuations in the spatial parameter $R(W_n)$ are so violent as well as why they span over such a large region (R_{min} = 9.5, R_{max} = 11.5) will be the main focus of the analysis to follow.

7.3 Error propagation and uncertainty analysis

Recalling that the extraction of the wavenumber axis is a four step process involving the use of phase signals from the four-wedge sensor (see Chapter-5 and [20]), it is possible that the accumulation of residual phase unwrapping errors in the intermediate steps ultimately lead to distortion of the Δk-axis that becomes apparent when intensity data other than that coming from the highest sensitivity wedge is used (refer to Chapter-6 for a more detailed description of the phenomenon). In this section, an in-depth investigation of the potential reasons for such errors is provided. In section-7.3.1 and in view of the violent fluctuations in the optimum R-ratio demonstrated earlier, a simple error propagation analysis is provided to see if differences between refractive index could potentially be the cause. In section-7.3.2 the effect of inaccuracies during the manufacturing stage of the four wedges is investigated using the sub-pixel peak detection algorithm used in chapter-6. In section-7.3.3, a simple method is described that attempts to extract the refractive index dispersion curves of the four wedges and the resulting three synthetic wedges is reported. Finally, error sources due to the behaviour of the *Ti:Sa* laser used here are discussed in section-7.3.4.

7.3.1 Effect of wedge thickness

Consider three wedges with central thicknesses d_1, d_2 and d_3 and refractive indices n_1, n_2 and n_3 respectively as shown in figure-7.6. As mentioned earlier (Chapter-5), the interferometric phase for each of the three wedges is given by:

$$\begin{aligned} \phi_1 &= 2kn_1d_1 \\ \phi_2 &= 2kn_2d_2 \\ \phi_3 &= 2kn_3d_3 \end{aligned} \quad , \qquad 7.5$$

where k is the wavenumber. Note that the $f(\theta,\alpha)$ term has been dropped here for simplicity. The interferometric phase changes for the two resulting synthetic wedges are then given by:

$$\begin{aligned}\Phi_{2,1} &= 2\delta k[n_2(k)d_2 - n_1(k)d_1] \\ \Phi_{3,2} &= 2\delta k[n_3(k)d_3 - n_2(k)d_2]\end{aligned} \quad . \qquad 7.6$$

For an infinite small change in k, i.e. $k = k_0$:

$$\begin{aligned}\delta\Phi_{2,1} &= \frac{d\Phi_{2,1}}{dk}\Big|_{k=k_0} = 2[n_2(k_0)d_2 - n_1(k_0)d_1] \\ \delta\Phi_{3,2} &= \frac{d\Phi_{3,2}}{dk}\Big|_{k=k_0} = 2[n_3(k_0)d_3 - n_2(k_0)d_2]\end{aligned} \quad . \qquad 7.7$$

The temporal phase unwrapping algorithm employed so far is a two-step process. At first, the unwrapped low sensitivity yet noisy signal is scaled up by a factor R. The scaled up version is then used to unwrap the higher sensitivity phase. Therefore, strictly speaking the correct R ratio is:

$$R = \frac{\delta\Phi_{3,2}}{\delta\Phi_{2,1}} = \frac{n_3(k_0)d_3 - n_2(k_0)d_2}{n_2(k_0)d_2 - n_1(k_0)d_1} \quad . \qquad 7.8$$

Assume that the refractive index of the wedges can be expressed as the sum of a nominal value $\bar{n}$ and a deviation δn from the latter, such that:

$$\begin{aligned}n_1(k_0) &= \bar{n}_1(k_0) + \delta n_1(k_0) \\ n_2(k_0) &= \bar{n}_2(k_0) + \delta n_2(k_0) \\ n_3(k_0) &= \bar{n}_3(k_0) + \delta n_3(k_0)\end{aligned} \quad . \qquad 7.9$$

Figure-7.7 shows a schematic representation of such behaviour. It, therefore, follows that the expression for R can be re-written as follows:

$$R = \frac{\bar{n}_3 d_3 - \bar{n}_2 d_2 + \delta n_3 d_3 - \delta n_2 d_2}{\bar{n}_2 d_2 - \bar{n}_1 d_1 + \delta n_2 d_2 - \delta n_1 d_1} \quad . \qquad 7.10$$

Note that the dependency of the refractive index to the wavenumber has been dropped to aid mathematical simplicity. By letting:

$$\begin{aligned}X &= \bar{n}_3 d_3 - \bar{n}_2 d_2\,,\ \delta X = \delta n_3 d_3 - \delta n_2 d_2 \\ Y &= \bar{n}_2 d_2 - \bar{n}_1 d_1\,,\ \delta Y = \delta n_2 d_2 - \delta n_1 d_1\end{aligned} \quad . \qquad 7.11$$

the expression for R can be simplified to:

$$R = \frac{X+\delta X}{Y+\delta Y} \ . \qquad 7.12$$

Assuming that $\delta X << X$ and $\delta Y << Y$:

$$R = \left(\frac{X+\delta X}{Y}\right)\left(1+\frac{\delta Y}{Y}\right)^{-1} \ . \qquad 7.13$$

Using a first order Taylor expansion for the second term, $(1+\delta Y/Y)^{-1}$, the equation above can be re-written as follows:

$$R = \frac{X}{Y} + \frac{\delta X}{Y} - \frac{X\delta Y}{Y^2}(+\ 2^{nd}\ order\ terms) \ . \qquad 7.14$$

Neglecting the higher order terms, the sought expression for R may be further simplified to a simple sum of a nominal value $\bar{R}$ and a deviation δR such that:

$$R = \bar{R} + \delta R \ , \qquad 7.15$$

where, $\bar{R} = X/Y$ and $\delta R = (Y\delta X - X\delta Y)/Y^2$. The aforementioned transformation allows one to investigate the error propagation in computing R, given that there will always be some fluctuations from the nominal value. Following some straight forward algebraic manipulation, the ratio of δR to the nominal value $\bar{R}$ can be reduced to:

$$\frac{\delta R}{\bar{R}} = \frac{\delta X}{X} - \frac{\delta Y}{Y} \ . \qquad 7.16$$

If we now treat the X and Y as random variables, then the refractive index fluctuations therefore give rise to an uncertainty σ_R in the calculated $\bar{R}$, which is described by the general expression:

$$\left(\frac{\sigma_R}{\bar{R}}\right)^2 = \left(\frac{\delta X}{X}\right)^2 + \left(\frac{\delta Y}{Y}\right)^2 \ , \qquad 7.17$$

The importance of the numerical expression above lies in that it allows in a straight forward manner the investigation of the individual contributions of $\delta X/X$ and $\delta Y/Y$ to the overall error in calculating R for a given fluctuation in δn.

Consider for example the simple case where the refractive indices for all three wedges have equal and constant nominal values throughout the scan duration, such that:

$$\begin{matrix}\bar{n}_3=\bar{n}_2\ ,\delta n_3=-\delta n_2\\ \bar{n}_2=\bar{n}_1\ ,\delta n_2=-\delta n_1\end{matrix}\ , \qquad 7.18$$

as shown in figure-7.7. The error contributions for such case are given by:

$$\begin{matrix}\frac{\delta X}{X}=\left(\frac{\delta n_3}{\bar{n}_3}\right)\left(\frac{d_3+d_2}{d_3-d_2}\right)\\ \frac{\delta Y}{Y}=\left(\frac{\delta n_2}{\bar{n}_2}\right)\left(\frac{d_2+d_1}{d_2-d_1}\right)\end{matrix}\ . \qquad 7.19$$

Substituting for the central thicknesses in equation-7.19, yields an error amplification factor of 41 and 127 respectively. Consequently, the error propagation equation becomes:

$$\left(\frac{\sigma_R}{\bar{R}}\right)^2=\left(41\frac{\delta n_3}{\bar{n}_3}\right)^2+\left(127\frac{\delta n_2}{\bar{n}_2}\right)^2\ . \qquad 7.20$$

It is worth noting that the mathematical derivation described so far leading to the error propagation equation above (equation-7.20) was developed on the assumption that the nominal value of the refractive index of the wedges remains constant with respect to the wavenumber. This of course is not the case for fused silica in the wavelength bandwidth of 750 to 850 nm where the *Ti:Sa* laser operates. Instead a linear behaviour in that region has been reported in the literature [210]. However, it can be shown that the analysis required to extracting the equivalent analytical expressions for the linear as well as for non-linear cases is similar. The reason for choosing the simplest case here was to demonstrate the effect of sample thickness in calculating the optimum *R*-ratio while keeping the mathematical complexity to minimum.

Finally, it is not clear whether the amplification factors in equation-7.20 are capable of causing such large and violent fluctuations in *R* as those illustrated in figure-7.4. It is possible that unaccounted errors related to the unwrapping process described in chapter-5 are also responsible for these large oscillations in the optimum *R*-ratio. For this reason the phenomenon is further investigated in section-7.4 where an in-depth assessment on the performance of the phase unwrapping algorithm developed so far is provided.

7.3.2 Uncertainty in instantaneous peak position

Consider a simple wedge with an angle α along the wedge direction such as that shown in figure-7.8. The difference in phase of the interference signal across the

wedge due to the reflections from the front and back surfaces of the wedge is given by:

$$\Delta\Psi = 2kn\Delta d \ , \qquad 7.21$$

where k is the wavenumber ($2\pi/\lambda$), n is the refractive index of the wedge and Δd is the change in the physical thickness of the wedge across the field of view due to the angle α. It follows that the number of interference fringes observed across the field of view is given by:

$$N_f = \Delta\Psi/2\pi \ . \qquad 7.22$$

An alternative way to calculate the number of fringes (N_f) is from the 2-D-Fourier transform of the recorded fringe pattern. After the removal of the d.c and any background artefacts, the location of the maximum positive spectral lobe in the Fourier domain can be determined using the same sub-pixel peak detection algorithm that was used earlier in chapter-6. The spatial coordinates k_x and k_y where the maximum of the 2-D Fourier peak appears in the Fourier domain given by the algorithm are in fact equivalent to the number of fringes in the x and y directions of the field of view. Therefore, for a perfectly formed wedge the total number of fringes across the field of view can be computed by the following expression:

$$N_f^{(i)}(t) = k_r^{(i)}(t) = \sqrt{\left(k_x^{(i)}(t)\right)^2 + \left(k_y^{(i)}(t)\right)^2} \ , \qquad 7.23$$

where t is a dimensionless time index and is equivalent to the frame index. Note that the superscript i in the parenthesis indicates the wedge index which in our case takes the values i = 1,2,3,4.

Figure-7.9 and figure-7.10 show the instantaneous 2-D Fourier peak position as a function of time, calculated according to equation-7.23. A close inspection of the figures yields a number of observations. Wedges 2 and 4 are seen to have a rather smooth variation of the number of fringes with frame index, whereas a rather curious fluctuation in the instantaneous peak position starting at t = 1 up to t~ 40,000 is observed for wedge 1, and from t~40,000 lasting until the end of the scan for wedge three. The origins of the fluctuations are rather difficult to determine at this stage. One possible reason for this behaviour is the laser behaviour, for example laser-beam

drift and/or beam clipping during the scan. A more detailed justification will be given in subsequent sections.

Table-7.2: List of the coefficients for the resulting polynomials after the LSF. Note that, the coefficients *a-f* appear in descending order i.e.5^{th} power to 0^{th}.

Wedge index (*i*)	**Polynomial coefficients**					
	a	*b*	*c*	*d*	*e*	*f*
1	-1.1×10^{-23}	1.7×10^{-18}	-9.6×10^{-14}	1.5×10^{-9}	-4.6×10^{-5}	42.3
2	-3.8×10^{-25}	1.6×10^{-19}	-1.7×10^{-14}	3.0×10^{-10}	-6.6×10^{-5}	37
3		4.6×10^{-19}	-3.3×10^{-14}	5.4×10^{-10}	-8.4×10^{-5}	45
4		3.3×10^{-19}	-3.7×10^{-14}	9.2×10^{-10}	-1.1×10^{-4}	47.7

The best fit curves illustrated by the red lines in figures 7.9 and 7.10 were obtained by least squares fitting 4^{th} or 5^{th} order polynomials to the raw data with the resulting coefficients given in Table-7.2 above.

Moreover, there are three parameters revealed in figures 7.9-7.10 which are of particular importance. These are the initial and final number of fringes and the total change in the number of fringes during the full scan and are summarized in table-7.3 below. By inserting the initial number of fringes in equations-7.21 and 7.22 the wedge angle α can be estimated. Note that the value used for the starting wavelength (λ_0 = 750 nm) was extracted from the recorded wavelength values by the embedded wavelength sensitive diode (WSD) in the *Ti:Sa* laser, while the refractive index at that wavelength was set to 1.45 in accordance with the Sellmeier equation for fused silica (equation-1 in [210]).

Table-7.3: Summary of parameters using the polynomials in table-7.2 for the four wedge cases. Note that t_0 and t_N in $N_f^{(i)}$, are used to indicate the initial and final time instances of the scan, while $\Delta N_f^{(i)}$ indicates the change in the number of fringes between these two instances.

Wedge index (*i*)	$N_f^{(i)}(t_0)$	$N_f^{(i)}(t_N)$	$\Delta N_f^{(i)}$	**Curve fitting: Least squares fit**	**Wedge angle (α) at $\lambda = \lambda_0 \sim$750nm**
1	42.3	39	3.3	5^{th} order polynomial	1.254 min
2	37	33.3	3.7	5^{th} order polynomial	1.096 min
3	45	41	4	4^{th} order polynomial	1.334 min
4	47.7	42.3	5.4	4^{th} order polynomial	1.408 min

The results show that the estimated angles for the four wedges are up to a factor of two lower than the manufacturer specified value of 2 min (± 0.2 min). On the other hand, the change in number of fringes at the start of the scan compared to that at the end is not quite the same for all four wedges, with the biggest the difference (2.1 fringes) observed between wedges one and four and the smallest (0.3 fringes) between wedges two and three. This suggests that the rate at which the fringe separation changes as the wavelength of the source is tuned is not the same (see later section for more details on this observation).

One concern with the analysis so far, is that it has been implicitly assumed that all four wedges comprising the optical sensor have been perfectly formed. It is, however, possible that during the manufacturing process of the four wedges, angles other than those along the required wedge direction have been introduced. Figure-7.11 shows a schematic representation of such a case. In fact the tilted fringes as well as the change in fringe orientation amongst the four wedges (see figure-7.12**)**, suggests rather clearly that this is the case. The presence of such spurious angles means that the number of fringes calculated using equation-7.23 is significantly underestimated.

To account for this discrepancy equation-7.23 was modified using a correction factor equal to the ratio of the number of pixels along the x-direction (N_x = 714 pixels) over the number of pixels in the y-direction (N_y = 86 pixels) in the region of interest, such that:

$$N_f^{(i)}(t) = k_r^{(i)}(t) = \sqrt{\left\{k_x^{(i)}\right\}^2 + \left\{\left(N_x/N_y\right)k_y^{(i)}\right\}^2} \ , \qquad 7.24$$

This represents in effect the number of fringes that would be observed across a square wedge with the same wedge angles. It should be noted that the modified version of equation-7.23 above only holds true for the case where the pixels in the CCD sensor are of square geometry, which is the case for the ICX285 EXview sensor in the Prosilica GC1380H model used in this thesis.

Figure-7.13 and figure-7.14 illustrate the updated tracking of $k_r^{(i)}(t)$ using equation-7.24. By comparing figures-7.9(a**)** and 7.13(a**)**, it is evident that the correction factor introduced had a significant impact on the estimated number fringes for wedge-1

with the updated number of fringes almost double to that predicted by equation-7.23 suggesting that the wedge is far from ideal. Another interesting fact revealed by using equation-7.24 is that the estimated difference between the number of fringes at the start of the scan to that at the end ($\Delta N_f^{(1)}$), is now almost three times higher to that estimated using equation-7.23.

The parameters, $N_f^{(i)}(t_0)$, $N_f^{(i)}(t_N)$ and $\Delta N_f^{(i)} = N_f^{(i)}(t_0) - N_f^{(i)}(t_N)$,where t_0 and t_N are dimensionless time indices indicating the start and end of the scan respectively, on the other hand, for the rest of the wedges (i.e. i = 2,3,4) remained almost unaffected. Table-7.4 below provides a list of the updated parameters.

Table-7.4: Same as table-7.3 but using equation-7.24 that accounts for wedge plane angles other than along the wedge angle direction. Comparing the parameters in table-7.3 previously and the current table, suggests that wedge-1 suffers the most compared to all other wedges from the presence of the additional angle.

Wedge index (i)	$N_f^{(i)}(t_0)$	$N_f^{(i)}(t_N)$	$\Delta N_f^{(i)}$	**Curve fitting: Piecewise spline**	**Wedge angle (α) at $\lambda = \lambda_0 \sim 750$nm**
1	84.9	75.1	9.8	5th order polynomial	2.516 min
2	37.8	33.9	3.9	5th order polynomial	1.120 min
3	48.2	43.6	4.7	5th order polynomial	1.428 min
4	48.6	43.0	5.6	5th order polynomial	1.440 min

One of the problems encountered in calculating the best fit curve using the least squares fit method (LSF) was that slow signal variations were not captured (see figure-7.9(a). In fact, a polynomial of degree *N* can possess *N-1* relative maxima and minima. A method that allows capturing this behaviour is by performing piecewise spline interpolation in which adjacent portions of the curve are tied together at the knot (common point shared by the two portions) forming a piecewise polynomial curve [249]. The best fit curves shown in figures 7.13 and 7.14 were extracted by sectioning the data in blocks of 2,500 data points to each of which a 5th order polynomial curve was fitted. The best fit polynomials for each section were then tied together to form the best fit curves. In contrast to the LSF method the slow signal variations are now better captured thereby clearly demonstrating the benefit of the

piecewise approach (see, for example, a comparison of figure-7.13(a) to its predecessor figure-7.9(a)).

7.3.3 Wedge refractive index dispersion curve estimation

The total change in the unwrapped phase $\Delta\Phi_u(t,0)$ due to the total change in wavenumber $\Delta k\,(t,0)$ from a starting wavenumber k_i to final value of k_f is:

$$\Delta\Phi_u(t,0) = 2\Delta k(t,0)n(t,0)\Delta d \ . \qquad 7.25$$

where t is the usual dimensionless time index which is equivalent to the frame index and in this case is equal to t_N where N is the total number of recorded frames (48,971 in this experiment). Consequently, the corresponding change in the recorded number of fringes for the scan duration may be written as follows:

$$\Delta k_r(t,0) = \Delta\Phi_u(t,0)/2\pi = (1/\pi)\Delta k(t,0)n(t,0)\Delta d \ . \qquad 7.26$$

At the starting instance of the scan ($t = 0$) the number of recorded fringes is given by:

$$k_r(0) = (1/\pi)k(0)n(0)\Delta d \ . \qquad 7.27$$

It follows that the normalised change $\Delta k_r\,(t,0)$ with respect to the starting value $k_r(0)$ at the beginning of the scan can be easily obtained by taking the ratio of the two quantities. After some straight forward algebraic simplification using the above two equations the normalised change in number of fringes with respect to the initial value is given by the expression:

$$\frac{\Delta k_r(t,0)}{k_r(0)} = \frac{\Delta k(t,0)}{k(0)}\frac{n(t,0)}{n(0)} \ , \qquad 7.28$$

where, $\Delta k(t,0) = k(0)\text{-}k(t)$, $n(t,0) = n(t)\text{-}n(0)$ is the change in the refractive index of the wedge as a function of time t and $n(0)$ is the refractive index at the start of the scan i.e. at $t = 0$.

The significance of the above expression lies in that the first term on the right hand side is the same for all four wedges, while the second term is the normalised change in the refractive index of the wedge. In the absence of any errors in computing the term on the left hand side, equation-7.28 provides a simple way for the estimation of the changes in the refractive index of each wedge and consequently a measure of the level of dispersion in each of the four wedges.

Figure-7.15 illustrates this point showing the normalised changes in the refractive index $\tilde{n}_i$ of each wedge as a function of *t*. Although in the first 4,000 frames the difference amongst the four plots is small a gap starts to build up around *t = 5,000* resulting to a significant deviation at the end of the scan in $\tilde{n}_i$ amongst the four wedges, suggesting that there is a mismatch in the dispersion curves. This is a rather surprising result as the material used to form the optical sensor was claimed to be the same for the four wedges. Similarly, figure-7.16 shows the normalised refractive index change $\tilde{n}_{i,j}$, as a function of time *t*, for the three synthetic wedges where:

$$\tilde{n}_{i,j}(t,0) = \left|\tilde{n}_i(t,0) - \tilde{n}_j(t,0)\right| \ , \qquad 7.29$$

with *i,j* used here to indicate wedges pairs (1,2), (2,3), (3,4) and (1,5) where 5 is a fictitious wedge with zero thickness. Once again the gap observed earlier in figure-7.15 is present. However, its starting point tends to drift as shown in figures-7.16(a)-(c) indicating that its location depends on the synthetic thickness of the wedge.

Although the study of the refractive index of fused silica as a function of wavelength dates back to the early 60's, reports of its behaviour in the 750-850 nm bandwidth, where the CW Ti:Sa laser source operates, are limited to one or two experimental data points [210, 250-253] at the start and end of the range. As a result, it is rather difficult to validate the behaviour shown in figure-7.15 with real experimental data reported in the literature. Nevertheless, it is worth pointing out that nonlinear behaviour of the refractive index of fused silica (SiO_2) has been reported on several occasions [251-253] and has been modelled based on the perturbation theory (see eqn-1 in [251]) such that:

$$n = n_0 + \Delta n \ , \qquad 7.30$$

where n_0 is the linear index of refraction and Δn is the intensity-dependent index change. According to equation-1 in [251] and the equation in the introduction of [252], the second term on the right hand side of equation-7.30 is given by:

$$\Delta n = \gamma I \ , \qquad 7.31$$

with γ defined as:

$$\gamma = \frac{m\lambda}{I_0 T(1+T^2)} \frac{\alpha}{(1-e^{-\alpha L})} \ , \qquad 7.32$$

where $m\lambda$ is a phase shift induced due to the change Δn, I_0 is the beam intensity incident on the sample, T is the fraction of the intensity transmitted by the sample surface, α is the absorption coefficient and L is the sample length (see equation-16 in [251]). The importance of equation-7.32 lies in that it includes a dependence of Δn on the sample thickness L. Assuming that all other parameters of equation-7.32 are the same for the four wedges, it becomes evident that refractive index n for the four wedges would be slightly different, therefore providing a possible explanation for the difference in the gradients of the four plots in figure-7.15 and the deviation in the refractive indices of the synthetic wedges in figure-7.16. However, the above is only a theory as if indeed the wedge material is fused silica then $\alpha = 0$.

7.3.4 Laser beam induced errors

One potential error source that has not been accounted for yet, is that related to the shape of the incident beam on the four-wedge optical sensor. Figure-7.17 provides a visual comparison between the first and last images in the scan sequence where it is clear that the shape of the incident beam on the four wedges is considerably different. Even though the beam appears to have shifted to the left compared to its initial location, the most likely reason for this change in shape is that the beam at the beginning of the scan has been clipped by the optical window at the exit of the Ti:Sa head.

Although a change in beam shape would practically leave the number of fringes seen by the CCD unaffected, this is unlikely to be the case for the phase calculated at that frequency. To clarify this point, one may consider for the moment that the shape of beam can be regarded as a natural window function multiplying the fringe pattern. It follows that a change in the shape of the window function would automatically result in a change in phase which is not necessarily linked to a change in the number of fringes.

A less obvious, yet rather important point associated with the clipping of the laser beam illustrated in figure-7.17 is that the estimated phase at the centre of each of the four wedge ROIs, resulting from the swapping of the image quadrants is most probably going to be affected. The issue has been partially suppressed by the removal of background artefacts (see section-6.2.3 equation-6.11 and figure-6.7), however, residuals may still exist that may well contribute towards degrading the

accuracy of the estimated phase signal as well as towards the appearance of residual phase unwrapping errors. For this reason the issue will be dealt with in more detail in section-8.3.5.

Finally, on closer inspection of figure-7.17(e) and figure-7.17(f) which refer to the first and last images of the scan sequence for wedge 3, it is clear that the shape of the beam in the last image is more complex with ring-like wrinkles clearly visible. This observation suggests that the shape of the beam for wedge 3 towards the end of the scan is the most likely reason for the increased fluctuation in $k_r^{(3)}(t)$ illustrated in figures 7.10(a) and 7.14(a) earlier. Although proof of this statement could be achieved by accurately tracking the shape of the beam in time, this falls outside the scope of this work and will, consequently, be left as a task to be dealt with in future. However, an alternative reason to the ring-like structure illustrated in figure-7.17(f) may be attributed to the different behaviour of the anti-reflecting coating, applied to the wedges, to different wavelengths. This observation was in fact pointed out by Yamamoto, A *et al.* (2001) in a study where the ability to perform surface shape measurements by wavelength scanning interferometry using an electronically tuned Ti:Sa laser was examined [26]. In this work, the authors concluded that even though all optical components were coated with wide-band anti-reflecting coatings, back reflections coming from optical components such as imaging lenses and the CCD cover slip were responsible for what is termed as 'coherent noise'. Non-compensated residuals of these 'coherent noises' were illustrated in figure-5 and figure-9 in [26] and were the main reasons for limiting the performance of the WSI system developed. The similarity between the aforementioned figures in [26] to figure-7.17(f) clearly suggests that a similar phenomenon is present in the current WSI system and a method to suppress it is worth investigating.

7.3.5 Material induced errors

From a material point of view, fused silica is a non-crystalline (glass) form of silicon dioxide (quartz, sand). Its atomic structure lacks long range structure, while its highly cross linked three-dimensional structure is responsible for the low thermal coefficient of thermal expansion the material possesses making it ideal for high temperature applications. In general there are different grades of fused silica. High purity sand deposits provide the raw material for bulk refractory grade which is electric arc

melted at extremely high temperatures. Optical and general purpose fused silica rods and tubing are drawn from a melt that is made from high purity chemicals, while fibre optic purity is made by thermal decomposition of chemicals that are rich in high purity gaseous silica. The glass may be clear or translucent, in which case it is often referred to as fused quartz. Its high viscosity allows the glass to be formed, cooled and annealed without crystallising [254]. From the above it is obvious that 'fused silica' is a term that encompasses a range of materials of different grades and therefore with slightly different properties tailored to match the application each of them is intended for. Although the criteria used to determine the grade of fused silica may alter depending on the manufacturer [254-260], these can be generically reduced to the following two: a) the impurities content and b) the optical homogeneity, both of which are linked to the manufacturing process used to produce the material.

Table-7.5: Summary of characteristics of different types of materials classified as fused silica from two different manufacturers (Heraeus and Corning).

Product name	**Production method**	**Impurities content**	**Homogeneity**	**$\Delta\lambda$ range**	**Application**	**Ref**
Heraeus HOMOSIL 101	Quartz glass manufactured by flame fusion of natural quartz crystals	Bubble size: ≤ 0.10 mm Free from inclusions and spots. OH content: ~150 ppm	From Δn: of ≤ 3 ppm to ≤ 1 ppm depending on grade	UV and visible range	Excellent for multiple axis optics such as prisms, steep lenses, beam splitters or etalons	[260]
Heraeus INFRASIL 301	Optical quartz glass grades manufactured by fusion of natural quartz crystals in electronically heated furnace.	Bubble size: ≤ 0.15 mm. Free from inclusions and spots. OH content: ≤ 8ppm	From Δn: of ≤ 5 ppm to ≤ 2 ppm depending on grade	IR and visible range	Multiple axis optics such as prisms, steep lenses, beam splitters or etalons.	[259]
Heraeus INFRASIL 302		Bubble size: ≤ 0.20 mm. Free from inclusions and spots. OH content: ≤ 8 ppm	From Δn: of ≤ 6 ppm to ≤ 3 ppm depending on grade		Demanding optics in one directional use such as lenses, IR-laser windows, optical flats etc.	

Table-7.5 continued

Product name	Production method	Impurities content	Homogeneity	Δλ range	Application	Ref
Heraeus INFRASIL 303		Bubble size: ≤ 0.30 mm. Free from inclusions and spots. OH content: ≤ 8 ppm	From Δ*n:* of ≤ 10 ppm to ≤ 6 ppm depending on grade		commercial optical IR application: light guide elements, beam delivery elements, microscope slides and IR-windows	
Heraeus SUPRASIL Standard	High purity synthetic fused silica materials manufactured by flame hydrolysis of $SiCl_4$.	Bubble size: ≤ 0.15 mm Free from inclusions and spots. OH content: < 1000 ppm	Not specified	Deep UV and visible range	Most economic grade within the SUPRASIL family. Used for substrates, mirrors, light guide elements, beam delivery elements, microscope slides and UV-windows.	[258]
Heraeus SUPRASIL 1		Bubble size: ≤ 0.1 mm Other: Same as above	From Δ*n:* of ≤ 5 ppm to ≤ 2 ppm depending on grade		Multiple axis optics such as prisms, steep lenses, beam splitters or etalons.	
Heraeus SUPRASIL 2		Bubble size: ≤ 0.15 to ≤ 0.25mm depending on weight. Other: Same as above	From Δ*n:* of ≤ 5 ppm to ≤ 2 ppm depending on grade		preferred materials for demanding optics in one directional use such as lenses, UV-laser windows, optical flats, etc.	
Heraeus SUPRASIL 3			From Δ*n:* of ≤10ppm to ≤ 5 ppm depending on grade			

Table-7.5 continued

Product name	Production method	Impurities content	Homogeneity	Δλ range	Application	Ref
HPFS® Standard Grade, Corning code 7980	High purity synthetic amorphous silicon dioxide manufactured by flame hydrolysis.	Inclusion size: ≤ 0.1mm to ≤ 1.27 mm-class (0 to 5) dependent. OH: 800 to 1000 ppm. Other:1 ppm	Grade dependent (AA to G): $\Delta n \leq 0.5$ ppm to ≤ 5 ppm	UV range	Microlithography	[255]
HPFS® KrF Grade, Corning code 7980,	High purity synthetic amorphous silicon dioxide manufactured by flame hydrolysis	Variable inclusion size (≤ 0.1 mm to ≤ 0.5 mm) depending on class (0 to 2). OH content: 800 to 1000 ppm. Other: ≤ 0.5 ppm	Grade dependent (AA to F): $\Delta n \leq 0.5$ ppm to ≤ 5 ppm	Deep UV range	248 nm lithography	[256]
HPFS® ArF Grade, Corning code 7980	High purity synthetic amorphous silicon dioxide manufactured by flame hydrolysis	Variable inclusion size (≤ 0.1mm to ≤ 0.5mm) depending on class (0 to 2). OH content: 800 to 1000 ppm. Other: < 0.1 ppm	Grade dependent (AA to F): $\Delta n \leq 0.5$ ppm to ≤ 5 ppm	Deep UV range	193 nm lithography	[257]

Table-7.5 above provides a list of the different types of fused silica from two of the main manufacturers, *Heraeus* and *Corning,* along with some of their characteristics based on the aforementioned two criteria. Generally speaking, the different types of impurities vary in size and content depending on the process and conditions under

which the material is formed affecting its optical homogeneity. The latter, is perhaps the most important parameter providing a measure of the variability of the refractive index Δn in all three dimensions which for fused silica varies from 10 ppm down to 1 ppm. In the technical reports describing the products from *Heraeus* [258-260], optical homogeneity is also assessed by the presence of striations in the functional and or all three dimensions. More specifically, the products INFRASIL-302,303 and SUPRASIL-2, 3 and Standard are likely to have weak striations that are parallel to the major faces of the material. This is a rather important point as it provides a possible reason that explains the formation of the striations observed on the estimated intensity background (recall figure-6.7 and section-6.2.3). On the other hand, *Corning* does not specify such artefacts. However, as these are most likely to be caused by the presence of certain types of impurities (see bubble size or inclusion size in table-7.5) it is possible that they can be observed in their products as well.

Generically speaking, crystalline and amorphous (non-crystalline) semiconductors and insulators are characterised by exponential optical absorption-edges that are generally referred to as the *Urbach* edges or region (see fig-1(b) in ref [261]). Over the past decade there have been a number of experimental and theoretical studies suggesting that disorder is responsible for affecting the features of the absorption edge in both crystalline and amorphous materials [261-267]. More specifically, the absorption edge in amorphous materials like fused silica (α-SiO_2) is affected by two contributing factors to disorder: a) thermal and b) non-thermal [261, 268]. According to *Vella, E. and R. Boscaino* (2009) the non-thermal component of disorder, also termed as structural disorder, for amorphous materials originates from the intrinsic lack in long-range order and from point defects such as dangling bonds and impurities [269]. The concentration of OH is one of the factors contributing to impurities that is responsible for the formation of silanol groups (Si–OH) [270]. The effect of these groups on structural disorder and the shape of the absorption-edges in amorphous SiO_2 have been studied by *Vella, E., R. Boscaino, and G. Navarra* (2008) and by *Vella, E. and R. Boscaino* (2009) [267, 269] respectively. More specifically, it was found that the intrinsic absorption edge is affected by the Si-OH concentration with high silanol group contents allowing for lower *Urbach* energy levels [267]. For this reason, a year later, the authors studied the effects of temperature on the absorption edge in the range of 4-300K for samples having negligible (dry, $<10^{17}$ cm^{-}

^{3}) and significant (wet, >10^{19} cm^{-3}) silanol groups contents [269]. It was found that a remarkable difference in the values of the absorption edge and in the temperature dependence of the Urbach energy occur in the comparison between the wet and dry samples. These were ascribed to the drastic reduction in the degree of disorder in wet materials which turn out to be characterised by an electronic structure more similar to that of crystalline quartz. The study concludes that silanol groups affect the thermal component of disorder by modifying the vibrational modes of the network. It is worth noting that the studies on the effect of disorder in amorphous silicon dioxide were predominantly carried out in the ultraviolet region of the light spectrum where absorption occurs.

Kitamura, R., L. Pilon, and M. Jonasz (2007) thoroughly and critically reviewed studies reporting the real (refractive index) and imaginary (absorption index) parts of the complex refractive index of silica glass over the spectral range from 30 nm to 1000 μm from the late twenties up to 2006. From their study it can be concluded that the general features of the optical constants over the aforementioned electromagnetic spectrum are fairly consistent throughout the literature. More specifically, silica glass can be regarded as optically opaque for wavelengths that are shorter than 200 nm and longer than 3.5-4.0 μm. Strong levels of absorption occurs in three distinct bands of the spectral range investigated; a) below 160 nm owing to, the interaction with electrons, absorption by impurities, the presence of OH groups and point defects, b) at ~ 2.73–2.85, 3.5, and 4.3 μm due to OH groups and c) at ~ 9–9.5,12.5, and 21–23 μm caused by Si-O-Si resonance modes of vibration. As far as absorption is concerned, the above is quite consistent with the more recent reports mentioned earlier. However, one important outcome of the critical review reported in [271] was that the actual values of the refractive and absorption indices can vary significantly. This is clearly demonstrated in figure-7.18, which is a reproduction of fig-1 in reference[271]. More specifically and as far as the refractive index values of silica glass are concerned, a rather significant mismatch between the calculated values is observed particularly in the region where the *Ti:Sa* laser operates. On the other hand, the absorption indices appear to be fairly consistent and clearly indicate that in that specific wavelength range absorption is practically negligible. According to the authors, some of the plausible reasons to explain such mismatches were ascribed to the following six factors:

a. due to the glass manufacturing process,
b. due to crystallinity,
c. due to wavelength range,
d. due to temperature effects,
e. due to the presence of impurities such as point defects, inclusions and bubbles,
f. and finally, due to the experimental uncertainties and approximations in the retrieval methods.

Although the origin of the material used for the four-wedge optical sensor was not specified by the supplier (see appendix-A4 for more information), the varying level of striations present in the four wedges (figure-6.7) suggests that it is possible that the four wedges were manufactured from slightly different grades of fused silica with optical homogeneity that is much lower than that specified by the high end products from *Heraeus* and *Corning* reviewed in table-7.5. Moreover, the extensive review in [271] indicates that a mismatch in the refractive index dispersion curves amongst different silica glasses is possible, thereby providing a potential explanation for the behaviour of the refractive index change trends shown in figure-7.15 and figure-7.16 earlier.

7.4 Discussion

In the view of the recent improvements reported in the previous chapter, in this chapter, an investigation of the error sources present in the full 100 nm scan using the wedge intensity data is presented. The reason behind this lies in that besides the ability to access the full 100 nm scan in contrast to the previous limit of 37 nm reported in [21] with the same setup, a phenomenon in the form of side lobe structure around the main spectral peak was observed. As the wavenumber change is the same for all four wedges, the re-registration of the raw intensity data onto the Δk-axis followed by Fourier transformation should yield clear spectral peaks at frequencies that are proportional to the thickness of the wedges in all four cases. Despite the fact that the resulting estimated frequencies closely matched the independent thickness measurements using a conventional micrometer, the presence of side lobe structure around the main spectral peaks, for wedges three and four, raises concerns about the accuracy of the estimated Δk axis that is crucial for the successful depth

reconstruction from the intensity of the interference signal and its associated phase. The aforementioned structure was attributed to residual phase unwrapping errors that are still present in the phase signal used for the estimation of Δk-axis and are therefore likely to cause distortions in Δk. Considering that the wavenumber-change monitoring sensor constitutes only a part of the phase-contrast, full-field, multi-axis tomographic interferometer under development and whose ultimate purpose is to provide accurate means of calculating the laser induced wavenumber changes onto which the interference signal from the 6 channels will be re-registered and subsequently analysed, it becomes clear that the identification of the error sources responsible for the residual phase unwrapping errors is of paramount importance for their subsequent suppression.

At first, a tool that is based on a time frequency analysis with the use of the short-time Fourier transform method has been employed to assess the performance of the algorithms developed so far. The resulting spectrograms are consistent with the presence of the structure observed around the main Fourier peak earlier by the occasional signal loss and in some cases the slow time-varying location of the spectral peak above or below the expected line of k_t =1. In the second step of the time frequency analysis a check on the optimum wedge thickness ratio variation was performed revealing unexpectedly large fluctuations in R as a function of time t. Strictly speaking, the ratio R is a spatial parameter which in the absence of any changes in the dimensions of the wedges, should in principle remain constant throughout the whole scan duration.

In previous studies on WSI systems developed for absolute thickness measurements and/or profilometry there have been no reports on a system with such a wide tuning range as that used in this work. More specifically, *de Groot, P* (2000) reported on a WSI system based on a Fizeau setup for the measurement of a 10 cm thick transparent plate with a tuning range of 7.5 pm [143]. Two years later *Deck, L.L* (2002) reported on a similar setup that was capable of measuring the optical thickness of a transparent flat (Fused silica 84 mm thick) with a tuning range of 4 nm [150]. *Hibino, K., B.F. Oreb, and P.S. Fairman* (2003) successfully measured the thickness of transparent plates (25 mm thick) with a tuning range of 0.028 nm [151], while *Deck, L.L.*, (2003) measured an 8-mm thick plate using a slightly larger range

of 0.134 nm [31]. *Hibino, K., et al*. (2004) reported on a similar system and measured a transparent near parallel flat BK7 glass sample that was 25 mm thick with a similar tuning range of 0.095 nm [77]. Within the same year, *Hibino, K., et al.* (2004) reported on a similar WSI setup that was used for the measurement of a BK7, 20 mm thick glass flat with a significantly larger tuning range of 0.25 nm [152]. A similar report was published two year later by the same authors [153]. Following a four year period of pause in the field of absolute thickness measurements, *Ghim, Y.-S., A. Suratkar, and A. Davies* (2010), reported on a reflectometry based WSI setup to measure the thickness of thin silicon wafers of 200 μm and 60 μm thick with a much wider wavelength tuning range of 4 nm [156]. Two years later, *Hibino, K., et al*. (2012), revisited the approach by reporting on the successful depth-resolved measurement of a synthetic fused silica glass plate with a thickness of 3.1 mm using a much larger tuning range than previously reported of 10 nm [158]. Finally, *Yu, H., C. Aleksoff, and J. Ni*, (2013), further pushed the tuning range limit, by an additional 6 nm to 16 nm, by measuring a 3 mm thick quartz block [159].

From the above brief review, it is clear that the larger the tuning range used, the smaller the thickness of the transparent plate measured. One of the main reasons that limit the measureable thickness is the effect of refractive index dispersion. Apart from the undesirable effect of degrading the depth resolution of the system, dispersion is also responsible for additional phase terms [230, 231] that in turn limit the accuracy of the phase measurement and thus the ability of the system to perform absolute thickness measurements. It follows that the longer the physical distance, in this case the thickness, the light has to travel inside the test sample the larger the effect of these additional phase terms. For this reason, the effect of the wedge thickness on the approach adopted so far was studied theoretically for the simple case of a nominal refractive index value that is constant and equal for all four wedges but with small variations that in the worst case scenario are diametrical opposite. The analysis showed that in the presence of these excursions, an error amplification factor of 41 and 127 in the error propagation expression in R (see equation-7.20) derived for the first unwrapping step appears. Considering that these get further amplified by the scaling ratios in steps two and three, it seems like a plausible explanation for the residual unwrapping errors still present in the signal. However, it is unlikely that the violent fluctuation in R for the first step can be explained solely by this reason.

In the brief review of similar studies provided earlier, all of the optical setups were realized in a Fizeau arrangement with the measurement volume (transparent flat surface to be measured) stacked behind a series of reference surfaces [77, 143, 150-153, 156, 159]. In contrast to the aforementioned studies, in the optical setup described in this work the four wedges are stacked on top of each other such that the intensity of the interference signal recorded and any artefacts associated with it are isolated to each individual wedge alone. Following the suppression of intensity background artefacts and with the use of the non-integer peak location algorithm introduced earlier in section-6.2.2 and section-6.2.3 respectively, a method of estimating the changes of the refractive index n of each of the wedges as function of wavenumber k was introduced. To limit errors owing to the potential existence of angles along directions other than the wedge direction, a simple correction factor was introduced. The resulting refractive index change curves for both the four individual wedges (recall figure-7.15) and the synthetic wedges (recall figure-7.16) used for the extraction of the Δk-axis, verify the presence of the non-linearities whose effect was previously investigated in the hypothetical scenario of a constant nominal value of the wedge refractive index but with the presence of excursions with opposite signs. More importantly, however, the results indicate: a) significant deviation from the expected linear behaviour of $n(k)$ for fused silica and b) a surprising, yet significant, difference in the gradient of the estimated dispersion curves that suggest there is a mismatch in the refractive index dispersion trend amongst the four wedges.

The theoretical model based on perturbation theory reported in the early study of *Weber, M.J., D. Milam, and W.L. Smith* (1978) [251] (see equation-7.32). provides one possible explanation for the observed $n(t)$ curves. The model predicts a dependence of n on the parameter L in equation-7.32 that is linked to the length of the path travelled by light inside the sample which of course is significantly different for the four wedges used in this work.

Finally a review of the potential material-induced errors was performed in section-7.3.5. The study revealed that the generic term fused silica encompasses a wide range of materials that may possess different optical properties depending on the manufacturing technique used. Moreover, a recent review (2007) on studies of the refractive index dispersion for fused silica that dates back to the early 30's and

stretches until the first decade of this millennium [271], confirmed that a small mismatch amongst the dispersion curves of the four wedges is after all quite possible.

7.5 Conclusion

As the title indicates, in this penultimate chapter, an attempt to identify the potential errors sources that may contribute towards degrading the accuracy and precision of the reconstructed wavenumber axis using the four-wedge optical sensor has been provided. These are: (a) residuals of intensity background artefacts, (b) a mismatch amongst the refractive index dispersion curves for the four wedges and (c) the amplifying effect that the wedge thickness has in the presence of such *n*-dispersion mismatches. Although all three effects are likely to play a role, residual phase unwrapping errors are still believed to be responsible for much of the undesirable structure in the observed spectra. Further attempts to reduce their influence will therefore be investigated in Chapter 8.

7.6 Figures

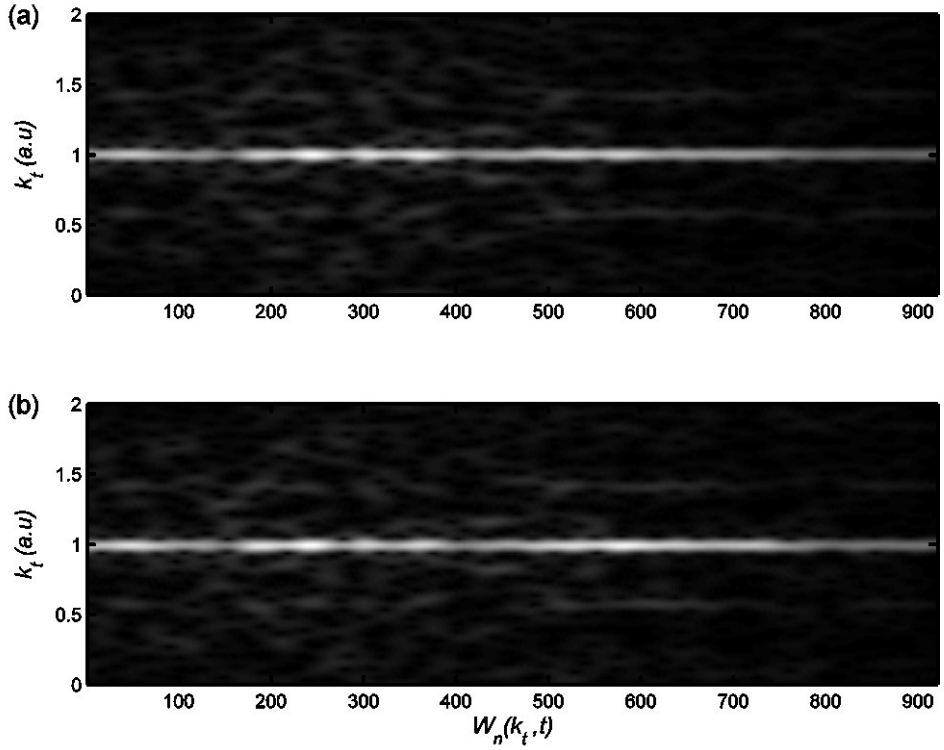

Figure-7.1: Time-frequency analysis using the short-time Fourier-transform for the intensity data from **wedge-1** (a) and **wedge-2** (b).

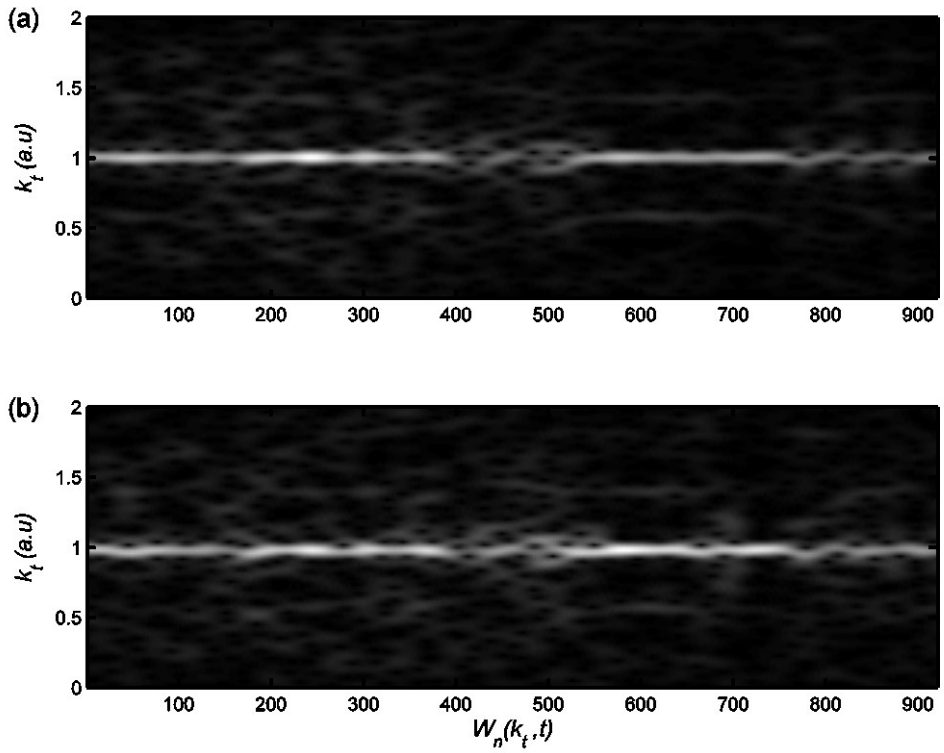

Figure-7.2: Time-frequency analysis using the short-time Fourier-transform for the intensity data from **wedge-3** (a) and **wedge-4** (b).

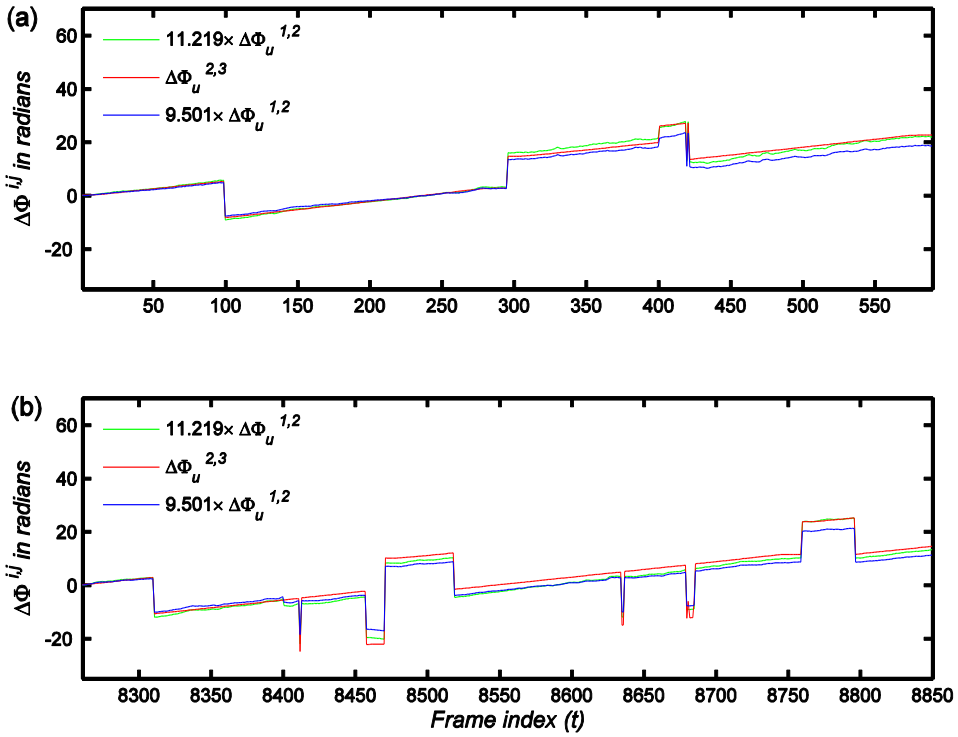

Figure-7.3: (a) Blue: temporally unwrapped phase change $\Delta\Phi_u^{1,2}(t,0)$ scaled by the optimum ratio for the 15th segment. Green: same as blue but scaled by the optimum ratio for the 1st segment of the scan. Red: unwrapped phase change $\Delta\Phi_u^{2,3}(t,0)$ using the green plot. (b) Same as (a) for the 15th segment of the scan.

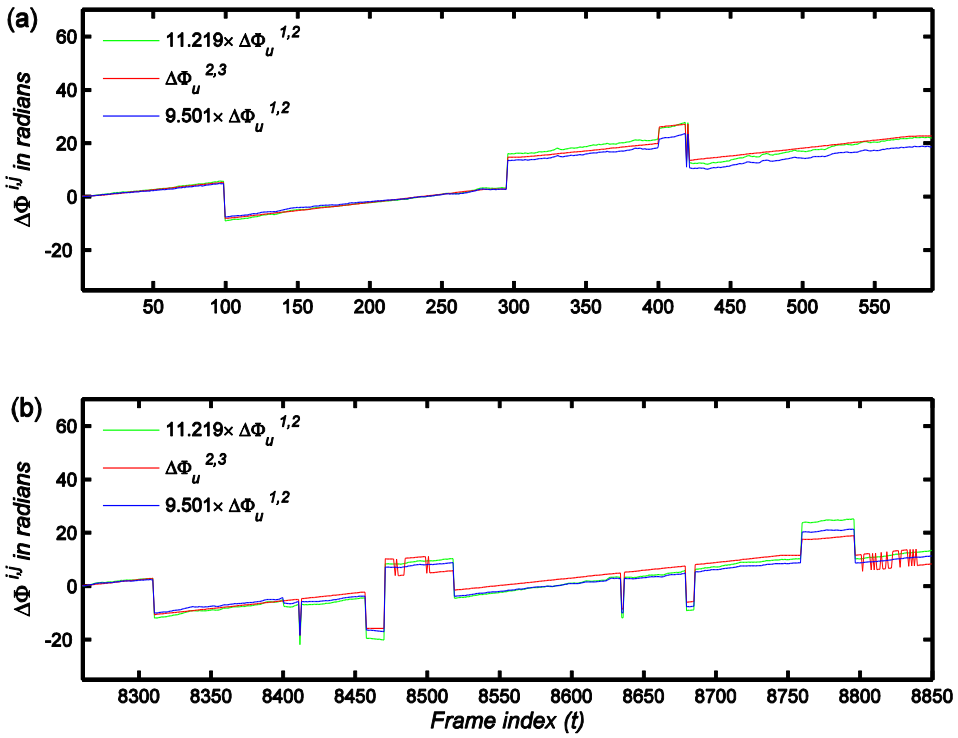

Figure-7.4: (a) Same as figure-7.3(a) to aid comparison. (b) Same as figure-7.3(b) but with the unwrapping performed using the blue line instead of the green used earlier.

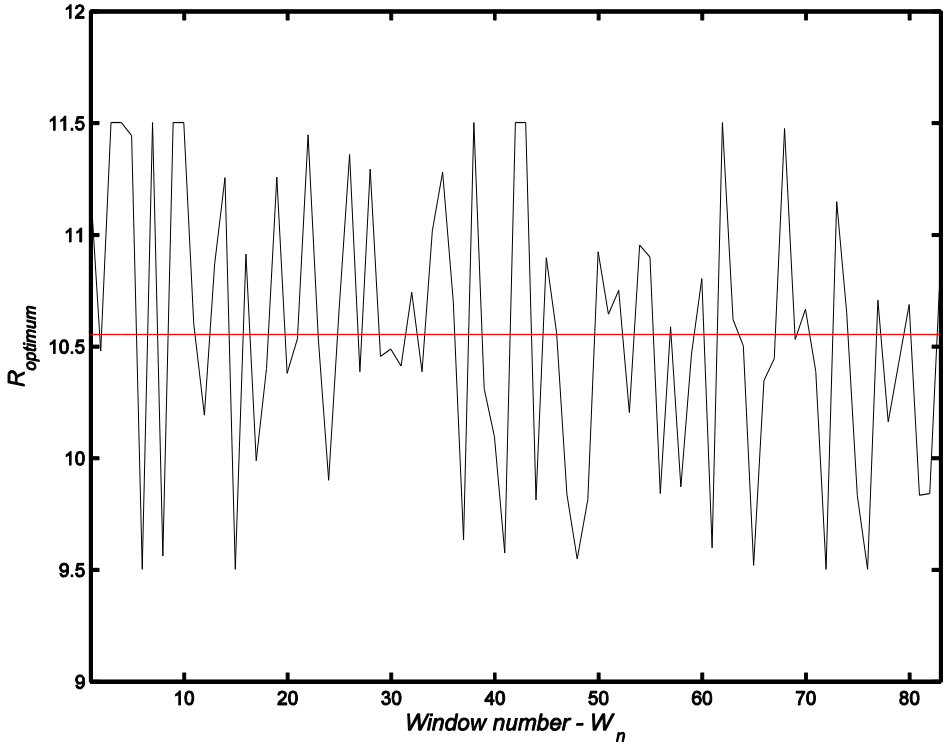

Figure-7.5: Black line: Optimum *R*-ratio variation as a function of scan position W_n with *n* indicating here the index of the 82 in total sections that the scan was divided to. Red line: Average optimum ratio (R = 10.250) over the total 82 segments.

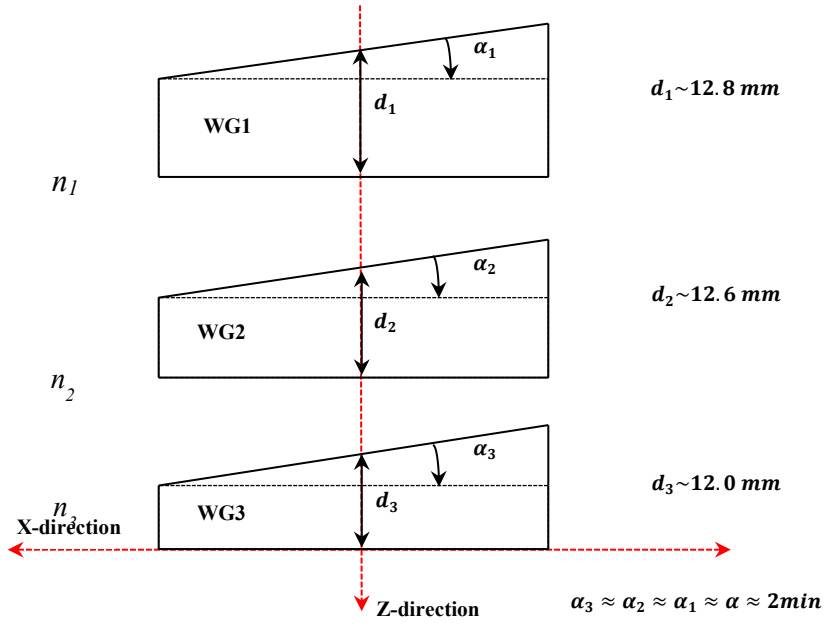

Figure-7.6: Schematic showing the three wedges considered for the error propagation analysis in section-7.3.1.

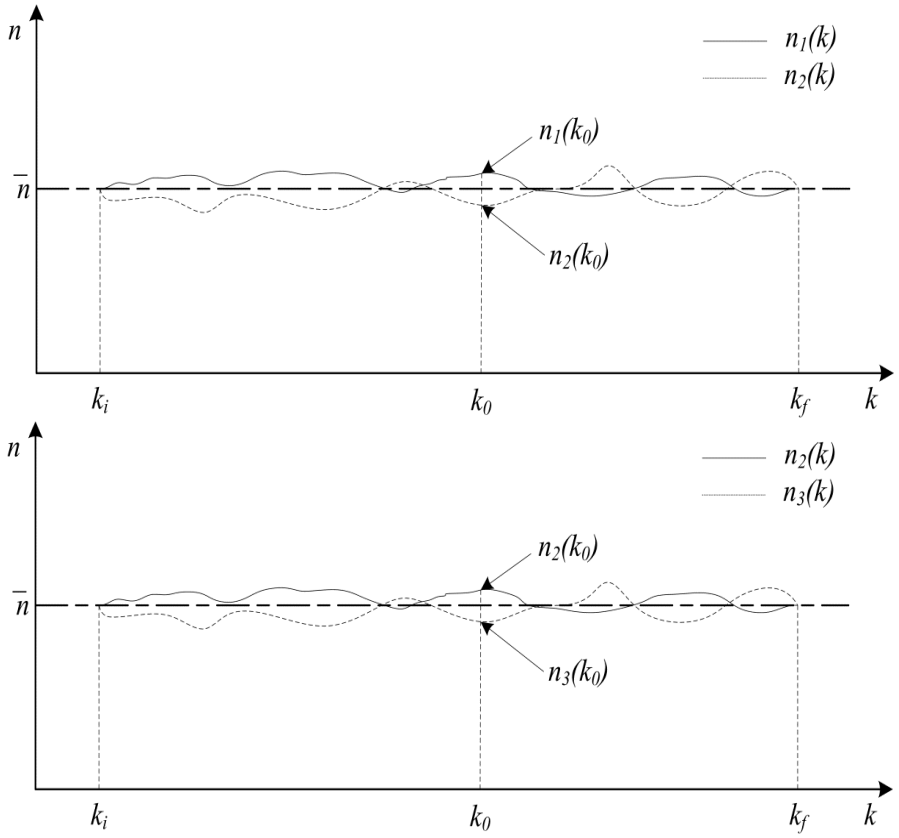

Figure-7.7: Hypothetical behaviour of the refractive index n with respect to the wavenumber k ($=2\pi/\lambda$) of the laser source for the analytical derivations involving the three wedges considered in section-7.3.1

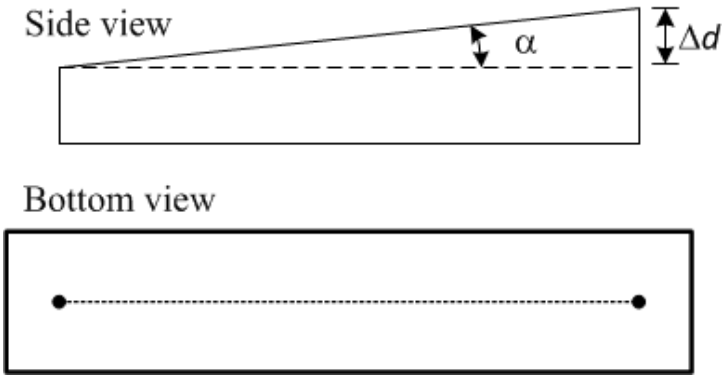

Figure-7.8: Schematic diagram showing a simple wedge. The interferometric change in phase due to the front and back reflections at the two points denoted by the black spots is given by $\Delta\Psi = 2kn\Delta d$, where k is the wavenumber, n is the refractive index and Δd the difference in thickness due to the wedge angle α.

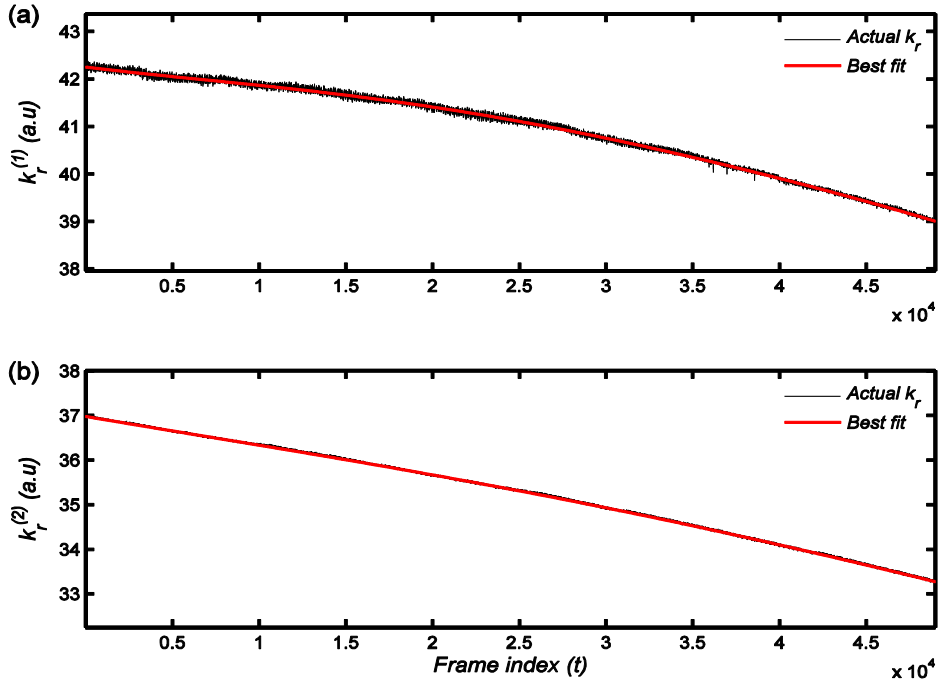

Figure-7.9: Instantaneous 2-D Fourier peak position as a function of time $k_r^{(i)}(t)$ using equation-7.23, for (a) **wedge-1** and (b) **wedge-2**, where i is the wedge index. Red lines indicate the best fit curve using LSF (see table-7.2); black lines show the row data extracted from the sub-pixel peak detection algorithm in section-6.2.2 after applying equation-7.23. $k_r^{(1)}(t)$ shows an increased level of fluctuation when compared to $k_r^{(2)}(t)$, the signal also shows some slow varying changes which are not present in (b) and are not captured by the best fit curve.

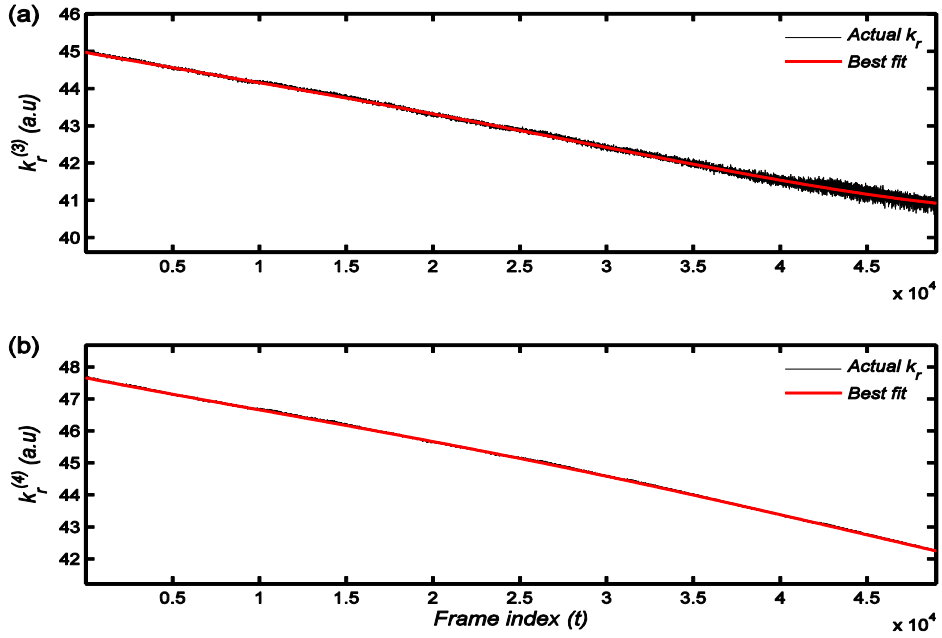

Figure-7.10: Same as figure-7.9 but for (a) **wedge-3** and (b) **wedge-4**. A rather curious increase in the fluctuation of $k_r^{(3)}(t)$ towards the end of the scan is clearly visible which is not present for $k_r^{(4)}(t)$.

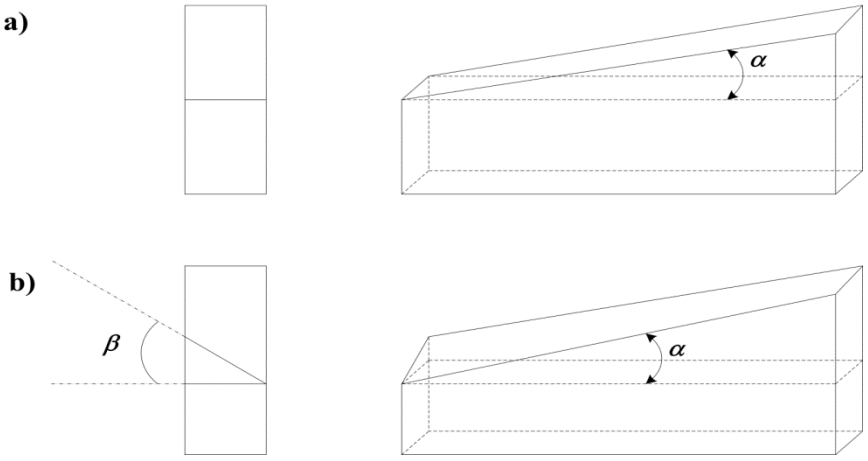

Figure-7.11: Schematic diagram showing (a) a perfectly formed wedge with a single wedge angle α, and (b) a wedge where apart from angle α an additional angle β exists.

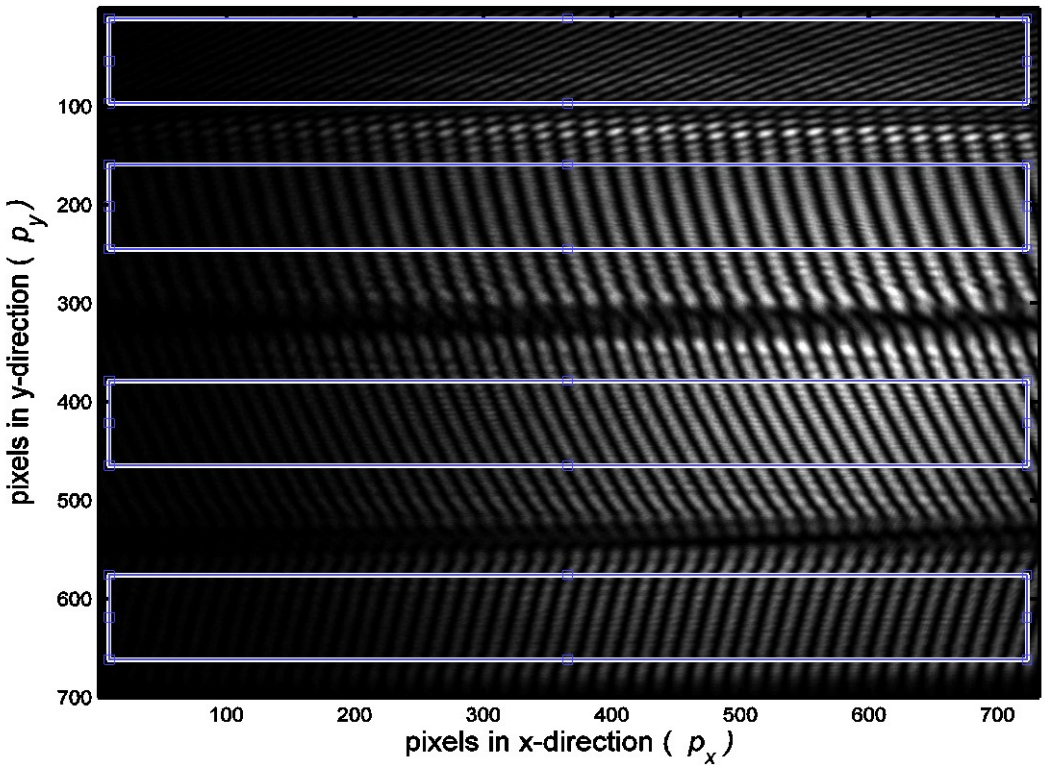

Figure-7.12: First image in the scan sequence illustrating the presence of tilted fringes as well as the difference in fringe tilt in the four wedges comprising the optical sensor developed in this thesis. Rectangles indicate the individual regions of interest (RoI) for each wedge with dimensions (N_x, N_y) = (714, 86) pixels.

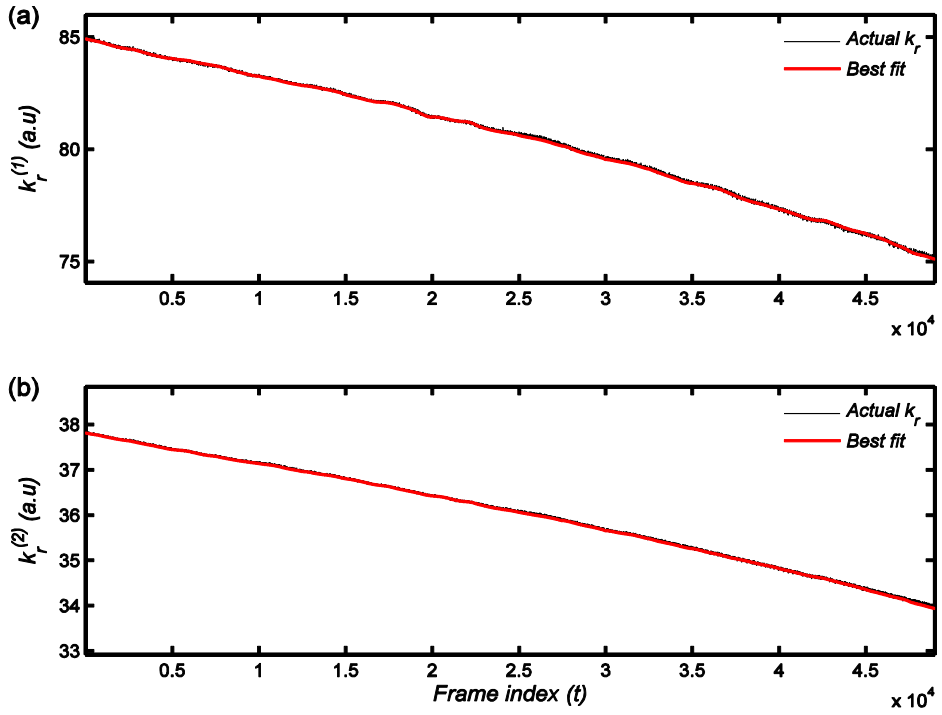

Figure-7.13: Instantaneous 2-D Fourier peak position as a function of time $k_r^{(i)}(t)$ using equation-7.24 for **wedge-1**(a) and **wedge-2** (b) where *i* is the wedge index. As previously, red lines indicate the best fit curve while black lines show the row data extracted from the sub-pixel peak detection algorithm. Note that the best fit curves were fitted using the piecewise method described in section-7.3.2 instead of the LSF method.

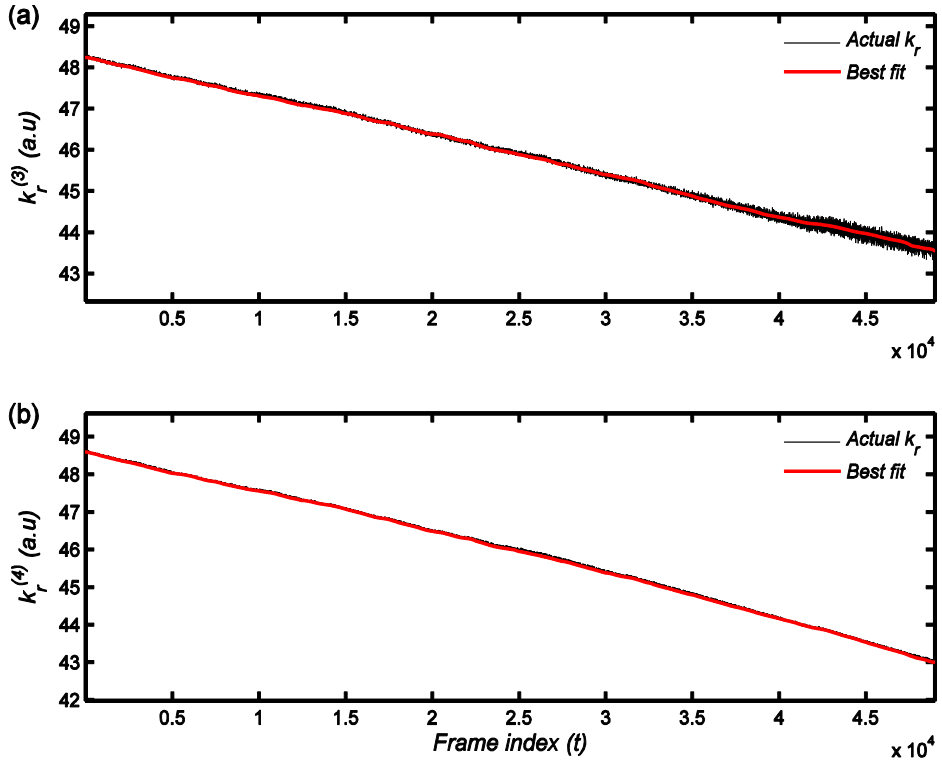

Figure-7.14: Same as figure-7.13 but for (a) **wedge-3** and (b) **wedge-4.**

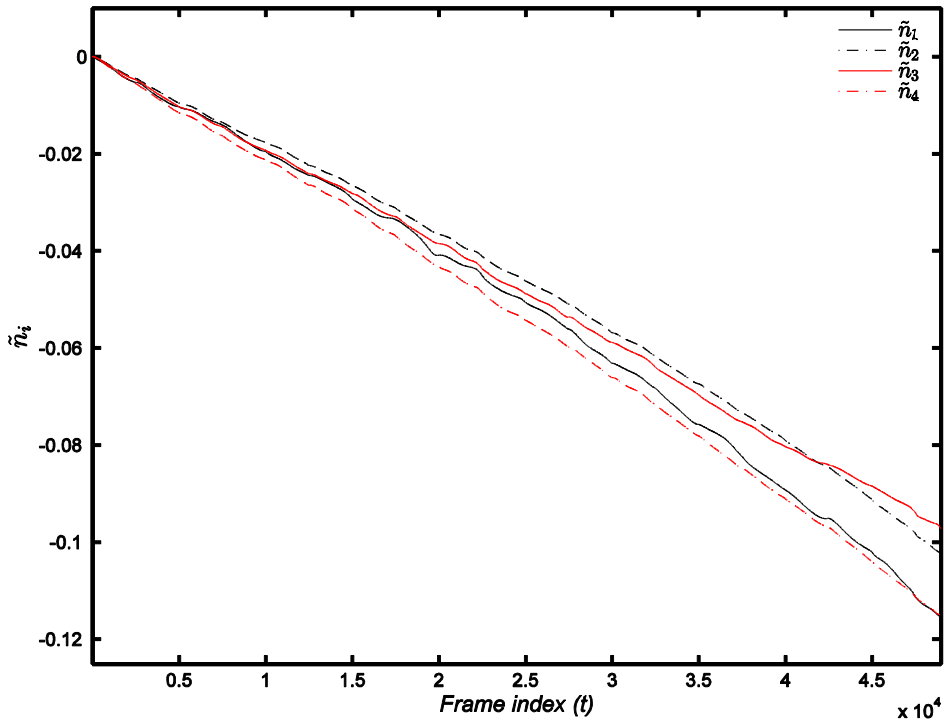

Figure-7.15: Plots showing the normalized change in the refractive index $\tilde{n}_i$ of each wedge as a function of time (t) using the piecewise curve fitting method to the raw data using equation-7.28, where i is the wedge index (i = 1,2,3,4).

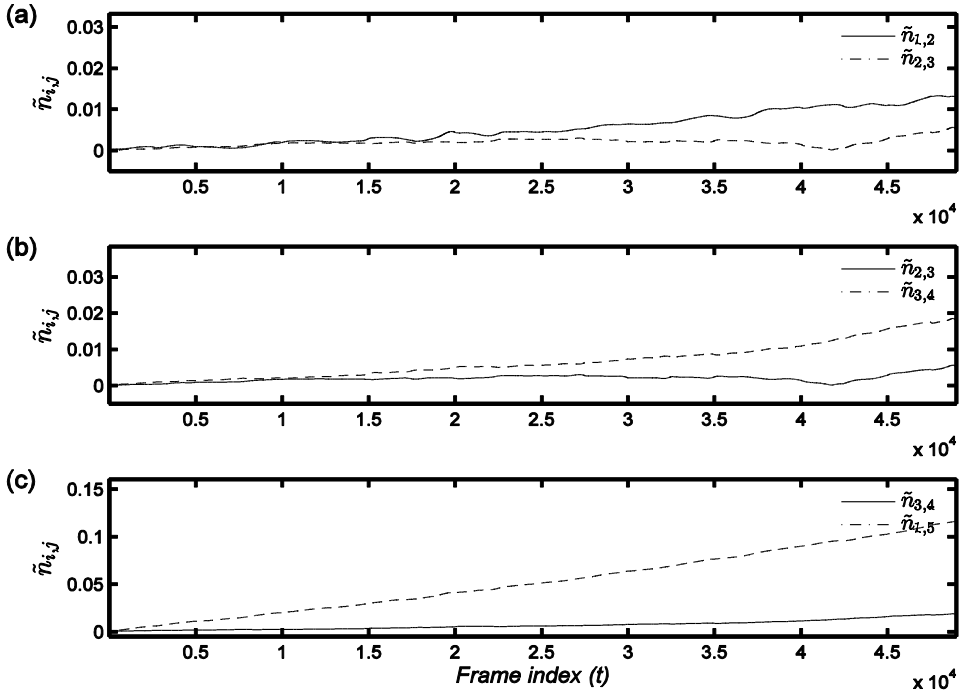

Figure-7.16: Comparison of the absolute changes in the refractive indices of the synthetic wedges (*i,j*) using equation-7.29: (a) Between synthetic wedge (*1,2*) and (*2,3*), (b) (*2,3*) and (*3,4*) and (c) (*3,4*) and (*1,5*) where *5* is a fictitious wedge of zero thickness. Note that the starting location of the gap that gradually increases as the scan progresses, between the pair of graphs gradually drifts to the left as the synthetic wedge thickness $d^{i,j}$ is exponentially increased.

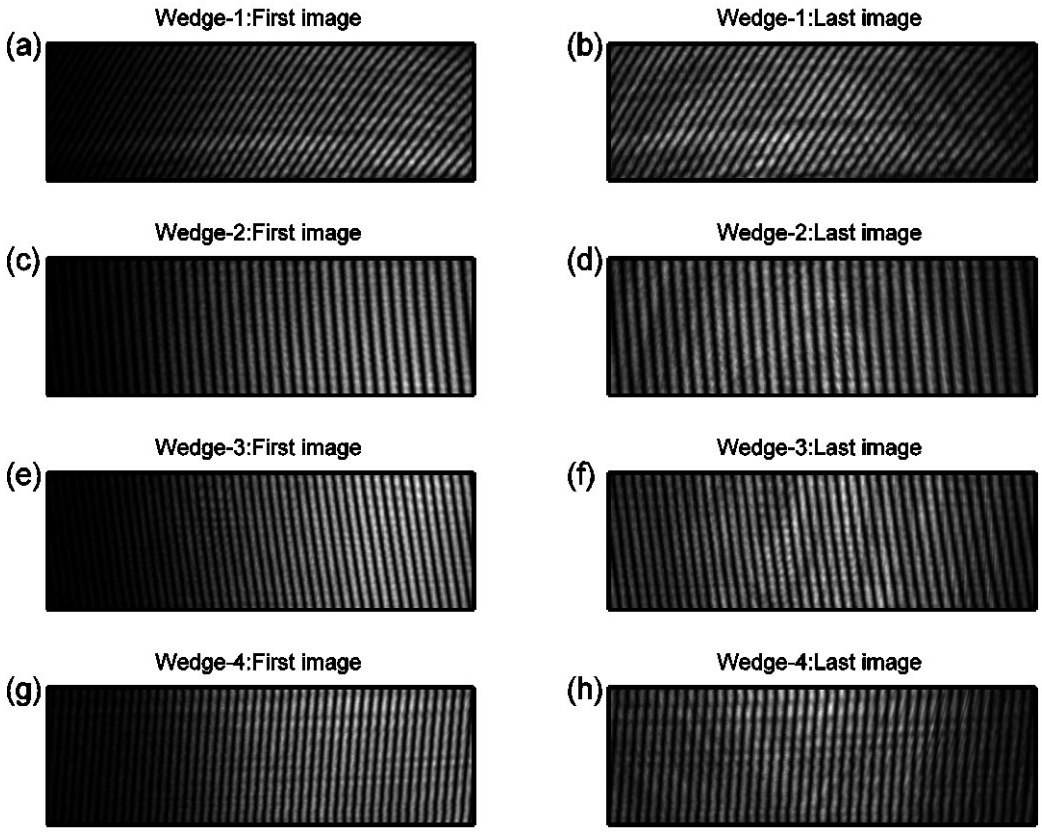

Figure-7.17: Left column (a, c, e, g) demonstrates the shape of the laser beam at the start of the scanning sequence while the right column (b, d, f, h) shows the shape of the beam in the last image of the sequence. Visual comparison of the two columns gives the impression that the beam has drifted to the left compared to its initial location.

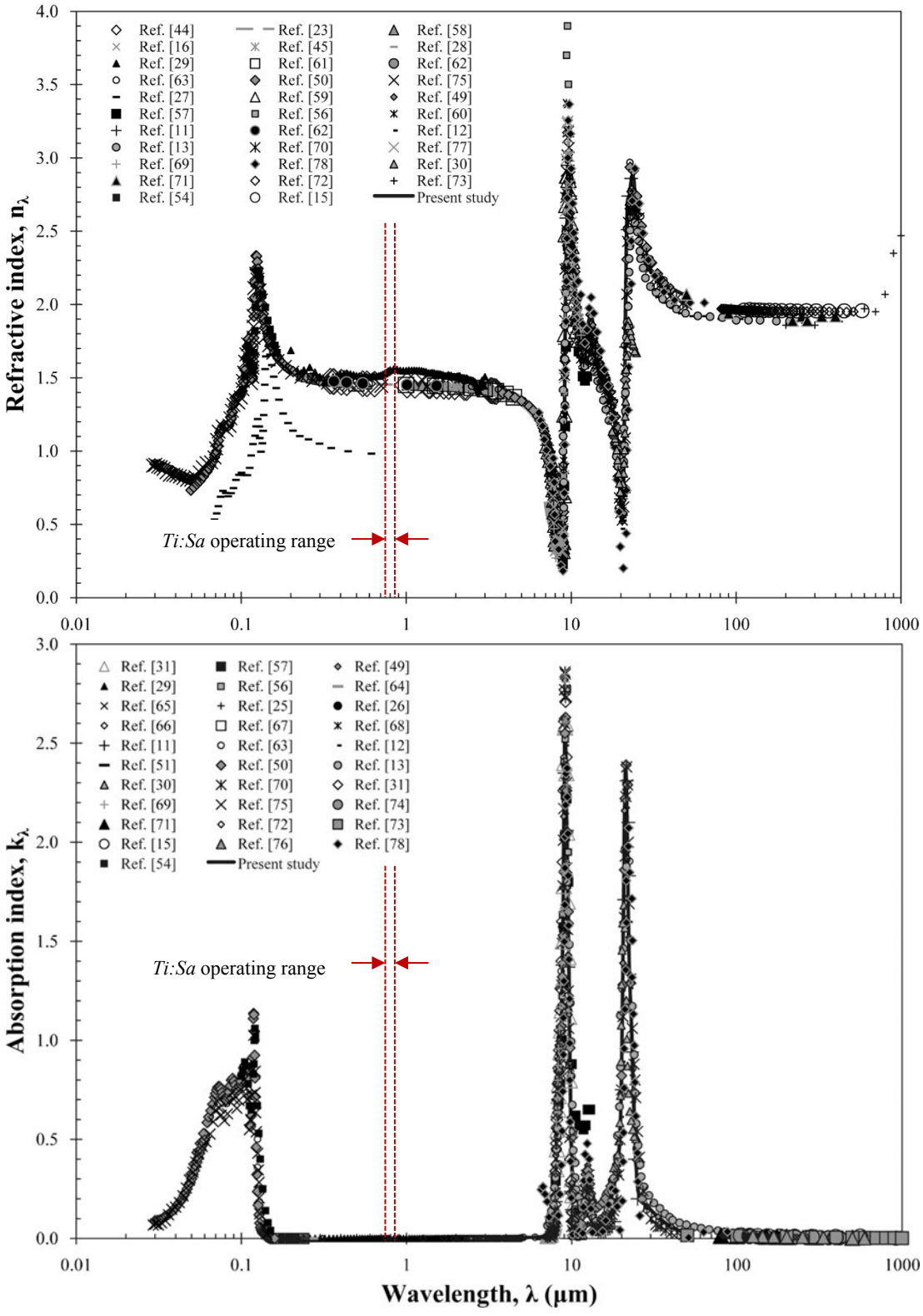

Figure-7.18: Copy of fig-1 in ref [271] showing the real (refractive index n_λ) and imaginary (absorption index, k_λ) of the complex refractive index of silica glass as function of wavelength for the 0.01 to 1000 μm range. Note the discrepancies in n_λ in the wavelength range where the Ti:Sa laser operates.

Chapter-8: Phase unwrapping for tomographic applications

8.1 Introduction

All phase-contrast optical techniques rely upon the evaluation of the phase of a fringe pattern (smooth wave-fronts) or speckled pattern, commonly known as interferograms, followed by the subsequent transformation of the latter to the parameter of interest [53, 54]. There are four main steps involved in the analysis of interferograms after the digitization of the intensity distribution as shown in the schematic diagram of figure-2.1. The first step involves the extraction of the phase (ϕ_w) by measuring the intensity as known shifts are introduced between the two interfering waves. In the next step, the phase-change ($\Delta\phi_w$) relative to some reference interferogram is calculated. In the case where the true phase-change value is slightly greater than π, the calculated value will appear to be 2π lower. In such cases, phase unwrapping is required where integral multiples of 2π are added to the phase-change values in order to remove the 2π discontinuities. Finally, in the last step the unwrapped phase map ($\Delta\phi_u$) is converted to the quantity of interest. If the sought parameter is a displacement field (u) or the extraction of the wavenumber axis (Δk) of a tuneable laser source as in our case, a simple scaling factor is required [54]. It is therefore obvious that the quality and reliability of the sought quantity highly depends on the robustness of the unwrapping algorithm used.

In this final chapter a detailed investigation on the performance of the temporal phase unwrapping algorithm used and described earlier in chapter-5 is provided. At first an overview of the temporal phase unwrapping strategies developed so far and their application is given in section-8.2. In view of the main error sources contributing towards the degradation in the accuracy of the Δk-axis being the refractive index dispersion and non-compensated residuals of intensity background artefacts owing to the multiple reflections inside the wedges, a set of new phase unwrapping strategies designed to address issues related to depth-resolved thickness measurements is provided in section-8.3. Finally in section-8.4 the ability of the different approaches to produce a more accurate and precise Δk axis is assessed by testing the accuracy with which the thickness of each of the wedges can be determined using as a reference the independent micrometer measurements. The importance of the work

presented in this chapter lies in that, to the best of the author's knowledge, this is the first time that established links between the error sources highlighted earlier in chapter-7 and phase unwrapping errors is provided.

8.2 Overview of temporal phase unwrapping strategies

Ideally, in wavelength scanning interferometry the wavelength of the source is tuned sequentially thus providing known phase shifts that are proportional to the change in wavelength. As each wavelength during the scan corresponds to a unique time instance, it becomes obvious that temporal as opposed to spatial phase unwrapping is, therefore, an appropriate strategy to use provided the signal is sampled sufficiently rapidly along the time axis.

From a historical point of view, it was in the early *90's* that *Huntley, JM* and *Saldner, H* proposed an alternative approach to the existing phase unwrapping strategies that at the time were restricted to searching the two-dimensional spatial domain for 2π discontinuities [172]. The new approach was based on a one-dimensional unwrapping strategy along the time axis, instead of the traditional two-dimensional spatial domain, thereby opening the ground to an important subclass of interferometry where the parameter of interest is phase differences as opposed to phase values [172]. Finally, as far as the applicability of the method was concerned, the authors clearly state that it is only suitable in situations where a) the phase map builds up slowly and b) where the parameter of interest is phase-changes as opposed to phase values. In other words, the gradient of the computed phase-changes should be such that:

$$|d\phi/dt| \leq \pi/\tau \ , \qquad 8.1$$

at all pixels throughout the experiment and where τ is the phase sampling interval.

It is worth noting, however, that almost a decade before the published work of [172] a similar approach was proposed in a short study by *Itoh, K* independently (compare equation-7 in [208] to equation-10 in [172]), albeit the applicability of the strategy to interferometry and in particular the transferring of the unwrapping problem from the spatial to the time domain was not highlighted.

A few years later, in an attempt to compare the success rate of two temporal phase unwrapping strategies where in the first the unwrapping was performed through a sequence of phase maps with a linear change in the spatial frequency with time and the second where only the first and last maps in the sequence were used, a new approach emerged [1]. That is, a method in which the spatial frequency is changed exponentially with time instead. The new method, termed temporal phase unwrapping using a forward exponential sequence to indicate the manner in which the fringe density is changed, was found to be superior to its linear contender [1].

In parallel to the discovery of the benefits associated with the use of the forward exponential algorithm, the same authors undertook a study on different methods aiming at reducing shape measurement errors rising from the use of four temporal phase unwrapping algorithms [211]. What follows is a brief description of the study published in [211] and the reasons for doing so will become clear shortly.

In practice measured phase values will almost always suffer from errors associated with them. Assuming that these errors are additive and of Gaussian nature, the measured sequence of unwrapped phase values is given by:

$$\Phi(t) = g(t) + \epsilon_{\phi} \ , \qquad 8.2$$

where ϵ_{ϕ} is a random variable taken from a Gaussian distribution, with a mean of zero and a standard deviation of σ_{ϕ}. On the other hand, the first term on the right hand side of equation-8.2 denoted by the letter *g* is a function of time *t* which in the case of a linear growth in fringe density becomes:

$$g(t) = \omega t \ , \qquad 8.3$$

where ω is a non-dimensional frequency that represents the rate of change in phase as a function of the non-dimensional time *t* which in other words is the slope of Φ(*t*). Note that after substituting equation-8.3 into equation-8.2 the resulting expression reduces to equation-9 in [211]. In order to reduce the error in estimating ω that would otherwise result by simply dividing the last term in the unwrapped sequence by the total number of terms in the presence of noise (see equation-10 in [211]), for the linear case, the authors proposed the use of least square fitting to equation-8.2. The proposed approach showed great improvement as far as the estimation of ω was

concerned for the linear case but very little for the case of the forward exponential algorithm. This was attributed to the fact that in the latter case, the phase values used for estimating ω were all clustered around the lower end of the Φ versus *t* plots. Naturally, these do not provide reliable estimates of the sought gradient and have therefore insignificant contribution to the least square estimate of ω. To overcome this issue, the number of fringes was decreased exponentially from a maximum value to zero instead, resulting to what is termed as 'the reverse exponential temporal phase unwrapping algorithm'. The method combined an increased reliability in unwrapping, a reduced data acquisition and processing time as well as lower number of measurement errors deeming it superior to its predecessor. This in fact is the underlying reason as to why the four wedges comprising the optical sensor developed in this thesis were designed such that their individual central thicknesses follow a reverse exponential sequence.

Last but not least, it should be noted that the non-dimensional frequency ω, mentioned earlier, practically corresponds to the thickness of each of the four wedges here. This is a rather important point in that it will form one of the two criteria used henceforth to assess the ability of the unwrapping algorithm in successfully estimating the true central thickness of the four wedges examined here; the other being the quality of the resulting spectrograms (i.e. the short-time Fourier transform method described in section-7.2.2).

Ever since its emergence as a valid method for phase measurements, the temporal phase unwrapping approach has found a wide range of applications. These include shape measurements using fringe projection methods [272-276], the study of dynamic events using high-speed phase-shifted speckle pattern interferometry [277-281], the measurement of subsurface delaminations in carbon fibre re-enforced polymers (CFRP) [282], the detection and sizing of delamination cracks in composite panels [283] and the real-time visualization of deformation fields [284] in speckle pattern interferometry as well as for stress analysis in photo-elasticity [285] to name a few. However, to the author's best knowledge, there have been no reports of phase unwrapping been used as a tool for dispersion compensation and the suppression of coherent noise induced errors [26] to date.

8.3 Dispersion and noise immune phase unwrapping

As mentioned earlier, dispersion [230-232] is one of the factors that limit the successful depth-resolved imaging of both intensity and phase. Moreover, multiple reflections inside the test sample give rise to spurious background artefacts termed 'coherent noise' [26, 89, 286-299] which in turn degrade the accuracy of phase measurements. Unlike previous studies in which appropriate filters are designed to suppress the effects of noise [89, 286-299] and refractive index dispersion [235-238], a different approach is adopted here in which links between these type of errors to phase unwrapping errors are established. As a result a group of different phase unwrapping strategies that are immune to dispersion and 'coherent noises' are investigated.

8.3.1 Initial dispersion correction considerations

One of the main assumptions to the analysis presented so far is that the dependency of the refractive index n on the instantaneous wavenumber of the light k is weak. Thus, a constant value of n = 1.4532 was assumed for the wedge material. If on the other hand, the wedge material is dispersive, a method for dispersion correction is required. One way of doing so is by modifying equation-5.28 to take account of the changing refractive index as the wavelength scan progresses. By rearranging equation-5.28, the following expression is obtained:

$$\Delta k(t,0) = \frac{\Delta\Phi_u^{i_{N_S+1},j_{N_S+1}}}{n(t)d_s^{max}f(\theta,\alpha)} - k(0)\left(\frac{n(0)}{n(t)} - 1\right), \qquad 8.4$$

where $k(t)$ and $n(t)$ denote the wavenumber and the refractive index for the t^{th} frame. According to the standard Sellmeier formula (equation-1 in ref [210]), the dependence of n on k for fused silica glass is almost linear over the wavelength range 750 to 850 nm, as was shown earlier in figure-5.20. Due to the dependency of n on k, the procedure to solve equation-8.4 is of iterative nature and is described by the following two steps. At first, the starting wavenumber, $k(0)$, and the refractive index, $n(0)$, at t = 0 are obtained iteratively through the use of equation-5.33. In the second step another iterative solution is required involving equation-8.4 in which at first $n(t)$ is assumed to be equal to $n(0)$. This allows an initial estimate for the time-varying wavenumber to be obtained according to:

$$k(t) = k(0) - \Delta k(t,0). \qquad 8.5$$

An improved estimate for $n(t)$ can then be calculated from the dispersion curve, which in turn [through equation-8.4] gives an improved estimate for $\Delta k(t,0)$, and hence for $k(t)$. In the case of the dispersion curve (see figure-5.20) used here, only five iterations are needed to achieve convergence to 11 significant figures.

8.3.2 Constant Fourier-peak re-referencing

Huntley, J.M., G.H. Kaufmann, and D. Kerr (1999) reported on a phase-shifting out-of-plane speckle interferometer operating at 1 kHz for the study of dynamic events in which phase extraction was performed using a standard four-frame algorithm (to calculate $\Delta\Phi_w$) and temporal phase unwrapping (to calculate $\Delta\Phi_u$) [277]. In their work it was pointed out that, if the deformation of the object (analogous to phase) to be measured becomes too large, the recorded speckled interferograms become completely de-correlated causing a significant increase in the noise of the calculated displacement fields. Figure-8.1(a) provides a schematic illustration of this phenomenon, where u denotes the speckle movement across the field of view of the CCD and D is the diameter of the entrance pupil. When the ratio $\rho = u / D$ is greater than or equal to unity (i.e. $u \geq D$), complete speckle decorrelation occurs, as schematically illustrated in figure-8.1(b). To overcome this issue, the authors proposed the updating of the initial reference state $t = 0$ to a new one at times $t = t_1$, t_2, t_3 etc. Figure-8.2 provides a schematic illustration of the proposed approach. The total unwrapped phase change over κ such referenced events is therefore given by the following expression:

$$\Delta\Phi_u(t,0) = \Delta\Phi_u(t,t_\kappa) + \sum_{k=2}^{\kappa} \Delta\Phi_u(t_k,t_{k-1}) + \Delta\Phi_u(t_1,0). \qquad 8.6$$

Wavelength changes can also cause speckles to move across the aperture thus making the above approach attractive for the analysis of speckle interferograms in WSI in the future. Although the analysis presented so far is not concerned with speckled interferograms but rather with the processing of the fringe patterns formed by the smooth wavefront (four-wedge sensor), an analogy can be drawn. That is, as the wavelength is tuned the position of the 2-D Fourier peak is gradually shifted and is, therefore, necessary to update the frequency at which the phase is evaluated after several wavelength increments. Strictly speaking this would be necessary regardless of whether the wedge material is dispersive or not. However, in the presence of dispersion an additional phase-term owing to the change of the refractive index as a

function of the wavelength will cause the computed phase-change to change faster than expected. Although, to date, there has been no reports on the actual relation between the position of the spectral peak position and its associated phase, the study by *Huntley, J.M. and H.O. Saldner* (1997) on error-reduction methods for shape measurements by temporal phase unwrapping suggested that it is of direct nature (visual comparison of fig.6 (b) to fig.6 (e) in ref [211]). In other words, a shift in the frequency at which the Fourier peak appears is directly encoded in the phase calculated using equation-6.3. Assuming that this holds true it follows that the change in phase due to the change in the refractive index is also encoded at the location of the Fourier peak. Therefore, the periodical updating of the frequency at which the Fourier peak appears and the phase estimated provides an effective way of correcting for phase errors caused by both the gradual drift owing to the changes in wavelength and dispersion.

With this in mind, the total unwrapped phase change for each of the four synthetic wedges considered here over κ such re-referenced phase maps is given by:

$$\Delta\Phi_u^{i,j}(t,0) = \Delta\Phi_u^{i,j}(t,t_\kappa) + \sum_{K=2}^{\kappa}\Delta\Phi_u^{i,j}(t_K,t_{K-1}) + \Delta\Phi_u^{i,j}(t_1,0), \qquad 8.7$$

where the superscripts *i,j* are used to denote the synthetic wedges as usual and K = 2,3,..κ. In the analysis presented so far an interval between re-referencing events of 400 frames (equivalent to approximately a 1 nm change in wavelength) was used. However, the time frequency analysis (TFA) results presented earlier, suggest that the approach adopted so far is not capable of resolving the issue. For this reason, a number of the assumptions made so far will be re-visited in the sections to follow and a more accurate treatment of dispersion will be given with emphasis on temporal phase unwrapping.

8.3.3 Performance of 1-D cost function for R_m optimization

One of the main observations revealed by the time frequency analysis so far was the violent fluctuation in the optimum wedge thickness ration R^{opt}. In this section the performance of the 1-D cost function used to estimate this ratio is examined. In brief, the optimised *R*-ratio in section-7.2.3 (refer to figure-7.5) was determined for the first unwrapping step by repeating the unwrapping process described earlier (see chapter-5) for a range of *R* values spanning the 9.5 to 11.5 region in steps of 0.001 for each

of the eighty two sections of the data sequence. The results of this process were stored in a 2×2 matrix where each row corresponded to the unwrapped phase change values for a unique *R*. An additional two-dimensional matrix was also stored in memory with each row containing the scaled version (by *R*) of the lower sensitivity phase change data. The data contained in each of the rows of the two matrices were then used to perform the 1-D optimisation through equation-5.30 and the *R* value corresponding to minimum RMSE between $R\Delta\Phi_u^{1,2}$ and $\Delta\Phi_u^{2,3}$ was chosen as the optimum for each of the scan sections. However, as it was pointed out earlier in section-7.2.3, even though the optimum ratio was used, in some cases, the unwrapped phase change $\Delta\Phi_u^{2,3}$ still suffered from phase unwrapping errors (recall figure-7.3(b) and figure-7.4(b)). Considering that the test was only performed for the first of the four unwrapping steps in each of which the previously unwrapped phase change is further amplified to help unwrap the next, higher sensitivity change, raises the concern that a significant number of unwrapping errors in the final phase change signal may originate from this process. Moreover, the optimization strategy used so far does not account for the presence of unwrapping errors, raising an additional concern as to how accurate the estimation of the optimum *R*-ratio is. It is therefore imperative to further investigate the issue and ensure that the signal is free from phase unwrapping errors owing to the incorrect choice of the optimum *R*-ratio.

Recall that the original assumption of the temporal phase unwrapping strategy used in this work was that a wrapped phase value Φ_A can be unwrapped using another phase value Φ_B that is notionally the same value but typically contains a higher noise level through the use of equation-5.21 (originally reported in ref [1] – eqn.3). Although here we are concerned with phase changes the principle idea remains the same with the only difference that the reference phase change is amplified by the ratio *R* (recall equation-5.24). As mentioned earlier, phase unwrapping refers to the process of adding the correct multiple of 2π to a phase signal that is wrapped in the region between -π and π. In the unwrapping operator $\mathcal{U}(\Delta\Phi^{2,3}, R \times \Delta\Phi^{1,2})$ defined earlier by equation-5.21, which is used to subtract the integral multiple of 2π from the wrapped phase change value $\Delta\Phi^{2,3}$ such that $\Delta\Phi^{2,3} - R \times \Delta\Phi_u^{1,2}$ lies within the range -π to π , NINT denotes a rounding operator which was implemented using the round function in the MATLAB programming language. It is, therefore, likely that

the amplified noise levels in the reference phase change $R \times \Delta\Phi_u^{1,2}$ are responsible for the appearance of phase unwrapping errors in places where there should not be any.

To examine the significance of the above observations, an additional check to the existing algorithm was introduced. At first the two dimensional matrix, $\boldsymbol{N^{m\times n}}$, containing the unwrapped phase change $\Delta\Phi_u^{2,3}$ for the different R values was loaded into the memory, where m is the number of rows and is equal to the number of different R values and n is the number of columns that is equal to the length of the scan section examined. The adjacent entries of each row were then compared, and in places where the difference was greater or equal to 2π, the difference between the adjacent entries of matrix, $\boldsymbol{M^{m\times n}}$, corresponding to the scaled by the R-ratio reference phase change was also taken, such that if the condition:

$$\begin{matrix} \left|\Delta\Phi_u^{2,3}(t-1,0) - \Delta\Phi_u^{2,3}(t,0)\right| \geq 2\pi \\ \left|R \times \Delta\Phi_u^{1,2}(t-1,0) - R \times \Delta\Phi_u^{1,2}(t,0)\right| < \pi \end{matrix} \quad , \qquad 8.8$$

is satisfied, the relevant entry on the unwrapped phase change is replaced by NaN:

$$\Delta\Phi_{\tilde{u}}^{2,3}(t,0) = NaN, \qquad 8.9$$

indicating that an unwrapping error has occurred due to the amplified noise levels in the reference phase change $R \times \Delta\Phi_u^{1,2}(t,0)$ which in turn can cause the incorrect estimation of the multiple of 2π (round operation in equation-5.21) that is necessary for the successful unwrapping of $\Delta\Phi_u^{2,3}(t,0)$. The outcome of this process is a new two dimensional matrix $\boldsymbol{L^{m\times n}} = \Delta\Phi_{\tilde{u}}^{2,3}(t,0)$ with the same dimensions and number of rows m and of columns n as previously but with its entries replaced by `NaN` in places where a phase jump of greater or equal to 2π occurs due to noise. Note that the ~ in equation-8.9 is used to denote the updated unwrapped phase change. The above constitutes a rather important achievement in that the strategy described thus far provides an easy way to distinguish between phase jumps that are due to noise in the signal to those arising from the wavenumber jumps that would otherwise be difficult to do so.

In the second and final step, the optimisation of the R-ratio is once again performed through the use of the 1-D cost function described by equation-5.30, as before, with

the only difference being that any of the rows in $\boldsymbol{L^{m\times n}}$ containing `NaN` entries and thus the corresponding *R* values are discarded from the process. It should be noted that the algorithm that performs the above steps is repeated until all sections of the scan are checked. Figure-8.3 provides a schematic of the flowchart for the modified optimisation algorithm implemented here.

In order to validate the proposed approach the same test as that described earlier in section-7.2.3 for the first unwrapping step is performed only for much longer scan sections. The reason for doing so is to ensure that the rms deviation between the reference phase change, $R \times \Delta\Phi_u^{1,2}$, and the unwrapped phase change, $\Delta\Phi_{\tilde{u}}^{2,3}$, approaches that of a random variable with uniform probability density function over the range -π to π, which is π/3, if the *R* value is chosen incorrectly. Consequently, the full ~100 nm scan of 48970 frames was divided into ten equal sections, as opposed to the previous eighty two segments, of 4897 frames long each (equivalent to approximately 12 nm). After the implementation of the modified 1-D cost-function optimisation procedure used for the estimation of the optimum *R*-ratio for each of the segments, the temporally unwrapped reference phase change $\Delta\Phi_u^{1,2}(t,0)$ was scaled using the optimum *R*-ratio for the first and fourth segments and the result was plotted onto the same graph to provide a visual comparison of the effect of changing *R*. In addition to that, the reference phase-change, $R_{opt}^1 \times \Delta\Phi_u^{1,2}(t,0)$, where the superscript 1 denotes the optimum *R*-value for the first segment of the scan, $t \in [1,4897]$, was used to unwrap the phase-change $\Delta\Phi_w^{2,3}(t,0)$ for the same *t*. The resulting unwrapped phase-change, $\Delta\Phi_{\tilde{u}}^{2,3}(t,0)$, was then plotted on the same graph to aid comparison (see figure-8.4(a)). The process was repeated but this time for the fourth segment of the scan where $t \in [19588,24484]$. Once again, the reference phase change was scaled up by the optimum ratios for the first and fourth segments with the only difference that this time the unwrapping of $\Delta\Phi_w^{2,3}(t,0)$ was performed using $R_{opt}^4 \times \Delta\Phi_u^{1,2}(t,0)$ instead and the results were plotted on the same graph as shown in figure-8.4(b). Last but not least, the optimum values of *R* were extracted and were subsequently plotted for each of the ten scan segments (W_n = 1, 2, .., 10) as it is illustrated in figure-8.4(c).

By comparing figure-8.5(a) to its equivalent for a shorter scan section figure-7.3(a), which did not include the modified algorithm described earlier, it is evident that the

behaviour of the phase signals is similar albeit the drift amongst them is now much smaller. A similar conclusion can be drawn by comparing figure-8.4(b) with figure-7.4(b). However, the phase unwrapping errors in $\Delta\Phi_u^{2,3}(t,0)$,that were previously present in figure-7.4(b), have now been fully supressed as illustrated in figure-8.4(b), suggesting that a clear improvement in the signal processing has been achieved. Moreover, the violent fluctuations in *R*, depicted in figure-7.5, are now significantly reduced as shown in figure-8.4(c).

As mentioned above, after the implementation of the modified algorithm the gap amongst the three phase change signals shown in figure-8.4(a) and figure-8.4(b) appears to be much smaller and in many cases insignificant. Considering that this is likely due to the much larger section examined here, a zoomed version showing a 1000 frame subsection towards the end of the section of figure-8.4(a) and figure-8.4(b) is shown in figure-8.5(a) and figure-8.5(b) respectively, confirming its presence. In contrast to the behaviour revealed by figure-7.3(a) and figure-7.4(b) earlier, the red line showing the unwrapped phase change $\Delta\Phi_u^{2,3}(t,0)$ in figures 8.5(a) and 8.5(b) always follows closely the temporally unwrapped and scaled by the optimum ratio for that section of the scan reference phase change $R_{opt}^{i} \times \Delta\Phi_u^{1,2}(t,0)$ (the green line for which $R_{opt}^{i} = R_{opt}^{1} = 10.264$ in the case of figure-8.5(a) and the blue line $R_{opt}^{i} = R_{opt}^{4} = 10.38$ in the case of figure-8.5(b)) ,which in turn further justifies the improvement in the data analysis by the modified algorithm.

In order to examine the effect of the aforementioned improvements to the data quality from the four wedge sensor the short time Fourier transform (STFT) tool, that was previously developed in section-7.2.2 with the same parameters, was once again employed. The resulting spectrograms for the raw intensity data from wedges one and two are shown in figures-8.6(a) and figure-8.6(b) ,while those corresponding to the intensity data from wedge three and four are shown in figure-8.8(a) and figure-8.8(b) respectively.

Considering the improvements introduced by the modified algorithm presented in this section, it would be reasonable to expect that the improvements would also be captured by the spectrograms in figure-8.7 and figure-8.8. Surprisingly, this clearly is not the case. By comparing figure-8.7(a) to figure-7.1(a) and figure-8.7(b) to figure-7.1(b), it is obvious that a strange '*zero*' structure is now present. In what is more, a

curious '*ghost*' spectral line just above $k_t = 1.5$ appears in the spectrograms for the intensity data of wedge three and four that was not present before (compare figure-8.8(a) to figure-7.2(a) and figure-8.8(b) to figure-7.2(b)).

In brief, although the unwrapping errors that were previously present in the phase change signals have been practically eliminated for the first unwrapping step the spectrogram quality appears to have degraded. One possible reason to explain the structure in the spectrograms may be that additional unwrapping errors, in steps two and three of the unwrapping strategy where $\Delta\Phi_{\tilde{u}}^{3,4}(t,0)$ and $\Delta\Phi_{\tilde{u}}^{1,5}(t,0)$ are estimated, creep in. As the wavenumber-change axis (Δk), used to resample and re-register the intensity distribution that is in turn used to perform the STFT, practically relies on the accuracy of $\Delta\Phi_{\tilde{u}}^{1,5}(t,0)$, it is possible that the presence of unwrapping errors for reasons that have not been addressed yet, cause distortions in Δk that are consequently responsible for the artefacts in the spectrograms. The following sections provide an in-depth investigation as to whether the above assumption holds true followed by methods of suppressing the curious structure in the spectrograms.

8.3.4 Adaptive Fourier-peak re-referencing

One of the main issues presented with analysis so far is that it has proven difficult to distinguish between phase unwrapping errors and phase jumps owing to the laser induced mode hops. In this section, an attempt to shed light into this area is provided starting with a simple thought experiment and followed by an improved strategy that establishes clear links with physical phenomena that are most likely to be responsible for the signal degradation mentioned in the previous section.

Consider the simple case where the reference phase change $R_m(W_n) \times \Delta\Phi_u^{i,j}(t,0)$ is free of the phase jumps caused by the laser mode hops. Note that *m* takes the value of one, two or three denoting the unwrapping step, Wn = 1, 2,…10 is a window containing all the *t* values corresponding to the segment of the scan examined and *i,j* are the usual indices denoting the wedges forming the synthetic wedge in question. As seen earlier, even though the violent fluctuations in *R* have been considerably reduced a relative amount of variation in *R* is still present in the unwrapped phase signal, suggesting that *R* is a slowly varying function of time. In the absence of any other non-linearities the reference phase signal would be a linear function of the non-

dimensional time index t with a gradient, $d\Phi/dt$, that is directly linked to the ratio R_m. Figure-8.8 provides a schematic illustration of such case showing the reference phase change $\Delta\Phi_u^{1,2}(t,0)$ scaled by the optimum ratios for two different segments of the scan.

In the analysis presented so far the fluctuations in R were handled by taking the average value of the optimized R values for each of the scan sections. The approach seemed to produce reasonable results and was therefore carried over to this point. However, one concern that has been overlooked is that the rounding operation for the estimation of the R value used to perform the unwrapping of the phase change signal may be responsible for phase unwrapping errors that are not captured by the approach adopted. As it is seen from the schematic illustration in figure-8.8, for the ideal case scenario described above, the deviation between the two linear graphs can be described by the error quantity ε_ϕ defined such that:

$$\begin{aligned} \varepsilon_\phi &= \left|\varepsilon_R \times \Delta\Phi_u^{1,2}(t,0)\right| \\ \varepsilon_R &= \left|R^{opt}(W_n=2) - R^{opt}(W_n=1)\right| \end{aligned}. \qquad 8.10$$

By comparing equation-8.1 to equation-8.10 it becomes obvious that the error quantity ε_ϕ is equivalent to the term on the left hand side of equation-8.1; that is the rate of change of phase with respect to time. Consequently, for the unwrapping operation to be successful, i.e. to avoid 2π oscillations, the following condition must be satisfied at all times:

$$\varepsilon_\phi \leq \pi. \qquad 8.11$$

Now, let the optimum R-ratio for the first scan segment be equal to 10.3 and that of the second to be equal to 10.1 such that: $R^{opt}(W_n=1)=10.3$ and $R^{opt}(W_n=2)=10.1$. Considering the relatively small fluctuation in the R ratio after the implementation of the modified algorithm described earlier, this is a reasonable assumption for the theoretical case investigated here. With this in mind, the aforementioned condition described by equation-8.11, reduces to the following simple expression:

$$\Delta\Phi_u^{1,2}(t,0) \leq 10\pi/2 \cong 15\,rad. \qquad 8.12$$

The condition described by the inequality-8.12 is of course applicable to the first unwrapping step. However, it is straight forward to show that the generalised condition is described by the following expression:

$$\Delta\Phi_u^{i,j}(t,0) \leq \pi/\left|R_m^{W_n} - R_m^{W_n+1}\right|, \qquad 8.13$$

where, m is the unwrapping step and W_n is the section of the scan. One way of implementing the above condition into the temporal phase unwrapping strategy developed so far would be by the periodical updating of the optimum R ratio such that the inequality-8.13 is satisfied for all $t \in [1,48970]$. To do so would require a robust algorithm to estimate the gradient of the phase signals in question which in the presence of the phase jumps owing to the laser mode hops could prove cumbersome and computationally expensive to achieve. Instead a slightly different approach is adopted in the analysis that follows.

In section-8.3.2 an approach of compensating for the phase shifts owing to the dependency of the refractive index on the instantaneous wavelength of the light emitted by the broadband tuneable laser source was proposed. The approach was based on the assumption that the corresponding instantaneous location of the main Fourier peak after the 2-D Fourier transformation of the fringe patterns from the four wedge sensor is directly linked to the sought phase quantity at that peak. Therefore, the periodical updating of the frequency, at which the Fourier peak appears, provides an easy way of compensating for phase errors due to the wedge sensor consisting of a dispersive material. The proposed technique was implemented through the use of equation-8.7 with an updating rate of 400 frames. The choice for that particular re-referencing rate was based on the assumption that the material (optical fused silica glass) used to manufacture the four wedges is the same for all four of them and, therefore, their dispersion curves should be identical. Furthermore, the refractive index behaviour of such material as a function of wavelength, in the wavelength spectrum that the laser is operating on, has been shown to be of the linear nature with its nominal value changing by as little as 0.0019 units over the 750 to 850 nm tuning range (recall figure-5.20 and ref [210]).

As was shown earlier in section-7.3.3, the estimated behaviour of the refractive index trends for the four wedges and the resulting three synthetic wedges, recall figure-7.15

and figure-7.16 respectively, deviates significantly from the assumed linear behaviour. This however, is most likely to be caused due to the fact that the refractive index change trends are plotted versus the non-dimensional time index *t* as opposed to the wavelength change ($\delta\lambda$) or the wavenumber change (δk). Although *t* is in fact associated with λ and *k* the mode hops present in the scan randomise the latter and therefore provide a possible explanation of the unexpected non-linear behaviour. One way of reducing the aforementioned non-linearity would of course be to sort the *t* values using the sorting vector *J* obtained earlier (see section-6.3.1). However, a more important observation is that the gradient of these trends is considerably different suggesting that there is a mismatch amongst the refractive index dispersion curves for the four wedges. As mentioned earlier (see section-7.3.5), one possible explanation to justify such a scenario could be that the four wedges were manufactured from different batches and thus have a slightly different behaviour. Assuming that this is the case, the remainder of this section is dedicated to developing a robust algorithm that is capable of accounting for such discrepancies that may well be the reason as to why the quality of the spectrograms (recall figure-8.6 and figure-8.7) appears to suffer from the '*zero*' like structure for all four wedges and the ghost line above the line $k_t = 1$, for wedges three and four.

In order to investigate whether the difference in the gradients of the refractive index change trends is indeed responsible for the signal degradation, a modified algorithm that is capable of accounting for these is pursued. Recalling that the plots describing the behaviour of the refractive index change for the four wedges are practically linked to the instantaneous location of the 2-D-Fourier peak $k_r^i(t)$, equation-8.7 can be modified such that the updating of the frequency at which the phase is evaluated for each of the four wedges is different but coincident to the gradient of the plots illustrated in figure-7.13 and figure-7.14 respectively. Consequently and in contrast to the constant peak re-referencing approach described earlier in section-8.3.2 the new algorithm is of an adaptive nature. Although introducing the adaptive re-referencing approach described above into equation-8.7 may at first seem tricky this can be easily achieved by the following expression:

$$\Delta\Phi_u^{i,j}(t,0) = \Delta\Phi_u^{i,j}\left(t, t_\kappa^{i,j}\right) + \sum_{K=2}^{\kappa} \Delta\Phi_u^{i,j}(t_K, t_{K-1}) + \Delta\Phi_u^{i,j}(t_1, 0), \qquad 8.14$$

where the superscript and subscript indices are the same as in equation-8.7. Note that the only difference between equation-8.7 and equation-8.14 is that the indices *i,j* are now applied to t_κ in order to account for the bias that may well be different due to the fact that the phase signal calculated is the synthesis of two phase signals which are individually estimated with different updating rates. As a consequence, and in contrast to equation-8.7 where t_K was regularly spaced, t_K is now irregularly spaced.

As far as the implementation of the modified adaptive peak re-referencing rate algorithm is concerned, a new threshold value is introduced that is based on the non-integer pixel spatial location of the 2-D-Fourier peak in the frequency domain such that if:

$$\delta k_r^i(t,0) \geq c_\tau \begin{cases} k_r^i(t) = k_r^i(t_K), K = 2,3..\kappa \\ t = 0 \end{cases}, \qquad 8.15$$

where i = 1,2,3,4 depending on which wedge is examined. In other words, each time the change in the peak position $\delta k_r(t,0)$ becomes greater or equal to the threshold c_τ (in units of pixels in the Fourier-domain) the frequency at which the phase is evaluated is updated. Once the re-referencing event has taken place the t value is reset to zero and the process is repeated until the entire t-range in the scan is covered and the necessary phase signals are computed.

In order to demonstrate the ability of the new approach to resolving the issues related to the quality of spectrograms a set of three different threshold values were chosen such that c_τ = 0.06, 0.045 and 0.005 pixels. Figures: 8.9 to 8.11 illustrate the time instances at which the peak re-referencing occur for the three c_τ values chosen. In the analysis to follow and before the visual inspection of the corresponding spectrogram quality, the simple test that involves the unwrapping of the phase signal $\Delta\Phi^{2,3}(t,0)$ using the optimum R-ratio for two different scan segments (the first and fifth segments in the following comparisons) is also employed so that:

a. it is ensured that the sought phase signal in the first unwrapping step remains free of unwrapping errors after the implementation of the adaptive updating of the Fourier-peak location,

b. the behaviour of the resulting plots is not affected by the modified algorithm, i.e. the unwrapped phase signal is always following closely the corresponding amplified signal $R\times\Delta\Phi^{1,2}(t,0)$ used to perform the unwrapping,
c. and finally in order to provide a visual tool of observing the impact of the new algorithm on the optimised *R*-ratio values for the ten different scan sections.

Figure-8.12 illustrates the above for Case-*A* in which $\delta k_r = c_\tau = 0.6$ pixels and confirms that the implementation of the modified algorithm does not induce any unwrapping errors in the phase signals. That being said the difference between the optimum *R* values for the first and fifth segments is rather small making it difficult to spot any differences amongst the signals as it is clearly indicated by the enlarged plots shown in figure-8.13. On the other hand, as far as the spectrogram quality is concerned, for the data of wedge-1 see figure-8.14(a) a significant improvement is observed when compared to figure-8.6(a) in that the '*zero'* like structure appears to have been suppressed. Unfortunately this is not the case for the rest of the wedges as illustrated in figure-8.14(b), figure-8.15(a) and figure-8.15(b) with the ghost line above $k_t = 1$ appearing more clearly.

To investigate as to whether any further improvement can be achieved the same tests are performed for *Case-B*, in which $\delta k_r = c_\tau = 0.45$ pixels, where the rate at which the updating is slightly faster. Once again the phase signals in figure-8.16 and figure-8.17 show no signs of phase unwrapping errors albeit their deviation from one another is now much more evident owing to the more significant difference between the optimum *R* values for the two scan segments. Although this behaviour was expected, the plots still follow closely each other and it is only after approximately 2,500 frames that the expected drift becomes apparent. Last but not least the slightly faster updating rate appears to have affected positively the spectrogram quality. More specifically, both spectrograms for wedge one and two appear to have improved with the zero artefacts almost eliminated as shown in figure-8.18(a),(b). Moreover, and although the ghost lines are still present for the spectrograms corresponding to the intensity data for wedges three and four (see figure-8.19(a),(b)), the main spectral lobe represented by $k_t = 1$ is more consistent and with less peak-splitting (*'zero'* structure).

For the last *Case-C* in which $\delta k_r = c_\tau = 0.05$ pixels, for which the rate of Fourier-peak updating is now considerably faster than in the previous two cases, the behaviour of the phase signals is once again free of unwrapping errors as expected (see figure-8.20(a),(b)). Furthermore, the unwrapping process seems to be insensitive to the deviation between the *R*-ratio values (a change of 0.025) used to obtain the unwrapped phase $\Delta\Phi^{2,3}(t,0)$, suggesting that it is only sensitive to changes in *R* of the order of one decimal place or more. This is verified by the enlarged plots shown in figure-8.21. However, on closer inspection of the latter small unwrapping errors start to appear at $t \sim 3500$ and $t \sim 4200$ in figure-8.21(a) and between $t = 2.33\times10^4$ and $t = 2.34\times10^4$ and $t = 2.35\times10^4$ and $t = 2.36\times10^4$ in figure-8.21(b) that cause the unwrapped phase signal to deviate slightly from its corresponding scaled version of the reference phase signal $R\times\Delta\Phi^{1,2}$. Recalling that in the original publication [277], where the updating of the reference speckle pattern was proposed as a method to suppress errors induced by large speckle motion, the authors suggest that too frequent updating induces bias and noise errors it is likely that the occurrence of these unwrapping errors is due to approaching this limit. For this reason, $c_\tau = 0.05$ pixels will constitute the last value examined here.

By visually inspecting figure-8.22 and figure-8.23, it is clear that the quality of the resulting spectrograms for this last case is clearly superior in that almost all artefacts are now suppressed suggesting that the adaptive peak re-referencing approach implemented here is an effective way of dealing with the potential mismatch in the refractive index dispersion curves amongst the four wedges. One concern with the proposed approach is that it is unable to suppress the presence of the *'ghost'* line shown in figure-8.23(a) and (b). Although at first sight one might ascribe this artefact to a frequency component owing to the multiple reflections in some physical component like the camera cover slip [26], the fact that it is only present in the spectrograms for the intensity data of wedge three and four as well as the fact that its location is not constant (its location moves towards $k_t = 1$ as the rate of updating is increased) for the three case studies presented here, rules out this explanation.

As mentioned earlier, the three-step unwrapping process described so far involves the scaling of an unwrapped yet noisy phase signal that is subsequently used for the unwrapping of a phase signal with higher sensitivity. In view of the variations in the

optimum R, an average value obtained by taking the mean of the optimum R values for each of the ten scan segments is used instead. In order to demonstrate the effect of the adaptive algorithm proposed here and its influence on the choice of R, the reference phase signal $\Delta\Phi^{1,2}(t,0)$ used for the first unwrapping step is scaled by the three different average R-ratios corresponding to the three different rates of updating. Figure-8.24 illustrates the behaviour of these phase signals for three different sections of the scan: a) $\forall t \in [0,4000]$, b) $\forall t \in [6000,10000]$ and c) $\forall t \in [3.95 \times 10^4, 4.35 \times 10^4]$ corresponding to the start, middle and the end of the scan sequence. Interestingly, the three signals are almost identical for the first 2,500 frames and it is only before the first downward laser induced jump that they start to deviate from each other as shown in figure-8.24(a). The deviation amongst the three signals is more evident in the mid and end scan sections as shown in figure-8.24(b) and (c), with the signal corresponding to the more frequent updating (black line) showing a reduced number of phase jumps compared to the other two (blue and red lines).

Finally, in figure-8.25 the RMSE (ε_{rms}) between the averaged R used for each of the three cases of c_τ and for each of the three unwrapping steps and the optimum R for each of the scan segments is shown, thereby providing a good indication as to where the estimated phase signals may suffer from numerical errors due to the averaging in R.

To conclude, the adaptive Fourier-peak updating approach appears to have resolved the majority of issues related to the quality of the spectrograms compared to that using the constant re-reference approach described in the previous section, although a numerically-induced artefact appeared in the shape of a ghost line above the line $k_t = 1$ that represents the location of the main spectral lobe. An analysis of the possible reasons that may give rise to this artefact and methods to suppress it will be given in the forthcoming section.

8.3.5 Phase unwrapping along the sensitivity direction

As clearly illustrated by the spectrograms in figure-8.23(a), and (b), the main issue with the adaptive Fourier-peak re-referencing method is that it suffers from what appears to be numerically induced artefacts that manifest themselves in the form of ghost lines. One possible reason for their appearance may be due to unresolved residual phase unwrapping errors that distort the sought Δk axis and therefore give

rise to these artefacts. In fact, and although the segmented unwrapping process for the first step seems to be completely free of these errors this may not necessarily be the case when the relevant averaged *R*-ratio is used for the unwrapping of the entire sequence. It is therefore possible that the accumulation of these residual unwrapping errors as the unwrapping of the higher sensitivity signals is progressing is in fact responsible for the ghost lines that appear around k_t = 1.5 for the spectrograms of wedges three and four.

In order to justify as to whether this is the case, the reference phase signal and the unwrapped phase signal are plotted for all three unwrapping steps and for c_τ = 0.05 pixels. As the data sequence is long and would be difficult to identify problematic areas, the RMSE plot in figure-8.25(a) is used as a guide to select three sections of the scan that are likely to contain unwrapping errors. These are situated at approximately W_n= 2, 6 and 9 in 8.25(a) where the deviation between the average *R* for the first unwrapping step and the optimum *R,* at that section of the scan, is at its maximum. The idea behind this approach is that if indeed the selected areas for the first unwrapping step contain 2π errors, these will in principle be carried to the next step and so on, thereby contaminating the highest sensitivity phase signal used to calculate the Δk axis.

As expected, all three of the chosen scan segments for the first unwrapping step contain a significant number of unwrapping errors as shown by the red lines depicting the unwrapped phase change $\Delta\Phi_u^{2,3}(t,0)$ in figure-8.26(a), figure-8.26(b) and figure-8.26(c). Figures-8.27(a)-(c) show the equivalent plots for the same three sections but for the second unwrapping step in which the previously unwrapped phase change $\Delta\Phi_u^{2,3}(t,0)$ is now scaled up and used as the reference to unwrap the higher sensitivity signal $\Delta\Phi_u^{3,4}(t,0)$. Once again the unwrapped signal seems to contain a large number of 2π phase jumps for all three sections. Unlike in the first step where the 2π discontinuities caused the unwrapped phase change (red line) to significantly deviate from the reference phase change (black line), in this step the two plots appear to follow each other more closely. This is however likely to be a result of the much wider phase range for the vertical scale which now spans over 250 rad in each case, or ca. 40× 2π phase jumps. The same behaviour is observed in figures-8.28(a)-(c) for the third and final unwrapping step. With this in mind, it

becomes obvious that a method of suppressing the errors in the first, and possibly also subsequent unwrapping steps, is likely to resolve the issue.

In simple terms, the main cause of the remaining unwrapping errors appears to be that over long time intervals, a gap starts to open up between the scaled low-sensitivity phase signal and the high sensitivity phase signal. This may be due to a small error in the value of R, or indeed small changes in R with wavelength due to different dispersion curves for the two pairs of wedges. By re-zeroing the phase change at regular intervals, and then subsequently adding up the re-referenced phase changes, the total phase change since the start of the scan can thus be computed but without the 2π phase errors that occurred previously.

The new unwrapping approach is somewhat similar to the '*constant'* and the '*adaptive Fourier-peak updating*' algorithms described earlier, in that it also involves updating. It does however differ from the latter in that the quantity that is being updated is now the phase itself as opposed to the spatial frequency components at which the phase is evaluated, hence justifying the name of phase unwrapping along the sensitivity axis. Moreover, and in contrast to the previous two algorithms which were based on the constant or adaptive re-referencing of the location of the instantaneous 2-D-Fourier peak of the signal corresponding to each of the four wedges, in this approach it is the phase change of the synthetic wedges that is updated instead.

A schematic illustration of the principal idea for the modified strategy that involves the regular and equally spaced updating of the phase change signals is shown in figure-8.29. One of the key aspects related to this approach is that the last and first element of adjacent sections is shared. These data points coincide with the instances at which the updating takes place and are consequently acting as pivot points that are in turn used to compensate for any changes in the nominal value of the gradients between adjacent scan segments.

As the direct derivation of the mathematical expressions that describe the new strategy is a little cumbersome to achieve, these will be first derived for the first unwrapping step that involves the pair of wedges $(i_2,j_2) = (2,3)$ and $(i_1,j_1) = (1,2)$ and will be generalized later. In the original temporal phase unwrapping algorithm

described in chapter-5, the unwrapped phase change for the higher sensitivity synthetic wedge (i_2,j_2) was calculated through the use of:

$$\Delta\Phi_u^{i_2,j_2}(t,0) = \mathcal{U}\{\Delta\Phi^{i_2,j_2}(t,0), R_1\Delta\Phi_u^{i_1,j_1}(t,0)\}. \quad 8.16$$

Note that equation-8.16 is practically identical to equation-5.20 but has been repeated here to aid the derivation of the necessary expressions. As mentioned above, in the new algorithm the same operation is performed only this time in a piecewise manner. In other words, the two phase change signals are first segmented before equation-8.17 is employed. To do so, a new threshold value that determines the length of each of the scan segments needs to be defined such that each time that:

$$c_\psi = \varrho, \quad 8.17$$

the counter t is reset to zero and the reference instance with respect to which the relevant phase changes are computed is updated to the last element of the segment, with c_ψ being the new threshold equal to a user defined constant ϱ such that:

$$2 \leq \varrho \leq N, \quad 8.18$$

and where N is used here to denote the total number of frames recorded by the CCD. Consequently, the unwrapped phase change $\Delta\Phi_u^{i_2,j_2}$ for a segment other than the first can be expressed as follows:

$$\Delta\Phi_u^{i_2,j_2}(t,t_\Psi) = \mathcal{U}\{\Delta\Phi^{i_2,j_2}(t,t_\Psi), R_1\Delta\Phi_u^{i_1,j_1}(t,t_\Psi)\}. \quad 8.19$$

where Ψ = 2,3,..ξ. Note that the phase change after the Ψ^{th} re-referencing event is given by:

$$\Delta\Phi^{i,j}(t,t_\Psi) = \Delta\Phi^{i,j}(t,0) - \Delta\Phi^{i,j}(t_\Psi,0), \quad 8.20$$

where the superscripts i,j take the value of i_1,j_1 or i_2,j_2 for the first and second terms inside the curly brackets on the right hand side of equation-8.19. It follows that after ξ such referenced events the total unwrapped phase change is given by:

$$\Delta\Phi_u^{i_2,j_2}(t,0) = \Delta\Phi_u^{i_2,j_2}(t,t_\xi) + \sum_{\Psi=2}^{\xi}\Delta\Phi_u^{i_2,j_2}(t_\Psi,t_{\Psi-1}) + \Delta\Phi_u^{i_2,j_2}(t_1,0). \quad 8.21$$

Similarly, the generic expressions for the m^{th} unwrapping step are given by the following set of equations:

$$\Delta\Phi_u^{i_{m+1},j_{m+1}}(t,t_\Psi) = \mathcal{U}\{\Delta\Phi^{i_m,j_m}(t,t_\Psi), R_m\Delta\Phi_u^{i_{m-1},j_{m-1}}(t,t_\Psi)\}$$
$$\Delta\Phi^{i_m,j_m}(t,t_\Psi) = \Delta\Phi^{i_m,j_m}(t,0) - \Delta\Phi^{i_m,j_m}(t_\Psi,0) \qquad .8.22$$
$$\Delta\Phi_u^{i_m,j_m}(t,0) = \Delta\Phi_u^{i_m,j_m}(t,t_\xi) + \sum_{\Psi=2}^{\xi}\Delta\Phi_u^{i_m,j_m}(t_\Psi,t_{\Psi-1}) + \Delta\Phi_u^{i_m,j_m}(t_1,0)$$

It is worth noting that the idea behind the approach described above emerged as a tool to suppress the gradual *'drift'* between the reference phase change and the sought unwrapped phase for each of the three steps. It should therefore be capable of dealing with the fact that the optimum *R*-ratio is in practice different for each of the ten scan segments and in turn compensate for any errors caused by the use of the average *R* value instead.

Once again the quality of the spectrograms should in principle reveal if this is the case for the new algorithm. Figure-8.30(a) and figure-8.30(b) show the corresponding spectrograms for the intensity data of wedges one and two, both of which appear to be clear of *'zero'* like structure and are of comparable quality to those produced using the adaptive Fourier-peak updating algorithm (for comparison, recall figure-8.22(a) and figure-8.22(b)). Similarly, figure-8.31(a) and figure-8.31(b) illustrate the corresponding spectrograms for the intensity data of wedge three and four respectively, using the modified phase unwrapping algorithm along the sensitivity axis, and are of particular importance as previously the data seemed to suffer from a spurious numerical artefact taking the form of a line. This, however, is clearly not the case anymore, highlighting the robustness of the proposed unwrapping strategy. That being said, the aforementioned spectrograms both show some level of deviation of the main spectral lobe from the expected location of $k_t = 1$ towards the end of the scan, making it difficult to decide which of the two algorithms is best.

8.3.6 Hybrid phase and Fourier-peak updating

In view of the success in suppressing the numerically induced ghost lines achieved by the unwrapping strategy along the sensitivity axis a hybrid approach is pursued in this section. That is, an unwrapping algorithm that is capable of combining the benefits of the adaptive Fourier-peak approach whose corresponding spectrograms showed that the main spectral lobe is situated consistently at $k_t = 1$ but suffered from the drawback of ghost lines and those offered by the last strategy in which the ghost

lines were fully suppressed at the expense of some level of variation in the location of spectral peak.

Before proceeding, it is worth revisiting the main principles behind the different unwrapping strategies proposed so far. In brief, the updating of the frequency at which the phase is evaluated was introduced as a means to limit errors owing to:

a) the gradual drift in the Fourier-peak position due to the incremental changes in the wavelength by the tuneable source,
b) the phase shifts caused by the refractive index dispersion of the wedges.

In view of the potential mismatch in the refractive index dispersion curves of the four wedges, a modified approach was proposed involving the adaptive updating of the frequency at which the phase is estimated based on a threshold value c_τ and the use of the estimated refractive index change dispersion curves for each of the four wedges. Using the time frequency analysis tool (spectrograms), it was shown that by increasing the adaptive rate of re-referencing, the quality of the spectrograms is improved. Despite the improvement, the spectrograms corresponding to the intensity data for wedges three and four were both contaminated by the presence of a spurious ghost line above the location of the main spectral lobe. As their spectral location was not fixed their nature was ascribed to unresolved numerically induced errors. These may well be caused by the fact that an average R value was used to scale the reference phase change of each of the three unwrapping steps which in turn has the undesirable effect of accumulating phase unwrapping errors over the three-step process. However, one of the factors that have been overlooked is that by introducing different updating rates for the estimation of the phase of each of the four wedges the risk of insufficient updating to compensate for the gradual drift in frequency due to the changes in wavelength caused by the laser source may arise. Strictly speaking the rate at which the updating should take place in order to avoid the errors caused by the light source should be constant. However, so long as the rate of re-referencing is fast enough the risk may be avoided. This is possibly the reason why the ghost line is approaching the main spectral lobe at $k_t = 1$ as the rate is increased. Although the obvious root would be to keep increasing the rate of updating, this runs the risk of introducing unwanted phase jumps owing to numerical errors. An indicative example of this can be seen in figure-8.21(a) at $t \sim 3500$, 3700 and 4200 and in figure-8.21(b)

at $t \sim 2.34\times10^4$ and 2.35×10^4 to point out a few. For this reason, further increase of the re-referencing rate was avoided.

Finally, in the last unwrapping strategy investigated and in an attempt to remove the spurious ghost lines in the spectrograms for the intensity data of wedges thee and four, an alternative re-referencing approach was proposed. The latter involved the constant updating of the sought synthetic wedge phase change quantity as opposed to updating the frequency at which the phase of each of the four wedges was evaluated. As already mentioned earlier, the reason for doing so was to compensate for unwrapping errors due to the fact that the R value used to scale up the reference phase change does not always correspond to that with the minimum rms error i.e. the optimum R-ratio (see section-8.3.3). As a result, the numerically induced artefacts in the spectrograms for wedges three and four were suppressed.

There is however an additional benefit associated with the unwrapping algorithm along the sensitivity direction. So far it has been implicitly assumed that following the 2-D-Fourier transform of the fringe patterns for each of the four wedges, the frequency at which the peak appears in the Fourier domain is directly linked to the phase corresponding to that peak. As pointed out earlier (see section-7.3.4), multiple reflections inside the wedges or back reflections from other optical components such as the camera cover slip give rise to background artefacts that take the form of a complex shaped ring like structure (recall figure-7.17). Although these were limited by the estimation and suppression of intensity background artefacts algorithm described in section-6.2.3 it is still possible that non-compensated residuals may still be present. Even though these are unlikely to cause significant shifts in the location of the Fourier-peaks it is possible that they alter the phase value. Therefore, by updating the reference phase-change constitutes a method of limiting phase excursions owing to the changing shape of the residual intensity background structure.

It follows that, by combining the adaptive Fourier-peak updating algorithm, originally developed to address the mismatch in the refractive index dispersion curves amongst the four wedges, with the phase unwrapping algorithm along the sensitivity axis that amongst others possesses the benefit of removing the numerically induced artefacts, it is possible to remove the variations in the peak

position while keeping the signal free from numerical errors. As usual, figure-8.32(a) and figure-8.32(b) show the corresponding spectrograms for the intensity data of wedge one and two, using the hybrid phase unwrapping method in which the adaptive Fourier-peak re-referencing rate is controlled using the threshold value c_τ = 0.05 pixels and a constant updating of the reference phase change that takes place every other frame i.e. ϱ = 2, both of which are free from artefacts. Figures-8.33(a) and (b) show the spectrograms for wedge three and four where the superiority of the hybrid algorithm becomes evident in that:

a. the variations in the location of the main spectral lobe previously seen in figure-8.31(a) and (b) have now been supressed,
b. and the numerically induced ghost lines present in figure-8.23(a) and (b) are now eliminated.

To conclude, and as far as the quality of the spectrograms is concerned, the hybrid phase unwrapping algorithm shows an increased robustness and noise immunity owing to the possible mismatch in the refractive index dispersion and noise residuals that are commonly termed ‘coherent noise’.

8.4 Phase unwrapping performance assessment

So far the quality of the spectrograms has been the main criterion used to assess the performance of the different algorithms developed so far. Although an excellent tool for the visual inspection of the signal, the short-time Fourier transform did not provide any information on the accuracy of the frequency at which the main spectral lobe occurs. It is therefore possible that despite the quality of the spectrograms being good that the resulting wavenumber axis is still distorted. In this final section of this chapter the accuracy of the different algorithms to producing highly accurate phase change measurements and thus leading to the correct reconstruction of the Δk axis and in future the accurate depth resolved imaging of both the interference signal and the phase is tested.

8.4.1 Initial performance considerations

One of the aspects that have been deliberately not mentioned so far is that the length of data points contained in the wavenumber change axis for the different unwrapping algorithms is not necessarily the same. By comparing the number of data sections W_n

in the spectrograms for the two cases of the adaptive Fourier-peak updating approach in which c_τ = 0.6 pixels (figures-8.14 to 8.15) and c_τ = 0.05 pixels (figures-8.22 to 8.23), it can be readily seen that W_n for c_τ = 0.05 pixels is larger than W_n for c_τ = 0.6 pixels. This in turn suggests that the wavenumber change axes corresponding to the two cases are different, with the latter being larger that the former.

As an initial approach to investigating the effect the different unwrapping strategies have on the resulting wavenumber change axis, the performance of the adaptive Fourier-peak updating approach is compared to that of the constant Fourier-peak updating. To do so, the corresponding spectrograms of (a) the adaptive Fourier peak re-referencing with c_τ = 0.05 pixels and (b) the constant Fourier peak re-referencing with a referencing rate of 400 frames are averaged along the W_n direction according to:

$$S = \sum_{W_n=1}^{\eta} \tilde{I}(x, y, W_n), \qquad 8.23$$

where η denotes the maximum value of W_n and $\tilde{I}(x_c, y_c, W_n)$ the Fourier transform of the intensity data for each data window W_n at the centre of each of the four wedge RoIs x_c,y_c. Figure-8.34(a) and figure-8.34(b) show the resulting averaged spectrograms and the location of their respective peaks for the intensity data of wedge one and two. As clearly illustrated by the aforementioned figures, the difference in the location of the two peaks is almost identical, albeit the signal to noise ratio of the signal for the adaptive algorithm (black line) appears to be slightly lower than that of the constant re-referencing rate algorithm (red line). The corresponding plots of the averaged spectrograms for wedges three and four are however significantly different. As clearly illustrated in figure-8.35(a) and figure-8.35(b), the location of the peak corresponding to the adaptive algorithm appears in both cases (intensity data of wedge three and four) to have shifted to the left with respect to the peak location of the constant re-referencing rate. Moreover, and apart from the expected ghost peaks that are situated next to the main spectral lobe, the process has revealed additional peaks. Although their high amplitude is likely to be the outcome of the averaging operation, their presence clearly indicates that the adaptive algorithm alone suffers from non-compensated errors.

8.4.2 Depth resolved thickness measurements

Although the averaged spectrogram approach can be successfully used as a tool to demonstrate that there is a difference in the estimated frequency at which the main spectral peak appears, the fact that the resulting wavenumber axis may expand or retract depending on which technique is used deems it inappropriate as a criterion to distinguish which of the algorithms developed so far yields the most reliable results. Despite the fact that optical metrology is a very powerful tool offering unparalleled high measurement sensitivity, it is susceptible to errors that are in many cases difficult to identify and therefore suppress. For this reason, in the most demanding applications and where possible, the optical measurements are often compared to mechanical measurements that are traceable to national standards. In line with this general rule of evaluation, the accuracy and precision of the different phase unwrapping techniques developed so far to estimating the sought wavenumber axis is tested by comparing the accuracy to which the central thickness of each of the four wedges can be measured against the independent micrometer measurements. In a similar way to that presented earlier in chapter-6 and to avoid the long names during the forthcoming comparison, the following notation will be adopted. Method-A will denote the unwrapping strategy with constant re-referencing rate of 400 frames, using the original integer based phase estimation algorithm and without the removal of the background intensity artefacts. Method-B will be the short name of the approach involving the same constant frame re-referencing rate as method-A, but with the non-integer phase estimation method and the removal of the background artefacts implemented. Method-C refers to the independent micrometer measurements, while method-D is the adaptive Fourier-peak updating (c_τ = 0.05 pixels) with both non-integer phase extraction and background removal implemented. Finally, method-E will denote the hybrid algorithm that combines the adaptive Fourier-peak updating (c_τ = 0.05 pixels) and the phase unwrapping along the sensitivity direction (ϱ = 2) and where once again the non-integer phase estimation and the background suppression procedures are both integrated in the technique. In addition to the short names attributed to the different methods used to estimate the central thickness of each of the four wedges and to avoid clustering the figures used for the following comparisons only the relevant Fourier peaks are plotted with the rest being represented by vertical lines where the peaks would occur.

In view of the fact that the spectrogram quality for method-E appears to be superior in that it is free from artefacts and without major variations in the location of the main spectral lobe, only the Fourier peaks of method-E and method-D which produced the second best spectrograms will be shown, Figure-8.36 provides a comparison amongst the five different methods used to estimating the central thickness of the thickest wedge (wedge-1). More specifically figure-8.36(a) shows the shape and location of the main spectral lobe using the adaptive Fourier-peak updating approach (method-D) as well as the location of the Fourier-peaks after conversion of the Δk-axis to distance d in mm. Similarly, figure-8.36(b) shows the shape of the main spectral lobe and its location using the hybrid approach (method-E), thereby providing a direct way of comparing the depth-resolved measurement accuracy and signal to noise ratio achievable by the different approaches. Although at this stage the estimated thickness values are reasonably close to each other making it difficult to decide which approach is best, the Fourier-peak corresponding to method-E appears to be narrower compared to that of method-D, indicating that method-E yields better results than method-D. By repeating this process for the intensity data from wedge-2 the superiority of the hybrid algorithm starts to become more obvious in that the estimated central thickness is much closer to that corresponding to the micrometer measurements compared to the other methods as illustrated in figures-8.37(a)-(b).

As the central thicknesses of wedges one and two are fairly close to each other and even though there is some evidence that suggests that the Δk-axis calculated using the hybrid algorithm is the more accurate, it is still unclear as to which method is best. For this reason, the same process is repeated for the intensity data of wedges three and four for which the central thicknesses are significantly smaller to that of wedge one. In doing so, any issues related to the fact that the wavenumber change axis is essentially computed from the high sensitivity phase changes resulting from the wedge-1 data will be revealed. As clearly illustrated in figure-8.38(a), the use of the adaptive Fourier-peak updating algorithm yields a sharp peak at a location that is significantly underestimating the central thickness of the third wedge. Moreover, a spectral artefact around the true thickness of the wedge is clearly visible. On the other hand the use of the hybrid approach shows in figure-8.38(b) demonstrates the ability to deal with the decoupling of the Δk-axis from the intensity data by resulting

in a sharp peak at a location that is much closer to the true wedge thickness and without any spectral artefacts. Finally figure-8.39(a) and figure-8.39(b) show the corresponding shapes and locations of the spectral peaks using method-D and method-E respectively. Unlike method-D in which the location of the Fourier-peak is dramatically underestimated while still suffering from spectral artefacts, the use of the hybrid temporal phase unwrapping algorithm (method-E) clearly illustrates the robustness and noise immunity of the technique by resulting in a clear Fourier-peak at the expected frequency and without any spectral artefacts.

Table-8.1: Tabular form of the estimated depth-resolved absolute thickness measurements of the four wedges using the five different methods (A-E) described throughout the thesis.

Method	***Wedge central thickness in mm***			
	Wedge-1	***Wedge-2***	***Wedge-3***	***Wedge-4***
A	12.7471	12.6740	11.9216	9.5747
B	12.7516	12.6780	11.9265	9.5813
C	12.7550	12.6600	12.4350	9.5900
D	12.7527	12.6613	11.7252	9.0855
E	12.7516	12.6783	11.9295	9.5874

Table-8.1 above provides the estimated central thicknesses of the four wedges comprising the optical sensor, using the five different methods described through the thesis in a tabular form. From this final and decisive test, it can be safely concluded that the hybrid phase unwrapping algorithm is the preferred method of computing the sought wavenumber change axis.

8.5 Conclusions

In this chapter, two modifications to the basic unwrapping algorithm used earlier have been introduced in an attempt to reduce the artefacts that were present in the Fourier reconstruction of the depth profile of the four wedges. Both approaches are adaptive and involve signal re-referencing at regular intervals throughout the scan. The first is designed to compensate for the gradual change in spatial frequency of the fringes that arises from the changing wavelength, and requires continual updating of the spatial frequency components at which the phase is evaluated. The second is designed to compensate for the gap that starts to open up between the scaled low-sensitivity phase signal and the high sensitivity phase signal. This may be due to a

small error in the value of R, or small changes in R with wavelength due to different dispersion curves for the two pairs of wedges. By re-zeroing the phase change at regular intervals, and then subsequently adding up the re-referenced phase change, the total phase change since the start of the scan can thus be computed but without the 2π phase errors that occurred previously.

The first was found to improve significantly the quality of the spectrograms apart from the 'ghost line' structure seen in the reconstructions from two of the wedges. The second largely eliminated the ghost lines. A hybrid approach combining both methods was therefore proposed and used to analyse the data from each of the four wedges which was then compared with independently measured wedge thickness values using a micrometer. The hybrid method was found to be the most robust of all the techniques considered, with a clear Fourier peak at the expected frequency and without any spectral artefacts.

8.6 Figures

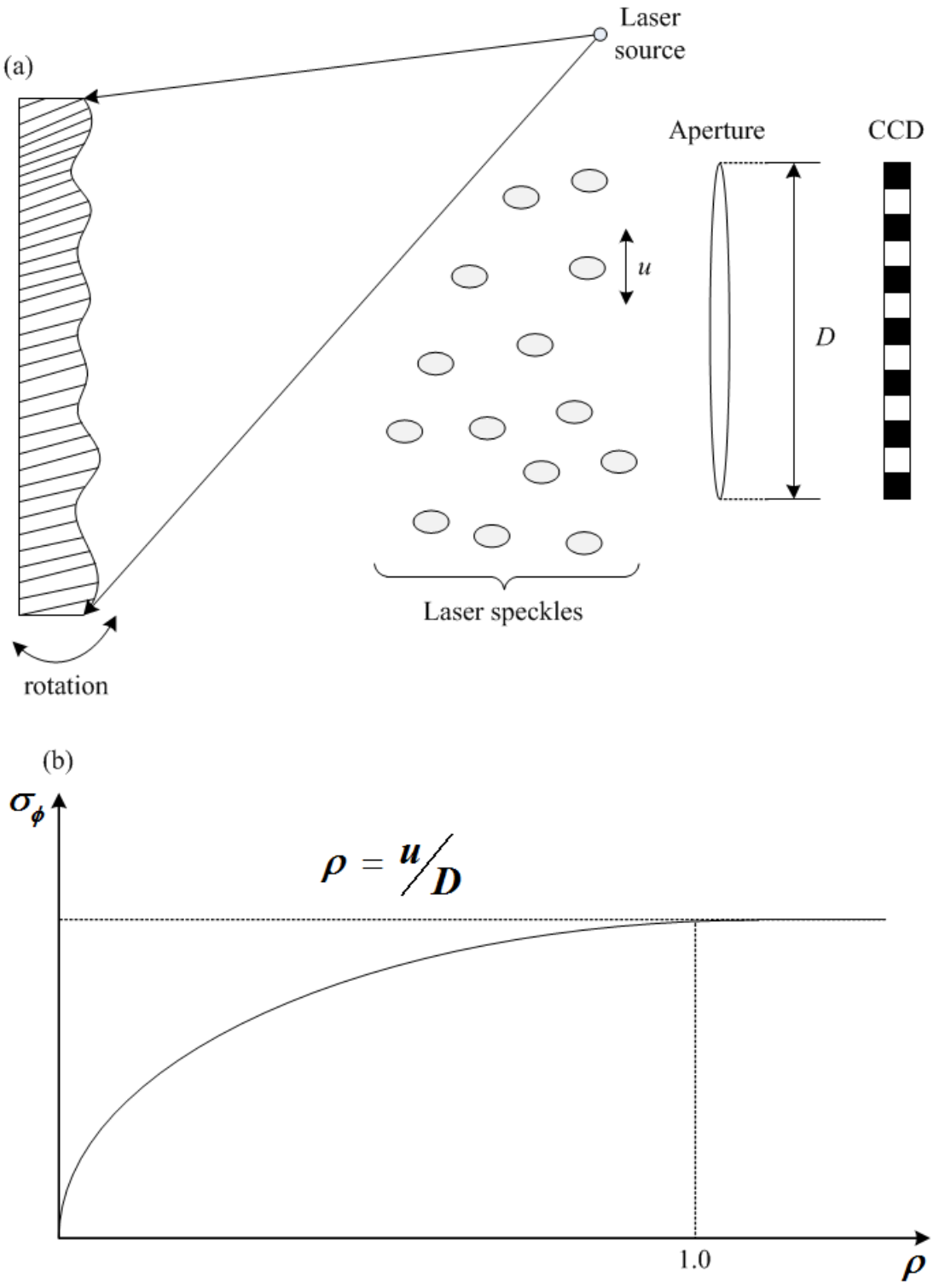

Figure-8.1: Schematic illustration of the laser speckle decorrelation phenomenon. (a) An induced rotation on the rough surfaced sample causes the speckles to move by an amount u across the field of view. (b) When the speckle movement u becomes greater or equal to the diameter of the entrance pupil D ($\rho \geq 1$), complete speckle decorrelation occurs causing a significant increase in the noise of the computed phase (σ_ϕ) and thus the measured displacement field of the sample.

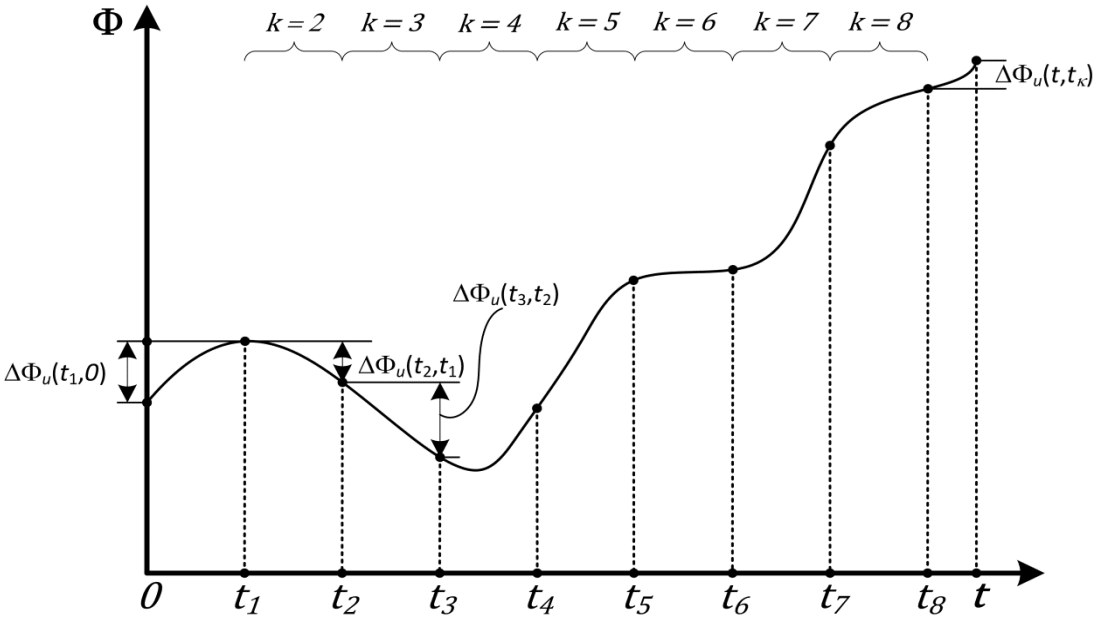

Figure-8.2: Schematic illustration of the original re-referencing approach proposed by [277] to overcome the phase errors caused due to complete speckle decorrelation.

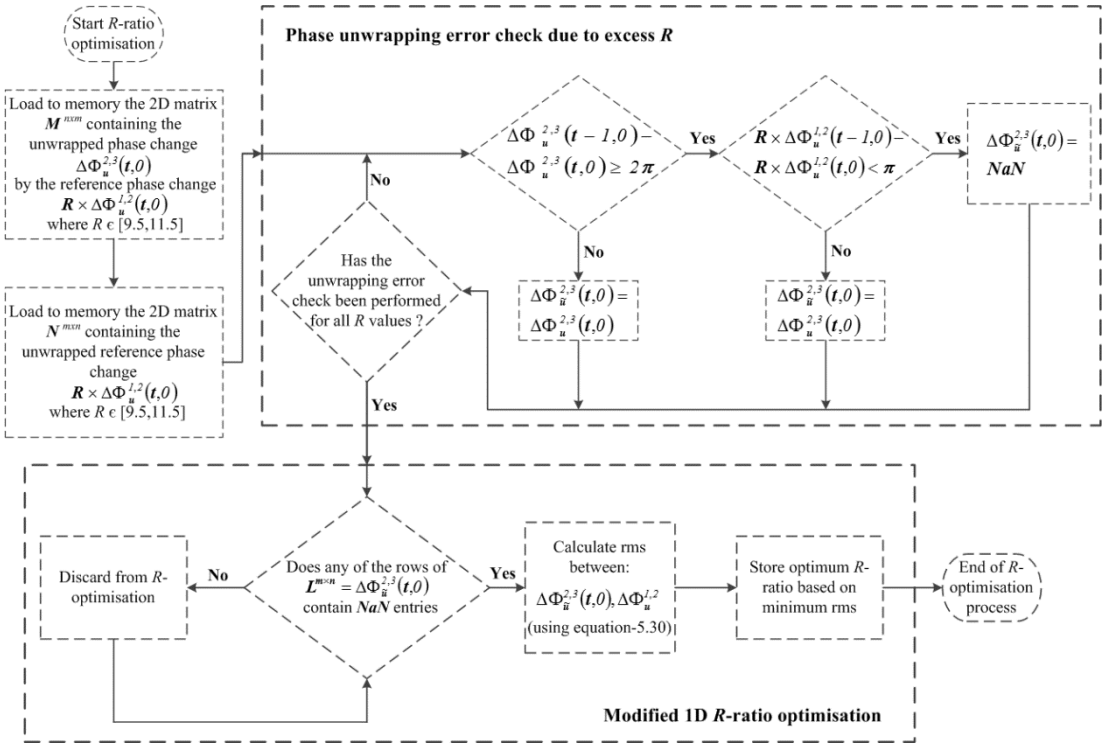

Figure-8.3: Flowchart showing the modified 1-D optimization for the estimation of the optimum *R*-ratio of each of the scan sections. At the top, shown in the dashed box, is the procedure implemented to avoid the inclusion of data containing unwrapping errors while on the bottom dashed box the steps for calculating the optimised *R*-ratio are described. Note that *m*,*n* superscripts are used to denote the number of rows and columns of the 2-D matrices (***M***,***N***,***L***) respectively, with *m* being determined by the number of different *R* values used and *n* by the length of the scan section examined.

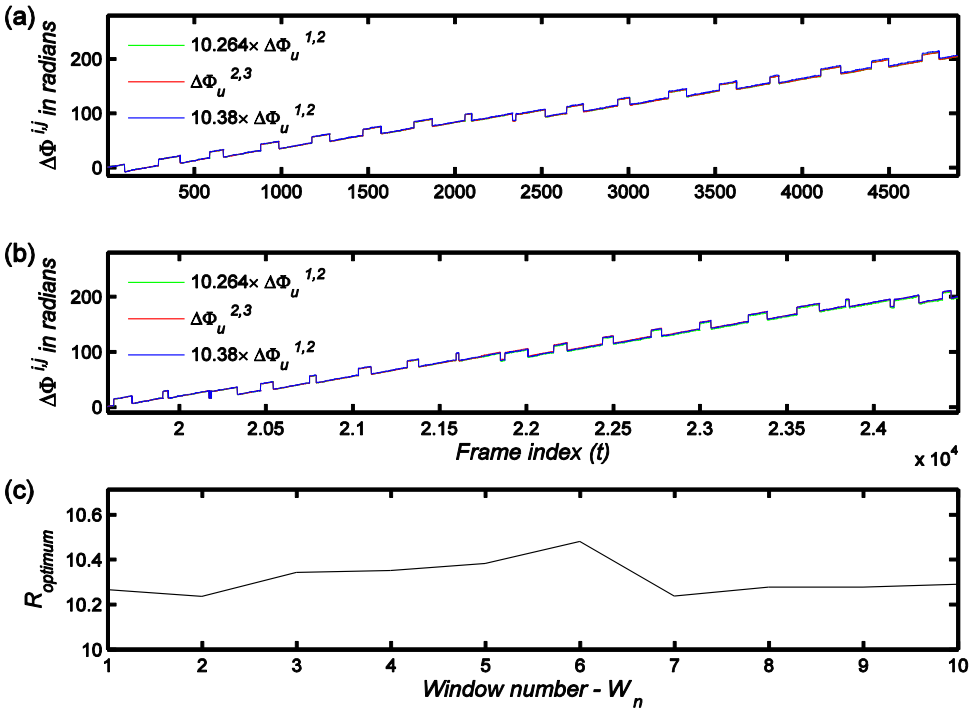

Figure-8.4: (a) Green: temporally unwrapped phase change $\Delta\Phi_u^{1,2}(t,0)$ scaled by the optimum ratio for the 1st scan segment. Red: unwrapped phase change $\Delta\Phi_u^{2,3}(t,0)$ using the green plot. Blue: same as green but scaled by the optimum ratio for the 4th segment of the scan. (b) Same as (a) for the 4th scan segment of the scan but with the $\Delta\Phi_u^{2,3}(t,0)$ (red line) unwrapped using the blue instead of the green line. (c) Variation in the optimum wedge thickness ratio as a function of W_n

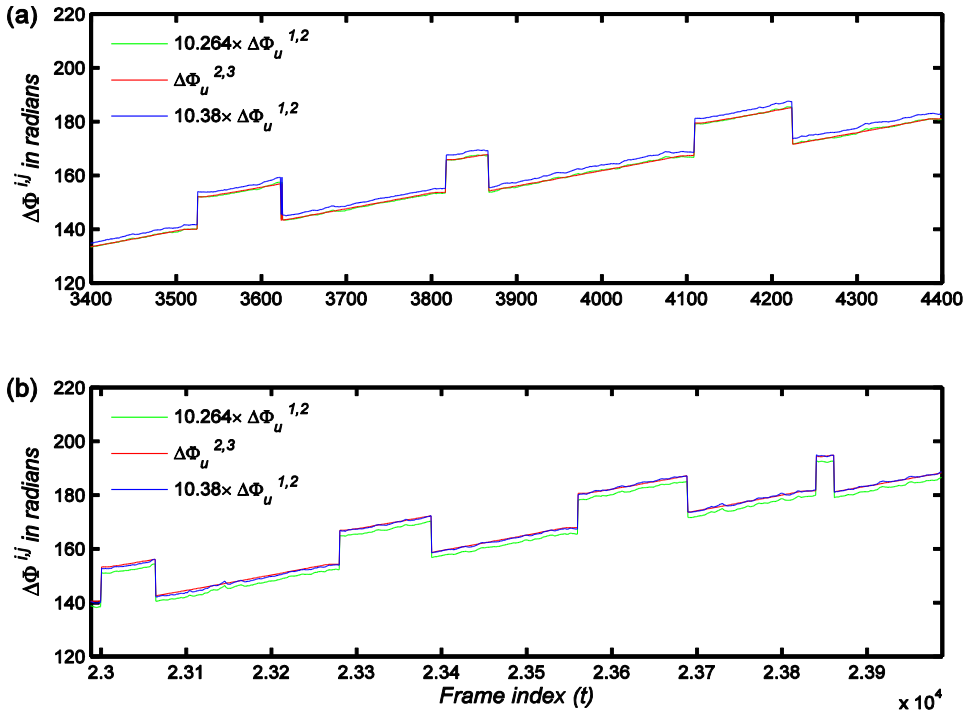

Figure-8.5: Zoomed in regions showing the last 1000 frames: (a) of figure-8.5(a) and (b) of figure-8.5(b)

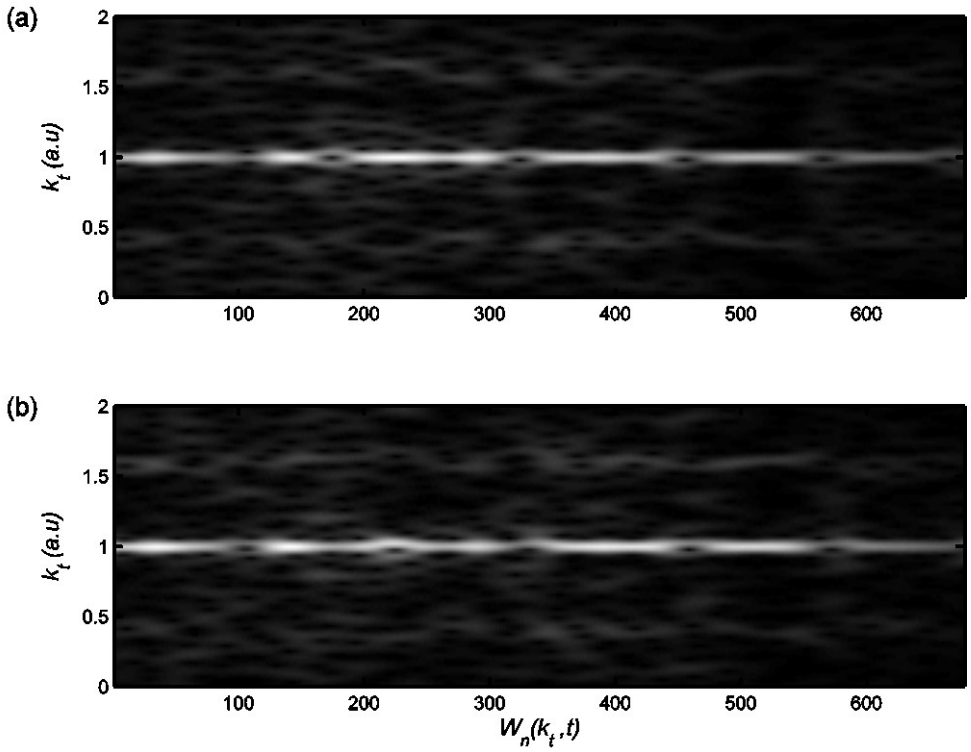

Figure-8.6: Time-frequency analysis using the short-time Fourier-transform for the intensity data from **wedge-1** (a) and **wedge-2** (b). The above spectral plots were produced using the `spectrogram` function in the MATLAB programming language (see section-7.2.2 for more details) after the improved optimization algorithm was implemented (see section-8.3.3 for more details)

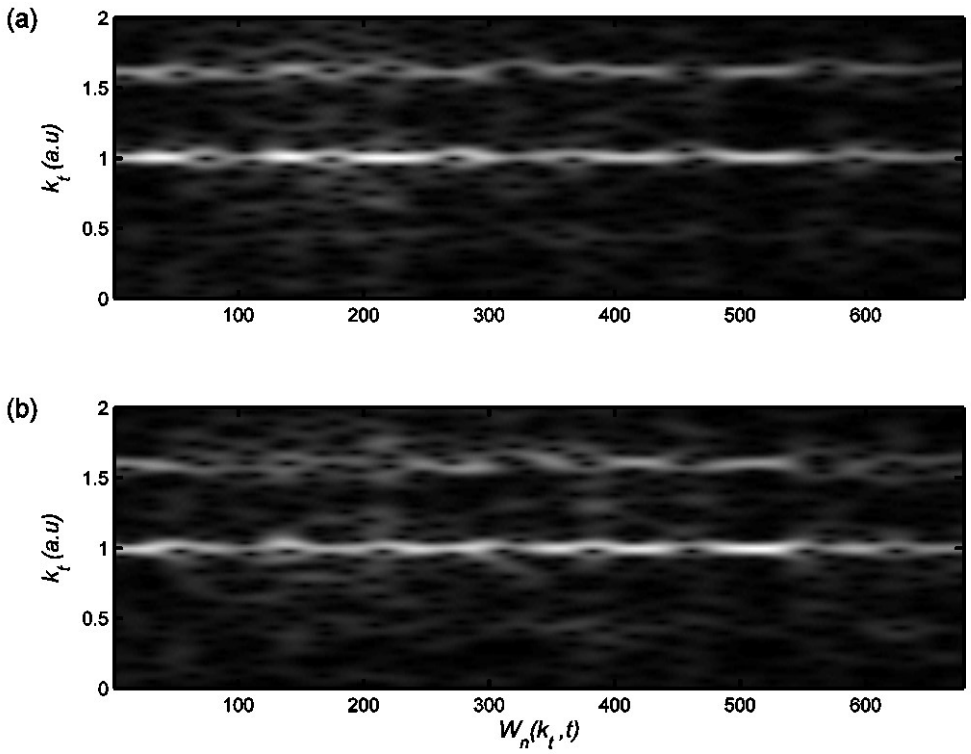

Figure-8.7: Same as figure-8.7 above but for (a) **wedge-3** and (b) **wedge-4**.

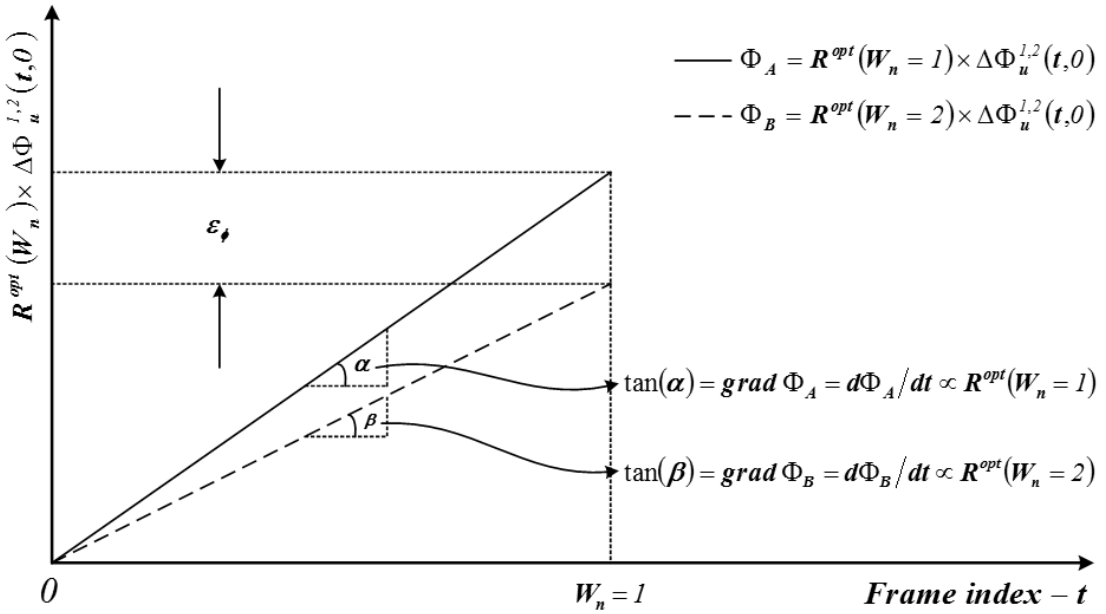

Figure-8.8: Schematic illustrating the hypothetical and ideal, in the absence of any non-linearities, linear trend of the reference phase change $\Delta\Phi_u^{1,2}(t,0)$ scaled by the optimum R-ratio: $R^{opt}(W_n = 1)$ where $W_n = 1 : t \in [1,4897]$ (shown in the black continuous line) and by $R^{opt}(W_n = 2)$ where $W_n = 2 : t \in [4897,9793]$(shown in the black dashed line). ε_ϕ: denotes the deviation between the two phase change signals for this ideal scenario and provides a useful measure to ensure successful unwrapping via the following condition: $\varepsilon_\phi < \pi$ (see section-8.3.4 for more details on this condition and its origin).

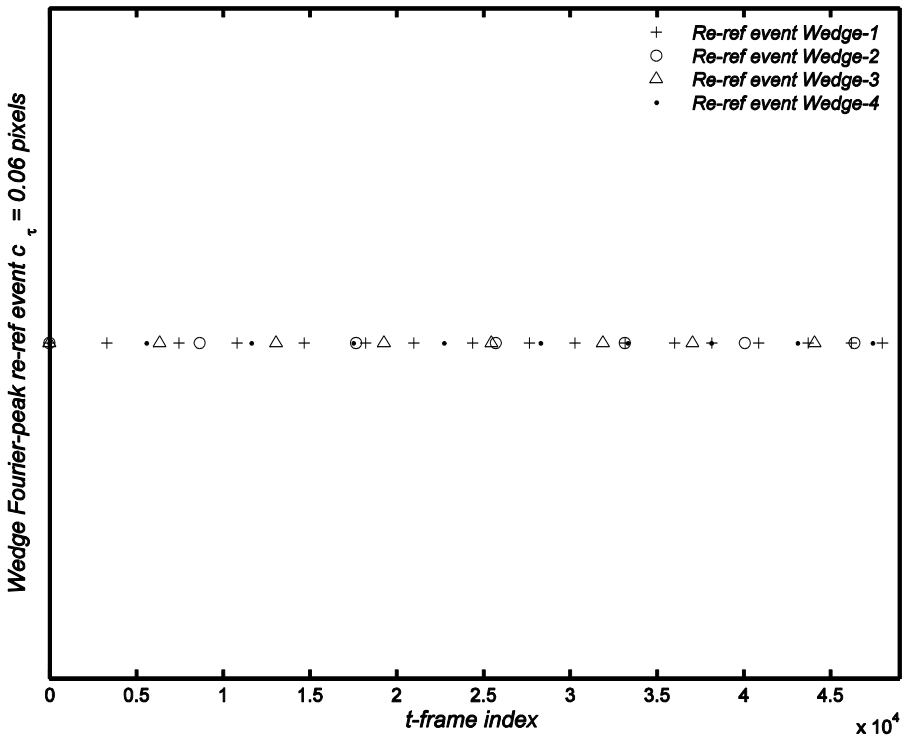

Figure-8.9: Graph showing the time instances at which updates of the frequency, at which the phase is evaluated, occur for c_τ = 0.6 pixels for the four wedges.

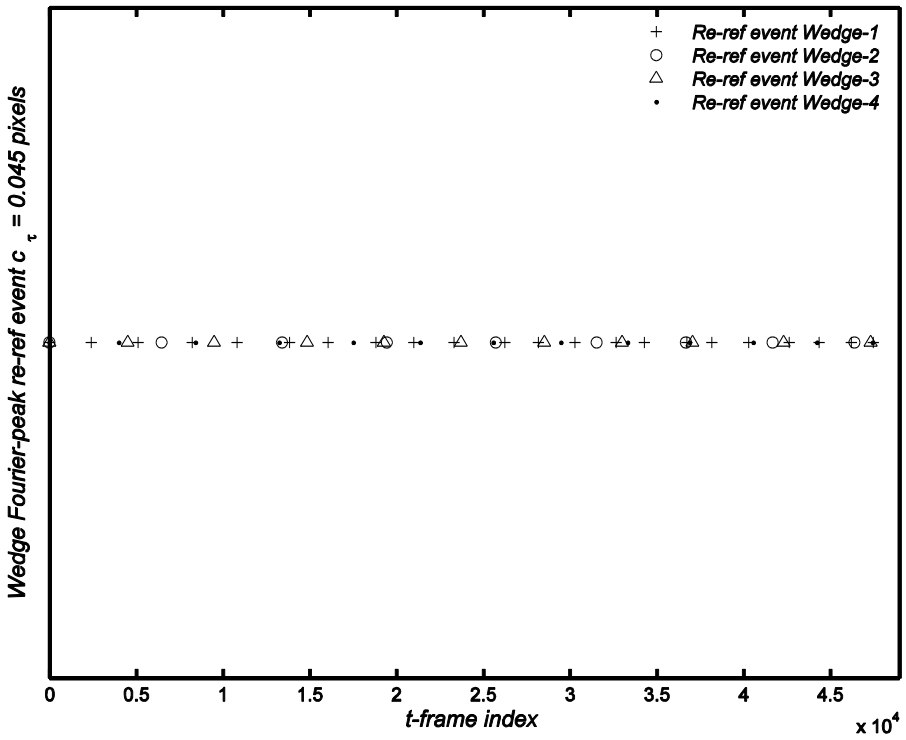

Figure-8.10: Graph showing the time instances at which updates of the frequency, at which the phase is evaluated, occur for $c_\tau = 0.45$ pixels for the four wedges.

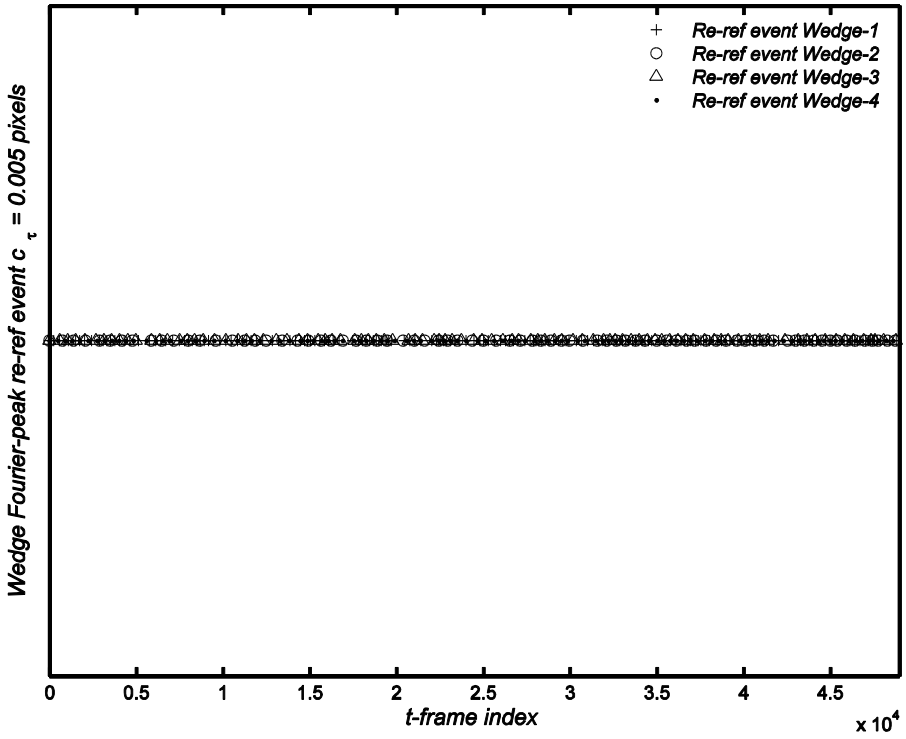

Figure-8.11: Graph showing the time instances at which updates of the frequency, at which the phase is evaluated, occur for $c_\tau = 0.05$ pixels for the four wedges.

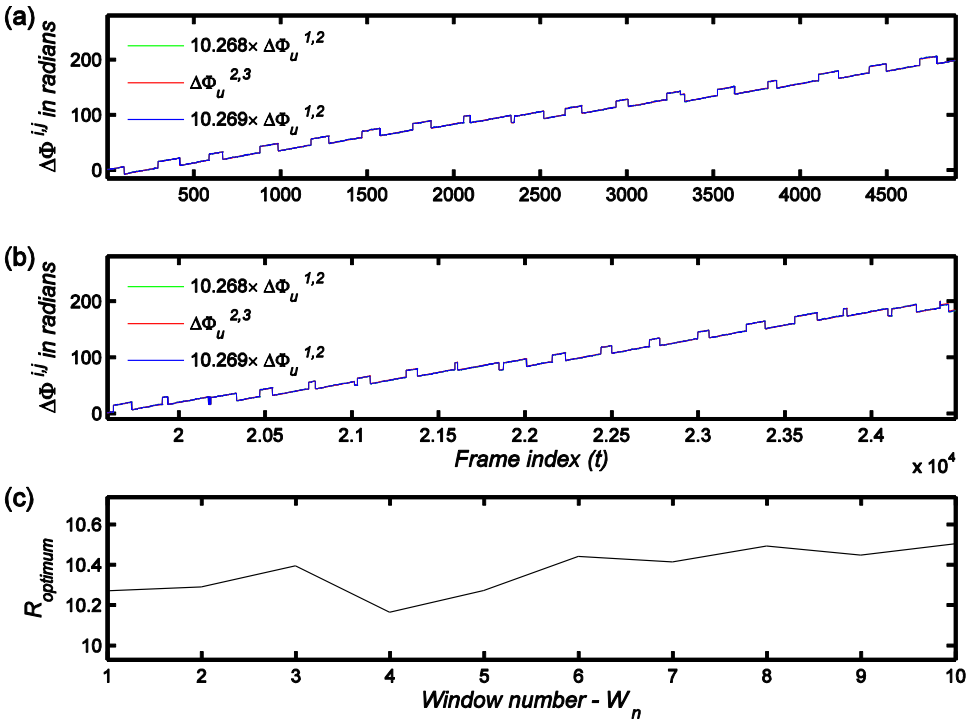

Figure-8.12: Case-***A***: $c_\tau = 0.6$ **pixels**. (a) Green: temporally unwrapped phase change $\Delta\Phi_u^{1,2}(t,0)$ scaled by the optimum ratio for the 1st scan segment. Red: unwrapped phase change $\Delta\Phi_u^{2,3}(t,0)$ using the green plot. Blue: same as green but scaled by the optimum ratio for the 1st segment of the scan. (b) Same as (a) for the 5th scan segment but with the $\Delta\Phi_u^{2,3}(t,0)$ (red line) unwrapped using the blue instead of the green line. (c) Variation in the optimum wedge thickness ratio as a function of W_n.

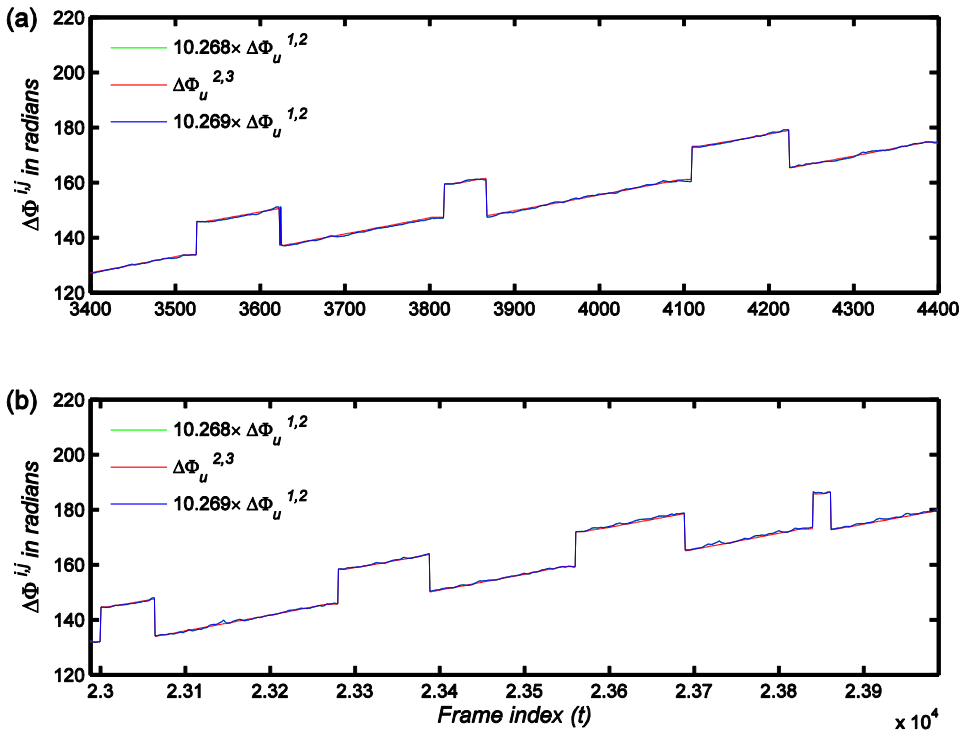

Figure-8.13: Zoomed in regions showing the last 1000 frames: (a) of figure-8.12(a) and (b) of figure-8.12(b)

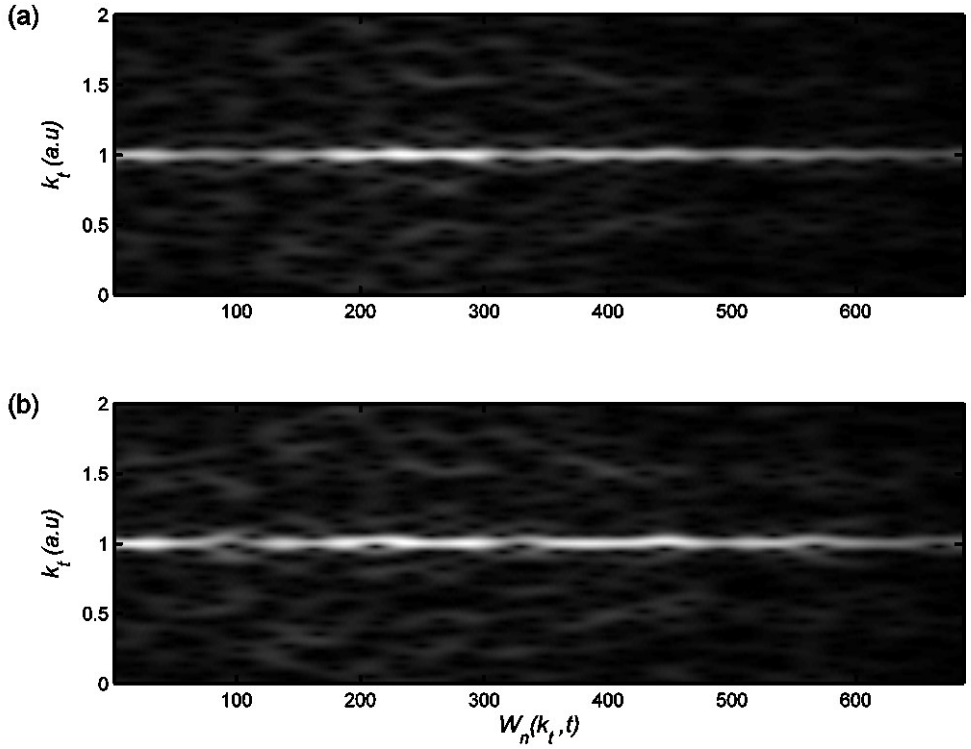

Figure-8.14: Time-frequency analysis using the short-time Fourier-transform for the intensity data from **wedge-1** (a) and **wedge-2** (b). The above spectral plots were produced using the `spectrogram` function in the MATLAB programming language of the data after the improved R-optimisation algorithm and the adaptive updating of the frequency at which the phase is calculated for *Case-A*: $\boldsymbol{c_\tau = 0.6}$ **pixels**.

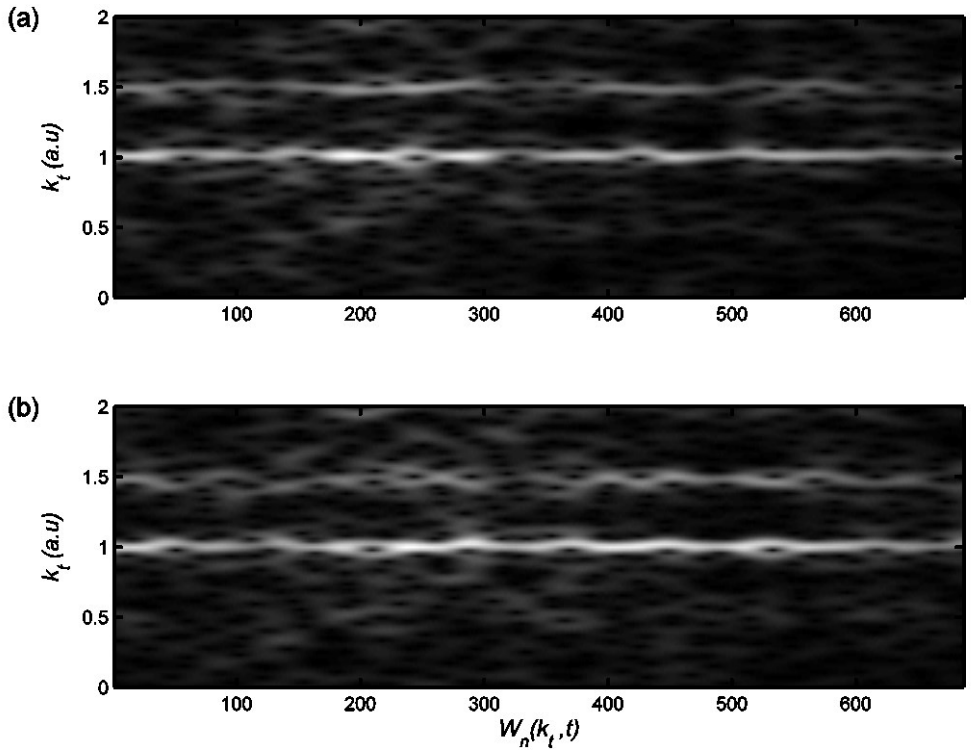

Figure-8.15: Same as figure-8.14 above but for (a) **wedge-3** and (b) **wedge-4**.

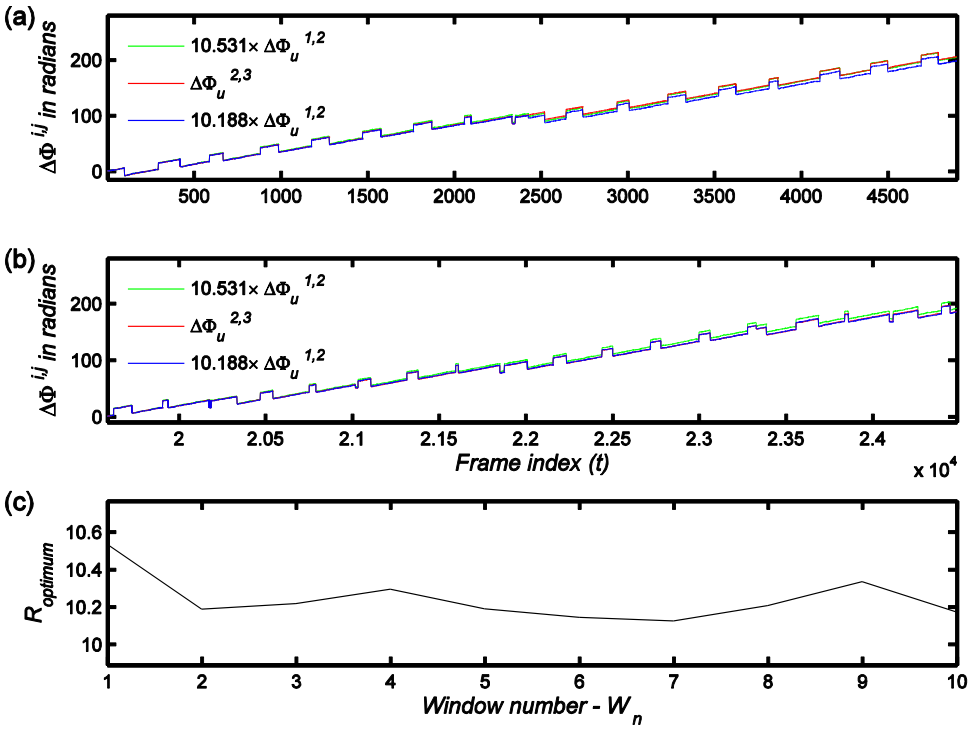

Figure-8.16: *Case-B*: $c_\tau = 0.45$ **pixels**. (a) Green: temporally unwrapped phase change $\Delta\Phi_u^{1,2}(t,0)$ scaled by the optimum ratio for the 1st scan segment. Red: unwrapped phase change $\Delta\Phi_u^{2,3}(t,0)$ using the green plot. Blue: same as green but scaled by the optimum ratio for the 1st segment of the scan. (b) Same as (a) for the 5th scan segment but with the $\Delta\Phi_u^{2,3}(t,0)$ (red line) unwrapped using the blue instead of the green line. (c) Variation in the optimum wedge thickness ratio as a function of W_n.

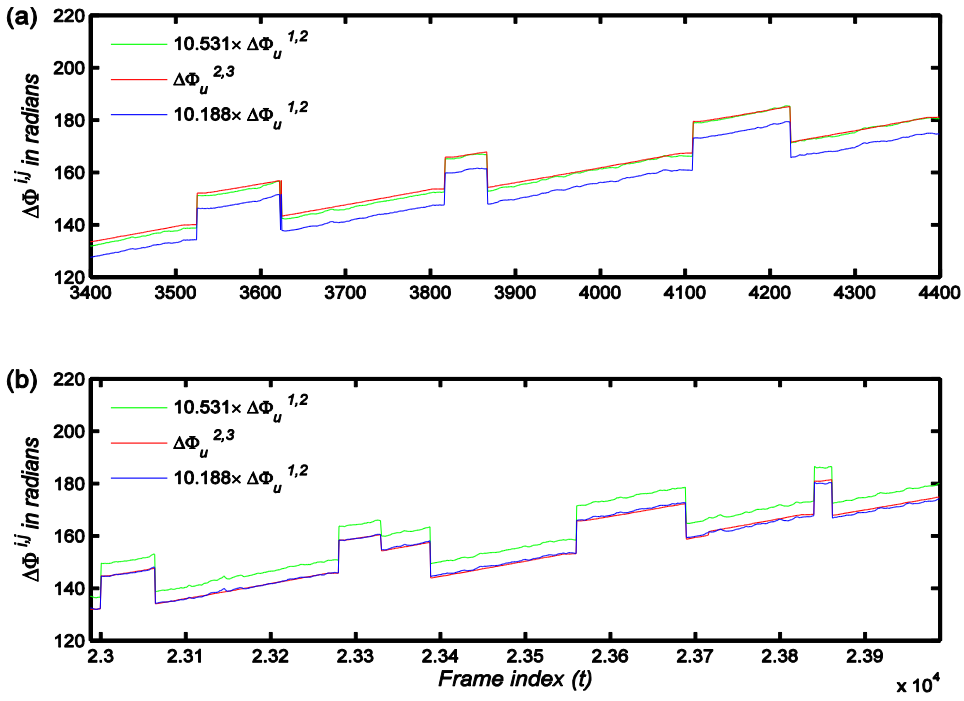

Figure-8.17: Zoomed in regions showing the last 1000 frames: (a) of figure-8.16(a) and (b) of figure-8.16(b).

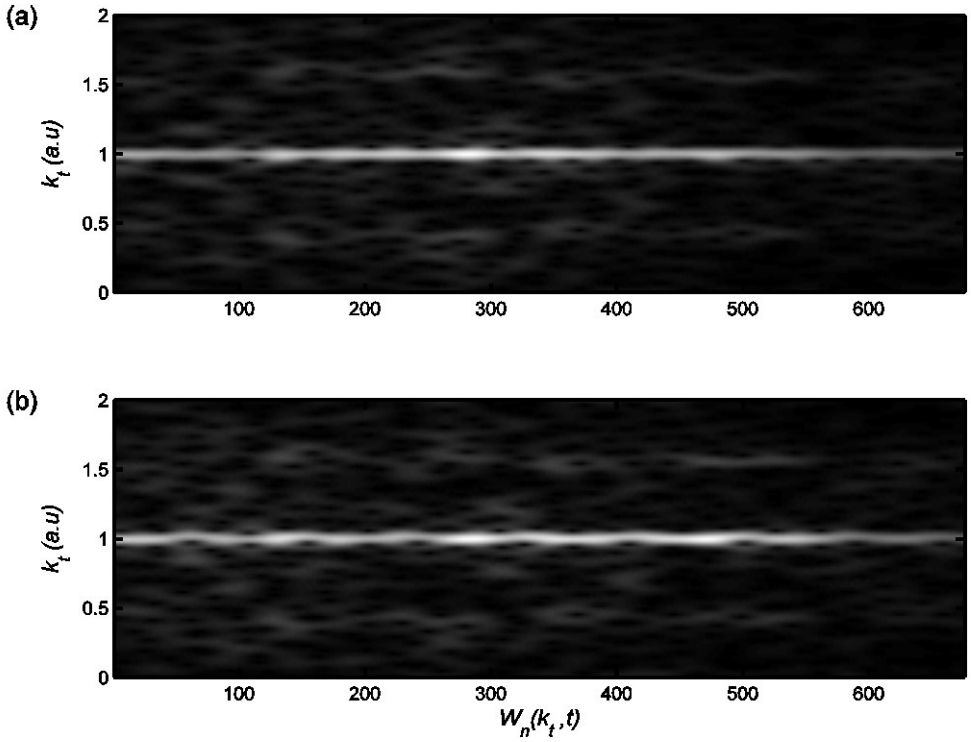

Figure-8.18: Time-frequency analysis using the short-time Fourier-transform for the intensity data from **wedge-1** (a) and **wedge-2** (b). The above spectral plots were produced using the `spectrogram` function in the MATLAB programming language of the data after the improved *R*-optimisation algorithm and the adaptive updating of the frequency at which the phase is calculated for *Case-B*: $\boldsymbol{c_\tau = 0.45}$ pixels.

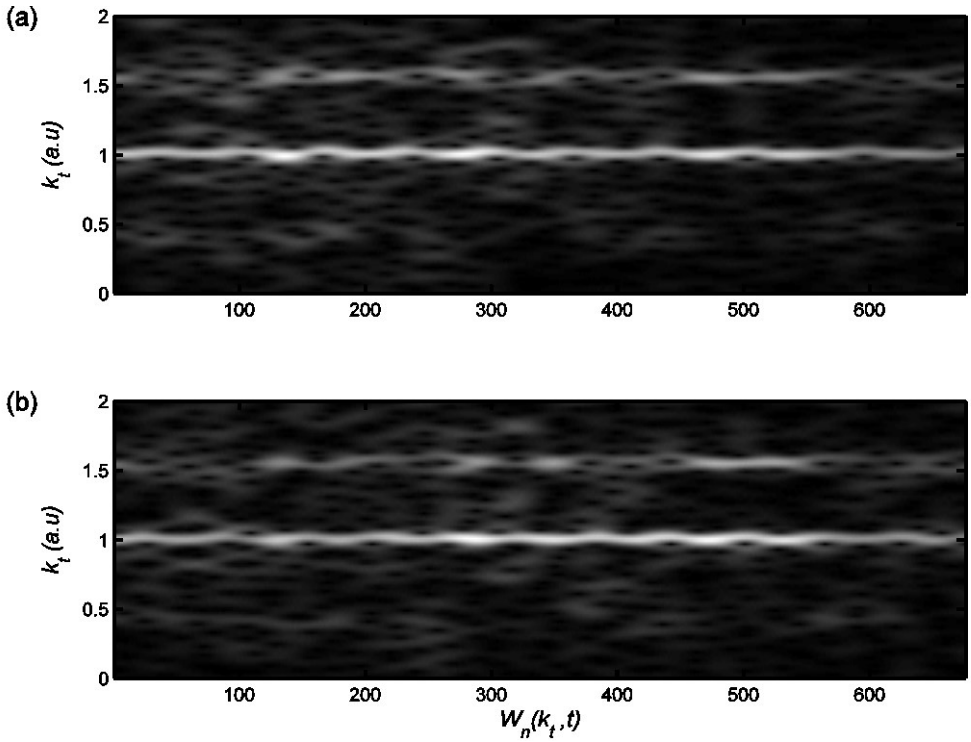

Figure-8.19: Same as figure-8.18 above but for (a) **wedge-3** and (b) **wedge-4**.

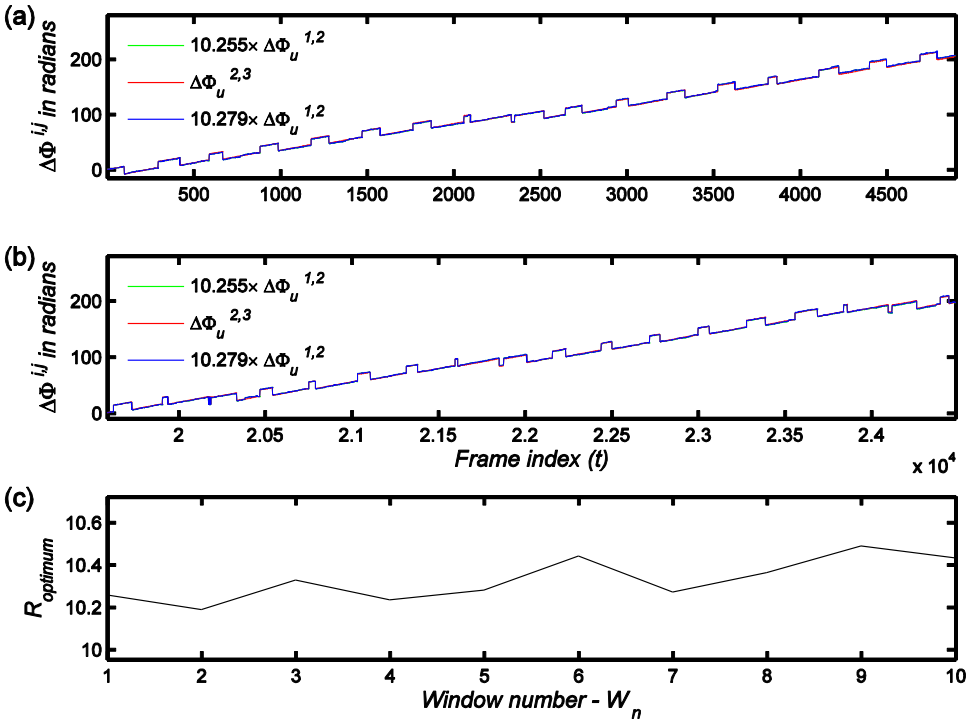

Figure-8.20: Case-*C*: $c_\tau = 0.05$ **pixels**. (a) Green: temporally unwrapped phase change $\Delta\Phi_u^{1,2}(t,0)$ scaled by the optimum ratio for the 1st scan segment. Red: unwrapped phase change $\Delta\Phi_u^{2,3}(t,0)$ using the green plot. Blue: same as green but scaled by the optimum ratio for the 1st segment of the scan. (b) Same as (a) for the 5th scan segment but with the $\Delta\Phi_u^{2,3}(t,0)$ (red line) unwrapped using the blue instead of the green line. (c) Variation in the optimum wedge thickness ratio as a function of W_n.

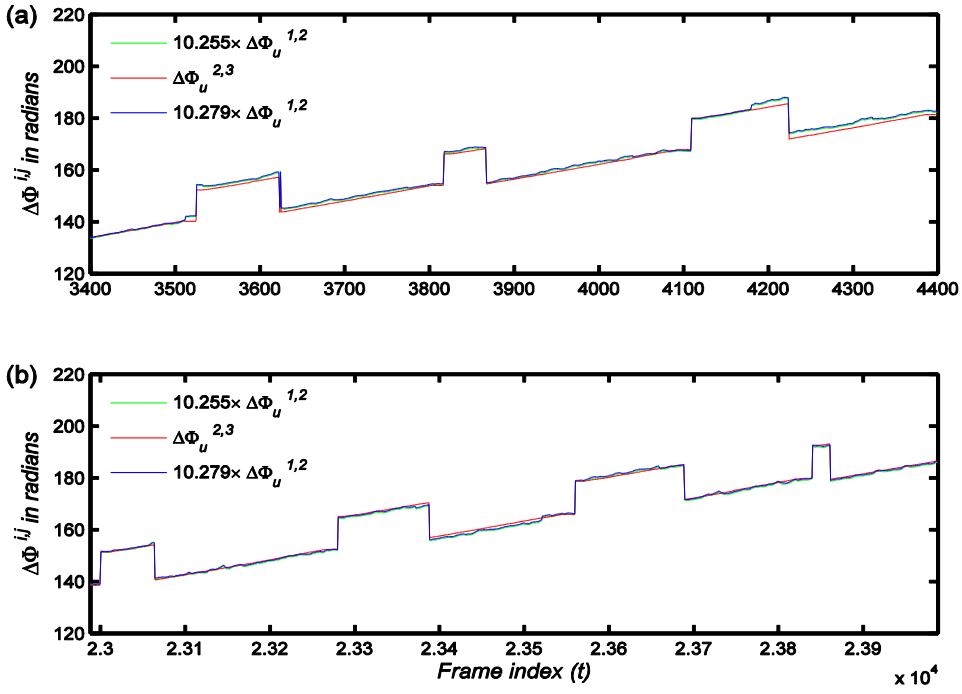

Figure-8.21: Zoomed in regions showing the last 1000 frames: (a) of figure-8.20(a) and (b) of figure-8.20(b).

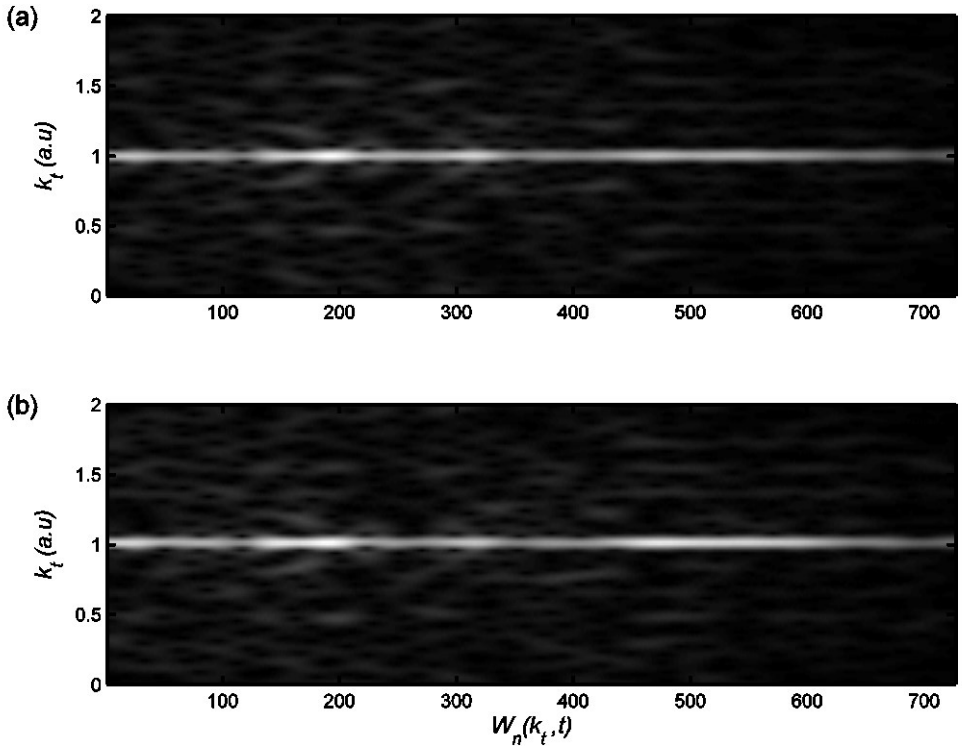

Figure-8.22: Time-frequency analysis using the short-time Fourier-transform for the intensity data from **wedge-1** (a) and **wedge-2** (b). The above spectral plots were produced using the `spectrogram` function in the MATLAB programming language of the data after the improved *R*-optimisation algorithm and the adaptive updating of the frequency at which the phase is calculated for *Case-C*: $\boldsymbol{c_\tau = 0.05}$ pixels.

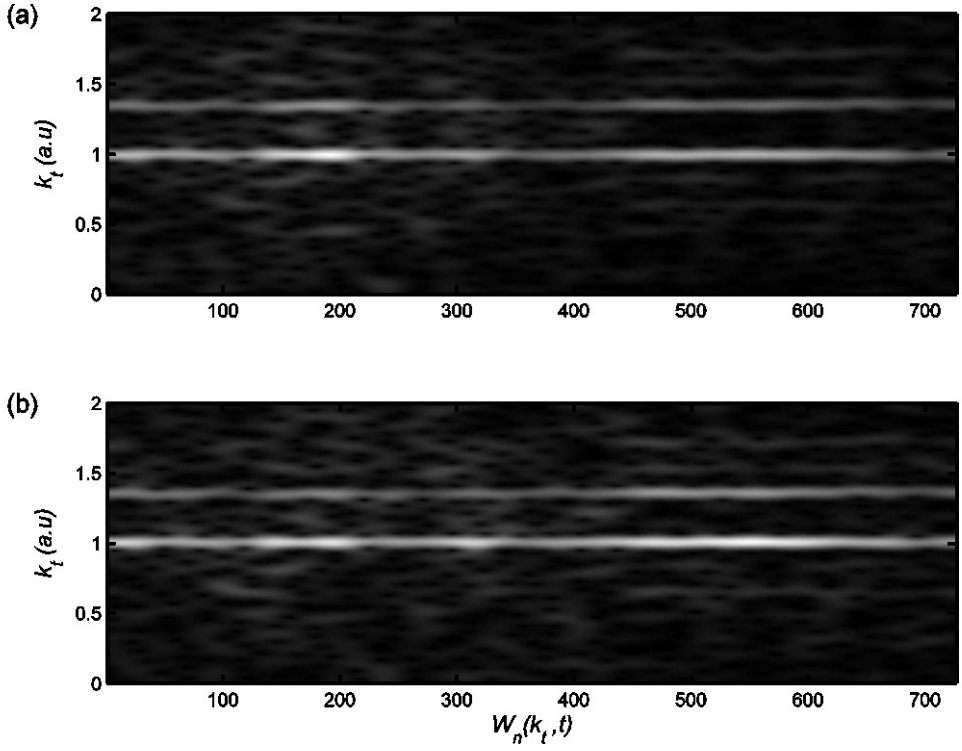

Figure-8.23: Same as figure-8.22 above but for (a) **wedge-3** and (b) **wedge-4**.

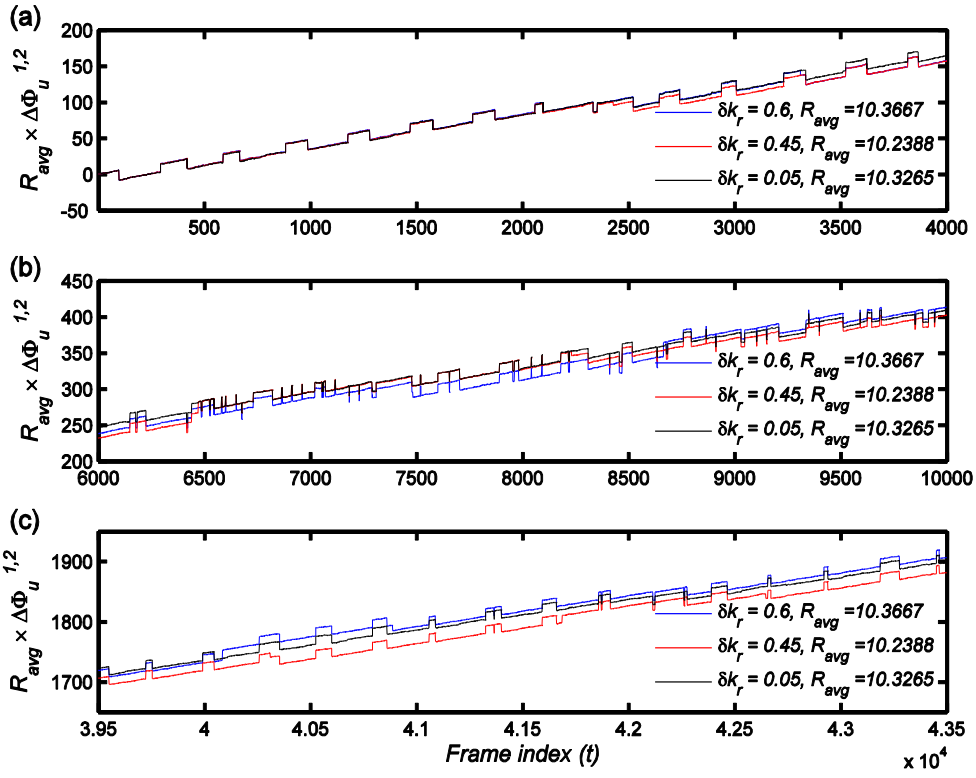

Figure-8.24: Comparison amongst the three different reference phase signals resulting from the scaling by three different averaged R ratios for the three cases of updating rates investigated (*Case-A*: $\delta k_r = c_\tau = 0.6$ pixels, *Case-B*: $\delta k_r = c_\tau = 0.45$ pixels and *Case-C*: $\delta k_r = c_\tau = 0.05$ pixels).

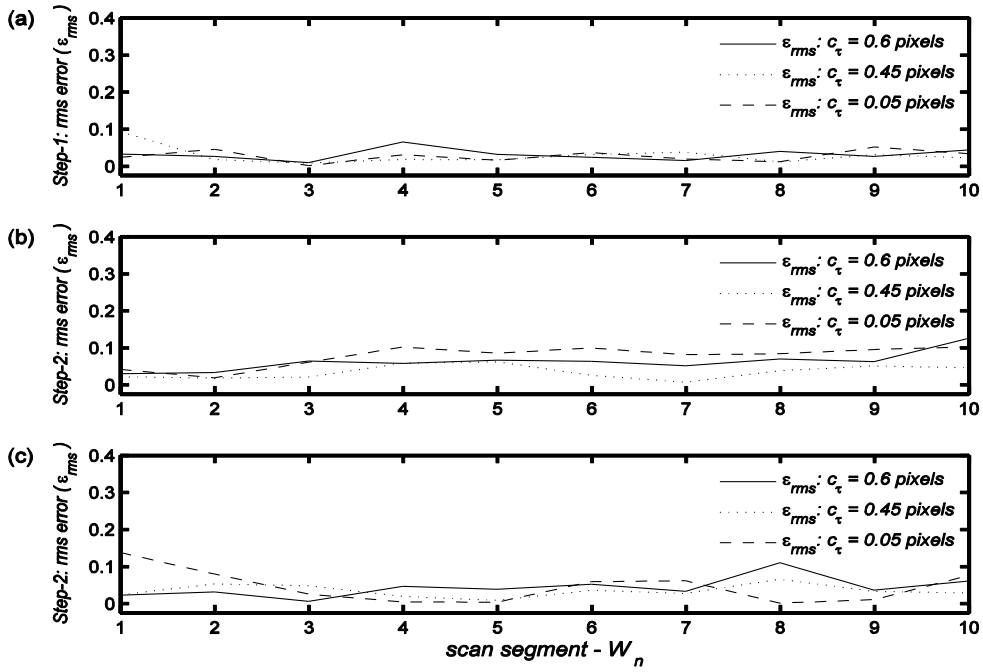

Figure-8.25: Plots showing the rms error between the averaged R value used to perform the unwrapping and the optimum R for each of the ten scan segments, for each of the three cases examined (a): 1st unwrapping step, (b) 2nd unwrapping step and (c) final unwrapping step.

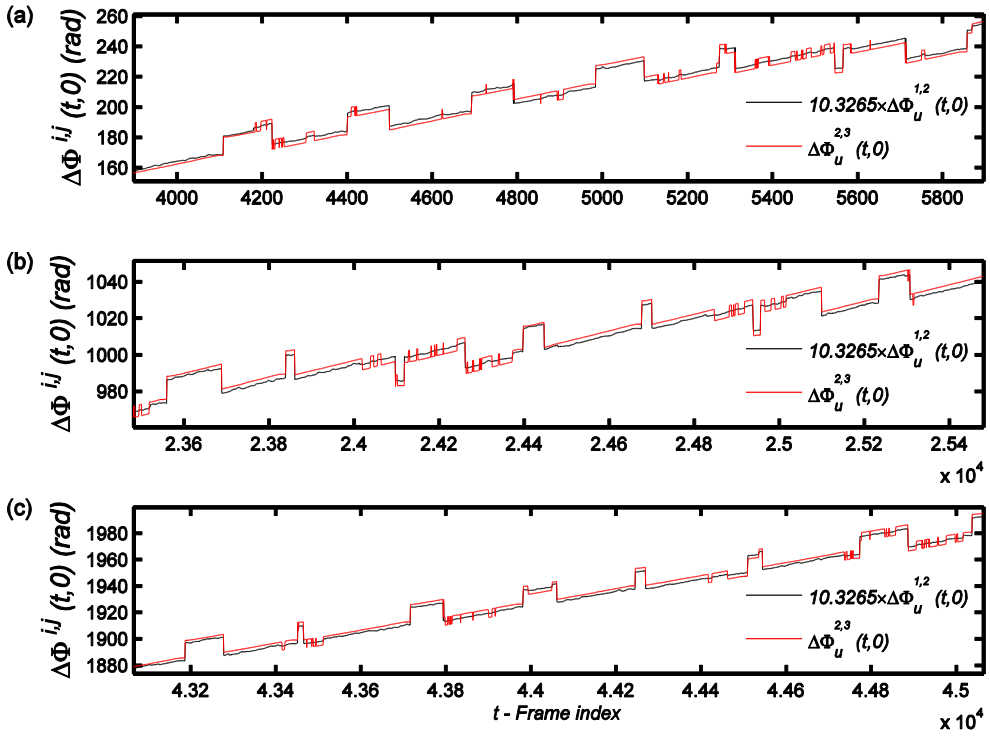

Figure-8.26: Phase plots of the reference phase signal $R \times \Delta\Phi_u^{1,2}(t,0)$ (black line) used to perform the unwrapping of $\Delta\Phi_w^{2,3}(t,0)$ and the resulting unwrapped phase change $\Delta\Phi_u^{2,3}(t,0)$ (red line) for the adaptive Fourier-peak algorithm for which the threshold value c_τ = 0.05 pixels for three different sections of the data sequence where unwrapping errors are most likely to occur. (a) Start of the scan, (b) middle and (c) towards the end of the scan.

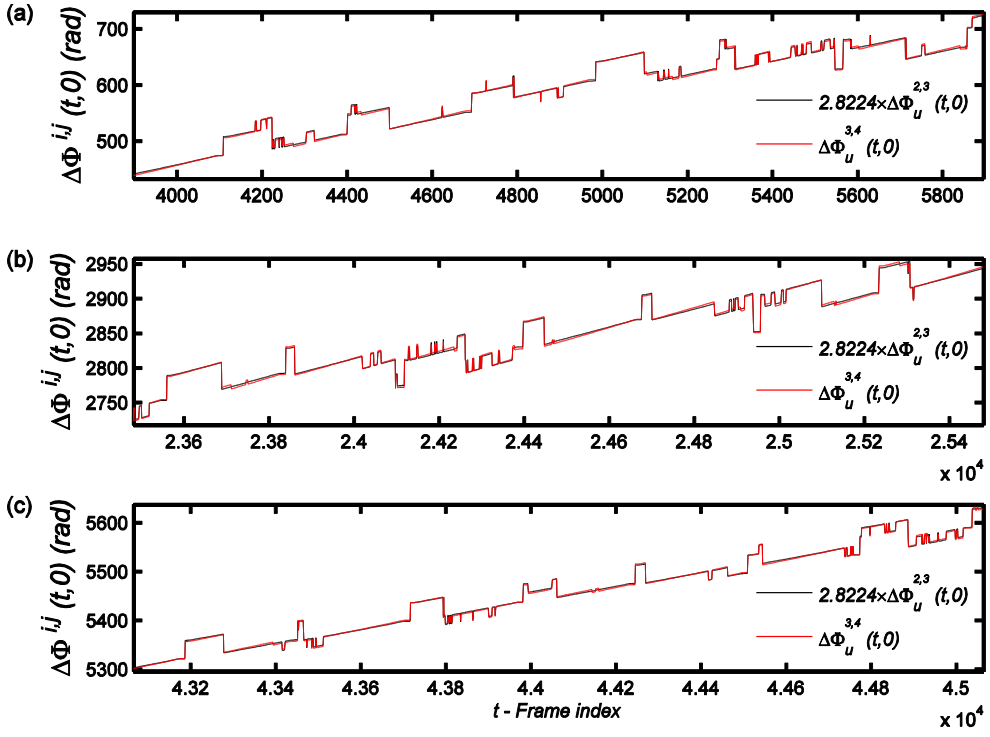

Figure-8.27: Same as above but for the second unwrapping step.

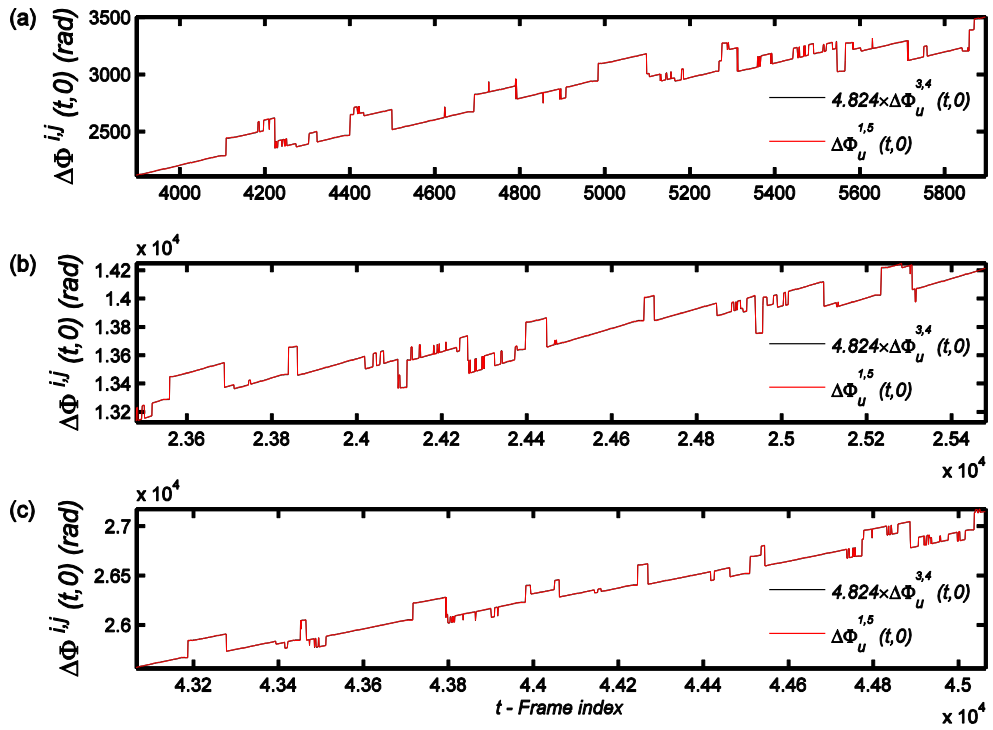

Figure-8.28: Same as above but for the third and final step of the unwrapping process.

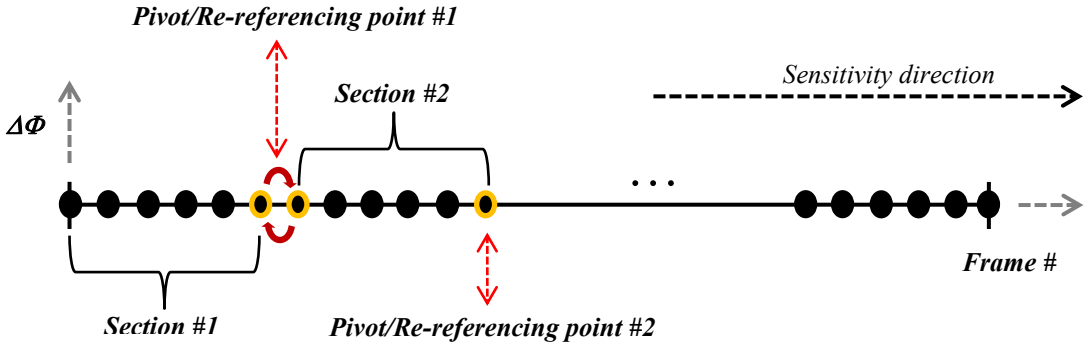

Figure-8.29: Schematic illustration of the principal idea for the unwrapping algorithm along the sensitivity direction with an updating rate of every six data points. The new approach involves the updating of the resulting phase change signal from the synthetic wedges $\Delta\Phi^{i,j}$ at regular and equally spaced intervals. The last element of each of the previous scan sections, termed as *'sections'* here, is shared by the next section (*'pivot'* or *'re-referencing points'*). This prevents gaps between the scaled low sensitivity phase signal, and the high sensitivity phase signal, that arise from the use of an average *R* scaling factor, from becoming large enough to cause a 2π phase unwrapping error.

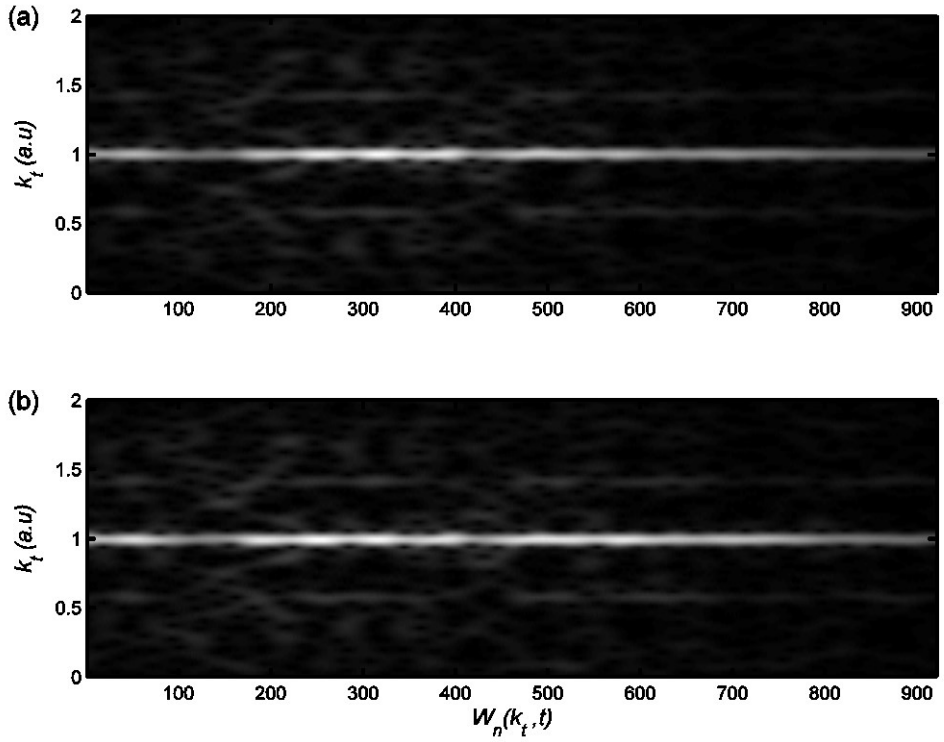

Figure-8.30: Time-frequency analysis using the short-time Fourier-transform for the intensity data from **wedge-1** (a) and **wedge-2** (b). The above spectral plots were produced using the `spectrogram` function in the MATLAB programming language of the data after the improved *R*-optimisation algorithm and the implementation of phase unwrapping algorithm along the sensitivity axis at the maximum updating rate of $\varrho = 2$.

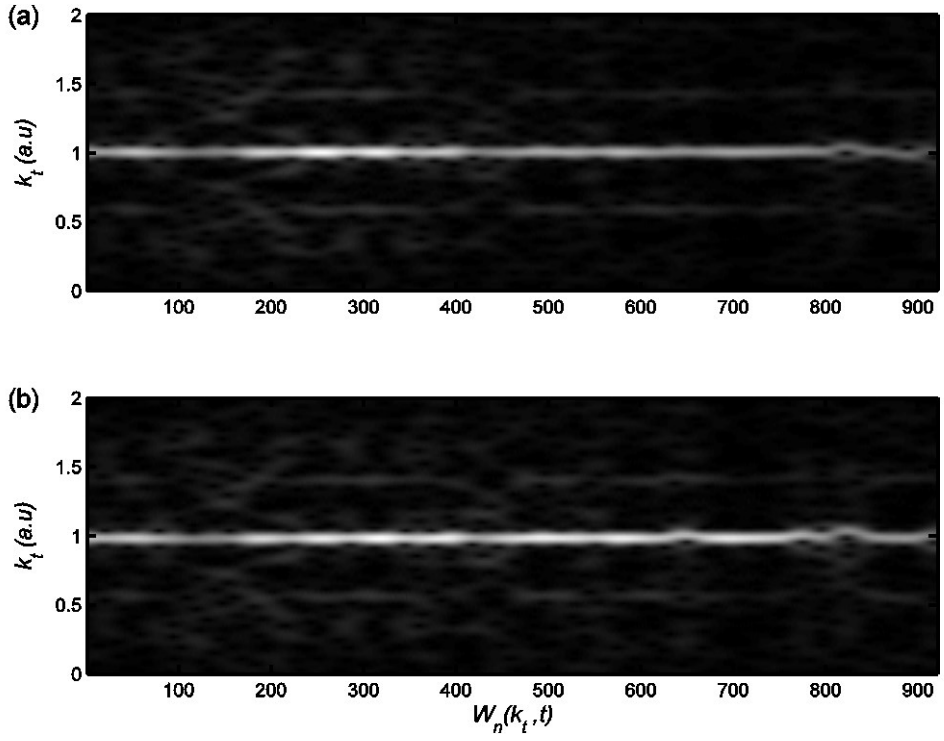

Figure-8.31: Same as figure-8.30 above but for (a) **wedge-3** and (b) **wedge-4**.

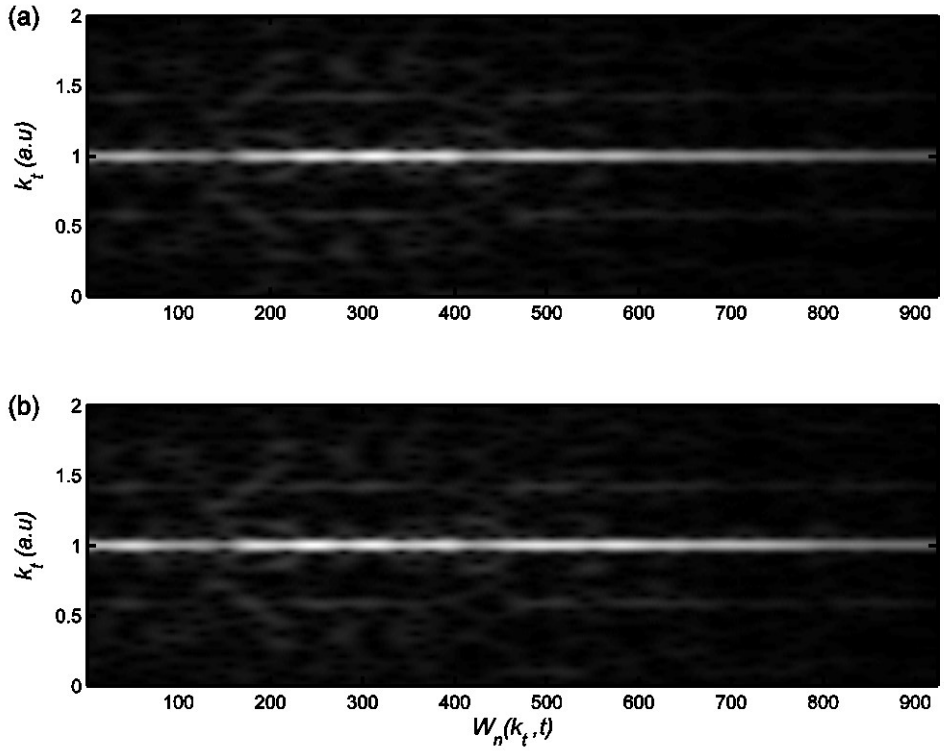

Figure-8.32: Time-frequency analysis using the short-time Fourier-transform for the intensity data from **wedge-1** (a) and **wedge-2** (b). The above spectral plots were produced using the `spectrogram` function in the MATLAB programming language of the data after the improved *R*-optimisation algorithm and the use of the hybrid approach with c_τ = **0.05** pixels and of $c_\psi = \varrho$ = **2** data points.

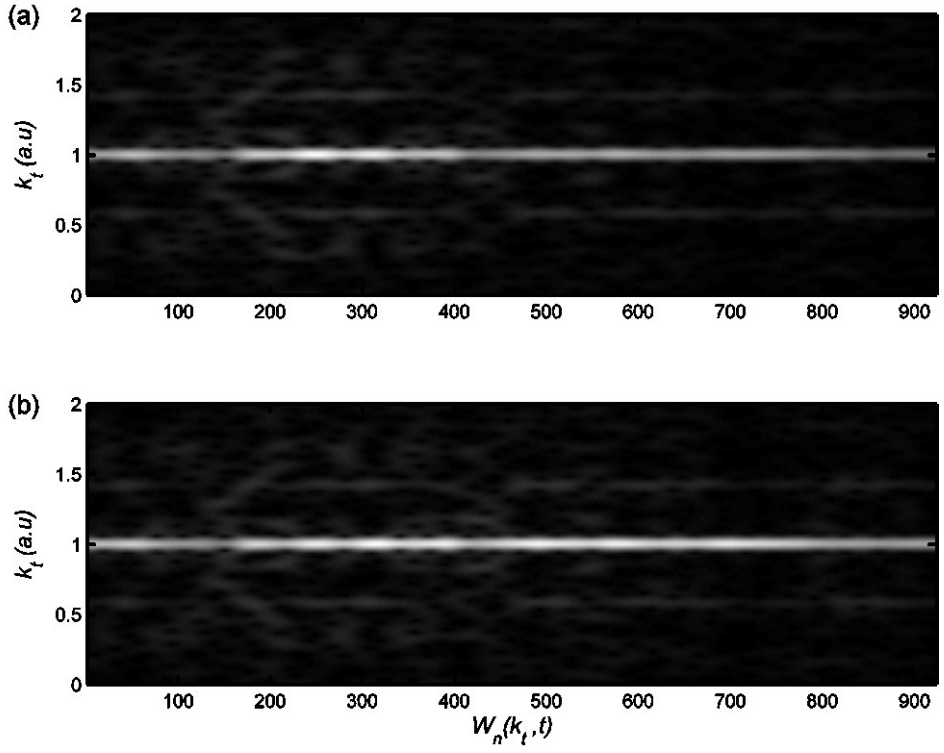

Figure-8.33: Same as figure-8.32 above but for (a) **wedge-3** and (b) **wedge-4**.

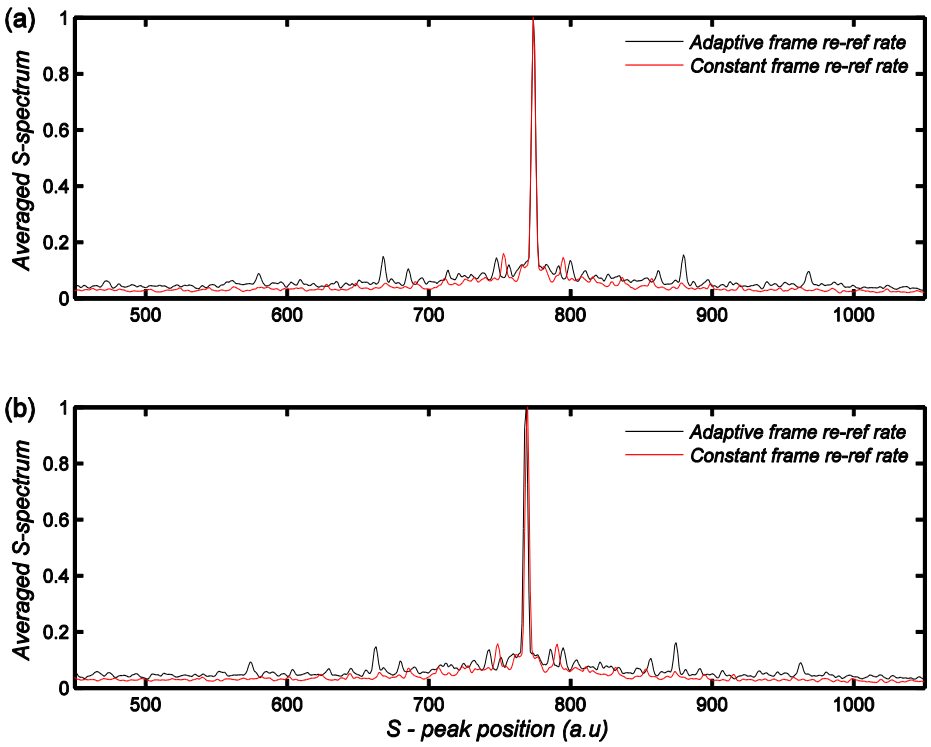

Figure-8.34: Comparison between the averaged spectrograms for the *'adaptive'* (black line) and *'constant'* (red line) frame re-referencing algorithms of the wedge intensity data for (a) **wedge-1** and (b) **wedge-2**.

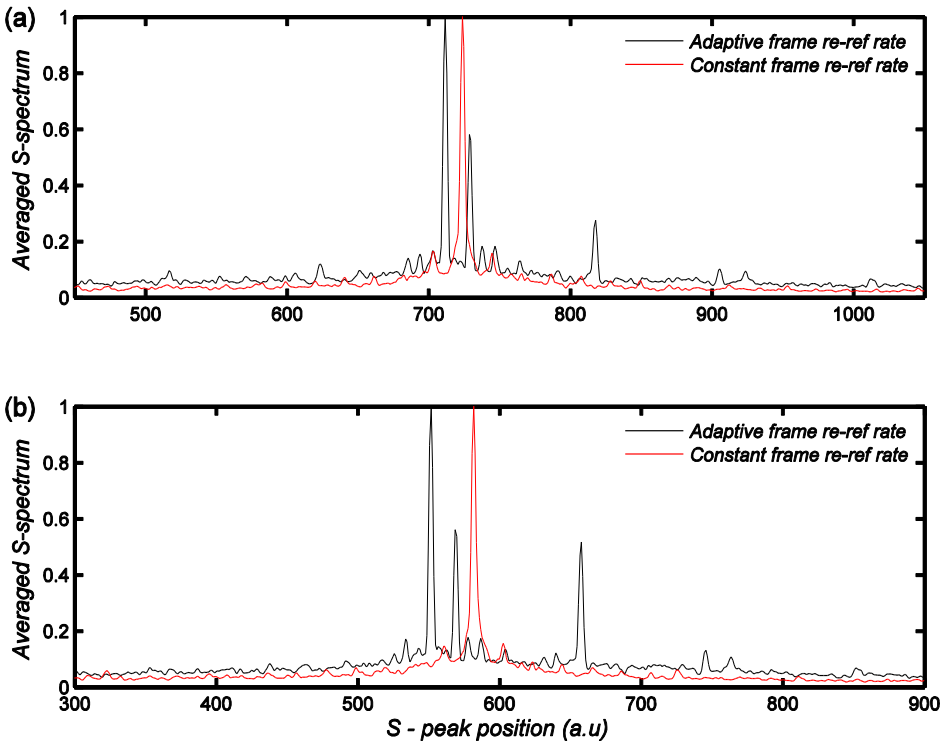

Figure-8.35: Same as figure-8.34 above but for (a) **wedge-3** and (b) **wedge-4**.

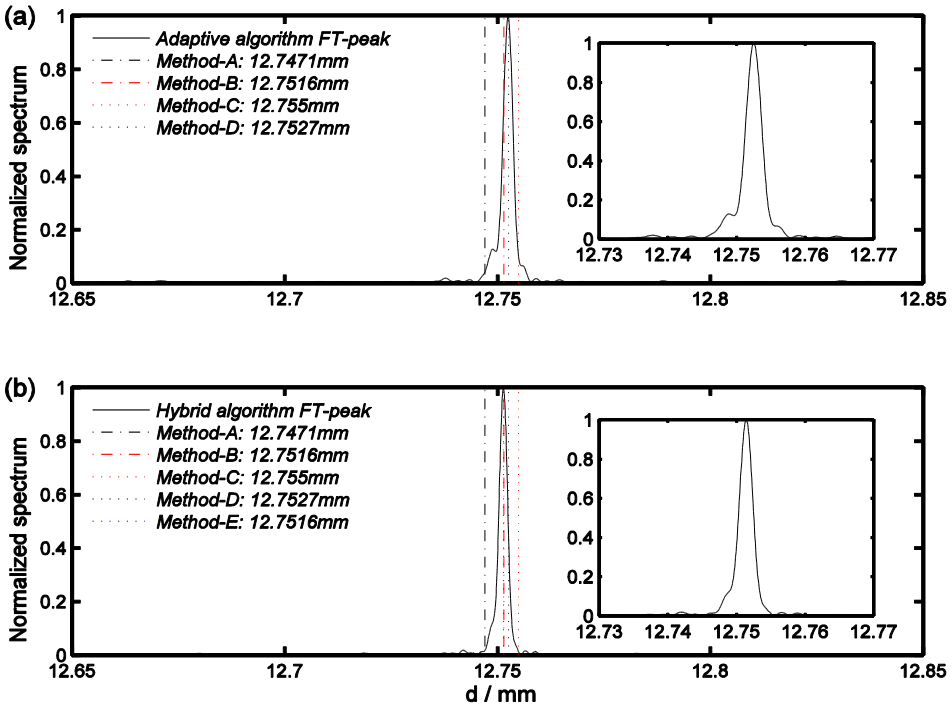

Figure-8.36: Comparison of the estimated central thickness of ***wedge-1*** using the five different methods (A-E). (a) Shape of the main spectral lobe using the adaptive Fourier-peak updating algorithm (Method-D) and its corresponding location (black dotted line) compared to the location estimated by methods A to C. (b) Shape of the main spectral lobe using the hybrid approach (Method-E) and its corresponding location (blue dotted line) compared to the location estimated by methods A to D. Insets show the corresponding 1-D Fourier peak zoomed for clarity.

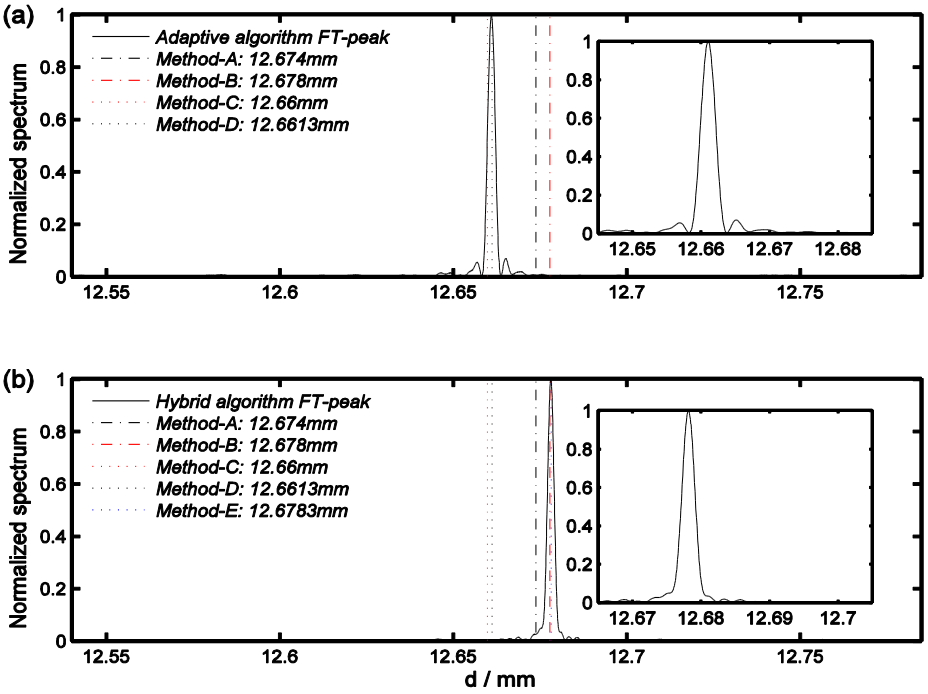

Figure-8.37: Same as figure-8.36 but for the intensity data of ***wedge-2***. Insets show the corresponding 1-D Fourier peak zoomed for clarity.

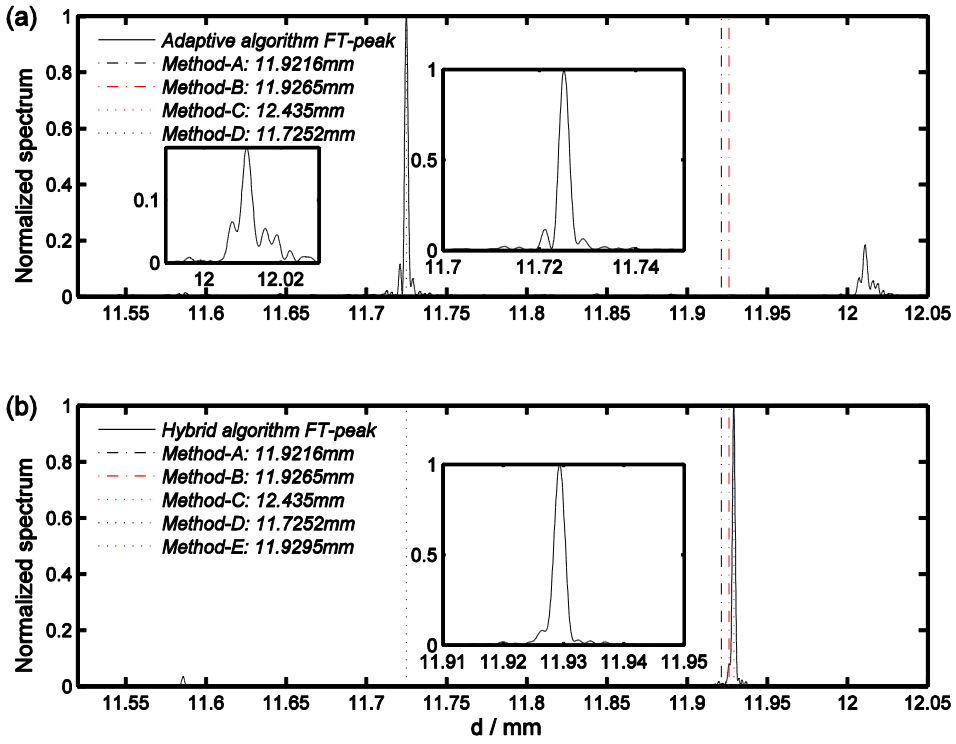

Figure-8.38: Same as figure-8.36 but for the intensity data of ***wedge-3***. Insets show the corresponding 1-D Fourier peak zoomed for clarity.

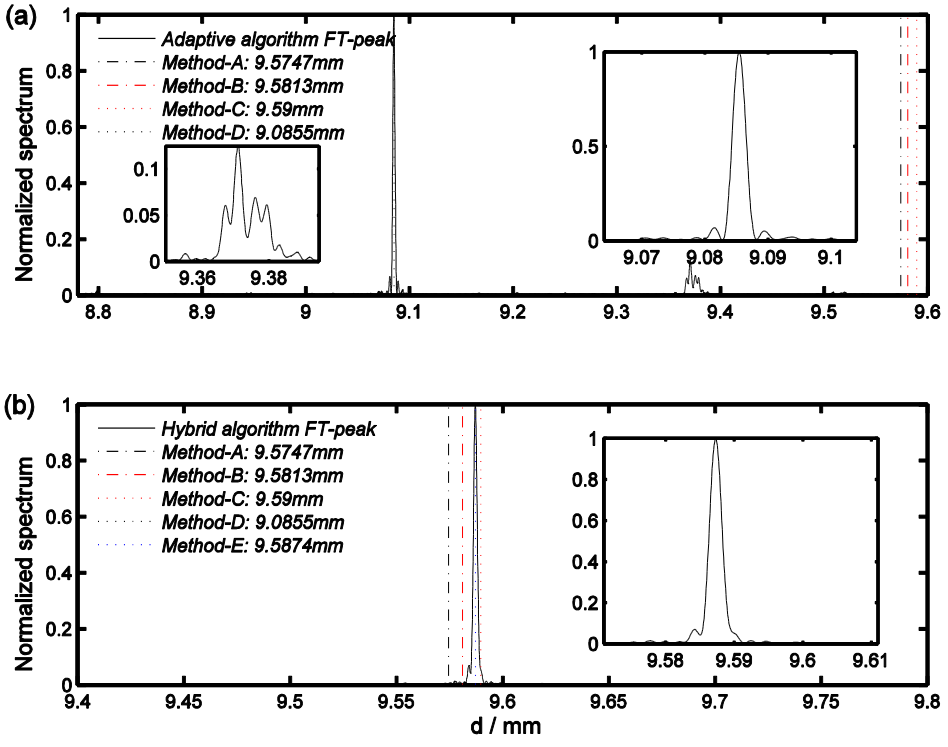

Figure-8.39: Same as figure-8.36 but for the intensity data of ***wedge-4***. Insets show the corresponding 1-D Fourier peak zoomed for clarity.

Chapter-9: TPU strategy validation using simulated data

9.1 Introduction

As phase unwrapping errors are believed to be the main source responsible for much of the undesirable structure, an attempt to link those to systematic and non-systematic errors during a wide range WSI scan using the electronically tuned CW Ti:Sa laser was presented earlier in chapter-7. More specifically, phase unwrapping errors due to (a) a small error in the value of the scaling factor R, (b) small changes in R with wavelength attributed at the time to different dispersion curves for the pairs of wedges, (c) laser-beam induced errors and (d) geometrical and material induced errors, were considered.

In chpter-8 and in order to reduce the artefacts present in the Fourier reconstructions of the depth profile of the four wedges, two modifications to the initial TPU algorithm described in chapter-5 were introduced. Both approaches were of adaptive nature and involved the re-referencing of the phase signal at regular intervals. The first, was designed to account for the gradual change in the spatial frequency of the fringes owing to the laser induced changes in the wavelength, and required the continual updating of the of the spatial frequency components at which the phase was evaluated. The second was designed to compensate for the gradual gap that started to open up between the scaled low-sensitivity unwrapped phase change signal and the assumed to be unwrapped higher-sensitivity phase change signal. By re-zeroing the phase change at regular intervals, and then subsequently adding up the re-referenced phase change, the total phase change since the start of the scan was thus computed but without the 2π phase errors that occurred previously.

The first method was found to improve significantly the quality of the spectrograms apart from the ‘ghost line’ structure seen in the reconstructions from two of the wedges, while the second largely eliminated the ghost lines. A hybrid approach combining both methods was, therefore, proposed and used to analyse the data from each of the four wedges. The hybrid method, a combination of several fixes, was found to be the most robust of all the techniques considered, with a clear Fourier peak at the expected frequency and without any spectral artefacts.

Naturally, the best way of validating the performance of the proposed hybrid approach would be the analysis of additional data sets. However, as already mentioned in the introductory chapter, this is not possible due to the permanent failure of the laser. Moreover, at the time the third data set (see section-1.4.3 and in particular table-1.1) was recorded, the laser behaviour had already started to show signs of malfunction – reduced power output and a rather curious reduction in the data size, suggesting the presence of much larger missing gaps. It was, therefore, decided not to include it in the analysis at this stage.

In the view of this limitation, in this final chapter, the performance of the proposed TPU strategy is investigated by using simulated data instead. The advantage in doing so lies in that, simulations provide a convenient platform where the performance of the proposed TPU strategy can be assessed in the absence of the inevitable noise and other non-linearities associated with the real experimental data. More specifically, in section-9.2 the principle onto which the simulated data are produced is discussed. In section-9.3 the method the two different simulated data sets are produced is described. In section-9.4 a comparison of the performance of the different TPU strategies described in this thesis in recovering the true phase-change signal is discussed. Finally, in section-9.5 the importance of the proposed approach is highlighted by discussing the findings from the analysis of the simulations and comparing them to the results from the real experimental data.

9.2 Proof of principle simulations: Theoretical aspects

The hybrid technique presented in chapter-8 is clearly the best solution so far. To ensure that the proposed solution is generic enough to handle other data scans when the laser will eventually be fixed and that the numerous fixes incorporated in the hybrid approach have not evolved to solve a particularly unique set of problems with the restricted experimental data available, a set of simulations that closely match in terms of the length of the scan range, the wavelength step, the size of the region of interest the characteristics of the real experimental data set analysed in chapters 6,7 and 8 under ideal conditions are described and are subsequently analysed.

9.2.1 Ideal tunning conditions

The fundamental condition for any WSI scheme requires a linear and monotonically increasing and or decreasing wavenumber k with time t such that:

$$k(t) = k_c + \delta k \cdot t, \qquad 9.1$$

where k_c denotes the centre wavenumber, δk is the wavenumber step between two successive frames and t is the frame number. Therefore, in order to maintain the consistency with the experimental data set analysed earlier but without the ambiguities caused by the Ti:Sa laser source (mode hops and missing gaps) the same wavelength range of 100 nm (750 nm to 850 nm) with a wavelength step of 2 pm is chosen for the simulated data sequence. Figure-9.1 shows the ideal tuning curves using equation-9.1.

9.2.2 Recovery of true phase change: *gold standard*

Once the wavelength, λ, and/or the wavenumber, k, at each time instance t are known, the instantaneous phase $\Psi_j(t)$ owing to the front and back reflections from each of the four wedges (j=1,2,3,4) can be calculated such that:

$$\Psi_j(t) = k(t) n d_j \{f(\theta, \alpha) + \lambda(t)/2\}, \qquad 9.2$$

where, t is a non-dimensional time index corresponding to a unique wavenumber k and is equivalent to the frame number. n is the refractive index of the medium (wedge material), d_j is the thickness at the centre of the wedge and $f(\theta,\alpha)$ is the term responsible for compensating for the wedge angle (recall section-5.2.1 and in particular equation-5.9). Finally, the term $\lambda(t)/2$ inside the parenthesis is included to account for the phase shift due to the internal reflection inside the wedges, in accordance to [300-302].

Equation-9.2 could serve as the reference signal for the comparison of the TPU algorithms. However, as the measurements performed involve phase-changes rather than absolute phase measurements, further mathematical manipulation is required. For this reason, the remaining of this section will focus on finding the appropriate mathematical expression capable of serving as the reference signal. Once this is achieved, the ability of the different TPU strategies to recover the true phase change signal can then be assessed.

The interferometric phase change $\delta\Psi_j$, owing to (a) the front and back reflections of a transparent wedge (j) of angle α and (b) to the inter-sample change in wavenumber k induced by the laser, can be expressed such that:

$$\begin{aligned}\delta\Psi_j(t,t-1) &= \Psi_j(t) - \Psi_j(t-1)\\ &= k(t)d_j\{f(\theta,\alpha)+\lambda(t)/2\} - k(t-1)d_j\{f(\theta,\alpha)+\lambda(t-1)/2\}\\ &= nd_jf(\theta,\alpha)\delta k + nd_j\{k(t)\,\lambda(t)/2 - k(t-1)\,\lambda(t-1)/2\}\\ &= nd_jf(\theta,\alpha)\delta k + \underbrace{nd_j\{\pi-\pi\}}_{=0}\\ &= nd_jf(\theta,\alpha)\delta k \end{aligned} \quad 9.3$$

By adding the incremental phase changes $\delta\Psi_j$ over time t (using the `cumsum` function in MATLAB), and provided that $f(\theta,\alpha)$ remains constant over the scan duration it follows that:

$$\Delta\Psi_j(t,0) = nd_j\Delta k(t,0)f(\theta,\alpha). \quad 9.4$$

Recall that the analysis presented in this thesis is concerned with phase differences between successive pairs of wedges because it would be impractical to make a wedge thin enough to satisfy the inequality-5.16. It follows that, the synthetic-wedge phase-change signal between a pair of wedges denoted here as j and j+1, owing to the incremental change in the wavenumber, δk, between two successive frames can be expressed using equation-9.3 such that:

$$\delta\Phi^{j,j+1}(t,t-1) = \delta\Psi_j(t,t-1) - \delta\Psi_{j+1}(t,t-1). \quad 9.5$$

Figure-9.2 provides a visual illustration of the working principle the optical sensor is based on, and is repeated here for consistency and clarity reasons. As $\delta\Psi_j$ and $\delta\Psi_{j+1}$ are each wrapped onto the range -π to π, $\delta\Phi^{j,j+1}$ lies in the range: -2π to 2π. It is, therefore, convenient to wrap this onto the principal range of -π to π [208] by the wrapping operator ($\mathcal{W}$) such that:

$$\delta\Phi_w^{j,j+1}(t,t-1) = \mathcal{W}\{\delta\Phi^{j,j+1}(t,t-1)\}. \quad 9.6$$

Note that, the wrapped phase-change ($\delta\Phi_w^{j,j+1}$) can be thought of as the phase signal produced by a wedge with a synthetic thickness:

$$d_s^{j,j+1} = d_j - d_{j+1}. \qquad 9.7$$

Provided $d_s^{j,j+1}$ satisfies the inequality-5.16 (note that the superscripts *i,j* are replaced here by *j,j+1* with *j* = 1,2,3,4), the incremental wrapped phase change between a given pair of successive frames equals the true (unwrapped) phase change between those frames. Therefore, the running sum of incremental wrapped phase changes represents the true unwrapped phase change between the first frame and the current frame *t*:

$$\Delta\Phi_u^{j,j+1}(t,0) = \overbrace{\delta\Phi_w^{j,j+1}(1,1)}^{=0} + \sum_2^t \delta\Phi_w^{j,j+1}(t,t-1) \qquad 9.8$$

Equation-9.8 above will formulate the reference, referred to henceforth as the *gold standard*, against which the performance of the different temporal phase unwrapping strategies in recovering the true phase change signal will be tested. Note that *t* = 1, 2, 3…, total number of frames.

9.3 Simulated wedge data sequence for a full 100 nm scan

Having established the mathematical expression that will provide the 'reference' against which the recovered phase signals resulting from the different TPU algorithms will be compared, in this section a description of the simulated data sets is given.

9.3.1 Wedge phase reconstruction

In order for the simulated data set to be as close to the experimental data set as possible, the majority of the constants that define the dimensions of the optical sensor are kept the same. These are summarised in tabular form in table-9.1 below. Note that the wedge angle α, has been deliberately chosen to be smaller than the ~ 2 min target value in order to match the number of fringes of the real experimental data and the estimated wedge angles (recall table-7.3) prior to the application of the square aperture correction factor (recall section-7.3.2) .

As the central thickness, d_c, and the angle, α, of each of the four wedges are known, the starting and final thicknesses along the wedge-direction can be determined as follows:

$$d_i^j = d_c^j - (l/2)\tan\alpha$$
$$d_f^j = d_c^j + (l/2)\tan\alpha \qquad 9.9$$

Table-9.1: Tabular form of the key optical sensor parameters used for the simulated data set.

	Wedge width		Central thickness d_c	Wedge height	θ	α
Wedge-1	30 mm	714 pixels	12.8 mm	86 pixels	2 degrees	1.200 min
Wedge-2	30 mm	714 pixels	12.6 mm	86 pixels	2 degrees	1.068 min
Wedge-3	30 mm	714 pixels	12.0 mm	86 pixels	2 degrees	1.362 min
Wedge-4	30 mm	714 pixels	9.60 mm	86 pixels	2 degrees	1.422 min

By interpolating between the starting and final thickness values, the profile of each of the four wedges can be reconstructed. Once the ideal wedge profiles are reconstructed, the 2-D phase distribution Ψ_j across the wedge can be obtained by inserting each of the elements of the 2-D matrix describing the wedge profiles into equation-9.2. Figure-9.3 shows these for the first two wedges at the first frame i.e. λ = 750 nm and for a refractive index value of n = 1.453.

9.3.2 Phase signal and fringe pattern reconstruction

By repeating the process described above for all the wavelengths in the scan range of 750 - 850 nm with a wavelength step of 2 pm and n = 1.453, the temporally unwrapped (due to the small difference in the central thickness between the first and second wedges) '*gold standard*' phase signal can be calculated using equations 9.5, 9.6 and 9.8.

In previous chapters a variety of error sources that are believed to contribute to phase unwrapping errors have been investigated. In brief, these included the effect of intensity artefacts, the wedge thickness, the uncertainty in the instantaneous peak position, the mismatch in the refractive index dispersion curves between successive pairs of wedges, laser beam induced errors as well as geometrical factors such as the presence of angles along directions other than that of the wedge direction (refer to section-7.3 for more details). The latter resulted in the introduction of a correction factor that demonstrated a rather dramatic mismatch in the number of fringes amongst the four wedges and the estimated wedge angle (recall table-7.3 and table-7.4).

Therefore, before proceeding with the description of the simulated fringe patterns, it is worth considering the effect of a mismatch amongst the wedge angles of the four wedges involved in the phase unwrapping procedure. To do so, consider the hypothetical scenario where the pair of wedges are characterised by the same refractive index and are also immune to dispersion such that:

$$n(\lambda) = n = 1.453, \lambda \in [750,850]nm \qquad 9.10$$

as illustrated in figure-9.4. If the wedge angles α_1, α_2 are the same i.e. $\alpha_1 = \alpha_2$, it follows that: $f(\theta, \alpha_1) = f(\theta, \alpha_2) = f(\theta, \alpha)$. Therefore, according to equation-9.5 the synthetic-wedge phase-change between two adjacent frames is given by:

$$\delta\Phi^{1,2}(t, t-1) = n\delta k f(\theta, \alpha)\{d_1 - d_2\} \qquad 9.11$$

If, on the other hand, $\alpha_1 = \alpha_2$ then, $f(\theta, \alpha_1) \neq f(\theta, \alpha_2)$ and the expression for the synthetic-wedge phase-change between two adjacent frames changes to:

$$\delta\Phi^{1,2}(t, t-1) = n\delta k\{d_1 f(\theta, \alpha_1) - d_2 f(\theta, \alpha_2)\} \qquad 9.12$$

Recall that the fundamental requirement for the temporal phase unwrapping described earlier and in chapter-5 requires that by first wrapping (equation-9.6) and then summing the incremental phase changes between adjacent frames (equation-9.8), gives the correctly unwrapped phase-change signal $\Delta\Phi_u^{1,2}(t, 0)$. This is scaled by a factor R (see equation-5.19) and is then used to unwrap the higher sensitivity phase-change signal $\Delta\Phi_w^{2,3}(t, 0)$ (recall equation-5.20) and so on until the highest sensitivity phase-change signal $\Delta\Phi_w^{1,5}(t, 0)$ is unwrapped and converted to the sought wavenumber axis Δk. From equation-9.11 and equation-9.12 it is clear that in the presence of unequal wedge angles, the role of the $f(\theta,\alpha)$ term is different. This is a rather important observation in that it suggests that the scaling factor R cannot be accurately calculated by taking the ratio of the respective central wedge thicknesses as suggested by equation-5.19. In order to quantify the deviations caused by this revelation and highlight the validity of the proposed hybrid approach, two simulated data sets will be processed. The first data set will be based on wedges with slightly unequal wedge angles ($\alpha_1 \neq \alpha_2$) and the second on identical wedge angles ($\alpha_1 = \alpha_2$), as shown in table-9.2.

Table-9.2: Wedge angles and the corresponding number of fringes of the two simulated data sets analysed in this chapter.

	Simulated data set-1: $\alpha_1 \neq \alpha_2$		**Simulated data set-2: $\alpha_1 = \alpha_2$**	
	Wedge angle	***Number of fringes***	***Wedge angle***	***Number of fringes***
Wedge-1	1.200 mins	42	0.9 mins	31
Wedge-2	1.068 mins	37	0.9 mins	31

With this in mind, the '*gold standards*' for the two different simulated data sets can be extracted through the use of equation-9.6 and equation-9.8. As expected, the two unwrapped phase change signals appear similar for the first few hundred frames but start to deviate from each other towards the end of the scan, with a mismatch of the order of 1.5 in 600 radians as illustrated in figure-9.5(a) and figure-9.5(b) respectively. The latter provides a useful quantitative measure of the deviation one should expect in the recovered phase-change signal when a mismatch in the wedge angle is present but in the absence of any other non-linearities.

Having established the reference phase-change signal, the last step towards producing the simulated WSI data sets is that of generating the relevant fringe patterns for each of the wedges. Recall that in interferometry the interference signal is practically given by the sum of the background intensity distribution I_0 and the modulation intensity I_M multiplied by the cosine of the phase, such that [81]:

$$I(x,y,t) = I_0(x,y,t) + I_M(x,y,t)\cos\phi(x,y,t)\,, \qquad 9.13$$

where x,y denote the pixel indices in the region of interest, t is the frame index corresponding to a unique wavelength (λ) or wavenumber (k) while ϕ is the phase shift between the reference and object waves. Therefore, by letting:

$$\phi(x,y,t) = \Psi_j(x,y,t) \qquad 9.14$$

where Ψ_j is the 2-D phase distribution at each time instance t (see figure-9.3), the sought fringe patterns can be generated. Figure-9.6 illustrates the resulting fringe patterns for the two scenarios considered here i.e. unequal wedge angles (left column) and equal wedge angles (right column). Note that in this example and in order to ensure maximum fringe contrast, the background and modulation intensities have been set equal to 10^5 in arbitrary units (a.u). By repeating the process described

in the previous section, the intensity data for all four wedges can be extracted and subsequently analysed

9.4 Comparison of TPU analysis algorithms in the absence of noise

The success of the 'hybrid' method that produced the best spectral peaks both in terms of the signal-to-noise ratio ('ghost line' fully suppressed) and the location corresponding to the thickness of each of the four wedges was the result of several fixes. Some of these were particularly introduced to the processing software in order to account for the various error sources associated with real experimental data such as:

a. the missing data gaps (see section-6.3.1) owing to the laser mode-hops,
b. the estimation and suppression of background intensity artefacts owing to the internal reflections inside the wedge material (see section-6.2.3),
c. the dependency of the refractive index of the wedge material on the instantaneous wavelength of the source and the potential mismatch in the dispersion curves amongst the four wedges (see section-7.3.3),
d. the presence of angles along directions other than the wedge direction (see section-7.3.2).

The majority of the above are no longer present in the simulated data. More specifically (a) has been replaced by the ideal tuning curve thereby eliminating the presence of gaps and thus resulting in a uniformly spaced k-vector, (b) is no longer an issue as there are no reflections and/or the location of the illuminating beam is no longer a function of time in the simulated data, (c) the refractive index of the wedges has been arbitrarily set to a constant value of 1.453 with its dependency on wavelength dropped (zero dispersion condition) and finally (d) there is only one wedge angle ,that is, along the wedge direction which in turn resulted in vertical fringes (recall figure-9.6) in place of the tilted fringes in the real experimental data (recall figure-7.12 for example).

As (a)-(d) constitute systematic and non-systematic errors that can all be categorised under the generic term 'noise', the remaining of this final chapter will be focused on the processing and analysis of data in the absence of noise. More specifically, the performance of the *integer* and *non-integer* phase extraction methods will be tested

for the two simulated data sets in recovering the true phase-change ('gold standard') by processing the intensities of the simulated fringe patterns for the first two wedges only i.e. wedge-1 and wedge-2. The reasons justifying the aforementioned decision are as follows:

a. If any phase unwrapping errors occur during this first step, they will be accumulated and amplified in the next steps.
b. It is believed that a large number of phase unwrapping errors and artificial wavenumber jumps have been suppressed after the implementation of the 2-D non-integer phase extraction method (see for example figure-6.9)
c. To investigate the validity of the adaptive vs the constant re-referencing TPU approach and its difference to the unwrapping strategy along the phase sensitivity direction in the presence and/or absence of unequal wedge angles.

The above aim at shedding some more light into a number of concerns that cannot at this stage be justified with real experimental data due to the permanent laser failure. First, the important question of whether the proposed 'hybrid' approach is in fact generic enough to be recommended for future WSI applications and has not evolved to solve the problems associated with one particular data set, will be clarified. Second, by testing the ability of the integer and non-integer phase extraction methods for equal and unequal angles will hopefully assist in understanding the rather large mismatch in the refractive index dispersion trend curves that was observed earlier (recall figure-7.15). Finally, the relevant contribution of phase unwrapping errors owing to the phase extraction process alone will be further clarified.

9.4.1 Recovery of $\Delta\Phi_u^{1,2}$ without updating the peak

As mentioned earlier, if an error occurs in the recovered, temporally unwrapped phase-change signal corresponding to the first synthetic-wedge (involving the pair of wedge 1, 2) phase-change that is used as the reference signal to unwrap the higher sensitivity synthetic-wedge phase change involving the next pair of wedges (2, 3), it follows that the unwrapped higher sensitivity phase-change $\Delta\Phi_u^{2,3}$ will also suffer from the same error amplified by the scaling factor R_1. This poses a major threat to the validity of the temporal phase unwrapping method described in chapter-5, in that it suggests that the reference signal is in fact not unwrapped. As a first step to highlight this point, the ability to recover the true phase change $\Delta\Phi_u^{1,2}$ using the

integer and the *non-integer* phase extraction methods without updating the Fourier-peak at which the phase is evaluated, is investigated for the two simulated data sets.

Figure-9.7(a) illustrates the effect of not updating the frequency at which the phase Ψ_j is evaluated on the recovered phase-change signals $\left(\Delta\Phi_{int}^{1,2}, \Delta\Phi_{non-int}^{1,2}\right)$ using the *integer* and *non-integer* phase evaluation methods for the case of unequal wedge angles ($\alpha_1 \neq \alpha_2$). As expected, significant deviations between the two recovered signals and the true phase change $\Delta\Phi_{gs_1}^{1,2}$ start to emerge from frame t = 10,000 onwards. These, manifest themselves as phase jumps that would be difficult to distinguish from the laser induced wavenumber jumps or, indeed, link them to any other possible physical phenomenon. Moreover, as indicated by the error plots in figure-9.7(b) and figure-9.7(c), even in the regions where the error function (erf) does not contain the jumps shown in figure-9.7(a), a curious deviation from the gold standard (gs_1) is observed that takes the form of a linear ramp convolved with an oscillating component (see detail D_1 in figures-9.7(b), 9.7(c)) of the order of 0.03 rad over a phase change of 10.8 rad for both cases.

On the other hand, figure-9.8(a), illustrates the same comparison as in figure-9.7(a) but this time for the case where the wedge angle is identical for both wedges forming the synthetic wedge (1,2) – $\alpha_1 = \alpha_2 = 0.9$ mins corresponding to 31 fringes at λ = 750 nm for both wedge-1 and wedge-2. By comparing figure-9.7(a) and figure-9.8(a), it becomes clear that the large phase jumps that were previously observed between the gold standard (gs_1) and the recovered phase-change signals (see figure-9.7(a)), for both the *integer* and the *non-integer* methods, are no longer present for the case of identical wedge angles (see figure-9.8(a)). Both the recovered phase-change signals seem to be in good agreement with the true phase-change (gs_2) with the exception of a downward phase jump of the order of 5 rad over a phase-change of 471.5 rad for the *integer* method and some small upward excursions occurring at frames t ~ 18470, 30800 and 43100 for the *non-integer* approach that are of the order of 3, 10 and 15 rad respectively as indicated by figure-9.8(b) and figure-9.8(c). More importantly, however, as it is illustrated by the error plots in both figures-9.8(b),(c) the linear ramp that was previously present right from the start of the scan sequence (recall detail D_1 in figure-9.7(b) and (c)) has been suppressed (see detail D1 in both figure-9.8(b) and (c)). Considering that the oscillating nature of the error plots illustrated in

detail D_1 of figure-9.8(b) and (c) describes much more closely the sensitivity of interferometric techniques than that illustrated in D_1 of figure-9.7(b) and (c), suggests that the linear ramp was in fact a numerical artefact owing to the mismatch in the wedge angles of wedge-1 and wedge-2.

Finally, as indicated by figure-9.7 and figure-9.8 the recovery of the true phase-change is always superior for the *non-integer* phase extraction method regardless of whether the wedge angles are identical or not, thereby highlighting its importance for WSI applications. Furthermore, the effect of not updating the frequency at which the phase is evaluated as well as the effect of the mismatch in the wedge angles is in fact very difficult to identify if only a few hundred frames are considered. The latter is a rather important observation in that it highlights the difficulties involved with recovering the correct temporally unwrapped phase signal over such a wide tuning range as that considered in this thesis.

9.4.2 Recovery of $\Delta\Phi_u^{1,2}$ using the constant peak updating TPU method

In the view of the observations presented above, in this section the effect of updating the Fourier-peak at which the phase is extracted in recovering the correct phase-change using the two simulated data sets ($\alpha_1 \neq \alpha_2$ and $\alpha_1 = \alpha_2$) using the two different phase extraction methods is investigated.

Following the same procedure as previously, the data set where $\alpha_1 \neq \alpha_2$ is considered first. Figure-9.9 provides a visual comparison between the recovered phase change signals using the *integer* and *non-integer* methods and the corresponding true phase change (gs_1). Additionally, in an attempt to investigate the effect of the re-referencing, two different re-referencing rates are chosen with first at 400 frames and the second at 4 frames. There are four important points revealed by the plots in figure-9.9. First, by introducing the concept of re-referencing, the principle idea that was stated earlier (recall section-8.3.2 and equation-8.6) suggesting that, after several wavelength increments during a wavelength scan the order position of the Fourier peak at which the phase is evaluated needs to be updated, is confirmed. Second, all of the recovered phase-changes, and regardless of the type of phase extraction method, are free from the phase jumps that were previously observed (recall figure-9.7(a)). Third, all four of the experimentally recovered phase changes seem to suffer from a deviation from the true phase change (gs_1) of the order of ~1.5 rad over the

total phase change of ~570 rad (see detail D_1 in figure-9.9). Fourth, by comparing the recovered phase changes for the two re-referencing rates, it becomes clear that under the ideal conditions considered here, it makes little if any difference whether one chooses a really high (4 frames) or medium (400 frames) re-referencing rate (see detail D_2 in figure-9.9). The latter is further illustrated in figure-9.10 and its accompanying details D_1, D_2 and D_3. Furthermore, the linear ramp in the error plots is once again confirmed for the case of unequal wedge angles.

As a last step, the recovered phase-changes are compared against each other and against the corresponding gold standard (gs_2) for the case of equal wedge angles in figure-9.11. As expected, by setting the wedge angles equal to each other, the majority of the discrepancies that were previously observed when $\alpha_1 \neq \alpha_2$ are once again by and large removed. More specifically, by comparing the corresponding error plots for the *integer* and *non-integer* methods for the two re-referencing rates chosen (400 frames and 4 frames) in figure-9.12, it is clear that when $\alpha_1 = \alpha_2$ the linear ramp is removed. Moreover, the superiority of the *non-integer* phase extraction approach proposed here is once again highlighted by the fact that the discrepancies between the gold standard (gs_2) and the *integer* method illustrated in figure-9.12 (a),(b) are not present for the *non-integer* method as shown in figure-9.12 (c),(d). Interestingly, the aforementioned phase jumps occur at the same frame indices. The most likely reason responsible for their occurrence is attributed to the order position of the Fourier peak being underestimated or overestimated due to some build-in rounding operation (figure-9.12 (a), (b)). This is confirmed by their absence in the corresponding error plots for the *non-integer* approach in figure-9.12 (c), (d).

9.4.3 Recovery of $\Delta\Phi_u^{1,2}$ by updating the peak at every frame

In this final section the effect of updating the position of the Fourier peak at which the phase is extracted at every frame, is investigated for the two simulated data sets and the two phase estimation methods (i.e. *the integer* and the *non-integer* methods). Although this is not quite the same as the 'hybrid' method (consisted of the adaptive peak updating TPU and the unwrapping along the phase sensitivity axis strategies – see chapter-8) used for the experimental data set, the fact that the peak location is updated at every frame can be considered similar in that it pushes the adaptive TPU strategy to its limit (if the re-referencing rate for the adaptive TPU method was to be

set to 1, the two methods become identical). The latter was not tested using the real experimental data due to the general noise aspects associated with the real experimental data. However, simulations provide the ideal platform where such conditions can be examined thereby, providing the necessary confidence to test whether there is a lower limit beyond which, the updating principle fails.

Once again, following the same procedure as before, the case where $\alpha_1 \neq \alpha_2$ is examined first. As illustrated in figure-9.13, and unlike the recovered phase using the *non-integer* method, the recovered phase change using the *integer* approach suffers from a large number of phase-jumps that gradually build up, starting from frame t = 10000 onwards (see detail D_1 in figure-9.13) confirming the superiority of the *non-integer* approach. As expected, the error plot in figure-9.14(a) confirms this as well as the presence of the linear deviation. In addition to the above expected remarks, the error plot in figure-9.14(a) suggests that the recovered phase change signal using the *integer* method suffers from phase unwrapping errors (i.e. unresolved 2π phase jumps). Considering that the recovered phase change from the first pair of wedges is assumed to be unwrapped, this is a rather disturbing observation. To test whether this is the case, a simple test is performed where the error plot erf is checked for 2π errors. This is done by choosing an arbitrarily threshold of $\pi/\sqrt{3}$ rad such that if:

$$erf(t) \geq \pi/\sqrt{3}\, rad \qquad 9.15$$

the corresponding frame t is marked with an asterisk (*). The results of this simple test are quite relieving. As shown in detail D_1 in figure-9.14(a), what initially appear as phase unwrapping errors are in fact the result of additive inter-frame phase jumps that are less than π. Apart from being reassuring, this also explains the stair-like shape of the error function (erf) for the integer method. On the other hand, the *non-integer* approach is free from this structure, once again demonstrating the importance of the *non-integer* phase extraction algorithm as illustrated by the corresponding error plot in figure-9.14(b). Another interesting fact, revealed by the error function for the *non-integer* method, is that although $\alpha_1 \neq \alpha_2$, the expected linear ramp is no longer present. This suggests that under the ideal conditions of a perfectly linear and free from gaps wavelength scan, the mismatch in the wedge angles can be resolved by simply updating the frequency at which the phase is evaluated at every frame (that is, provided that the *non-integer* method is used).

Last but not least, the recovered phase changes using the *integer* and *non-integer* algorithms with the maximum re-referencing rate are compared for the case of identical wedge angles. As expected, the superiority of the *non-integer* approach versus its *integer* contender is once again confirmed, as it is illustrated in figure-9.15. Moreover, by comparing figure-9.15 to figure-9.13, it can be seen that the deviation point between the recovered phase change signal using the *integer* method and the corresponding *gold standard*, is now shifted by several thousands of frames thereby highlighting the important effect of having equal wedge angles. The effect is further justified by the error plots illustrated in figure-9.16(a) and figure-9.16(b) for the integer and non-integer phase extraction algorithms respectively.

As it has already been pointed out, from the comparisons presented this far, the large phase jumps observed in the error plots for the *integer* method are not to be confused with phase unwrapping errors. These, are in fact, the result of accumulated phase errors of magnitude less than π that occur between adjacent frames as illustrated by the zoomed region in figure-9.16(a). The most likely reason for their occurrence is linked to the fact that it takes several thousands of frames until the order position of the Fourier peak is changed when using the *integer* method. In simple terms, as the position of the peak where the phase is evaluated, is estimated as an integer number using the integer method, it is only after several thousands of frames that its position is in fact updated, even when the maximum re-referencing rate of 1 is used. It is, therefore, reasonable for one to expect the recovered phase-change to be significantly underestimated. This can be further realised by comparing the estimated instantaneous peak positions using the *integer* and *non-integer* 2-D Fourier peak position estimation algorithms.

Figure-9.17 illustrates this point for the case of unequal wedge angles, while figure-9.18 refers to the case where the wedge angles are set to equal each other. As it is clearly illustrated, the location at which the curious phase jumps were previously observed perfectly coincides with the location at which the order position of the peak changes (compare figure-9.17(b) to figure-9.14(a) and figure-9.18(b) to figure-9.16(a) for example). On the other hand, the natural question as to why the phase jumps seem to not be present for the case of constant peak updating is not as straight forward. However, by comparing figure-9.12(a) and figure-9.12(b) to figure-9.18(a) and figure-9.18(b), it becomes clear that they are in fact present but are more

diffucult spot due to their much smaller case. The above justifies the sensitivity of the location of the Fourier peak and the corresponding phase. This last point further justifies the suspicion that the accuracy of the estimated phase is directly linked to the accuracy the corresponding Fourie-peak position is determined.

9.5 Discussions and conclusions

In this final chapter, and in the absence of additional experimental results, a set of simulated data that closely matched the real experimental data set analysed in chapters-6 to 8 were produced and subsequently analysed. There are two reasons that justify this decision. The first one is related to the lack of additional experimental data due to the permanent failure of the lase source. As a result, it is possible that the 'hybrid' approach that has clearly given the best results (recall chapter-8) may have evolved to solve the problems associated with one particular data set, thereby questioning whether the technique ('hybrid' approach) is generic enough to be recommended for future WSI applications. The second one is related to the relative contribution of phase unwrapping errors compared to the error sources discussed earlier in chapter-7. As it has already been pointed out, simulations provide the ideal platform to test the performance of the numerous TPU strategies tested in this thesis, in the absence of the inevitable noise associated with the recording and analysis of real experimental data.

On this note, the effect of a potential mismatch in the wedge angles of the two wedges forming the pair of synthetic wedges and the corresponding recovered phase change signals that would have otherwise been impossible to examine, was investigated. It was found that the number of fringes that appear across the field of view of each of the individual four wedges is, in fact, predominantly controlled by the wedge angle. Recalling the observed gradual drift that occurred between the recovered phase changes and the corresponding *gold standard* (gs_1) for both the *integer* and the *non-integer* methods when $\alpha_1 \neq \alpha_2$ with constant peak updating in figure-9.10, it is possible that the mismatch in the wedge angles is partially responsible for the variation in the optimum wedge thickness ration R observed in the numerous tests performed in chapter-8 – recall figures-8.4(c), 8.12(c), 8.16(c) and 8.20(c)). Considering that the mismatch in the wedge angles had already been experimentally verified earlier in chapter-7 (recall table-7.3) but at the time its

significance had not been realised, one possible way of testing this in the future could be to modify equation-5.23 such that the estimation of the scaling factor R includes the $f(\theta, \alpha)$ term.

Furthermore, closer inspection of the recovered phase change signals using the *integer* and the *non-integer* approaches for two simulated data sets has revealed that the former suffers from small phase jumps of magnitude less than π that are of additive nature. As already pointed out, these are not to be confused with 2π phase jumps that are successfully dealt with by the original temporal phase unwrapping strategy which was described in chapter-5 and reference [20] and are not of additive nature. However, as the recovered phase change signal resulting from the first pair of wedges is amplified by the scaling factor R prior to it being used as the reference signal to unwrap the higher sensitivity phase change signal of the next pair, it follows that these phase jumps are also amplified. As a result, they can be easily misinterpreted as phase unwrapping errors or even artificial wavenumber jumps. This is most likely the reason as to why the accessing to the scan range was limited to 37 nm in reference [21] (the *integer* method was used). Once again, the above would have been impossible to reveal using real experimental data as the small phase jumps are camouflaged within the high noise levels that characterise the reference signal of the real experimental data sets analysed in this thesis (data set-1 and data set-2 of table-1.1). In contrast to the recovered phase change signal obtained using the *integer* method, the corresponding *non-integer* one is free from these issues thereby highlighting its importance in PC-WSI.

As far as the assumption of a mismatch in the refractive index of the four wedges comprising the optical sensor is concerned, the simulations analysed in this chapter have provided some important information. Most importantly, it is now much clearer that the large mismatch observed in the extracted refractive index trend curves (recall figure-7.15 and figure-7.16) is most likely produced by the mismatch in the wedge angles that at the time was not considered to be a significant factor. It is worth noting that the aforementioned observation does not invalidate the method of estimating the refractive index trends nor does it eliminate the possibility that there is a mismatch in the dispersion curves of the wedge materials but rather it rather highlights the importance of equal wedge angles in the hardware design of the four-wedge sensor.

As already pointed out, the TPU strategy concerning the unwrapping along the phase sensitivity direction was not employed in the simulated data sets analysed in this final chapter. However, as the simulations provide a convenient platform to test the effect of physical parameters such as ideally formed wedges with $\alpha_1 \neq \alpha_2$ and $\alpha_1 = \alpha_2$, it becomes clear that the major contribution of the unwrapping along the phase sensitivity axis is to compensate for the mismatch between the wedge angles of the pair of wedges used to construct the synthetic wedge phase change signals. In other words, the latter constitutes a way of compensating for the gradual build-up of the gap observed between the true phase change signal and the recovered phase change signal by placing regular pivot points in places where a phase change discrepancy is likely to occur owing to the mismatch in the wedge angles. On this note, it is possible that the 'ghost lines' that were observed in the spectrograms during the analysis of the real experimental data set prior to the implementation of the temporal phase unwrapping along the phase sensitivity direction, was an artefact attributed to the mismatch between the wedge angles (predominantly between the first pair of wedges (recall table-7.3 and table-7.4) that was carried through the unwrapping steps). This, in turn, potentially explains the reason as to why the position of the aforementioned artefacts start to approach the main spectral lobe (line $k_t = 1$) as the adaptive re-referencing rate was increased.

Recalling that the real experimental data set used to validate the performance of the wavenumber change sensor developed in this thesis only consisted of 400 frames, further highlights (a) the difficulty in accessing the full scan range and (b) the importance of the various fixes that were introduced to the original algorithm and have eventually led to the successful 1-D depth reconstructions using the full scan range in the absence of any reference signal i.e. the high-end wavelength meter that was used for the short scan proof of principle validation.

To conclude, the above, hopefully, provides the reader with the necessary confidence that the proposed technique detailed earlier in chapter-8 is generic enough to be considered for future users of this particular WSI setup or, indeed, for other PC-WSI applications concerned with the processing of large scans (> 100 nm) and wavelength steps down to the picometers level.

9.6 Figures

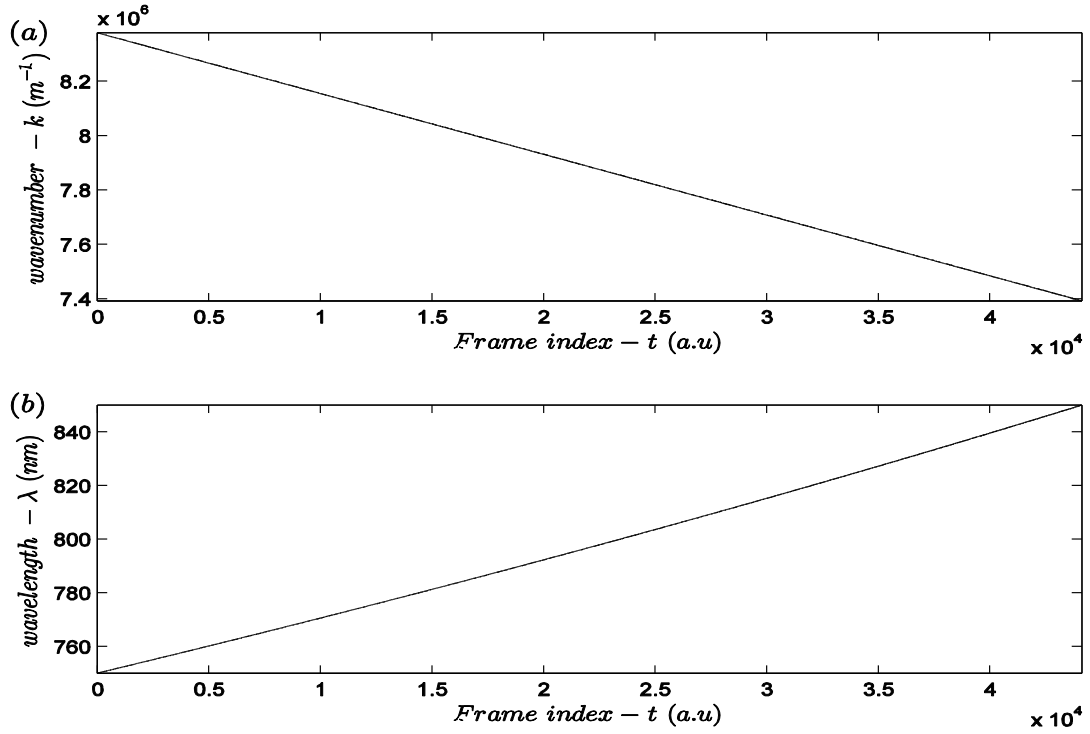

Figure-9.1: Ideal laser tuning curves: (a) linear wavenumber k as a function of frame index t and (b) corresponding ideal wavelength λ tuning curve as a function of frame index t. Note the importance of a non-linear $\lambda(t)$ in order to get a linear $k(t)$ ramp.

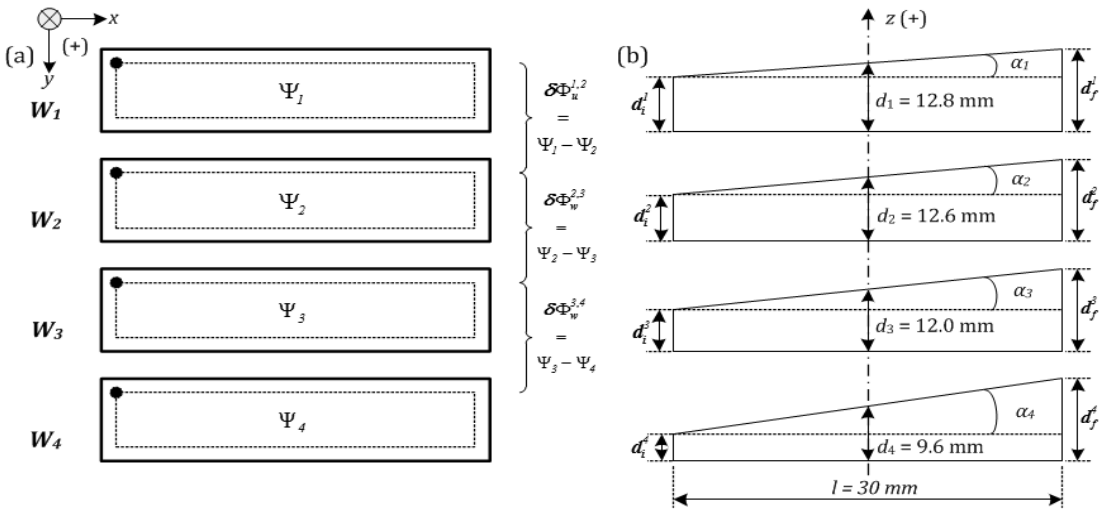

Figure-9.2: Schematic diagram showing the working principle of the four-wedge optical sensor. (a) Expanded front-view of the four-wedge sensor: the black dots indicate where the phase Ψ_j is evaluated for each region of interest (dotted rectangles), with j = 1, 2, 3, 4 for each wedge. δΦ is the synthetic-wedge phase-change parameter that is used to calculate the sought Δk parameter, while the subscripts u, w denoting whether the phase signal is unwrapped or wrapped respectively. (b) Expanded side-view of the sensor showing the central thickness for each of the four wedges. α_j is the wedge angle with $\alpha_1 \sim \alpha_2 \sim \alpha_3 \sim \alpha_4 \sim 2$ min for the ideal case scenario.

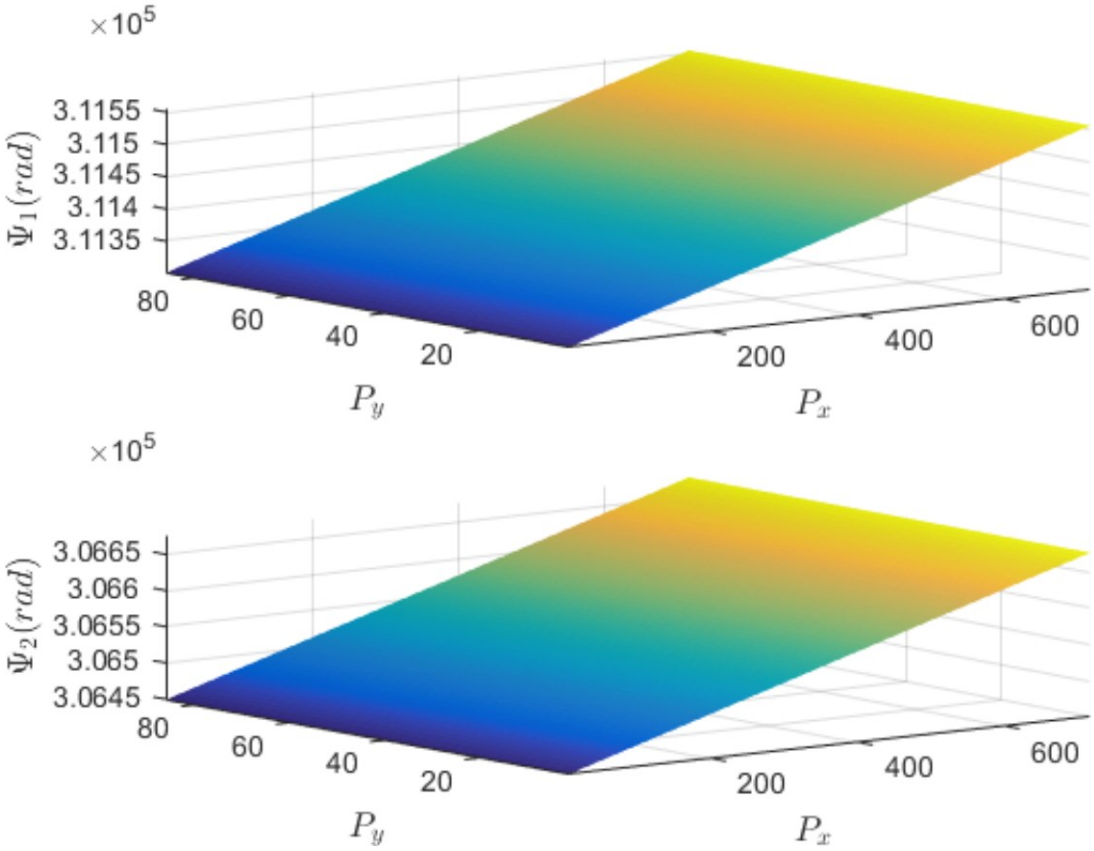

Figure-9.3: 2-D phase distribution due to the wedge profile at λ = 750 nm for wedge-1 (Top) and for wedge-2 (bottom) and for n = 1.453. P_x and P_y are the pixel counts along the x and y directions.

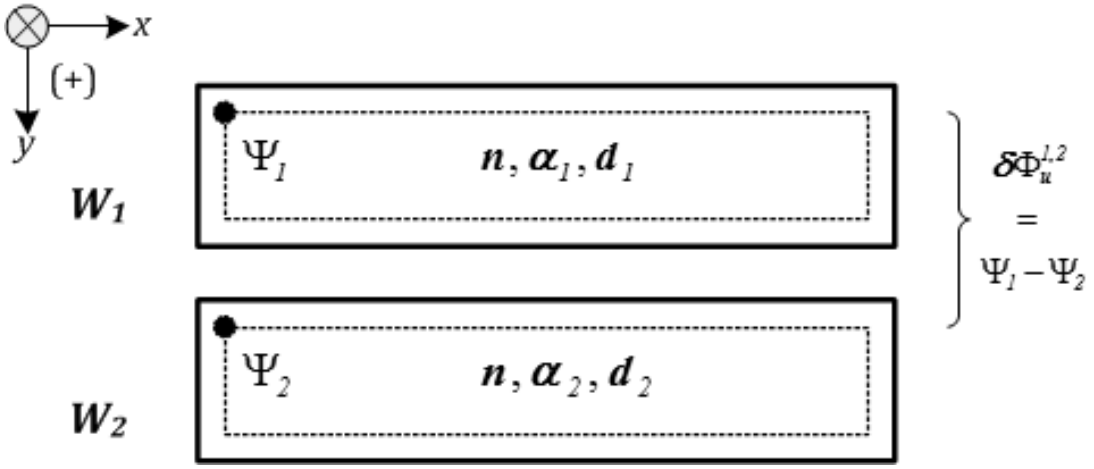

Figure-9.4: Hypothetical scenario of a pair of wedges (W_1, W_2) with the same refractive index that are insensitive to dispersion i.e. $n(\lambda) = n$ = 1.453 for all wavelengths in the wavelength range of 750-850 nm. α_1, α_2 and d_1, d_2 are the wedge angles and central thicknesses of wedge-1 and wedge-2 respectively. The black spots indicate the location at which the phase is evaluated.

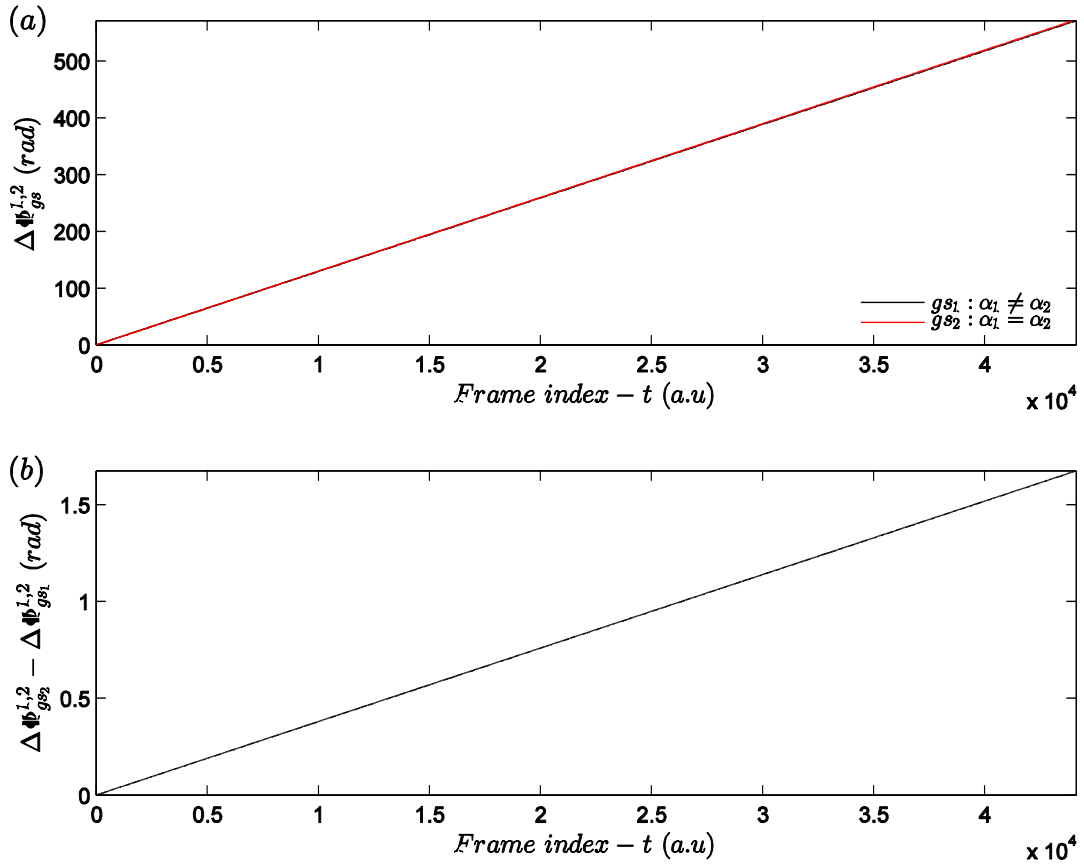

Figure-9.5: (a) True temporally unwrapped phase-changes $\Delta\Phi_u^{1,2}(t,0)$ for the two different simulated data sets. Black-line: $\Delta\Phi_u^{1,2}(t,0) = \Delta\Phi_{gs_1}^{1,2}(t,0)$ for the case of different wedge angles. Red-line: $\Delta\Phi_u^{1,2}(t,0) = \Delta\Phi_{gs_2}^{1,2}(t,0)$ for the case of equal wedge angles. Note that *gs,* stands for gold standard. (b) Difference between the two gold standards that illustrates the deviation in the recovered unwrapped phase-change expected in the case of unequal angles and in the absence of any other non-linearities.

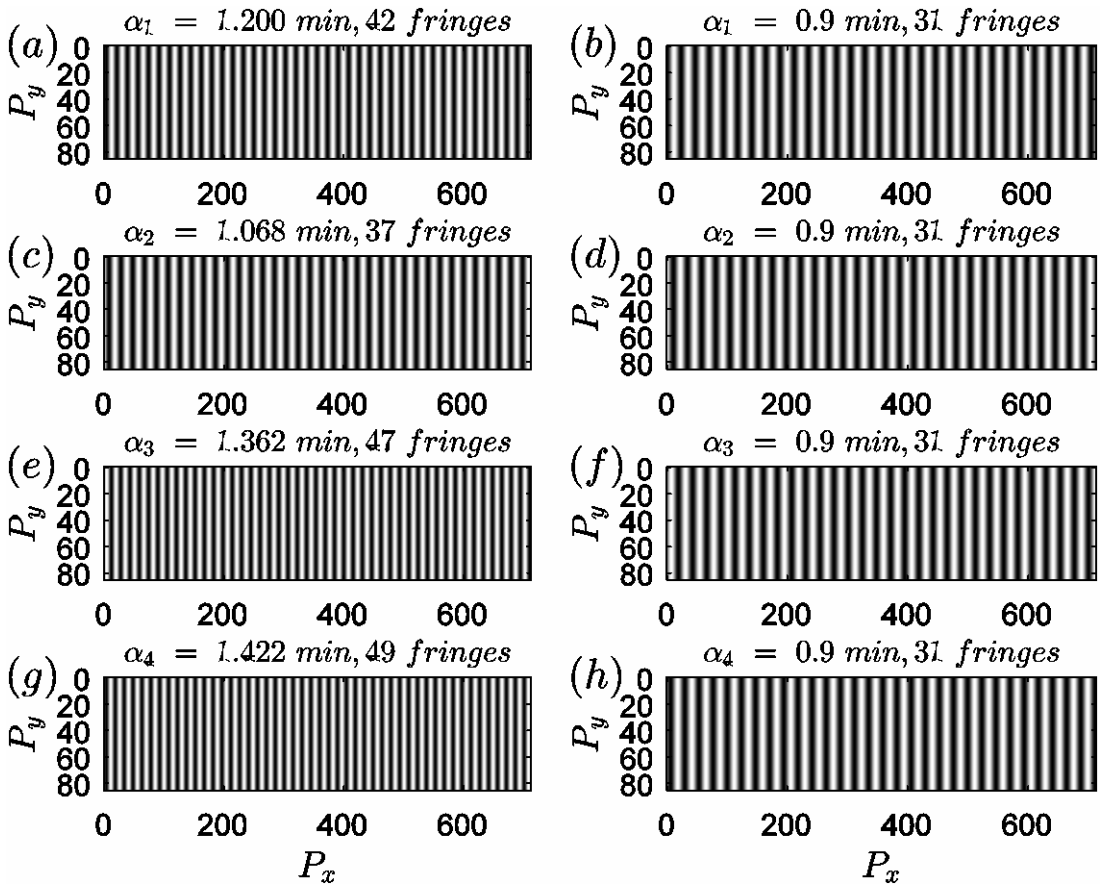

Figure-9.6: Simulated fringe patterns at the starting wavelength λ = 750 nm of an ideal WSI scan for the four wedges. Left column (a), (c), (e), (g): for the case where $\alpha_1 \neq \alpha_2 \neq \alpha_3 \neq \alpha_4$. Right column (b), (d), (f), (h): for the case where $\alpha_1 = \alpha_2 = \alpha_3 = \alpha_4$.

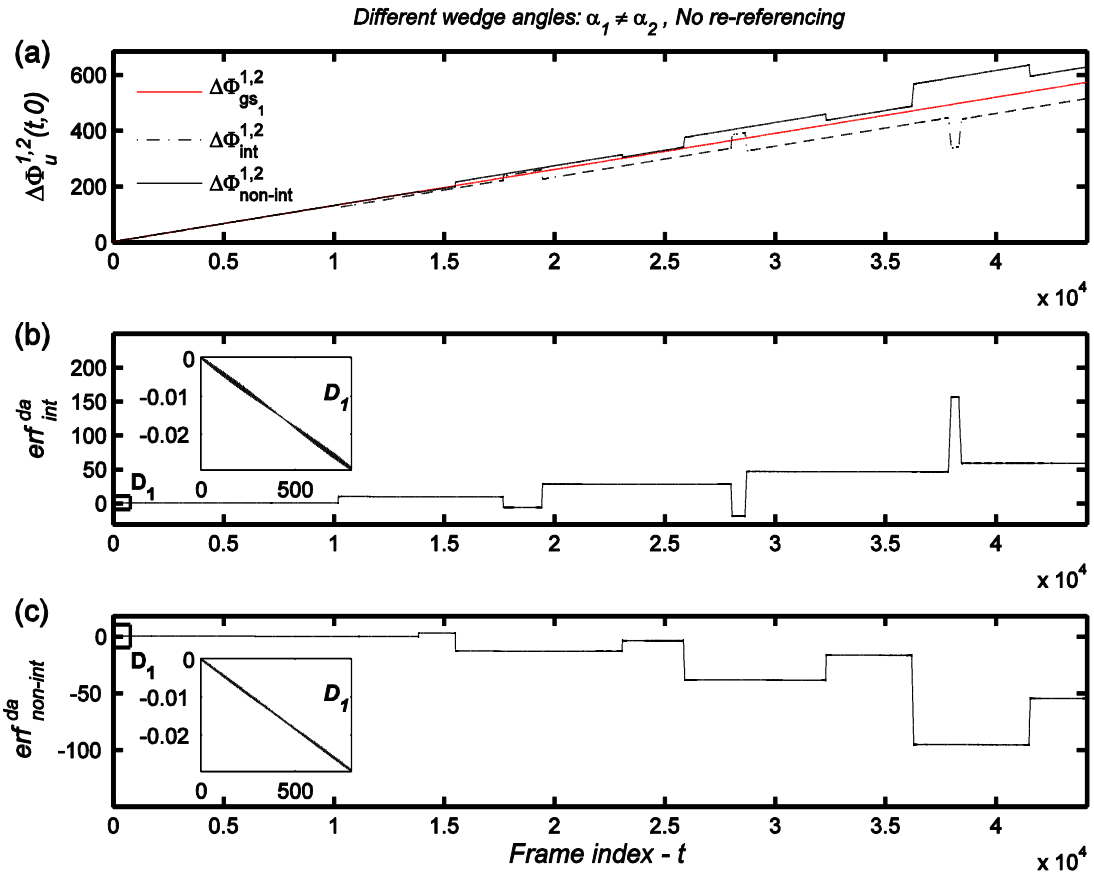

Figure-9.7: (a) Comparison of phase-change signals illustrating the detrimental effect on the recovered phase-change signals in the absence of re-referencing for both the *integer* and the *non-integer* phase extraction methods when compared to the gold standard with wedge angles that are slightly different from each other (α_1 = 1.2 mins and α_2 = 1.068 mins) The red line indicates the gold standard while the solid black and dotted black line indicate the recovered phase-change signals using the *non-integer* and the *integer* phase extraction approaches respectively. (b) Difference between the gold standard (gs_1) and the recovered phase change signal using the *integer* approach. (c) Difference between the gold standard (gs_1) and the recovered phase change signal using the *non-integer* approach. Note that *erf* stands for error function and is expressed in units of radians, while the superscript *da* stands for different angles.

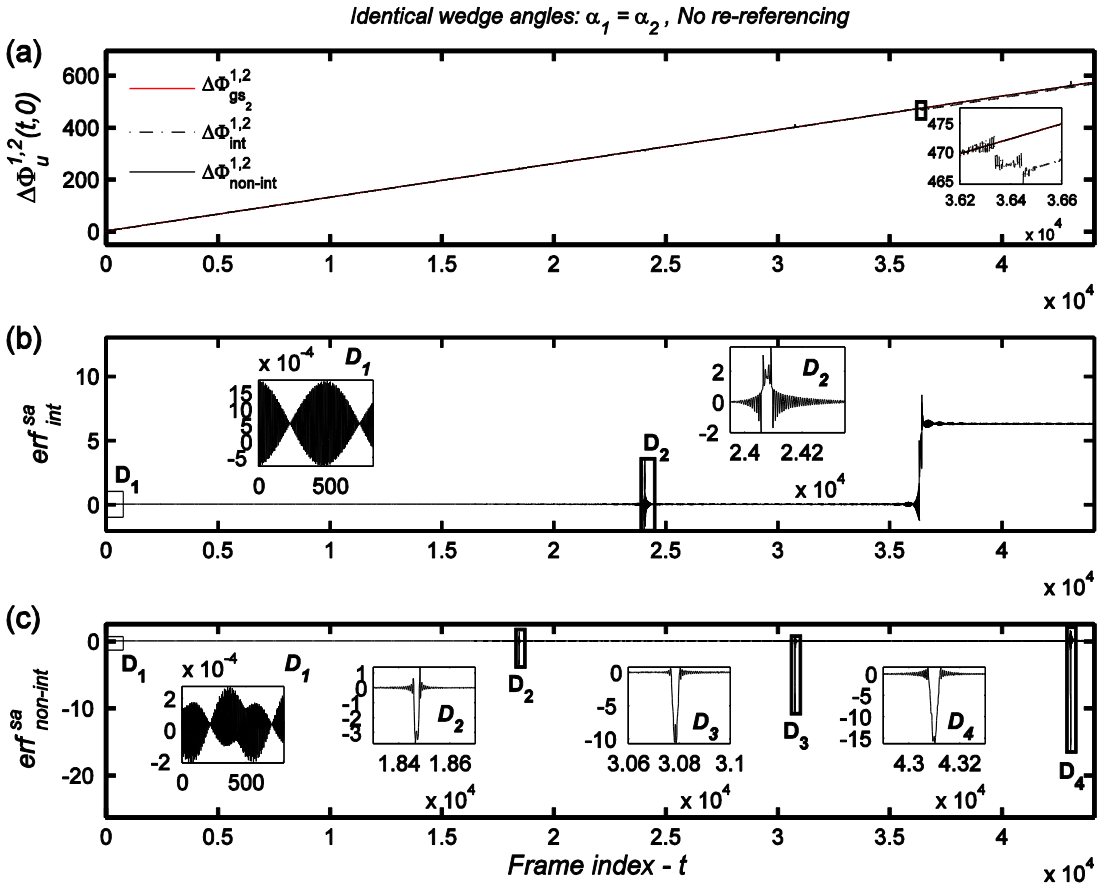

Figure-9.8: (a) Comparison of phase-change signals illustrating the improvement on the recovered phase-change signals in the absence of re-referencing for both the *integer* and the *non-integer* phase extraction methods when compared to the gold standard but with equal wedge angles this time ($\alpha_1 = \alpha_2 = 0.9$ mins) The red line indicates the gold standard (gs_2) while the solid black and dotted black line indicate the recovered phase-change signals using the *non-integer* and the *integer* phase extraction approaches respectively. (b) Difference between the gold standard (gs_2) and the recovered phase change signal using the *integer* approach. (c) Difference between the gold standard (gs_2) and the recovered phase change signal using the *non-integer* approach. Note that *erf* stands for error function and is expressed in units of radians, while the superscript *sa* stands for same angles.

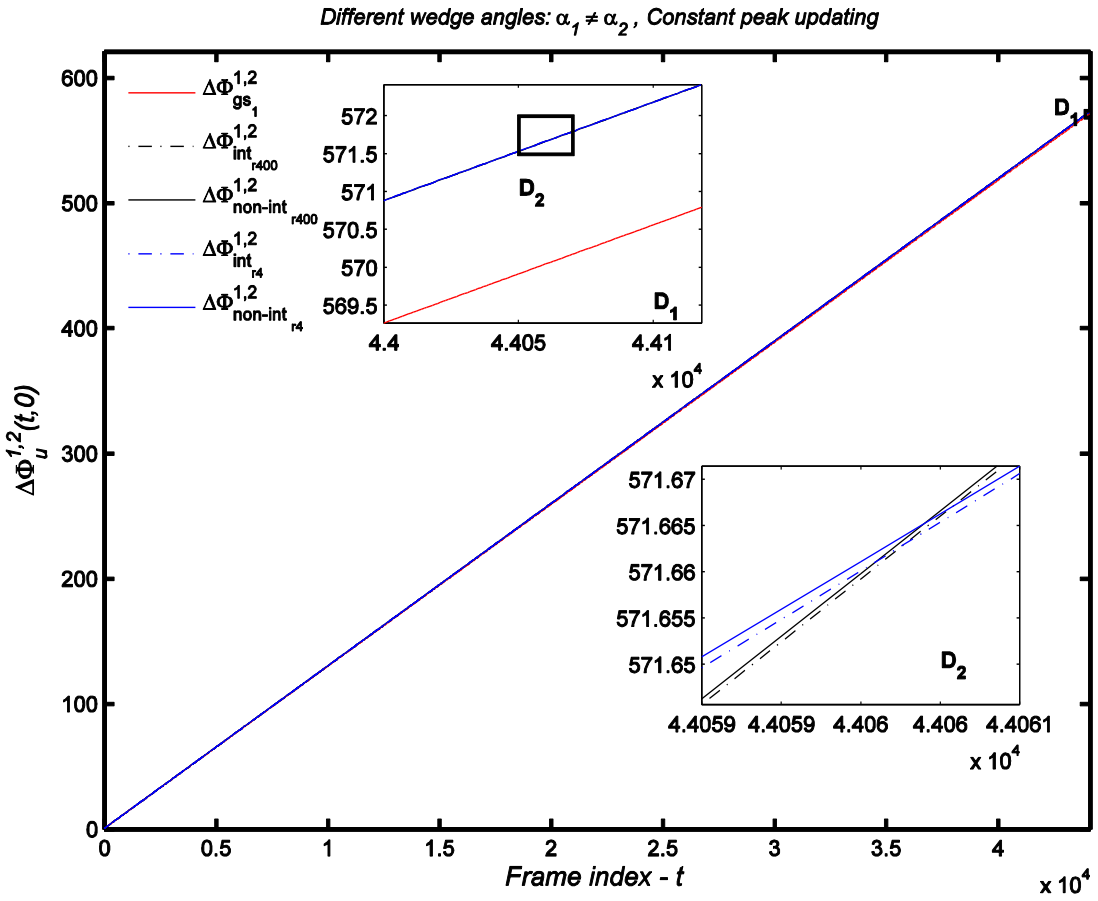

Figure-9.9: Comparison that illustrates the effect that re-referencing (by updating the location at which the phase is evaluated) has on the recovered phase-change signals for the *integer* and the *non-integer* phase extraction methods, versus the gold standard (gs_1) in the presence of unequal wedge angles. Two re-referencing rates have been chosen: at 400 frames and 4 frames. D_1 and D_2 denote the two zoomed regions. Note that all phase changes are in units of radians.

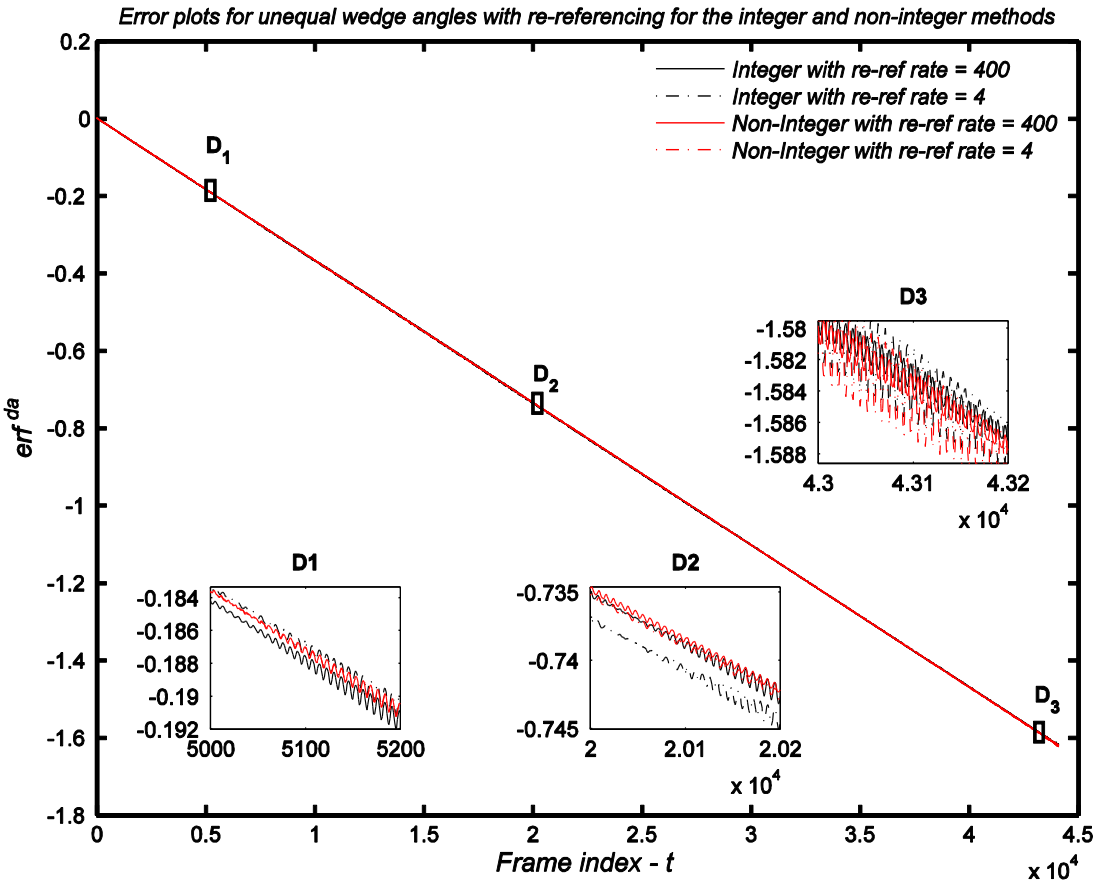

Figure-9.10: Error as a function of the frame index t, between the gold standard (gs_1) for wedge angles that are slightly different from each other (α_1 = 1.2 mins and α_2 = 1.068 mins) and the recovered phase-change signals using the integer and the non-integer phase extraction approaches with regular (constant) updating of the peak at which the phase is evaluated. Solid black line: Difference between the gs_1 and the recovered phase-change using the *integer* method and a constant re-referencing rate of 400 frames. Dotted black line: Difference between the gs_1 and the recovered phase-change using the *integer* method and a constant re-referencing rate of 4 frames. Solid red line: Difference between the gs_1 and the recovered phase-change using the *non-integer* method and a constant re-referencing rate of 400 frames. Dotted red line: Difference between the gs_1 and the recovered phase-change using the *non-integer* method and a constant re-referencing rate of 4 frames. D_1, D_2 and D_3 denote the three zoomed regions. Note that all error plots are in units of radians.

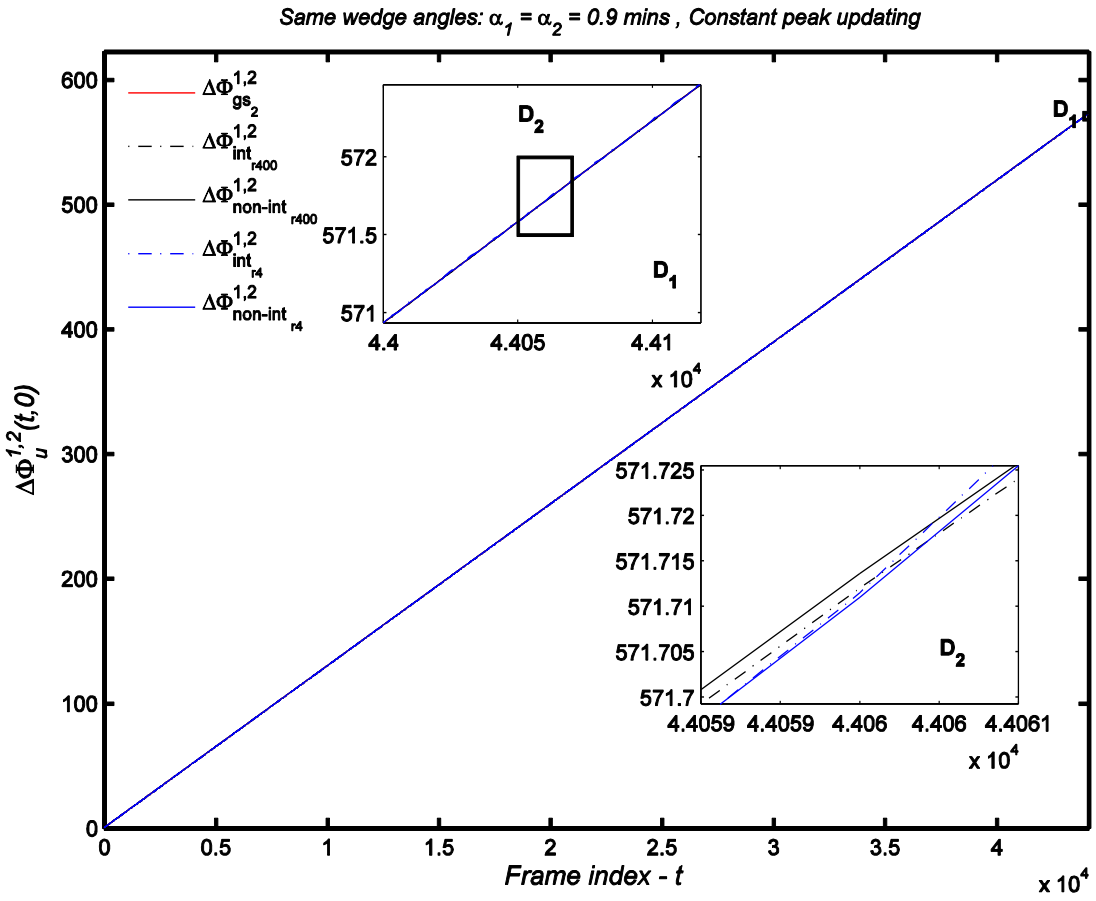

Figure-9.11: Comparison that illustrates the effect that re-referencing (by updating the location at which the phase is evaluated) has on the recovered phase-change signals for the *integer* and the *non-integer* phase extraction methods, versus the gold standard (gs_2) for the case of identical wedge angles. Two re-referencing rates have been chosen: at 400 frames and 4 frames respectively. D_1 and D_2 denote the two zoomed regions. Note that all phase changes are in units of radians.

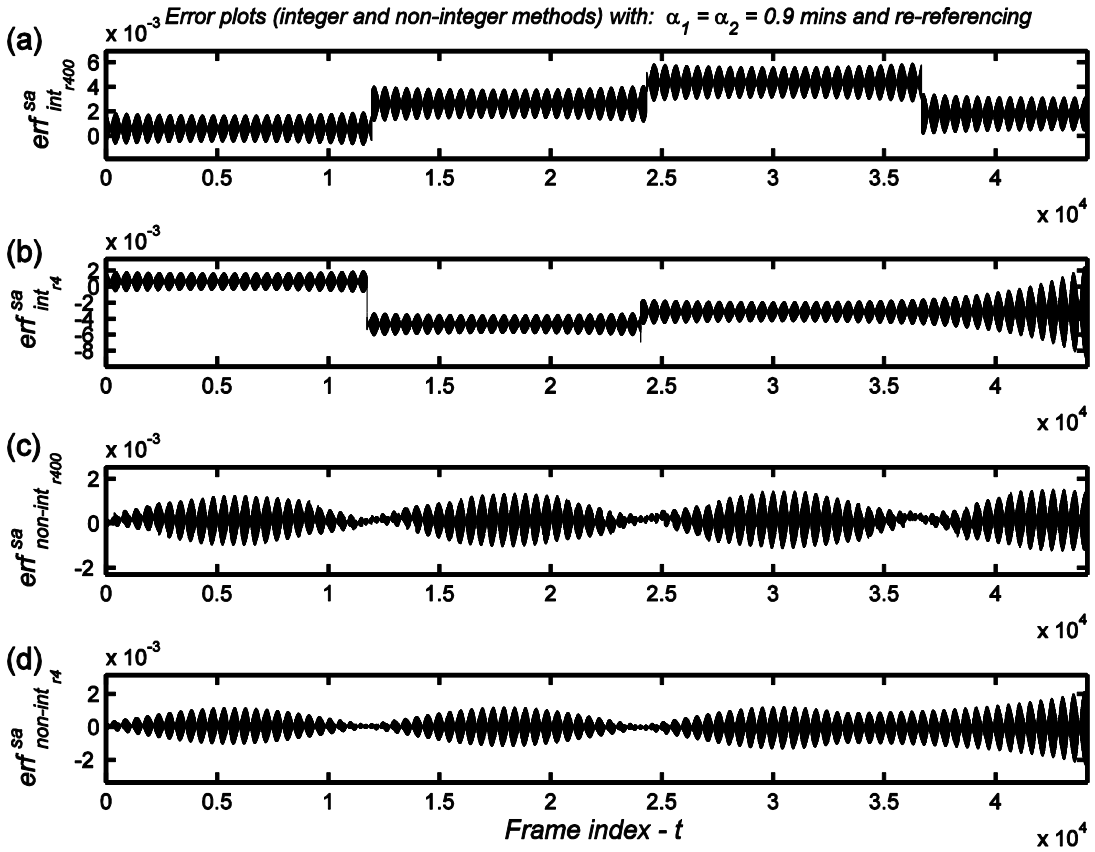

Figure-9.12: Comparison of the difference, denoted here as erf, between the gold standard for identical wedge angles (gs_2) and the recovered phase-change signals using the *integer* and the *non-integer* phase extraction approaches for two re-referencing rates (at 400 and at 4 frames respectively). Note that erf is expressed in radians while, the superscript *sa* stands for same angles.

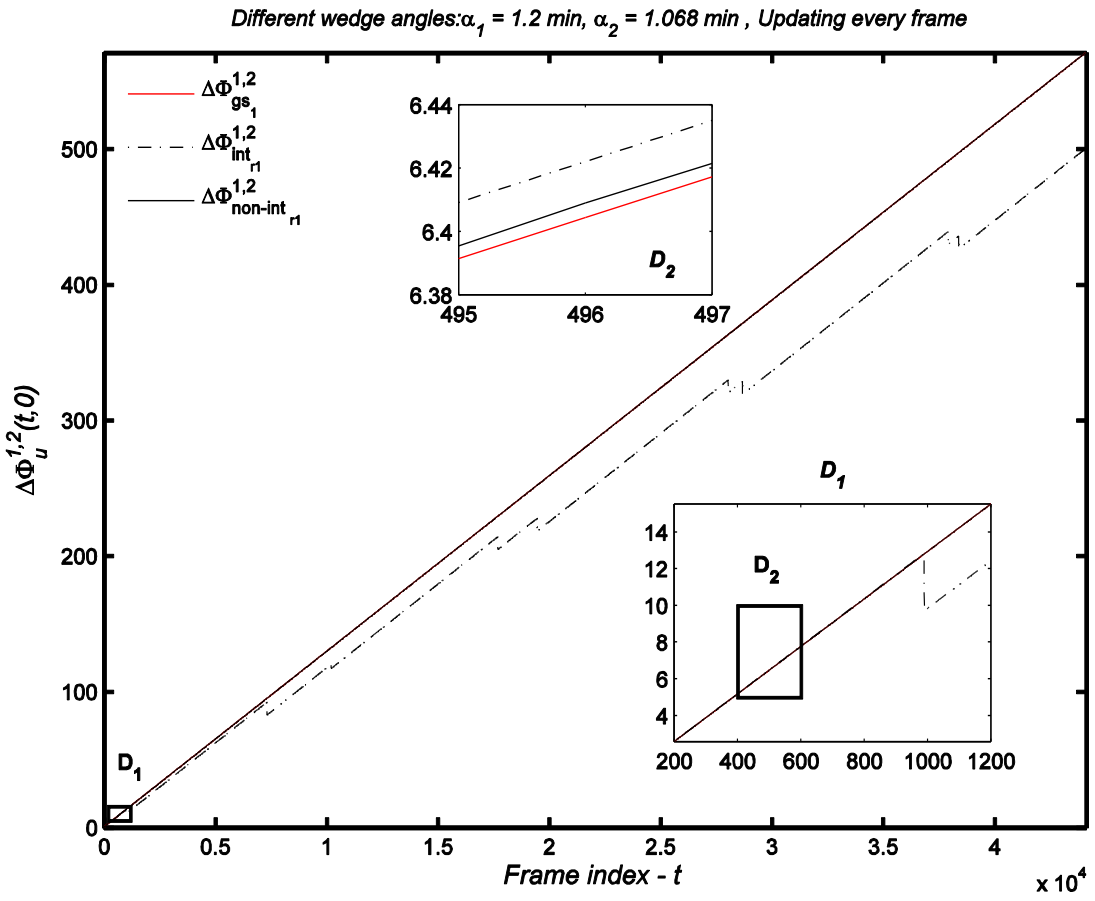

Figure-9.13: Comparison that illustrates the effect that updating the Fourier peak at which the phase is extracted at every frame has, on the recovered phase-change signals for the *integer* and the *non-integer* phase extraction methods, versus the gold standard (gs_1) for the case of unequal wedge angles. D_1 and D_2 denote the two zoomed regions. Note that all phase changes are in units of radians.

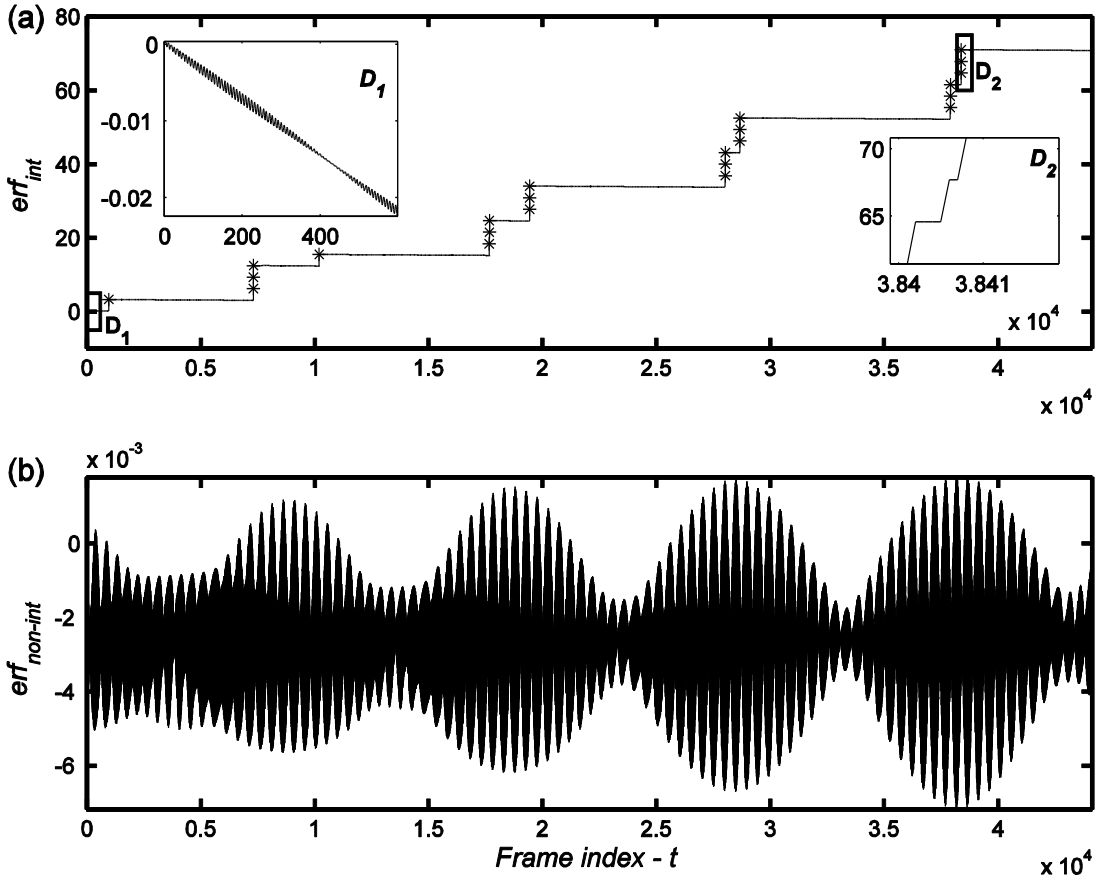

Figure-9.14: Corresponding error plots erf(t) (for different wedge angles), showing the difference between the recovered phase-change signal and the gold standard (gs_1) using the TPU strategy where the peak at which the phase is evaluated is updated at every frame t. (a) Using the *integer* method – D_1 and D_2 denote the zoomed regions highlighted, while the asterisks (*) indicate the places where a phase jump $\geq \pi/\sqrt{3}$ rad occurs between adjacent frames. (b) Using the *non-integer* approach.

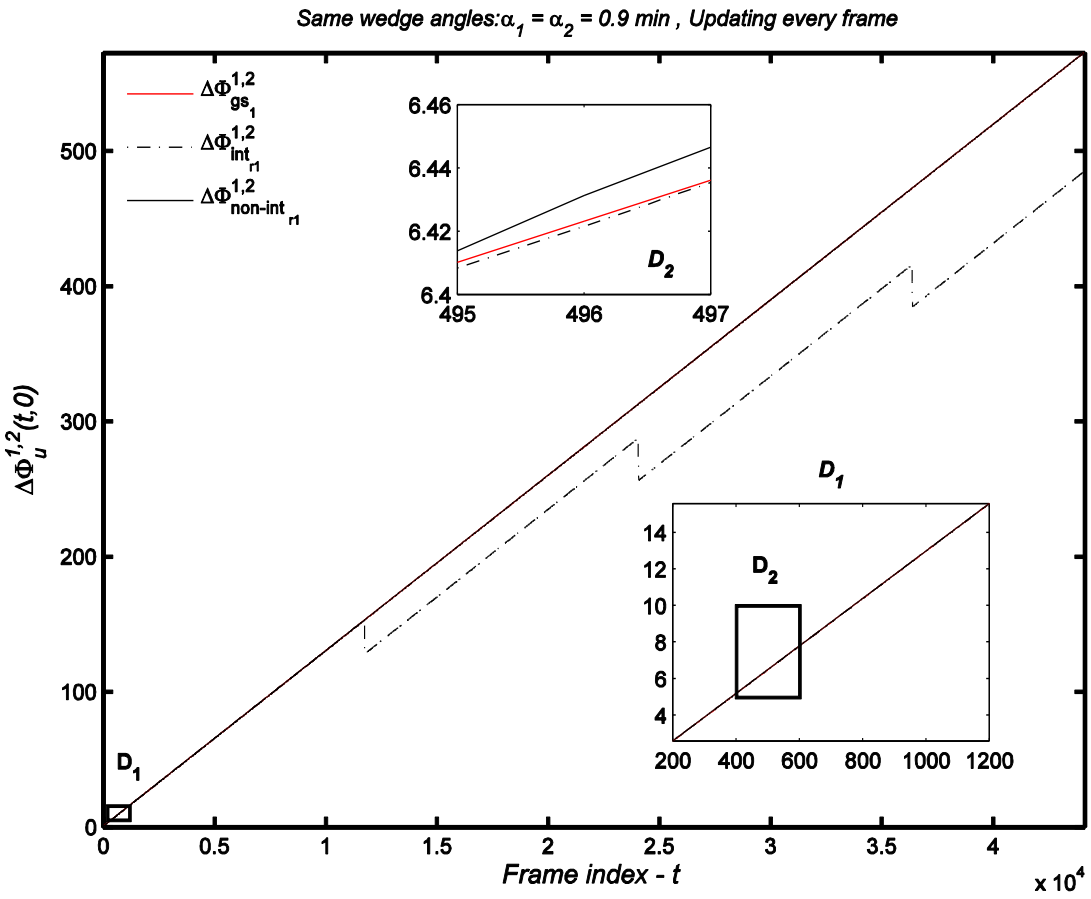

Figure-9.15: Comparison that illustrates the effect that updating the Fourier peak at which the phase is extracted at every frame has, on the recovered phase-change signals for the *integer* and the *non-integer* phase extraction methods, versus the gold standard (gs_2) for the case of identical wedge angles. D_1 and D_2 denote the two zoomed regions. Note that all phase changes are in units of radians.

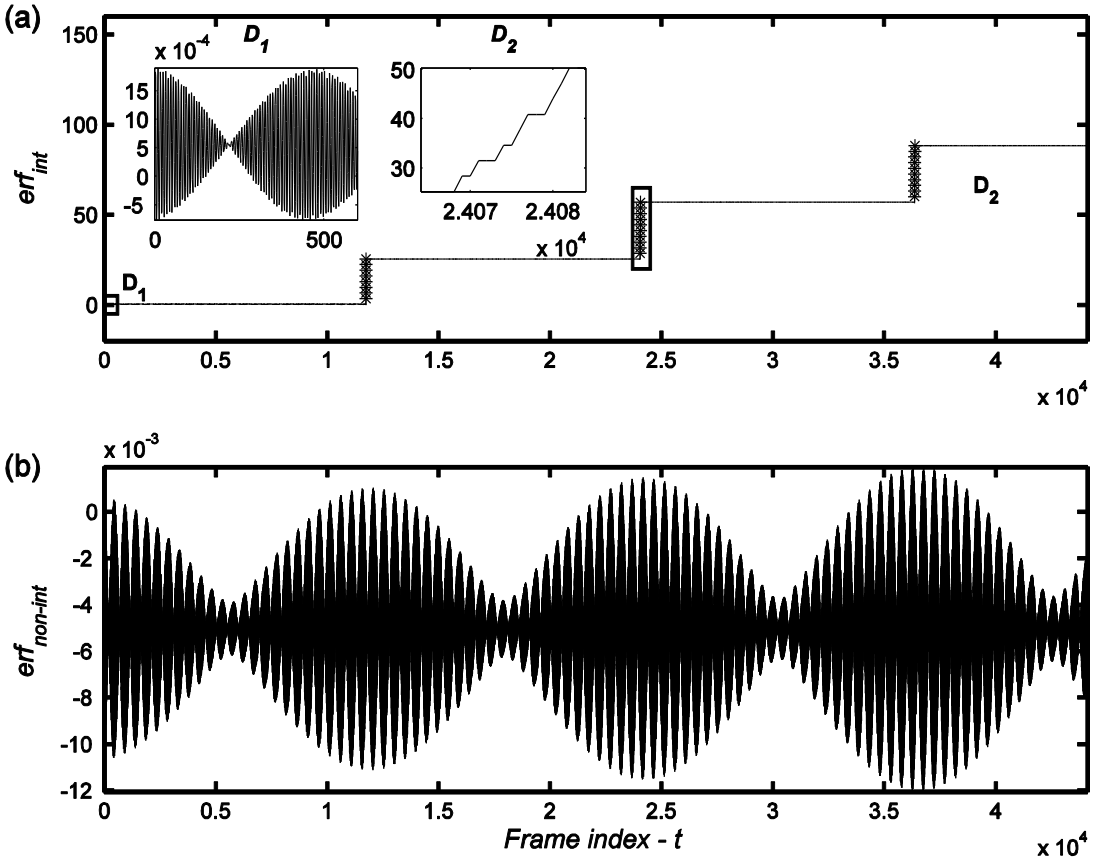

Figure-9.16: Corresponding error plots (for identical wedge angles), erf(t), showing the difference between the recovered phase-change signal and the gold standard (gs_2) using the TPU strategy where the peak at which the phase is evaluated is updated at every frame t. (a) Using the *integer* method – D_1 and D_2 denote the zoomed regions highlighted, while the asterisks (*) indicate the places where a phase jump $\geq \pi/\sqrt{3}$ rad occurs between adjacent frames. (b) Using the *non-integer* approach.

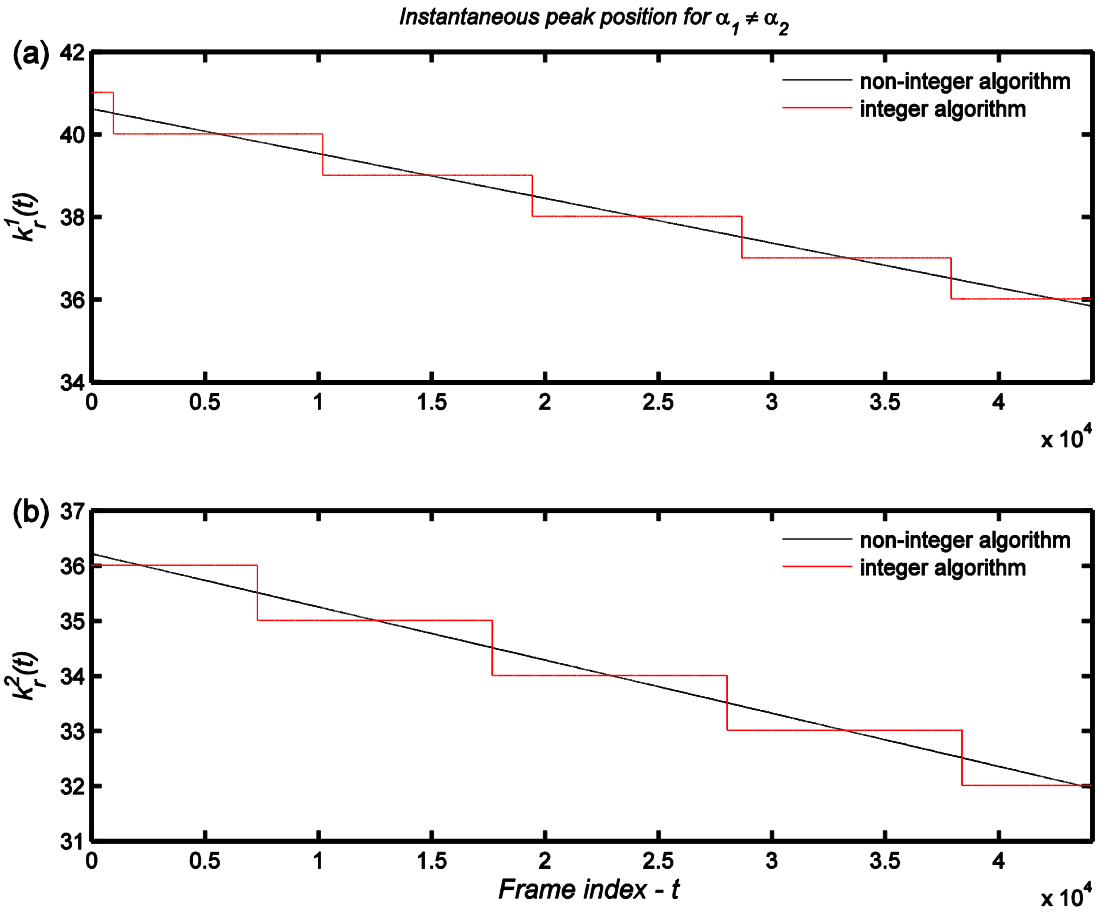

Figure-9.17: Comparison of the estimated instaneous peak position k_r as a function of the frame index t for the *integer* and *non-integer* algorithms with different wedge angles. (a) For ***wedge-1*** and (b) for ***wedge-2***. Note that k_r is expressed in pixel units in the Fourier domain and corresponds to the instantaneous number of fringes appearing across the field of during the simulated, ideal 100 nm scan range. The superscripts 1 and 2 denote the wedge.

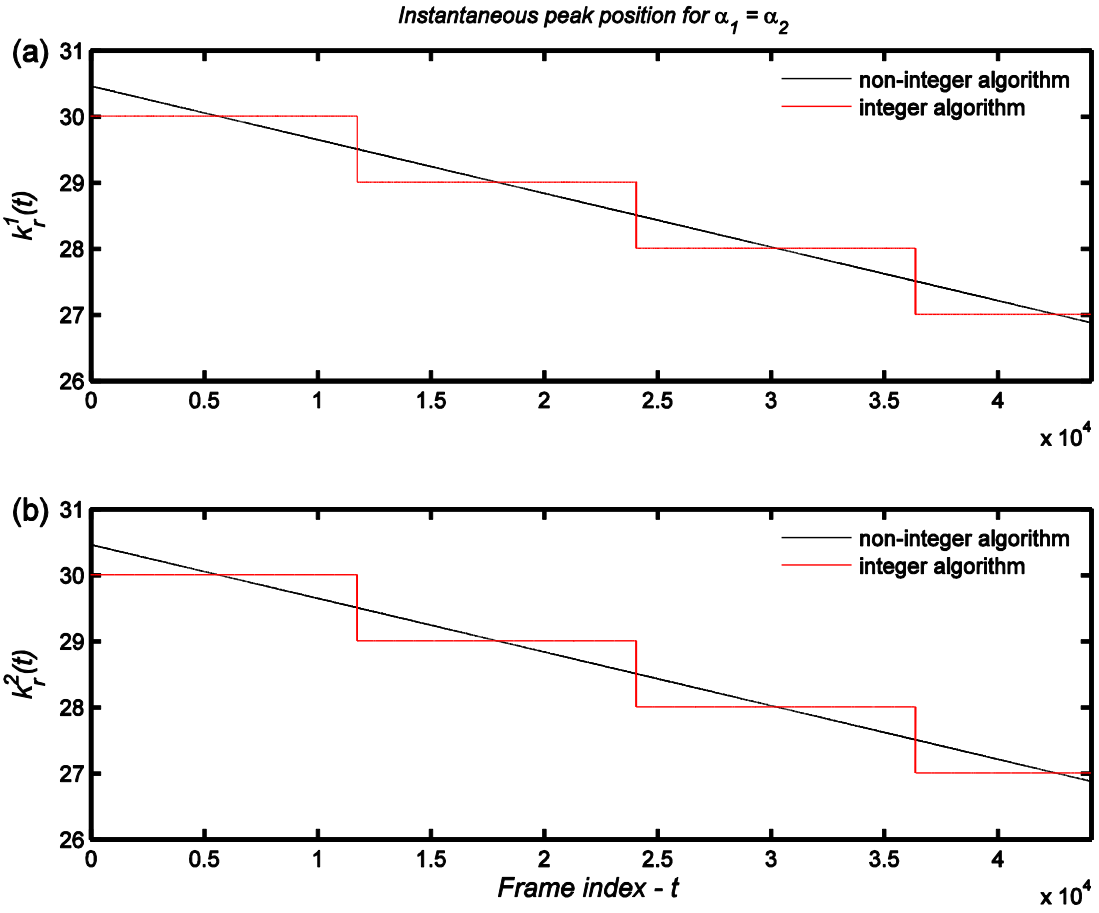

Figure-9.18: Comparison of the estimated instaneous peak position k_r as a function of the frame index t for the *integer* and *non-integer* algorithms with same wedge angles. (a) For ***wedge-1*** and (b) for ***wedge-2***. Note that k_r is expressed in pixel units in Fourier domain and corresponds to the instantaneous number of fringes appearing across the field of during the simulated ideal 100 nm scan range. The superscripts 1 and 2 denote the wedge.

Summary, conclusions, discussions and future work

Brief summary

Optical coherence tomography (OCT) is the generic term used to encompass a wide range of optical techniques able to perform depth resolved measurements. Over the past decade, it has been extensively used to image the microstructure of biomedical materials with great success. Phase-contrast OCT (PC-OCT) belongs to the family of techniques that combine the imaging capabilities of traditional OCT with the measurement sensitivity of digital speckle pattern (DSPI) interferometry and its predecessor electronic speckle pattern interferometry (ESPI) through the imaging of both intensity and phase of the interference signal, thereby allowing the through-the-thickness study of inhomogeneous structures governed by complex mechanical behaviour. Wavelength scanning interferometry (WSI) is one specific type of OCT commonly known by the term swept source OCT (SS-OCT) in which the wavelength of a tuneable source is scanned sequentially. The performance of OCT systems is determined by two critical parameters, the depth resolution and the depth range, both of which are linked to the tuneable laser source. In general, the wider the tuning range the better the depth resolution while the smaller the wavelength step the larger the depth range. In this work, a widely tuneable Ti:Sa with high output power is used which allows the construction of a multi axis, tomographic interferometer. Despite its wide tuning range, the tuneable source suffers from mode hops that randomize the recorded signal and prevent depth reconstructions. To resolve this issue, an optical sensor consisting of four glass wedges has been designed and integrated into the system. The sensor, together with the implementation of temporal phase unwrapping algorithms, allowed the accurate reconstruction of the wavenumber induced changes by the laser and has consequently led to the accessing of the full ~100 nm tuning range. Apart from resolving the laser-induced mode hops, the use of temporal phase unwrapping revealed that key issues that limit the performance of tomographic instruments, like dispersion and multiple reflections, can be successfully dealt with. The ability of the phase unwrapping strategy in resolving these issues was demonstrated by successfully measuring the absolute thickness of four fused silica glasses using real experimental data. The results were compared with independent micrometer measurements and showed good agreement.

Discussions and conclusions

The study of depth resolved displacement fields within weakly scattering materials is of particular importance to study the mechanical behaviour of composite materials. In this work, the development of a full field, multi-axis, tomographic interferometer is described. At first, two important hardware devices, namely a miniature tensile testing device and a rotation stage, for the tomographic setup were described. These were designed and manufactured to induce controlled displacements of a sufficiently low magnitude and be small enough to fit into the multi-axis interferometer without obstructing any of the beams. Hardware failure of the tuneable Ti:Sa source used in the setup ultimately prevented the use of the aforementioned devices. However, preliminary experiments at a single wavelength on the cuboid calibration device (rotation stage), have demonstrated that the main elements of the interferometer are working as expected.

Preliminary experiments on glass wedges have demonstrated that without precise knowledge of the wavenumber changes during the scan, the imaging of the interference signal of the wavelength scanning interferometer under development and consequently the accuracy of the phase contrast measurements is significantly compromised. More specifically, the experiments revealed the presence of a significant number of mode hops throughout the scan duration that were confirmed by the wavelength sensitive diode that was put in place to ensure the selection of a single wavelength at each time instance. These mode hops have the undesirable effect of causing the wavenumber to deviate significantly from the linear behaviour required for wavelength scanning interferometry applications. As a result, the phase of the recorded interference signal is randomised causing significant artefacts in the calculated optical thickness distribution.

In the view of these limitations, an optical sensor, based on the recording of interferograms from multiple wedges was developed, which is capable of providing simultaneously high wavenumber resolution and immunity to the ambiguities caused by large wavenumber jumps. All the data required to compute a wavenumber shift are provided in a single image, thereby allowing dynamic wavenumber monitoring. In addition, loss of coherence of the laser light is detected automatically. From a software point of view, the analysis algorithms used for the wavenumber changes

monitoring are based on phase detection by a two-dimensional Fourier transform method followed by temporal phase unwrapping. The performance of the optical sensor was confirmed for a limited scan of ~1 nm using a commercial wavemeter. A root mean square (rms) difference in measured wavenumber shift between the two of ~4 m^{-1} has been achieved, equivalent to an RMSE wavelength shift error of ~0.4 pm. In the light of this achievement, the ability to process the intensity data for a scan range 100× larger than the preliminary tests of 1 nm was investigated. It was found that mode hops and other nonlinearities in the scans prevent successful depth reconstructions by the standard approach of 1-D Fourier transformation of the image sequences on a pixel wise basis. A solution to this problem has been developed, which involves measuring wavenumber changes from the phase changes in the interferograms from the four wedges. The measured wavenumber changes are then used to resample the intensity signals on a regularly spaced wavenumber vector. With these improvements, depth-resolutions approaching the theoretical values are achievable for the full scan. Missing gaps in the data, due to upward etalon mode hops, have negligible effect on the depth resolution, but result in some long range signal leakage. Although the missing data gaps are a contributory source of the side lobe structure, the main cause is believed to be residual phase unwrapping errors.

An attempt to identify as many of the potential error sources that may contribute towards degrading the accuracy and precision of the reconstructed wavenumber axis using the four-wedge optical sensor has been provided. These are: (a) residuals of intensity background artefacts, (b) a mismatch amongst the refractive index dispersion curves for the four wedges and (c) the amplifying effect that the wedge thickness has in the presence of such *n*-dispersion mismatches. Although all three effects are likely to play a role, residual phase unwrapping errors are still believed to be responsible for much of the undesirable structure in the observed spectra.

With the above in mind, improvements to the original temporal phase unwrapping strategy have been introduced to account for the physical phenomena believed to give rise to the aforementioned phase unwrapping errors. More specifically, two modifications to the basic unwrapping algorithm used earlier have been introduced in an attempt to reduce the artefacts that were present in the Fourier reconstruction of the depth profile of the four wedges. Both approaches are adaptive and involve signal

re-referencing at regular intervals throughout the scan. The first is designed to compensate for the gradual change in spatial frequency of the fringes that arises from the changing wavelength, and requires continual updating of the spatial frequency components at which the phase is evaluated. The second is designed to compensate for the gap that starts to open up between the scaled low-sensitivity phase signal and the high sensitivity phase signal. This may be due to a small error in the value of R, or small changes in R with wavelength due to different dispersion curves for the two pairs of wedges. By re-zeroing the phase change at regular intervals, and then subsequently adding up the re-referenced phase change, the total phase change since the start of the scan can thus be computed but without the 2π phase errors that occurred previously.

The first was found to improve significantly the quality of the spectrograms apart from the 'ghost line' structure seen in the reconstructions from two of the wedges. The second largely eliminated the ghost lines. A hybrid approach combining both methods was therefore proposed and used to analyse the data from each of the four wedges which was then compared with independently measured wedge thickness values using a micrometer. The hybrid method was found to give the most robust results of all the techniques considered, with a clear Fourier peak at the expected frequency and with significantly reduced spectral artefacts. More specifically, as far as the central wedge thicknesses are concerned:

a. For ***wedge-1***: A difference of 3.4 μm between the results of the hybrid approach and the independent micrometer measurements was obtained, equivalent to a RMSE of 46.7 μm from the target value of 12.8 mm that is well within the ± 0.5 mm tolerance claimed by the manufacturer.
b. For ***wedge-2***: A difference of 18.3 μm between the results of the hybrid approach and the independent micrometer measurements was obtained, equivalent to a RMSE of 69.8 μm from the target value of 12.6 mm that is well within the ± 0.5 mm tolerance claimed by the manufacturer.
c. For ***wedge-3***: A difference of 505.5 μm between the results of the hybrid approach and the independent micrometer measurements was obtained, equivalent to a RMSE of 311.6 μm from the target value of 12.0 mm. This large discrepancy is attributed to human error in reading the value measured

by the micrometer (see chapter-6 and in particular table-6.6) and was impossible to repeat as at the time the labs went through a 1.5 years renovation during which all equipment was inaccessible.

d. For ***wedge-4***: A difference of 2.6 μm between the results of the hybrid approach and the independent micrometer measurements was obtained, equivalent to a RMSE of 11.4 μm from the target value of 9.6 mm that is well within the ± 0.5 mm tolerance claimed by the manufacturer.

Finally, in the lack of additional experimental data and in order to ensure that the proposed 'hybrid' approach has not evolved to solve the problems associated with the particular data set, a set of two simulated data sets that closely matched the parameters used for the real experimental data set was produced and was subsequently analysed. In the first data set, the wedge angles were deliberately chosen such that they slightly differ, while in the second these were set to be identical to each other. This allowed the assessment of the performance of the different TPU strategies under ideal scanning conditions i.e. without (a) the mode hops owing to the physics of the wavelength selection mechanism associated with Ti:Sa laser source (b) refractive index dispersion (c) any other laser induced non-linearities such as beam drifting and/or change in the reflectivity of the wedges and (d) multiple reflections taking place inside the wedges.

The analysis of the aforementioned simulated data sets revealed a number of important points that would have been impossible to identify otherwise. The most important one is related to the effect that wedge angle has on the number of fringes that appear across the field of view and the corresponding impact of the mismatch in the wedge angles between the pair of wedges used to construct the synthetic wedges and the recovered phase change signal. More specifically, it was found that when the *integer* phase extraction method is used in the presence of a mismatch in the wedge angles, a large number of artificial phase-jumps that are less than π occur between the recovered phase change signals and the true phase change (*gold standard*). Unlike phase unwrapping errors (2π phase jumps), these were of additive nature and would have been impossible to distinguish as their magnitude is comparable to the noise level present in the recovered phase-change signal of the real experimental data sets (both for the short scan data set-1 and the full scan data set-2). As this signal is amplified by scaling factor R, prior to it being used as the reference to unwrap the

higher sensitivity synthetic wedge phase-change, the aforementioned small phase-jumps are also amplified. As a result, it is possible that during the three-step unwrapping process their magnitude is magnified beyond the 2π threshold, therefore, making it extremely difficult to distinguish them from true phase unwrapping errors or, in fact, the laser induced phase-jumps. This is possibly the reason as to why in the second publication (see reference [21]) where the *integer* method was used, the maximum scan range before the corresponding Fourier peak started to split was limited to 37 nm. The majority of these are, however, removed when the *non-integer* phase extraction method is employed instead, thereby, justifying its importance in PC-WSI applications. The reason for this is simply because the location of the 2-D Fourier peak where the phase Ψ_j is evaluated is no longer estimated as an integer but rather as a decimal number, highlighting the sensitivity of the technique and reinforcing the assumption that the position of the Fourier peak and its associated phase are directly linked.

Following the analysis of the two ideal scans ($\alpha_1 \neq \alpha_2$ and $\alpha_1 = \alpha_2$), it is now much clearer that the large mismatch observed in the extracted refractive index trend curves (recall figure-7.15 and figure-7.16) is most likely produced by the mismatch in the wedge angles that at the time was not considered to be a significant factor. It is worth noting that the aforementioned observation does not invalidate the method of estimating the refractive index trends nor does it eliminate the possibility that there is a mismatch in the dispersion curves of the wedge materials but it rather highlights the importance of equal wedge angles in the hardware design of the four-wedge sensor and of course the ability of the proposed 'hybrid' TPU strategy to compensate for the errors associated in the presence of such mismatches.

More specifically, it should now be more clear that the phase unwrapping along the sensitivity axis constitutes a way of compensating for the gradual build-up of the gap observed between the true phase change signal and the recovered phase change signal by placing regular pivot points in places where a phase change discrepancy is likely to occur owing to the mismatch in the wedge angles. On this note, it is possible that the 'ghost lines' that were observed in the spectrograms during the analysis of the real experimental data set, prior to the implementation of the temporal phase unwrapping along the phase sensitivity direction, was an artefact associated to the mismatch between the wedge angles (predominantly between the first pair of wedges

(recall table-7.3 and table-7.4) that was carried through the various unwrapping steps). This, in turn, provides a possible explanation as to why the position of the aforementioned artefacts start to approach the main spectral lobe (line $k_t = 1$ in figure -8.19 and figure-8.23) as the adaptive re-referencing rate was increased.

Finally, recalling that the real experimental data set used to validate the performance of the wavenumber change sensor developed in this thesis only consisted of 400 frames and that the simulations suggest that the aforementioned issues become evident much later in the scans, further highlights (a) the difficulty in accessing the full scan range and (b) the importance of the various fixes that were introduced to the original algorithm and have eventually led to the successful 1-D depth reconstructions using the full scan range in the absence of any reference signal i.e. the high-end wavelength meter that was used for the short scan proof of principle validation.

Future work

In this final section, a list of the various aspects that in the author's opinion can offer improvements on the overall performance of the multi-channel PC-WSI system under development are presented. At first, general hardware aspects are considered. Second, lists of actions that have the potential to further improve the software developed so far are presented followed by some thoughts of how the work can proceed from this point onwards. Finally, the work plan for publishing the improvements introduced to the software so far (i.e. the work documented from and including chapter-6 onwards which is the outcome of the author's work only).

Hardware improvements

In this section, the various possibilities that can offer improvements to the hardware used in the current setup are mentioned. These include hardware concerning the existing mechanical rigs, the laser source, the wavelength sensor and the CCDs.

The laser source

As far as improvements of the hardware concerning the multi-axis interferometer, the most obvious and critical one is the replacement of the electronically tuned CW Ti:Sa laser source. As it has already been mentioned, the team at M-squared Lasers

Ltd, have implemented several improvements to the laser cavity design that have removed the requirement of manual alignment of the beam each time a scan is performed (see ref [201] for more details). The most up-to-date models possess much larger tuning ranges with typical values in excess of 175nm, better wavelength stability owing to the combined effect of multiple BRF stages instead of the single BRF stage of the current model and the etalon fine selection stage. Moreover, with the addition of eternal reference cavity, linewidths of < 5 kHz are achievable in place of the < 5 MHz that the current model possesses (recall that this option was available at the time the laser source was purchased, however, it was traded for the set of etalons with the much finer FSR) – linewidth refers to a property that is directly linked to how close monochromatic the light emitted is. Considering the offer for replacing the current source with the new improved cavity design at reduced price due to the numerous issues with the laser source right from the start of its purchase, the Ti:Sa laser is the preferred option. Apart from cost, the benefit of keeping the Ti:Sa as the laser source for the future measurements is that the wedge material (optical quality fused silica) can be maintained as it is practically the less sensitive in dispersion within its operating tuning range.

As an alternative to the Ti:Sa laser, the New Focus TLM-8700 is an attractive solution offering similar tuning range of 110 nm in the wavelength range of 835-1630 nm with tuning speeds of 2000nm/s or greater (see ref [303]). Unlike the Ti:Sa laser, this particular laser source belongs to the family of external cavity diode lasers (ECDL) designed for metrology applications and is OEM (original manufacturer equipment) certified with proven reliability (> 100 million cycles tested). Its disadvantage is mainly the much lower output power that is in the 10 mW range. Although the manufacturer provides amplifiers such as the VAMP^{TM} tapered optical amplifiers that can increase the optical power output in excess of 2 W, these have an operating range that is at its best a quarter of the actual tuning range of the tunable laser. This leaves the erbium doped fibre amplifier (EDFA) (see ref [304]) as the only option for raising the power output to the required ~0.4 W. However, like all amplifiers, these have the undesired effect of amplifying the noise of the input signal, too. Finally, to the best of the author's knowledge, there have been no reports in the literature of such combination being used in the OCT community. Consequently, and

besides its multiple drawbacks the solid state Ti:Sa is still the preferred laser for the multi-axis interferometer.

CCD

As already mentioned, the CCD is perhaps equally important as the choice of the laser source SS-OCT and WSI for tomographic applications. Its importance lies in the fact that not only does it provide the hardware for the recording of the interference intensity distributions but it also limits the acquisition speed. Considering that for reliable results in WSI synchronisation between the CCD frame grabber and the laser tuning speed is required, it follows that no matter how fast the laser frequency sweep is, it needs to be matched by the CCD, too. Furthermore, the bit-depth offered by the sensor is another factor that controls the accuracy with which the 2-D Fourier transform is represented in the Fourier spectrum, as the higher it is the more the grey scale levels available and thus the less QE during the digitisation of the recorded intensity distribution. Last but not least, the sensitivity of the sensor in the region the tunable laser operates also needs to be considered for optimum results. Moreover, the size of the sensor and the shape of the corresponding number of pixels is another factor that requires consideration as it is linked to the spatial resolution. Finally, the type of connection between the electronic devices (i.e. USB, Firewire or Ethernet (E) to name a few) determines the speed at which the triggering pulses between the PC, the laser source and the CCD are communicated. From the above, it becomes obvious that the choice of the CCD requires careful consideration of a number of parameters that are not always easy to optimize. For example, choosing a CCD with high frame rate of the order of 208 fps and 14 A/D bits like the Allied Vision Pike-032 B/C Firewire Camera with the On-Semi KAI-0340 sensor available from [305], comes at the expense of a reduced number of pixels and sensitivity in the NIR region. Another example is that of the Allied Vision Manta G-031B/C GigE Camera with the Sony ICX618 sensor available from [306] offering 128 fps the same bit depth, better sensitivity in the NIR but different port for data transferring (Gigabit Ethernet). Therefore, the Prosilica GC1380H with the Sony ICX285 EXview sensor CCD used in the current setup is still amongst the best options available in the market.

Wedge sensor hardware

The four wedges comprising the wedge sensor are perhaps amongst the few components that if replaced have the potential of a positive impact on the performance of the system. As it has been already pointed out, these seem to suffer from dimensional manufacturing errors such as (a) the presence of angles along directions other than the wedge direction as it is suggested by the tilted fringe patterns, (b) curved edges as suggested by the curved fringes towards the edges of the wedges, (c) striations across the functional dimension that may be the outcome of crude polishing or low grade fused silica containing impurities (d) mismatch in the wedge angles (e) flatness issues on the faces where they have been cemented with each other. Therefore, it is worth investing in replacing them with ones possessing better dimensional accuracy, fused silica quality grade, smaller and of course consistent wedge angles and better flatness. The latter could perhaps be completely eliminated by making the entire sensor from a single piece of fused silica depending on how big a manufacturing challenge this may be. Finally and regardless of whether the sensor is replaced by a completely new one, it should be fully characterised if possible. This should include its measurement with traceable means like the CMM at the metrology lab of the Wolfson school and possibly the measurement of the refractive index of the four wedges at selected wavelengths that span the tuning range of the laser to ensure there is no mismatch in the amongst the refractive index dispersion characteristics.

Software

As far as the development of the software is concerned, one of the areas that renders improvement is the estimation and suppression of intensity background artefacts. Although a method has already been devised and described in this thesis based on the averaging of the intensity along the *k*-axis, the fact that the laser beam appears to be drifting across the field of view during a 100 nm scan, suggests that the method has not completely resolved the issue. It is believed that the issue can be possibly addressed better by performing the same procedure but in a piecewise manner instead. That is, by segmenting the scan in smaller sections as it was done for the estimation of the instantaneous peak position earlier in chapter-7 and then averaging the intensity of the recorded interference signal along the wavenumber axis. This has the potential of better capturing the time dependent changes that are believed to be

responsible for the partial suppression of the d.c component in the Fourier spectrum. Moreover, the rather long processing time required to analyse the wedge data sequence for a full 100 nm scan (approximately 6 hours to complete) constitutes another area of improvement. This can be easily reduced by suppressing functions that are computationally expensive and are of no particular use. This is particularly true for the procedure introduced for the estimation of the 2-D Fourier peak width for each of the four wedges. The aforementioned was implemented in the software in an attempt to investigate the assumption of different dispersion characteristics on the basis that the width of the 2-D Fourier peak should remain constant over the scan duration in the absence of *n*-dispersion. However, as it was shown in chapter-6 (figure-6.3 and figure-6.5) non-integer number of fringes can give the impression that the width of the peak is changed. This, however, is in fact an artefact caused by the fact that the sampling of the Fourier spectrum lobes is still done at integer number of pixels (there are no decimal pixel positions in the digital world) giving the false impression that the peak is widened and is consequently not to be confused with the general principle that associates the widening of the peak to the presence of dispersion. By removing and/or suppressing this part of the code is expected to significantly improve the processing time of the data sequences by at least 2 hrs if not more, due to the high computational expense of temporarily storing the 2-D Fourier spectrum in the memory and sectioning it along the *x* and *y* directions prior to performing the necessary curve fitting for the estimation of its width along the *x* and *y* directions.

As already demonstrated earlier in chapter-6, the effect of missing gaps is believed to have negligible if no contribution to the depth resolution of the system. However, it is believed to be responsible for much of the undesirable long range structure illustrated in figure-6.17. This is most likely caused by the lower sharp edges of the experimental window function in the places where the data are set to zero due to failure of the interpolation function (`interp1` in the MATLAB programming) to recover the intensity data in places where there is insufficient information. To test this, the experimental function could be altered so that its lower sharp edges are smoothened.

Finally, considering the success of the 'hybrid' TPU strategy in successfully analysing the entire 100 nm scan for the wedge data, its implementation for absolute

wavelength measurements with better accuracy than that reported in [20], is a real possibility that is worth investigating.

Work plan for future publications

The extensive literature review included in this work that is in excess of three hundred relevant scientific publications in established journals in the field of optics and in particular interferometry, have provided the necessary confidence that the achievements documented in this thesis are worthy of publishing.

Immediate action

To this end, the numerous improvements introduced to the software used for the analysis of the real experimental data sets that have allowed the unambiguous accessing of the full 100 nm scan range can be safely assumed to constitute enough material for at least two more publications. Considering the complex nature of the problem and to assist the understanding of the not at all obvious problems encountered when dealing with such large tuning ranges and such small wavelength steps, it is believed that a two-part paper intended for the Applied Optics journal (*Noise immune temporal phase unwrapping algorithm for depth-resolved measurements using PC-WSI*) is the best option. In brief, the first part will consist of a description of the simulated data sets produced and analysed in chapter-9. This will provide the reader with the necessary motivation with regards to the challenges presented while at the same time it will assist with the mathematical description of the complex 'hybrid' method – a combination of several fixes to the original software that would be otherwise difficult to describe to the unprepared reader. The second part will consist of the analysis of the real experimental data presented in chapters-6 to 8.

Future

A short letter describing the optical setup of the multi-axis interferometer with examples showing the imaging capabilities of the system is also possible. However, this will require the analysis of the second part of data set-2 referring to the micro-fluidic device (MFD) that was used as the sample and is expected to take some time. Moreover, the performance of the system could be further reinforced by the processing of data set-3 concerning the reconstruction of the step object from speckle

images. Although this is still possible, there are serious concerns with the quality of this data set, as the laser source had already started to malfunction at the time it was captured.

Finally, a short paper detailing the ability of the proposed technique to reconstruct the wedge profiles and the corresponding fringe patterns at each time instance is another real possibility addressing the ability of the proposed method to act as a 16,000 frame phase shifting formula.

Appendices

A1 Engineering drawings

In this section of the appendix, the engineering drawings for the aluminium cube that host the samples to be inspected by the phase-contrast, multi-axis tomographic interferometer and those used for the manufacturing of the calibration artefacts are provided.

A1.1 Sample-host aluminium cube

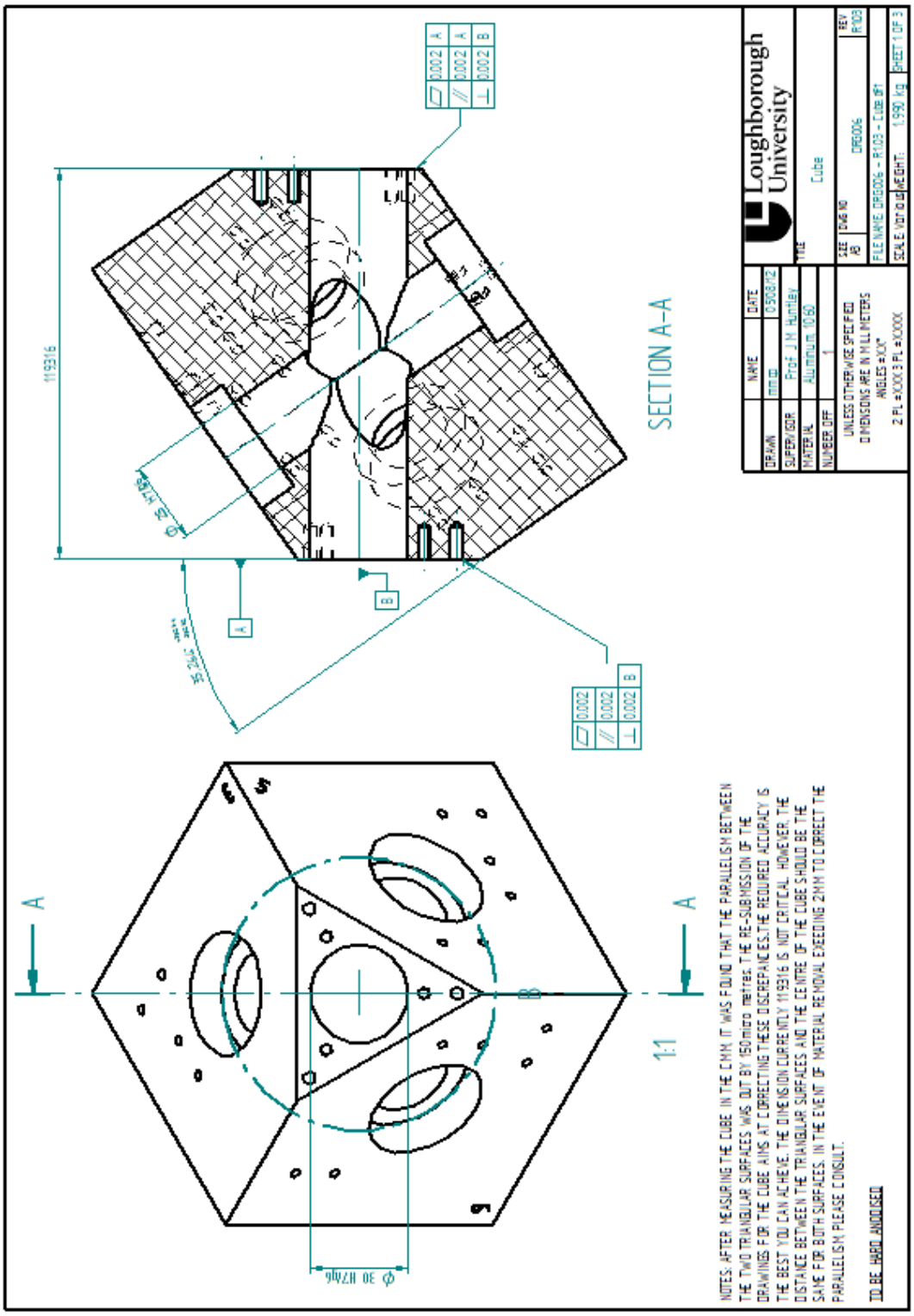

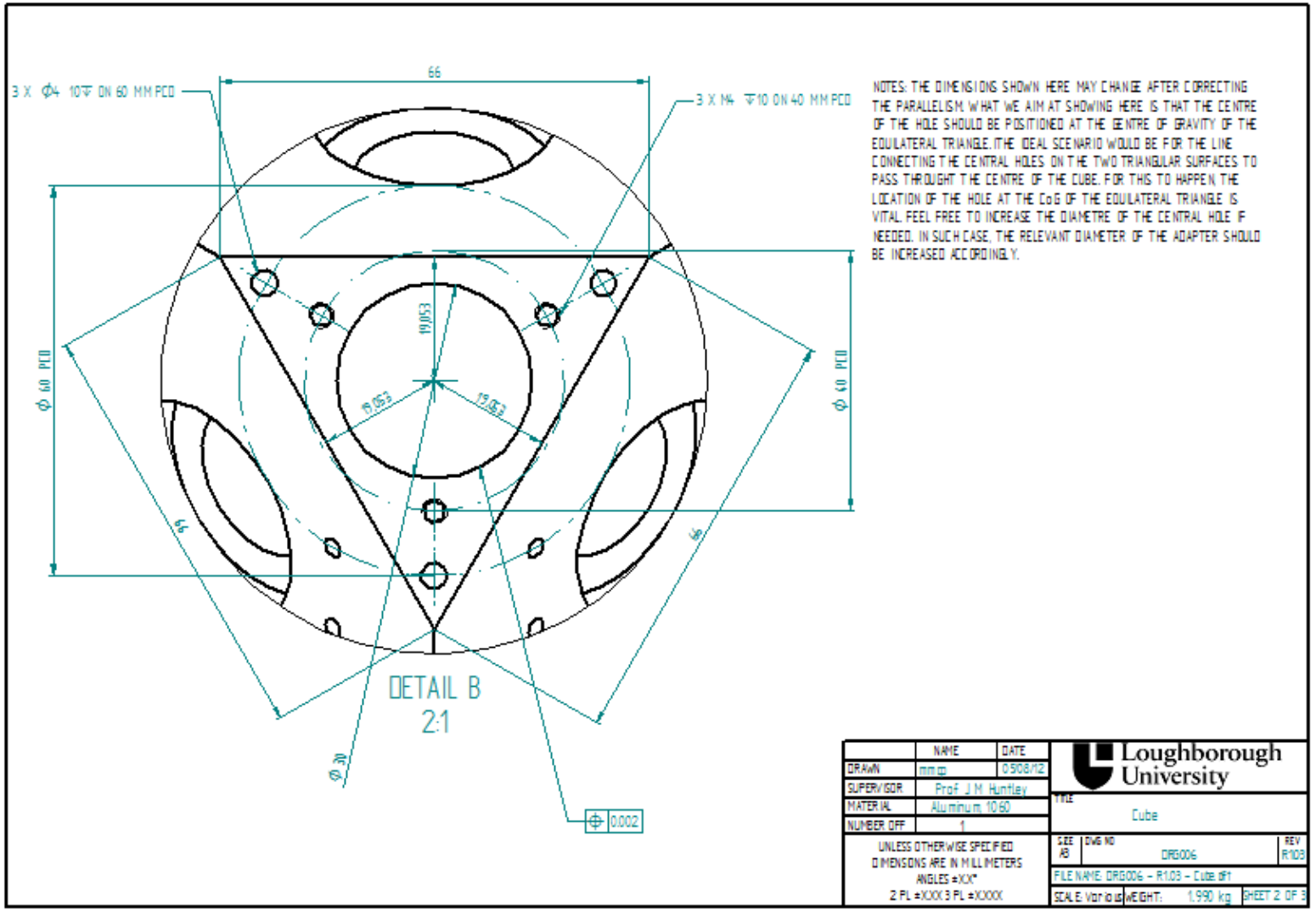
3 X Φ4 10↧ ON 60 MM PCD
66
3 X M4 ↧10 ON 40 MM PCD
NOTES: THE DIMENSIONS SHOWN HERE MAY CHANGE AFTER CORRECTING THE PARALLELISM. WHAT WE AIM AT SHOWING HERE IS THAT THE CENTRE OF THE HOLE SHOULD BE POSITIONED AT THE CENTRE OF GRAVITY OF THE EQUILATERAL TRIANGLE. ITHE IDEAL SCENARIO WOULD BE FOR THE LINE CONNECTING THE CENTRAL HOLES ON THE TWO TRIANGULAR SURFACES TO PASS THROUGHT THE CENTRE OF THE CUBE. FOR THIS TO HAPPEN, THE LOCATION OF THE HOLE AT THE CoG OF THE EQUILATERAL TRIANGLE IS VITAL. FEEL FREE TO INCREASE THE DIAMETRE OF THE CENTRAL HOLE IF NEEDED. IN SUCH CASE, THE RELEVANT DIAMETER OF THE ADAPTER SHOULD BE INCREASED ACCORDINGLY.
19.053
19.053
19.053
Φ 60 PCD
Φ 60 PCD
66
66
Φ 30
DETAIL B
2:1
0.002
NAME
DATE
DRAWN
mm cp
0.5108.12
SUPERVISOR
Prof. J.M. Huntley
MATERIAL
Aluminum 1060
NUMBER OFF
1
UNLESS OTHERWISE SPECIFIED
DIMENSIONS ARE IN MILLIMETERS
ANGLES ±XX°
2 PL ±XXX 3 PL ±XXXX
Loughborough University
TITLE
Cube
SIZE A3
DWG NO
DRG006
REV R103
FILE NAME: DRG006 – R103 – Cube.iPT
SCALE: Various
WEIGHT: 1.990 kg
SHEET 2 OF 3

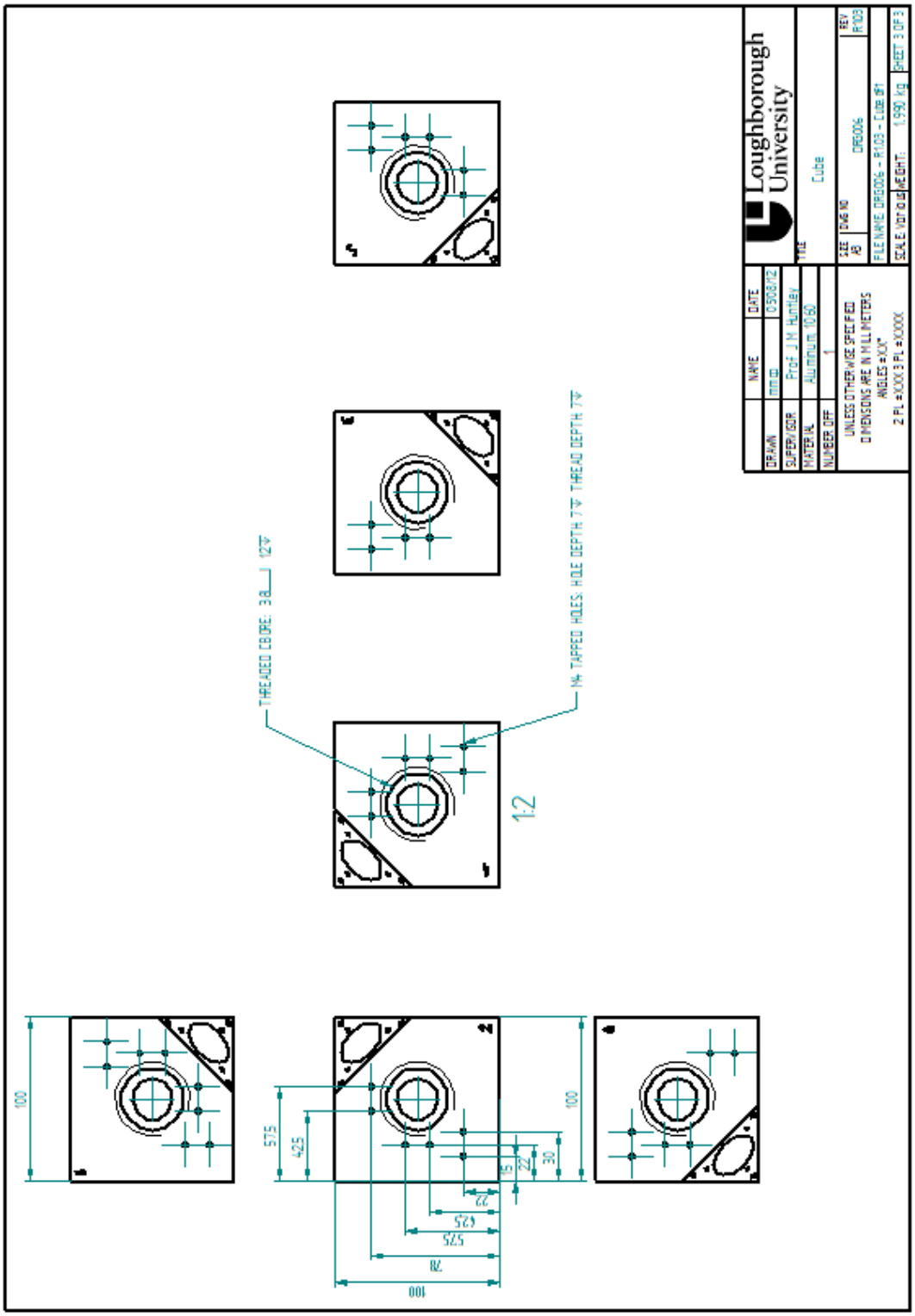
Loughborough University
NAME
DATE
DRAWN
mmp
05/08/12
SUPERVISOR
Prof J.M. Huntley
MATERIAL
Aluminium 1060
NUMBER OFF
1
TITLE
Cube
SIZE A3
DWG NO
DR0006
REV R103
UNLESS OTHERWISE SPECIFIED DIMENSIONS ARE IN MILLIMETERS ANGLES ±XX° 2 PL ±XXX 3 PL ±XXXX
FILE NAME DR0006 - R103 - Cube.dft
SCALE 1:2
WEIGHT: 1.990 kg
SHEET 3 OF 3
THREADED CBORE: 3.8 ⌴ 12
M4 TAPPED HOLES: HOLE DEPTH 7 ↧ THREAD DEPTH 7 ↧
1:2
100
57.5
42.5
15
22
30
22
62.5
57.5
78
100
100

A1.2 Calibration artefact setup

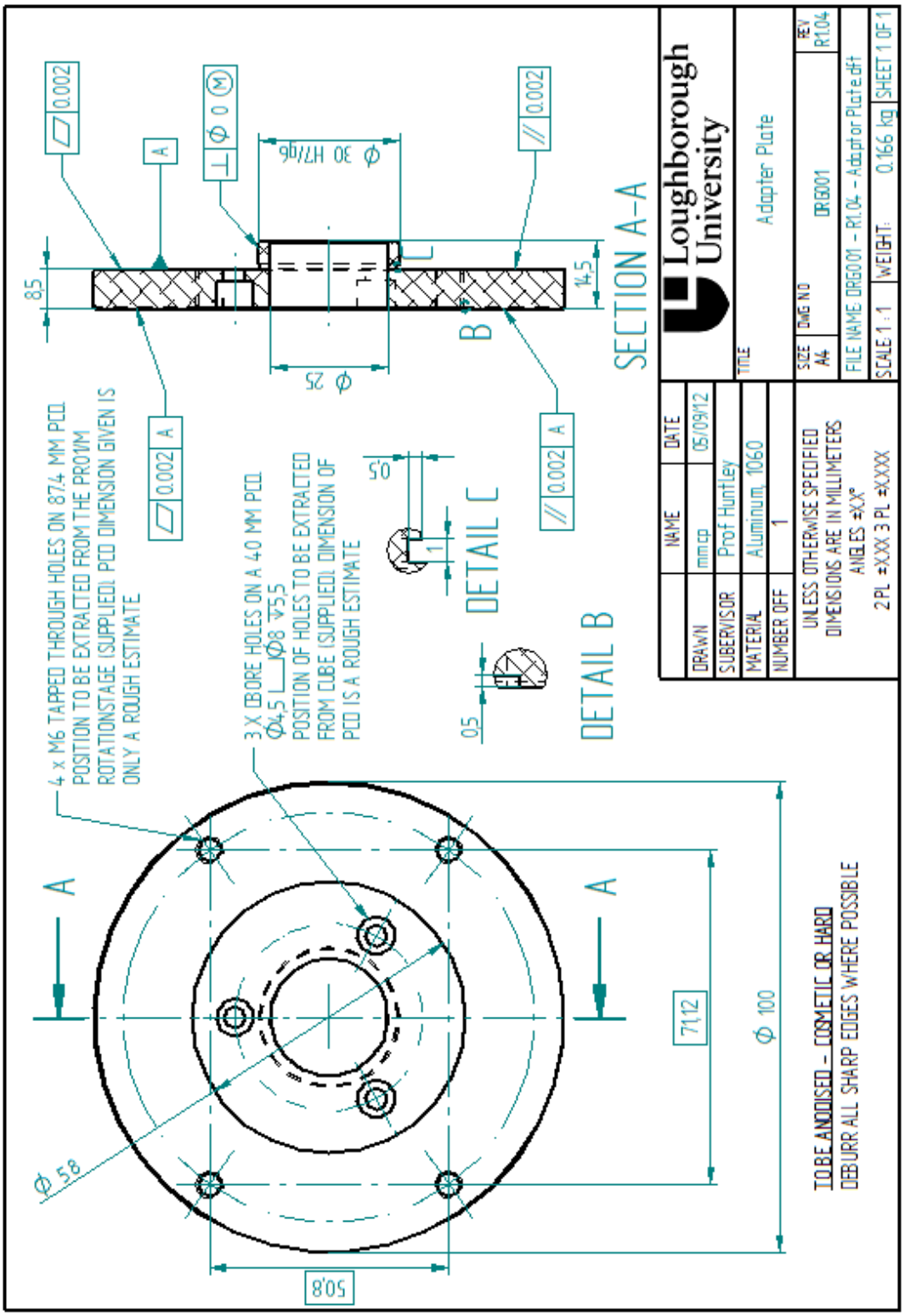

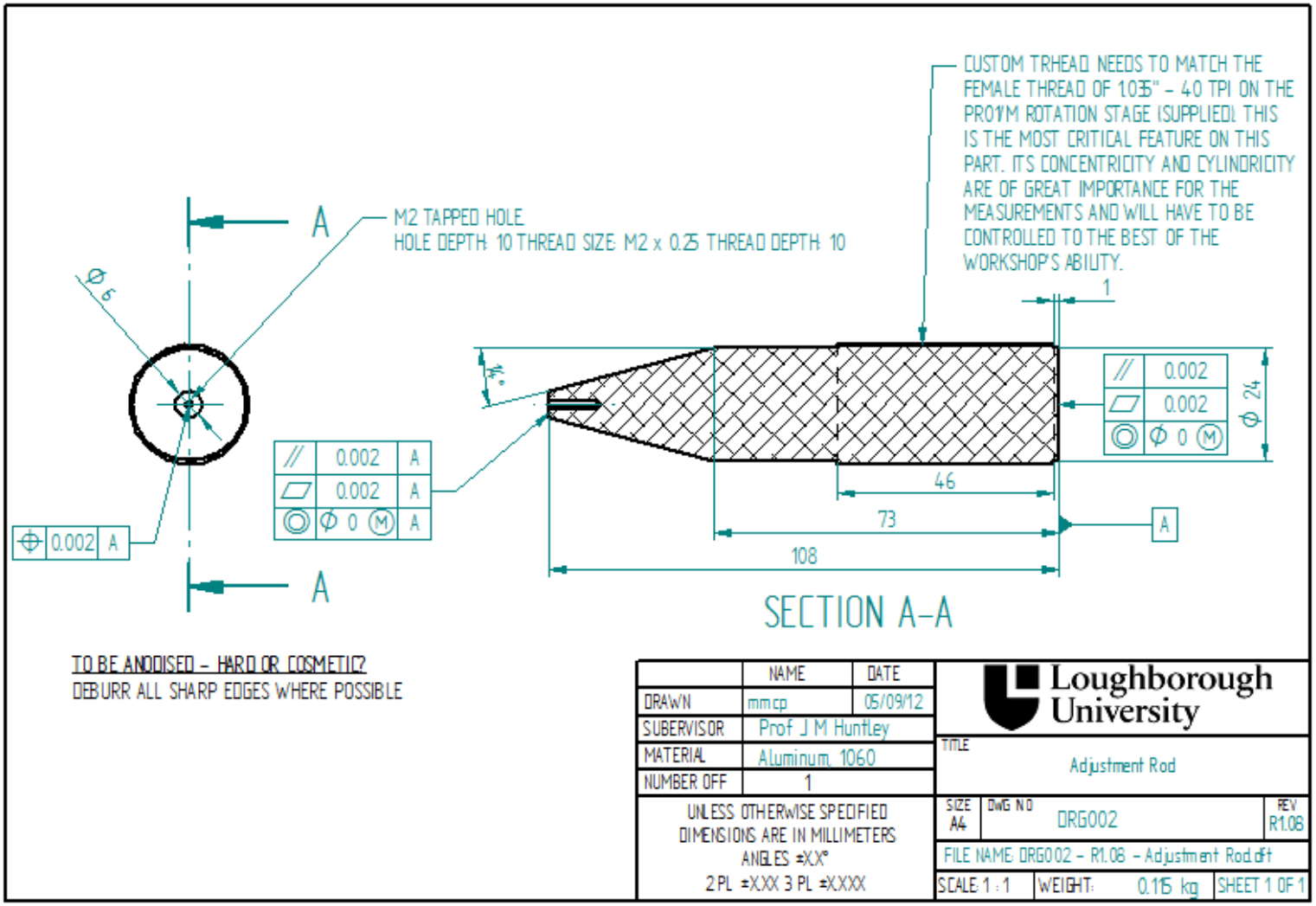
CUSTOM THREAD NEEDS TO MATCH THE FEMALE THREAD OF 1.035" – 40 TPI ON THE PROTM ROTATION STAGE (SUPPLIED). THIS IS THE MOST CRITICAL FEATURE ON THIS PART. ITS CONCENTRICITY AND CYLINDRICITY ARE OF GREAT IMPORTANCE FOR THE MEASUREMENTS AND WILL HAVE TO BE CONTROLLED TO THE BEST OF THE WORKSHOP'S ABILITY.
A
M2 TAPPED HOLE
HOLE DEPTH: 10 THREAD SIZE: M2 x 0.25 THREAD DEPTH: 10
Ø6
0.002 A
0.002 A
0.002 A
Ø 0 M A
1
4°
0.002
0.002
Ø 0 M
Ø 24
46
73
108
A
A
SECTION A-A
TO BE ANODISED – HARD OR COSMETIC?
DEBURR ALL SHARP EDGES WHERE POSSIBLE
NAME
DATE
DRAWN
mmcp
05/09/12
SUBERVISOR
Prof J M Huntley
MATERIAL
Aluminum, 1060
NUMBER OFF
1
UNLESS OTHERWISE SPECIFIED
DIMENSIONS ARE IN MILLIMETERS
ANGLES ±X.X°
2 PL ±X.XX 3 PL ±X.XXX
Loughborough University
TITLE
Adjustment Rod
SIZE
A4
DWG NO
DRG002
REV
R1.08
FILE NAME: DRG002 – R1.08 – Adjustment Rod.dft
SCALE: 1 : 1
WEIGHT: 0.115 kg
SHEET 1 OF 1

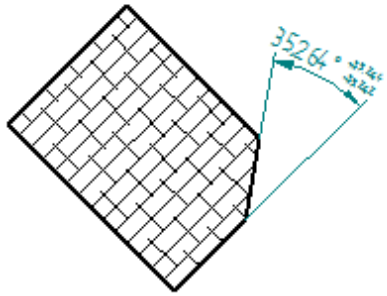

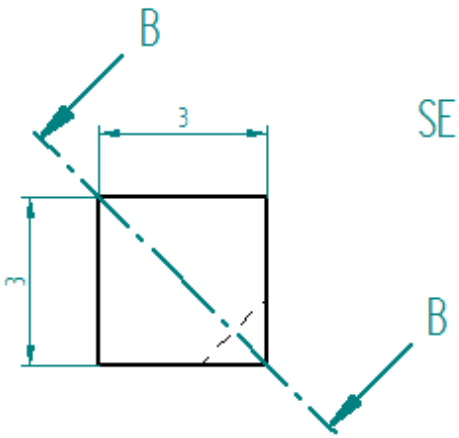

SECTION B-B

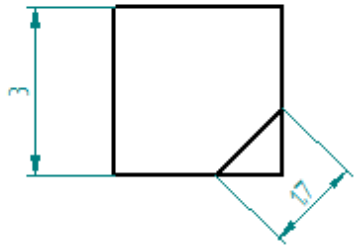

NOTE: THIS CUBIC SPECIMEN IS TO BE USED FOR MEASUREMENT OF SURFACE DISPLACEMENT FIELDS USING AN INHTEFEROMETRIC INSTRUMENT TO A FRACTION OF A WAVELENGTH. THE CUBIC SPECIMEN WILL BE ROTATED BY MEANS OF A PRECISION ROTATION STAGE (PR01/M) AND SUCCESIVE MEASUREMENTS WILL BE TAKEN. CONSEQUENTLY, ALL SIX SIDES OF THE CUBIC SPECIMEN SHOULD BE FLAT TO WITHIN 0.002MM. OPPOSITE SIDES SHOULD BE PARALLEL TO WITHIN 0.002 MM WHILE ADJACENT ONES SHOULD BE PERPENDICULAR TO EACH OTHER TO WITHIN 0.002MM. THE TRIANGULAR SURFACE SHOWN SHOULD ALSO BE FLAT TO WITHIN 0.002MM

	NAME	DATE
DRAWN	mmcp	05/10/12
SUBERVISOR	Prof J M Huntley	
MATERIAL	Aluminum, 1060	
NUMBER OFF	1	

UNLESS OTHERWISE SPECIFIED
DIMENSIONS ARE IN MILLIMETERS
ANGLES ±0.002°
2 PL ±0.01 3 PL ±0.002

Loughborough University

TITLE: Cubic Specimen 3x3x3 mm

SIZE	DWG NO	REV
A4	DRG005	R1.02

FILE NAME: DRG005 – R1.02 – Cubic Specimen 3x3x3 mm.drft

SCALE:	WEIGHT: 0.000 kg	SHEET 1 OF 2

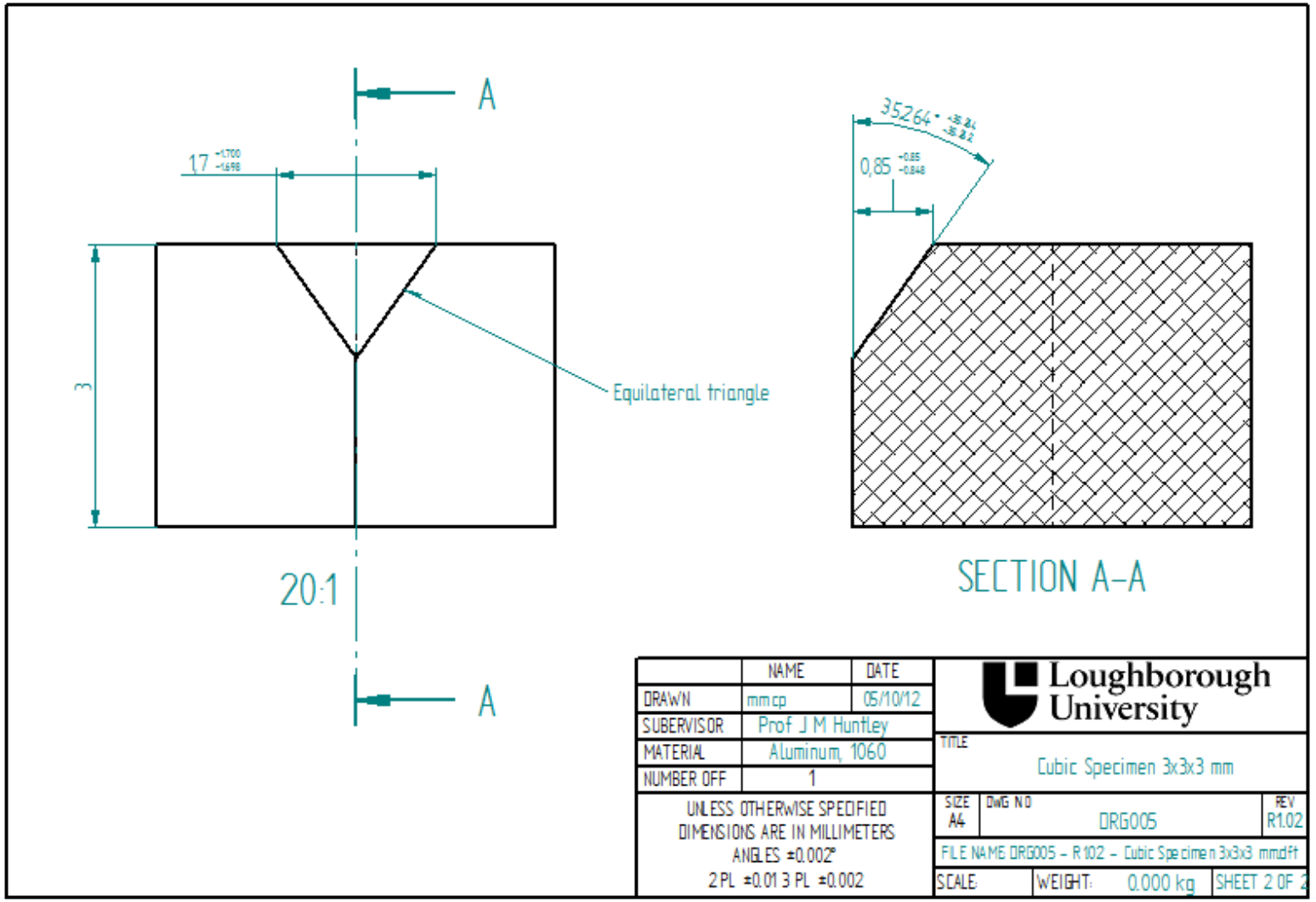
A
17 +1.700 -1.698
3
Equilateral triangle
20:1
A
35.264° +35.26 -35.27
0,85 +0.85 -0.848
SECTION A-A
NAME
DATE
DRAWN
mmcp
05/10/12
SUBERVISOR
Prof J M Huntley
MATERIAL
Aluminum, 1060
NUMBER OFF
1
UNLESS OTHERWISE SPECIFIED
DIMENSIONS ARE IN MILLIMETERS
ANGLES ±0.002°
2 PL ±0.01 3 PL ±0.002
Loughborough University
TITLE
Cubic Specimen 3x3x3 mm
SIZE A4
DWG NO
DRG005
REV R1.02
FILE NAME DRG005 - R102 - Cubic Specimen 3x3x3 mmdft
SCALE:
WEIGHT: 0.000 kg
SHEET 2 OF 2

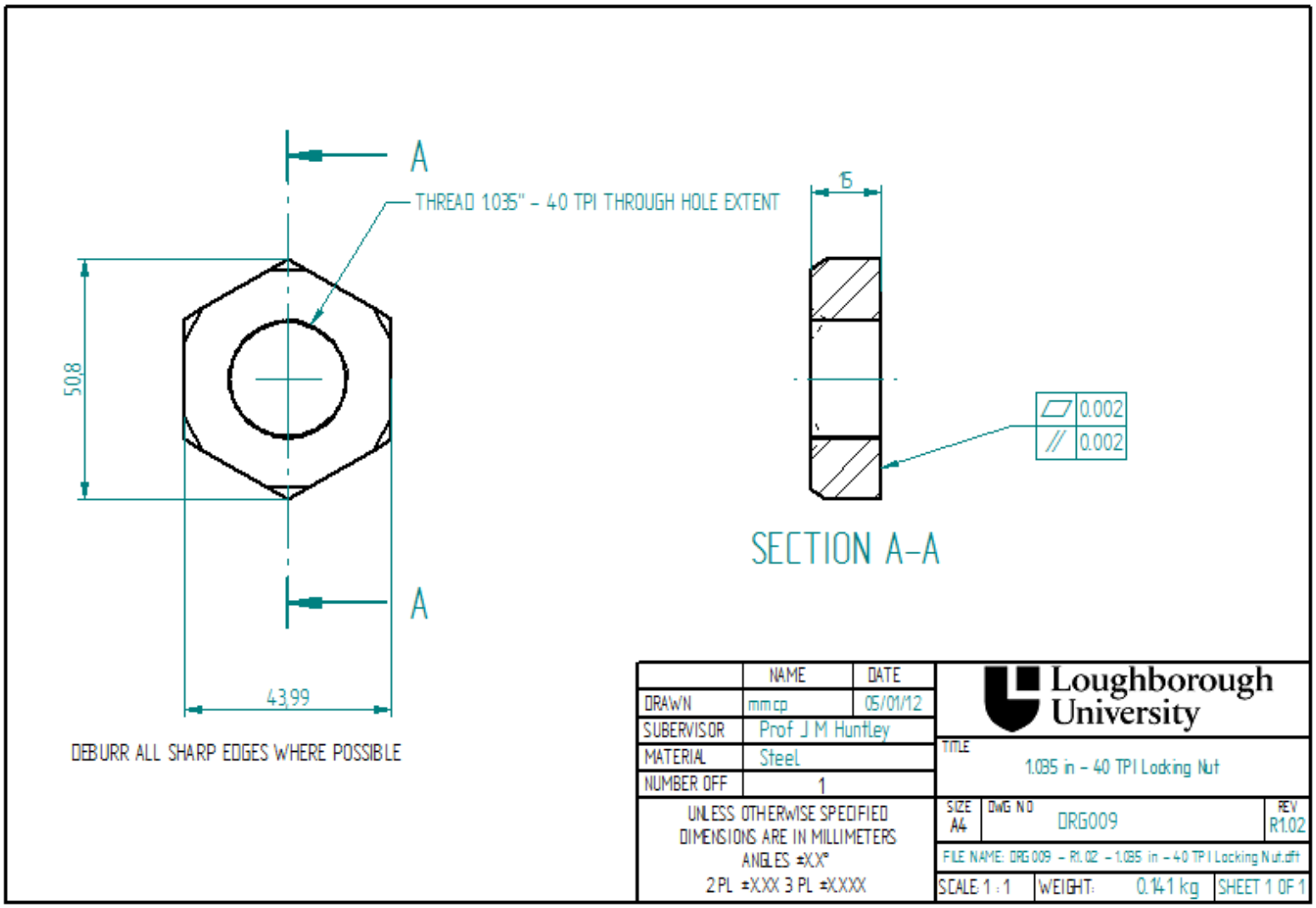
A
THREAD 1.035" – 40 TPI THROUGH HOLE EXTENT
50.8
A
43.99
15
0.002
0.002
SECTION A–A
DEBURR ALL SHARP EDGES WHERE POSSIBLE
NAME
DATE
DRAWN
mmcp
05/01/12
SUBERVISOR
Prof J M Huntley
MATERIAL
Steel
NUMBER OFF
1
UNLESS OTHERWISE SPECIFIED
DIMENSIONS ARE IN MILLIMETERS
ANGLES ±X.X°
2 PL ±X.XX 3 PL ±X.XXX
Loughborough University
TITLE
1.035 in – 40 TPI Locking Nut
SIZE
A4
DWG NO
DRG009
REV.
R1.02
FILE NAME: DRG 009 – R1.02 – 1.035 in – 40 TPI Locking Nut.dft
SCALE: 1 : 1
WEIGHT:
0.141 kg
SHEET 1 OF 1

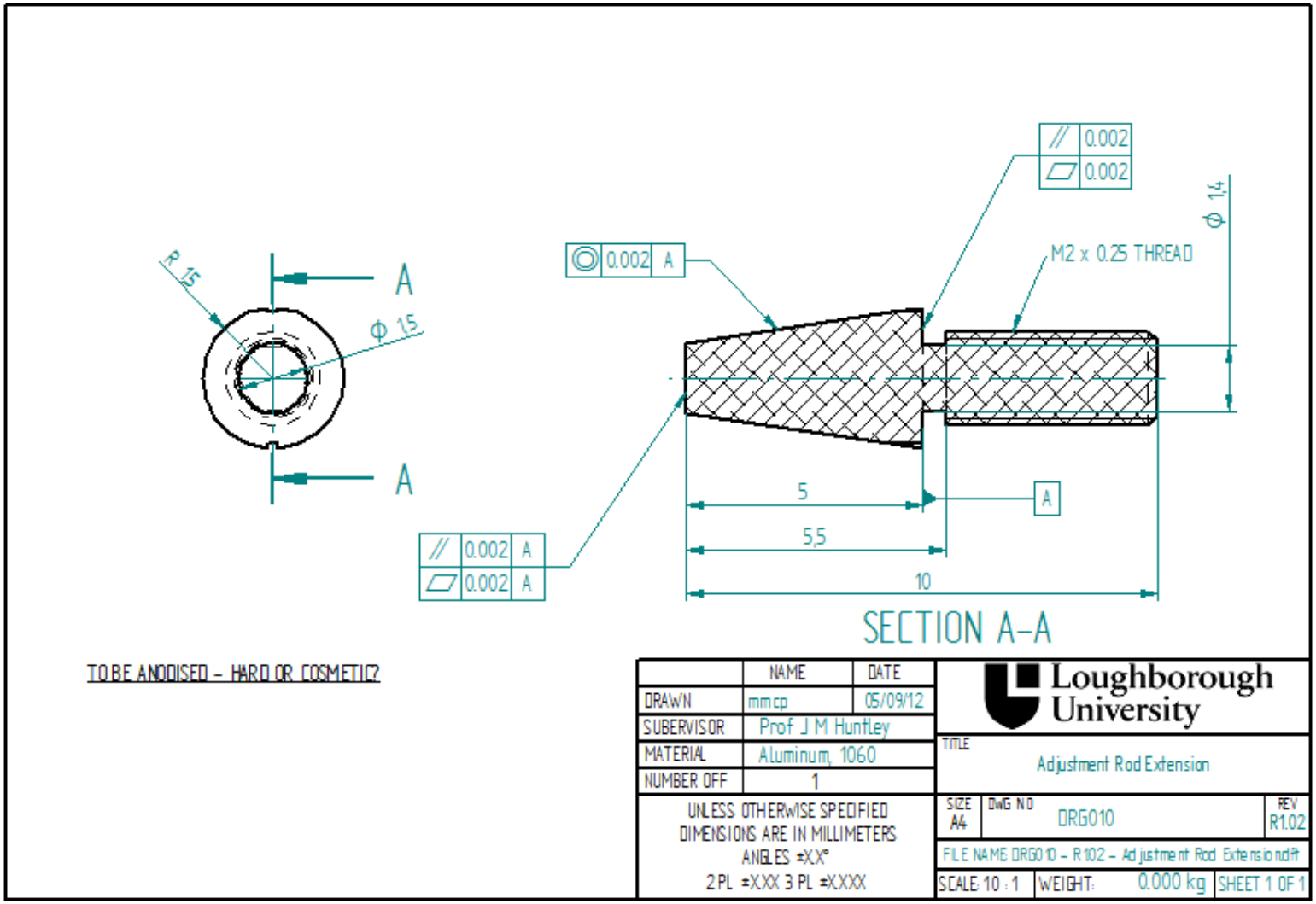
R 1.5
A
Φ 1.5
A
0.002 A
// 0.002
0.002
Φ 1.4
M2 x 0.25 THREAD
// 0.002 A
0.002 A
5
5.5
10
A
SECTION A-A
TO BE ANODISED - HARD OR COSMETIC?
NAME
DATE
DRAWN
mmcp
05/09/12
SUBERVISOR
Prof J M Huntley
MATERIAL
Aluminum, 1060
NUMBER OFF
1
UNLESS OTHERWISE SPECIFIED
DIMENSIONS ARE IN MILLIMETERS
ANGLES ±X.X°
2 PL ±X.XX 3 PL ±X.XXX
Loughborough University
TITLE
Adjustment Rod Extension
SIZE
A4
DWG NO
ORG010
REV
R1.02
FILE NAME ORG010 - R102 - Adjustment Rod Extension.dft
SCALE 10 : 1
WEIGHT:
0.000 kg
SHEET 1 OF 1

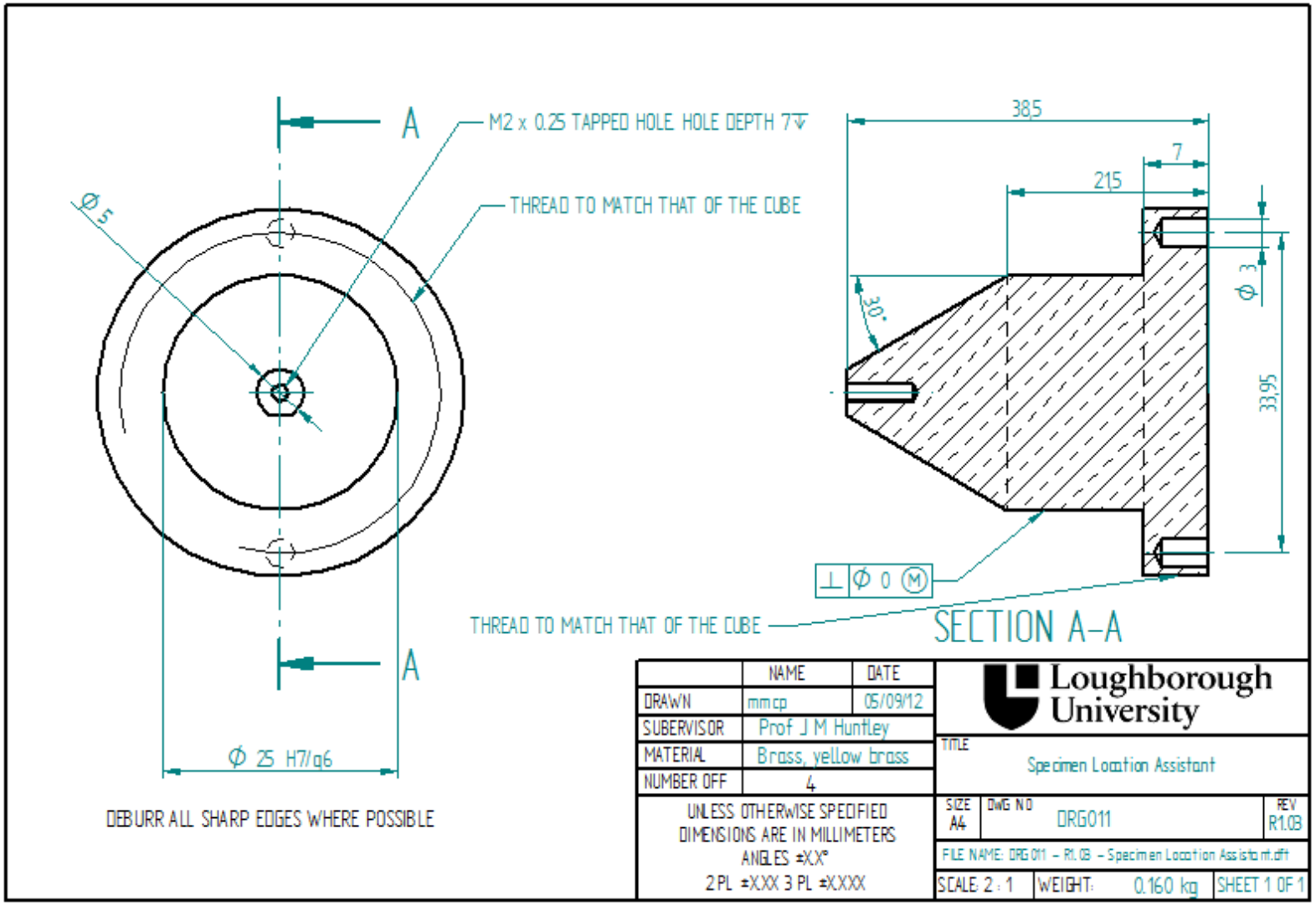
A
M2 x 0.25 TAPPED HOLE HOLE DEPTH 7↧
THREAD TO MATCH THAT OF THE CUBE
Ø5
A
Ø 25 H7/g6
38,5
7
21,5
Ø 3
30°
33,95
⊥ Ø 0 Ⓜ
THREAD TO MATCH THAT OF THE CUBE
SECTION A-A
DEBURR ALL SHARP EDGES WHERE POSSIBLE
NAME
DATE
DRAWN
mmcp
05/09/12
SUBERVISOR
Prof J M Huntley
MATERIAL
Brass, yellow brass
NUMBER OFF
4
UNLESS OTHERWISE SPECIFIED
DIMENSIONS ARE IN MILLIMETERS
ANGLES ±X.X°
2 PL ±X.XX 3 PL ±X.XXX
Loughborough University
TITLE
Specimen Location Assistant
SIZE
A4
DWG NO
DRG011
REV
R1.03
FILE NAME: DRG 011 – R1.03 – Specimen Location Assistant.dft
SCALE: 2 : 1
WEIGHT:
0.160 kg
SHEET 1 OF 1

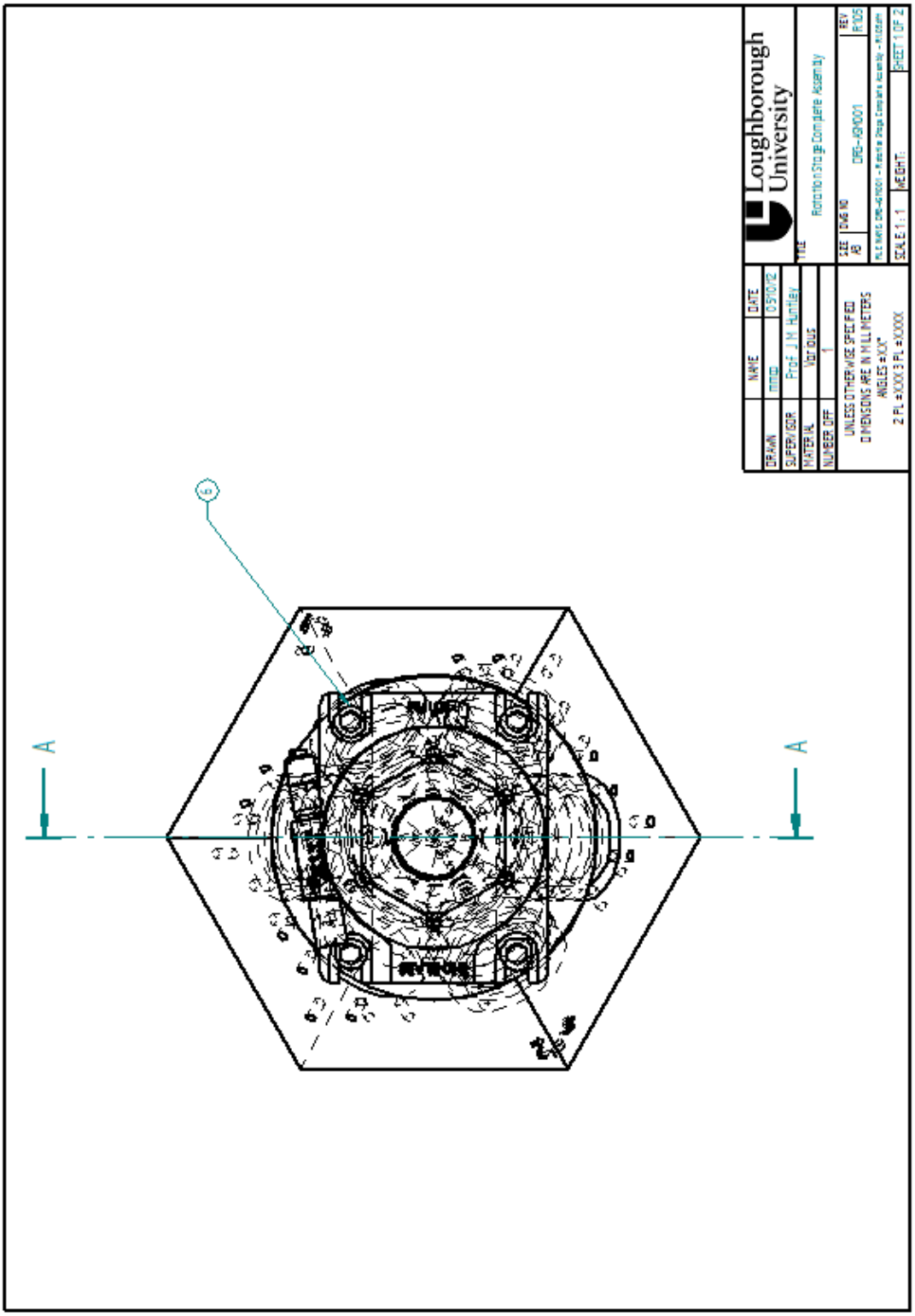
A
A
6
Loughborough University
NAME
DATE
DRAWN
mmp
05/10/12
SUPERVISOR
Prof J.M. Huntley
MATERIAL
Various
NUMBER OFF
1
UNLESS OTHERWISE SPECIFIED
DIMENSIONS ARE IN MILLIMETERS
ANGLES ± 0.5°
2 PL ± 0.XX 3 PL ± 0.XXX
Rotation Stage Complete Assembly
SIZE
A3
DWG NO
DRS-491001
REV
R105
SCALE 1 : 1
WEIGHT:
SHEET 1 OF 2

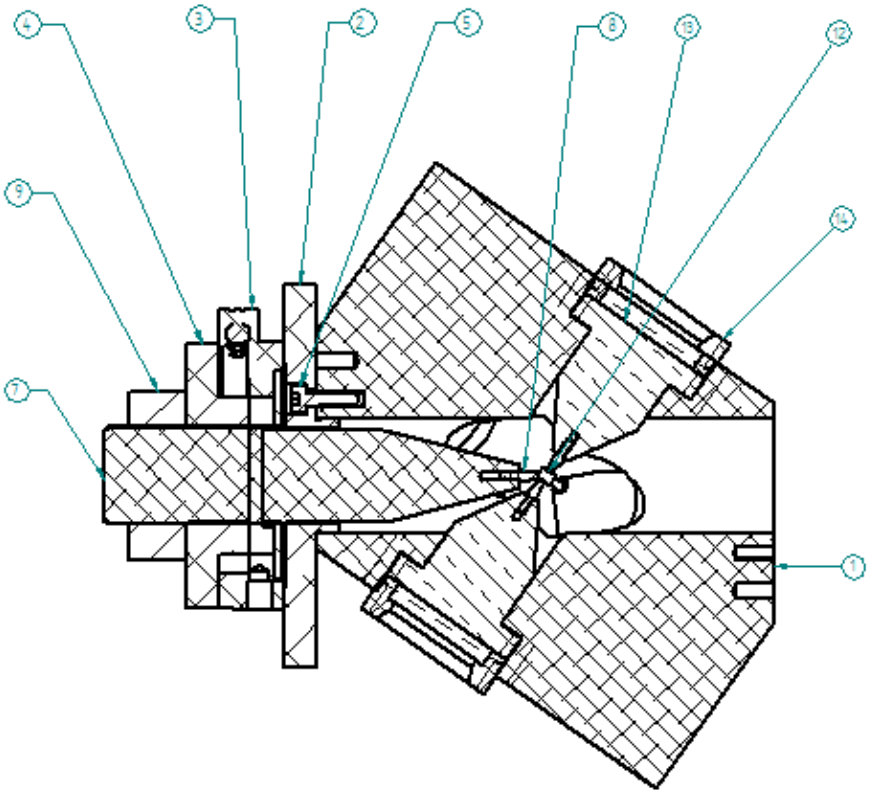

SECTION A–A

Item Number	Document Number	Title	Material	Quantity	Status	Revision number
1	DRB006	Cube	Aluminum, 1060	1	ADDUSTMENTS NEEDED	R1.03
2	DRB001	Adaptor Plate	Aluminum, 1060	1	TO BE MANUFACTURED	R1.04
3	PRT004a	PR01/M	Aluminum, 1060	1	ThorLabs – Stock	R1.01
4	PRT004b	PR01/M Rotating Disc	Aluminum, 1060	1	Thorlabs – Stock	R1.02
5	PRT007	M4 Cap Head Screw	Steel	3	Stock Item	R1.01
6	PRT008	M6 Cap Head Screw	Steel	4	Stock Item	R1.02
7	DRB002	Adjustment Rod	Aluminum, 1060	1	TO BE MANFUCTURED	R1.08
8	DRB010	Adjustment Rod Extension	Aluminum, 1060	5	TO BE MANUFACTURED	R1.02
9	DRB009	Locking Nut	Steel	1	TO BE MANUFACTURED	R1.02
12	DRB005	Cubic Specimen 3x3x3 mm	Aluminum, 1060	1	N/A	R1.02
13	DRB011	Specimen Potition Assistant	Brass, yellow brass	4	TO BE MANUFACTURED	R1.02
14		Retaining Ring	Aluminum, 1060	5		R1.01

	NAME	DATE
DRAWN	mmp	05/10/12
SUPERVISOR	Prof. J.M. Huntley	
MATERIAL	Various	
NUMBER OFF	1	

UNLESS OTHERWISE SPECIFIED
DIMENSIONS ARE IN MILLIMETERS
ANGLES ±XX°
2 PL ±XXX 3 PL ±XXXX

Loughborough University

TITLE
Rotation Stage Complete Assembly

SIZE	DWG NO	REV
A3	DRB–ASM001	R1.05

FILE NAME: DRB–ASM001 – Rotation Stage Complete Assembly – R1.05.sldprt

SCALE: 1 : 1 | WEIGHT: | SHEET 2 OF 2

A2 CMM measurements

Measurements of the calibration cube and the sample host cube using the coordinate measurement machine at the metrology lab of the Wolfson School at Loughborough University that is traceable to national standards.

A2.1 Calibration artefact

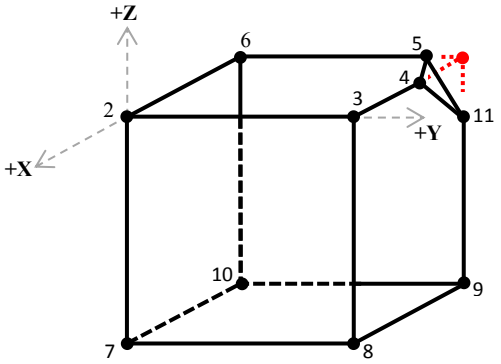

Plane Number	Points on Plane	Flatness	Parallelism (//) in µm	Squareness (⊥) in µm
PLN2	(2,3,4,5,6)	1.1 µm	PLN2/PLN4: 30.8	PLN2/PLN3: 6.5
PLN3	(2,6,7,10)	1.5 µm	PLN3/PLN6: 2.9	PLN2/PLN5: 30.6
PLN4	(7,8,9,10)	10.9 µm	PLN5/PLN7: 4.1	PLN2/PLN6: 7.0
PLN5	(2,3,7,8)	1.1 µm	**Plane to Plane Dist.**	PLN2/PLN7: 33.0
PLN6	(3,4,11,9,8)	0.7 µm	PLN2/PLN4: 2.7964 mm	PLN4/PLN3: 22.8
PLN7	(6,5,11,9,10)	1.0 µm	PLN3/PLN6: 2.9840 mm	PLN4/PLN5: 28.0
			PLN5/PLN7: 2.9793 mm	PLN4/PLN6: 22.6
Point Coordinates				PLN4/PLN7: 30.3
Point Number	**X (µm)**	**Y (µm)**	**Z (µm)**	PLN3/PLN5: 4.1
2	0	0	0	PLN5/PLN6: 2.3
3	-2.8	2985	0	PLN6/PLN7: 1.3
6	-2978.6	0	0	PLN3/PLN7: 3.3
7	-41.5	-8	-2798.6	
8	-44.6	2976.3	7.9	
9	-3024.9	2975.1	-2774.9	
10	-3023	-7.9	-2774.9	

Spatial Orientation of Cube-Edges					
Line Number	**On Plane**	**Points on Line**	**X (μm)**	**Y (μm)**	**Z (μm)**
LN2	PLN2	(2,3)	-1.6	1669.6	0
LN3	PLN2	(2,7)	-23	-4.4	-1554.8
LN4	PLN2	(7,8)	-43.1	1495.5	-2809.7
LN5	PLN2	(8,3)	-23.9	2980.6	-1424.5
LN6	PLN6	(3,4)	-1604.2	2984.3	0
LN7	PLN6	(8,9)	-1541.4	2975.7	-2808.7
LN8	PLN6	(9,11)	-3001.3	2979.6	-1322.2
LN9	PLN2	(6,5)	-2979.3	1436	0
LN10	PLN4	(9,10)	-3023.8	1216.3	-2784.3
LN11	PLN3	(6,10)	-3001.8	-4.2	-1452.5
LN12	PLN2	(2,6)	-1728	0	0
LN13	PLN4	(7,10)	-1663.9	-8	-1785.7

A2.2 Sample-host aluminium cube

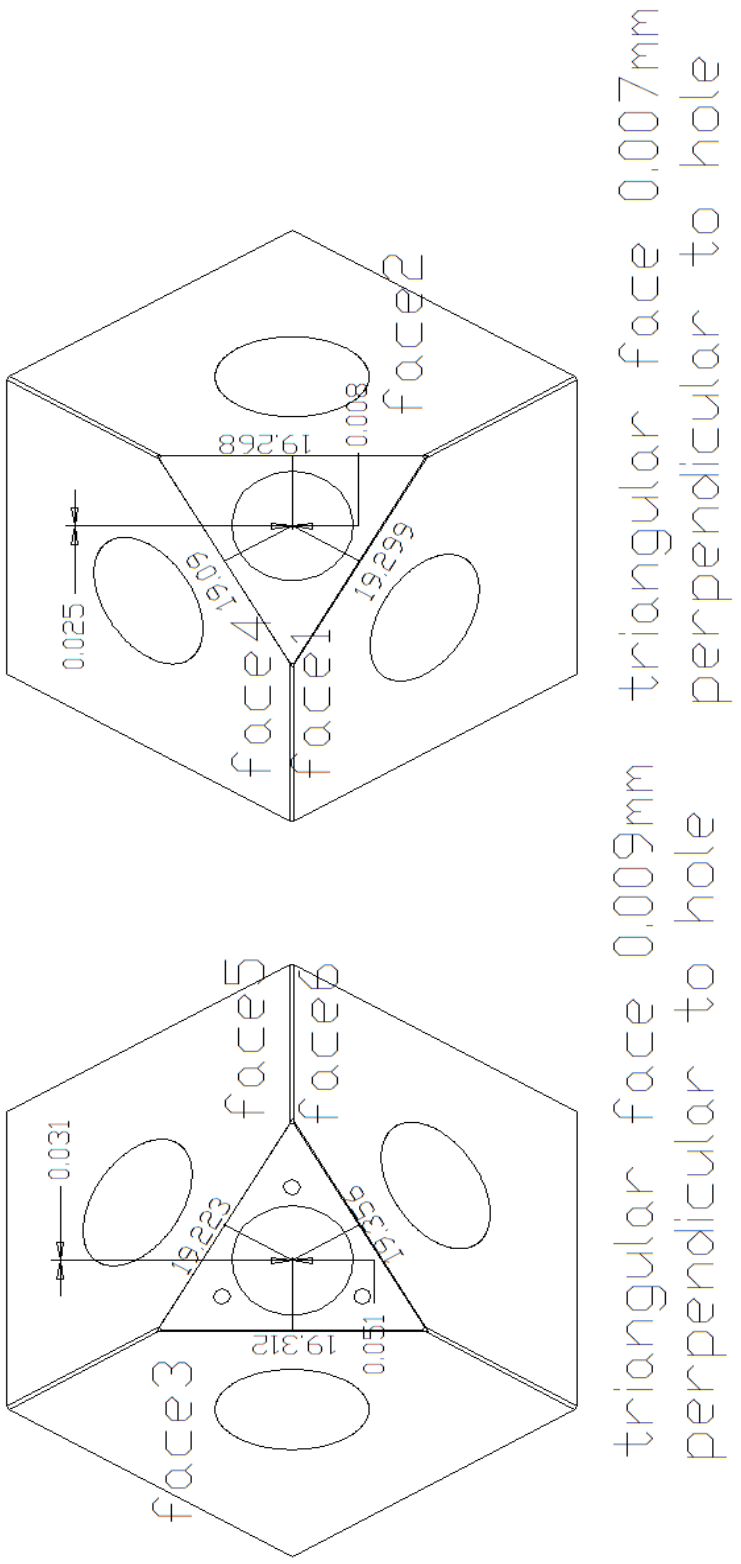

A3 Laser operating procedure

Description of the operating and alignment procedures for initiating the data capturing.

A3.1 Verdi and SolsTi:S operating procedure

1. Switch cameras ON inside the laser Box.
2. Lock all doors – Both front and back doors for T.0.18 Lab
3. Turn switch for '*Laser in operation'* to ON. This is located behind the metal box and activates the interlocks.
4. Make sure that the light outside the main door of T.0.18 is ON (Red light) and that the light indicators for ALL the interlocks are ON. This should ensure that all interlocks are working properly.
5. Make sure that the interlock override is OFF.
6. Make sure that the SHUTTER is closed on Verdi and that the power level is set to LEVEL 1 (0.5W).
7. Insert key into key slot and switch Verdi from STANDBY to ON.
8. Wait until all servos are locked.
9. Open SHUTTER and switch to power LEVEL 2 (5W) – wait until all servos are locked.
10. Start cameras from StreamPix in *'FixedRate'* trigger mode – Although the scan has not started yet this should give an image from the *Workspace* named *Cam1* (Wedges). This is an indicator that the SolsTi:S is lasing. If no image is received from the wedge camera this means that the laser has become misaligned – Refer to **Alignment and Power Adjustment Procedures**
11. Switch trigger mode from the ***Adjustments tab*** in ***Hardware Properties*** in StreamPix to '*SyncIn2'* – This will now synchronize the cameras to the

SolsTi:S. NOTE that the cameras will probably stop acquiring images after this change. This is normal.

12. Double click on the *internet explorer* shortcut on the desktop. This will open the operating control panel for the SolsTiS.
13. Select '*Configure'* and then '*Scan*'.
14. Make sure that the wavelength sensitive diode (WSD) reading is stable (minor fluctuations). This means that the laser is still lasing and everything is working properly.
15. Adjust parameters as appropriate i.e. wavelength step, scan type, stop wavelength, scan frequency (Hz) etc.
16. Start scan by pressing the START SCAN button.
17. Check that the cameras have started to acquire images again!
18. Press on the STOP SCAN button
19. Start recording from StreamPix – See **Recording Image Sequence Procedures** document for more info.
20. Restart Scan from the required wavelength

A3.2 Alignment and power adjustment procedure of SolsTi:S

1. Put GOGGLES ON
2. Check everyone else in the room have their goggles ON
3. Lock BOTH lab doors.
4. Remove any shiny/metal object you - watches, rings, bracelets etc.
5. Turn the power to 0.5 Watts, proceed to alignment without IR Viewer looking for the output green light.
6. Move in x, and y to center the green output light on the exit aperture of the SolsTi:S.

7. Once centered (Check this carefully as damage to the internal components can happen if not centered carefully) turn the intensity to 5Watts and turn on to the IR viewer for detecting IR light emission.

8. Look for the fluorescence halo by very small adjustments on the horizontal direction until suddenly a bright IR spot appears.

9. Now turn to the Power meter for further adjustment, and moving by fine adjustment until the power is optimized.

A4 Wedge manufacturer data

CENTRO DE INVESTIGACIONES EN OPTICA, A.C. ®

DIRECCIÓN DE TEGNOLOGIA E INNOVACION

OFFER: I
DATE: February 16th 2009

BILL TO:

Name: Loughborough University
Attention: Dr. Abundio Davila Alvarez
Address: Loughborough, Leics. LE11 3TU
City: Loughborough
Country: England, UK
Phone: +44 (0) 1509 22 7636
ZC: LE11 3TU
Email: A.Davila-Alvarez@lboro.ac.uk

SHIP TO:

Name: Loughborough University
Address: Loughborough, Leics. LE11 3TU
City: Loughborough
Country: England, UK
Phone: +44 (0) 1509 22 7636
ZC: LE11 3TU
TAX ID:

QUANTITY	DESCRIPTION	UNIT PRICE	TOTAL
1	Optical wedge, material: fused silica, dimensions: 30 x 7.5 mm, centre thickness de **9.6** mm +/- 0.05 mm, wedge angle: 2 min +/- 0.2 min, polish both sides to lambda /10	**£ 48.00**	**£ 48.00**
1	Optical wedge, material: fused silica, dimensions 30 x 7.5 mm, centre thickness: **12** mm +/- 0.05 mm, wedge angle: 2 min +/- 0.2 min, polish both side to lambda/10.	**£ 48.00**	**£ 48.00**
1	Optical wedge, material: fused silica, dimensions: 30 x 7.5 mm, centre thickness: **12.6** mm +/- 0.05mm, wedge angle: 2 min +/- 0.2 min, polish both sides to lambda/10	**£ 48.00**	**£ 48.00**
1	Optical wedge, material: fused silica, dimensions: 30 x 7.5 mm, central thickness: **12.8** mm +/-0.05 mm, wedge angle: 2 min +/- 0.2 min, polish both sides to lambda/10	**£ 48.00**	**£ 48.00**
-	Note: S/D: 60/40, bevel: 0.1 mm @45°	-	-

TERMS AND CONDITIONS

** NOTE: COST DOES NOT INCLUDE SHIPPING EXPENSES NOR CUSTOMS PROCESSING FEES
** TIME FOR DELIVERY: 4 TO 5 WEEKS AFTER DOWN PAYMENT HAS BEEN DEPOSITED
** PAYMENT IS TO BE MADE BY DEPOSIT OR ELECTRONIC TRANSFER TO THE BANK ACCOUNT STATED BELOW, UNDER THE NAME OF "CENTRO DE INVESTIGACIONES EN ÓPTICA A.C." A COPY OF THE DEPOSIT SLIP IS TO BE FAXED, TO THE ATTENTION OF MS. MARILÚ SILVA, TO PHONE NUMBER (477) 441 42 09 IN MEXICO, INDICATING QUOTATION NUMBER

MERCHANDISE TOTAL	£ 192.00
FREIGHT COST	£ 28.37
HANDLING AND DELIVERY	£ 23.64
INSURANCE	£ -
TOTAL (POUNDS)	£ 244.01

BANK	"CLABE" NUMBER	ACCOUNT NUMBER	BRANCH	LOCATION
BANORTE	072225001052349453	10523494 - 5	175	LEÓN INSURGENTES

SINCERELY

Carlos Javier Martínez
UNIDAD DE GESTIÓN
E-MAIL: cj@cio.mx
TEL: (477) 441 42 00 EXT: 103

OBSERVATIONS:
P ST DS A
* Para uso exclusivo interno CIO

ACCEPTANCE OF QUOTATION BY COMPANY
DATE: February 16th 2009
Name: Dr. Abundio Davila Alvarez
Signature:

References

1. Huntley, J.M. and H.O. Saldner, *Shape measurement by temporal phase unwrapping: comparison of unwrapping algorithms.* Measurement Science and Technology, 1997. **8**(9): p. 986-992.
2. Huntley, J.M., *An image processing system for the analysis of speckle photographs.* Journal of Physics E: Scientific Instruments, 1986. **19**(1): p. 43.
3. Pablo D. Ruiz, et al., *Depth-resolved whole-field displacement measurement using wavelength scanning interferometry.* Journal of Optics A: Pure and Applied Optics, 2004. **6**(7): p. 679.
4. Ruiz, P.D., J.M. Huntley, and R.D. Wildman, *Depth-resolved whole-field displacement measurement by wavelength-scanning electronic speckle pattern interferometry.* Applied Optics, 2005. **44**(19): p. 3945-3953.
5. Manuel De la Torre-Ibarra, H., P.D. Ruiz, and J.M. Huntley, *Double-shot depth-resolved displacement field measurement using phase-contrast spectral optical coherence tomography.* Optics Express, 2006. **14**(21): p. 9643-9656.
6. Ruiz, P.D., J.M. Huntley, and A. Maranon, *Tilt scanning interferometry: a novel technique for mapping structure and three-dimensional displacement fields within optically scattering media.* Proceedings of the Royal Society of London A: Mathematical, Physical and Engineering Sciences, 2006. **462**(2072): p. 2481-2502.
7. Manuel De la Torre-Ibarra, H., P.D. Ruiz, and J.M. Huntley, *Simultaneous measurement of in-plane and out-of-plane displacement fields in scattering media using phase-contrast spectral optical coherence tomography.* Optics Letters, 2009. **34**(6): p. 806-808.
8. Ruiz, P.D., M. de la Torre-Ibarra, and J.M. Huntley. *Single-shot depth-resolved displacement field measurement using phase-contrast polychromatic speckle interferometry*. in *Proc. SPIE 6341*. Speckle06: Speckles, From Grains to Flowers,63410U (September 15, 2006);doi:10.1117/12.695305; http://dx.doi.org/10.1117/12.695305
9. Pierron, F. and M. Grediac, *The virtual fields method : extracting constitutive mechanical parameters from full-field deformation measurements*. First ed, ed. M. Grediac. 2012, New York, London: Springer.
10. Rousseau, D., et al., *Fast virtual histology using X-ray in-line phase tomography: application to the 3D anatomy of maize developing seeds.* Plant Methods, 2015. **11**(1): p. 55.
11. Lyons, J.S., J. Liu, and M.A. Sutton, *High-temperature deformation measurements using digital-image correlation.* Experimental Mechanics, 1996. **36**(1): p. 64-70.
12. Sutton, M.A., et al., *The effect of out-of-plane motion on 2D and 3D digital image correlation measurements.* Optics and Lasers in Engineering, 2008. **46**(10): p. 746-757.
13. Germaneau, A., P. Doumalin, and J.C. Dupré, *Full 3D Measurement of Strain Field by Scattered Light for Analysis of Structures.* Experimental Mechanics, 2007. **47**(4): p. 523-532.
14. Germaneau, A., P. Doumalin, and J.C. Dupré, *3D Strain Field Measurement by Correlation of Volume Images Using Scattered Light: Recording of Images and Choice of Marks.* Strain, 2007. **43**(3): p. 207-218.

15. Lenoir, N., et al., *Volumetric Digital Image Correlation Applied to X-ray Microtomography Images from Triaxial Compression Tests on Argillaceous Rock.* Strain, 2007. **43**(3): p. 193-205.
16. Carrion, L., et al., *Comparative study of optical sources in the near infrared for optical coherence tomography applications.* Journal of Biomedical Optics, 2007. **12**(1): p. 014017-014017-8.
17. Hecht, J., *Short history of laser development.* Optical Engineering, 2010. **49**(9): p. 091002-091002-23.
18. Svelto, O., *Principles of lasers*. 4th ed.. ed. 1998, New York

London: Plenum Press.
19. Davila, A., et al., *Instantaneous Wavelength Detection by a Whole-Field k-space Method*, in *Fringe 2009: 6th International Workshop on Advanced Optical Metrology*, W. Osten and M. Kujawinska, Editors. 2009, Springer Berlin Heidelberg: Berlin, Heidelberg. p. 1-6.
20. Davila, A., et al., *Simultaneous wavenumber measurement and coherence detection using temporal phase unwrapping.* Applied Optics, 2012. **51**(5): p. 558-567.
21. Davila, A., et al., *Wavelength scanning interferometry using a Ti:Sapphire laser with wide tuning range.* Optics and Lasers in Engineering, 2012. **50**(8): p. 1089-1096.
22. Wiesauer, K., et al. *Ultra-high resolution optical coherence tomography for material characterization and quality control*. in *Proc. SPIE 5714*. 2005. Commercial and Biomedical Applications of Ultrafast Lasers V, 108,doi:10.1117/12.593612; http://dx.doi.org/10.1117/12.593612
23. Wiesauer, K., et al., *En-face scanning optical coherence tomography with ultra-high resolution for material investigation.* Optics Express, 2005. **13**(3): p. 1015-1024.
24. Humbert, G., et al., *Supercontinuum generation system for optical coherence tomography based on tapered photonic crystal fibre.* Optics Express, 2006. **14**(4): p. 1596-1603.
25. Wiesauer, K., et al., *Investigation of glass–fibre reinforced polymers by polarisation-sensitive, ultra-high resolution optical coherence tomography: Internal structures, defects and stress.* Composites Science and Technology, 2007. **67**(15–16): p. 3051-3058.
26. Yamamoto, A., et al., *Surface Shape Measurement by Wavelength Scanning Interferometry Using an Electronically Tuned Ti:sapphire Laser.* Optical Review, 2001. **8**(1): p. 59-63.
27. Chakraborty, S. and P.D. Ruiz, *Measurement of all orthogonal components of displacement in the volume of scattering materials using wavelength scanning interferometry.* Journal of the Optical Society of America A, 2012. **29**(9): p. 1776-1785.
28. Reiser, C. and R.B. Lopert, *Laser wavemeter with solid Fizeau wedge interferometer.* Applied Optics, 1988. **27**(17): p. 3656-3660.
29. Alipieva, E.A., E.V. Stoykova, and V. Nikolova, *Wavemeter with Fizeau interferometer for cw lasers*, in *Proc. SPIE 4397*. (April 9, 2001): 11th International School on Quantum Electronics: Laser Physics and Applications, 129;doi:10.1117/12.425118; http://dx.doi.org/10.1117/12.425118 p. 129-133.

30. Lee, L.S. and A.L. Schawlow, *Multiple-wedge wavemeter for pulsed lasers.* Optics Letters, 1981. **6**(12): p. 610-612.
31. Deck, L.L., *Fourier-transform phase-shifting interferometry.* Applied Optics, 2003. **42**(13): p. 2354-2365.
32. Liu, Y., et al., *Deconvolution methods for image deblurring in optical coherence tomography.* Journal of the Optical Society of America A, 2009. **26**(1): p. 72-77.
33. Bousi, E. and C. Pitris, *Axial resolution improvement by modulated deconvolution in Fourier domain optical coherence tomography.* Journal of Biomedical Optics, 2012. **17**(7): p. 071307-071307.
34. Mousavi, M., et al., *Iterative re-weighted approach to high-resolution optical coherence tomography with narrow-band sources.* Optics Express, 2016. **24**(2): p. 1781-1793.
35. Coupland, J.M. and J. Lobera, *Holography, tomography and 3D microscopy as linear filtering operations.* Measurement Science and Technology, 2008. **19**(7): p. 074012.
36. Ruiz, P.D., J.M. Huntley, and J.M. Coupland, *Depth-resolved Imaging and Displacement Measurement Techniques Viewed as Linear Filtering Operations.* Experimental Mechanics, 2011. **51**(4): p. 453-465.
37. Waller, L., et al., *Phase and amplitude imaging from noisy images by Kalman filtering.* Optics Express, 2011. **19**(3): p. 2805-2815.
38. Jones, R.M., *Mechanics of Compoiste Materials*. Second ed. 1998, London: Taylor & Francis Ltd. p 93.
39. Barbero, E.J., *Introduction to Composite Materials Design*. 1999: Taylor & Francis.
40. Chamis, C.C. and G.P. Sendeckyj, *Critique on Theories Predicting Thermoelastic Properties of Fibrous Composites.* Journal of Composite Materials, 1968. **2**(3): p. 332-358.
41. Chamis, C.C., *Polymer Composite Mechanics Review — 1965 to 2006.* Journal of Reinforced Plastics and Composites, 2007. **26**(10): p. 987-1019.
42. Cantwell, W.J. and J. Morton, *The significance of damage and defects and their detection in composite materials: A review.* The Journal of Strain Analysis for Engineering Design, 1992. **27**(1): p. 29-42.
43. I.A Ashcroft, S. Erpolat, and J. Tyrer, *Damage assessment in bonded composite joints.* Key Engineering Materials, 2003. **245-246**: p. 501-508.
44. Erpolat, S., et al., *Fatigue crack growth acceleration due to intermittent overstressing in adhesively bonded CFRP joints.* Composites Part A: Applied Science and Manufacturing, 2004. **35**(10): p. 1175-1183.
45. Erpolat, S., et al., *A study of adhesively bonded joints subjected to constant and variable amplitude fatigue.* International Journal of Fatigue, 2004. **26**(11): p. 1189-1196.
46. Loh, W.K., et al., *Modelling interfacial degradation using interfacial rupture elements.* The Journal of Adhesion, 2003. **79**(12): p. 1135-1160.
47. Ashcroft, I.A., *A simple model to predict crack growth in bonded joints and laminates under variable-amplitude fatigue.* The Journal of Strain Analysis for Engineering Design, 2004. **39**(6): p. 707-716.
48. Hariharan, P., *Basics of Interferometry*. 1992, Academic Press Limited: London. p. 91-92.

49. Jones, R. and C. Wykes, *Electronic Speckle Pattern Correlation Interferometry*, in *Holographic and Speckle Interferometry*. 1989, Cambridge U. Press: Cambridge. p. 165-196.
50. Moore, A.J., J.R. Tyrer, and F.M. Santoyo, *Phase extraction from electronic speckle pattern interferometry addition fringes.* Applied Optics, 1994. **33**(31): p. 7312-7320.
51. Alcalá Ochoa, N., et al., *Multiplicative electronic speckle-pattern interferometry fringes.* Applied Optics, 2000. **39**(28): p. 5138-5141.
52. Leendertz, J.A., *Interferometric displacement measurement on scattering surfaces utilizing speckle effect.* Journal of Physics E: Scientific Instruments, 1970. **3**(3): p. 214.
53. Dorrío, B.V. and J.L. Fernández, *Phase-evaluation methods in whole-field optical measurement techniques.* Measurement Science and Technology, 1999. **10**(3): p. R33.
54. Huntley, J.M., *Automated analysis of speckle interferograms*, in *Digital speckle pattern interferometry and related techniques*, P.K. Rastogi, Editor. 2001, John Wiley & Sons Ltd.: Baffins Lane, Chichester, West Sussex, PO19 1UD, England. p. 59-139.
55. Bone, D.J., *Fourier fringe analysis: the two-dimensional phase unwrapping problem.* Applied Optics, 1991. **30**(25): p. 3627-3632.
56. Schmitt, J.M., *Optical coherence tomography (OCT): a review.* Selected Topics in Quantum Electronics, IEEE Journal of, 1999. **5**(4): p. 1205-1215.
57. Fujimoto J, G., *Optical Coherence Tomography : Principles and Applications.* The Review of laser engineering, 2003. **31**(10): p. 635-642.
58. Fujimoto, J.G., *Optical coherence tomography for ultrahigh resolution in vivo imaging.* Nature Biotechnology, 2003. **21**(11): p. 1361-1367.
59. Drexler W, F.J., ed. *Optical Coherence Tomography - Technology and Applications*. 2008, Springer: Berlin Heidelberg.
60. Mariampillai, A., et al., *Speckle variance detection of microvasculature using swept-source optical coherence tomography.* Optics Letters, 2008. **33**(13): p. 1530-1532.
61. Spaide, R.F., H. Koizumi, and M.C. Pozonni, *Enhanced Depth Imaging Spectral-Domain Optical Coherence Tomography.* American Journal of Ophthalmology, 2008. **146**(4): p. 496-500.
62. Prati, F., et al., *Expert review document on methodology, terminology, and clinical applications of optical coherence tomography: physical principles, methodology of image acquisition, and clinical application for assessment of coronary arteries and atherosclerosis.* European Heart Journal, 2010. **31**(4): p. 401-415.
63. Dunkers, J.P., et al., *The application of optical coherence tomography to problems in polymer matrix composites.* Optics and Lasers in Engineering, 2001. **35**(3): p. 135-147.
64. Stifter, D., et al., *Investigation of polymer and polymer/fibre composite materials with optical coherence tomography.* Measurement Science and Technology, 2008. **19**(7): p. 074011.
65. Duncan, M., M. Bashkansky, and J. Reintjes, *Subsurface defect detection in materialsusing optical coherence tomography.* Optics Express, 1998. **2**(13): p. 540-545.
66. Fercher, A.F., et al., *Optical coherence tomography - principles and applications.* Reports on Progress in Physics, 2003. **66**(2): p. 239.

67. Dunsby, C. and P.M.W. French, *Techniques for depth-resolved imaging through turbid media including coherence-gated imaging.* Journal of Physics D: Applied Physics, 2003. **36**(14): p. R207.
68. Bien, F., et al., *Absolute distance measurements by variable wavelengthinterferometry.* Applied Optics, 1981. **20**(3): p. 400-403.
69. Stone, J.A., A. Stejskal, and L. Howard, *Absolute interferometry with a 670-nm external cavity diode laser.* Applied Optics, 1999. **38**(28): p. 5981-5994.
70. Cabral, A. and J. Rebordão, *Accuracy of frequency-sweeping interferometry for absolute distance metrology.* Optical Engineering, 2007. **46**(7): p. 073602-073602-10.
71. Dändliker, R., Y. Salvadé, and E. Zimmermann, *Distance measurement by multiple-wavelength interferometry.* Journal of Optics, 1998. **29**(3): p. 105.
72. Gibson, S.M., et al., *Coordinate measurement in 2-D and 3-D geometries using frequency scanning interferometry.* Optics and Lasers in Engineering, 2005. **43**(7): p. 815-831.
73. Yang, H.-J., et al., *High-precision absolute distance and vibration measurement with frequency scanned interferometry.* Applied Optics, 2005. **44**(19): p. 3937-3944.
74. Swinkels, B.L., N. Bhattacharya, and J.J.M. Braat, *Correcting movement errors in frequency-sweeping interferometry.* Optics Letters, 2005. **30**(17): p. 2242-2244.
75. Yang, H.-J., S. Nyberg, and K. Riles, *High-precision absolute distance measurement using dual-laser frequency scanned interferometry under realistic conditions.* Nuclear Instruments and Methods in Physics Research Section A: Accelerators, Spectrometers, Detectors and Associated Equipment, 2007. **575**(3): p. 395-401.
76. Yamamoto, A. and I. Yamaguchi, *Profilometry of Sloped Plane Surfaces by Wavelength Scanning Interferometry.* Optical Review, 2002. **9**(3): p. 112-121.
77. Hibino, K., et al., *Simultaneous measurement of surface shape and variation in optical thickness of a transparent parallel plate in wavelength-scanning Fizeau interferometer.* Applied Optics, 2004. **43**(6): p. 1241-1249.
78. Costantino, S., O. Martinez, and J. Torga, *Wide band interferometry for thickness measurement.* Optics Express, 2003. **11**(8): p. 952-957.
79. Fukano, T. and I. Yamaguchi, *Separate measurement of geometrical thickness and refractive index by an interference confocal microscope*, in *Proc. SPIE 3897*. 1999: Advanced Photonic Sensors and Applications, 342,doi:10.1117/12.369325; http://dx.doi.org/10.1117/12.369325 p. 342-354.
80. Suratkar, A., Y.-S. Ghim, and A. Davies, *Uncertainty analysis on the absolute thickness of a cavity using a commercial wavelength scanning interferometer*, in *Proc. SPIE 7063*. 2008: Interferometry XIV: Techniques and Analysis, 70630R,doi:10.1117/12.793772; http://dx.doi.org/10.1117/12.793772. p. 70630R-70630R-12.
81. Ruiz, P. and J. Huntley, *Depth-resolved displacement field measurement*, in *Advances in speckle metrology and related techniques*, G.H. Kaufmann, Editor. 2011, Wiley-VCH: Weinheim. p. 37-104.
82. de Groot, P., *Derivation of algorithms for phase-shifting interferometry using the concept of a data-sampling window.* Applied Optics, 1995. **34**(22): p. 4723-4730.

83. Surrel, Y., *Design of phase-detection algorithms insensitive to bias modulation.* Applied Optics, 1997. **36**(4): p. 805-807.
84. Surrel, Y., *Design of algorithms for phase measurements by the use of phase stepping.* Applied Optics, 1996. **35**(1): p. 51-60.
85. Liu, G.Y., et al., *High power wavelength linearly swept mode locked fiber laser for OCT imaging.* Optics Express, 2008. **16**(18): p. 14095-14105.
86. Marks, D.L., et al., *Inverse scattering for frequency-scanned full-field optical coherence tomography.* Journal of the Optical Society of America A, 2007. **24**(4): p. 1034-1041.
87. Marks, D.L., et al., *Partially coherent illumination in full-field interferometric synthetic aperture microscopy.* Journal of the Optical Society of America A, 2009. **26**(2): p. 376-386.
88. Karamata, B., et al., *Multiple scattering in optical coherence tomography. II. Experimental and theoretical investigation of cross talk in wide-field optical coherence tomography.* Journal of the Optical Society of America A, 2005. **22**(7): p. 1380-1388.
89. Steiner, P., C. Meier, and V.M. Koch, *Influence and compensation of autocorrelation terms in depth-resolved spectroscopic Fourier-domain optical coherence tomography.* Applied Optics, 2010. **49**(36): p. 6917-6923.
90. Wojtkowski, M., et al., *In vivo human retinal imaging by Fourier domain optical coherence tomography.* Journal of Biomedical Optics, 2002. **7**(3): p. 457-463.
91. Huntley, J.M., T. Widjanarko, and P.D. Ruiz, *Hyperspectral interferometry for single-shot absolute measurement of two-dimensional optical path distributions.* Measurement Science and Technology, 2010. **21**(7): p. 075304.
92. Yanzhou, Z., R.D. Wildman, and J.M. Huntley, *Improved measurement of grain–wall contact forces in granular beds using wavelength scanning interferometry.* Journal of Optics A: Pure and Applied Optics, 2005. **7**(6): p. S453.
93. Stumpf, M.C., et al., *Compact Er:Yb:glass-laser-based supercontinuum source for high-resolution optical coherence tomography.* Optics Express, 2008. **16**(14): p. 10572-10579.
94. Alex, A., et al., *Multispectral in vivo three-dimensional optical coherence tomography of human skin.* Journal of Biomedical Optics, 2010. **15**(2): p. 026025-026025-15.
95. Superlum. *Broadband Light Sources. Superlum BroadLighters.* 2015 [cited 2002 15-11-2015]; Available from: https://www.superlumdiodes.com/broadband-light-sources.htm.
96. Drexler, W., et al., *In vivo ultrahigh-resolution optical coherence tomography.* Optics Letters, 1999. **24**(17): p. 1221-1223.
97. Bouma, B., et al., *High-resolution optical coherence tomographic imaging using a mode-locked Ti:Al_2O_3 laser source.* Optics Letters, 1995. **20**(13): p. 1486-1488.
98. Tae Joong, E., et al., *Wavelength-Tunable Broadband Frequency-Domain OCT Source Based on Spatially Filtered Sub-10-fs Pulsed Laser.* Photonics Technology Letters, IEEE, 2008. **20**(12): p. 994-996.
99. Bouma, B.E., et al., *Self-phase-modulated Kerr-lens mode-locked Cr:forsterite laser source for optical coherence tomography.* Optics Letters, 1996. **21**(22): p. 1839-1841.

100. Wagenblast, P., et al., *Ultrahigh-resolution optical coherence tomography with a diode-pumped broadband Cr^{3+}:LiCAF laser.* Optics Express, 2004. **12**(14): p. 3257-3263.
101. Krupke, W.F., S.A. Payne, and L.L. Chase, *Cr:LiCAF and Cr:LiSAF: New Materials for Tunable Solid-State Lasers* https://lasers.llnl.gov/multimedia/publications/pdfs/etr/1991_09_10.pdf, 1991.
102. Schmitt, J.M., *Array detection for speckle reduction in optical coherence microscopy.* Physics in Medicine and Biology, 1997. **42**(7): p. 1427.
103. Corporation, N.E. *Photonics*. 2015 [cited 2002 15-11-2015]; Available from: http://www.ntt-electronics.com/en/solutions/index.html.
104. Bashkansky, M., et al., *Characteristics of a Yb-doped superfluorescent fiber source for use in optical coherence tomography.* Optics Express, 1998. **3**(8): p. 305-310.
105. Bouma, B.E., et al., *Optical Coherence Tomographic Imaging of Human Tissue at 1.55 μm and 1.81 μm Using Er- and Tm-Doped Fiber Sources.* Journal of Biomedical Optics, 1998. **3**(1): p. 76-79.
106. Hartl, I., et al., *Ultrahigh-resolution optical coherence tomography using continuum generation in an air–silica microstructure optical fiber.* Optics Letters, 2001. **26**(9): p. 608-610.
107. Povazay, B., et al., *Submicrometer axial resolution optical coherence tomography.* Optics Letters, 2002. **27**(20): p. 1800-1802.
108. Aguirre, A., et al., *Continuum generation in a novel photonic crystal fiber for ultrahigh resolution optical coherence tomography at 800 nm and 1300 nm.* Optics Express, 2006. **14**(3): p. 1145-1160.
109. Fercher, A.F., et al., *A thermal light source technique for optical coherence tomography.* Optics Communications, 2000. **185**(1–3): p. 57-64.
110. Vabre, L., A. Dubois, and A.C. Boccara, *Thermal-light full-field optical coherence tomography.* Optics Letters, 2002. **27**(7): p. 530-532.
111. Carrasco, S., et al., *Broadband light generation by noncollinear parametric downconversion.* Optics Letters, 2006. **31**(2): p. 253-255.
112. Barnes, N.P. and B.M. Walsh, *Amplified spontaneous emission-application to Nd:YAG lasers.* Quantum Electronics, IEEE Journal of, 1999. **35**(1): p. 101-109.
113. Blazek, M., et al., *Unifying intensity noise and second-order coherence properties of amplified spontaneous emission sources.* Optics Letters, 2011. **36**(17): p. 3455-3457.
114. Paschotta, R., *'amplified spontaneous emission'*, in *Encyclopedia of Laser Physics and Technology,accessed on 2015-11-16*. RP photonics encyclopedia: https://www.rp-photonics.com/amplified_spontaneous_emission.html.
115. Ko, T., et al., *Ultrahigh resolution optical coherence tomography imaging with a broadband superluminescent diode light source.* Optics Express, 2004. **12**(10): p. 2112-2119.
116. Gong, J., et al., *Optimal spectral reshaping for resolution improvement in optical coherence tomography.* Optics Express, 2006. **14**(13): p. 5909-5915.
117. Fingler, J., et al., *Phase-contrast OCT imaging of transverse flows in the mouse retina and choroid.* Investigative ophthalmology & visual science, 2008. **49**(11): p. 5055-5059.

118. Wang, R.K., Z. Ma, and S.J. Kirkpatrick, *Tissue Doppler optical coherence elastography for real time strain rate and strain mapping of soft tissue.* Applied Physics Letters, 2006. **89**(14): p. 144103.
119. Ophir, J., et al., *Elastography: Ultrasonic estimation and imaging of the elastic properties of tissues.* Proceedings of the Institution of Mechanical Engineers, Part H: Journal of Engineering in Medicine, 1999. **213**(3): p. 203-233.
120. Wilson, L.S., D.E. Robinson, and M.J. Dadd, *Elastography - the movement begins.* Physics in Medicine and Biology, 2000. **45**(6): p. 1409.
121. Jacques, S.L. and S.J. Kirkpatrick, *Acoustically modulated speckle imaging of biological tissues.* Optics Letters, 1998. **23**(11): p. 879-881.
122. Schmitt, J., *OCT elastography: imaging microscopic deformation and strain of tissue.* Optics Express, 1998. **3**(6): p. 199-211.
123. Liang, X., V. Crecea, and S.A. Boppart, *Dynamic optical coherence elastography: A review.* Journal of Innovative Optical Health Sciences, 2010. **03**(04): p. 221-233.
124. Sun, C., B. Standish, and V.X.D. Yang, *Optical coherence elastography: current status and future applications.* Journal of Biomedical Optics, 2011. **16**(4): p. 043001-043001-12.
125. Kennedy, B.F., K.M. Kennedy, and D.D. Sampson, *A Review of Optical Coherence Elastography: Fundamentals, Techniques and Prospects.* Selected Topics in Quantum Electronics, IEEE Journal of, 2014. **20**(2): p. 272-288.
126. Kirkpatrick, S.J., R.K. Wang, and D.D. Duncan, *OCT-based elastography for large and small deformations.* Optics Express, 2006. **14**(24): p. 11585-11597.
127. Song, S., Z. Huang, and R.K. Wang, *Tracking mechanical wave propagation within tissue using phase-sensitive optical coherence tomography: motion artifact and its compensation.* Journal of Biomedical Optics, 2013. **18**(12): p. 121505-121505.
128. Bercoff, J., M. Tanter, and M. Fink, *Supersonic shear imaging: a new technique for soft tissue elasticity mapping.* Ultrasonics, Ferroelectrics, and Frequency Control, IEEE Transactions on, 2004. **51**(4): p. 396-409.
129. Kennedy, K.M., et al., *Needle optical coherence elastography for tissue boundary detection.* Optics Letters, 2012. **37**(12): p. 2310-2312.
130. Huang, D., et al., *Optical coherence tomography.* Science, 1991. **254**(5035): p. 1178-1181.
131. Wang, Q., et al., *Thermoelastic optical Doppler tomography of biological tissues*, in *Proc. SPIE 6847*. 2008: Coherence Domain Optical Methods and Optical Coherence Tomography in Biomedicine XII, 68471B, doi:10.1117/12.766962; http://dx.doi.org/10.1117/12.766962 p. 68471B-68471B-6.
132. Stifter, D., et al., *Polarisation-sensitive optical coherence tomography for material characterisation and strain-field mapping.* Applied Physics A, 2003. **76**(6): p. 947-951.
133. Heise, B., et al., *Spatially Resolved Stress Measurements in Materials With Polarisation-Sensitive Optical Coherence Tomography: Image Acquisition and Processing Aspects.* Strain, 2010. **46**(1): p. 61-68.
134. Røyset, A., T. Støren, and T. Lindmo. *Speckle noise in polarization sensitive optical coherence tomography*. in *Proc. SPIE 6079, Coherence Domain Optical Methods and Optical Coherence Tomography in Biomedicine X*. 2006. 60792F, doi:10.1117/12.647743; http://dx.doi.org/10.1117/12.647743

135. Hitzenberger, C., et al., *Measurement and imaging of birefringence and optic axis orientation by phase resolved polarization sensitive optical coherence tomography.* Optics Express, 2001. **9**(13): p. 780-790.
136. MacDonald, R.I., *Frequency domain optical reflectometer.* Applied Optics, 1981. **20**(10): p. 1840-1844.
137. Eickhoff, W. and R. Ulrich, *Optical frequency domain reflectometry in single‐mode fiber.* Applied Physics Letters, 1981. **39**(9): p. 693-695.
138. Fercher, A.F., et al., *Measurement of intraocular distances by backscattering spectral interferometry.* Optics Communications, 1995. **117**(1–2): p. 43-48.
139. Lexer, F., et al., *Wavelength-tuning interferometry of intraocular distances.* Applied Optics, 1997. **36**(25): p. 6548-6553.
140. Coe, P.A., D.F. Howell, and R.B. Nickerson, *Frequency scanning interferometry in ATLAS: remote, multiple, simultaneous and precise distance measurements in a hostile environment.* Measurement Science and Technology, 2004. **15**(11): p. 2175.
141. Takeda, M. and H. Yamamoto, *Fourier-transform speckle profilometry: three-dimensional shape measurements of diffuse objects with large height steps and/or spatially isolated surfaces.* Applied Optics, 1994. **33**(34): p. 7829-7837.
142. Kuwamura, S. and I. Yamaguchi, *Wavelength scanning profilometry for real-time surface shape measurement.* Applied Optics, 1997. **36**(19): p. 4473-4482.
143. de Groot, P., *Measurement of transparent plates with wavelength-tuned phase-shifting interferometry.* Applied Optics, 2000. **39**(16): p. 2658-2663.
144. Tiziani, H.J., et al., *Surface topometry by multiwavelength technique and temporal Fourier transformation*, in *Proc. SPIE 3407*. 1998: International Conference on Applied Optical Metrology;doi: 10.1117/12.323299; http://dx.doi.org/10.1117/12.323299 p. 96-103.
145. Yamaguchi, I., A. Yamamoto, and S. Kuwamura, *Speckle decorrelation in surface profilometry by wavelength scanning interferometry.* Applied Optics, 1998. **37**(28): p. 6721-6728.
146. Yamaguchi, I., A. Yamamoto, and M. Yano, *Surface profilometry by wavelength scanning interferometry*, in *Proc. SPIE 3407*. 1998: International Conference on Applied Optical Metrology;doi:10.1117/12.323305; http://dx.doi.org/10.1117/12.323305 p. 141-146.
147. Kato, J.-i. and I. Yamaguchi, *Height gauging by wavelength-scanning interferometry with phase detection*, in *Proc. SPIE 3740*. 1999: Optical Engineering for Sensing and Nanotechnology (ICOSN '99); doi:10.1117/12.347753; http://dx.doi.org/10.1117/12.347753 p. 594-597.
148. Geng, J., et al., *Widely tunable, narrow-linewidth, subnanosecond pulse generation in an electronically tuned Ti:sapphire laser.* Optics Letters, 1999. **24**(10): p. 676-678.
149. Paulsson, L., et al., *Temporal phase unwrapping applied to wavelength-scanning interferometry.* Applied Optics, 2000. **39**(19): p. 3285-3288.
150. Deck, L.L., *Absolute distance measurements using FTPSI with a widely tunable IR laser*, in *Proc. SPIE 4778*. 2002: Interferometry XI: Applications,p218-226;doi:10.1117/12.473544; http://dx.doi.org/10.1117/12.473544 p. 218-226.

151. Hibino, K., B.F. Oreb, and P.S. Fairman, *Wavelength-scanning interferometry of a transparent parallel plate with refractive-index dispersion.* Applied Optics, 2003. **42**(19): p. 3888-3895.
152. Hibino, K., et al., *Tunable phase-extraction formulae for simultaneous shape measurement of multiple surfaces with wavelength-shifting interferometry.* Optics Express, 2004. **12**(23): p. 5579-5594.
153. Hibino, K., et al., *Multiple-surface testing by a wavelength-scanning interferometer for refractive index inhomogeneity measurement.* Optics and Spectroscopy, 2006. **101**(1): p. 18-22.
154. Aleksoff, C.C., *Multi-wavelength digital holographic metrology*, in *Proc. SPIE 6311*. 2006: Optical Information Systems IV, doi:10.1117/12.686727; http://dx.doi.org/10.1117/12.686727. p. 63111D-63111D-7.
155. Moore, E.D. and R.R. McLeod, *Correction of sampling errors due to laser tuning rate fluctuations in swept-wavelength interferometry.* Optics Express, 2008. **16**(17): p. 13139-13149.
156. Ghim, Y.-S., A. Suratkar, and A. Davies, *Reflectometry-based wavelength scanning interferometry for thickness measurements of very thin wafers.* Optics Express, 2010. **18**(7): p. 6522-6529.
157. Yu, H., C. Aleksoff, and J. Ni, *A multiple height-transfer interferometric technique.* Optics Express, 2011. **19**(17): p. 16365-16374.
158. Hibino, K., et al., *Simultaneous measurement of surface shape and absolute optical thickness of a glass plate by wavelength tuning phase-shifting interferometry.* Optical Review, 2012. **19**(4): p. 247-253.
159. Yu, H., C. Aleksoff, and J. Ni, *Thickness measurement of transparent plates by wavelength stepping and a phase unwrapping algorithm.* Measurement Science and Technology, 2013. **24**(7): p. 075201.
160. Hyo Jin, K., et al., *Three-dimensional surface phase imaging based on integrated thermo-optic swept laser.* Measurement Science and Technology, 2014. **25**(3): p. 035201.
161. Huntley, J.M., *Higher - dimensional phase imaging.* AIP Conference Proceedings, 2010. **1236**(1): p. 29-34.
162. Samuel, D., *Design and Manufacture of a Miniature Tensile Testing Machine*. 2010 - 2011, Loughborough University: Loughborough, England, UK. p. 1-68.
163. Abdin, A.H., *Design and manufacture of miniature tensile testing machine*. 2009 - 2010, Loughborough University: Loughborough,England,UK. p. 1-64.
164. Moulart, R., *Banc de Traction Miniature*. 2003 - 2006 ENSAM: CHÂLONS-EN-CHAMPAGNE. p. 17-48.
165. Moulart, R., *Développement et mise en oeuvre d'une méthode de mesure de champs de déformation à l'échelle micrométrique*, in *Laboratoire de Mécanique et Procédés de Fabrication*. 2007, ENSAM: ENSAM, CER de Châlons-en-Champagne. p. 1-162.
166. R. Moulart, et al., *Development of a full-field displacement measurement technique at the microscale and application to the study of strain fields in a tensile steel specimen.* Applied Mechanics and Materials, 2007. **7-8**: p. 181-186.
167. Raphaël Moulart, René Rotinat*, and F. Pierron. *Full-field measurement at the micrometric scale: application of the grid method to steel samples under tensile load*. in *Proceedings of the XIth International Congress and*

Exposition. 2008. Orlando, Florida USA: ©2008 Society for Experimental Mechanics Inc.
168. Hodginson, J.M., *Tension*, in *Mechanical Testing of Advanced Fibre Composites*, E.W. Godwin, Editor. 2000, Woodhead Publishing Ltd. p. p43-p74.
169. Gedney, R. *Tensile Testing Basics, Tips and Trends*. Quality test & Inspection, Admet, http://www.qualitymag.com/articles/84035-quality-test-inspection-tensile-testing-basics-tips-and-trends, 2005.
170. Hojo, M., Y. Sawada, and H. Miyairi, *Influence of clamping method on tensile properties of unidirectional CFRP in 0° and 90° directions — round robin activity for international standardization in Japan.* Composites, 1994. **25**(8): p. 786-796.
171. Gibson, R.F., *Analysis of Viscoelastic and Dynamic Behavior*, in *Principles of Composite Material Mechanics*. 2007, CRC Press, Taylor & Francis Group. p. 377-380.
172. Huntley, J.M. and H. Saldner, *Temporal phase-unwrapping algorithm for automated interferogram analysis.* Applied Optics, 1993. **32**(17): p. 3047-3052.
173. Judge, T.R. and P.J. Bryanston-Cross, *A review of phase unwrapping techniques in fringe analysis.* Optics and Lasers in Engineering, 1994. **21**(4): p. 199-239.
174. Huntley, J.M., *Automated fringe pattern analysis in experimental mechanics: A review.* Journal of Strain Analysis for Engineering Design, 1998. **33**(2): p. 105-125.
175. Davila A*, et al. *Whole-field wavelength scanning interferometry using a tunable Ti:Sapphire laser* in *Proceedings of Photon10*. (23-26 August) 2010. in Fringe Analysis Special Interest Group (FASIG),University of Southoumpton,UK: Private communication.
176. Stetson, K.A., *Fringe interpretation for hologram interferometry of rigid-body motions and homogeneous deformations.* Journal of the Optical Society of America, 1974. **64**(1): p. 1-10.
177. Stetson, K.A., *Homogeneous deformations: determination by fringe vectors in hologram interferometry.* Applied Optics, 1975. **14**(9): p. 2256-2259.
178. Pryputniewicz, R. and K.A. Stetson, *Holographic strain analysis: extension of fringe-vector method to include perspective.* Applied Optics, 1976. **15**(3): p. 725-728.
179. Pryputniewicz, R.J., *Determination of the sensitivity vectors directly from holograms**. Journal of the Optical Society of America, 1977. **67**(10): p. 1351-1353.
180. Stetson, K.A., *Use of projection matrices in hologram interferometry.* Journal of the Optical Society of America, 1979. **69**(12): p. 1705-1710.
181. Pryputniewicz, R.J. and K.A. Stetson, *Determination of sensitivity vectors in hologram interferometry from two known rotations of the object.* Applied Optics, 1980. **19**(13): p. 2201-2205.
182. Stetson, K.A., *Use of sensitivity vector variations to determine absolute displacements in double exposure hologram interferometry.* Applied Optics, 1990. **29**(4): p. 502-504.
183. Takatsuji, T., et al., *Simultaneous measurement of three orthogonal components of displacement by electronic speckle-pattern interferometry and the Fourier transform method.* Applied Optics, 1997. **36**(7): p. 1438-1445.

184. Takatsuji, T., et al., *Simultaneous measurements of vector components of displacement by ESPI and FFT techniques*, in *Proc. SPIE 2544*. 1995: Interferometry VII: Techniques and Analysis, 309,doi:10.1117/12.211870; http://dx.doi.org/10.1117/12.211870 p. 309-316.
185. Sun, P., *Three-dimensional displacement measurement by using reversed phase-shifting electronic speckle pattern interferometry.* Optical Engineering, 2006. **45**(9): p. 093602-093602-5.
186. Saucedo-A, T., et al., *Digital holographic interferometer using simultaneously three lasers and a single monochrome sensor for 3D displacement measurements.* Optics Express, 2010. **18**(19): p. 19867-19875.
187. Bhaduri, B., et al., *Two wavelength simultaneous DSPI and DSP for 3D displacement field measurements.* Optics Communications, 2011. **284**(10–11): p. 2437-2440.
188. Arai, Y., *Development of in-plane and out-of-plane deformations simultaneous measurement method for the analysis of buckling.* Optical Engineering, 2015. **54**(2): p. 024102-024102.
189. Arai, Y., *Development of three-dimensional speckle deformation measurement method with same sensitivities in three directions*, in *Proc. SPIE 9576*. 2015: Applied Advanced Optical Metrology Solutions, 957606,doi:10.1117/12.2187353; http://dx.doi.org/10.1117/12.2187353 p. 957606-957608.
190. Muñoz Moreno, G. and N. Alcalá Ochoa, *Phase deformation measurements using a swept-source OCT system.* Optics and Lasers in Engineering, 2014. **52**: p. 53-60.
191. Chakraborty, S., *Tomographic measurement of all orthogonal components of three-dimensional displacement fields within scattering materials using wavelength scanning interferometry*, in *Wolfson school of mechanical and manufacturing engineering*. 2013, Loughborough University: 2013 LOUGH DSP: https://dspace.lboro.ac.uk/2134/13493.
192. Brophy, C.P., *Effect of intensity error correlation on the computed phase of phase-shifting interferometry.* Journal of the Optical Society of America A, 1990. **7**(4): p. 537-541.
193. Skydan, O.A., et al., *Quantization error of CCD cameras and their influence on phase calculation in fringe pattern analysis.* Applied Optics, 2003. **42**(26): p. 5302-5307.
194. Shiyuan, Y. and T. Hiroaki, *Quantization Error Reduction in the Measurement of Fourier Intensity for Phase Retrieval.* Japanese Journal of Applied Physics, 2004. **43**(8S): p. 5747.
195. Maallo, A.M.S., P.F. Almoro, and S.G. Hanson, *Quantization analysis of speckle intensity measurements for phase retrieval.* Applied Optics, 2010. **49**(27): p. 5087-5094.
196. Hu, E., Y. Hu, and H. Fang, *A novel phase-recovering algorithm for the intensity quantization error in the digital grating phase-shifting profilometry.* Optik - International Journal for Light and Electron Optics, 2011. **122**(24): p. 2227-2229.
197. Song, L. and D.S. Elson, *Effect of signal intensity and camera quantization on laser speckle contrast analysis.* Biomedical Optics Express, 2013. **4**(1): p. 89-104.

198. Moreno, G.M. and N.A. Ochoa, *Phase calculation with a swept source in optical coherence tomography: Jitter influence.* Optics and Lasers in Engineering, 2011. **49**(6): p. 663-667.
199. Siltanen, M., M. Vainio, and L. Halonen, *Pump-tunable continuous-wave singly resonant optical parametric oscillator from 2.5 to 4.4 μm.* Optics Express, 2010. **18**(13): p. 14087-14092.
200. M-SquaredLasers, *SolsTiS manual V9.2*. Sept. 2010: http://www.m2lasers.com/media/74139/solstis_datasheet_1014.pdf.
201. M-SquaredLasers, *SOLSTIS*. 2016: http://www.m2lasers.com/products/laser-systems/ti-sapphire-laser.aspx.
202. NorPix. *Multiple camera software for digital video camera*. 2016 [cited 2016 09-01-2016]; Available from: https://www.norpix.com/products/streampix/streampix.php.
203. COHERENT. *MBR-EL Single Frequency Ti:Sapphire Laser Data Sheet.* 2011 [cited 2011 22-09-2011]; Available from: http://www.coherent.com/downloads/MBR110EL_DSrevA_0510n.pdf.
204. SantecCorporation. *HSL-2100-LC /1100-LC*. Available from: http://www.santec.com/jp/wp-content/uploads/HSL2100_1100LC-C-E-v10print.pdf.
205. HighFinesse. *WS7 Angstrom*. Available from: http://www.highfinesse.com/Brochure/LowRes/07_WS7_low.pdf.
206. Françon, M., *Optical interferometry*. 1966, New York,London: Academic Press.
207. Hariharan, P., *Basics of interferometry*. 2006, London: Academic Press.
208. Itoh, K., *Analysis of the phase unwrapping algorithm.* Applied optics, 1982. **21**(14): p. 2470.
209. Takeda, M., H. Ina, and S. Kobayashi, *Fourier-transform method of fringe-pattern analysis for computer-based topography and interferometry.* Journal of the Optical Society of America, 1982. **72**(1): p. 156-160.
210. Malitson, I.H., *Interspecimen Comparison of the Refractive Index of Fused Silica.* Journal of the Optical Society of America, 1965. **55**(10): p. 1205-1208.
211. Huntley, J.M. and H.O. Saldner, *Error-reduction methods for shape measurement by temporal phase unwrapping.* Journal of the Optical Society of America A, 1997. **14**(12): p. 3188-3196.
212. Huntley, J.M., *Speckle photography fringe analysis: effect of imaging geometry on displacement errors.* Applied Optics, 1991. **30**(32): p. 4602-4604.
213. Kaufmann, G.H., et al., *An electro-optical read-out system for analysis of speckle photographs.* Journal of Physics E: Scientific Instruments, 1980. **13**(5): p. 579.
214. Zhang, K. and J.U. Kang, *Graphics processing unit accelerated non-uniform fast Fourier transform for ultrahigh-speed, real-time Fourier-domain OCT.* Optics Express, 2010. **18**(22): p. 23472-23487.
215. Peter, H.T. and K.W. Ruikang, *Digital phase stabilization to improve detection sensitivity for optical coherence tomography.* Measurement Science and Technology, 2007. **18**(11): p. 3365.
216. Abdulhalim, I. and R. Dadon, *Multiple interference and spatial frequencies' effect on the application of frequency-domain optical coherence tomography*

to thin films' metrology. Measurement Science and Technology, 2009. **20**(1): p. 015108.
217. Nikola, K., et al., *Common path Michelson interferometer based on multiple reflections within the sample arm: sensor applications and imaging artefacts.* Measurement Science and Technology, 2011. **22**(2): p. 027002.
218. Hanayama, R., et al., *Phase Measurement Algorithm in Wavelength Scanned Fizeau Interferometer.* Optical Review, 2004. **11**(5): p. 337-343.
219. Lomb, N.R., *Least-squares frequency analysis of unequally spaced data.* Astrophysics and Space Science, 1976. **39**(2): p. 447-462.
220. Gu, Y.H. and M.H.J. Bollen, *Time-frequency and time-scale domain analysis of voltage disturbances.* Power Delivery, IEEE Transactions on, 2000. **15**(4): p. 1279-1284.
221. Radil, T., et al., *PQ Monitoring System for Real-Time Detection and Classification of Disturbances in a Single-Phase Power System.* Instrumentation and Measurement, IEEE Transactions on, 2008. **57**(8): p. 1725-1733.
222. Bollen, M.H.J., et al., *Bridging the gap between signal and power.* Signal Processing Magazine, IEEE, 2009. **26**(4): p. 12-31.
223. Granados-Lieberman, D., et al., *Techniques and methodologies for power quality analysis and disturbances classification in power systems: a review.* Generation, Transmission & Distribution, IET, 2011. **5**(4): p. 519-529.
224. Pineda-Sanchez, M., et al., *Diagnosis of Induction Motor Faults in the Fractional Fourier Domain.* Instrumentation and Measurement, IEEE Transactions on, 2010. **59**(8): p. 2065-2075.
225. Chatterjee, A., et al., *A Postural Information-Based Biometric Authentication System Employing S-Transform, Radial Basis Function Network, and Extended Kalman Filtering.* Instrumentation and Measurement, IEEE Transactions on, 2010. **59**(12): p. 3131-3138.
226. Berger, E., et al., *Approach for the evaluation of speckle deformation measurements by application of the wavelet transformation.* Applied Optics, 1997. **36**(29): p. 7455-7460.
227. Berger, E., et al., *Reconstruction of surfaces from phase-shifting speckle interferometry: Bayesian approach.* Applied Optics, 1999. **38**(23): p. 4997-5003.
228. Cherbuliez, M., P.M. Jacquot, and X. Colonna de Lega. *Wavelet processing of interferometric signals and fringe patterns*. 1999.
229. Kruger, S., et al., *Fault detection and feature analysis in interferometric fringe patterns by the application of wavelet filters in convolution processors.* Journal of Electronic Imaging, 2001. **10**(1): p. 228-233.
230. Fercher, A., et al., *Numerical dispersion compensation for Partial Coherence Interferometry and Optical Coherence Tomography.* Optics Express, 2001. **9**(12): p. 610-615.
231. Fercher, A.F., et al., *Dispersion compensation for optical coherence tomography depth-scan signals by a numerical technique.* Optics Communications, 2002. **204**(1–6): p. 67-74.
232. Tomlins, P.H. and R.K. Wang *Simultaneous analysis of refractive index and physical thickness by Fourier domain optical coherence tomography*. IEE Proceedings - Optoelectronics, 2006. **153**, 222-228.

233. Chen, Y. and X. Li, *Dispersion management up to the third orderfor real-time optical coherence tomography involving a phase or frequency modulator.* Optics Express, 2004. **12**(24): p. 5967-5978.
234. Lee, K.-S., et al., *Dispersion control with a Fourier-domain optical delay line in a fiber-optic imaging interferometer.* Applied Optics, 2005. **44**(19): p. 4009-4022.
235. Marks, D.L., et al., *Digital algorithm for dispersion correction in optical coherence tomography for homogeneous and stratified media.* Applied Optics, 2003. **42**(2): p. 204-217.
236. Wojtkowski, M., et al., *Ultrahigh-resolution, high-speed, Fourier domain optical coherence tomography and methods for dispersion compensation.* Optics Express, 2004. **12**(11): p. 2404-2422.
237. Tumlinson, A.R., et al., *Inherent homogenous media dispersion compensation in frequency domain optical coherence tomography by accurate k-sampling.* Applied Optics, 2008. **47**(5): p. 687-693.
238. Lippok, N., et al., *Dispersion compensation in Fourier domain optical coherence tomography using the fractional Fourier transform.* Optics Express, 2012. **20**(21): p. 23398-23413.
239. Kaufmann, G.H. and G.E. Galizzi, *Speckle noise reduction in TV holography fringes using wavelet thresholding.* Optical Engineering, 1996. **35**(1): p. 9-14.
240. Stoica, P., L. Jian, and H. Hao, *Spectral Analysis of Nonuniformly Sampled Data: A New Approach Versus the Periodogram.* Signal Processing, IEEE Transactions on, 2009. **57**(3): p. 843-858.
241. Babu, P. and P. Stoica, *Spectral analysis of nonuniformly sampled data – a review.* Digital Signal Processing, 2010. **20**(2): p. 359-378.
242. Zhiguo, Z., C. Shing-Chow, and W. Chong, *A New Regularized Adaptive Windowed Lomb Periodogram for Time-Frequency Analysis of Nonstationary Signals With Impulsive Components.* Instrumentation and Measurement, IEEE Transactions on, 2012. **61**(8): p. 2283-2304.
243. Kemao, Q., *Windowed Fourier transform for fringe pattern analysis.* Applied Optics, 2004. **43**(13): p. 2695-2702.
244. Kemao, Q., *Two-dimensional windowed Fourier transform for fringe pattern analysis: Principles, applications and implementations.* Optics and Lasers in Engineering, 2007. **45**(2): p. 304-317.
245. Kemao, Q., H. Wang, and W. Gao, *Windowed Fourier transform for fringe pattern analysis: theoretical analyses.* Applied Optics, 2008. **47**(29): p. 5408-5419.
246. Widanage, W.D., J.L. Douce, and K.R. Godfrey, *Effects of Overlapping and Windowing on Frequency Response Function Estimates of Systems With Random Inputs.* Instrumentation and Measurement, IEEE Transactions on, 2009. **58**(1): p. 214-220.
247. Antoni, J. and J. Schoukens. *Optimal Settings for Measuring Frequency Response Functions withWeighted Overlapped Segment Averaging*. in *Instrumentation and Measurement Technology Conference, 2006. IMTC 2006. Proceedings of the IEEE*. 2006.
248. Antoni, J. and J. Schoukens, *Optimal Settings for Measuring Frequency Response Functions With Weighted Overlapped Segment Averaging.* Instrumentation and Measurement, IEEE Transactions on, 2009. **58**(9): p. 3276-3287.

249. Mathews, J.H. and K.D. Fink, *Curve fitting*, in *Numerical methods using MATLAB*. 1999, Prentice Hall: Upper Saddle River, N.J. London. p. 252-310.
250. Wray, J.H. and J.T. Neu, *Refractive Index of Several Glasses as a Function of Wavelength and Temperature.* Journal of the Optical Society of America, 1969. **59**(6): p. 774-776.
251. Weber, M.J., D. Milam, and W.L. Smith, *Nonlinear Refractive Index Of Glasses And Crystals.* Optical Engineering, 1978. **17**(5): p. 175463-175463-.
252. Milam, D., *Review and assessment of measured values of the nonlinear refractive-index coefficient of fused silica.* Applied Optics, 1998. **37**(3): p. 546-550.
253. Leviton, D.B. and B.J. Frey, *Temperature-dependent absolute refractive index measurements of synthetic fused silica*, in *Proc. SPIE 6273*. 2006: Optomechanical Technologies for Astronomy, doi:10.1117/12.672853; http://dx.doi.org/10.1117/12.672853 p. 62732K-62732K-11.
254. ULC. *Fused Silica*. 2016 [cited 2016 11-02]; Available from: http://www.unitedlens.com/materials-fused-silica.
255. Corning, *HPFS® Fused Silica Standard Grade*. 2016: United Lens Company (ULC): http://www.unitedlens.com/pdf/hpfs_fused_silica_standard_grade.pdf.
256. Corning, *HPFS®Fused Silica KrF Grade*. 2016: United Lens Company (ULC): http://www.unitedlens.com/pdf/hpfs_fused_silica_krf_grade.pdf.
257. Corning, *HPFS® Fused Silica ArF Grade*. 2016: United Lens Company (ULC): http://www.unitedlens.com/pdf/hpfs_fused_silica_arf_grade.pdf.
258. Heraeus, *SUPRASIL® 1, 2, 3 and SUPRASIL® Standard* 2016: United Lens Company (ULC): http://www.unitedlens.com/pdf/suprasil.pdf.
259. Heraeus, *INFRASIL® 301, 302 and 303*. 2016: United Lens Company (ULC): http://www.unitedlens.com/pdf/infrasil.pdf.
260. Heraeus, *HOMOSIL® 101* 2016: United Lens Company (ULC): http://www.unitedlens.com/pdf/homosil.pdf.
261. Saito, K. and A.J. Ikushima, *Absorption edge in silica glass.* Physical Review B, 2000. **62**(13): p. 8584-8587.
262. Hosono, H., et al., *Physical Disorder and Optical Properties in the Vacuum Ultraviolet Region of Amorphous SiO_2.* Physical Review Letters, 2001. **87**(17): p. 175501.
263. Saito, K. and A.J. Ikushima, *Effects of fluorine on structure, structural relaxation, and absorption edge in silica glass.* Journal of Applied Physics, 2002. **91**(8): p. 4886-4890.
264. Skuja, L., et al., *Urbach absorption edge of silica: reduction of glassy disorder by fluorine doping.* Journal of Non-Crystalline Solids, 2004. **345–346**: p. 328-331.
265. Vella, E., et al., *Irradiation effects on the absorption edge of silica glass.* Journal of Non-Crystalline Solids, 2007. **353**(5–7): p. 559-563.
266. Tamura, T., et al., *First principles analysis of the optical properties of structural disorder in SiO_2 glass.* Physical Review B, 2008. **77**(8): p. 085207.
267. Vella, E., R. Boscaino, and G. Navarra, *Vacuum-ultraviolet absorption of amorphous SiO_2: Intrinsic contribution and role of silanol groups.* Physical Review B, 2008. **77**(16): p. 165203.
268. Cody, G.D., et al., *Disorder and the Optical-Absorption Edge of Hydrogenated Amorphous Silicon.* Physical Review Letters, 1981. **47**(20): p. 1480-1483.

269. Vella, E. and R. Boscaino, *Structural disorder and silanol groups content in amorphous SiO_2.* Physical Review B, 2009. **79**(8): p. 085204.
270. Zhuravlev, L.T., *The surface chemistry of amorphous silica. Zhuravlev model.* Colloids and Surfaces A: Physicochemical and Engineering Aspects, 2000. **173**(1–3): p. 1-38.
271. Kitamura, R., L. Pilon, and M. Jonasz, *Optical constants of silica glass from extreme ultraviolet to far infrared at near room temperature.* Applied Optics, 2007. **46**(33): p. 8118-8133.
272. Coggrave, C.R. and J.M. Huntley, *High-speed surface profilometer based on a spatial light modulator and pipeline image processor.* Optical Engineering, 1999. **38**(9): p. 1573-1581.
273. Huntley, J.M. and C.R. Coggrave, *Optimization of a shape measurement system based on spatial light modulators.* Shape Measurement and Surface Inspection 1999. **3823**(Laser Metrology and Inspection): p. 104-114.
274. Coggrave, C.R. and J.M. Huntley, *Optimization of a shape measurement system based on spatial light modulators.* Optical Engineering, 2000. **39**(1): p. 91-98.
275. Kinell, L. and M. Sjödahl, *Robustness of reduced temporal phase unwrapping in the measurement of shape.* Applied Optics, 2001. **40**(14): p. 2297-2303.
276. Tian, J., X. Peng, and X. Zhao, *A generalized temporal phase unwrapping algorithm for three-dimensional profilometry.* Optics and Lasers in Engineering, 2008. **46**(4): p. 336-342.
277. Huntley, J.M., G.H. Kaufmann, and D. Kerr, *Phase-shifted dynamic speckle pattern interferometry at 1 kHz.* Applied Optics, 1999. **38**(31): p. 6556-6563.
278. Svanbro, A., J.M. Huntley, and A. Davila, *Optimal re-referencing rate for in-plane dynamic speckle interferometry.* Applied Optics, 2003. **42**(2): p. 251-258.
279. Svanbro, A., *In-plane dynamic speckle interferometry: comparison between a combined speckle interferometry/speckle correlation and an update of the reference image.* Applied Optics, 2004. **43**(21): p. 4172-4177.
280. Davila, A., et al., *High-speed dynamic speckle interferometry: phase errors due to intensity, velocity, and speckle decorrelation.* Applied Optics, 2005. **44**(19): p. 3954-3962.
281. Kai, L. and Q. Kemao, *Dynamic phase retrieval in temporal speckle pattern interferometry using least squares method and windowed Fourier filtering.* Optics Express, 2011. **19**(19): p. 18058-18066.
282. Davila, A., et al., *Measurement of sub-surface delaminations in carbon fibre composites using high-speed phase-shifted speckle interferometry and temporal phase unwrapping.* Optics and Lasers in Engineering, 2003. **40**(5–6): p. 447-458.
283. Huntley, J.M., et al. *Detection and sizing of delamination cracks in composite panels using speckle interferometry and genetic algorithms*. 2003.
284. Coggrave, C.R. and J.M. Huntley, *Real-time visualisation of deformation fields using speckle interferometry and temporal phase unwrapping.* Optics and Lasers in Engineering, 2004. **41**(4): p. 601-620.
285. Baldi, A., F. Bertolino, and F. Ginesu, *A temporal phase unwrapping algorithm for photoelastic stress analysis.* Optics and Lasers in Engineering, 2007. **45**(5): p. 612-617.

286. Gelikonov, V.M., et al., *Coherent noise compensation in Spectral-Domain optical coherence tomography.* Optics and Spectroscopy, 2009. **106**(6): p. 895-900.
287. Gelikonov, G.V., et al., *Coherent noise compensation improvement in spectral-domain optical coherence tomography*, in *Proc. SPIE 7554*. 2010: Optical Coherence Tomography and Coherence Domain Optical Methods in Biomedicine XIV, 755431; doi:10.1117/12.841337; http://dx.doi.org/10.1117/12.841337 p. 755431-755431-8.
288. Gelikonov, V.M., I.V. Kasatkina, and P.A. Shilyagin, *Suppression of image artifacts in the spectral-domain optical coherence tomography.* Radiophysics and Quantum Electronics, 2010. **52**(11): p. 810-821.
289. Gelikonov, V.M., et al., *Suppression of image autocorrelation artefacts in spectral domain optical coherence tomography and multiwave digital holography.* Quantum Electronics, 2012. **42**(5): p. 390.
290. Moiseev, A.A., et al., *Digital refocusing in optical coherence tomography*, in *Proc. SPIE 8213*. 2012: Optical Coherence Tomography and Coherence Domain Optical Methods in Biomedicine XVI, 82132C; doi:10.1117/12.911297; http://dx.doi.org/10.1117/12.911297 p. 82132C-82132C-6.
291. Seck, H.L., Y. Zhang, and Y.C. Soh, *Autocorrelation noise removal for optical coherence tomography by sparse filter design.* Journal of Biomedical Optics, 2012. **17**(7): p. 0760291-0760296.
292. Matveev, L.A., et al., *Correlation-stability approach in optical microelastography of tissues*, in *Proc. SPIE 8699*. 2013: Saratov Fall Meeting 2012: Optical Technologies in Biophysics and Medicine XIV; and Laser Physics and Photonics XIV, 869904; doi:10.1117/12.2018377; http://dx.doi.org/10.1117/12.2018377 p. 869904-869904-10.
293. Zaitsev, V.Y., et al., *A correlation-stability approach to elasticity mapping in optical coherence tomography.* Laser Physics Letters, 2013. **10**(6): p. 065601.
294. Zaitsev, V.Y., et al., *Elastographic mapping in optical coherence tomography using an unconventional approach based on correlation stability.* Journal of Biomedical Optics, 2013. **19**(2): p. 021107-021107.
295. Zaitsev, V.Y., et al., *Correlation-stability elastography in OCT: algorithm and in vivo demonstrations*, in *Proc. SPIE 8802*. 2013: Optical Coherence Tomography and Coherence Techniques VI, 880208; doi:10.1117/12.2032631; http://dx.doi.org/10.1117/12.2032631 p. 880208-880208-11.
296. Jaedu, C., G. Gultekin, and K. Chang-Seok, *800-nm-centered swept laser for spectroscopic optical coherence tomography.* Laser Physics, 2014. **24**(4): p. 045605.
297. Moiseev, A.A., et al., *Improvement of lateral resolution of spectral domain optical coherence tomography images in out-of-focus regions with holographic data processing techniques.* Quantum Electronics, 2014. **44**(8): p. 732.
298. Shilyagin, P.A., et al., *Achromatic registration of quadrature components of the optical spectrum in spectral domain optical coherence tomography.* Quantum Electronics, 2014. **44**(7): p. 664.
299. Shilyagin, P.A., et al. *Over-depth artifacts elimination in spectral-domain optical coherence tomography*. in *Proc. SPIE 8934*. 2014. Optical Coherence

Tomography and Coherence Domain Optical Methods in Biomedicine XVIII, 89343H; doi:10.1117/12.2038106; http://dx.doi.org/10.1117/12.2038106
300. Hariharan, P., *Phase shifts on reflection*, in *Basics of Interferometry*. 1992, Academic Press Limited: London. p. 171-172.
301. Azzam, R.M.A., *Phase shifts that accompany total internal reflection at a dielectric–dielectric interface.* Journal of the Optical Society of America A, 2004. **21**(8): p. 1559-1563.
302. Azzam, R.M.A., *Phase shifts in frustrated total internal reflection and optical tunneling by an embedded low-index thin film.* Journal of the Optical Society of America A, 2006. **23**(4): p. 960-965.
303. NewFocus, *Tunable Diode Lasers*, in *Simply Better™ Photonics*. 2016: https://www.newport.com/medias/sys_master/images/images/h3d/h9b/8797219749918/New-Focus-Tunable-Diode-Lasers-Brochure.pdf. p. 1-28.
304. OptiWave. *EDFA — Basic concepts*. 2016 27-11-2016]; Available from: https://optiwave.com/resources/applications-resources/optical-system-edfa-basic-concepts/.
305. 1stVision. *Allied Vision Pike-032 B/C Firewire Camera*. 2016; Available from: https://www.1stvision.com/cameras/AVT/Pike-032-B-C.html.
306. 1stVision. *Allied Vision Manta G-031B/C GigE Camera*. 2016 15-10-2016]; Available from: https://www.1stvision.com/cameras/AVT/Manta-G-031B-C.html.